

**PROCEEDINGS OF THE 7TH PATA DAYS, 2016**

**The 7th International INQUA Workshop on  
Paleoseismology,  
Active Tectonics and  
Archaeoseismology  
30 May-3 June 2016  
Crestone, Colorado USA**

# Proceedings of the 7th International INQUA Workshop on Paleoseismology, Active Tectonics and Archaeoseismology ("PATA Days")

**30 May- 3 June 2016**  
**Crestone, Colorado, USA**

## **Editors**

James P. McCalpin  
Christoph Gruetzner

*This event was organized by* **GEO-HAZ Consulting, Inc.**  
*This event was hosted by the* **Crestone Science Center**  
*This event was supported by:*  
INQUA Focus Group 'Earthquake Geology and Seismic Hazards - EGSHaz'  
Adams State University  
Colorado College  
Colorado School of Mines  
University of Colorado-Boulder



**GEO-HAZ Consulting, Inc.**

- *Engineering Geology*
- *Environmental Geology*
- *Hazards Assessment and Mitigation*



**Crestone Science Center, Inc.**

Education and Research  
in the Earth Sciences



**paleoseismicity.org**

**Published by**

Crestone Science Center  
P.O. Box 837  
600 East Galena Avenue  
Crestone, CO 81131 USA  
www.crestonescience.org

**Edited by**

James P. McCalpin  
GEO-HAZ Consulting, Inc.  
Crestone, CO USA  
&  
Christoph Gruetzner  
Department of Earth Sciences, University of Cambridge  
United Kingdom

ISBN: 978-0-9974355-2-8

Digital edition.

**PROCEEDINGS VOLUMES OF PATA DAYS:**

**Vol. 7:** Proceeding of the 7th International INQUA Meeting on Paleoseismology, Active Tectonics and Archeoseismology (*J.P. McCalpin & C. Gruetzner, eds.*). ISBN 978-0-9974355-2-8, 2016. Published digitally by the Crestone Science Center, Crestone, CO 81131 USA, Guidebook No. 12; 7<sup>th</sup> International INQUA Meeting on Paleoseismology, Active Tectonics and Archeoseismology, Crestone (USA).

**Vol. 6:** Abstracts Volume, 6th International INQUA Meeting on Paleoseismology, Active Tectonics and Archeoseismology (*Blumetti, A.M., Cinti, F.R., De Martini, P.M., Galadini, F., Guerrieri, L., Michetti, A.M., Pantosti, D. and Vittori, E., eds.*), 19-24 April 2015, Pescina, Fucino Basin, Italy: Miscellanea INGV, Anno 2015\_ Numero 27, ISSN 2039-6651, printed in Italy by Istituto Nazionale di Geofisica e Volcanologia, Rome, Italy, 545 p.

**Vol. 5:** Proceeding of the 5th International INQUA Meeting on Paleoseismology, Active Tectonics and Archeoseismology (*C. Grutzner, J.-H. Choi, P. Edwards & Y.-S. Kim, eds.*). ISBN 9791195344109 93450. Printed in Korea, 2014. 5<sup>th</sup> International INQUA Meeting on Paleoseismology, Active Tectonics and Archeoseismology, Busan (Korea).

**Vol. 4:** Seismic Hazard, Critical Facilities and Slow Active Faults (*C. Grutzner, A. Rudersdorf, R. Perez-Lopez & K. Reicherter, eds.*). ISBN 978-3-00-0427-96-1. Printed in Germany, 2013. 4th International INQUA Meeting on Paleoseismology, Active Tectonics and Archeoseismology, Aachen (Germany).

**Vol. 3:** Earthquake Geology and Archeoseismology: Society and Seismic Hazard (*R. Perez-Lopez, P.G. Silva, M.A. Rodriguez Pascua, V.H. Garduno Monroy, G. Suarez & K. Reicherter, eds.*) Printed in Mexico, 2012. 3rd INQUA-IGCP 567 International Workshop on Earthquake Geology, Paleoseismology and Archeoseismology, Morelia (Mexico).

**Vol. 2:** Earthquake Geology and Archeoseismology: Society and Seismic Hazard (*C. Grutzner, R. Perez-Lopez, T. Fernandez-Steeger, I. Papanikolaou, K. Reicherter, P.G. Silva & A. Vott, eds.*) ISBN: 978-960-466-093-3. Printed in Greece, 2011. 2nd INQUA-IGCP 567 International Workshop, Corinth (Greece).

**Vol. 1:** Archaeoseismology and Paleoseismology in the Alpine-Himalayan Collisional Zone (*R. Perez-Lopez, C. Grutzner, J. Lario, K. Reicherter & P.G. Silva, eds.*) ISBN: 978-84-7484-217-3. Printed in Spain, 2009. 1st INQUA-IGCP 567 International Workshop, Baelo Claudia, Cadiz (Spain).

## Preface [I]

Dear friends and colleagues,

Seven years ago, a hundred geoscientists assembled in sunny southern Spain for what can be seen as the birth of the PATA Days conference series. Klaus Reicherter who initiated and actively supported these meetings decided that we need more time for discussions and interaction both in conference halls and in the field. The huge AGU and EGU type of meetings leave no time or space for both. Therefore these regular topical workshops have been set up, providing enough time for discussions, fieldtrips, socialising and student focused summer schools. The high attendance and the planned future meetings testify for their success.

In 2009, after having studied the active faults of the Strait of Gibraltar, the tsunami deposits along the beautiful coast, and the earthquake damage at the ruins of Baelo Claudia, the meeting moved to Corinth, Greece, in 2011. This place is probably the best laboratory on Earth to study fast continental extension and it is also the birthplace of archaeoseismology. In 2012 the PATA Days were held in Morelia, Mexico, commemorating the centenary of the November 19, 1912 Acambay Earthquake (M~7). Active faulting in the Acambay Graben and the seismic hazard in Mexico were brought to the attention of the paleoseismology community. The extremely slowly deforming region of Western Germany was the topic of the 2013 meeting in Aachen. Although the ongoing extension in the Lower Rhine Graben is so low that it cannot even be measured with geodesy in the time span that is covered by modern techniques, strong earthquakes happened here in the past and left their traces in the sedimentological and archaeological record. The 2014 PATA Days led us to Busan, South Korea, and we focussed much on the issue of slow faults and hazard to critical facilities like nuclear power plants. Plus, we enjoyed the excellent South Korean food and landscape. In 1915, the strongest earthquake on record in Italy reduced the Fucino area to rubble. We visited the Fucino plain one hundred years later in 2015 to learn about the state of the art of paleoseismology in Italy and to visit L'Aquila, the city that was so badly stricken by a strong earthquake in 2009 and which made it to international news with the convict of seismologists.

Now, in 2016, we are very happy to have the PATA Days in the United States for the first time. Here is the cradle of paleoseismology, here are some of the most spectacular and best-studied surface ruptures in the world, and here in Crestone, CO, is where Jim McCalpin wrote his 'bible' of paleoseismology. Here is earthquake country. We are happy that Jim is the lead organiser of this meeting.

The last decades have brought us an immense new toolbox of geoscience methods. With permanent GPS and latest DInSAR technology we are now able to observe the deformation of the crust almost in real-time and to detect phenomena that we weren't even aware of a few years ago. Dense seismic networks, broadband stations, and strong motion instruments allow us to examine the anatomy of large earthquakes in many parts of the world. Stereo satellite imagery, LiDAR, and photogrammetry help us to create the most precise digital elevation models which are used to trace the surface expression of active faulting. Cosmogenic isotope dating and other advanced dating techniques offer unprecedented temporal resolution. Turbidity paleoseismology and interdisciplinary tsunami studies gave us invaluable insights into coastal hazards. But it is not only the methodology that improved, it is also the increasing co-operation with scientists from neighbouring or even more distant disciplines that helped to advance the study of paleoseismology, active tectonics, earthquake geology, and archaeoseismology.

Fostering co-operation among scientists and supporting early career researchers (ECRs) is the main aim of our new INQUA Focus Group 'Earthquake Geology and Seismic Hazards - EGSHaz'. With the INQUA congress in Nagoya in 2015, the old structure ceased to exist and something new was born. Active tectonic studies were hitherto supported by our former focus group PALACTE (Paleoseismology and Active Tectonics) within the TERPRO Commission (Terrestrial Processes) of INQUA. The PALACTE leaders Pablo Silva, Klaus Reicherter and Luca Guerrieri stepped back after having done a fantastic job during the past years- the current group has now 445 members from 54 countries. They established the EEE catalogue of environmental earthquake effects and supported countless ECRs to participate in our activities. Now the new focus group EGSHaz will support networking and the exchange of ideas during the ongoing intercongress period 2015-2019. We are happy to have the support of the TERPRO (INQUA's Commission on Terrestrial Processes, Deposits and History) president Alessandro M. Michetti who also served as a past leader of the group. The group is now led by Ioannis Papanikolaou, Petra Štěpančíková, and Christoph Grützner, with support from Yael Braun, Beau Whitney, and Jakub Stemberk.

For the upcoming years we have established two main projects that will form the focus of our work: 'SURfaceFaulting Catalogue – Earthquakes (SURFACE)' coordinated by Stéphane Baize and 'Geological Earthquake Mapping of recent, historical and paleoseismic events; Quaternary Geology for Seismic Hazard Analyses (GEMAP)' coordinated by Ioannis Papanikolaou. We are currently establishing a new focus group website, which will contain all information about our ongoing work, collaborators, scientific reports, and meetings: [www.earthquakegeology.org](http://www.earthquakegeology.org). For regular updates, news and announcements follow the blog over at [www.paleoseismicity.org](http://www.paleoseismicity.org) and find us on Twitter and Facebook.

We wish you an exciting and wonderful conference and we thank Jim for the amazing job he has done.

*Ioannis Papanikolaou (leader), Petra Štěpančíková (co-leader), Christoph Grützner (co-leader)*

## **Preface [II]**

The 7th International Workshop on Paleoseismology, Active Tectonics and Archeoseismology (7th PATA Days) is being held in Crestone, Colorado, USA from 30-May through 3-June, 2016. The Workshop was preceded by the 1<sup>st</sup> PATA Road Trip, "*Faults of the Wild West*", a 2000-km, 6-day, limited attendance field trip led by Jim McCalpin to classic faults of the western USA. The "Wild West" theme continues with our 2016 venue of Crestone, a small former gold-mining town on the eastern margin of the Neogene Rio Grande rift zone. Crestone lies on the rift valley floor at 2500 m elevation, nestled at the base of the 4000+-meter mountains of the rift-flank uplift.

This is the first PATA Days meeting in the USA, and the second in North America (after Morelia, Mexico in 2012). However, unlike the Morelia and Fucino (2015) workshops, this one does not celebrate the anniversary of a damaging historic earthquake, for the simple reason that the rift-bounding faults in Colorado have been seismically quiescent throughout historic time (1850-present). The Rift is thus similar to the larger Basin and Range Province, having many late Pleistocene and Holocene fault scarps, but very few surface-rupturing earthquakes in our short 150-year written history. When paleoseismology was beginning in the 1970s in the USA, the conventional wisdom in Colorado and New Mexico was that the rift had developed in the Miocene and Pliocene, and that rift faults were no longer active and posed no seismic risk. Like much of the Western USA outside of California, these large extensional regions had low historic & instrumental seismicity and were shown on national/regional seismic hazard maps as having very low seismic risk. Yet studies in the 1970s began to document recent geologic evidence (fault scarps) for M>7 earthquakes in the Holocene, on the faults that were supposedly inactive! To some of us in graduate school at that time, it seemed that the contribution of paleoseismology was even more critical in these regions, than in the more seismically active areas (such as California) where seismic risk was already accepted as high. This story of rift paleoseismology will unfold on the Pre-Meeting, Intra-Meeting, and Post-Meeting Field Trips.

The 2016 Workshop will include a 4 days with keynote lectures, talks and posters in seven sessions spanning these topics: Earthquake Geology, Paleoseismology, Archeoseismology, Secondary Effects of Earthquakes, Remote Sensing & Geomorphology, and Seismic Hazard Assessment. More than 50 scientific papers from 23 countries will be presented, as well as about 20 posters. And if you do not go to the Poster Sessions, you will not get any coffee.

In addition, 3 field trips are occurring before, during, and after the meeting. The Pre-and Post-Meeting Field Trips provide a convenient way for attendees to travel from Denver to Crestone and return, while learning about the neotectonic development of Colorado.

The meeting is organized by the Crestone Science Center ([www.crestonescience.org](http://www.crestonescience.org)) and GEO-HAZ Consulting, Inc. ([www.geohaz.com](http://www.geohaz.com)) of Crestone. We appreciate the assistance of the INQUA Focus Group 'Earthquake Geology and Seismic Hazards' for their support for young scientists and students. We also acknowledge for the support of The Colorado College ([www.coloradocollege.edu](http://www.coloradocollege.edu)).

On behalf of the Organizing Committee  
James P. McCalpin

We gratefully acknowledge for the help and work of:

**Organizing Committee:**

*James McCalpin (USA)*  
*Rich Koehler (USA)*  
*Kathy Haller (USA)*  
*Ed Nissen (USA)*  
*Alan Nelson (USA)*  
*Christoph Gruetzner (UK)*

**Scientific Committee:**

*James McCalpin (USA),*  
*Rich Koehler (USA)*  
*Tony Crone (USA)*  
*Ramon Arrowsmith (USA)*  
*Eldon Gath (USA)*  
*Rich Briggs (USA)*  
*Christoph Gruetzner (UK)*  
*Young-Seog Kim (KOR)*  
*Rob Langridge (NZ)*  
*Luca Guerreri (ITAL)*  
*Yael Braun (ISR)*  
*Beau Whitney (AUS)*

**Keynote Speakers:**

*Vince Matthews (USA)*  
*Takashi Azuma (JPN)*  
*Ruben Tatevossian (RUS)*

**Invited Speakers:**

*Vince Matthews (USA)*  
*Tom Rockwell (USA),*  
*Takashi Azuma (JPN)*

# Program

***Before the Conference (limited attendance)***

**The 1<sup>st</sup> PATA Road Trip; “Faults of the Wild West”**

**24-29 May 2016; led by James McCalpin**

**29 May (SUNDAY)**

**Arrival in Denver, Colorado and Icebreaker Party**

Attendees arrive in Denver throughout the day

19:00 Icebreaker Party at the Sporting News Grill, in the Holiday Inn Airport hotel, Tower Road; this is SW and across the street from the Best Western Plus-DIA hotel

**30 May (MONDAY, morning)**

**Pre-Meeting Field Trip (8 am-1 pm)**

6:30 - 8:00 Breakfast; check out of hotel, transfer luggage to the bus

8:00- board bus at Best Western Plus-DIA hotel, 7020 Tower Road, Denver; depart Denver Airport hotels

8:00-13:00- field trip bus travels on highways I-70W, C-470, US 285, and CO 17 to Moffat, CO, then CR “T” to Crestone

13:00- arrive at the Desert Sage Restaurant

**30 May (MONDAY, afternoon)**

**Opening Ceremony, Keynote Lectures, Poster Session 1, Dinner at Desert Sage**

13:00-14:00 Lunch

14:00 - 15:00 Check -In

15:00 Opening ceremony:

15:00-15:10 - Organization of the workshop: James McCalpin

15:10-15:20 - INQUA TERPRO in the Inter-Congress Period 2015-2019; Advisory Board Member  
Takashi Azuma

15:20-15:30 - INQUA Focus Group ‘Earthquake Geology and Seismic Hazards - EGSHaz’;  
Christoph Gruetzner

15:30-15:40 -INQUA ‘SURFACE’ Project: Stephane Baize

15:40 – 16:50 Key notes, Poster Session 1, talks & wine

30 May Monday afternoon	Session 1: Keynotes	Chaired by: Robert Kirkham
(1) 15:40-16:00	Vincent MATTHEWS	Neogene Tectonism in Colorado
(2) 16:00-16:20	Koji OKUMURA	The Kumamoto, JAPAN earthquakes of April 2016
(3) 16:20-16:40	Ruben TATEVOSSIAN	Scarps associated with non-tectonic activity
(4) 16:40-17:00	James MCCALPIN	Paleoseismology of the Sangre de Cristo fault

17:00 – 17:30; set up Posters

17:30-20:00 Poster Session 1 (2.5 hours)

20:00 Dinner at the Desert Sage Restaurant; drinks afterward

## 31 May (TUESDAY) - Technical Talks, Keynote Lectures, Poster Sessions 2 and 3, Dinner at Old Crestone Schoolhouse

7:00 - 8:30 Breakfast

9:00 - 11:00 Key note lectures and talks

31 May Tuesday morning	Session 2: Paleoseismology- Strike Slip Faults	Chaired by: Young-Seog KIM
(5) 9:00-9:15	Sean BEMIS	The Elizabeth Lake paleoseismic site: Rupture pattern constraints for the past ~800 years for the Mojave section of the south-central San Andreas Fault
(6) 9:15-9:30	Kate SCHARER	Testing geomorphology-derived rupture histories against the paleoseismic record of the southern San Andreas Fault
(7) 9:30-9:45	Glenn BIASI	Does paleoseismology forecast the historic rates of large earthquakes on the San Andreas Fault system?
(8) 9:45-10:00	Tom ROCKWELL	Is the Southern San Andreas Fault Really Overdue For a Large Earthquake or Just Late in the Cycle?
(9) 10:00-10:20	Takashi AZUMA KEYNOTE	Paleoseismological surveys and studies of active faults in Japan

10:20-11:00 break (40 minutes)

11:00- 12:30 key note lectures, talks

31 May Tuesday morning	Session 2: Paleoseismology- Strike Slip Faults	Chaired by: Young-Seog KIM
(10) 11:00-11:15	Eldon GATH	Tectonic geomorphic and paleoseismic investigation of the Gatún fault in central PANAMA
(11) 11:15-11:30	Stephane BAIZE	Earthquake fault segmentation in the Central Andes, ECUADOR
(12) 11:30-11:45	Laurence AUDIN	Neotectonic activity in Ecuador and Peru, from geomorphic to geodetic data, focus around Andean megapoles
(13) 11:45-12:00	Sung-Il CHO	Geological evolution of Quaternary fault at Dangu-ri, Gyeong-ju area, SE Korea
(14) 12:00-12:15	Jinhyun LEE	Seismic activity in SE Korea based on a trench survey(Dangu fault) and historical earthquake data around the Yangsan fault

12:15- 13:00 Posters (45 minutes)

13:00 - 14:00 Lunch

14:00 - 15:00 poster session (1 hour)

31 May Tuesday afternoon	Session 3: Paleoseismology- Reverse Faults and Stable Continental Interiors	Chaired by: Tina NIEMI
(15) 15:00-15:20 KEYNOTE	Christoph GRUETZNER	Paleoseismological challenges in Central Asia
(16) 15:20-15:35	<i>Paula</i> <i>FIGUEIREDO</i>	Late Pleistocene deformation at Aljezur fault system, SW Portugal: Seismicity triggering within a slow tectonic rate setting and relationships with sea-level rise (speaker- Tom Rockwell)
(17) 15:35-15:50	Colby SMITH	Holocene paleo-seismicity of the Bollnäs fault derived from terrestrial and hydroacoustical records

(18) 15:50-- 16:05	Gabriel VARGAS- EASTON	The San Ramon thrust fault at the eastern border of Santiago city, Chile: Paleoseismological implications from the linkage between piedmont units and fluvial terraces
(19) 16:05- 16:20	Yukari MIYASHITA	Paleoseismic investigation of the Yunodake fault, Fukushima Prefecture, Japan
(20) 16:20- 16:35	Reed BURGETTE	Late Quaternary Offset of Alluvial Fan Surfaces along the Central Sierra Madre Fault, Southern California

16:35 - 17:15 break (40 minutes)

17:15 - 18:30 talks

30 May Tuesday evening	Session 3: Paleoseismology- Reverse Faults and Stable Continental Interiors	Chaired by: Tina NIEMI
(21) 17:15- 17:30	R. SUTINEN	Postglacial faults and paleolandslides in western Finnish Lapland
(22) 17:30- 17:45	Sarah BOULTON	When did the Moroccan High Atlas Mountains get high? Constraints on neo- and active tectonics from fluvial geomorphology and palaealtimetry
(23) 17:45- 18:00	C. Goswami INDIA	On Linkage between Present Geomorphology and Substrate Geology in a Tectonically Active Terrain along the North Eastern Himalayan Foothills
(24) 18:00- 18:15	Javed MALIK	Surface rupture of a Great Himalayan 1905 Kangra earthquake (Mw7.8), NW Himalaya, India
(25) 18:15- 18:30	Biju JOHN	Issues pertaining to active fault identification in cratonic regions: example from Peninsular India

18:30-20:00 free time and posters (1.5 hours)

20:00 evening dinner at the Old Crestone Schoolhouse , 240 North Cottonwood Street (NE corner of Cottonwood Street and Carbonate Avenue); **(but sorry, no alcohol)**; after dinner, attendees can walk 2 blocks south to the Crestone Brewery, 187 West Silver Avenue)

# 1 June (WEDNESDAY) - Technical Talks, Intra-Meeting Field Trip, Dinner at McAlpine Ranch

7:00 - 8:30 Breakfast

9:00 - 11:00 talks

1 June Wednesday morning	Session 4: Paleoseismology- Normal Faults	Chaired by: Klaus REICHERTER
(26) 9:00-9:15	Martha GOMEZ	Paleoearthquake history and extension rates of the Waihi and Poutu faults in the Tongariro Volcanic Centre, New Zealand
(27) 9:15-9:30	Gabriel GONZALEZ	Quaternary deformation in the Atacama Fault System in northern Chile: new discoveries from trenching and OSL dating of colluvial wedges
(28) 9:30-9:45	Lorenzo LO SARDO	Paleoseismological techniques applied to different surface rupturing morpho-tectonic processes: case studies from tectonically active areas of the Abruzzi Region, central Apennines, Italy
(29) 9:45--10:00	Dean OSTENAA	Updates to the Seismic Hazard Characterization of the Cheraw Fault, Southeast Colorado
(30) 10:00-10:15	Rich KOEHLER	Reconnaissance geologic observations along the Petersen Mountain fault zone northwest of Reno, Nevada, U.S.A.
(31) 10:15-10:30	Stefano PUCCI	Structural complexity and Quaternary evolution of the 2009 L'Aquila earthquake causative fault system (Abruzzi Apennines, Italy): a three-dimensional image supported by deep ERT, ground TDEM and seismic noise surveys

10:30 - 11:15 break (45 minutes)

11:15-- 13:00 talks

1 June Wednesday morning	Session 5: Paleoseismology- Subduction Zones and Coasts	Chaired by: Yoshi KINUGASA
(32) 11:15-11:30	Sascha SCHNEIDERWIND	The Geometry of Tidal Notches – What do they reveal about historic coastal tectonics?
(33) 11:30-11:45	Jose GONZALEZ-ALFARO	Accelerated upper crustal uplift since MIS3 at the southern edge of the northern Chile megathrust seismic gap
(34) 11:45-12:00	Angelo VILLALOBOS	New evidences of the cortical origin of the seismic crisis of 2007 in the Aysén Region, Southern Chile
(35) 12:00-12:15	Beth ARCOS	Interaction of tsunamis with inland sediment sources: implications for interpreting deposits
(36) 12:15-12:30	Beau WHITNEY	Seismic source characterization in the Western Australia Shear Zone using 2D seismic data: the Dampier fault.
(37) 12:30-12:45	Daniel GARCES	Geomorphologic and Stratigraphic relationships as indicators of Quaternary climate change and Tsunami Hazard, central coast of Ecuador
(38) 12:45-13:00	Daniel GARCES	Geological effects of the 16-April-2016 Pedernales earthquake (M7.8), Ecuador

13:00 - 14:00 Lunch

14:00 - 18:30 Intra-Meeting Field Trip

20:00 Western BBQ dinner at the McAlpine Ranch, 600 East Galena Avenue, Crestone; (719) 256-5227; (719) 588-4279

## 2 June (THURSDAY) - Technical Talks, Student Training Sessions, Dinner at Desert Sage

7:00 - 8:30 Breakfast

9:00 - 11:00 Key note lectures and talks

2 June Thursday morning	Session 6: Seismites & Neotectonics	Chaired by: Tom VAN LOON
(39) 9:00-9:20 KEYNOTE	Victor GARDUNO- MONROY	Coseismical stratigraphy; A concept useful in the study of active tectonics in Mexico
(40) 9:20-9:35	Greg BROOKS	Paleoseismic assessment of multi-MTD event horizons preserved within the deposits of glacial Lake Ojibway, near Rouyn-Noranda, northwestern Quebec, Canada
(41) 9:35-9:50	Gosia PISARSKA- JAMROZY	Earthquake-induced versus periglacially-induced load structures in clastic sediments
(42) 9:50- 10:05	Oxana LUNINA	Clastic dikes induced by strong earthquakes in southern Siberia and their paleoseismic significance
(43) 10:05- 10:20	Petra JAMSEK RUPNIK	Fault characterization field campaign related to probabilistic seismic hazard assessment for nuclear infrastructure in the Krško Basin, Slovenia
(44) 10:20- 10:35	Jakub STEMBERK	Valley evolution of the Biala Łądecka drainage network during late Cenozoic, Lower Silesia, Poland

10:35- 11:15 break [40 minutes]

11:15- 13:00 talks

2 June Thursday morning	Session 7: Seismic Hazard, Remote Sensing, Geophysics	Chaired by: Gerry STIREWALT
(45) 11:15- 11:30	Edward CUSHING	Close to the lair of Odysseus Cyclops : the SINAPS@ postseismic campaign and accelerometric network installation on Kefalonia island – Site effect characterization experiment
(46) 11:30- 11:45	Jure ATANCKOV	Database of active faults in Slovenia
(47) 11:45- 12:00	M. Logan CLINE	Tectonic geomorphology supporting a probabilistic seismic hazard analysis in the Krško Basin, Slovenia: implications for critical infrastructure
(48) 12:00- 12:15	Rob LANGRIDGE	Assembling lidar swaths along the distributed South Island plate boundary, NZ: The South Island 'b4' project
(49) 12:15- 12:30	Thomas LEGE	Integrated InSAR Based Copernicus Ground Motion Service for Germany - Paleoseismic aspects
(50) 12:30- 12:45	Rob LANGRIDGE	Preview of 2017 PATA Days—New Zealand

13:00 - 14:00 Lunch

14:00 - 18:30 Student Training Sessions; ~1 hours in Baca Campus auditorium, remainder in field sites north of Crestone (bus trip)

14:00 - 18:30 Free time for attendees not at Training Session. Possible activities include:

0-INQUA Business Meeting

1-all afternoon bus trip to Great Sand Dunes National Park; play in Medano Creek, unique surging stream; hike the high dune (600 ft high); look at Holo fault scarps and range-front landslide formed by backsliding on a valleyward-dipping old thrust fault

2- in Crestone; 2-3 hour hike to the crest of terminal moraine complex of Willow Creek; drop down into old lake bed, now a meadow; lakebed was cored in 1979 with C14 dates on postglacial sequence of mud vs peat beds

3-in Crestone; Western horseback trail ride at the Baca Grande Stables

4-on-your-own nudist experience at Valley View Hot Springs

5-stop at Recreational Marijuana store in Moffat, 12 mi W of Crestone

20:00 dinner at the Desert Sage

## Poster Sessions (Monday, May 30, 5:30-8:00 pm; Tuesday, May 31, 2:00-3:00 pm; 6:30-8:00 pm)

No.	Author	Title
1	Robyn DANIELS	Developing a paleoseismic age model for large-magnitude earthquakes on fault segments of the Himalayan Frontal Thrust in India
2	James DUNAHUE	Paleoliquefaction and possible surface deformation along New Madrid Seismic Zone in Yarbrow, Arkansas
3	Francisco GOMEZ	Re-evaluation of late Quaternary deformation in the northern Wind River Basin, Wyoming
4	Chandreyee GOSWAMI	Manabhum Anticline: An apparent key to the genesis of the Eastern Himalayan Syntaxial Zone
5	Brian GRAY	Seamless Photomosaic Trench Logging Using Trench-Based Photogrammetry Methods: Workflow and Case-Studies
6	Christoph GRUETZNER	Large strike-slip faults in a convergent continental setting - the Dzhungarian Fault in the Northern Tien Shan
7	Keene KARLSSON	Paleoseismicity of the Laguna Salada fault, northern Baja California
8	Oksana LUNINA	Style of deformations in the Mondy active fault zone investigated with ground-penetrating radar and structural observations (southern East Siberia)
9	Genaro MARTINEZ	Investigation of uplifted marine and fluvial terraces in the Santa Rosalía basin of central Baja California, México
10	Alan NELSON	AMS 14C tests of correlations of great earthquakes along the Cascadia Subduction Zone, coastal Oregon
11	Christine REGALLA	Evidence for late Quaternary surface rupture along the Leech River fault near Victoria, British Columbia, Canada
12	Sascha SCHNEIDERWIND	Numerical modelling of tidal notch sequences on rocky coasts
13	Thomas SPIES	Establishment of an up-to-date database for seismic hazard assessment in Germany and Central Europe using paleoseismic, neotectonic and historical evidence
14	Petra STEPANCIKOVA	Applicability of complex geophysical surveying in paleoseismic studies: three case studies from Bohemian Massif
15	Jessica THOMAS	Towards an active fault assessment in the southern Upper Rhine Graben
16	Neta WECHSLER	On the accuracy of topographic models derived from UAV photography
17	Alana WILLIAMS	Shorter and variable recurrence intervals along the Cholame segment of the San Andreas Fault
18	Asmita MOHANTY	Tectonic geomorphology of Late Pleistocene-Holocene landscape evolution and drainage migration, NW Himalaya, India
19	Shao YANXIU	Fault slip behavior of North Danghe Nanshan Thrust (NDNT) from high resolution topography data and paleoearthquakes

### **3 June (FRIDAY) - Post-Meeting Field Trip (8 am-6 pm)**

7:00 - 8:00 Breakfast; drop off room keys at Desert Sage Restaurant

8:00- board buses for field trip and depart Crestone

8:00-18:00- field trip travels north from Crestone to the Upper Arkansas Valley of the Rio Grande Rift; includes multiple (~10) field stops

18:00 to 19:00- bus arrives at Best Western Plus-DIA hotel, 7020 Tower Road, Denver; **END OF 7<sup>th</sup> PATA DAYS!!**

### **4 June (SATURDAY) – attendees return home**

6:30 - 8:00? Breakfast; check out of hotels

Attendees take airport shuttle buses or taxis to Denver International Airport for departure home

**ON THE FOLLOWING PAGES ARE THE 4-  
Page Extended Abstracts, ARRANGED  
ALPHABETICALLY BY LAST NAME OF  
THE AUTHOR**



## Interaction of tsunamis with inland sediment sources: implications for interpreting deposits

Arcos, Maria (1), Kruawun Jankaew (2), Joanne Bourgeois (3), SeanPaul LaSelle (4), Bruce Jaffe (4)

- (1) Amec Foster Wheeler, 180 Grand Avenue, Suite 1100, Oakland, CA 94612 USA. Email: Beth.arcos@amecfw.com
- (2) Department of Geology, Faculty of Science, Chulalongkorn University, Phayathai Road, Phatumwan, Bangkok, 10330, Thailand.
- (3) Department of Earth and Space Sciences, University of Washington, Seattle, Washington 98195-1310
- (4) U.S. Geological Survey, Pacific Science Center, 400 Natural Bridges Drive, Santa Cruz, CA, 95060, United States

**Abstract:** Tsunami deposits are increasingly being used to interpret various characteristics of tsunami wave flow including inundation and velocity. The simple model of tsunami deposition involves the erosion of sediment near the coast and then deposition from suspension as the water flows inland. Locations where tsunamis entrain new sediment a kilometer or more inland can aid in interpreting the development of the tsunami flow as it travels inland. Here we examine a modern record of the 2004 Indian Ocean tsunami in Thailand and paleotsunami deposits in the Puget Lowland to the extent of influence of inland sediment sources on deposit thickness and grain size distribution. As hypothesized, these deposits indicate the slowing of the tsunami flow as it extends inland. Tsunami deposits with inland sediment sources can help refine how tsunamis evolve as they flow inland.

**Key words:** Paleotsunami, liquefaction, flow speed, Thailand, Washington.

### Introduction

The next frontier of tsunami deposit research is to use paleodeposits to determine characteristics of the tsunami flow and perhaps, tsunami source. Various avenues have been pursued including analyzing grain-size (from sand to boulders) to determine the flow necessary to both

erode and transport the sediments and the use of sedimentary structures such as upward fining to distinguish tsunamis from other flows. Much of the work done on sandy deposits uses the assumption that sediments are picked up near the coast and transported in suspension until they are deposited. Therefore, many of the conclusions made by these analyses are primarily

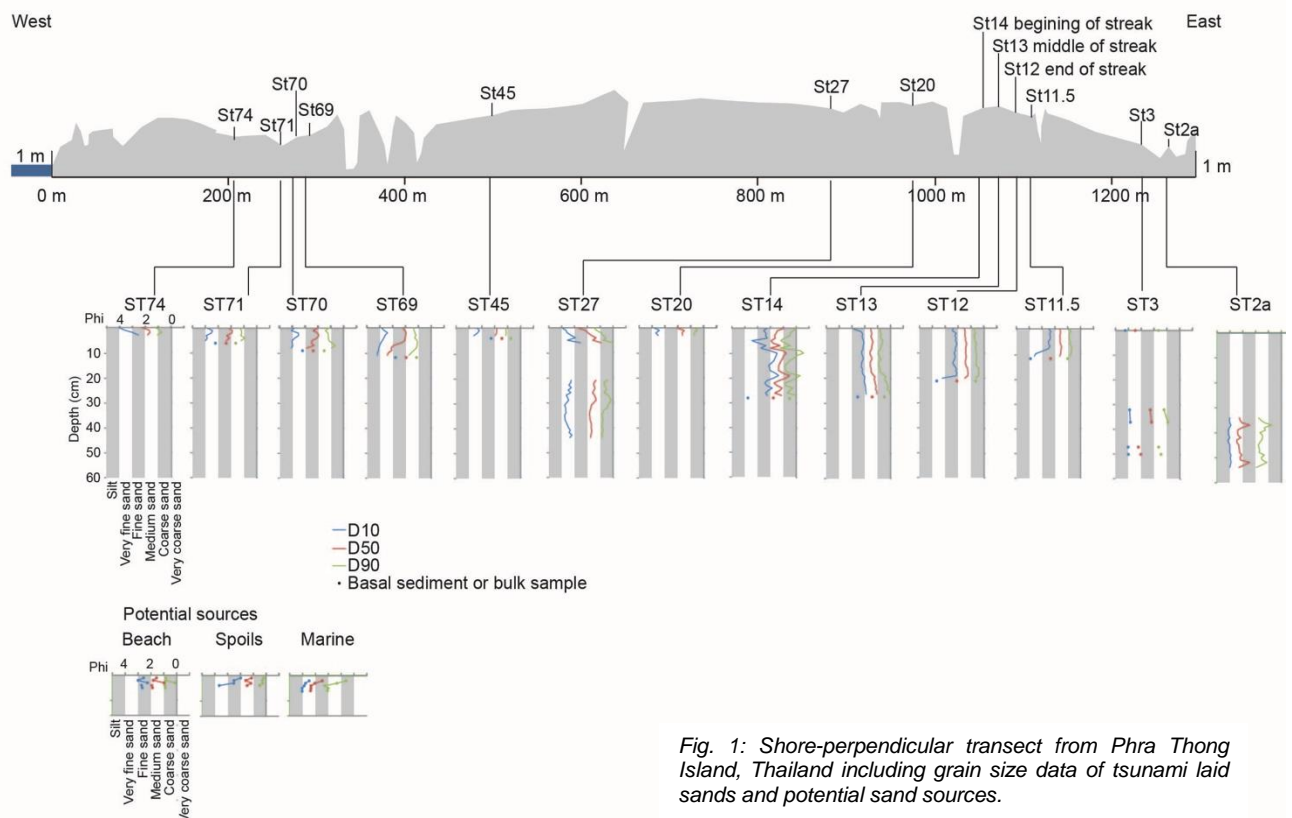


Fig. 1: Shore-perpendicular transect from Phra Thong Island, Thailand including grain size data of tsunami laid sands and potential sand sources.



focused near the shoreline and are less applicable to tsunami flow velocities and depths farther inland.

Taking into account new sources of sediment available for transport far from the coast can help interpret tsunami flows as they evolve. Potential sediment sources could be anthropogenic, in the coastal plain system (e.g. river sediment or dune sand), or related to the earthquake (e.g., liquefaction deposits). This study uses anthropogenic mining spoils. The inland flow characteristics of tsunamis could be used to validate models of tsunami velocities and inform hazard analysis and tsunami mapping for inland sites.

On Phra Thong Island on the Andaman coast of Thailand, the 2004 tsunami reached depths of up to 20 m (Tsuji et al., 2006) and inundated over two kilometers inland across the low elevation (< 3 m) coastal plain. Deposits of both the 2004 and older tsunamis were mapped by Jankaew et al., (2008). Although the island is currently sparsely populated, the mining of tin modified portions of the islands ridge-and-swale geomorphology by excavating swales and leaving spoils piles on the adjacent ridges. The 2004 tsunami remobilized the sand from some of these spoils piles.

The Thailand case study is compared to 1,000 year-old tsunami deposits in the Puget Lowland in Washington State. On the Snohomish delta, sediment, likely extruded as a result of liquefaction, locally thickens tsunami deposits (Martin and Bourgeois, 2011). These deposits serve as a potential case where the characteristics of inland flows from paleotsunami can be estimated. Our methods can be applied to paleotsunami deposits with an inland sediment source. Vented sands related to liquefaction are an ideal test case because liquefaction is commonly associated with local earthquakes, especially in deltas where tsunamis may inundate and the "new" sediment source can be sampled from dikes.

## Discussion

This study of the 2004 tsunami focuses on an almost 1.3 km long, shore perpendicular transect (Fig. 1). The 2004 tsunami eroded the sand from the spoils pile and deposited a wedge-shaped "streak" in the landward direction (Fig. 2). Along the transect we surveyed distance and elevation in addition to thickness of the 2004 tsunami deposit. The tsunami deposits were sampled at 1 cm vertical increments. These samples were bleached in the lab to remove organic material and the grain size was analyzed using a CamSizer.

The focus of this study is the analysis of the sediment from a tin mining spoils pile just over 1 km inland. The redeposited sand from the spoils pile has a clear bimodal grain size distribution that is distinct from the deposits both landward and seaward (St 20 and St 3, respectively).

Seaward of the spoils pile at St 20 the 2004 deposit is 4 cm thick and consists of mostly medium sand (Fig. 1). The streak deposit consists mainly of medium sand as well, but does not fine upward like the seaward deposits and contains coarser sediments than any of the landward deposits we sampled. Bulk samples of uneroded spoils piles are similar to beach sand and coarser than samples taken offshore (Fig. 1).



Fig. 2: 2004 tsunami deposit at St 14 on Phra Thong Island. See Fig. 1 for the location of the excavation along the profile.

Based on the geomorphology of the wedge and structure within the deposit, the sediment making up the streak is interpreted to have been transported as bedload. This is an ideal scenario for interpreting flow speeds because there is a narrow range of shear stresses where bedload transport occurs, relative to grain size, as quantified by the Rouse number (see below). Higher stresses result in the sediment being transported as suspended load; lower stresses do not have enough force to initiate movement.

To determine the flow characteristics we calculated an estimate of the tsunami flow depth at ST 14. The closest post-tsunami survey flow height observation to the site is 7 m near the coast and the inundation was approximately 2.5 km (Fujino et al., 2008). We assumed a uniform slope of the top of the flow from the 7 m at the coast to 0 at the limit of inundation. Factoring in the 2.2 meter elevation of St 14, the water flow depth is estimated to have been approximately 1.75 m at the spoils pile.

The Rouse parameter is a non-dimensional number that distinguishes between bedload, suspended load and wash load transport (Rouse & Howe, 1953). Calculations of the Rouse parameter indicate bedload transport for the coarsest grains in the streak deposit at 1.75 m flow depth. In the calculation of the Rouse parameter, in the calculations, shear velocity, the square root of boundary shear stress divided by the fluid density, was calculated.

To calculate the minimum shear velocity to transport the grains in question, we used a modified Shields diagram (Wiberg and Smith, 2001), which is an experimentally derived plot used to determine the threshold at which grains will begin to move. The shear velocity needed to



initiate motion for D90 of the coarsest unit in St 14 is 8.6 cm/sec.

Using the Law of the Wall an estimate of flow speeds at ST 14 two meters above the bed would be no less than ~180 cm/s for the lower boundary based on Shields criterion and no more than ~280-990 cm/s at the upper bound based on the Rouse bed load limit when not considering flow depth. The shear velocity based on the calculated 1.75 m flow depth at ST14 indicates a flow speed of approximately 60 cm/s based on the Rouse calculations.

An approximately 1,000 year old tsunami sand sheet at the Snohomish delta coincides with a period of several large earthquakes around the Puget Lowland (Bourgeois & Johnson, 2001; Martin and Bourgeois, 2012). In at least two locations where the tsunami deposit is well mapped, the deposit thickens near dikes and in some locations where no dikes were mapped. This is interpreted as vented sands locally augmenting the tsunami deposit. Cases such as this could be used to test the methods outlined above on paleotsunami deposits.

Bracketing flow speeds from paleotsunamis would facilitate assessing tsunami hazard in locations where there has not been a historical tsunami. In addition, estimates of flow speed could aid in determining tsunami inundation in conjunction with numerical modelling in cases where the landward extent of the deposit cannot be traced either due to lack of preservation or human development.

There are several potential limitations to this methodology. Determining the flow depths of paleoevents can be difficult and there are not well established methodologies, especially in flat topography. Fortunately, sediment transport equations become less sensitive to changes in depths greater than one meter (Jaffe and Gelfenbaum, 2007). Bioturbation and other processes can through time can rework sedimentary structures that indicate bedload transport, thus this methodology may only be applicable in well preserved deposits. A second challenge with this methodology is determining that the thickening of the tsunami deposit is due to an additional sediment source and not a factor of deposition such as paleotopography or backwash.

There are two distinct advantages to determining flow speed from bedload transported sediments over the use of suspended load transported sediments as has been more common (e.g., Jaffe and Gelfenbaum, 2007; Moore et al., 2007). First, the equations give both an upper and lower bound to flow speed. The lower bound is the speed necessary to initiate motion and the upper bound is the speed at which the grains would become fully transported as suspended load. Second and related to the above point, the interpretations of flow speed from suspended load transport are limited by the grain size available for transport. For example, if only fine sand is available for the tsunami to entrain, the interpreted flow speeds will be lower than if coarse sand is available.

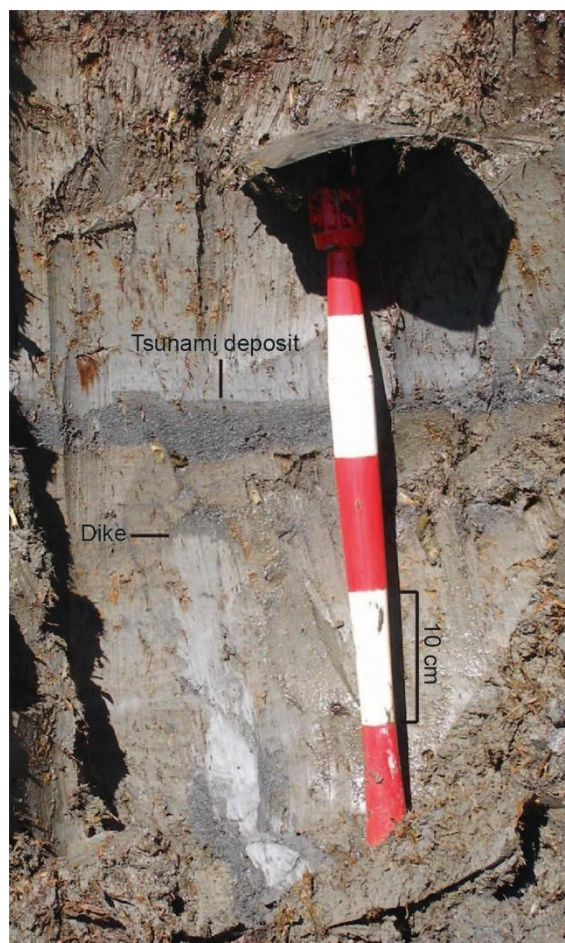


Fig. 3: Paleotsunami deposit locally thickened above a dike filled with sand and mud at the Snohomish delta, Washington State.

**Acknowledgements:** This work was funded in part through a graduate student research grant from the University of Washington. Dr. K. Huntington at the University of Washington allowed the use of the CamSizer.

## References

- Boggs, S. (2001) *Principles of Sedimentology and Stratigraphy*. Third Edition. Prentice Hall, NJ. 726 p.
- Bourgeois, J., & Johnson, S.Y. (2001) Geologic evidence of earthquakes at the Snohomish delta, Washington, in the past 1200 yr. In: *Geological Society of America Bulletin* 113, 482-494.
- Fujino, S., Naruse, H., Suphawajrksakul, A., Jarupongsakul, T., Murayama, M., & Ichihara, T. (2008) Thickness and Grain-Size Distribution of Indian Ocean Tsunami Deposits at Khao Lak and Phra Thong Island, South-Western, Thailand. In: *Tsunamiites—Features and Implications* (eds. Shiki, T., Tsuji, Y., Minoura, T., & Yamakazi, T.) 124-131.
- Jaffe, B.E., Gelfenbaum, G. (2007) A simple model for calculating tsunami flow speed from tsunami deposits. In: *Sedimentary Geology*, doi:10.1016/j.sedgeo.2007.01.013
- Jankaew, K., Atwater, B.F., Sawai, Y., Choowong, M., Charoentitirat, T., Martin, M.E., & Pendergast, A. (2008) Medieval Precursor to the 2004 Tsunami in Thailand. In: *Nature* 455, 1228-1231.



INQUA Focus Group on Paleoseismology and Active Tectonics



paleoseismicity.org

- Martin, M.E. & Bourgeois, J. (2012) Vented sediments and tsunami deposits in the Puget Lowland, Washington – differentiating sedimentary processes. In: *Sedimentology* 59, 419–444.
- Moore, A.L., McAdoo, B.G., Ruffman, A. (2007) Landward fining from multiple sources in a sand sheet deposited by the 1929 Grand Banks tsunami, Newfoundland. In: *Sedimentary Geology* 200, 336-346.
- Rouse, H., & Howe, J.W. (1953) *Basic Mechanics of Fluids*. John Wiley and Sons, New York, 245 p.
- Tsuji, Y. et al. (2006) The 2004 Indian tsunami in Thailand; surveyed runup heights and tide gauge records. In: *Earth Planets Space* 58, 223–232.



## Database of active faults in Slovenia

Jure Atanackov (1), Petra Jamšek Rupnik (1), Jernej Jež (1), Blaž Milanič (1), Matevž Novak (1), Bogomir Celarc (1), Anže Markelj (1), Miloš Bavec (1)

(1) Geological survey of Slovenia, Dimičeva ulica 14, SI-1000 Ljubljana, Slovenia. jure.atanackov@geo-zs.si

**Abstract:** The first database of active and potentially active faults in Slovenia was compiled, as a basis to derive a new national Design ground acceleration map. 89 faults with 217 segments have been seismotectonically parametrized using an adapted and expanded European SHARE database format. Faults were defined, evaluated and parametrized using geologic, geomorphic, geodetic, geodynamic, geophysical and seismological data.

**Key words:** active, faults, map, database, Slovenia

### INTRODUCTION

Slovenia occupies a seismically active region characterized by moderate seismic activity caused by faulting at the contact of the Adriatic microplate and the European plate. Earthquake catalogues span approximately 1000 yrs (Ribarič, 1982; Živčič, 2009; Grünthal and Wahlström, 2012; Stucchi et al., 2013), recording many significant earthquake events. A number of damaging to devastating historical earthquakes have occurred in the area (M 6.8 Idrija 1511, M 6.4 Villach 1348, M 6.1 Ljubljana 1895, M 5.9 Villach 1690, M 5.7 Brežice 1917, M 5.7 Bovec 1998). No historic surface ruptures were recorded, but paleoseismic evidence has been found for surface rupture during the M 6.8 1511 event (Bavec et al., 2013).

The primary goal of the project is to provide a base input to derive a new Design ground acceleration map of Slovenia (Environmental Agency of Slovenia) for regulation of earthquake resistant engineering. Seismological data alone do not sufficiently reflect the earthquake hazard, with the record length shorter than expected recurrence times of major earthquakes (hundreds to thousands of years) on faults with slip rates on the order of several tenths to several mm per year. A map of active faults was developed to provide a geological input on active faulting to assess the earthquake hazard.

### GEOLOGIC SETTING

Faulting in Slovenia and its general vicinity is caused by accommodation of deformation at the contact of the Adriatic microplate and the European plate. Slovenia is located at the contact zone between these two converging plates. Active faults accommodate the relative northward movement and counterclockwise rotation of Adria microplate with rates of shortening at approximately 2-4 mm/yr across the country (approximately 200 km). Maximal horizontal compression is oriented N-S (Weber et al., 2010; Nocquet, 2012).

Active faults form five zones: a) South Alpine thrust zone, b) Istria-Friuli thrust zone, c) Dinaric strike-slip fault zone, d) Periadriatic strike-slip fault zone and e) Zagreb Mid-Hungarian shear zone.

### DATABASE FORMAT AND WORKFLOW

To provide input for the database of active faults we used: 5 m DEM and LiDAR DEM, geologic maps of Slovenia at scales 1 : 100 000 and 1 : 25 000, manuscript geologic maps of various areas at different scales (GeoZS archive), borehole data, geodetic data, including GNSS, GPS and terrestrial networks, deep and shallow geophysical data, seismological data, and paleoseismic data. A large volume of research papers covering the geologic structure and active faulting in Slovenia and the vicinity were analysed and their findings critically evaluated and included in fault trace definition and seismotectonic parametrization. Active faults with surface traces longer than 5 km were included. The workflow is presented in Figure 1.

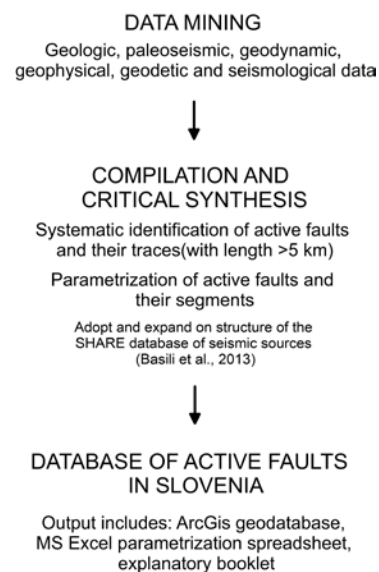


Fig 1. Data processing workflow.

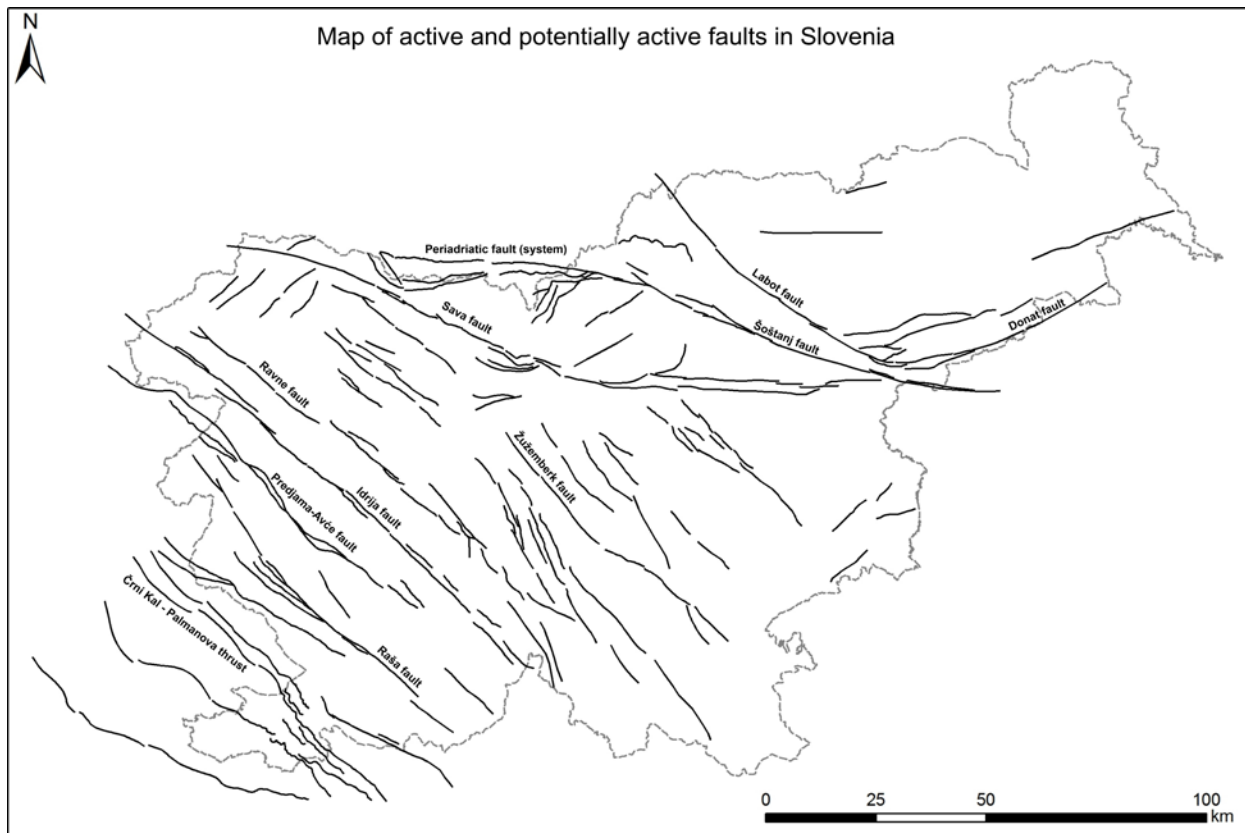


Fig 2. Map of active faults in Slovenia with labeled faults outstanding by their length, slip rate or historic seismicity. Istria-Friuli thrust zone (Črni Kal – Palmanova faults); Dinaric strike-slip fault zone (Predjama-Avče, Raša and Idrija faults); Periadriatic strike-slip fault zone (Sava and Šoštanj faults); and Zagreb Mid-Hungarian shear zone (Donat fault).

The SHARE - Seismic Hazard Harmonization in Europe project database format was used (Basili et al., 2013), with each fault and its individual segments described with: fault name, type, strike (min, max, median), dip (min, max, median), rake (min, max, median), depth, length (along trace and end-to-end), width, area, segmentation type, slip rate (min, max, average) and possible maximum earthquake magnitude (according to empirical relationships by Wells and Coppersmith, 1994). Quality designators were assigned to each parameter (LD – Literature Data, OD – Original Data, ER – Empirical Relationship, EJ – Expert Judgement; Based on, inferred from, assumed from, calculated from + data source and reference).

The database contains four components: an ArcGis geodatabase, an MS Excel parametrization spreadsheet, an MS Excel spreadsheet of XY coordinates of all nodes on each fault segment and an explanatory booklet with the descriptions of all faults in the database. The description includes fault name, fault type, description of the fault trace, including geographic description of individual segments and their type, and a description and discussion on geometric and kinematic parameters, including discussion on relevant published data as well

as original data used in parameter determination.

## RESULTS

The map and database currently contains 89 faults and 217 segments. All have a full set of seismotectonic parameters, as required for further use in determination of seismic hazard. Some interesting statistics can also be gleaned from the database, such as slip rate distribution (global, per fault system) and maximum possible magnitudes.

The longest faults include the 141 km Sava dextral strike-slip fault, the 124 km Idrija dextral strike-slip fault, which was the source of the destructive M 6.8 1511 I<sub>max</sub>=X Idrija earthquake (Bavec et al., 2013), the 90 km Predjama-Avče dextral strike-slip fault, the 89 km Šoštanj dextral strike-slip fault, the 87 km Raša dextral strike-slip fault, the 80 km Črni Kal-Palmanova thrust fault, and the Labot (Lavanttal) dextral-strike slip fault, for which only segments in Slovenia have been parametrized so far (70 km total length), but the fault extends far north into Austria and its parametrization will be finalized shortly.

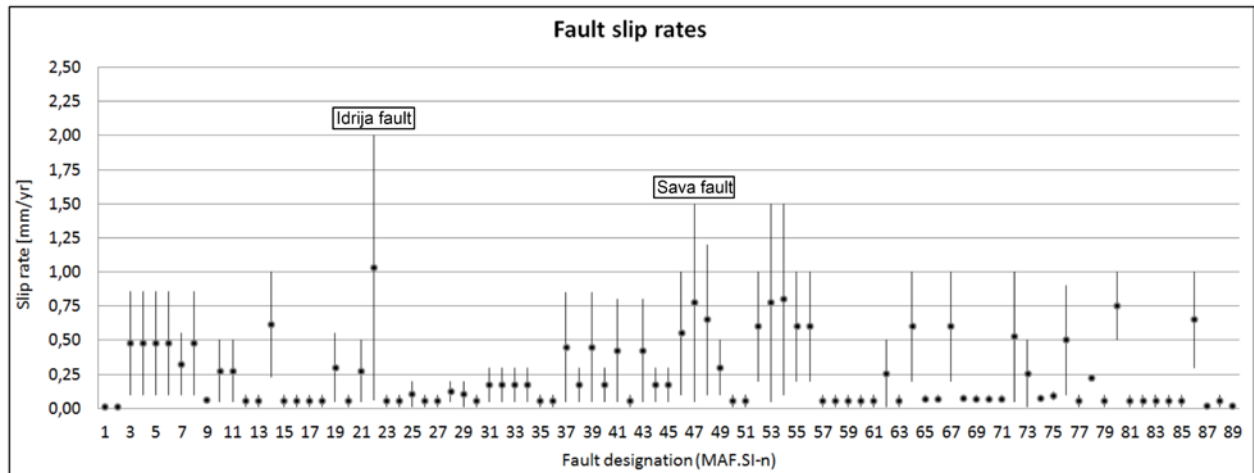


Fig 3. Fault slip rates. Each fault in the database is denoted by its designation MAF.SI-n (MAF – Map of Active Faults). Lines mark the uncertainty in slip rate values.

The highest slip rates are estimated on the Idrija fault 0.06-2.00 mm/yr, the Sava fault 0.05-1.50 mm/yr, the Labot fault 0.50-1.00 mm/yr, the Donat fault 0.30-1.00 mm/yr, the Raša fault 0.23-1.00 mm/yr, the Žužemberk fault 0.10-1.00 mm/yr, the Celje fault 0.05-1.00 mm/yr, and the Črni Kal-Palmanova, Petrinje, Hrastovlje, Kubed thrusts 0.10-0.86 mm/yr. However, average slip rates between 0.01 and 0.25 mm/yr prevail. See Figure 3 for slip rates on all mapped faults.

Among the active faults in the database, only two have major historic seismicity undoubtedly attributed to them: the Idrija fault (M 6.8 1511  $I_{max}=X$ ) and the Ravne fault (M 5.7 1998  $I_{max}=VIII$ ). The Sava fault may potentially be linked with the M 6.4 Villach 1348 (Merchel et al., 2014) and M 5.9 Villach 1690 earthquakes, however, at this time the link to the 1690 is speculative and other faults may well be responsible.

## DISCUSSION

The primary goal of the project to provide a base input to derive a new Design ground acceleration map of Slovenia has been achieved. The map is being used in cooperation with seismologists of the Slovenian Environmental Agency, to define seismogenic sources as the next step towards the Design ground acceleration map.

In two years, active faults on the territory of Slovenia were analyzed. Work continues in 2016 on faults that extend into neighboring countries.

In addition to providing a basis for future assessments of seismic hazard, the database also produced a number of secondary, yet important and highly useful results: a) the basis for detailed mapping of individual faults for future projects, b) additional structural input for engineering applications (such as civil engineering and hydrogeologic mapping), c) identification of a number of

potential paleoseismic trenching sites on several major active faults.

**Acknowledgements:** the Slovenian Environmental Agency financed the projects “Map of Active Faults in Slovenia” and “Elaboration of seismotectonic maps of Slovenia”.

## References

- Bavec, M., Atanackov, J., Celarc, B., Hajdas, I., Jamšek Rupnik, P., Jež, J., Kastelic, V., Milanič, B., Novak, M., Skaberne, D., Žibret, G. 2013. Evidence of Idrija fault seismogenic activity during the Late Holocene including the 1511 Mm 6.8 earthquake. In: Grütznér, C. (ed.) [etc.]. Proceedings of the 4th International INQUA meeting on Paleoseismology, Active Tectonics and Archeoseismology: Seismic Hazard, Critical Facilities and Slow Active Faults, 9-15 October 2013, p. 23-26.
- Grünthal, G., Wahlström, R. 2012. The European-Mediterranean Earthquake Catalogue (EMEC) for the last millennium. *Journal of Seismology* 16, 3: 535-570.
- Merchel, S., Mrak, I., Braucher, R., Benedetti, L., Repe, B., Bourlès, D., Reitner, J. M. 2014. Surface exposure dating of the Veliki vrh rock avalanche in Slovenia associated with the 1348 earthquake. *Quaternary Geochronology* 22: 33-42.
- Nocquet, J. M. 2012. Present-day kinematics of the Mediterranean: A comprehensive overview of GPS results. *Tectonophysics* 579: 220-242.
- Ribarič, V. 1982. Seizmičnost Slovenije. Katalog potresov (792 n.e.–1981). = Seismicity of Slovenia. Catalogue of earthquakes (792 A.D.–1981). Ljubljana, Seizmološki zavod SR Slovenije: 649 p.
- Stucchi, M., Rovida, A., Capera, A. A. G., Alexandre, P., Camelbeeck, T., Demircioglu, M. B., Gasperini, P., Kouskouna, V., Musson, R. M. W., Radulian, M., Sesetyan, K., Vilanova, S., Baumont, D., Bungum, H., Fah, D., Lenhardt, W., Makropoulos, K., Solares, J. M. M., Scotti, O., Zivcic, M., Albini, P., Batlo, J., Papaioannou, C., Tatevossian, R., Locati, M., Meletti, C., Viganò, D., Giardini, D. 2013. The SHARE European



INQUA Focus Group on Paleoseismology and Active Tectonics



[paleoseismicity.org](http://paleoseismicity.org)

Earthquake Catalogue (SHEEC) 1000-1899. *Journal of Seismology* 17: 523-544.

Weber, J., Vrabec, M., Pavlovčič Prešeren, P., Dixon, T., Jiang, Y., Stopar, M. 2010. GPS-derived motion of the Adriatic microplate from Istria Peninsula and Po Plain sites, and geodynamic implications. *Tectonophysics* 483: 214–222.

Wells, D. L., Coppersmith, K. J. 1994. New Empirical Relationships among Magnitude, Rupture Length, Rupture Width, Rupture Area, and Surface Displacement. *Bulletin of the Seismological Society of America* 84, 4: 974-1002.

Živčič, M. 2009. Katalog potresov v Sloveniji. Internal documentation. Ljubljana, Ministry of Agriculture and Environment, Slovenian Environment Agency, Seismology and Geology Office.



## NEOTECTONIC ACTIVITY IN ECUADOR AND PERU, from GEOMORPHIC to GEODETIC data, FOCUS AROUND ANDEAN MEGACITIES

Audin, Laurence (1), Carlos Benavente (2,1), Alexandra Alvarado (3), Swann Zerathe (1), Yepes Hugo (3), Champenois Johann (4), Baize Stéphane (5), Delgado Fabrizio (2), Beauval Céline (1), Robert Xavier (1)

- (1) ISTerre, UGA, France. Email: [laurence.audin@ird.fr](mailto:laurence.audin@ird.fr), [laurence.audin@univ-grenoble-alpes.fr](mailto:laurence.audin@univ-grenoble-alpes.fr)
- (2) INGEMMET, Peru.
- (3) IG QUITO, Ecuador.
- (4) CEA DASE, France.
- (5) IRSN, France.

**Abstract:** *The Andean range stretches for thousands of kilometers from Patagonia to Venezuela and its recent tectonic evolution results from the ongoing subduction of the Nazca plate. Less studied than the subduction mega earthquakes, several  $M > 7$  continental earthquakes did affect the Andean human settlements since the Pre Incaic period. Although neglected in terms of archaeoseismic or neotectonic studies, the impacted regions display exponentially growing megacities, highly exposed to seismic hazards. In this study, we focus on investigating crustal deformation along newly described fault systems, in a seismically active urban setting (in Peru and Ecuador). High resolution satellite images, geodetic data, georadar and field studies provide striking examples and evidences of the ongoing tectonic deformation that can be the longer-term Quaternary geomorphic record. We focus here on the Quito and Ibarra regions in northern Ecuador, and on Arequipa and Cuzco regions in southern Peru.*

**Key words:** *Active tectonics, Geomorphology, Andes, Seismic Hazards.*

### NEOTECTONICS ALONG THE ANDEAN RANGE: STATE OF THE ART and OBJECTIVES

Along the Pacific flank of the high Andes, the recent geodetic measurements do not provide informations on the long term continental deformation rates, due to the strong coupling and the ongoing subduction (Nocquet et al., 2014). Therefore tectonic geomorphology provides a unique and necessary tool to address longer term deformation. Over the past decades the urban population has been increasing in the Andean region. And since the return period of continental earthquakes is much longer than the periods of recent urbanization, further tectonic geomorphology studies in and around megacities are needed. Moreover, the instrumental crustal seismicity is also rather sparse in comparison to megathrust seismicity, so little is known about the active tectonics and fault sources in the continental Andes.

Here, we propose to provide combined data sets to study the ongoing tectonic deformation around an urbanized area in order to constrain the seismic activity rates on prominent crustal faults that could impact the megacities in Peru and Ecuador.

### ACTIVE FAULTING IN ECUADOR

The Quito megacity (in terms of Ecuador's total population) lies at 2800 m elevation within the Interandean Depression (ID), in an active seismic and volcanic province (*Figure 1*) in northern Ecuador. Quito basin and the city itself are located on a structural bench, along the western border of the ID (Soulas et al., 1991). Beneath Quito, the subduction interface is located at a depth of ~120 km, without known influence on superficial tectonics of the upper plate (Yepes et al., 2016).

#### *IS QUITO BLIND THRUST CREEPING?*

The Quito Fault System (QFS) extends over 60 km and appears to be segmented en echelon. Multidisciplinary studies support an interpretation in which two major contemporaneous fault systems affect Quaternary volcanoclastic deposits (*Figure 1*). Hanging paleovalleys and disruption of drainage networks attest to ongoing crustal deformation and uplift in this region, further indicated by 15 years of GPS measurements and seismicity. The resulting new map displays an eastward migrating Quito Fault



System. Northeast of this major tectonic feature, the strike-slip Guayllabamba Fault System (GFS) aids the eastward transfer of the regional strain northeastward to Colombia. A new GPS data set and INSAR studies indicates active shortening rates for Quito blind thrust of up to 4 mm/yr, which decreases northward along the fold system as it connects to the strike-slip Guayllabamba Fault System (*Figure 2*). These two tectonic fault systems are active today, and the local focal mechanisms are consistent with the direction of relative GPS velocities and the regional stress tensors (Alvarado et al., 2014). Moreover, a sharp velocity gradient is observed across the Quito fault system and only a fraction of the fault plane is presently accumulating elastic stress, available for future earthquakes (Champenois et al., 2013, *Figure 2*). Alvarado et al. (2014) proposed that the depth over which elastic stress is presently accumulated is in the range of 3–7 km. We estimated a maximum magnitude range of Mw 5.7 to 7.1 for the GFS and QFS. But the best constrained estimation derives from the geodetic data and corresponds to a maximum value of Mw = 6.6 (Alvarado et al., 2014).

Finally, as for the urban setting, the capital is lying over the hanging wall of the reverse fault system. In case of a large earthquake, ground motions are expected to be much higher in Quito than in the suburbs (Beauval et al., 2015; Yepes et al., 2016). The 1797 Riobamba earthquake (MI 7.6) occurred 160 km south of Quito, but produced an intensity VII in the city. Years later, Quito experienced a similar shaking level during another large earthquake, the 1868 Ibarra event 80km north of Quito (MI 7.2, in Beauval et al., 2010).

#### 1868 IBARRA LOST SCARP?

The 4m-resolution DEM of Ecuador reveals a sharp geomorphic lineament cutting through the western shoulder of the ID near Ibarra city. This scarp is developed within the volcanic formation of Chachimbiro edifice (Andrade et al., 2009). Along the lineament, we document evidences of captures, sag ponds and normal faulting of the volcanic and sedimentary deposits (*Figure 3*). This systematic offset could be due to previous large earthquakes in the area, possibly the M7.2 1868 Ibarra event (Beauval et al., 2010).

#### ACTIVE FAULT SCARPS in PERU

##### FIRST DIRECT DATING OF A FAULT SCARP by <sup>10</sup>Be

Commonly in southern Peru, most of the previous studies have argued that low tectonic activity is recorded along the Andean forearc, and despite recent updating of the active fault map (INGEMMET, Neotec, Benavente and Audin, 2009), no direct quantification of the deformation rates have been proposed. To bring new constrains, we focus on the transpressive Purgatorio fault (*Figure 4*), located between the cities of Moquega and Mirave. The fault is 45 kilometers long and connects to the major and active Incapuquio fault system (Hall et al., 2008). It trends along the Western Cordillera piedmont where it disrupts the rocky and smooth landscape of the Atacama Desert (*Figure 4*). It forms a fresh vertical scarp ~4 m in height coseismic displacements and offers the opportunity to constrain the age of the last events and fault slip rates (Benavente et al., in prep). We performed direct <sup>10</sup>Be surface exposure dating of the fault scarp along a vertical profile. Five samples were collected along a 4 m high profile (*Figure 4*). We systematically selected pebbles cut by the fault movement and marked by tectonic slickensides (Benavente et al., in prep, *Figure 4*). The obtained exposure ages suggest that 4 m of coseismic uplift happened during the last 2 thousands years (*Figure 4*). Based on the assumption that the scarp is coseismic, we can derived a new minimum vertical tectonic motion rate (~2 mm/yr) that is one order of magnitude higher than the previously obtained one from terraces river offsets (0.2 mm/yr, Hall et al., 2012). Our results challenge the accuracy of the recurrent vision defining the Peruvian Andean forearc as a non-deforming block, and raise up the question of the seismic hazard in the nearby cities, potentially exposed to strong shallow earthquakes of depth <10 km and Mw > 7 (Benavente et al., in prep).

#### ARE CUZCO FAULT SEGMENTS ACTIVE?

Unlike the Andean forearc, the tectonic regime in the High Peruvian Andes is mainly extensional and result from the competing convergence and gravity forces (Sébrier et al., 1988; Mercier et al., 1992; Benavente et al., 2013). The Cuzco normal fault system (Cabrera & Sébrier, 1998) limits the Altiplano basin from the Eastern Cordillera. The Cuzco fault and the associated fault system in southern Peru cross Cuzco city and is chosen here as an example to illustrate the needs of multidisciplinary approach for neotectonic studies in this touristic region.

Normal faulting during the historical times (back to 1650) indicate that N-S oriented extension is characteristic of the present-day tectonic regime. Prior to 1986, several Mw 6 shallow earthquakes



affected the Cuzco region (Silgado, 1978) in 1650, 1950 and 1986. In 1650, a massive earthquake hit Cuzco, the Inca capital at the time. For the 1986 event, Cabrera et al., 1998 consider that the rupture at depth is rather shallow (<10 km) after the coseismic scarps and the instrumental low magnitude (Mw 5.3). It is consistent with the longitudinal extension of well-preserved Holocene scarps along other regional active faults, that extend all the way from Cuzco to Puno region along the Altiplano basin.

## CONCLUSIONS

Even if strong seismic events are not unfamiliar to Peru and Ecuador, appropriate earthquake engineering highly depends on the mapping, knowledge and detailed studies of the active fault systems and the related seismic hazard.

The proximity of previously unrecognized active structures to the densely populated Andean cities highlights the need for additional archaeoseismic, palaeoseismic, geomorphic and tectonic studies to characterize seismic sources and develop parameters for input to hazard assessments. Interdisciplinary studies must be pursued to better understand the recurrence and magnitude of crustal earthquakes that may affect the capital cities and megacities in South America.

**Acknowledgements:** This publication was made possible thanks to the Institut de Recherche pour le Développement (IRD), which provided support to UMS 2572 LMC14 (CNRS-CEA-IRD-IRSN-Min. Culture et Comm.) and to the PhD grant of some of the authors. ADN and REMAKE ANR projects and LMI "Séismes et Volcans dans les Andes du Nord". The data for this paper are available by contacting the first author. This contribution is part of an Ecuadorian-French and Peruvian -French cooperation program between the INGEMMET in Peru, Instituto Geofísico, Escuela Politécnica Nacional (IG-EPN), Quito, Ecuador; Institut de Recherche pour le Développement and the UMR ISTerre in France.

## References

Alvarado A., L. Audin, J. M. Nocquet, S. Lagreulet, M. Segovia, Y. Font, G. Lamarque H. Yepes, P. Mothes, F. Rolandone, P. Jarrín, X. Quidelleur (2014) Active tectonics in Quito, Ecuador, assessed by geomorphological studies, GPS data, and crustal seismicity. *Tectonics*. (2014) doi: 10.1002/2012TC003224.

Andrade, D., 2009. The influence of active tectonics on the structural development and flank collapse of Ecuadorian arc volcanoes. PhD Thesis, Université Blaise Pascal, France, p. 239.

Beauval C., H. Yepes, W. Bakun, J. Egred, A. Alvarado and J-C. Singaicho (2010). Locations and magnitudes of historical earthquakes in the Sierra of Ecuador (1587-1996), *Geophys. J. Int.*, DOI: 10.1111/j.1365-246X.2010.04569.x

Beauval C., H. Yepes, A. Alvarado, L. Audin, J.-M. Nocquet, D. Monelli, and L. Danciu. (2014) Probabilistic seismic hazard assessment in Quito, estimates and uncertainties *Seismological Research Letters*, 85:1316-1327.

Benavente, C., Zerathe, S., Audin, L., Robert, X., Delgado, F., Hall, S., Faber, D. ASTER TEAM (*In preparation*). Using 10Be cosmogenic surface exposure dating to determine the evolution of the Purgatorio active fault in the Andean forearc, southern Peru.

Benavente C. & Audin L. (2009) Geometry, Morphology And Seismic Hazard Of The Purgatorio Mirave Fault-Forearc Southern Peru, *Bol. Soc. geol. Perú*, 103: 15.

Benavente, C.; Delgado, F.; Taipe, E.; Audin, L & Pari, W. (2013) - Neotectónica y peligro sísmico en la región Cusco, INGEMMET. Boletín, Serie C: Geología Ambiental y Riesgo Geológico, 55, 245p.

Cabrera J. & Sébrier M. (1998) - Surface rupture associated with a 5.3 mb earthquake: the 5 April 1986 Cuzco earthquake and kinematics of the Chincheros-Qoricocha faults of the High Andes, Peru. *Bull. Seism. Soc. Am.*, 88, 242-255.

Champanois J., L. Audin, S. Baize, JM Nocquet, A. Alvarado (2013), Interseismic deformations along Ecuador active fault systems: Contribution of space-borne SAR Interferometry. AGU Cancun Meeting of the Americas T22A-01. 2013, Mexico.

2008 Hall S.R., Farber, D.L., **Audin L.**, Finkel, R.C., Mériaux, A.S.; Geochronology Of Pediment Surfaces In Southern Peru: Implications For Quaternary Deformation Of The Andean Forearc, *Tectonophysics*, doi: 10.1016/J.Tecto.2007.11.073; 459 (2008) 186-205.

Hall S., Farber, D.L., Audin L. and Finkel, R.C.; Recently active contractile deformation in the forearc of southern Peru *Earth and Planetary Science Letters* 337-338 (2012) 85-92.

Mercier, J.L.; Sébrier, M.; Lavenu, A.; Cabrera J.; Bellier, O.; Dumont, J.F. & Macharé, J. (1992) - Changes in the tectonic regime above a subduction zone of Andean type—The Andes of Peru and Bolivia during the Pliocene-Pleistocene: *Journal of Geophysical Research*, v. 97, no. B8, p. 11,945-11,982.

Sébrier, M.; Lavenu, A.; Fornari, M. & Soulas, J.P. (1988) - Tectonic and uplift in Central Andes (Perú, Bolivia and northern Chile) from Eocene to present. *Géodynamique*, 3(1-2): 85-106.

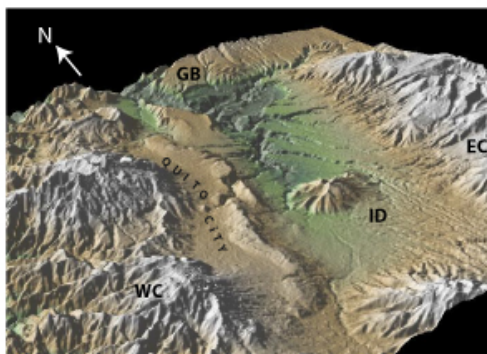
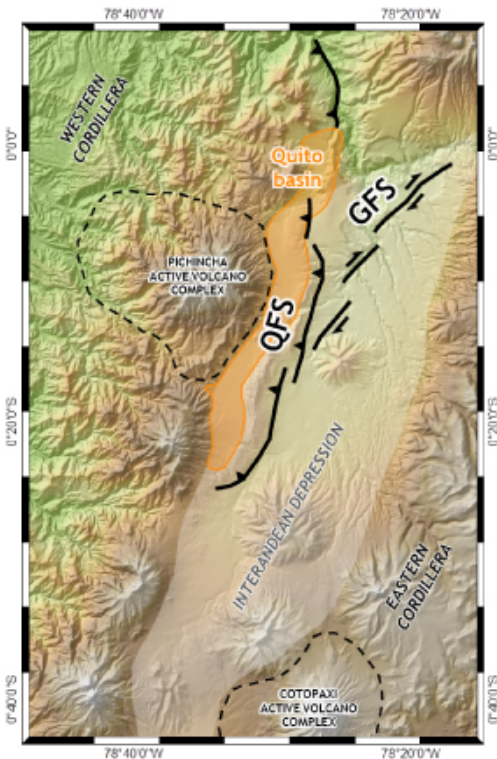


Silgado, E. (1978). Historia de los sismos más notables ocurridos en Perú, 1513-1974. Inst. Geol. Minero de Perú, 131 pp.

Yepes H., L. Audin, A. Alvarado, C. Beauval, J. Aguilar, Y. Font, F. Cotton (2016), A new view for the geodynamics of Ecuador: implication in seismogenic sources definition and seismic hazard assessment. 35. Tectonics.

**Figures**

Figure 1: A/ Quito region, topography and fault systems, B/ 3D topography.



ID Interandean Depression      WC Western Cordillera  
 GB Guayllabamba Basin &      EC Eastern Cordillera  
 GFS Guayllabamba Fault System      QFS Quito Fault System

Figure 2: Quito region, 1993-2000 PS InSAR versus GPS deformation across the Quito Fault System after Champenois et al., 2013.

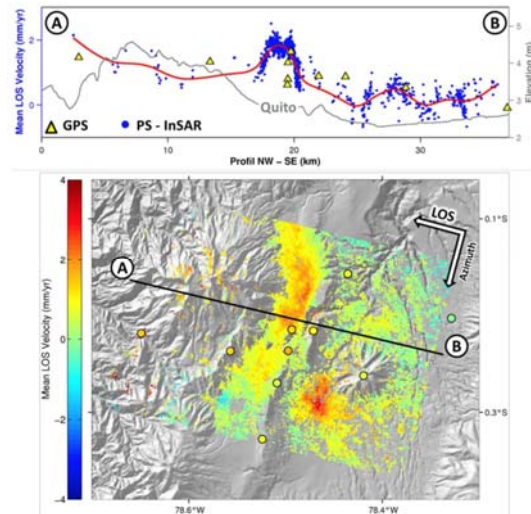


Figure 3: Ibarra region and a Google Earth photo of a potential scarp associated to the seismic source of historic 1868 Mw 7 earthquake.



Figure 4: Southern Peru region and the active fault systems (Benavente et al., in prep)



## Paleoseismological nature and character of active faults in Japan -Analysis of parameters in the Active Fault Database of AIST-

Takashi Azuma (1)

(1) Research Institute of Earthquake and Volcano Geology, Geological Survey of Japan/AIST, Site Central 7, 1-1-1 Higashi, Tsukuba, Ibaraki, 305-8567 JAPAN . Email: t-azuma@aist.go.jp

**Abstract:** After the 1995 Kobe Earthquake, Geological Survey of Japan/AIST constructed the Active Fault Database of Japan. It includes active fault parameters obtained from surveys by local governments, universities as well as our institute. This database contains fault parameters (location, length, angle of fault plane, slip per event, age of the last faulting event, recurrence interval, and slip rate) for 583 segments. By analysis of these data, we can consider the nature and characters of active faults in Japan.

**Key words:** active fault, fault parameters, database, Japan.

### 1. INTRODUCTION

After the 1995 Kobe Earthquake, the Japanese government founded "the Headquarters for Earthquake Research Promotion (HERP)" and conducted paleoseismological surveys of major active faults in Japan as well as other seismological observations. 10 years after the Kobe earthquake, HERP published reports on the long-term evaluation of 98 major active fault zones as well as the probabilistic seismic hazard map of Japan based on a huge collection of data on active faults, subsurface structures and seismological data.

Geological Survey of Japan/AIST has gathered active fault parameters obtained from surveys by local governments, universities as well as our institute to construct the Active Fault Database of Japan ([https://gbank.gsj.jp/activefault/index\\_e\\_gmap.html](https://gbank.gsj.jp/activefault/index_e_gmap.html)). This database contains fault parameters (location, length, angle of fault plane, slip per event, age of the last faulting event, recurrence interval, and slip rate) for 583 segments. These data allow us to consider the nature and character of active faults in Japan.

### 2. ACTIVE FAULT DATABASE OF AIST

Geological Survey of Japan/AIST opened the Active Fault Database in 2005. It includes 310 fault systems and 569 segments, as well as information of 10 fault systems (14 segments) that were evaluated as non-active faults. It is composed of three databases; fault parameter, survey information, and reference databases. We can find information about active faults from map or key words. The fault parameter database includes fault name, length, strike, dip angle, type and sense of faulting, age of the last event, average recurrence interval, and probability of rupture for next 30 years. The survey information database includes the name of site, coordinate system, type of survey, reference for displacement, amount of displacement, age of

reference geological layer, and related references. Reference database links to Japanese scientific contents service sites (CiNii, J-Stage) as well as PDF files of survey reports of Geological Survey of Japan. Also this database shows the geological map and distribution of seismicity in Japan, with links to a visualization system for subsurface structures.

### 3. CHARACTER OF ACTIVE FAULTS IN JAPAN FROM THE DATASET

#### (1) Fault systems and segments

Fault systems and segments in the Active Fault Database of AIST were defined several ways, such as by distance of separation, change of fault trace strike, and the age of faulting events based on geological surveys. A segment means a range of typical faulting events and a fault system shows a combination of segments which could act during an earthquake. About 40 % of fault systems have multi-segments (Figure 1) and maximum number of segment in a fault system is 16 (MTL and ISLT fault systems).

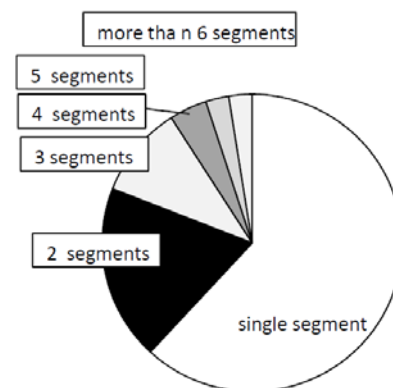


Fig. 1: Number of fault segments contained in a fault system



(2) Strike and dip angle of fault (Figure 2)

Reverse faults are concentrated to a N-S trend and a NNE to NE group are more than a NNW-NW group. Strike-slip faults are consistent with the stress orientation of E-W compression related to the motion of the Pacific Plate. Right-lateral slip faults are concentrated in a NE and left-lateral slip faults are in NW. Normal faults are few but they were concentrated in a EW trend.

(3) Length of fault segment

In any fault type, about half of segments have lengths of 10-19 km, and about a quarter of segments have lengths of 20-29 km (Figure 3). A few reverse faults and right-lateral strike-slip faults have lengths more than 50 km as a single segment.

(4) Type of displacement

More than half of segments were reverse faults (298 segments). Strike slip faults were divided into right-lateral slip faults (143 segments) and left-lateral slip faults (85 segments). Less than one-tenth of segments are normal faults (45 segments).

(5) Slip rate

Slip-rates for each of segment was basically based on geological data (amount of displacement / age of reference layer). Topographic features were also used to estimate fault slip rates. Nearly half of segments have slip-rate between 0.1-0.4 m/ka in Japan (Figure 4). The maximum slip-rate value is 9.1 m/ka for the Gofukuji fault of the ISTL in central Japan.

(6) Average recurrence interval

Recurrence intervals were estimated by geological surveys for 63 segments. For 33 segments, recurrence intervals are estimated by the ages of more than 3 events, whereas recurrence intervals for the other 30 segments are calculated based on the ages of 2 faulting events. For the other 135 segments, average recurrence intervals are calculated by the slip-rate and amount of slip per event. The distribution of average recurrence intervals shows two peaks of around 4 kyr and 13 kyr from all data, although there is a peak around 1 kyr based on only geological data (Figure 5).

(7) Age of the last faulting event and related historical earthquake

Data of the age of the last faulting event were obtained for 208 segments. The most recent event on 47 segments are obtained from historical records.

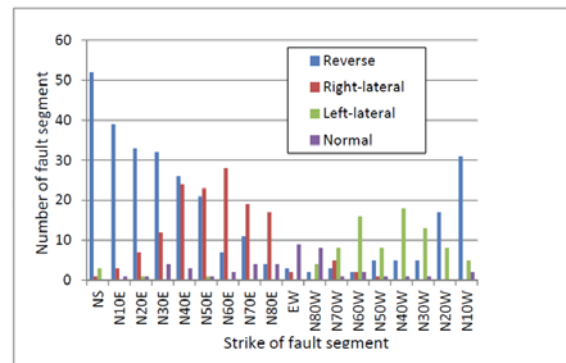


Fig. 2: General strike of fault segments with different sense of deformation in Japan

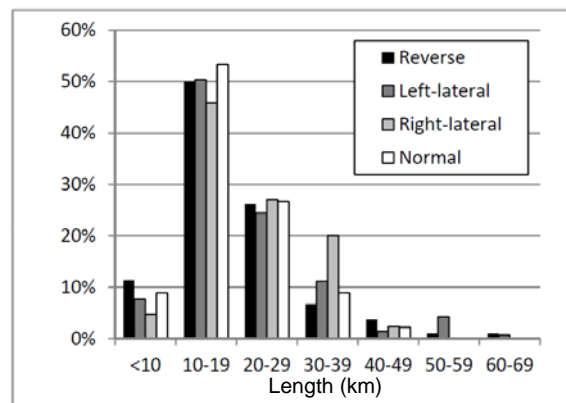


Fig. 3: Length of fault segment in Japan

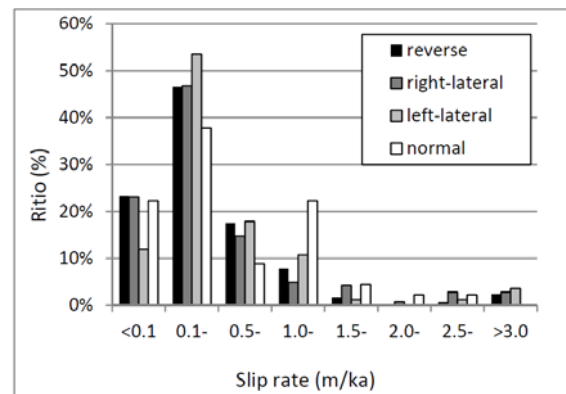


Fig. 4: Slip rate of fault segment with type of deformation in Japan

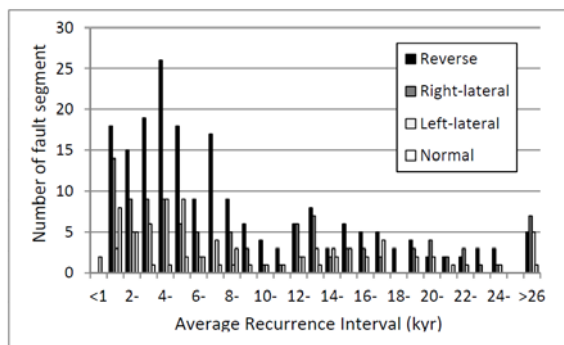


Fig. 5: Average recurrence interval of fault segment with different type of deformation in Japan

#### 4. FUTURE ISSUES

Using the Active Fault Database of AIST, we discuss the relationship between several fault parameters, such as length-slip rate, slip rate-recurrence interval, and so on. We hope this discussion will further our collective understanding of the nature of active faults and their evaluation. Furthermore, the occurrence of non-characteristic earthquakes on active faults is another problem for evaluation.

#### References

Miyamoto, F., and T. Yoshioka (2011). Active Fault Database of Japan of AIST (in Japanese). *Monthly Chikyū*, 33 (12), 759-769.

#### (8) Ratio of elapsed time

Ratio of elapsed time is calculated based on the data of average recurrence interval and age of the last faulting event. This ratio has been calculated for 185 segments. About half of those segments (89) exhibits a ratio between 0.1-0.4. 23 segments have a ratio more than 1.0, suggesting they are likely to failure.

#### (9) Probability of 30 years (BPT / Poisson)

Probability of occurrence of future faulting with BPT model (time dependent model) was obtained for segments the ratio of elapsed time is known (185 segments). Other 223 segments have only Poisson probability based on the data of average recurrence interval. The Gofukuji segment has the maximum BPT probability of 25 % and Poisson probabilities of 4 %.

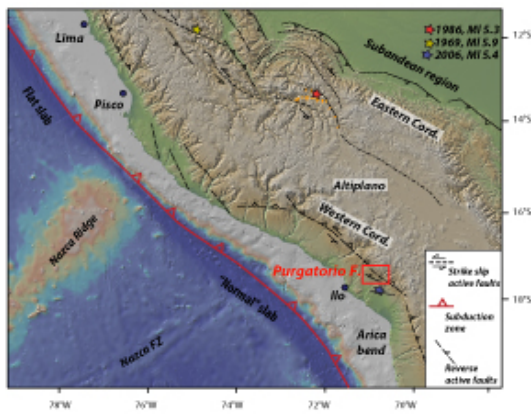


Figure 5: Field evidences of the recent co-seismic activity of the Purgatorio Fault in Southern Peru forearc region. B/ Sampled scarp along the thrust fault. C/ Broken pebbles along the fault plane, sampled for  $^{10}\text{Be}$  dating. D/ Folded recent ashes and sediments in the Purgatorio plain along the fault trace.



## Earthquake Fault Segmentation In The Central Andes, Ecuador

Baize, Stéphane (1), Laurence Audin (2), Alexandra Alvarado (3), Hervé Jomard (1), Johann Champenois (1)

- (1) Institut de Radioprotection et de Sécurité Nucléaire, BP 17, 92262 Fontenay-aux-Roses, France ([stephane.baize@irsn.fr](mailto:stephane.baize@irsn.fr))
- (2) ISTERre, IRD-CNRS-OSUG, Université de Grenoble, 1381 rue de la Piscine, 38400 Saint Martin d'Hères, France
- (3) Escuela Politécnica Nacional, Instituto de Geofísica, Ladrón de Guevara E11-253 y Andalucía, P.O. Box 2759, Quito, Ecuador

**Abstract:** Field investigations have been carried out along the fault system that accommodates the relative motion between the North Andean Sliver and the South American Plate in Ecuador. The project aims at mapping the segmentation of this major active fault system. A series of fault strands newly mapped in direct continuation to the Pallatanga Fault (PF) to the north allow the definition of a large structure capable of triggering large events. This is confirmed by the presence of historical well-preserved scarps and decametric offsets (probably due to the 1797 M7.5 Riobamba event) disrupting the Iqualata volcano. We could not find evidence for any structural continuity between the PF and the fault mapped in the Huisla volcano to the NE. We suggest that a 5-10 km wide step over separates the two segments and probably blocked the 1797 rupture. A recent surface rupture has also been recently discovered during the M5 Pisayambo quake along the Cosanga Fault (CF) system, with uncommon surface rupture length and displacement. From the few unearthed evidences, we estimate at a first glance that the mean slip rate along the PF and CF is similar ( $\approx 1$  mm/yr).

**Key words:** Earthquake Geology, Historical Surface ruptures, Segmentation, Ecuador.

### GEOLOGICAL FRAMEWORK

Relative motion between the North Andean Sliver (NAS) and the South American Plate (SAP) is accommodated along a large continental fault zone at 8 mm/yr rate, including the Pallatanga Fault (PF). The PF crosses the entire Western Cordillera and localizes the deformation between the SAP and NAS (Alvarado et al., 2016), and is suspected to have hosted large historical earthquakes (1698?, 1797, 1911, 1949) reported by Beauval et al. (2010). Its 65+ km surface trace is quite well known from Juan de Velasco (SW) to the Cajabamba area (NE) where three trenches were excavated, evidencing the occurrence of large prehistorical earthquakes, and among them the 1797 event (Baize et al., 2015). North of this, towards the Cosanga Fault (CF) in the Cordillera Real, the fault mapping is much less constrained and was the target of a 4m-high-resolved DEM analysis and field investigations.

### NEW INVESTIGATIONS

Our recent efforts focused on mapping and documenting the fault in this transition area between PF and CF. We aim both at mapping the active fault traces, characterizing their long-term activity and evidencing recent or historical surface ruptures. These topics are relevant steps to infer the rupture segmentation during large past events and to contribute to a better assessment of seismic hazard. During these last campaigns, we could characterize several fault strands that continue the PF to the north, defining a large fault capable to trigger large events. Three sectors were investigated: San Andres, Iqualata volcano, Huisla volcano (Figure 1).



Fig. 1: Location of the study areas, between the known and mapped segments (Pallatanga Fault and Cosanga Fault) in red (fault traces from Alvarado, 2012). White dashed lines are fault traces investigated. Yellow pins locate the main historical earthquakes. In green, the major active or dormant volcanoes in the area. Insert: the blue dashed line depicts the shear zone that separates the North Andean Sliver (NAS) from the South-America Plate (SAP). Red star: study area.

The structural continuity between the PF on top of the Pliocene Iqualata Volcano (IV) and the CF in the Pleistocene Huisla volcano (HV) is unknown but, at the end of our field investigation, we defined a 5-10 km step-over which seems to have blocked the most recent surface rupture to the south. Finally, Holocene activity has been unearthed along the CF system, close to the



Pisayambo Lake, and we were able to document a new and clear surface rupture associated with a M5 earthquake in 2010 as described below. We hereafter describe the geological evidences and their analysis from south to north.

### **SURFACE RUPTURE EVIDENCES BETWEEN SAN ANDRES AND THE IGUALATA VOLCANO**

#### *The San Andres Village and the IV slopes*

The 4m-resolution DEM reveals several lineaments aligned with the known trend of the Pallatanga Fault segments. These are developed within volcanic avalanche deposits (hereafter called "VAD") that filled the Riobamba basin 50 to 60 ka ago after the partial collapse of the Chimborazo edifice (Bernard et al., 2008). Along the lineament, we document evidences of folding and faulting of the volcanic and sedimentary deposits. Interestingly, the general course of a fault-perpendicular incised creek is deflected about 60 meters in the right-lateral sense, including a localized 10 meters nearby an abandoned water-mill. This latter smaller-scale offset could be due to the last large earthquake of the area, i.e. the M7.5 1797 Riobamba event. Considering the age of the VAD and assuming that this creek initially incised in a linear course across the fault, we can preliminary estimate the slip rate at  $\approx 1$  mm/yr.

Along the IV slopes north of San Andres, we could trace a series of compelling evidences of surface faulting affecting the thick Holocene organic soil, as well as large

(5-10 m) cumulative NE-SW scarps, individual scarplets (1 m) and right-lateral displacements of creeks (several tens of meters).

#### *The Igualata Volcano*

The best evidence of recent surface faulting crops out nearby the IV summit, with cumulative displacements of morphologic features and coseismic signs of a major historical event (scarp with free-face, en echelon fractures). The 1797 quake seems to be the best candidate, because of the vicinity of the epicenter. However, we cannot completely rule out the M $\approx$ 7.2 1698 event (Beauval et al., 2010).

The general geomorphic expression is of a right-lateral fault zone generating a counter-slope scarp and related sag ponds (Figure 2). The right-lateral kinematics are attested by left-stepping en-echelon fractures during the last quake, and by successive displacements of morphological features, especially an erosional "channel" (CH) for which we could identify at least 5 remnants in the downthrown block (Figure 2). Successive dextral displacements of this "CH" are between 8 (last event) and 18 m. The cumulative vertical component is about 4 meters. These displacement values are really high, even for M $\approx$ 7.5 events like the 1797 Riobamba quake, and we suggest that they could correspond to multi-event offsets. The fault trace can be mapped up to the northern IV slope, displacing moraine, terrace risers, Holocene marsh deposits.

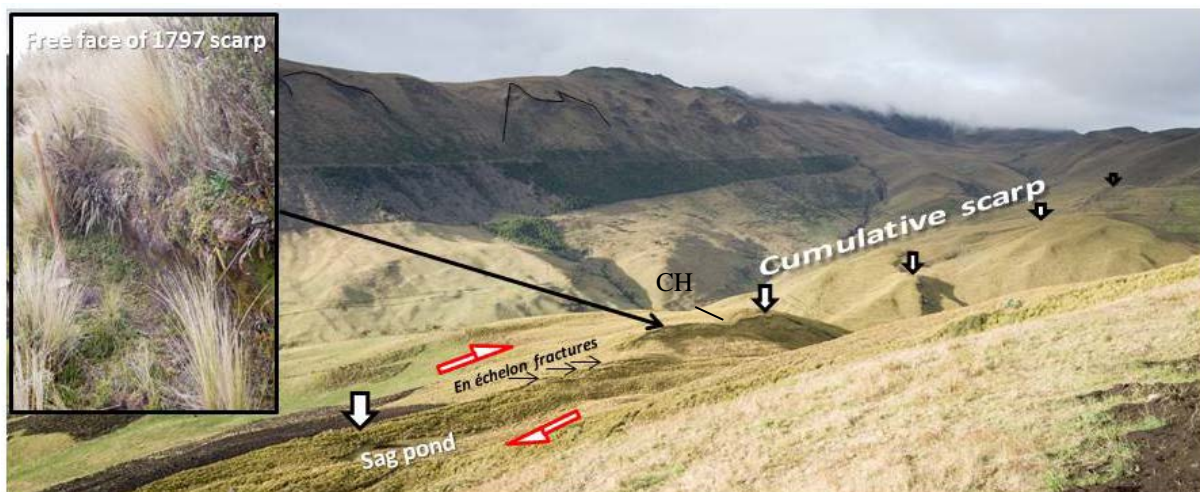


Fig. 2: Cumulative fault trace across the Igualata volcano (IV) summit. En echelon left-stepping fractures and recent free face scarps represent the most recent surface rupturing event, probably the 1797 Riobamba earthquake (northern end of the same rupturing event observed in Baize et al., 2014). They reveal a prevailing right-lateral mechanism, consistent with current regional kinematics.

### **DISLOCATION OF THE HUISLA VOLCANO CLOSE TO PELILEO**

In this area, we report evidences of cumulative fault displacement, but no clear proof of historical surface rupture. Five kilometers north of the trace in the IV, the dislocation of the inactive Huisla volcano is the closest

recent geomorphic sign of coseismic deformation. The morphology of the edifice is symptomatic of a large sudden collapse of the cone, which beheaded the edifice and formed the large and hollowed valleys on top. The related slide and accumulation of avalanche debris reached the Patate River valley. According to P. Mothes (personal communication), the Huisla avalanche could have occurred 30 ka. Therefore, all the tectonic features



that are described hereafter are younger (Upper Pleistocene to Holocene).

An overview of the edifice from the south enables roughly locating the fault zone (Figure 3) and, at closer distance, a series of benches which disrupt the major slope could indicate the fault trace. On its eastern flank, the HV also is cut by the fault which displaces an incised valley with a significant ( $\approx 60$  m) right-lateral component. Down to the Rio Patate valley, the road-cuts of the new Pelileo - Riobamba highway offers massive outcrops. In one of these, we could document a Quaternary NE-SW fault between the Huisla VAD and a series of stratified deposits mixing colluvial layers and volcanic falls. The strike-slip fault kinematics of the shear zone there attests

to a tectonic origin, despite the very steep slope which is affected by numerous mass movements. The northernmost fault segment investigated during our November 2015 field session was inferred from morphological analysis: a pressure ridge dams a paleo-valley on the right side of the Patate valley, in the exact continuation of the NE-SW shear zone described before. The area did not reveal any evidence of historical surface rupture and, to date; it seems that both the 1797 and 1949 earthquake faults did not reach the surface there. The road cut outcrop suggests that the most recent colluvial deposits are not deformed.

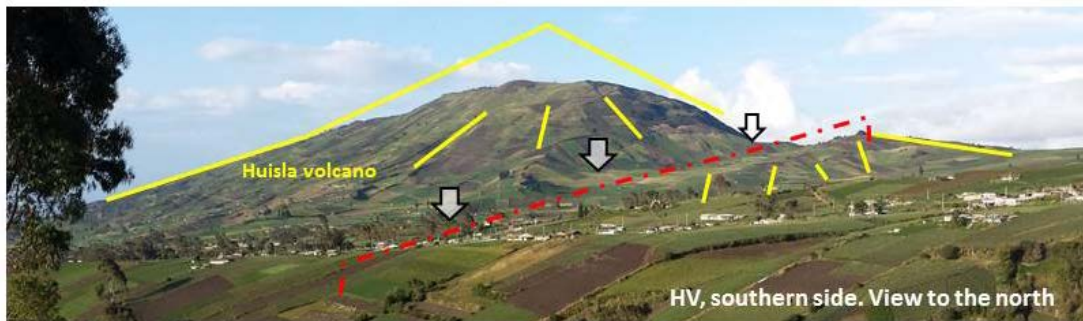


Fig. 3: View from south of the Huisla volcano (HV) disrupted by a dextral fault (red dashed line). Yellow lines represent the hypothetical flanks and slopes of the former edifice.

The epicentral area of the 1949 Pelileo earthquake suffered many landslides and other secondary effects during shaking. The former Pelileo city (nowadays rebuilt; La Moya) was destroyed by superficial movements during the 1949 quake. Archives also report that most of the Patate River valley slopes were affected by heavy and deep-seated movements mobilizing several millions of cubic meters.

### THE PISAYAMBO EARTHQUAKE ON THE COSANGA FAULT ZONE

In 2010, a magnitude 5 earthquake occurred in the Pisayambo Lake region, 25 km north-east of Pelileo city. Surprisingly, this quake produced significant surface faulting that could still be discovered four years after from InSAR analysis. This study (Champenois et al., in prep.) has shown the occurrence of a 9 km long linear anomaly in interferograms, with relative displacements in the Line-of-Sight of about 50-60 cm, which we interpret as the evidence of a surface faulting event. During a field reconnaissance in 2014, we could check the "InSAR" surface rupture trace and geologically map the field clues that have been preserved. The "coseismic" evidences are located along a cumulative fault which displaces the Pleistocene moraines and the Holocene soils. All along the investigated fault, we could document right-lateral offsets of 10 to 20 meters versus 1 to 2 meters of vertical throw. At some places, these offsets are distributed over several parallel segments. A stratigraphic section in a hand-made trench allowed the

verification of the coseismic activity of the fault during the Holocene, with two major morphogenic quakes that produced a moraine free-face scarp between 2500-1000 years BC and between 800-400 years BC. The fault segment here described is assigned to the Cosanga Fault zone (Alvarado, 2012).

Four years after the quake, we could unearth the traces of surface faulting, which were conspicuously preserved: open cracks, ENE-WSW left stepping en-échelon fissures, NE-SW fractures with relative displacement and pop-up features. Fault strike is generally around N30°-N50°E consistent with the InSAR results (Alvarado, 2012). The overall deformation pattern is consistent with right-lateral kinematics. Average (AD) and maximum (MD) values of displacement are really high for such a moderate earthquake, respectively of 22 to 26 cm and 37 to 61 cm (according to field and InSAR measurements, respectively). Applying the classical empirical relationships (Wells and Coppersmith, 1994), these fault parameters should be associated with a M6.2-6.5 earthquake.

According to the InSAR data and their inversion, we can summarize the fault parameters as follows: surface rupture length is 9 km, fault width 2 km, fault dip 60° to the east (Champenois et al., in prep.). When converting the average slip (about 25 cm) over the fault surface area (18 km<sup>2</sup>), the equivalent moment magnitude of such an event is Mw=5, assuming realistic shallow conditions for the local crust (i.e. Vs=2000 m/s, density 2.5 and therefore a shear modulus of 10 GPa). This is completely consistent with the seismological data (Figure 4) and we here emphasized that the Wells and Coppersmith (1994)



relationships are to be applied carefully, especially when trenching data like AD or MD are used. One question still remains open: we cannot rule out that part of the measured surface slip has been released

aseismically during the 16 days-time period covered by the successive radar data.

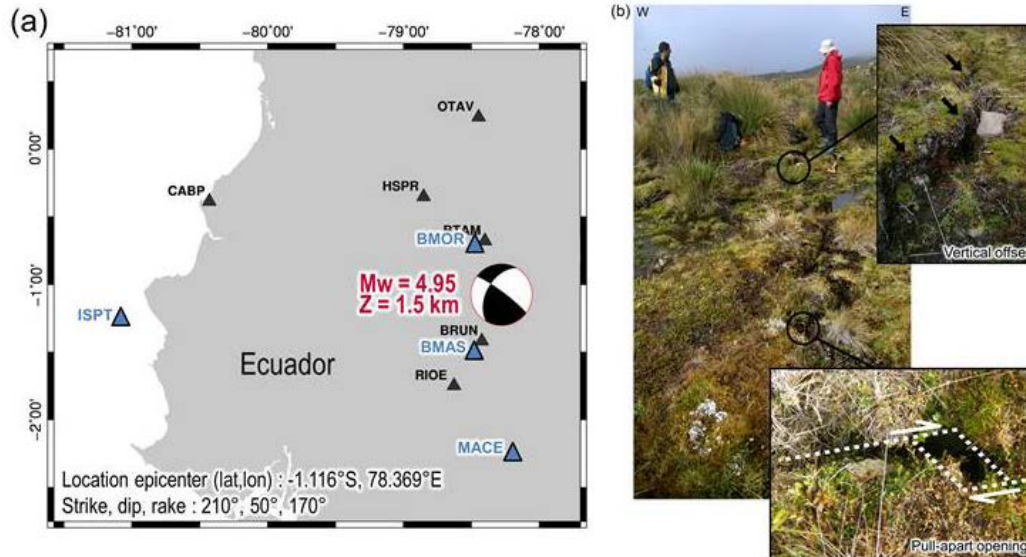


Fig. 4: Focal parameters of the 26/3/2010 M5 Pisayambo earthquake and associated surface rupture as observed in 2014 (from Champenois et al., in prep.). Surface right lateral and vertical offsets are around 25 cm and ~10 cm, respectively, coherent in scale from both the field observations and the INSAR imagery.

## FUTURE WORKS

Future field surveys and optical imagery analyses will focus on completing the active fault and surface rupture mapping, in the framework of the newly re-funded "REMAKE" project. To date, we could drastically refine the fault segmentation of the PF and CF, but the final product is not achieved yet. The paleoearthquake history of the fault zone has not been continued since the successful trenches in Rumipamba (Baize et al., 2015). We emphasize that, with the future segmentation map of the fault system, we would be able to propose scenarios for the earthquake rupture propagation through the system which was able to cause magnitude 7.5 quakes in the past. Trenching in the Iqualata summit area or in the Huisla zone could be relevant targets for achieving that project.

In addition, we emphasize that the CF and PF system only accommodates 1 mm/yr over the 8 mm/yr of dextral shearing between NAS and SAP: further works will also have to focus on figuring this deficit out: how this deformation is absorbed; or is this due to other unmaped active faults?

**Acknowledgements:** This work has been founded by the "Laboratoire Mixte International Séismes et Volcans des Andes du Nord", a cooperation structure between France (Institut pour le Développement) and Ecuador (Escuela Politécnica Nacional-Instituto Geofísico de Quito). IRSN and CNES provided a grant for the post-doctoral contract of Johann Champenois.

## References

- Alvarado, A. (2012). Néotectonique et cinématique de la déformation continentale en Equateur. Thèse de Doctorat, Université de Grenoble.
- Alvarado A. et al. (2016). Migration history of a continental plate boundary in Ecuador: Delimiting the North Andean Sliver's eastern boundary with active faulting, seismicity, GPS and geology. *Tectonics*, accepted.
- Baize, S., L. Audin, T. Winter, A. Alvarado, L. Pilatasig Moreno, M. Taipei, P. Reyes, P. Kauffmann & H. Yepes, (2015). Paleoseismology and tectonic geomorphology of the Pallatanga fault (Central Ecuador), a major structure of the South-American crust. *Geomorphology* 237, 14–28
- Beauval, C., H. Yepes, W. H. Bakun, J. Egred, A. Alvarado & J. C. Singaicho, (2010). Locations and magnitudes of historical earthquakes in the Sierra of Ecuador (1587–1996). *Geophys. J. Int.*, doi: 10.1111/j.1365-246X.2010.04569.x
- Bernard, B., B. vanWyk, B. de Vries, D. Barba, H. Leyrit, C. Robin, S. Alcaraz, P. Samaniego, (2008). The Chimborazo sector collapse and debris avalanche: deposit characteristics as evidence of emplacement mechanisms. *J. Volcanol. Geotherm. Res.* 176, 36–43.
- Champenois, J., S. Baize, M. Vallée, H. Jomard, A. Alvarado, L. Audin, (in prep.). Evidences of surface rupture associated with a low magnitude (M5.0) shallow earthquake in the Ecuadorian Andes. To be submitted to *J. Geophys. Research*.
- Wells, D. L., & K. J. Coppersmith, (1994). New empirical relationships among magnitude, rupture length, rupture width, rupture area and surface displacement. *Bull. Seismo. Society America* 84, 974-1002.



INQUA Focus Group on Paleoseismology and Active Tectonics



paleoseismicity.org

## The Elizabeth Lake paleoseismic site: Rupture pattern constraints for the past ~800 years for the Mojave section of the south-central San Andreas Fault

Bemis, Sean P. (1), Scharer, Kate (2), Dolan, James (3), Rhodes, Edward (4)

- (1) University of Kentucky, Lexington, KY. Email: [sean.bemis@uky.edu](mailto:sean.bemis@uky.edu)
- (2) U.S. Geological Survey, Pasadena, CA. Email: [kscharer@usgs.gov](mailto:kscharer@usgs.gov)
- (3) University of Southern California, Los Angeles, CA. Email: [dolan@usc.edu](mailto:dolan@usc.edu)
- (4) University of California Los Angeles/University of Sheffield: [ed.rhodes@sheffield.ac.uk](mailto:ed.rhodes@sheffield.ac.uk)

**Abstract:** Critical gaps remain in constraining the variability in extent and timing of latest Holocene paleo-ruptures along the south-central San Andreas Fault (SAF). We developed the Elizabeth Lake paleoseismic site in the center of the Mojave section of the southern SAF, near the middle of the 100 km span between the Frazier Mountain and Pallett Creek sites, to fill one of these paleoearthquake gaps. We completed three field campaigns at the site, documenting 10 trenches that span portions of an elongate geomorphic depression formed by a bedrock-cored shutter ridge on the NW side. Radiocarbon dates establish that the excavations expose >2000 years of stratigraphy deformed by a narrow 3-7 m wide fault zone. The best stratigraphic resolution occurs within the past ~800 years where we have documented evidence for 4-5 earthquakes.

**Key words:** paleoseismology; strike-slip fault; rupture patterns

### INTRODUCTION

The southern San Andreas Fault in California has hosted two historic surface-rupturing earthquakes, the ~M7 1812 Wrightwood earthquake and the ~M7.9 1857 Fort Tejon earthquake (e.g., Sieh, 1978; Jacoby et al., 1988). Numerous paleoseismic studies have established chronologies of historic and prehistoric earthquakes at sites along the full length of the 1857 rupture (e.g., Sieh, 1978; Scharer et al., 2014). These studies provide an unparalleled opportunity to examine patterns of recent ruptures; however, at least two significant spatial gaps in high-quality paleoseismic sites remain. At ~100 km long each, these gaps contribute up to 100 km of uncertainty to paleo-rupture lengths and could also permit a surface rupture from an earthquake up to ~M7.2 to go undetected [using scaling relationships of Wells and Coppersmith (1994)]. Given historic evidence of ~M7 earthquakes on this portion of the SAF (1812), it is critical to fill these gaps reduce the probability of missing 1812-like events in the prehistoric record.

In this study, we target a new site within the 100 km long stretch of the San Andreas Fault between the Frazier Mountain and Pallett Creek paleoseismic sites (Figure 1), near Elizabeth Lake, California. Prior excavations at the site during 1998-1999 encountered promising stratigraphy but these studies were hindered by shallow groundwater throughout the site. We began our current phase of investigations in 2012, targeting the northwestern end of a 40 x 350 m fault-parallel depression that defines the site (Figure 2). Subsequent investigations in 2013 and 2014 focused on the southeastern end of the depression where the fault trace is constrained between topographic highs and is proximal to an active drainage. In total, our paleoseismic

investigations consist of 10 fault-perpendicular trenches that cross the depression (Figure 2) and expose a >2000 year depositional record. These trenches reveal that the thickest section of young stratigraphy occurs at the southeastern end of the site where the fault zone projects through an area of relatively continuous sediment accumulation from a northeast-flowing drainage. This portion of the site contains a 3-m-wide pop-up within the fault zone that separates alternating alluvial and paludal (marsh) deposits south of the fault zone from a thick organic-rich loam on the north side of the fault zone. Faults, fissures, and tilted blocks provide evidence for 4 to 5 paleoearthquakes since ca. 1250 A.D. Radiocarbon dating established that the site has a significant component of detrital charcoal producing an age spread of up to 500 years. To supplement our age chronology we incorporated ages from collections of micro-scale organic fractions and post-IR infrared stimulated luminescence dating in order to better estimate true layer ages.

### ELIZABETH LAKE PALEOSEISMIC SITE

Elizabeth Lake is a natural freshwater lake trapped within the topographic trough formed by the San Andreas Fault system along the northeast flank of the San Gabriel Mountains (Figure 2). The modern, active trace of the San Andreas Fault occupies the southwest margin of this valley, upslope from Elizabeth Lake. The fault zone forms an uphill-facing geomorphic scarp that dams and offsets north-flowing drainages emanating from the adjacent mountains. Geomorphic and vegetation patterns indicate that much of the fault zone has shallow groundwater present as well as intermittent fine sediment accumulation in a series of fault parallel depressions. For our studies we targeted the largest of these depressions, situated in an undeveloped zone between Blue Hills Drive



## INQUA Focus Group on Paleoseismology and Active Tectonics



paleoseismicity.org

and Ranch Club Road (Figure 2). Satellite imagery from as recent as 2008 shows standing water filling the depression; however, when our current phase of investigations began in 2012, surface water covered only a few square meters. Alluvial fans and channels show that most sediment at the site is derived from three small drainages (<0.3 sq. km each). We suspect that the southeasternmost margin of our site has at times received additional sediment from a larger drainage (2.2 sq. km) farther to the southeast.

Our investigations at the Elizabeth Lake site consisted of 10 trenches (Figure 2); ultimately three of these trenches provided compelling evidence for the past ~800 years. These trenches (T4, T4b, and T9; Figure 2) are the easternmost excavations at the site and were excavated up to the eastern margin of the property. Prior investigations and the local geomorphology interpreted from airborne lidar suggests these depressions have received recent, episodic sediment deposition. For example, the southeastern portion of the site received ~1 m of sediment during the 1998 El Nino event (Figures 3 and 4). Below the 1998 El Nino sand and gravel, the stratigraphy in T4 and T9 thickens to the south-southeast (away from the fault) and is composed primarily of sandy horizons interbedded with organic-rich silt and clay. Faulting occurs within a <7 m wide zone through these trenches (Figures 3 and 4). Upslope (southwest) of and within this fault zone the stratigraphy is well-preserved, whereas the stratigraphy on the downslope (north) side of the fault consists primarily of massive, organic-rich sandy loam.

### EARTHQUAKE EVIDENCE

The upper portion of the stratigraphic section at the Elizabeth Lake site, unit 60 and above, contains evidence for as many as 5 earthquakes. This sequence of units is ~3.7 m thick in T9 (Figure 4) and thins northwestward to ~2.3 m in T4 (Figure 3). Most of this thickness change occurs within unit 50, which is a ~0.5 m thick massive organic-rich clayey silt in T4 and expands to a 1.4 m thick succession of interbedded sand and clayey silt in T9.

The most recent event recorded at Elizabeth Lake (EL1) is defined by a southwest-side-up vertical displacement extending into the uppermost pre-1998 deposits. Unit 45.3 is sharply truncated by a fault zone and the younger sand layer, 45.1, overlaps this offset and is not deformed (Figure 4). South of the fault offset, unit 45.3 is absent and 45.2 and 45.1 thin across a structural high at the fault zone. Unit 45.2 in particular exhibits thickness changes across the fault-related deformation, indicating that EL1 occurred while 45.2 was the ground surface.

Evidence for the penultimate earthquake at Elizabeth Lake (EL2) generally consists of faults penetrating into the uppermost part of unit 50 (50.1 through 50.3) and are difficult to distinguish from the most recent event. For example, T4 and T4b both exhibit fault traces that terminate within 10-15 cm of the 45.3 basal contact, but

due to the massive nature of unit 50 in those trenches, more specific constraints on the timing and stratigraphic relationships are ambiguous. However, in T9 there is sufficient stratigraphic resolution to identify a cross-cutting relationship where a fault has truncated unit 50.2, resulting in a southward tapering wedge of sediment that is capped by the unit 45.3 basal contact (Figure 4). This is the key relationship that provides evidence of a distinct earthquake that occurred within the top of subunit 50.1.

A prior deformation event occurs in the middle portion of unit 50, involving units 50.5 and 50.6. The most obvious deformation is in T4b, where stratigraphic relationships show faulting that truncates unit 50.7. The upward termination of these faults is less clear because unit 50.4 is not clearly preserved in T4b, but layers continuous with the upper section of unit 50 appear to be unfaulted, placing broad constraints on faulting associated with EL3 between the base of 50.6 and the base of 50.3. In T9 where the units are better stratified, a possible fault termination just below the 50.5/50.6 contact on the south side of the pop-up has an unclear upward termination as it is overprinted by later faulting. Parallel to the fault, there is about 1 m of thickening of the middle section of unit 50 (~units 50.5 and 50.6) in the seven meters between T4 and T9. This reflects deposition following a folding event that could have occurred sometime between the top of 50.7 and the base of 50.3 that could be correlative with EL3 (in T4b) or be a separate folding event (EL3.5?). We are currently developing a 3D reconstruction to test interpretations of one versus two earthquakes in this interval.

Evidence for the fourth earthquake back (EL4) consists of the cross-trench relationship between unit 60 and the overlying subunits of 50.7. In both T4b and T9, the basal contact of 50.7 has a steeper dip than the top of that unit, and the sublayers pinch out over 1-2 m toward the main fault zone. From this evidence we interpret a folding event that warps the 50.7c/60.1 contact and creates accommodation space for the lower section of unit 50.

We document evidence for another deformational event (ELX) northeast of the main fault zone in T4, T4b, and T9. (e.g., Figures 3 and 4). Within an unbedded section of unit 50, a trough-shaped, thin sand horizon is bounded by faults. This is likely EL2 faulting, thus the thin sand horizon was probably formed in the lower half of unit 50. The massive character of unit 50 north of the main fault zone renders us unable to confidently associate this event with the earthquake evidence documented elsewhere in the base of unit 50 (EL3 or EL3.5?) or determine if it is in fact a separate earthquake.

### DISCUSSION

The earthquake chronology at Elizabeth Lake provides evidence of 4, and possibly 5, paleo-ruptures of the San Andreas Fault since ~1250 AD. With a final suite of radiocarbon and IRSL samples currently pending, we



refrain from including a detailed discussion of earthquake ages in this extended abstract.

**Acknowledgements:** This research was supported by awards #14202, #13136, and #12157 from the Southern California Earthquake Center to Pls Bemis, Scharer, Dolan, and Rhodes and a 1998 award to Dolan. Thanks to Ridgetop Range Properties for access to their property and Bob's Backhoe of Quartz Hill for excavation services. Field assistance provided by A. Hatem, C. Wespestad, C. Milliner, J. Grenader, L. DeVore, T.P. Taylor, C. Burkett, A. Hislop, J. Lucas, R. Witkosky, and others. Any use of trade, firm, or product names is for descriptive purposes only and does not imply endorsement by the U.S. Government.

### References

Bevis, M., Hudnut, K., Sanchez, R., Toth, C., Grejner-Brzezinska, D., Kendrick, E., Caccamise, D., Raleigh, D., Zhou, H., Shan, S., Shindle, W., Yong, A., Harvey, J., Borsa, A., et al., 2005, The B4 Project: Scanning the San Andreas and San Jacinto Fault Zones: AGU Fall Meeting Abstracts, v. 34, p. 01.  
 Jacoby, G.C., Sheppard, P.R., and Sieh, K.E., 1988, Irregular Recurrence of Large Earthquakes Along the San Andreas Fault: Evidence from Trees: *Science*, v. 241, no. 4862, p. 196–199, doi: 10.1126/science.241.4862.196.

Rockwell, T., Scharer, K., Dawson, T., in press, Paleoseismology of the San Andreas Fault Zone, in *Applied Geology of California*, eds. Anderson R., and Ferriz, R., Association of Environmental and Engineering Geology Special Publications Number 26.  
 Scharer, K.M., Biasi, G.P., and Weldon, R.J., 2011, A reevaluation of the Pallett Creek earthquake chronology based on new AMS radiocarbon dates, San Andreas fault, California: *Journal of Geophysical Research: Solid Earth*, v. 116, no. B12, p. B12111, doi: 10.1029/2010JB008099.  
 Scharer, K., Weldon, R., Streig, A., and Fumal, T., 2014, Paleoeearthquakes at Frazier Mountain, California delimit extent and frequency of past San Andreas Fault ruptures along 1857 trace: *Geophysical Research Letters*, v. 41, no. 13, p. 2014GL060318, doi: 10.1002/2014GL060318.  
 Sieh, K.E., 1978a, Prehistoric large earthquakes produced by slip on the San Andreas Fault at Pallett Creek, California: *Journal of Geophysical Research: Solid Earth*, v. 83, no. B8, p. 3907–3939, doi: 10.1029/JB083iB08p03907.  
 Sieh, K.E., 1978b, Slip along the San Andreas fault associated with the great 1857 earthquake: *Bulletin of the Seismological Society of America*, v. 68, no. 5, p. 1421–1448.  
 Wells, D.L., and Coppersmith, K.J., 1994, New empirical relationships among magnitude, rupture length, rupture width, rupture area, and surface displacement: *Bulletin of the Seismological Society of America*, v. 84, no. 4, p. 974–1002.

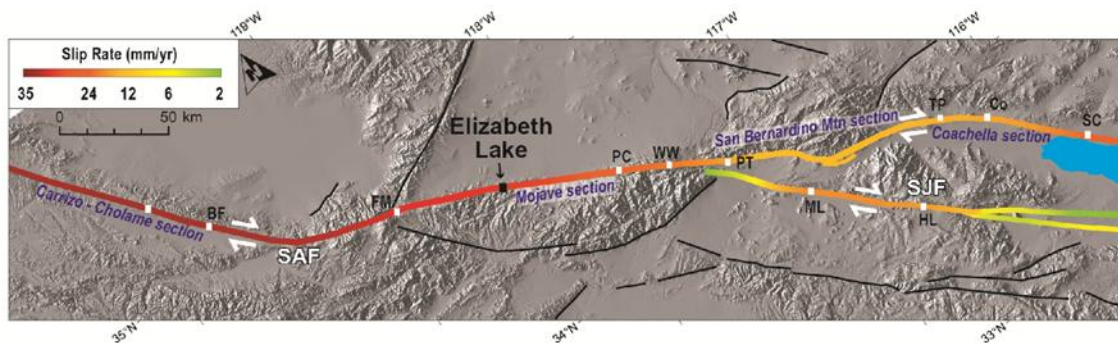


Figure 1. Map of the southern San Andreas/San Jacinto Fault systems (SAF/SJF). The Elizabeth Lake paleoseismic site is approximately halfway between Frazier Mountain (FM) and Pallett Creek (PC). Other labeled paleoseismic sites: BF = Bidart Fan, Co = Coachella, HL = Hog Lake, ML = Mystic Lake, PT = Pitman Canyon, SC = Salt Creek, TP = Thousand Palms, WW = Wrightwood. Slip rates interpolated along the faults based upon data summarized by Rockwell et al. (in press). Base from National Elevation Dataset.

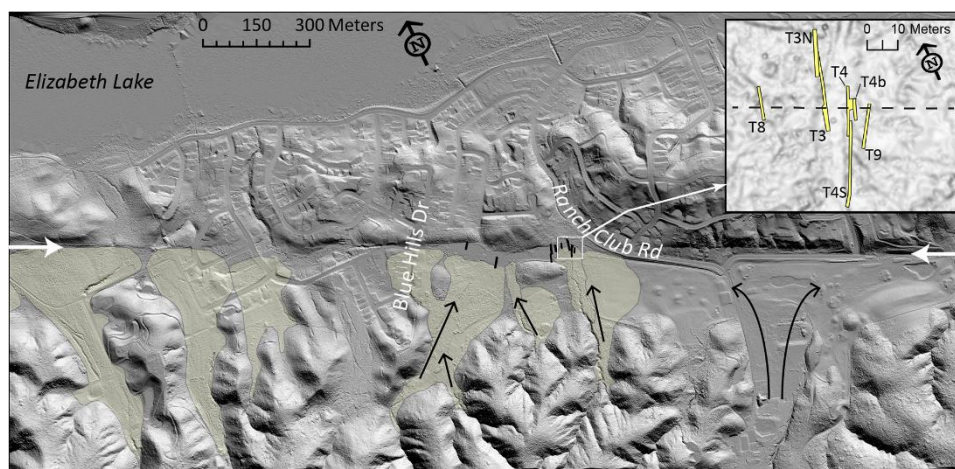


Figure 2. Elizabeth Lake study area. Bare-earth lidar hillshade (derived from the B4 dataset; Bevis et al., 2005) rotated counterclockwise; the San Andreas Fault runs between the two large white arrows. The Elizabeth Lake paleoseismic site is between Blue Hills Drive and Ranch Club Rd where the north-northeast flowing drainages are partially impounded behind a shutter ridge. Black arrows show flow direction and yellow polygons show well-defined alluvial fans associated with these drainages. The short



black lines show the locations of all 10 paleoseismic trenches we excavated at the site; the white box and inset image show the southeasternmost trenches where the best record of recent paleoearthquakes is preserved.

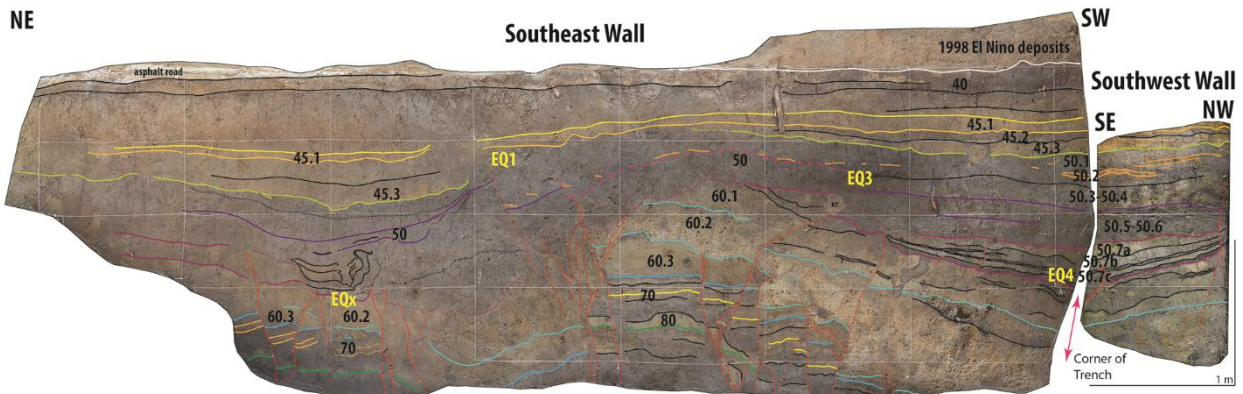


Figure 3. Southeast wall of T4b at the Elizabeth Lake site. Black numbers define stratigraphic units and yellow labels illustrate the locations of primary earthquake event evidence. The small photomosaic from the southwest end of the trench which was oriented perpendicular to the southeast wall. The oldest stratigraphy is exposed within the structural high where units 70 and 80 are labeled. The more massive character of unit 50 continues to the northwest (left) and the unit 50 growth strata thickens from this trench to the south-southeast towards T9 (Figure 4).

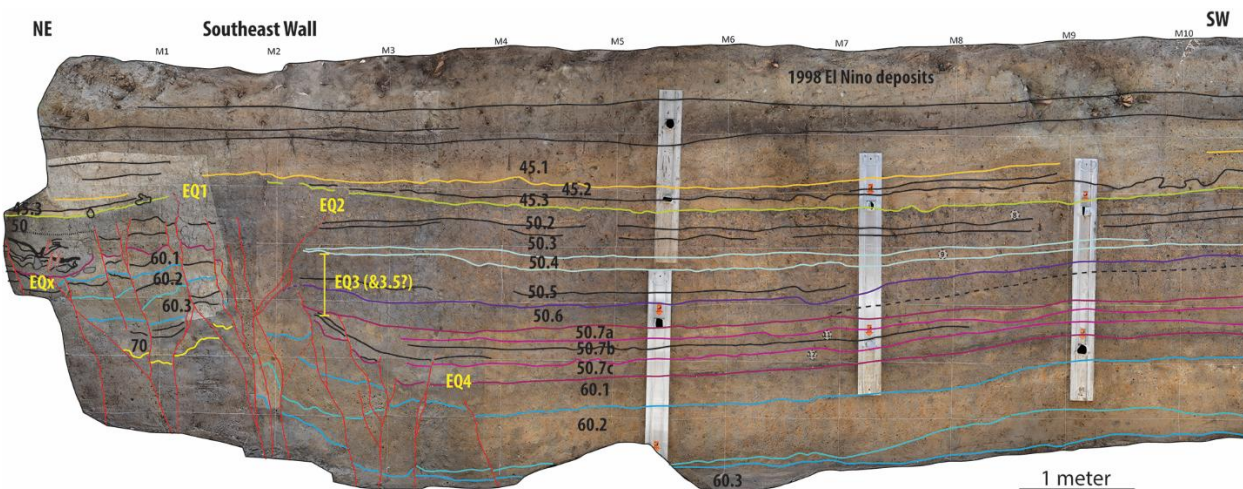


Figure 4. Southeast wall of T9 at the Elizabeth Lake site. Since ~1250 AD (all of unit 50 and above), alluvial and paludal sediments have progressively filled a topographic depression that formed behind a structurally controlled topographic high within the fault zone.



## Does paleoseismology forecast the historic rates of large earthquakes on the San Andreas fault system?

Glenn Biasi (1), Katherine Scharer (2), Ray Weldon (3), Timothy Dawson (4)

- (1) University of Nevada, Reno, NV, USA. Email: glenn@seismo.unr.edu
- (2) U.S. Geological Survey, Pasadena CA, 91104 USA. Email: kscharer@usgs.gov
- (3) University of Oregon, Eugene, OR USA. Email: ray@uoregon.edu
- (4) California State Geological Survey, Menlo Park CA, USA. Email: Timothy.Dawson@conservation.ca.gov

**Abstract:** The 98-year open interval since the most recent ground-rupturing earthquake in the greater San Andreas boundary fault system would not be predicted by the quasi-periodic recurrence statistics from paleoseismic data. We examine whether the current hiatus could be explained by uncertainties in earthquake dating. Using seven independent paleoseismic records, 100 year intervals may have occurred circa 1150, 1400, and 1700 AD, but they occur in a third or less of sample records drawn at random. A second method sampling from dates conditioned on the existence of a gap of varying length suggests century-long gaps occur 3-10% of the time. A combined record with more sites would lead to lower probabilities. Systematic data over-interpretation is considered an unlikely explanation. Instead some form of non-stationary behaviour seems required, perhaps through long-range fault interaction. Earthquake occurrence since 1000 AD is not inconsistent with long-term cyclicity suggested from long runs of earthquake simulators.

**Key words:** paleoseismology, earthquake recurrence.

### INTRODUCTION

The conditional probability estimate of a future earthquake depends on the dates of past events, their uncertainties, and the probability model assumed to characterize recurrence. A less recognized assumption is that the recurrence process is stationary; that is, that statistics derived from past earthquakes can be applied to future occurrences. Jackson (2015) recently called this assumption into question using recurrence models and parameter estimates from paleoseismic data in the Uniform California Earthquake Rupture Forecast 3 (UCERF3) model (Field et al., 2014; Biasi, 2013). For the paleoseismic sites in UCERF3, an open interval of 98 years has elapsed since the historic 1918 earthquake on the San Jacinto Fault. Jackson (2015) finds the joint probability of such a long interval since 1918 to be very small. He offers as potential explanations that perhaps the geologic record is misinterpreted, with ~30% too many earthquakes, or that earthquake occurrence is governed by some physics or correlation process such that recurrence is not a stationary process. In the former case, data underlying UCERF3 are impeached; in the latter, recurrence parameters from past earthquakes would not be useful for future occurrences, and the whole time-independent rupture rate forecast is put on shaky ground.

Jackson (2015) considers a set of seven paleoseismic sites with long paleoseismic records, including the San Andreas Santa Cruz Mountains, southern Hayward, central Garlock, San Andreas Wrightwood, San Jacinto Hog Lake, Elsinore Temecula, and Compton (Figure 1;

event ages, Figure 2, obtained from UCERF3 Appendix G, Weldon et al., 2013). The sites were chosen as they are spatially separated and therefore each paleoearthquake record is likely to be independent and would not reflect the same earthquake(s). In this study, we use the same dataset except we use an updated Hog Lake record by Rockwell et al. (2014), which has slightly different age distributions and a historic 1918 event. Records for the seven sites are considered complete for the most recent ~1000 years.



Figure 1. Selected paleoseismic sites on the plate boundary fault system. Sites considered by Jackson (2015): HS, Hayward South; SC, Santa Cruz; GC, Central Garlock; WW, Wrightwood; C, Compton; ET, Elsinore Temecula; and HL, Hog Lake. Site CO, Coachella, among others, also have long records.

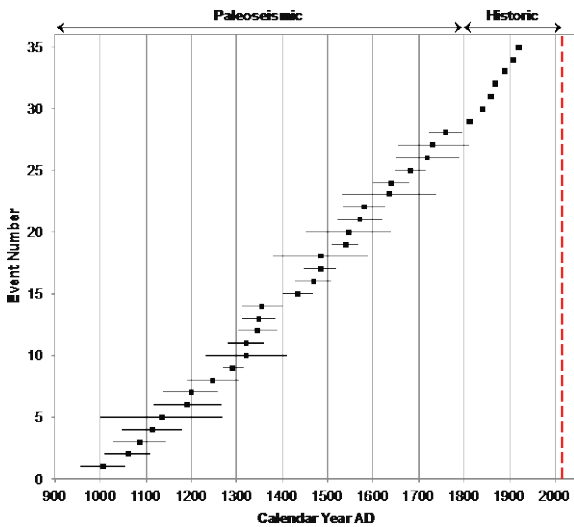


Figure 2. Mean age of 35 historic and paleoearthquakes in the dataset. Horizontal bars show 95% range of radiocarbon-dated paleoearthquake ages, red vertical line on current year (2016).

### Impact of age uncertainties

Prehistoric earthquake ages are derived from Bayesian modeling of radiocarbon dates obtained from organic material in sediments bracketing the paleoearthquake horizon. As a consequence, the timing of prehistoric paleoearthquakes are defined by probability distribution functions (PDFs) rather than an individual year. We first consider whether the conclusions of Jackson (2015) might be affected by inclusion of paleoseismic age PDFs. This is accomplished by testing interval lengths. We sample within event distributions, sort event occurrence, and tabulate incidence and length of “gaps,” or periods with no earthquakes. One view of this sampling is provided in Figure 3. On average the record since 1000 AD has had 2-4 earthquakes per century, but the periods from 1100-1200 and near 1700 have 1 or fewer in many samples. Roughly 20% of samples drawn this way include gaps of 100 years or more. Gaps concentrate around 1150, but can occur near 1400, and 1700 A.D (Figure 3). Thus century-long hiatuses are not frequent, but neither are they completely unlikely outliers. Interestingly, periods also occur with as many as 7 events per century, or nearly twice the long-term average. The record is obviously short, but the apparent cycles of 200-300 years in Figure 3 are interesting potential support for the existence of super-cycles recognized in long runs of earthquake simulators (Milner and Jordan, 2015).

### How much wiggle room?

We now consider a second approach in which a gap is inserted as a given length of time, and the probability consequences evaluated. It is helpful to consider how probabilities are affected using the familiar example of two fair 6-sided dice. There are 15 ways out of the 36 possible combinations in which the second die has more spots than the first, a condition equivalent to age

ordering between them. By comparison, there are only six ways out of 36 in which a gap of two or more spots can occur between the first and second die (1:4,5,6; 2:5,6; 3:6). Thus, relative to simply having more spots in the second dice, the requirement of an extra gap of 2 spots reduces the probability by 9/15. When gaps are forced into paleoseismic event dates, larger separations push distributions to their edges. We examine this effect with a sampling method that evaluates how probabilities of gaps evolve with gap size and location in the record.

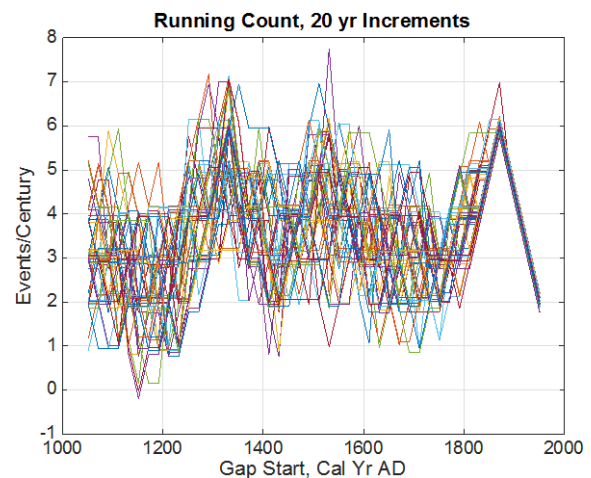


Figure 3. Running count of the number of events per century since 1000 AD is estimated by sampling from event distributions and counting in a sliding 100 year window starting at 20 year points. Each line reflects one of 100 picks through the paleoearthquake event PDFs. It is tempting to see 200-300 year cycles in these data.

We illustrate how sampling works and redistributes the earthquake age PDFs in Figure 4. As a matter of efficiency and because the gap really only affects a few paleoearthquake ages before and after the forced gap, we subsample the total record in this testing phase, a method demonstrated in Biasi and Weldon (1994). In Figure 4 we show the posterior earthquake age PDFs based on 500 successful samples through the event PDFs.

Three PDFs before the gap and three after are shown in Figure 4 for gap widths from 20 to 120 years. By comparing upper PDFs to the 20-year gap case, a sense for the probability of the gap can be inferred. For a gap of 100 years near AD 1150, event dates are moved slightly later, and the two dates before the gap have to be chosen in the early part of their prior ranges.

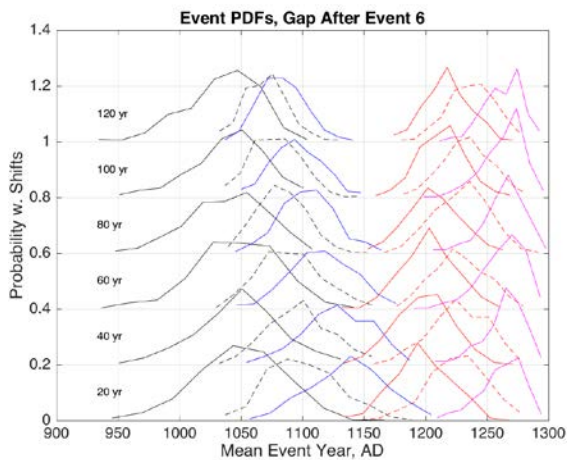


Figure 4. Posterior event PDFs conditioned on a gap after event 6 (blue pdf) in the mid-1100's. Colors and dashed lines are to distinguish individual event date distributions and make it easier to follow how individual cases change with gap size. Successive sets of PDFs are displaced upward as a plotting device.

Figure 5 generalizes the process in Figure 4 across all events in the combined record. In Figure 4 the vertical axis shows the number of trials to obtain 500 sample series from the event PDF's conditioned on including the indicated gap. The upper limit number of trials is set to 500,000. If this number of trials is reached before finding 500 successes, the sampling success rate is lower than 1 in 1000. We cannot fit gaps of all sizes between all events. For example, at 1300 AD, gaps of 20 or 40 years are possible, gaps of 60 years barely work under the 1:1000 criteria, and gaps of 80 years or larger do not fit. This occurs because PDFs before and after the gap are relatively narrow, and a gap larger than 60 years would push surrounding age PDFs beyond the tails of the prior distributions. The vertical axis with numbers of trials can be used to compare probability estimates if the 20-year gap case is considered a lower likely average separation. This approach corresponds to the dice analogy introduced earlier, with the second die showing more spots than the first. As in the dice illustration, the number of trials divided by 500 for a larger gap is an approximate measure of its relative probability. Thus a gap of 100 years near 1200 AD would be associated with an ~order of magnitude lower probability than a 20 year gap based on the event PDFs. Although a century-long gap near 1200 AD is not preferred by the data, it is not impossible either.

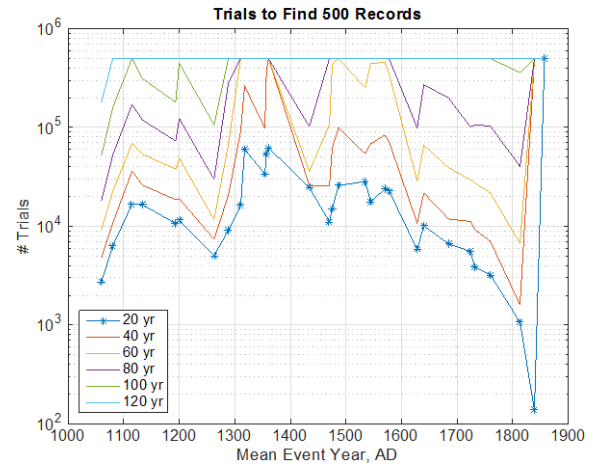


Figure 5. Proxy probability measure for gaps from 20 to 120 years at various times in the paleoseismic record. Larger gaps require more trials to find 500 successes. In some spaces large gaps are incompatible. Gaps after 1812 are historically identified.

### Discussion

When gaps in the paleoseismic record are approached as conditions on the data, a similar view emerges to results from direct sampling within uncertainties. Gaps of 100 or more years are not favored in this dataset, but neither are they strongly contradicted. With event age uncertainties included, gaps of 100 years or more occur in about 20% of the samples, with long intervals concentrated in the 12<sup>th</sup>, 15<sup>th</sup>, and 18<sup>th</sup> centuries. We do not calculate actual probabilities for the whole set here, but a rough estimate would include them with a likelihood of 3 to 10%. This small probability confirms that for the data considered, the present open interval is unusual, but perhaps not so unusual as to entirely discard chance as its explanation.

The probabilities of gaps depend strongly on the event set being considered. We have used the set considered by Jackson (2015) to provide corresponding values from the paleoseismic data. Two qualifications should be noted. First, the sites selected are extremely heterogeneous and not favorable for generalizing about the San Andreas system. Legitimate statistical conclusions may be drawn from the record ensemble of Jackson (2015), but the sites selected are, by design, unconnected, and thus not representative of the fault system in a paleoseismic sense. Records include long and short recurrence sites (Wrightwood vs. central Garlock, thrust faults (Compton), and records where completeness could be questioned (Elsinore Temecula). Second, probabilities of gap sizes depend on the site selection. Adding more sites (e.g., the southern San Andreas Coachella record, Figure 1, Philibosian et al., 2012) will make it increasingly difficult to explain the current long open interval as a chance occurrence on the basis of dating uncertainty. At the same time such an addition would strengthen the statistical argument in Jackson (2015). In principle, without rejecting the whole paleoseismic record as over-interpreted (Jackson, 2015), strategic removal of an event from the record could



## INQUA Focus Group on Paleoseismology and Active Tectonics



paleoseismicity.org

make room for a gap of 100 years or more, but we restrict our consideration to the data as reported. We would consider it unlikely that records have been systematically over-interpreted. While locally an extra earthquake may creep in, missed events also occur and are discovered only later with further excavation. While each of these records contains multiple lines of evidence for individual earthquakes, most of the original field studies recognize that evidence for individual paleoearthquakes is of variable quality. Future studies may examine the inclusion of low-quality events, but long-range interactions, stress shadow effects from large historical ruptures, and changes in seismicity rates seem to be better possibilities than systematic recording or dating problems to explain the current open interval.

**Acknowledgments:** Data used in this work were adopted from UCERF3 Appendix. We thank Dave Jackson for discussions on these issues, and USGS reviewers S. DeLong and D. Schwartz for their thoughtful reviews.

### References

- Biasi, G. P. (2013). Maximum likelihood recurrence intervals for California paleoseismic sites, *U.S.G.S Open-File Report 2013-1165, Uniform California Earthquake Rupture Forecast Version 3 (UCERF3) – The Time-Independent Model, Appendix H*, 25 pp.
- Biasi, G. P. and R. J. Weldon II (1994). Quantitative refinement of calibrated  $^{14}\text{C}$  distributions, *Quaternary Research*, 41, 1-18.
- Field, E. H., R. J. Arrowsmith, G. P. Biasi, P. Bird, T. E. Dawson, K. R. Felzer, D. D. Jackson, K. M. Johnson, T. H. Jordan, C. Madden, A. J. Michael, K. R. Milner, M. T. Page, T. Parsons, P. M. Powers, B. E. Shaw, W. R. Thatcher, R. J. Weldon II, and Y. Zeng (2014). Uniform California Earthquake Rupture Forecast Version 3 (UCERF3) – The Time-Independent Model, *Bulletin of the Seismological Society of America*, 104, 1122-1180.
- Jackson, D. (2015). Recurrence implications of California Paleo-event hiatus, AGU Annual Meeting 2015, S23A-2695.
- Milner, K. and T. H. Jordan (2015). Supercycles and synchronization signatures in synthetic seismic sequences, AGU Annual Meeting 2015, S21D-06.
- Philibosian, B., T. E. Fumal, and R. J. Weldon II (2011). San Andreas fault earthquake chronology and Lake Cahuilla history at Coachella, California: *Bulletin of the Seismological Society of America*, 101, 13-38.
- Rockwell, T. K., T. E. Dawson, J. Young, and G. Seitz (2014). A 21 event, 4,000-year history of surface ruptures in the Anza Seismic Gap, San Jacinto Fault and implications for long-term earthquake production on a major plate boundary fault, *Pure and Applied Geophysics*, doi: 10.1007/s00024-014-0955-z
- Weldon, R. J. II, T. E. Dawson, G. Biasi, C. Madden, and A. Streig (2013). Paleoseismic Sites Recurrence Database, *U.S.G.S Open-File Report 2013-1165, Uniform California Earthquake Rupture Forecast Version 3 (UCERF3) – The Time-Independent Model, Appendix G*, 73 pp.



## When did the Moroccan High Atlas Mountains get high? Constraints on neo- and active tectonics from fluvial geomorphology and palaeoaltimetry

Sarah J. Boulton<sup>1</sup>, Martin Stokes<sup>1</sup>, Justin H. VanDeVelde<sup>1</sup>, Anne E. Mather<sup>1</sup>

(1) School of Geography, Earth and Environmental Sciences, Plymouth University, Plymouth, U.K. sarah.boulton@plymouth.ac.uk

**Abstract:** *The surface uplift of mountain belts can have profound effects on precipitation patterns and moisture distribution, potentially resulting in the development of orographic rain shadows and aridification. Within Africa, the Moroccan High Atlas Mountains are the highest (2-4km elevation) topographic relief formed by Alpine tectonics. However, the uplift history of the Moroccan High Atlas has been a matter of debate for many years. New palaeoaltimetry data from Late Miocene lacustrine limestones that suggest that the High Atlas had a mean altitude of  $1200 \pm 500$  m through the Middle-Late Miocene. While geomorphic data (river long profiles and river terrace data) support models that propose ~1000 m of elevation have been gained during the Plio-Quaternary. These new data provide independent constraints on the timing and magnitude of orogenic development in the High Atlas that is driven by mantle upwelling and fault reactivation.*

**Key words:** Morocco, Neotectonics, Palaeoelevation, Fluvial Geomorphology, Uplift

### Introduction

The High Atlas Mountains are a Cenozoic mountain belt trending ENE-WSW for over 2000 km from Morocco in the west to Tunisia in the east, and have the most significant relief in North Africa rising to over 4000 m in elevation. Alpine shortening resulted in the inversion and uplift of Mesozoic rift basins sometime between the Late Eocene and Quaternary (e.g., Frizon de Lamotte et al., 2000; Balestreri et al., 2009), developing a bivergent mountain chain.

However, the timing of topographic growth of the High Atlas Mountains of Morocco has proved to be a contentious topic. Several lines of evidence point to two phases of surface uplift. Deposition of two distinct conglomeratic units within the Ouarzazate foreland basin (Fig. 1) have been related to phases of active uplift triggering enhanced erosion in the hinterland (e.g., El Harfi et al., 2001) with intervening lacustrine facies being interpreted by El Harfi et al. (2001) as evidence for a period of tectonic quiescence during the Middle Miocene. Similarly, the regional unconformities of the late Eocene/Oligocene (~ 35 – 25 Ma) and early Pliocene (~ 5 – 1 Ma) have been attributed to pulses of deformation separated by tectonic quiescence (Fraissinet et al., 1988). In contrast, apatite fission-track analyses (Missenard et al., 2006; Barbero et al., 2007; Balestrieri et al., 2009) have constrained the onset of exhumation to the late Oligocene (~27 Ma). While continuous tectonic activity and structural shortening throughout the Oligocene to Pliocene has been deduced by Teson and Teixell (2008) using syn-sedimentary relationships in the fold and thrust belt, all suggesting a single continuous deformation event.

Here we investigate the palaeoelevation of the High Atlas from the Middle/Late Miocene to the present using

dual stable isotope ratios (Horton and Oze, 2012) from lacustrine carbonates deposited in the Ouarzazate Basin to investigate when topography was generated in the High Atlas Mountains prior to the Plio-Quaternary. We then address the magnitude and rate of Plio-Quaternary uplift using fluvial geomorphology of rivers flowing southwards into the Ouarzazate Basin.

### Ouarzazate Basin

The Ouarzazate Basin (Fig. 1) developed as the southern foreland basin to the High Atlas Mountains in the Cenozoic and contains a comprehensive record of sedimentation from that time (Teson et al., 2010). From 20 Ma to ~ 0.5 Ma, the basin was characterized by endorheic drainage and continental sedimentation in alluvial fan and palustrine environments (El Harfi et al., 2001). The ~ 1000 m sedimentary fill of the basin is tripartite, with Middle Miocene conglomerates (Aït Ouglif Fm.), Middle-Late Miocene lacustrine limestones, marls and gypsum layers, and Plio-Quaternary conglomerates (Aït Ibrirn and Aït Seddrat members of the Aït Kandoula Fm., respectively (El Harfi et al., 2001). Magnetostratigraphy of the succession (Benammi et al., 1996; Teson et al., 2010) demonstrates that the deposition of lacustrine facies of the Aït Ibrirn Mb. took place from ~13.5 – 5 Ma. Therefore, the carbon and oxygen isotope composition of these sediments can provide a record of the mean catchment elevation for Ouarzazate Basin lakes in the Middle-Late Miocene. At ~0.5 Ma the headward erosion of the Draa River captured the drainage of the Ouarzazate Basin resulting in incision of the earlier deposits. The present day drainage pattern is dominated by the Dades-Draa River system and associated tributaries that drain southwards across the Southern Atlas Thrust front, exiting the basin south of the town of Ouarzazate (Fig. 1).

### Miocene Palaeoelevation



Lake sediments can serve as powerful archives of palaeoclimatic and palaeoenvironmental information, including palaeotopography (Talbot, 1990). Carbonate sediments precipitated in lakes typically form in chemical equilibrium with lake water, reflecting the input of surface precipitation from the surrounding catchment, because the oxygen isotopic composition of modern precipitation exhibits a well-documented relationship with surface elevation (Bowen and Wilkinson, 2002). However, this original isotopic composition can be subsequently modified by evaporation, masking the original elevation signal. Comparisons of lake carbonate  $\delta^{13}\text{C}$  and  $\delta^{18}\text{O}$  with the composition of lake inflow show that a strong covariance exists between the two isotope ratios (Horton and Oze, 2012). This covariant relationship has a consistent slope (Horton et al., 2015) allowing combined  $\delta^{13}\text{C}$  and  $\delta^{18}\text{O}$  measurements to be used to correct for evaporative enrichment. The resulting parameter,

referred to as  $^{13}\text{C}$ -excess, is strongly correlated to lake catchment elevation (Horton and Oze, 2012).

We sampled lacustrine carbonates from five sections of the Ait Ibrirn Mb. in the Ouarzazate Basin, spanning 7.5 Myrs for palaeoelevation estimates. Two sections exhibit relatively constant isotope ratios, with no stratigraphically coherent shifts in either  $\delta^{13}\text{C}$  or  $\delta^{18}\text{O}$ . By contrast, the other three sections exhibit a  $\sim 3\text{‰}$  negative shift in both  $\delta^{13}\text{C}$  and  $\delta^{18}\text{O}$  (Fig. 2). Determining catchment elevation from  $^{13}\text{C}$ -excess first requires accounting for the impacts of other factors known to influence  $\delta^{18}\text{O}$ ; latitude, continentality and temperature of carbonate precipitation. We apply normalizations of  $-2.9\text{‰}$  and  $0.6\text{‰}$  to  $\delta^{18}\text{O}$  for the modern latitude of  $31^\circ\text{N}$  and coastal distance of 300 km, respectively. Accounting for lake temperature is more difficult, due to the absence of independent regional temperature estimates; we therefore apply a range of possible lake

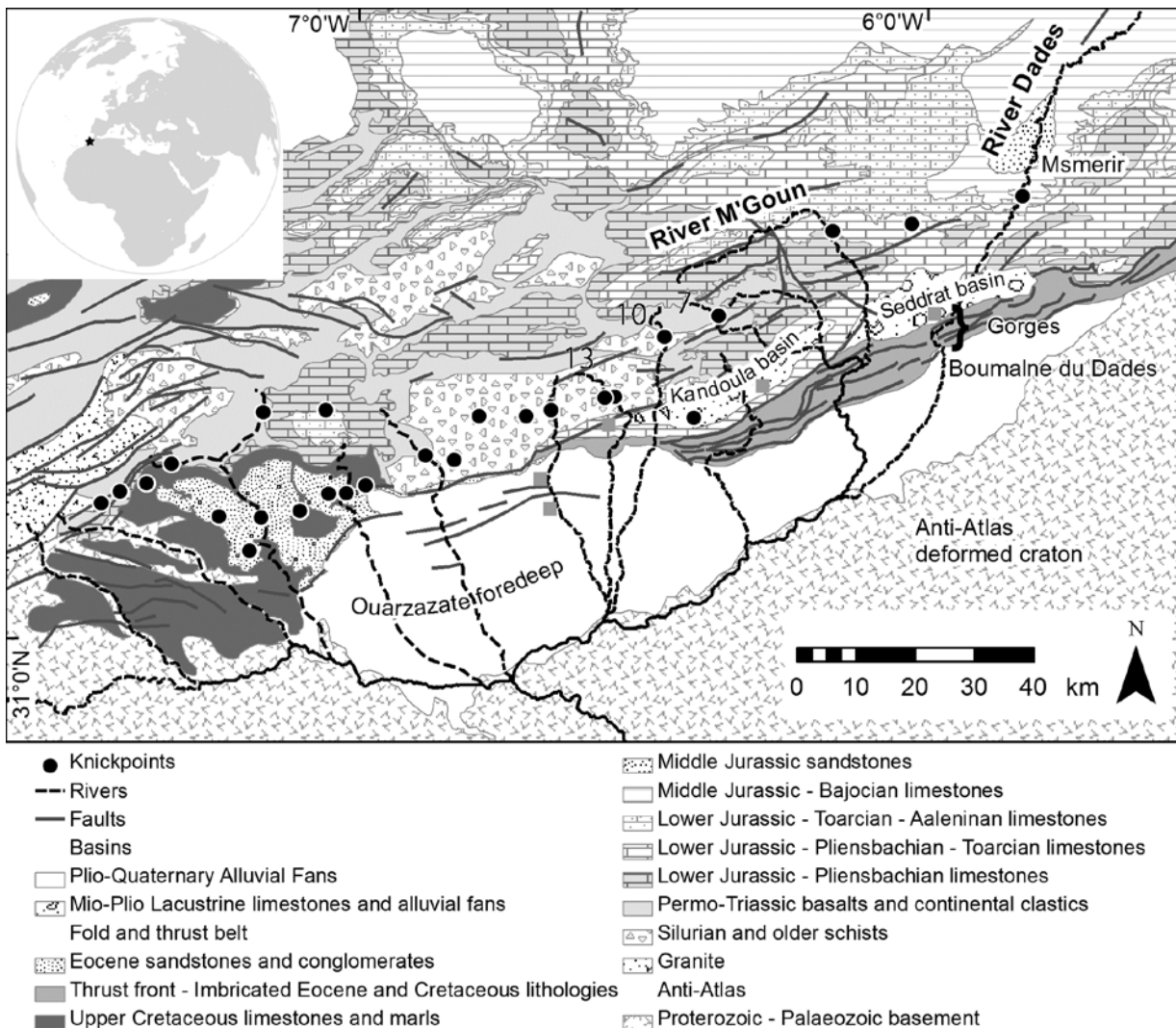


Fig. 1 Simplified geological map of the Ouarzazate region showing the main geological units present, key locations, trunk rivers and (where present) knickpoints (black circles). Rivers 7, 10 and 13 shown in Fig. 2 are also indicated. Light grey squares indicate locations sampled for isotope analysis (modified from Boulton et al., 2014).



water temperatures of 20-35°C, resulting in normalizations of -1.0 to 1.9 ‰ for  $\delta^{18}\text{O}$  and -0.7 to 1.3 ‰ for  $\delta^{13}\text{C}$ . As temperature is a second-order effect on lacustrine carbonate  $\delta^{18}\text{O}$ , this imposes an additional uncertainty to the elevation estimates of only  $\sim\pm 150$  m. After correcting for these effects on our data, these sections produce catchment elevation estimates of  $1.2 \pm 0.5$  km for the Middle-Late Miocene, suggesting that surface elevation was relatively stable for the  $\sim 7.5$  Myr that these data span.

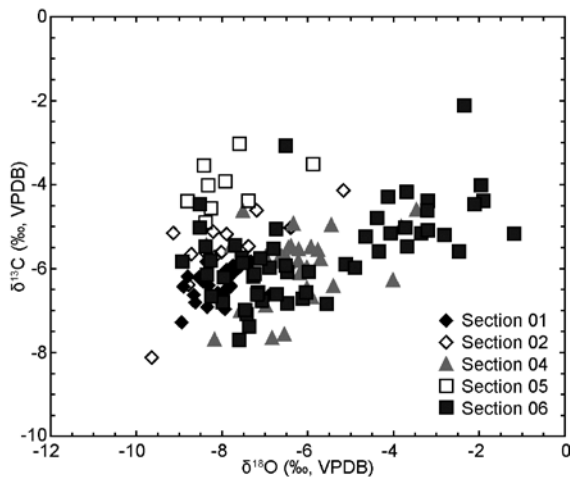


Fig. 2. Cross-plot showing  $\delta^{18}\text{O}$  versus  $\delta^{13}\text{C}$  measurements from lacustrine carbonates in the Ouarzazate Basin.

#### Plio-Quaternary Uplift

Modern mean elevation of the High Atlas Mountains north of the sampled locations is  $\sim 2300$  m and ranges from 1800 – 2600 m, further suggesting that  $\sim 1000$  m of surface uplift has occurred in the post-Miocene period. Similar magnitudes of surface uplift have also been proposed for Middle Atlas Mountains by Babault et al., (2008) who recognised Messinian marine deposits at 1200 m elevation and Pastor et al., (2015) using reconstructed river profiles indicating up to 1000 m of rock uplift.

We quantitatively analysed the long profiles of 32 rivers that drain southwards across the Southern Atlas Fault (SAF) into the Ouarzazate Basin (Boulton et al., 2014). The majority of the rivers exhibit at least one knickpoint upstream of the thrust front (Fig. 3). The height of the knickpoints varies from 100 – 1300 m, with calculated incision at the range bounding fault ranging from 80-1040 m (Fig. 3). In map view, knickpoint locations generally plot along sub-parallel lines and there are no obvious relationships with lithological units for knickpoints exhibiting slope-break morphology. Channel reaches below slope-break knickpoints have higher mean concavities (0.76) than above the knickpoint. This observation combined with a lithological or river-capture origin for the knickpoints having been ruled out indicates that an increase in uplift rate along a planar fault zone during the Plio-Quaternary caused the initiation of the transient response (i.e., knickpoint

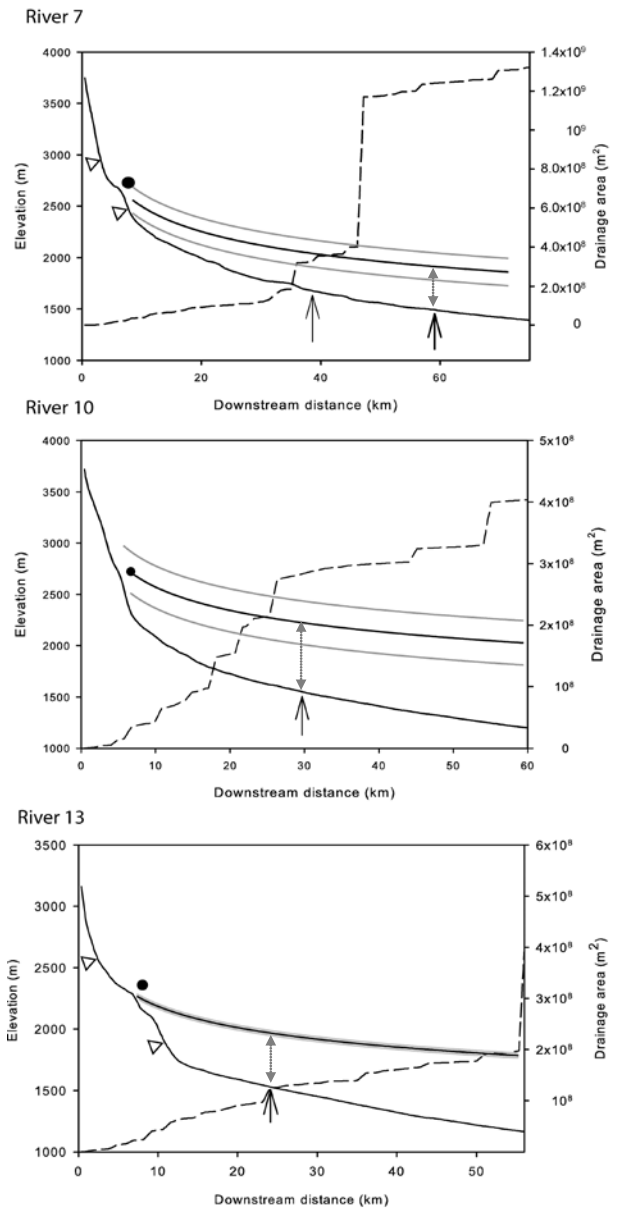


Fig. 3. Representative examples of river profiles (solid lines) that exhibit knickpoints (circles) and segmented power-law scaling characteristic of slope-break knickpoints, each river is labelled with a number that corresponds to those shown in figure 1. Reconstructed relict profiles (with 1 sigma error), magnitude of range front incision (grey dashed arrow) and position of the frontal thrust (black arrow) are also shown, modified from Boulton et al. (2014).

formation) to a change in base-level observed in the river profiles.

The knickpoint elevation and magnitude of incision indicated by the river profile analysis indicates  $\sim 1000$  m of surface uplift has taken place in the Plio-Quaternary, supporting previous estimates and in accordance with Pre-Pliocene estimates of palaeoelevation.



## Discussion and Conclusions

We show that the mean elevation of the catchments feeding the Tortonian Ouarzazate Basin lake system was ~ 1000 m lower than the present day mean elevation of the same region, consistent with estimates of rock uplift determined from river profile analysis of rivers flowing across the Southern Atlas Fault system (Boulton et al., 2014) and previous estimates for the magnitude of Quaternary surface uplift in the Middle Atlas (Babault et al., 2008). This result supports models for a two-phase development for the topography of the High Atlas. The sections measured span > 8 Myr during the Late Miocene, yet the derived paleoelevations are similar for each section, suggesting either that any uplift during this time period was balanced by denudation, or it was a period of tectonic quiescence. Both interpretations imply that tectonic deformation was not significantly changing the mean elevation of the mountain range; during the Late Miocene period and thus supporting increased rates of uplift during the Quaternary. This pulse of uplift is recorded in the fluvial systems through knickpoint generation and landscape rejuvenation as a response to reactivation of crustal-scale reverse faults. Offset Quaternary terraces in the Ouarzazate basin also suggest that active thrusting is occurring at the thrust front and may have stepped forward into the foreland basin (i.e., Arboleya et al., 2008; Pastor et al., 2012a). Therefore, although current levels of seismicity along the SAF are low, the evidence of Quaternary active faulting combined with historical events (i.e., the 1960 Agadir earthquake) that are generally < 70 km in depth (Medina and Cherkaoui, 1991) suggests that the seismic hazard along the SAF may be higher than previously recognised.

**Acknowledgements** We thank National Geographic and the Royal Geographical Society (with IBG) for providing the funding for this research, and Ramon Arrowsmith for constructive comments on this extended abstract.

## References

- Arboleya, M-L. et al., 2008, Timing and nature of Quaternary fluvial incision in the Ouarzazate foreland basin, Morocco: *Journal of the Geological Society* [London], 165, p. 1059-1073.
- Babault, J. et al., 2008. A late Cenozoic age for long-wavelength surface uplift of the Atlas Mountains of Morocco. *Terra Nova*, 20(2), p.102-107.
- Balestrieri, M.L. et al., 2009. Neogene exhumation of the Marrakech High Atlas (Morocco) recorded by apatite fission-track analysis. *Terra Nova*, 21(2), p.75-82.
- Barbero, L. et al., 2007. Jurassic-to-present thermal history of the central High Atlas (Morocco) assessed by low-temperature thermochronology. *Terra Nova*, 19(1), p.58-64.
- Benammi, M. et al., 1996. Magnetostratigraphy and paleontology of Ait Kandoula basin (High Atlas, Morocco) and the African-European late Miocene terrestrial fauna exchanges. *Earth and Planetary Science Letters*, 145(1-4), p.15-29.
- Boulton, S.J., Stokes, M. & Mather, A.E., 2014. Transient fluvial incision as an indicator of active faulting and Plio-Quaternary uplift of the Moroccan High Atlas. *Tectonophysics*, 633, p. 16-33.
- Bowen, G. J., and Wilkinson, B., 2002, Spatial distribution of  $\delta^{18}O$  in meteoric precipitation. *Geology*, v. 30, p. 315-318.
- El Harfi, a. et al., 2001. Cenozoic sedimentary dynamics of the Ouarzazate foreland basin (Central High Atlas Mountains, Morocco). *International Journal of Earth Sciences*, 90(2), p.393-411.
- Frizzon de Lamotte, D. et al., 2009. Mesozoic and Cenozoic vertical movements in the Atlas system (Algeria, Morocco, Tunisia): An overview. *Tectonophysics*, 475(1), p.9-28. Available at: <http://dx.doi.org/10.1016/j.tecto.2008.10.024>.
- Horton, T. W., and Oze, C., 2012, Are two elements better than one? Dual isotope-ratio detrending of evaporative effects on lake carbonate paleoelevation proxies. *Geochemistry, Geophysics, Geosystems*, 13, p. Q0AK05.
- Medina, F., Cherkaoui, T-E., 1991. Focal mechanisms of the Atlas earthquakes, and tectonic implications. *Geologische Rundschau*, 80, p. 639 - 648.
- Missenard, Y. et al., 2006. Crustal versus asthenospheric origin of relief of the Atlas mountains of Morocco. *Journal of Geophysical Research: Solid Earth*, 111(3), p.1-13.
- Pastor, A. et al., 2015. Extracting dynamic topography from river profiles and cosmogenic nuclide geochronology in the Middle Atlas and the High Plateaus of Morocco. *Tectonophysics*, 663, p.95-109.
- Talbot, M. R., 1990, A review of the paleohydrological interpretation of carbon and oxygen isotopic ratios in primary lacustrine carbonates. *Chemical Geology*, 80, p. 261-279.
- Tesón, E. & Teixell, A., 2008. Sequence of thrusting and syntectonic sedimentation in the eastern Sub-Atlas thrust belt (Dadès and Mgoun valleys, Morocco). *International Journal of Earth Sciences*, 97(1), p.103-113.
- Tesón, E. et al., 2010. Magnetostratigraphy of the Ouarzazate Basin: Implications for the timing of deformation and mountain building in the High Atlas Mountains of Morocco. *Geodinamica Acta*, 23(4), p.151-165.



## Paleoseismic assessment of multi-mass transport deposit signatures preserved within the deposits of glacial Lake Ojibway, northwestern Quebec, Canada

Brooks, Gregory, R. (1)

(1) Geological Survey of Canada, Natural Resources Canada, 601 Booth Street, Ottawa, Ontario, Canada, K1A0E8. Email greg.brooks@canada.ca.

**Abstract:** Eight event horizons, consisting of 74 mass transport deposits (MTDs), were mapped using high-density sub-bottom profiles surveyed at Lac Dasserat, northwestern Quebec, Canada. Five of the event horizons (H-D) are intercalated within glaciolacustrine deposits of glacial Lake Ojibway, the other three (C-A) are at the interface of the glaciolacustrine-lacustrine deposits. Event horizons H, G and E exhibit are interpreted to be the products of paleoearthquakes, respectively, based on the relative strength of the multi-MTD signatures, the lack of likely alternative aseismic interpretations, and the occurrences of similarly-aged disturbed deposits regionally in NW Quebec-NE Ontario.

**Key words:** paleoearthquakes, mass transport deposits, varves, glacial Lake Ojibway, eastern Canada

### INTRODUCTION

Large areas of central and eastern Canada were inundated for periods up to several thousand years by large glacial lakes that evolved during the recession of the Laurentide Ice Sheet (LIS). Thick accumulations of glaciolacustrine deposits aggraded within these water bodies that are well preserved within the basins of modern lakes. Submarine mass transport deposits (MTDs) can be present within glaciolacustrine or early post-glacial lacustrine deposits and some have been inferred to be evidence of paleoearthquakes (Adams, 1982; Shilts et al., 1992; Ouellet, 1997; Doughty et al., 2014). Some of the latter MTDs may be evidence of deglacial seismicity that is related to crustal unloading associated with the retreat of the LIS. Although examples of late glacial seismicity are described by a number of studies in Fennoscandia, there is a lack of similar well-documented examples from eastern Canada.

Lac Dasserat is a moderately-sized lake covering ~28 km<sup>2</sup> that is located in NW Quebec, about 425 km NW of Ottawa, Ontario (Fig. 1). The presence of multiple MTDs within the lake was initially discovered within sub-bottom acoustic profile (SAP) returns collected in 2010 in support of an environmental investigation of metal contamination from a nearby former mining site. This extended abstract assesses the possible seismogenic origin of three event horizons that exhibit multi-MTD signatures and which are intercalated with glaciolacustrine deposits of glacial Lake Ojibway.

### STUDY AREA

Lac Dasserat is up to 12.4 km long, 6.5 km wide and locally 17 m deep. Typical of many lakes on the Canadian Shield, the lake is irregular in shape and bathymetry, reflecting the relief of the underlying bedrock. The local surficial geology is mapped predominately as deep

water glaciolacustrine sediments with numerous outcrops of bedrock, pockets of glacial deposits, and wetlands. The lake is located within an intracratonic setting ~150 km north of the belt of concentrated historical seismicity of the Western Quebec Seismic Zone (WQSZ), which encompasses parts of SW Quebec, SE Ontario, and N New York State (Fig.1). The 1935 Temiskaming earthquake ( $M$  6.1) is the most significant to occur historically within the northern portion of the WQSZ; its epicenter was located ~165 km to the south of Lac Dasserat (Lamontagne et al. 2008).

Lac Dasserat is situated within a large area of NW Quebec-NE Ontario that was inundated by a glacial lake impounded against the retreating LIS to the north. This water body, referred to at different stages as lakes Barlow, Barlow-Ojibway, or Ojibway, evolved within the isostatically-depressed landscape of the Timiskaming and Hudson Bay basins between about 11.0 and 8.4 <sup>14</sup>C

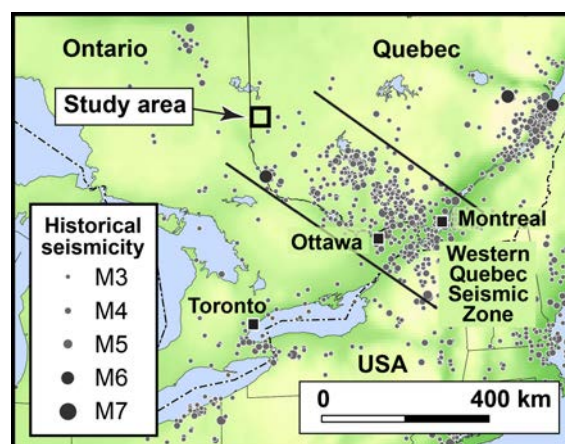


Fig. 1: Map showing the location of the Lac Dasserat study area, Quebec, and historical seismicity of the Western Quebec Seismic Zone, eastern Canada (Source: Natural Resources Canada).

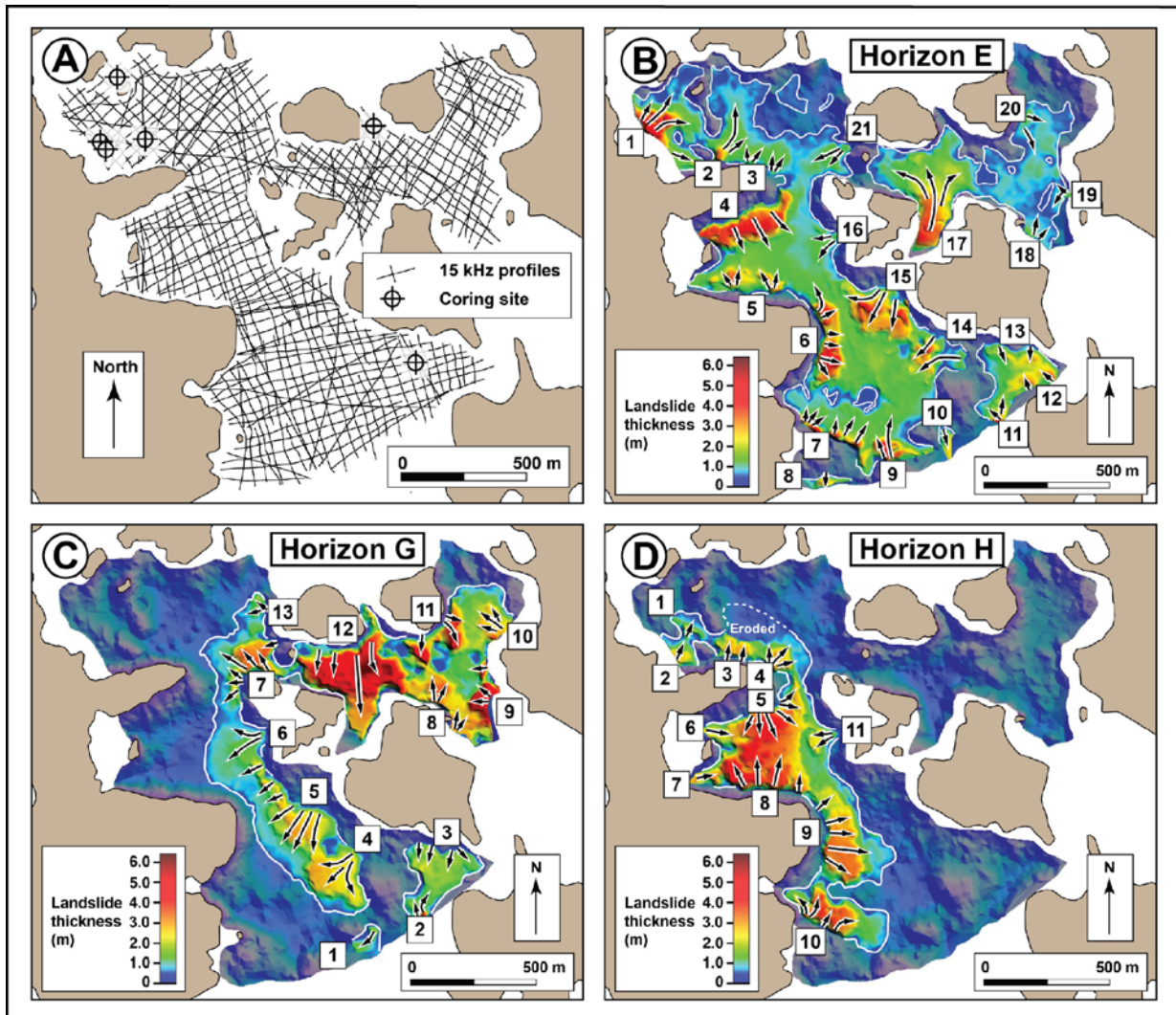


Fig. 2: Maps of the Lac Dasserat study area depicting A) the grid of 15 kHz profile lines used to compile the event horizon maps and the six coring sites, and in B), C) and D) the lateral extent and thickness of the mass transport deposits (MTDs) within event horizons E, G and H (stratigraphically youngest to oldest), respectively. All three event horizons are intercalated within glaciolacustrine deposits of glacial Lake Ojibway. The arrows on the maps represent the interpreted direction of mass transport flow. The MTDs interpreted to originate from separate source areas are numbered on each map. The majority of the source areas are located above the modern water level of Lac Dasserat. Not shown are event horizon D, which overlies horizon E, or horizon F situated between horizons E and G. Horizons D and F consist of single and paired MTDs, respectively.

cal BP (Vincent and Hardy 1979; Veillette 1994). The succession of lake stages ended when glacial Lake Ojibway drained catastrophically northwards into the James and Hudson basins through a breach in the LIS. For simplicity, the glaciolacustrine deposits in Lac Dasserat are referred to as glacial Lake Ojibway deposits.

## METHODOLOGY

The SAP survey at Lac Dasserat was undertaken between September 9 and 17, 2014, using a Knudsen CHIRP Pinger SBP™ echosounder system. Profiling data was collected using low frequency (LF) 15 or 3.5 kHz and high frequency 200 kHz transducers. About 144 line-km of profiles were collected within a dense sampling grid spaced mostly 40 to 60 m apart (Fig. 2A). On each 15 kHz profile, the top and bottom surfaces of the MTDs

were picked within the upper portion of the lake stratigraphy to map and identify the stratigraphic levels of the MTD occurrences. These stratigraphic levels defined eight event horizons composed of one to multiple MTDs, reflecting the stratigraphic distribution of the MTDs. The MTDs within a common event horizon are inferred to have occurred synchronously within the resolution of the SAP returns. Maps were compiled that depict the lateral extent and thickness of the MTDs occurring within each event horizon.

Six locations within the surveyed area were cored using a Livingston piston corer from an ice cover in March 2015 to recover glaciolacustrine deposits overlying or interbedded with the event horizons (Fig. 2A). The thicknesses of 548 rhythmic laminations (couplets) within a composite sequence of the recovered



glaciolacustrine deposits were measured on full-scale, high-contrast, radiograph images of the cores. The thickness pattern of the couplets were correlated to the regional Timiskaming varve series, which is composed of about 2100 rhythmites that have been interpreted to be annual varves and dated tentatively as accumulating between  $10,570 \pm 200$  and  $8470 \pm 200$   $^{14}\text{C}$  cal BP (Antevs, 1925; 1928; Breckenridge et al., 2012). This correlation allows varve numbers (i.e., varve ages) relative to the regional series to be assigned to the individual measured varves in the Lac Dasserat cores. Possible error in the numbering of the Dasserat varves relative to the Timiskaming varve series is estimated to be  $\pm 2$  varves.

## Results

Mapping of the upper portion of the sub-bottom identified eight event horizons composed of an interpreted 74 mass transport deposits (MTDs). Forty eight of the MTDs are within five event horizons (H to D from stratigraphically oldest to youngest) that are intercalated between glaciolacustrine deposits. The remaining MTDs form three stacked horizons (C to A) at the interface of the glaciolacustrine-lacustrine deposits; these horizons are not discussed in this paper. No MTDs are present within the postglacial lacustrine deposits.

Horizon E contains 21 MTDs that are distributed widely throughout the study area (Fig. 2B). Many of the deposits are coalesced and the lateral boundaries are indistinguishable in the SAP returns. Overall, horizon E exhibits a strong multi-MTD signature relative to the other event horizons. Event horizons H and G are composed of 11 and 13 MTDs, respectively (Fig. 2C and D). The MTDs in horizon H are located predominately on the western portion of the study area, while those of horizon G are located in the central and eastern portions. Horizons H and G both represent moderately-strong multi-MTD signatures relative to the strong signature of horizon E. In contrast, horizon D is composed of a pair of small MTDs within the southern and northern portions of the study area, while horizon F consists of a single MTD located in the northwestern area that is the thickest and most laterally extensive MTD within the study area. Both of the single and paired MTDs of these two horizons represent minor MTD signatures within the study area.

The correlation of the Dasserat varves to the Timiskaming varve series indicates that the oldest and youngest measured varves span varve years (vyr) 1039 to 1637. An additional 13 varve numbers were assigned to couplets that were too thin and/or deformed to be measured, extending the series to vyr 1650. Based on the varve year (less one year) of the couplet(s) immediately overlying a given event horizon in one or more cores, horizons H, G, F and E are interpreted to have formed in vyr 1268 1324, 1364, and 1483, respectively. Horizon D was not penetrated by any of the cores, but it formed between vyr 1484 and 1650, from its

stratigraphic position in the SAP returns between horizon E and the top of the varve sequence.

## Discussion

Occurrences of post-glacial multi-MTD event horizons have been interpreted to be evidence of paleoearthquakes, based on analogous MTD signatures from historical earthquakes in the same lake basin (Schnellman et al., 2002; Strasser et al., 2013). There is no historical analogue at Lac Dasserat because of the absence of post-glacial MTDs in the lake and its location outside of the WQSZ. Nevertheless, the strong and moderately-strong multi-MTD signatures of horizons E, and H and G, respectively, could be evidence of paleoseismicity. This inference is circumstantial, however, and requires consideration of possible aseismic mechanisms as well as supporting evidence outside of Lac Dasserat to be better substantiated. Neither horizons F and D, consisting of single and paired MTDs, respectively, are considered to be evidence of paleoseismicity, based on available data.

With respect to aseismic mechanisms, these are considered from the context of a large glacial lake, as horizons E, G and H aggraded within glacial Lake Ojibway. The setting is assumed to be a deep water, distal depositional environment; a deep water location is inferred because water depths in excess of 30 m are considered necessary for varves to form in glacial Lake Ojibway (Veillette, 1994), and a distal location with respect to the sediment source is interpolated from the fine clay-silt texture of the varve sediments. The grounding of icebergs and the oversteepening-overloading of slopes from sedimentation could account for isolated failures in the study area, but both seem unlikely to explain the occurrences and lateral extent of the observed multi-MTD signatures. In particular, the near absence of dropstones in the varve deposits implies that few icebergs were in the study area during the interval of interest. The distal location precludes high localized sedimentation from a nearby sediment source. Similarly, both wind-generated waves and rapid drawdown of the lake level also are considered to be unlikely mechanisms. While undoubtedly there were significant wind storms on glacial Lake Ojibway, the influence of wave action on the lake bed would be limited in deep water conditions. There are no known rapid drawdown events of glacial Lake Ojibway during the time interval of interest. Overall none of the aseismic mechanisms are considered to represent good explanations for the occurrence of multi-MTD signatures of horizons E, G and H.

In summary logs of the varve measurement sites, Antevs (1925; 1928) and Hughes (1959) recorded the presence of zones of 'disturbed' varves interbedded within sequences of numbered varves of the Timiskaming varve series. The number of the lowest couplet (less one year) in the immediately overlying varve sequence provides a minimum age for the disturbed deposit. Also,



Breckenridge et al. (Fig. 5, 2012) report the presence of deformed varves in a core collected from Lac Duparquet. From these records, disturbed deposits with minimum ages of *vyr* 1483-1489, 1323 and 1325, and 1263 are present at nine, two and one sites, respectively, located 32 to 135 km from the study area. Also, from a varve study in NW Quebec-NE Ontario, Adams (1982) mentions that the best-developed synchronous deformation of varves at a number of sites happened in *vyr* 1487. Because of the tight chronological control provided by the varves, it is reasonable to assume that these disturbed or deformed deposits are synchronous with the nearly identical varve ages of horizon E (*vyr* 1483), G (*vyr* 1324) or H (*vyr* 1267). It thus follows that the failures within each group are the product of a common trigger. Although the varves at all of the sites accumulated within glacial Lake Ojibway, as opposed to independently in detached lake basins, a paleoearthquake mechanism best accounts for the presence of commonly-aged MTD/disturbed deposits at the widely-spaced locations. The case is compelling with the numerous sites of the *vyr* 1483-1489 group (including horizon E), although less, but still notably with the fewer sites of the two older groups (containing horizons G or H), especially considering that Antevs, Hughes and Breckenridge et al. were interested in studying varve sequences *per se* and not disturbed deposits. Horizons E, G and H, thus, are interpreted to be evidence of paleoearthquakes, but with high, medium and medium levels of interpretative confidence, respectively, in consideration of the relative strength of the multi-MTD signatures, the relative correlation to other disturbed deposits of similar age in the region, and the lack of likely alternative aseismic mechanisms. The paleoseismic interpretation of horizon E concurs with that of Adams (1982, 1989) for the synchronous deformation that he identified in *vyr* 1487.

The stratigraphic position of horizons E, G and H reveal that the interpreted paleoearthquakes occurred during deglaciation when glacial Lake Ojibway was impounded behind the LIS. As such, these paleoearthquakes may represent eastern Canadian examples of seismicity associated with relatively rapid crustal unloading during deglaciation, especially as Lac Dasserat is located ~150 km north of the historical seismicity of the WQSZ. Of note, there may be additional paleoseismic evidence in Lac Dasserat; event horizon B, situated at the glaciolacustrine-lacustrine interface, also has a strong multi-MTD signature, and there are unmapped, deeper MTDs in Lac Dasserat.

## Conclusions

The multi-MTD signatures of event horizons E, G and H are interpreted to have been triggered by paleoearthquakes reflecting the relative strength of the multi-MTD signatures, the regional occurrence of similarly-aged disturbed deposits, as well as the lack of alternative aseismic triggering mechanisms.

The three interpreted paleoearthquakes occurred during regional deglaciation when glacial Lake Ojibway was impounded behind the LIS. They may be evidence of seismicity caused by crustal unloading associated with the retreat of the LIS.

**Acknowledgements:** Comments from Hazen Russell are sincerely appreciated. I am most gratefully to Alain Grenier (GSC) for assistance in the field. This research was supported by Earth Sciences Sector (ESS), Natural Resources Canada and the Nuclear Waste Management Organization. This paper represents ESS Contribution 20150436.

## References

- Adams, J. (1982). Deformed lake sediments record prehistoric earthquakes during the deglaciation of the Canadian Shield (abstract): *EOS, Transactions, American Geophysical Union* 63, 436.
- Adams, J. (1989). Postglacial faulting in eastern Canada: Nature, origin and seismic hazard implications. *Tectonophysics* 163, 323-331.
- Antevs, E. (1925). Retreat of the last ice-sheet in eastern Canada. *Geological Survey of Canada Memoir* 146, 142 p.
- Antevs, E. (1928). *The last glaciation with reference to the retreat in northeastern North America*. American Geographical Society Research Series No. 17, New York, 292 p.
- Breckenridge, A., T.V. Lowell, J.S. Stroup, & G. Evans, (2012). A review and analysis of varve thickness records from glacial Lake Ojibway (Ontario and Quebec, Canada). *Quaternary International* 260, 43-54.
- Doughty, M., N. Eyles, C.H. Eyles, K. Wallace, & J.L. Boyce, (2014). Lake sediments as natural seismographs: Earthquake-related deformations (seismites) in central Canadian lakes: *Sedimentary Geology*, 313, 45-67.
- Hughes, O.L. (1959). *Surficial geology of Smooth Rock and Iroquois Falls map areas, Cochrane District, Ontario*. Department of Geology, University of Kansas, unpublished Ph.D. thesis, 190 p.
- Lamontagne, M., S. Halchuk, J.F. Cassidy, & G.C. Rogers, (2008). Significant Canadian earthquakes of the period 1600–2006. *Seismological Research Letters* 79, 211-223.
- Quellet, M. (1997). Lake sediments and Holocene seismic hazard assessment within the St. Lawrence Valley, Quebec. *Geological Society of America Bulletin* 109, 631-642.
- Schnellmann, M., F.S. Anselmetti, D. Giardini, J.A. McKenzie & S.N. Ward, (2002). Prehistoric earthquake history revealed by lacustrine slump deposits. *Geology* 30, 1131–1134.
- Shilts, W.W., M. Rappol, A. Blais, (1992). Evidence of late and postglacial seismic activity in the Témiscouata-Madawaska Valley, Quebec-New Brunswick, Canada. *Canadian Journal of Earth Sciences* 29, 1043-1069.
- Strasser, M., K. Monecke, M. Schnellmann & F.S. Anselmetti, (2013). Lake sediments as natural seismographs: A compiled record of Late Quaternary earthquakes in Central Switzerland and its implication for Alpine deformation. *Sedimentology* 60, 319–341.
- Veillette, J.J. (1994). Evolution and paleohydrology of glacial Lakes Barlow and Ojibway. *Quaternary Science Reviews* 13, 945-971.
- Vincent, J.-S. & L. Hardy, (1979). The evolution of glacial lakes Barlow and Ojibway, Quebec and Ontario. *Geological Survey of Canada Bulletin* 316, 18 p.



## Late Quaternary Offset of Alluvial Fan Surfaces along the Central Sierra Madre Fault, Southern California

Reed J. Burgette (1), Austin M. Hanson (1), Katherine M. Scharer (2), Nikolas Midttun (2)

- (1) Department of Geological Sciences, New Mexico State University, Las Cruces, NM 88003 USA. Email: burgette@nmsu.edu  
(2) U.S. Geological Survey Pasadena Field Office, 525 South Wilson Ave., Pasadena, CA USA.

**Abstract:** The Sierra Madre Fault is a reverse fault system along the southern flank of the San Gabriel Mountains near Los Angeles, California. This study focuses on the Central Sierra Madre Fault (CSMF) to provide numeric dating on surfaces with ages previously estimated from soil development alone. We have refined previous geomorphic mapping conducted in the western portion of the CSMF near Pasadena, CA, with the aid of new lidar data. This progress report focuses on our geochronology strategy employed in collecting samples and interpreting data to determine a robust suite of terrace surface ages. Sample sites for terrestrial cosmogenic nuclide and luminescence dating techniques were selected to be redundant and to be validated through relative geomorphic relationships between inset terrace levels. Additional sample sites were selected to evaluate the post-abandonment histories of terrace surfaces. We will combine lidar-derived displacement data with surface ages to estimate slip rates for the CSMF.

**Key words:** Sierra Madre fault, slip rate, terrestrial cosmogenic nuclide dating, luminescence dating, lidar.

### INTRODUCTION

The Sierra Madre fault (SMF) system juxtaposes the San Gabriel Mountains against a series of basins north of the broader Los Angeles basin (Crook et al., 1987; Dolan et al., 1995; Rubin et al., 1998). This study focuses on the Central Sierra Madre fault (CSMF), the longest (85 km) of the four SMF segments, and one of the least studied with modern Quaternary geochronological techniques (Fig. 1). Our understanding of the Quaternary history of the

CSMF range front builds on previous investigations by Crook et al. (1987) and McFadden (1982). Terrace ages in those studies were estimated from soil development and limited radiocarbon dates, and thus have wide uncertainties. McFadden (1982) estimated the ages of two of the lower terraces in Arroyo Seco area as 13-4 ka and 70-13 ka based on regional soil development correlation. The suites of terraces on which we have focused were mapped as Qal2 and Qal3 by Crook et al., with age estimates of 11-2 ka and 200-11 ka,

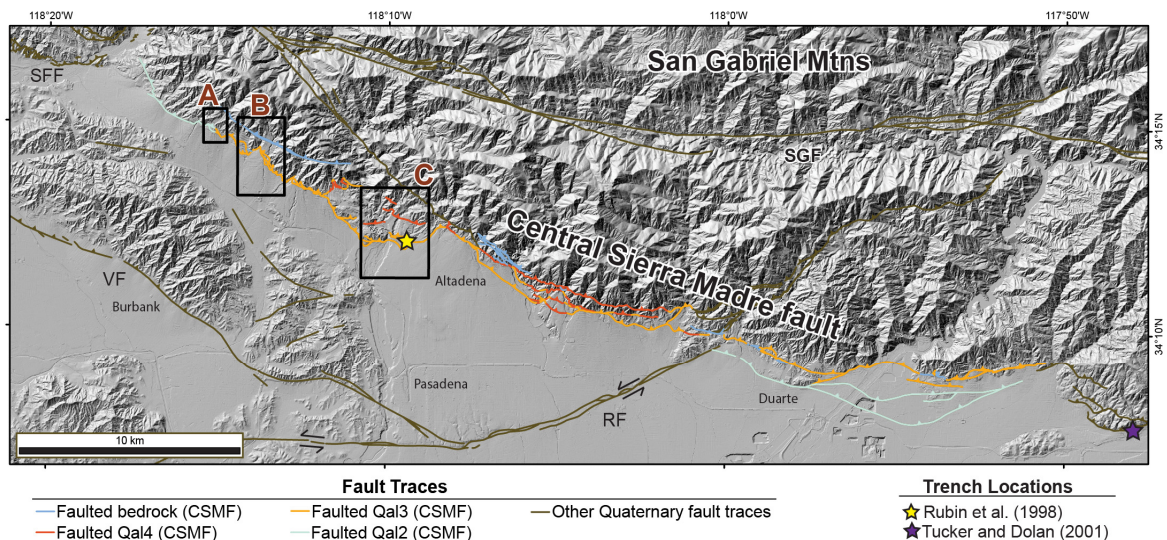


Fig. 1: Central Sierra Madre fault map. Fault traces are from the USGS Fault and Fold Database (USGS & CGS, 2006). Faulted CSMF units are based on mapping and nomenclature of Crook et al. (1987), with Qal4 being the oldest alluvial unit. Labeled faults include: San Fernando fault (SFF), Verdugo fault (VF), Raymond fault (RF), and the San Gabriel fault (SGF). Labeled boxes show our areas of focus: A, Dunsmore Canyon; B, Pickens Canyon; and C, Arroyo Seco (Fig. 2). Shaded relief basemap derived from USGS 1/3 arc second digital elevation model.



respectively. To refine slip rate estimates for the CSMF, this project includes (1) detailed mapping of faulted terraces along the range front and (2) newly-obtained numeric ages for the terraces using cosmogenic and luminescence techniques.

*Surface correlation and offset estimation*

We focused our investigation on fans at the mouths of three catchments along the western portion of the CSMF (Fig. 1). We examined and refined interpretations of previous mapping with field observations aided by 3 to 0.5 m resolution lidar-derived digital elevation models. Based on soil development and surface characteristics, as well as examination of terrace elevations, we subdivided the Qal3 terrace of Crook et al. (1987) to reflect the full range of distinct geomorphic surfaces present in these catchments. The best area in terms of terrace preservation is in Arroyo Seco (Fig. 1), where we found up to four distinct terrace levels within the Qal3

map unit in some catchments (Fig. 2). We are focusing our effort on estimating slip rates for fault strands that cut dateable surfaces that are preserved on both sides of the faults. To obtain the displacement, we have analyzed swath profiles extracted from lidar bare-earth DEMs in a series of 2 m-wide subswaths (Fig. 2). Dip-slip displacements are estimated from vertical separations of surfaces, fault dips, and surface slopes.

*Dating*

We collected profiles consisting of five to six samples each at five locations for <sup>10</sup>Be terrestrial cosmogenic nuclide (TCN) dating. We have received results from PRIME lab and are currently modeling surface ages based on the profile <sup>10</sup>Be data using a previously published calculator (Hidy et al., 2010). We collected a suite of nine samples for luminescence analysis. The IRSL samples are currently being analyzed and we expect final results later this spring.

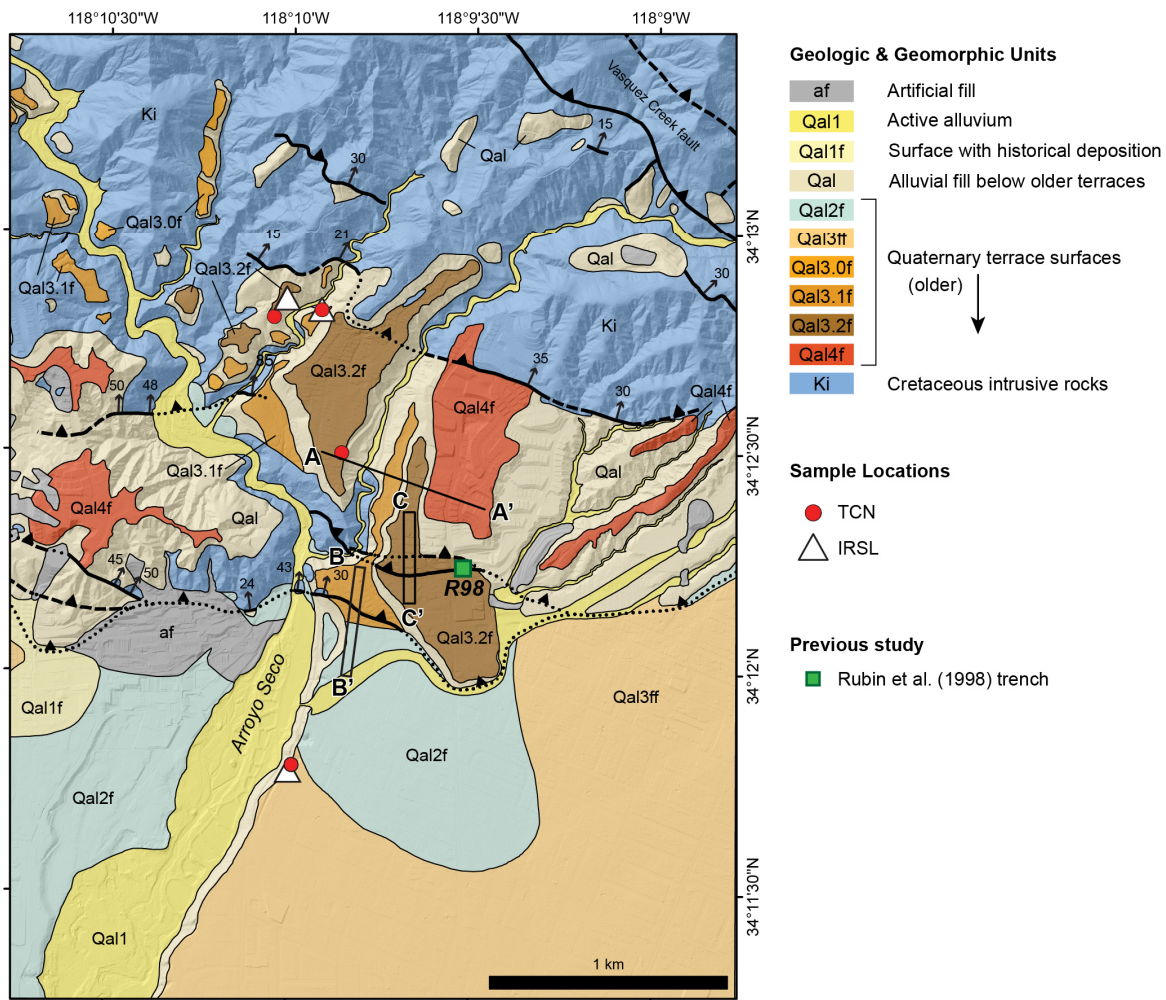


Fig. 2: Geologic and geomorphic map of the Arroyo Seco area showing locations of samples collected for dating. Mapping is modified from Crook et al. (1987), and basemap is shaded relief derived from a USGS 0.5 m resolution lidar digital elevation model. Boxes B-B' and C-C' show locations where we have made preliminary swath profile estimates of vertical separations of terrace surfaces (Hanson et al., 2015).



Fig. 3: Photo of sample locations on the Qal3.2f terrace surface. View is to west-northwest, across the eastern tributary of Arroyo Seco (Fig. 2). White arrows indicate the top of the terrace (geomorphic surface) and the top of fine-grained cover sediment deposited above the terrace gravel. Black arrows show the top of the cobble-boulder terrace gravel. The terrace gravel is exposed to the base of the image, with a total thickness > 25 m. We collected a  $^{10}\text{Be}$  depth profile from the terrace gravel near the edge of the cover sediment deposit. We collected two samples for IRSL dating from the cover sediment 95 m to the north, where the exposure of terrace sediment is closer to the local hillslopes, and the cover sediment is over 4 m thick.

## DISCUSSION

Our dating strategy is designed to establish numeric landform ages by using synergies provided by our two primary dating techniques, with ages validated by relative geomorphic relationships. We focused most of our resources in the Arroyo Seco area, where there are three distinct Qal3-age terrace surfaces on the hanging wall of the CSMF and a prominent footwall surface that may have a more complex history. The inset geomorphic relationships at Arroyo Seco will allow us to interpret our geochronologic results for consistency. Likewise, we have targeted inset pairs of surfaces at Dunsmore Canyon (IRSL dating), and Pickens Canyon (combination of TCN and IRSL dating) (Fig. 1). Our sample sites for IRSL dating are complementary with our TCN sites: for example, two IRSL samples on the young Qal2 surface will give an age where we did not sample TCN surface exposure dating. Our other IRSL samples are co-located with the TCN sampling sites to obtain the best estimates of the ages of two important units: (1) terrace gravels, and (2) capping sediment above these terrace gravels.

Sampling the same sediment for both TCN surface exposure dating and IRSL dating allows us to test for both systematic issues in dating techniques and the depositional and geomorphic histories of the fan terraces. As the luminescence signal begins to grow at the time of burial, the true burial age of a terrace deposit dated by IRSL should be at least slightly older than the geomorphic surface which caps it. In the case of a surface cut across a much older fill, this deposit-surface age discrepancy could be significant. In the case where the surface was established soon after the upper ~2 m of

gravel aggraded, the TCN and IRSL ages should be nearly equivalent.

The sections we sampled for TCN dating generally include an upper layer of fine-grained cover sediment. This characteristic gives us greater confidence in the stability of the top surface of the gravel deposit, but the history of the cover sediment deposit impacts the age that we estimate from the  $^{10}\text{Be}$  concentrations. IRSL samples collected from fine-grained cover sediment provide a limiting minimum age for the upper, buried gravel surface. Two of our IRSL samples are from a 4.25-m thick wedge of cover sediment that thins to ~10 cm at the TCN site (Fig. 3). The two IRSL samples are spaced 1.5 m apart vertically, and will allow us to evaluate whether the wedge slowly grew to its present geometry, or was rapidly deposited following abandonment of this terrace level.

### Conclusion and future work

Once the IRSL ages are complete, we will combine our data to obtain surface age estimates that are consistent with the numerical age data, relative geomorphic criteria, and previous age data where available (e.g., Rubin et al., 1998). Ages of the surfaces capping Qal3 and Qal2 deposits will permit estimation of slip rates at three locations along strike where these surfaces are offset and preserved across strands of the CSMF. We will calculate slip rates with full uncertainties using the methodology of Thompson et al. (2002). This work will result in the first numerically-constrained slip rate estimates for the western half of the CSMF.

The existing paleoseismic records for the CSMF suggest infrequent and large earthquakes, with reverse displacements of 4 m or more (Rubin et al., 1998; Tucker



## INQUA Focus Group on Paleoseismology and Active Tectonics



paleoseismicity.org

& Dolan, 2001). Rubin et al. (1998) trenched the northern strand of the CSMF active in the late Quaternary in the Arroyo Seco area (Fig 2). They interpreted the most recent earthquake occurred in the last 10 ka, and at least two earthquakes with a cumulative 10.5 m of slip occurred in the past 18 ka. A paleoseismic study on the eastern end of the CSMF yielded an estimate of the last earthquake of  $> 8$  ka, and estimated  $\geq 14$  m of cumulative reverse slip in the past 24 ka (Tucker & Dolan, 2001).

Taken together, the results of the paleoseismic studies, the latest Pleistocene-to-Holocene terrace ages from previous soil correlation work, and our preliminary TCN age estimates suggest that our in-progress slip rates based on Qal2 and Qal3 surfaces may capture only two or three earthquake cycles. If the events are clustered (as the combined paleoseismic data tentatively suggest), the resulting latest Pleistocene slip rate may not represent the long-term rate on the system. Although this represents a challenge for estimating an accurate time-averaged slip rate, our strategy to date and measure offsets on surfaces of at least two ages in three locations offers an opportunity to better understand earthquake-cycle related slip variation on the CSMF.

**Acknowledgements:** Research supported by the U.S. Geological Survey (USGS), Department of the Interior, under USGS award number G15AP00039 to Burgette. The views and conclusions contained in this document are those of the authors and should not be interpreted as necessarily representing the official policies, either expressed or implied, of the U.S. Government. Additional funding and support for luminescence dating was provided by the Southern California Earthquake Center. Any use of trade, firm, or product names is for descriptive purposes only and does not imply endorsement by the U.S. Government.

## References

- Crook, R. Jr., C.R. Allen, B. Kamb, C.M. Payne & R.J. Proctor, (1987). Quaternary geology and seismic hazard of the Sierra Madre and associated faults, western San Gabriel Mountains. *Recent Reverse Faulting in the Transverse Ranges, California, US Geological Survey Professional Paper 1339*, 27-64.
- Dolan, J.F., K. Sieh, T.K. Rockwell & R.S. Yeats, (1995). Prospects for larger or more frequent earthquakes in the Los Angeles metropolitan region. *Science* 267, 199-205.
- Hanson, A.M., R.J. Burgette, K.M. Schärer & N. Midttun, (2015). Late Quaternary Offset of alluvial fan surfaces along the Central Sierra Madre fault, southern California, Abstract T41A-2857, presented at 2015 Fall Meeting, AGU, San Francisco, Calif., 14-18 Dec.
- Hidy, A. J., J.C. Gosse, J.L. Pederson, J.P. Mattern & R.C. Finkel, (2010). A geologically constrained Monte Carlo approach to modeling exposure ages from profiles of cosmogenic nuclides: An example from Lees Ferry, Arizona. *Geochemistry, Geophysics, Geosystems*, 11(9), Q0AA10.
- McFadden, L.D., (1982), The Impacts of temporal and spatial climatic changes on alluvial soils genesis in southern California, Ph.D. Dissertation, University of Arizona.
- Rubin, C.M., S.C. Lindvall & T.K. Rockwell, (1998). Evidence for large earthquakes in metropolitan Los Angeles. *Science* 281 (5375), 398-402.
- Thompson, S.C., R.J. Weldon II, C.M. Rubin, K. Abdrakhmatov, P. Molnar & G.W. Berger, (2002). Late Quaternary slip rates across the central Tien Shan, Kyrgyzstan, central Asia. *Journal of Geophysical Research: Solid Earth* 107 (B9), 2203.
- Tucker, A. Z., & J.F. Dolan, (2001). Paleoseismologic evidence for a  $> 8$  ka age of the most recent surface rupture on the eastern Sierra Madre fault, northern Los Angeles metropolitan region, California. *Bulletin of the Seismological Society of America*, 91(2), 232-249.
- U.S. Geological Survey & California Geological Survey, (2006). Quaternary fault and fold database for the United States, accessed 1/24/2014, from USGS web site: <http://earthquakes.usgs.gov/regional/qfaults/>.



## Geological evolution of active fault at Dangu-ri, Gyeong-ju area, SE Korea

Sung-il Cho(1), Weon-hack Choi(1), Daiei Inoue(2), Young-Seog Kim (3)

- (1) Central Research Institute, Korea Hydro & Nuclear Power Co., Ltd. Daejeon 305-343, Korea (chosi4476@khnp.co.kr)
- (2) Tokyo Electric Power Services Co., Ltd. 1-7-12 Shinonome, Koto-ku, Tokyo, Japan
- (3) Department of Earth & Environmental Sciences, Pukyong National University, Busan 608-737, Korea

**Abstract:** We evaluated the age of the latest activity and the return period by adding age data of the stratigraphic layers at Dangu-ri along the northern part of the Yangsan fault, southeast Korea. The Quaternary sediments at the trench site are classified into eight layers from the bottom: 6, 1, 2, 3, 4, 4', 5 and 7 based on their texture and composition. The age of layers 1 - 4 are assumed to be 25 - 35 ka B.P., the age of layer 4' is 4,809±30, 3,990±40 and 2,145 ± 40, and layer 7 is 1,132 ± 24, 1,000 ± 40 and 247 ± 31 y B.P., all determined by <sup>14</sup>C dating. We interpret three events at this site. The youngest event is at fault F<sub>1</sub>; this fault cuts layer 4' and has been buried by layer 7. This event is estimated to have occurred between the 15<sup>th</sup> century and 2,145 y B.P. The penultimate fault event on fault F<sub>2</sub>, cut layers 1 - 4 and terminates in layer 4. The timing of this fault is estimated to be younger than 24,440 ± 110 y B.P. an older penultimate event interpreted by the deformation of layers 1 and 2. The timing of this faulting event is interpreted to be younger than 25,480 ± 110 y B.P. The return period of the active fault at Dangu-ri may be 10 - 15 ka B.P. based on these three events.

**Key words:** Quaternary fault, Return period, <sup>14</sup>C dating, Lineament, Terrace.

### INTRODUCTION

There are many locations that show evidence of young displacements on the Yangsan and Ulsan fault system in the southeastern part of the Korean Peninsula (Fig. 1). Rezaei, et al. (2015) and Lee, et al. (2015) reported evidence of the most recent and penultimate ruptures on the fault at Dangu-ri, along the northern part of the Yangsan fault, SE Korea. In this study, we re-evaluate the age of the latest activity, and the return period by reporting age data for stratigraphic layers at the same site. Rezaei, et al. (2015) and Lee et al. (2015) concluded the latest activity occurred between 300 and 7,000 y BP based on the dating results of both <sup>14</sup>C and OSL (Optically Stimulated Luminescence) methods. However, the OSL method yielded ages that were too older for a deposit that contained man-made objects. We use only <sup>14</sup>C dating results in this paper for the discussion of the events and the return period. The <sup>14</sup>C results in this study are inconsistent in that the analyses yielded different values for samples that were taken from the same position but were analyzed by different measuring organizations.

We studied two parallel E-W trenches in the Dangu-ri area, which are the same trenches mentioned in the above papers (Fig 2). The Dangu-ri study site is located in the alluvial plain that is formed along the western side of the main river running from the east to the west. Alluvial deposits in the trench area are mainly controlled by the river's flow direction. They mainly consist of fluvial sediments of silt, sand, and gravel. The gravels contain some large, angular cobbles and pebbles that were released during instantaneous floods. The trench exposed two faults and eight sedimentary layers. The main fault contact separates granitic basement rocks on the east from the Quaternary sediments on the west. The fault attitude is N10°E/80°SE; the direction of fault

movement, which was recorded from slickensides in the fault gouge, is almost horizontal. This suggests that the recent movement is mainly strike slip.

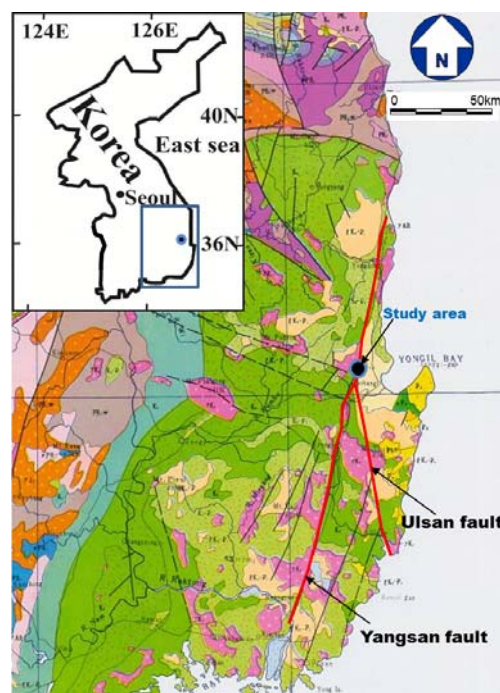


Fig.1: Geological map of the Korean Peninsula and the location of the study area (modified after KIGAM, 1995).

### LINEAMENT STUDY

We analyzed the lineaments and terraces in the study area using aerial photographs to define the extent of fault. The characteristics of lineaments and terraces were classified on the basis of the classification criteria provided

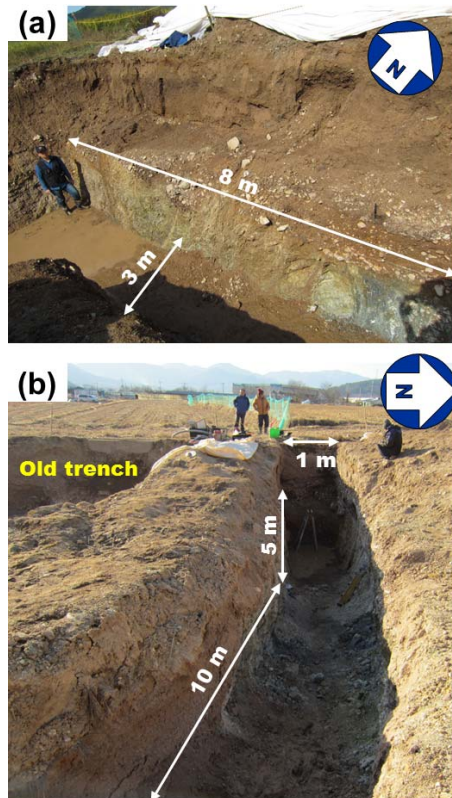


Fig. 2: Overview of the trench site. (a) Old trench, (b) New trench.

by Inoue and Choi (2006). Several lineaments around the trench of the Dangu-ri area are unclear, except for L1 and L4 (Fig. 3). Several short lineaments also run parallel to them with NNE-SSW orientation. These lineaments branch off to the south and southwest. One interpretation is that this area may be the southern termination of one segment of the Yangsan fault.

1. Area south of the trench site

There is a ridge that trends E-W about 100 meters south of the trench. It is very difficult to interpret dextral offsets in small ridges and streams due to the small scale of the photograph, however we identified, small breaks of slope in this ridge. A H<sub>3</sub> terrace that may correspond to MIS 8 because similar terraces have been recognized to the south. A gentle flexure-like feature is interpreted on the H<sub>3</sub> terrace surface 1.5 km south of the trench site. This lineament is tentatively named lineament L1 with a rank of LB. Those of LB rank have discontinuity in large topographic features between mountain and plain, and the altitudinal discontinuity in the mountain region. A flexure is present in the H<sub>3</sub> terrace, but this flexure is not visible on the M terrace due to modifications of the ground surface in the rice fields.

2. Lineament L1 north of the trench site

The M terrace is located 400m north of the trench site. Flexure scarps on the M terraces are interpreted (Fig. 3; A), and the lineament is located at the projection of the fault we identified in the trench. Across the lineament, the terrace elevation of the eastern side is five meters

higher than on the western side. This lineament is given as LB rank.

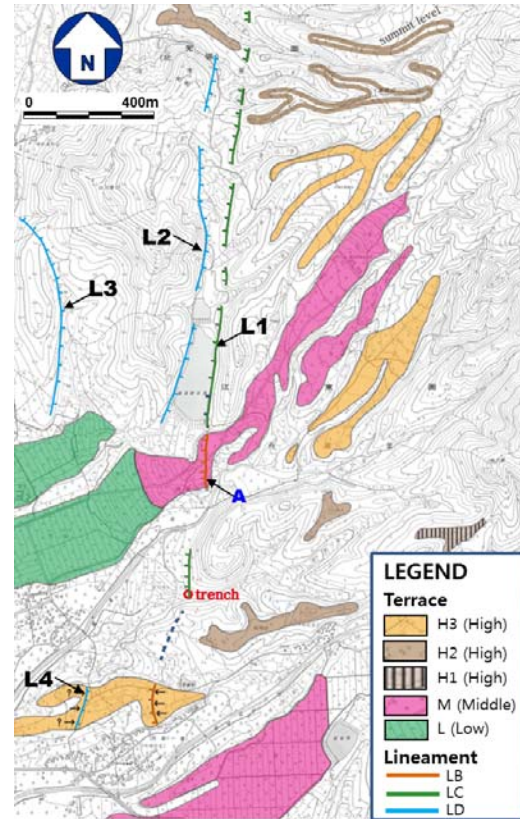


Fig. 3: Lineament and terrace map by aerial photos interpretation.

TRENCH STUDY

Stratigraphy

The Quaternary sediments exposed in the trench are divided into eight layers from the bottom: 6, 1, 2, 3, 4, 4', 5, and 7, from their sedimentary order based on texture and composition (Fig. 4 and Fig 5).

Layer 1 is mainly composed of humus silt, sand and gravel. This layer is deformed and inclines 30 degrees to the east. The <sup>14</sup>C dating samples from layer 1 were collected at the west wall of the trench from the humus sediment. The age was 25,480 ± 110 y B.P. and 39,045 ± 351 y B.P. Layer 2, which cuts layer 1, is composed of semi-angular pebbles and granules. The sorting in this layer is not homogeneous and no sedimentary structures were visible. There may be a minor discontinuity between layers 1 and 2. These layers of 1 and 2 are the series of one sedimentary unit.

The lower part of layer 3 is composed of horizontally bedded, matrix-supported granules, sand, and unsorted silt, and the thickness of its upper horizontal sand layer is 20 cm. Layer 3 unconformably covers layers 1 and 2. The geological structure between layers 1, 2 and 3 is different, as layers 1 and 2 are inclined due to tectonic movement, while layer 3 is horizontal. The age of this layer is 32,932 ± 227 y B.P. This age is older than layers 1 and 2, in spite of the fact that layer 3 was deposited on layers 1 and 2.

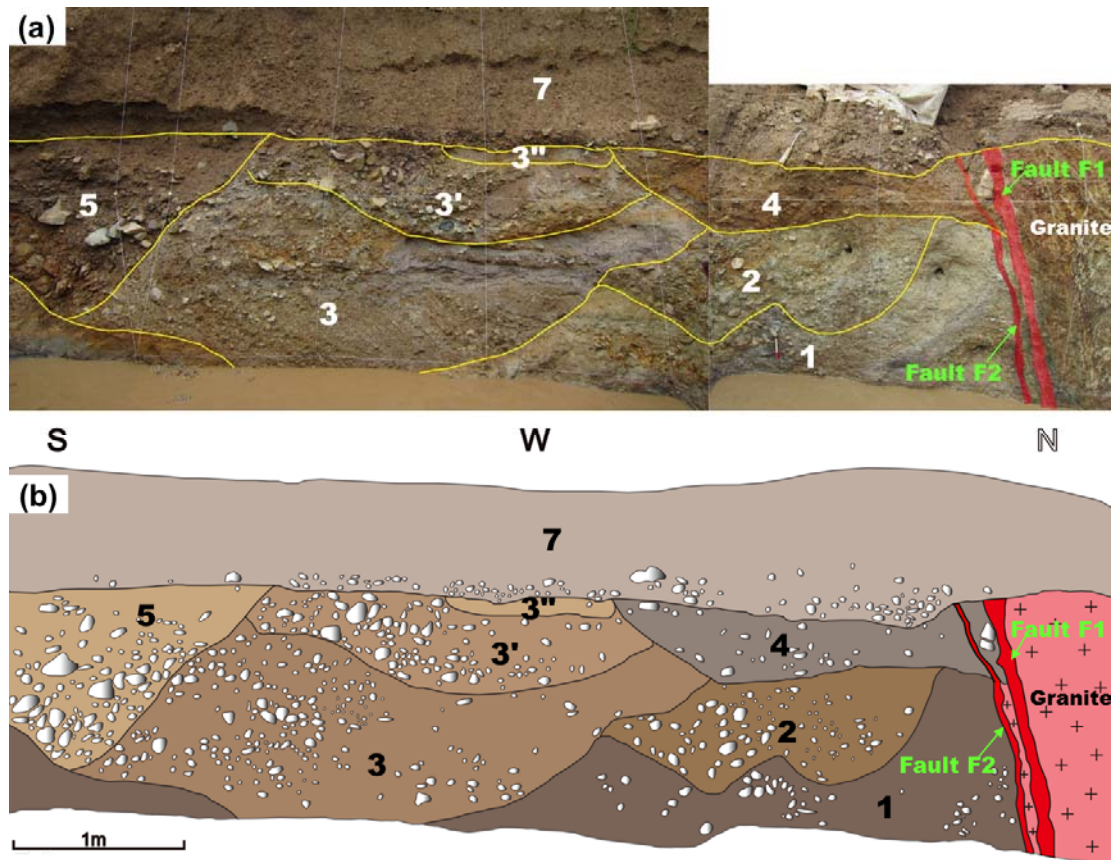


Fig.4: Field photo (a) and sketch (b) of the old trench. The fault contact is observed between the basement granitic rocks to the east and the Quaternary young sediments(Layer 1 ~ 7) to the west.

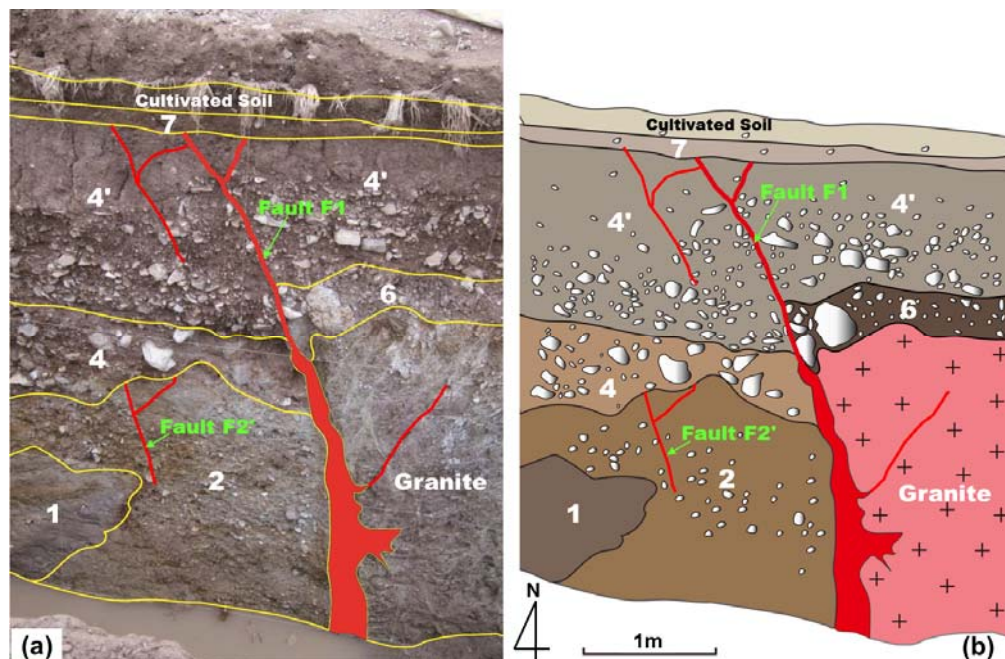


Fig.5: Northern wall of the new trench. Field observations indicate that the fault F1 affected young sediments (Layer 4').



Layers 3' and 3" are composed of sub rounded pebbles, granules and sands. Both these layers are composed of various rock types. Layer 3' was deposited on eroded layer 3 while layer 3" was deposited on eroded layer 3'. The time gaps among the ages of layers 3, 3' and 3" are not long. These layers are mainly fluvial sediments.

Layer 4 is present only in the north wall of the old trench. It is almost horizontally bedded and is composed of matrix-supported silt with angular pebbles. It is obvious that this layer unconformably overlies layers 1, 2 and 3. Its age is  $24,440 \pm 110$  y B.P. and  $35,632 \pm 279$  y B.P. Layer 4' unconformably lies over layer 4, and is mainly composed of pebble and gravel with sand as matrix. Layer 4' is thick in the new trench and thinner in the old trench. The age of layer 4' is  $4,809 \pm 30$ ,  $3,990 \pm 40$  and  $2,145 \pm 40$  y B.P. The sample in this layer is charcoal, which may or may not be reworked from the older deposits, and thus its age may be in-situ sediment. It is very difficult to determine whether this is accurate. The age of layer 4' may be 2,000 - 4,000 y B.P., therefore, the time gap between 4 and 4' is a long time. The differences of oxidation and weathering condition between them support above large time gap.

Layer 5 is present in the south and west walls of the old trench and was eroded into layers 1 and 3 (3, 3', 3"). There is no direct exposure where we could observe the relation between layer 5 and layers 4 - 4'.

Layer 5 is a clast-supported gravel composed of angular cobbles and pebbles. This may be a flood deposit from an instantaneous tributary flood. Pottery fragments and roof-tile fragments were found in layer 5. This pottery was made during the years 1550 ~ 1700 AD (Lee, 2015).

Layer 6 is composed of sand and rounded granules, pebbles, and cobbles. It is approximately 10 cm thick. Layer 6 is present only at the eastern side of the fault. This layer lies unconformably over the basement rock. Thus, the age of layer 6 is unknown - it may be the oldest in this succession. However, it is very difficult to estimate the horizon of layer 6 in this investigation, because layer 6 appeared only at the east side of the fault. Layer 6 may be the weathered colluvium on the top of granitic bedrock.

Layer 7 is composed of coarse sand deposited as a flood loam. At the bottom of this layer, there is thin black silt with manganese-tinted, small, angular pebbles. Layer 7 is the youngest of all the sediments, and horizontally covers layer 4' at the west of the fault and layer 6 at the east of the fault. The thickness of layer 7 is different in the new and old trench. The thickness in the new trench is 10 - 20 cm and that of the old trench is  $\pm 1$  m. The  $^{14}\text{C}$  dating samples show the age to be  $1,132 \pm 24$ ,  $1,000 \pm 40$  and  $247 \pm 31$  y B.P. This age is younger than that of layer 5, which was formed in the 15<sup>th</sup> century. The samples of  $1,132 \pm 24$  and  $1,000 \pm 40$  y B.P. might be reworked sediments. We also found apparently manmade charcoal and roof-tile fragments at layer 7 in the north wall of the old trench.

#### Fault activity

We recognize three possible fault events from the two trenches (Fig. 4 and Fig. 5). The most recent movement occurred along the F1 fault. The fault contact is the

boundary between the sheared granitic basement that is covered by layer 6 on the east side of the fault, and layers 1 and 4 on the west side of the fault in the northern wall of the old trench. This boundary fault is marked by a thin fault gouge. The fault contact in the northern wall of the new trench separates granitic rock and layers 6, 4' at the east side of the fault from layers 2, 4, 4' at the west side of the fault. Layer 7 covers the F1 fault in both the old and the new trench.

The fault structure is sprayed in layer 4', a flower-like structure at the upper part of the layer 4' in the new trench. The latest event at fault F1 may have occurred between the 15<sup>th</sup> century and 2,145 y B.P. The  $^{14}\text{C}$  values in layer 7 are ignored because the samples are probably from charcoal fragments.

We estimate another fault event by using the fault F2. Fault F2 is separated by several centimeters to the west from fault F1. Fault F2 is a branch fault at the upper part of the fault. Black manganese deposits have penetrated and tinted the fault plane. Fault F2 cuts layers 1 and 4 at the south wall (Fig. 4). Fault F2 may be the same position of fault F1 at the north wall, and Fault F2' moved concurrently as cracks (Fig. 5). The timing of the event is estimated to be younger than  $24,440 \pm 110$  y B.P., during or after deposition of layer 4. There is a small fault that is 2 m apart from the main fault. This branch fault has cut layers 2 and 4. The minor fault is regarded as the branch of fault F2. In order to limit the time of a penultimate event, the  $^{14}\text{C}$  age of the layer 4 is a key issue, but this sample is derived from charcoal, and thus it is very difficult to estimate real age of the deposit.

Another event is inferred based on the deformation of layers 1 and 2. Layer 1 dips to about 30 degrees near the fault. This deformation could be caused by tectonic fault movements. This deformation could be the result of three or more events after deposition of layer 1. Layers 1 - 4 are distributed at the lower elevation than the interpreted lower terrace. Furthermore, layers 1 - 4 are located beneath the alluvial deposits. The sediments of layers 1-4 suggest that they were laid during the period of lowest sea level at the latest glacier. Therefore, we adopted the age of about 25,000 y B.P. that is the period of the lowest sea level. However the large deformation of layer 1 suggests that there may be more than two events. Therefore, the second penultimate event is estimated by the deformation of layers 1 and 2. The timing of this fault event may be later than  $25,480 \pm 110$  y B.P. The  $^{14}\text{C}$  samples from layer 1 are humus silt that is in-situ. This age determination may be reliable but there is another value of  $39,045 \pm 351$  y B.P. from the same sample that was carried out by the other organization. This silt may have been deposited during the last glacial period in a stable environment.

The return period of the active fault at Dangu-ri is estimated to be 10 - 15 ka B.P., considering these three different events during the 25 - 40 ky, and the latest event is between 15<sup>th</sup> century and 2,145 y B.P.

There is an exposure of the fault in the left bank of a small valley, which is 100 m south of the trench (Ryoo et al., 1999). Here, the fault separates granite on the east side



from a consolidated, round cobble gravel on the west side. The colors of the cobble formation range from brown to red. The fault gouge is several centimeters wide, and its character is the same as that of the trench site. The trend of this fault is N10°W/85°NE. This is the extension of fault F<sub>1</sub>. The fault is also presumed at the adjacent small valley as boundary between the basement rock and the cobble layer. We were unable to identify the fault boundary itself geologically due to the cover of the overburden. The small tributary seems to have a dextral offset of about 1.5 - 2.0 meters. This offset is regarded to be single-event displacement. This area is a suitable trench site to evaluate a single-event dislocation.

## DISCUSSION

We conclude the investigation by proposing difficulties that may be addressed in the future. The structural model of geological evolution at the Dangu-ri area is shown in Fig. 6.

1. It is very difficult to reconcile the differences between the stratigraphy and the age-dating results. For example, the dating samples from layers 4 and 7 are from charcoal, which is easily reworked by erosion and deposition. We need more studies determine how to interpret the age results. The age view from stratigraphy, and some <sup>14</sup>C ages from layers 4 and 7 are excluded in this study.
2. It was difficult to correlate the fluvial sediments because of repeated episodes of erosion and deposition. Even if the faces are similar, there can be large time differences.
3. The most recent event occurred between the 15th century and 2,145 y B.P., as fault F<sub>1</sub> deformed layer 4' and has been covered by layers 5 and 7. Lee (2015) estimated that the latest movement of this fault was between 300 y B.P. and 7,000 y B.P. Also, Kyung (2003) reported that the faults were activated after 1,345 y B.P. from a study at Yuge-ri on the northern part of the Dangu-ri fault. We suspect that these differences in age results are due to differences in analysis methods and in the age dating. We plan to undertake another trench survey between the Dangu-ri and Yuge-ri area in the future.
4. The penultimate event occurred during or after deposition of layer 4. The <sup>14</sup>C age of layer 4 is 24,440 y BP. As mentioned above, the age is too old based on stratigraphic interpretation, so we estimate that the age of layer 4 may be 10,000 - 15,000 y B.P.
5. A second penultimate event is interpreted based on the steep dip of layer 1 near fault F<sub>1</sub>. Such deformation is not generally formed by only one or two events. It is better to consider other events, therefore, the timing of the second penultimate event is regarded as being after deposition of layer 1 after 25,000 y BP.

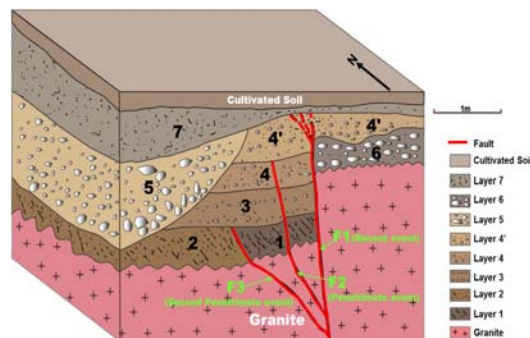


Fig.6: Structural model for the evolution of the Dangu-ri fault.

## CONCLUSION

We identify eight Quaternary deposits and three faulting events at this trench site. We limit the age of the latest fault event to be between the 15<sup>th</sup> century and 2,145 y B.P., but prefer a better estimate to be close to the 15<sup>th</sup> century by combining the Yuge-ri results. An older penultimate event is estimated to have occurred later than 25,480 ± 110 y B.P. Therefore, the return period of the fault at Dangu-ri may be 10 - 15 ka. We plan to continue future investigations to verify the ages of faulting events along the northern part of the Yangsan fault.

## References

- Inoue D. and Choi W.H., 2006, The activity of the Ulsan fault system based on marine terrace age study at the southeastern part of the Korean Peninsula. CRIEPI Report, No512, pp. 83.
- KIGAM(Korea Institute of Geoscience and Mineral Resources), 1995. Geological map in Korea (1:1,000,000).
- Kyung, J.B., 2003. Paleoseismology of the Yangsan fault, southeastern part of the Korean Peninsula. Ann. Geophys. 46, p. 983-996.
- Lee, J-H, Rezaei, S., Hong, Y., Choi, J.H., Choi, J.H., Choi, W.H., Lee, G.W. and Kim, Y-S., 2015, Characteristic of Quaternary fault movement from the trench survey on the northern part of the Yangsan fault at the Dangu-ri, Gyeng-ju area, SE Korea. Journal of the Geological Society of Korea, v. 51, no. 5, p. 471-485.
- Rezaei, S., Lee, J-H, Hong, Y. Gwon, S-H, Kim, Y-S., Rockwell, T.K., 2015, Paleoseismicity on the northern part of the Yangsan Fault, S-E Korea 6<sup>th</sup> International INQUA Meeting on PATA.
- Ryoo, C.-R., Lee, B.-G., Cho, D.-L., Chwae, U.-C, Choi, S.-J. and Kim J.-Y., 1999, Quaternary fault of Dangu-ri in Gyeongju Gangdong-myeon: Byeokgye fault. The Korean Society of Economic and Environmental Geology/The Korean Society of Mineral and Energy Resources Engineers/Korean Society of Earth and Exploration Geophysicists, spring joint conference-east-north Asia ore deposit of cause of formation, pp. 334.



## Geomorphologic and Stratigraphic relationships as indicators of Geologic Hazard and Paleoseismicity, central coast of Ecuador

Kervin Chunga (1), Maurizio Mulas(1), María F. Quiñónez(2), Daniel Garcés (1), Angelo Constantine (1)

(1) Escuela Superior Politécnica del Litoral, Facultad de Ingeniería en Ciencias de la Tierra, Campus Gustavo Galindo Km 30.5 Vía Perimetral, P.O. Box 09-01-5863, Ecuador. Email: kchung@espol.edu.ec.

(2) Dirección de Análisis de Riesgos. Secretaría de Gestión de Riesgos, Guayaquil, Ecuador.

**Abstract:** The Jaramijó sea-cliff and the surrounding deposits recorded a series of natural disaster that affected Ecuador's central coast during Upper Pleistocene to Holocene. Stratigraphic and geomorphologic studies between Manta and Jaramijó recognized volcanic fine ash layers (related to secondary rain-triggered lahars) interbedded with fine sand to silt layers related to tsunami events. These alternations were discovered on different terrace levels T1 to T4. This work recognized two new terraces (T1 and T2) related to the T3 and T4 terraces previously described. These new terraces were dated to 1ky and 43ky, respectively. The stratigraphic, geomorphologic and palaeoseismologic features allow us to understand the sequence of catastrophic geological events that affected the landscape and the coastal changes at the Jaramijó site.

**Key words:** Coastal uplift, Geologic Hazard, Tsunami deposit, paleogeographic reconstruction, Central Ecuador.

### Introduction

The coast of Ecuador (South America) is highly prone to natural disasters, especially those caused by active tectonics. Its short historical seismicity record (1787 – 2015) includes a series of catastrophic earthquakes. The main seismogenic structure capable to generate strong earthquakes ( $M_w \geq 8$ ) is the subduction zone where the Nazca plate underthrusts the adjacent South American plate in the eastern Pacific Ocean, 60 to 150 km from the coast (Kelleher, 1972; Carena, 2011).

Several secondary coseismic geological phenomena (ie., Michetti et al, 2007) can generate other earthquake related hazards such as tsunami inundation in littoral plains, (b) landslides and rockfalls on unstable slopes and coastal cliffs, (c) an increasing rate of natural or anthropogenic subsidence, (d) soil liquefaction focusing in water saturated sand sediments confined by semi-permeable layers of silt and clay materials, and (e) tectonic uplift of subtidal platforms forming marine terraces. The last process allows the formation of well preserved Quaternary sedimentary sequences. Furthermore, the most distal occurrences of ash fallouts and lahar flow deposits also modelled the landscape of Ecuador's central coast. These deposits are related with volcanic vents situated at a distance between of 150 - 190 km in the northern Andes (ie., Mothes & Hall, 2008; Usselman, 2006). Only few studies concerned with volcanic hazard and the modelling of volcanic risk exist for the Ecuadorian littoral sectors (Mulas et al., 2015).

The site selected to study the paleoseismic and paleogeographic reconstruction of the central coast of Ecuador is the Jaramijó canton (total area 96 km<sup>2</sup>), (Figure 1). The Upper Pleistocene to Holocene sedimentary and volcanic sequences crop out on sea cliffs and in quarries in the inner Jaramijó Canton.

Their deposits occurred between MIS 3 (59 - 24 ka BP) and MIS 1 (18 ka to present).

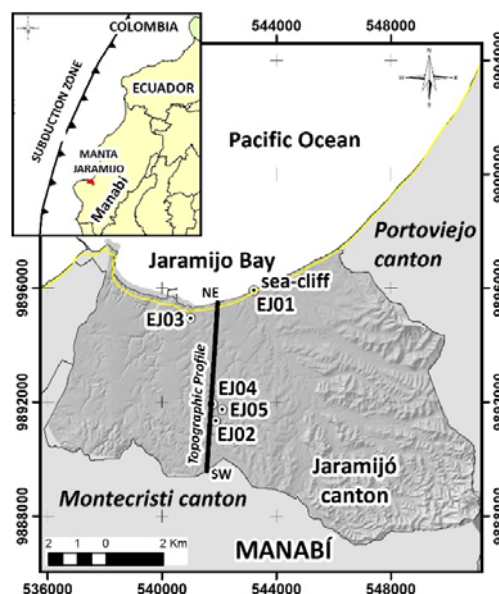


Fig 1: Location of Upper Pleistocene - Holocene stratigraphic sequences on the Jaramijó bay sea cliff in the central area of Ecuador's Pacific coast.

### Geomorphological setting and natural hazard

The Jaramijó site is characterized by different types of hilly relief contrasting with the coastal and alluvial plains. The cliffs are mostly made of sandstones, siltstones, and claystone layers of Tertiary age (Baldock, 1982). The rock mass is fractured by the regional active tectonics and is easily erodible by ocean waves. These processes formed geomorphologic structures such as wave-cut notches and cracks at the base of the sea-cliffs. Upper Pleistocene to Holocene sediments lie on the basement rocks and are well-preserved. Thus, they provide information to



understand the paleogeography and paleoseismicity of the region.

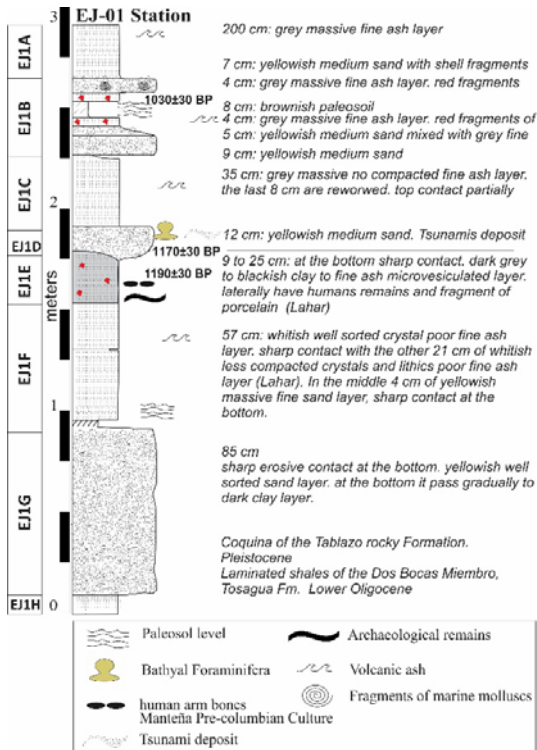


Fig 2. Stratigraphic column of EJ-01 geological sampling site on the Jaramijó sea-cliff.

The geological long-term and hydro-meteorological hazards associated with climatic changes can cause major landscape changes on the coast, i.e. marine erosion and coastal cliff retreat (Bloom & Yonekura, 1985). The main geomorphological features on the Jaramijó site are a wave-cut beach platform, permanently exposed on the lowest tides and an 18 m-high coastal cliff retreating with an estimated rate of ca. 2.5 m/a (Chunga et al., 2015).

Moreover, volcanic fine ash and lahar layers are well distinguished on the sea-cliffs and are related with volcanic activities of northern Andes of Ecuador volcanoes such as Quilotoa, Cotopaxi, Guagua Pichincha, and Pululahua (Mothé and Hall, 2008; Usselman, 2006). It cannot be ruled out that pre-Columbian cultures may have been displaced in the last 2,000 years by disastrous geological events such as subduction earthquakes, local tsunamis, and volcanic lahar-ash deposits (Lim et al., 2013; Zeidler, 2015).

### Paleoseismicity and coastal uplift

The tectonic uplift of the Ecuadorian central coast is associated with tectonic transport of the high bathymetric relief of the Carnegie ridge, which is subducting below the South American continental plate (Cantalamesa & Di Celma, 2004).

This regional geodynamic process uplifted sublittoral platforms and the beach-shore, now visible as uplifted marine terraces. It preserved volcanic and sedimentary sequences dating from Upper Pleistocene to Holocene (Cantalamesa & Di Celma, 2004; Pedoja et al., 2006; Chunga et al., 2015). Geological records of coseismic uplift can be identified in Quaternary sedimentary sequences at the Jaramijó site.

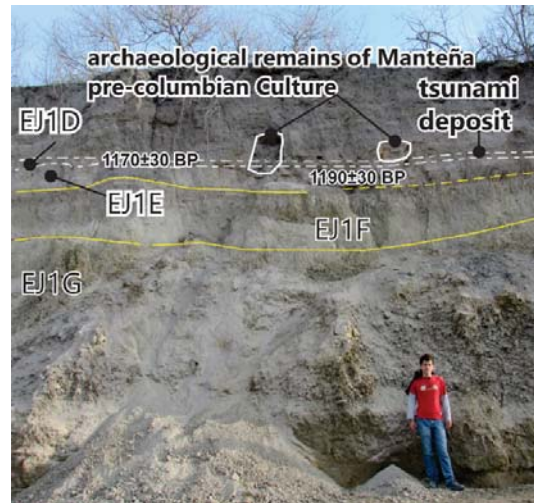


Fig 3. Sea-cliff at Jaramijó site EJ-01 sampling station.

In this study we selected five geological sampling stations, named EJ-01 to EJ-05, located on the sea-cliff and abandoned quarries on the inner coastal margin (ca. 4 km away from coastline). Geomorphic and stratigraphic studies as well as radiometric dating techniques applied to Quaternary sedimentary sequences allow recognizing upper Pleistocene to Holocene uplifted terraces. The marine terraces, from bottom to the top, are: T1 at an altitude of 20 meters a.s.l. (above sea level) (dated 1.190 ± 30 BP to 1.030 ± 30 years BP), T2 terrace at 30 meters a.s.l. (43.245 ± 460 years B.P.) and T3 at an altitude between 43 to 57 meters a.s.l. (ca. 120,000 years). The T3 terrace was previously recognized by Pedoja et al. (2006), but our research outlined two new terraces (here named T1 and T2) mostly covered by volcanic-ash deposits. Our first results for estimating a tectonic uplift rate are ca. 0.5 mm/yr to 0.98 mm/yr, obtained from altimetry data and the ages of the terraces and coastal paleocliffs. On the contrary, Pedoja et al. (2006) estimated a rate of 0.31 mm/yr to 0.39 mm/yr, considering marine terraces ages 120,000 years (MIS 5e), 220,000 years (MIS 7) and 330,000 years (MIS 9).

Here, the paleoseismologic reconstruction of coastal uplift is linked with the continental margin active tectonics and also to the MIS1 to MIS 3 glacial and interglacial stages. EJ-02 sample is from the T2 terrace and lithological unit EJ-02E is composed by a medium sand layer with bivalve molluscs (i.e.,



*Trachycardium* –*Mexicardia*– *procerum*, and *Divalinga perparvula*, both species of neritic marine environment) indicating a sublittoral environment. Radiocarbon dating and oxygen isotope analysis ( $^{18}\text{O}$  ratio), were carried out at the Beta Analytic Laboratory. Our research results show that these sediments probably were deposited in a water column -10 to -30 m below the present sea level. The

radiocarbon age of this unit is 41.295 to 40.140 years BC (cal. 43.245 to 42.090 years BP). The  $\delta^{18}\text{O}$  and -1 to -1.5 o/oo values can be associated with a short interstadial stage within the MIS 3glacial stage, associated with a rapid sea level rise that reached -10 to -20 m below respect to the current sea level.

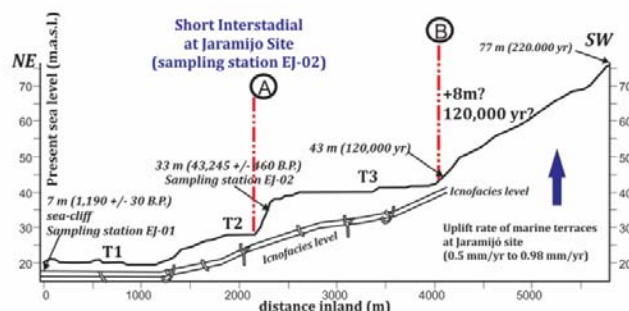
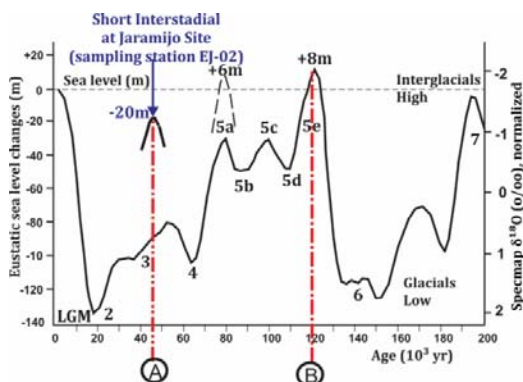


Fig. 4: Uplift model using marine terrace ages corresponding to Marine Isotope Stages (MIS) from 1 to 5e. Left: sea-level history since 200 ka (Chappel & Shackleton, 1986). Right: Topographic profile and Marine terrace inner edge elevations and geological sampling stations at the Jaramijo site.

#### Tsunami deposit and potential seismic source

Sites EJ-01 and EJ-03 are situated on the T1 terrace. This terrace is composed of late Holocene sequences of sand and clay interbedded with loose to weakly consolidated fine volcanic-ash layers. One of the most remarkable geoarchaeological findings in this outcrop (sample EJ-01E) were human bones related to the Manteña culture integration period, within a 8 to 25 cm-thick volcanic ash layer (radiocarbon dating of  $1.190 \pm 30$  B.P. - Mulas et al., 2015). Stratigraphically above lies an erosive contact with a well-sorted medium to fine-grained sand layer (unit EJ-01D), characterized in the lower part by rip-up clasts. Biostratigraphical analysis of the matrix revealed *Melonis sphaerodis* foraminifera, typical of bathyal environments. These data indicate a tsunami event characterized by 6.3 meters a.s.l. run-up height (estimated age of ca.  $1.170 \pm 30$  B.P.). Unit EJ-01D is one of the most important sedimentary levels that provide evidence for tsunamis (Fig. 3).

The seismic source linked with this event is uncertain. Contreras-López (2014) suggests the following classification of tsunami in Ecuador: (a) near-field tsunami, when the seismic source is adjacent to the continental platform of Ecuador near the borders of Colombia and Peru. (b) intermediate-field tsunami if the earthquake epicentre is sited at distance less than 1,000 km from Ecuadorian coastline. (C) far-field tsunami if the epicentres have trans-oceanic distances (i.e Japan or Russian megathrust seismic sources).

We searched the NOAA global historical tsunami database (<http://www.ngdc.noaa.gov>) for great tsunamigenic earthquake events that would fit our

dates. The following tsunamigenic earthquakes in Japan are possible candidates: AD 745 Osaka Bay earthquake (Mk 7.9), AD 818 Tokaido earthquake (Mk 7.9), and AD 869 Jogan Sanriku earthquake (Mk 8.9).

Sedimentological analysis and hydrodynamic simulations showed that on July 13, 869 the Jogan tsunami was triggered by a Mk 8.3 (other measures indicate M 8.9) earthquake. The tsunami inundated more than 4 km inland into the Sendai plain (Minoura et al., 2001). There is no evidence that this trans-oceanic tsunami reached the coast of Ecuador. We then analysed the recent seismic event of March 11, 2011 (Mw 9). Both earthquakes were compared by Suguwara et al., (2013), who studied the inundated area in the Sendai plain. This strong 2011 Japan tsunamigenic event, if it had reached the southern Ecuadorian coast, would have caused run-up heights of ca. 1.61 m only on the Libertad site. These historical and contemporaneous events indicate that our  $1.210 \pm 30$  B.P tsunami event at the Jaramijó site was not a far-field event, but a near-field tsunami. If this is true, it means that large local tsunami of ca. 5 to 8 meters run-up height can strike the central coast of Ecuador.

#### Conclusion

Stratigraphic, geomorphologic and paleoseismologic studies performed on the central coastal area of Ecuador from Manta to Jaramijó allowed us to recognize different volcanic and coseismic events that affected this area. The stratigraphic and biostratigraphic studies allowed to recognize fall-out and lahar events alternated with tsunamis events. The volcanic events are related with the volcanic



activity of the North Andes (Quilotoa, Guagua Pichincha, Cotopaxi, and Pululahua). These volcanoes primarily generated distal fine ash fall-out deposits in the last 5 ky. Lately the same deposits were remobilized by weakly to strong meteorological events that triggered secondary rain-triggered flow.

Tsunamis events were recognized with biostratigraphic and stratigraphic studies that revealed foraminifera typical of bathyal environments. Detailed geomorphological studies, and  $^{14}\text{C}$  and  $^{18}\text{O}$  analysis permitted to recognize and date two new terraces (T1 and T2) previously not described in this sector.

Our data indicate that a local tsunami hit Ecuador's coast ~1000 years BP.

In this multidisciplinary study we recognized a new geological hazard that affected the Ecuadorian coastal area in the past. This is an important contribution to understanding the geological risk of this area.

#### References

- Baldock J.W. (1982). Geology of Ecuador. Explanatory Bulletin of the National Geological Map of Republic of Ecuador, 1: 1.000.000 scale, Division de Investigación Geológico-Minera, Quito, 55pp.
- Bloom A.L., Yonekura N. (1985). Coastal terraces generated by sea level change and tectonic uplift. In: Woldenberg, M.J., (Ed), Models of Geomorph., Allen and Unwin, Boston, MA, pp. 139-155.
- Cantalamessa G., Di Celma C. (2004). Origin and chronology of Pleistocene marine terraces of Isla de la Plata and of flat, gently dipping surfaces of the southern coast of Cabo San Lorenzo (Manabí, Ecuador). *Journal of South American Earth Sciences* 16, 633-648.
- Cerena S. (2011). Subducting-plate topography and nucleation of great and giant earthquakes along the South American trench. *Seismological Research Letters*, vol. 82, Number 5. doi:10.1785/gssrl.82.5.629
- Chappell J., Shackleton N. (1986). Oxygen isotopes and sea level. *Nature*, 324: 137-140.
- Chunga K., Mulas M., Peña-Carpio E., Garcés D. (2015). Paleoseismic and Paleogeographic Reconstruction of the Central Coastal of Ecuador: Insights from Quaternary Geological Data for the Jaramijó bay area. American Geophysical Union, AGU Meeting.
- Contreras-López, M. (2014). Riesgo de Tsunami en Ecuador. *Ingenius N.* 12, (Julio-Diciembre). pp. 68-75. ISSN: 1390-650X.
- Hall M., Mothes P. (2008). Quilotoa volcano — Ecuador: An overview of young dacitic volcanism in a lake-filled caldera. *Journal of Volcanology and Geothermal Research*, Volume 176, Issue 1, 10 September 2008, Pages 44-55
- Kelleher, J. (1972). Rupture zones of large South American earthquakes and some predictions. *Journal of Geophysical Research*, vol 77, No. 11, pp. 2087-2103.
- Lim S., Marie-Pierre L., et al. (2013). Ecological effects of natural hazards and human activities on the Ecuadorian Pacific coast during the late Holocene. *Palaeogeogr. Palaeoclimat. Palaeoecol.* Palaeo-06701.
- Michetti, A.M., Esposito, E. et al. (2007). Environmental Seismic Intensity Scale 2007 – ESI 2007. In: Vittori, E. & Guerrieri, L. (eds) *Memorie. Descrittive della Carta Geologica d'Italia, LXXIV Servizio Geologico d'Italia, Dipartimento Difesa del Suolo, APAT, System Cart Srl, Roma, Italy, 7 – 54.*
- Minoura K., Imamura F., et al. (2001). The 869 Jogan tsunami deposit and recurrence interval of large-scale tsunami on the Pacific coast of northeast Japan. *Journal of Natural Disaster Science*, volume 23, Number 2, pp 83-88.
- Mothes, P.A., Hall, M.L. (2008). The Plinian Fallout Associated with Quilotoa's 800 yr BP Eruption, Ecuadorian Andes. *J. Volcanol. Geotherm. Res.* (Ecuadorian Special Issue). 176, 56–69.
- Mulas K., Chunga K., et al. (2015). Stratigraphic and Lithofacies Study Of Distal Rain- Triggered Lahars: The Case Of West Coast Of Ecuador. American Geophysical Union, AGU Meeting.
- National Geophysical Data Center / World Data Service (NGDC/WDS): Global Historical Tsunami Database. National Geophysical Data Center, NOAA. doi:10.7289/V5PN93H7 [access date].
- Pedoja, K., Dumont, J.F., et al., (2006). Plio- Quaternary uplift of the Manta Peninsula and La Plata Island and the subduction of the Carnegie Ridge, central coast of Ecuador, *Journal of South American Earth Science*, 22, 1-21.
- Suguwara D., Imamura F., et al. (2013). The 2011 Tohoku-oki earthquake Tsunami: similarities and differences to the 869 Jogan Tsunami on the Sendai Plain. *Pure and Applied Geophysics*. 170, 831-843. DOI: 10.007/s00024-012-0460-1.
- Usselman P. (2006). Dinámica geomorfológica y medio ambiente en los sitios arqueológicos Chitije y San Jacinto / Japoto (costa del Manabí central, Ecuador). *Bulletin de L'institut Francais d'Etudes Andines*, 35 (3): 257-264.
- Zeidler, J.A. (2015). Modeling cultural responses to volcanic disaster in the ancient JamaeCoaque tradition, coastal Ecuador: A case study in cultural collapse and social resilience, *Quaternary International*, <http://dx.doi.org/10.1016/j.quaint.2015.09.011>.



## Tectonic geomorphology and geochronology supporting a probabilistic seismic hazard analysis in the Krško Basin, Slovenia: implications for a critical infrastructure

Cline, M. Logan (1), K. Michael Cline, (1), Petra Jamšek Rupnik, (2), Jure Atanackov(2), Miloš Bavec(2), Sally Lowick(3)

(1) Rizzo Associates. 500 Penn Center Boulevard, Pittsburgh, PA 15214, USA mlogan.cline@rizzoassoc.com

(2) Geological Survey of Slovenia. Dimičeva ulica 14. SI-1000 Ljubljana, Slovenia.

(3) Institute of Geological Sciences, Universität Bern. Baltzerstrasse 1+3 CH-3012 Bern, Switzerland

*Krško Basin in southeastern Slovenia is being investigated as a potential site for a new nuclear power plant. The basin is in a region of low to moderate tectonic activity. The post-Miocene Krško Syncline defines the basin's axis, which has been driven by generally N-S convergence of the Adriatic Microplate and the European Plate. Three major obstacles have precluded accurate assessments of fault deformation rates in the region: 1) the sparse chronometric data; 2) The geochronology that exists is biased toward the latest Pleistocene and Holocene due to the inherent limitations of methods applied in the past; and 3) the lack of outcrop or near-surface evidence of deformed Quaternary sediments due to relatively low strain rates. To overcome these impediments we are utilizing methods in tectonic geomorphic analysis of LIDAR data and multiple age dating methods to develop a robust geochronology that targets the Neogene-Quaternary.*

**Key words:** geochronology, paleoseismology, tectonic geomorphology, PSHA.

### Introduction

Field investigations supporting a probabilistic seismic hazard analysis (PSHA) are being performed for a new nuclear power plant (NPP) in the Krško Basin, Slovenia. Tectonic geomorphic analysis and field geological mapping have demonstrated that larger faults in the local area are highly segmented and have relatively low deformation rates, thus making fault recognition challenging. As a result, fault constraints (e.g. slip rates) remain elusive in the region. There are several major impediments to developing faulting constraints: (1) a regional unconformity that accounts for ~1.5 Ma of missing sediment from the Quaternary record, (2) relatively low strain rates along faults, (3) a sparse geochronology, and (4) difficult subsurface conditions for very shallow geophysical surveys. Coupling these factors presents hurdles for paleoseismic data acquisition. To address these challenges we are applying a suite of methods that include multiple geochronology methods that target a wide range of ages from the Holocene to the Pliocene, tectonic geomorphic analysis, geological mapping, multiple geophysical methods, paleoseismic trenching, and sediment and rock coring. These investigations are part of an ongoing, multi-year effort to evaluate potential fault capability and to develop a seismic source model that will be used to provide inputs to the PSHA. The work reported herein focusses on the tectonic geomorphology and geochronology to assess the potential presence of faulting and associated strain rates, and also to identify uncertainties associated with previous work in the region. An accompanying document (Jamšek Rupnik et al., 2016) presents results from the field mapping, mountain front sinuosity measurements, and the high resolution geophysical survey campaign.

Paleoseismology and tectonic geomorphology exploit earth's topographic expression of neotectonic activity to constrain the seismic history, spatial patterns of faulting, and fault behaviour. In some cases, however, strain markers are masked, particularly in areas where geomorphic processes outpace tectonic processes. There are also areas where faults don't break to the surface (e.g. blind faults), which often impedes their detection. These sorts of issues are ever-present in the Krško region. While seismicity is moderate, surface expressions of faulting are difficult to discern and only clearly seen in Miocene and older bedrock. An additional complication is that relief controlled by transpression or transtension typically produce a great deal of spatial variability in uplift or subsidence related to complex strain partitioning (e.g. Delong et al., 2010). It is therefore necessary to utilize high quality data and detailed analyses to detect expressions of tectonic deformation.

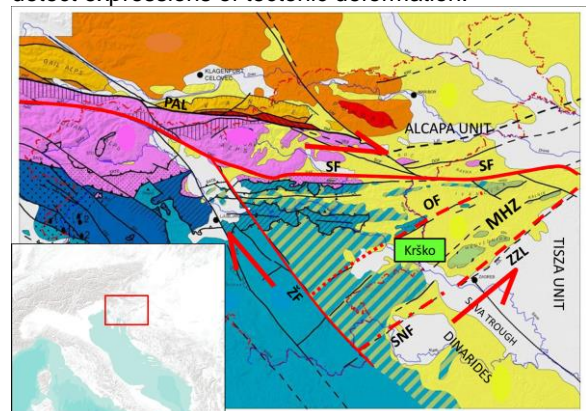


Fig 1: Inset map in lower right shows the geographic location of Krško relative to the regional tectonic model (modified from Placer, 2008).

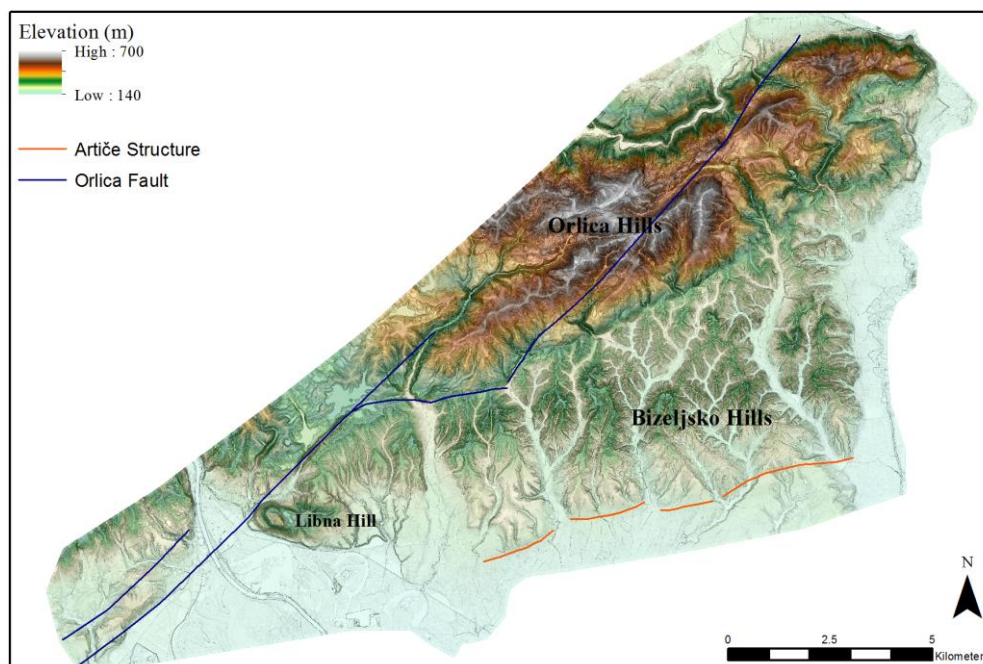


Fig. 2: Elevation-enhanced slopeshade digital elevation model of study region. Locations of the Orlica and Artiče faults are shown from the existing 1:100,000 geological maps.

The proposed NPP, whose location is roughly shown in *Figure 1*, lies within a transition zone between the northern Dinarides and the Alps and has experienced multiple phases of deformation from the Mesozoic through most of the Cenozoic (e.g. Van Gelder et al., 2015). As a result, the present topography expresses Dinaric and Alpine structural styles, as well as Balaton structures associated with the Mid Hungarian Shear Zone (MHZ) (Brückl et al., 2010; Hetényi et al., 2015). Related to these three structural domains is the Sava Compressive Wedge (SCW) (Placer, 1999), which is a zone of east-west trending, high-frequency folds and associated thrust faults. Each deformation phase has unique structural orientations, leaving the Krško region with four dominant deformation styles. The broader tectonic setting is shown in *Figure 1* (Modified from Placer, 2008), which shows the four major structural zones. The SCW is roughly delimited by the Žužemberk Fault, Sava Fault and the MHZ, whose locations are shown on *Figure 1*.

Within a 25 km radius from site, the largest faults are Balaton structures, which are left-lateral strike slip faults with a significant reverse component. These faults are associated with the northern side of the southwestern extent of the ENE-striking MHZ. Also present is the Krško Syncline, a large fold associated with the SCW.

### Geomorphic Analysis

We have applied numerous quantitative and qualitative methods including stream profiling (Kirby and Whipple, 2001) and morphometric analysis (e.g. topographic ruggedness, hypsometric curves) to extract information from the topography, including the areas defined by the Orlica Fault and the Artiče Structure (AS) shown in *Figure 2*. The morphometric and stream profile analyses have identified important

aspects of the landscape that are not entirely identifiable through interpretation of the hillshade or slopeshade (shown in *Figure 2*). The most striking feature in *Figure 2* is the ENE-trending lineament that divides the Orlica Hills from the Bizeljsko Hills. Geologic mapping has demonstrated, repeatedly, that the abrupt lineament is related to differential rock strength as opposed to a fault. The Orlica Hills comprise Mesozoic carbonate rocks, juxtaposed against weaker Neogene marls and sandstones that comprise the Bizeljsko Hills. Another evident feature is the swath of steeper slopes within the Bizeljsko Hills that extends from Libna Hill in the west, to the eastern edge of the Bizeljsko Hills. The area is roughly coincident with the mapped position of Pontian (Late Miocene) sands and gravels.

Longitudinal stream profiles reflect base level changes (via uplift or climate change), and can therefore show critical information about relative uplift (Hack, 1957; Kirby and Whipple, 2012; Kirby and Whipple, 2001). Previous stream profiling efforts in the Krško region utilized the Hack's (1973) stream gradient index for channels that cross the AS (Baize, 2008). Small knickpoints were recognized and attributed to tectonic deformation along the AS; however, the topographic data was coarse (12.5 m pixel spacing), and had numerous artefacts. To evaluate those results we extracted longitudinal stream profiles from channels that cross the Orlica and Bizeljsko hills based on a high quality DEM produced by reprocessing a LiDAR point cloud (sampling rate >16 laser returns/m<sup>2</sup>) with 1 m pixel spacing. The profiles were extracted and analyzed in Matlab and ArcGIS using the Stream Profiler Tools (<http://geomorphtools.org/>), following theory presented in Wobus et al., (2006; Kirby and Whipple (2012, and references therein).

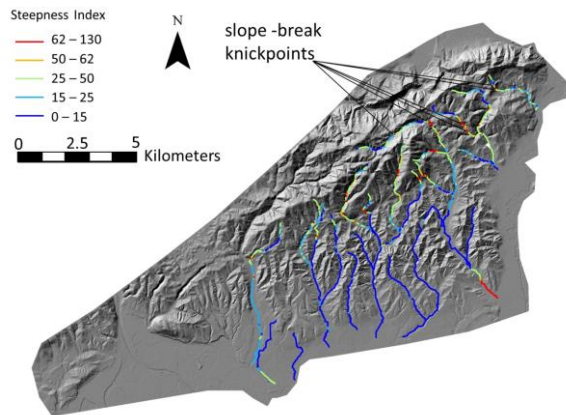


Fig 3: Stream steepness index on major drainages crossing the Orlica and Bizeljsko hills

Our analysis demonstrates a lack of knickpoints near the projection of the AS, suggesting there is either lack of persistent base level change along the AS, or that the AS's deformation rate is very slow relative to surface process rates. Upstream, however, within the Orlica Fault Zone (OFZ), there are several slope-break knickpoints, i.e. those defined by a break in slope-area scaling. Above the slope-break knickpoints are relict channel profiles that have not adjusted to the modern base level (Kirby and Whipple, 2012). The geographic positions of the slope-break knickpoints are shown in Figure 3 and one of the accompanying river profiles shown in Figure 4. Slope-break knickpoints are often indicative of persistent uplift; moreover, the spatial distributions of the slope-break knickpoints align well with the position of the OFZ. Combined, these factors suggest the fluvial system in the northeastern Orlica Hills is being affected by the OFZ.

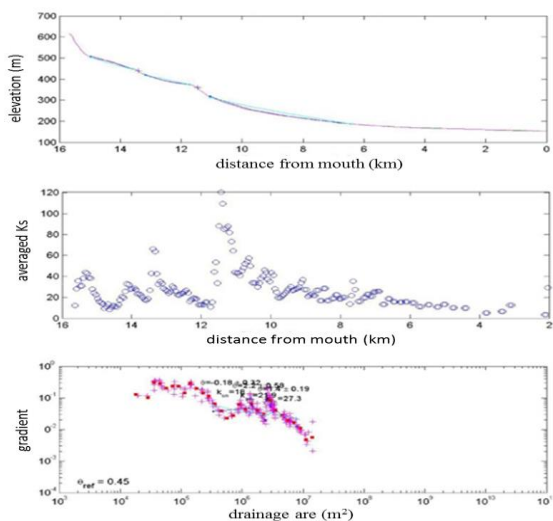


Fig 4: Result from one of the stream profiles exhibiting a slope-break knickpoint within the Orlica Fault Zone

### Geochronology

A possible fault was trenched to investigate its paleoseismicity on Libna Hill (location shown in Figure 2). The trench revealed displaced bedrock and Pliouaternary (>1.8 Ma) sediment; however, the

sediment had not been dated reliably and regional age correlations did not exist. Optically stimulated luminescence (OSL) dating was used and resulted in a <200 Ka age, a full order of magnitude younger than the long-held regional understanding of the sediment's age. The surprisingly young age caused GeoZS to question its validity (Bavec, 2010). To further evaluate the previous OSL ages, we used <sup>26</sup>Al/<sup>10</sup>Be cosmogenic radionuclide (CRN) burial dating and also dated Quaternary sediments using OSL and infrared stimulated luminescence (IRSL). The CRN burial ages returned ages consistent with the regional knowledge of Pliouaternary sediments, and illuminated the possibility that the OSL and IRSL ages were reaching their saturation limits, i.e. not recording the full burial history due to the 'filling' of the crystal lattice with free electrons. Complicating the interpretation, the OSL dose response curve was not clearly indicating that the samples had reached saturation, although IRSL measurements of the same samples' feldspar fraction suggested the Quartz OSL signals were underestimating the ages.

The age extent of OSL dating is limited by the environmental dose rate and the internal properties of the quartz lattice. This upper (old) age limit typically occurs in the Upper, and occasionally Middle Quaternary. We plotted ages against elevation of all of the absolute ages from the Krško Basin (Figure 5). At the ~0.2 Ma position, there is a significant stack of similarly aged samples with a significant elevation range from the same unit, suggesting that >120 m of sediment were deposited in an extremely short period of time. In effect, OSL dating caps the sample ages in Krško Basin at ~200 ka, whereas CRN has a much broader age range that can span the Holocene to most of the Pliocene.

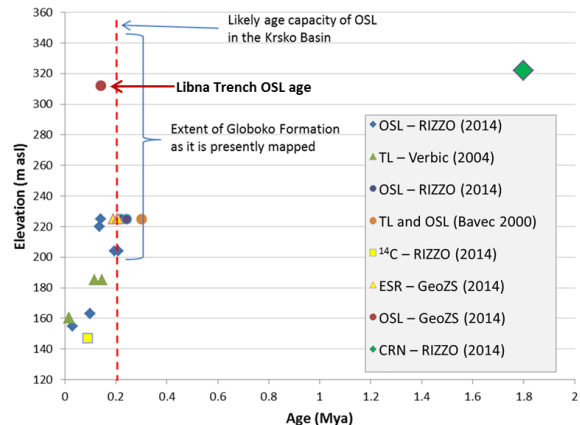


Fig 5: Age-elevation plot of all ages from the Krško Basin

There are several envisaged scenarios that can explain the indistinguishable ages of the same depositional unit but from very different elevations. The first three options assume the >1.8 Ma CRN ages are not representative of the depositional age. Scenario 1 requires that the entire Krško Basin would have deposited >120 m of fluvial sediment at an extreme rate. Scenario 2 requires a modest rate of alluviation followed by a >120 m net incision



occurring at an unreasonably high rate, while also leaving fill terraces at various elevations. Scenario 3 requires unreasonably high localized uplift of Libna Hill, on the order of 140 m, over a very short period of time. A fourth, more plausible, scenario assumes the <200 Ka age of the OSL sample from the Libna trench represents an age minima of the unit's deposition, and accepts the  $^{26}\text{Al}/^{10}\text{Be}$  CRN ages as the true age of deposition. This is consistent, too, with the regional understanding of the depositional age for the Plioquaternary sediment. This 4<sup>th</sup> scenario requires modest, long-term net incision with rates averaging  $\sim 0.1 \text{ mm yr}^{-1}$ , which is consistent with global rates of incision in places with similar relief from around the world (Montgomery and Brandon, 2002).

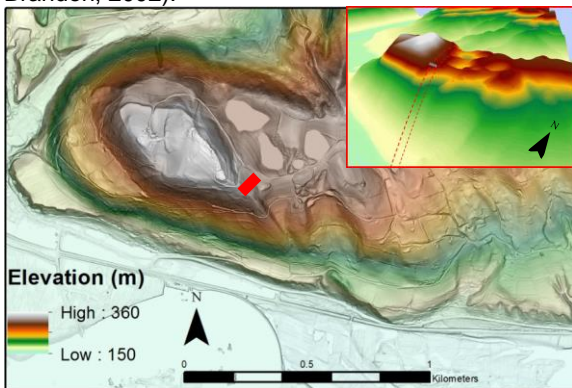


Fig. 6: Karstic and hillslope features on Libna Hill. Inset box in upper right provides an oblique view (3X vertically exaggerated).

When the trench was excavated on Libna Hill (Bavec, 2010), GeoZS did not have high quality LiDAR data, but recently acquired LiDAR revealed that the trench location (shown by red rectangle in Figure 6), and likely its interpretation, may have been complicated by surface processes that are known to produce fault-like appearances in paleoseismic trenches (e.g. Hart et al., 2012). Specifically, the trench was excavated on the edge of a breached karstic depression associated with a landslide (Figure 6).

## Conclusions

Using the best analytical tools and data available helps to reduce uncertainty, and in some cases, helps to recognize important uncertainties that were not previously identified. This work, albeit in a preliminary state, provides several examples that demonstrate the importance of acknowledging the limitations of data and methods, and the value of utilizing the most suitable methods to investigate the best possible topographic data, especially in regions that experience low to moderate tectonic deformation rates. The geochronology that is currently being developed for the Krško Basin is demonstrating that multiple geochronology methods should be used, whenever possible, to detect erroneous ages that may result from inherent, physical limitations of dating methods. Within the Krško Basin and the surrounding area we are starting to develop more robust constraints on deformation rates that we are

using to assess fault capability, and to revise and enhance the seismic source model for the PSHA.

**Acknowledgements:** This work is being performed for a PSHA that is being performed for JEK 2, Krško, Slovenia. The work is being funded by GEN energija, d.o.o.

## References

- Baize, S. (2008): Geological contribution of the SARG/BERSIN to the GG&S project (Krško, Slovenia). Phase 1. DEI/SARG/2008-047. – *Internal report*, 52 pp, IRSN.
- Bavec, M., ed., (2010): Geology report – Phase 1. - Project report for Phase 1 of Geotechnical, Geological, and Seismological (GG&S) Evaluations for the New Nuclear Power Plant at the Krško Site (NPP Krško II).
- Brückl, E., Behm, M., Decker, K., Grad, M., Guterch, A., Keller, G. R., & Thybo, H. (2010). Crustal structure and active tectonics in the Eastern Alps. *Tectonics*, 29(2) 1-17.
- DeLong, S. B., Hilley, G. E., Rymer, M. J., & Prentice, C. (2010). Fault zone structure from topography: Signatures of an echelon fault slip at Mustang Ridge on the San Andreas Fault, Monterey County, California *Tectonics*, 29(5) 1-16.
- Hack, J. T. (1957). Studies of longitudinal stream profiles in Virginia and Maryland, *USGS Professional Paper No. 294-B*.
- Hart M.W., Shaller P.J., Farrand G.T. (2012). When landslides are misinterpreted as faults: Case studies from the western United States. *Environmental and Engineering Geoscience*, 18, 313-325.
- Hetényi, G., Ren, Y., Dando, B., Stuart, G. W., Hegedűs, E., Kovács, A. C., & Houseman, G. A. (2015). Crustal structure of the Pannonian Basin: The AlCaPa and Tisza Terrains and the Mid-Hungarian Zone. *Tectonophysics*, 646, 106-116.
- Jamšek Rupnik, P., Atanackov J., Cline M. L., Cline K. M., Rižnar I., Celarc B., Markelj A., Milanič B., Jež J., Novak M., Bavec, M. (2016). Fault characterization and field campaign related to probabilistic seismic hazard assessment for nuclear infrastructure in the Krško Basin, Slovenia, *7th International INQUA Meeting on Paleoseismology, Active Tectonics and Archeoseismology*, Crestone, CO USA.
- Kirby, E., & Whipple, K. (2001). Quantifying differential rock-uplift rates via stream profile analysis. *Geology*, 29(5), 415-418.
- Kirby, E., & Whipple, K. X. (2012). Expression of active tectonics in erosional landscapes. *Journal of Structural Geology*, 44, 54-75.
- Montgomery, D. R., & Brandon, M. T. (2002). Topographic controls on erosion rates in tectonically active mountain ranges. *Earth and Planetary Science Letters*, 201(3), 481-489.
- Placer, L. (1999) Structural meaning of the Sava Folds. *Geologija* 41, 191-221, Ljubljana, Slovenia
- Placer, L., (2008). Principles of the tectonic subdivision of Slovenia: *Osnove tektonske razčlenitve Slovenije*.
- Van Gelder, I. Matenco E., Willingshofer L., Tomljenovic E., B., Andriessen, P., Ducea, M. N., & Gruič, A. (2015). The tectonic evolution of a critical segment of the Dinarides-Alps connection. *Tectonics*, 34(9), 1952-1978.
- Wobus, C., Whipple, K. X., Kirby, E., Snyder, N., Johnson, J., Spyropolou, K., B. Crosby & Sheehan, D. (2006). Tectonics from topography: Procedures, promise, and pitfalls. *Geological Society of America Special Papers*, 398, 55-74



## Close to the lair of Odysseus Cyclops : the SINAPS@ postseismic campaign and accelerometric network installation on Cephalonia island – Site effect characterization experiment

Edward Marc Cushing (1), Fabrice Hollender (2), Cedric Guyonnet-Benaize (2), Vincent Perron (1,2), Afifa Imtiaz (3), Angkeara Svay (4), Armand Mariscal (3), Pierre-Yves Bard (3), Régis Cottureau (4), Fernando Lopez Caballero (4), Nikolaos Theodoulidis (5), Denis Moiriat (1), Céline Gélis (1)

- (1) IRSN, Fontenay-aux-Roses, France Edward.cushing@irsn.fr.
- (2) CEA Cadarache, St Paul-lez-Durance.
- (3) Univ. Grenoble Alpes, ISTERre / IRD, Grenoble, France
- (4) MSSMat, CNRS, Centrale Supélec, Université Paris-Saclay, 92290 Châtenay-Malabry, France
- (5) ITSAK, Thessalonique, Grèce

**Abstract:** The Cephalonia Island (Greece) area is located at the north-western end of the Aegean subduction frontal thrust linked to the dextral Cephalonia Transform Fault (CTF west of Cephalonia). Since the mean slip rate and the CTF length are large, seismic hazard is high in terms of earthquake frequency and magnitude. The Koutavos-Argostoli site was selected within the French Research Agency (ANR) PIA SINAPS@ project ([www.institut-seism.fr/projets/sinaps/](http://www.institut-seism.fr/projets/sinaps/)) to host a vertical accelerometric array. The long term goal aims at validating 3D nonlinear numerical simulation codes in order to assess site specific amplifications and non-linearities in the framework of seismic hazard assessment for nuclear installation. Herein are presented the first results of the post-seismic campaign organized following the seismic sequence of January-February 2014 including two M6 + shocks and numerous aftershocks and recent accelerometric records performed during the last Levkada Earthquake. Recording of the 2015 Levkada earthquake 50 km away shows that the vertical network is operational and confirms the expected amplifications of the Koutavos Plio-Quaternary basin. The present network is now ready to record strong motion for non-linearity studies.

**Key words:** Cephalonia, seismic experiment, site effects, active faults.

### Introduction

In order to validate 3D non-linear computer codes and to be able to record a great number of earthquake motions, the Koutavos site in Cephalonia (western Greece) was chosen considering both the geological and geotechnical structure and the high seismicity rate. This favourable site is constituted by a lagoonal poorly consolidated quaternary basin overlying infilling of an active Neogene synclinal. Local active tectonics is shown by faulted quaternary terraces exposed on the western shore. This experimental site was previously equipped in the 90's by Athens University Protopapa et al., 1998) then in 2011-2012 in the framework of NERA experiments (Network of European Research Infrastructures for Earthquake Risk Assessment and Mitigation, projet FP7 n° 262330, [www.nera-eu.org](http://www.nera-eu.org)). 62 seismometers were settled from September 2011 to April 2012 by a European laboratories consortium (ITSAK, ISTERre, INGV and GFZ).

In 2013, a first survey was performed to collect geological and geophysical data in the framework of the French Research Agency (ANR) PIA SINAPS@ project ([www.institut-seism.fr/projets/sinaps/](http://www.institut-seism.fr/projets/sinaps/)). In the beginning of 2014, a post seismic campaign was performed. In 2015, 3 boreholes were drilled in the Koutavos area and several accelerometers were installed at different depths to assess site specific amplifications and non-linearities in the framework of seismic hazard assessment for nuclear installations.

### Geodynamical and seismic context

North-western Greece is one of the main active tectonics areas of the Mediterranean region and presents the highest seismic activity in Europe. Located at the boundary of the Eurasian/African plates, the convergence rate is up to few centimetres per year. In the Cephalonia area, this limit is constituted by the north-western end of the Aegean subduction frontal thrust linked to the dextral Cephalonia Transform Fault (CTF west of Cephalonia). This major fault plays the role of a transition zone between the African subducting plate and the continental Apulian plate (Figure 1). Since the mean slip rate and the CTF length are large, seismic hazard is high in terms of earthquake frequency and magnitude. This was the cause of the major 1953, Mw 7.2 earthquake and provoked about 0,5 to 1 meter uplift of a great part of the Cephalonia island. Previously, two events occurred in 1915 (Mw ~ 6.6 & 6.7) in Cephalonia island. This major structure is associated with secondary ones which are the source of more recent, lower but significant earthquakes (e.g. Mw 6.2 Levkada, 2003, Lixourion doublet - Mw 6.0 and 6.1, 2014, Mw ~6.4 Levkada, 2015).

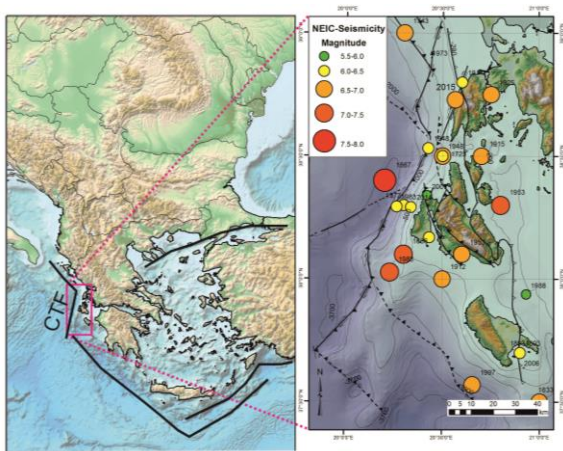


Figure 1: Geodynamical setting of the experiment (structural sketch from Cushing, 1985)

### Test site geology

The Plio-Quaternary Koutavos basin is located in the Argostoli area and is located on a NE striking syncline bounded to the west by a thrustured asymmetric anticline (Figure 2). This anticline is faulted by two east-dipping reverse faults (White Rock or Minies Fault and Argostoli Fault).



Figure 2 : Geological map and cross section.

Based on all available observations collected in the field and previous mapping (Sorel, 1974, Underhill, 1985, Sorel, 1989), the lithostratigraphic series limestones can be described as presented in figure 3.

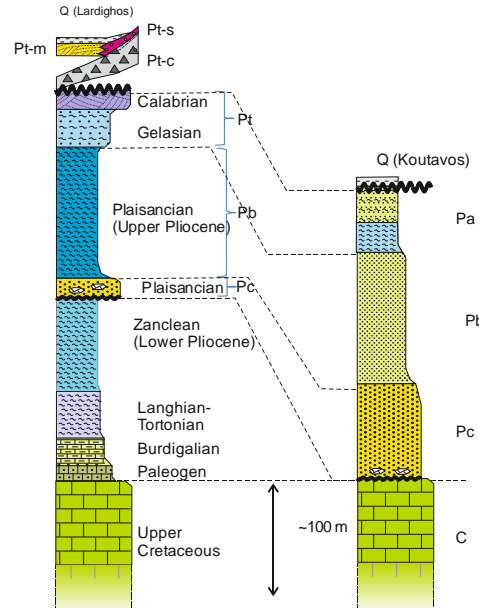


Figure 3: Lithostratigraphic sketch of the Minies anticline (west-left) and Argostoli basin (east-right)

From bottom to top, overlying Cretaceous limestones:

Eastern part (Argostoli area) :

- Unconformably lying on the previous series : Lower Pliocene calcarenites (Pc);
  - Pliocene (Plaisancian ?) sands and sandstones (Pb);
  - Lower Pleistocene sandy shales (Pa);
  - Quaternary (recent) lagoonal deposits.
- Western part (Minies and Lardighos areas) :
- Paleogen carbonates to lower Pliocene clayey series (Zanclean);
  - Unconformably lying on the previous series : Lower Pliocene calcarenites (Pc);
  - Plaisancian blue marls (Pb);
  - Lower Pleistocene sandy marls and gravels (Gelasian) and calcarenites (Calabrian) (Pt);
  - Unconformably lying on the previous series, Early to middle Pleistocene cemented slopes breccia (Pt-c)
  - Middle to upper Pleistocene screens laterally connected to Pleistocene marine calcarenite terraces (raised beaches) (Pt-s/Pt-m);
  - Recent to present Quaternary deposits (Q).

### Database

#### Post seismic campaign:

More than 6000 events have been recorded during the post seismic campaign from February 2014 to June 2015. Each record has been checked, validated and picked manually considering the access to a very large database for Europe. Most of the events have epicentral distance less than 30 km. Some records show Pick Ground Acceleration (PGA) close to 0.1g (Figure 4).

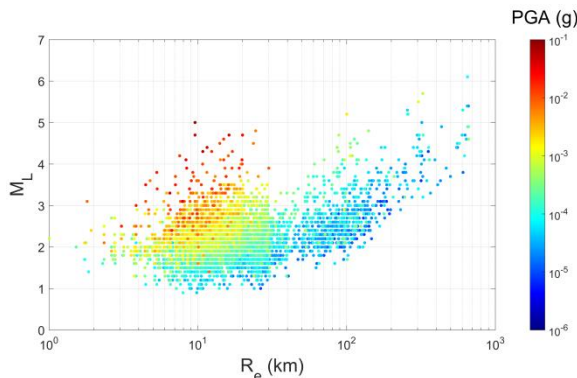


Figure 4: Post-seismic database. PGA (color scale) are represented according to the epicentral distance and to the local magnitude. Each point corresponds to an earthquake recorded at the rock site station.

Koutavos boreholes :

Boreholes were performed in June 2015 in Koutavos park close to the Argostoli town (see location in Figure 2):

- Two 84.5 m deep boreholes: one cored borehole (B1) and one destructive borehole (B2) where a probe was installed:
  - Three destructive boreholes at 40.1 (B3), 15.6 (B4) and 5.5 (B5) meters deep, very close to the previous one (see Figure 5).
- Boreholes were drilled in the Plio-Quaternary units, the deep borehole almost reached Cretaceous Limestones.

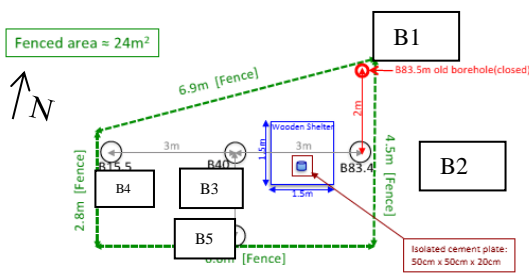


Figure 5: Geotechnical measurements.

One Standard Penetration Test (SPT) was performed in B1. Two crossholes : CH1 (between B2 and B3) and CH2 (between B3 and B4) and two downholes : DH1 in B2 and DH2 in B3.

Borehole Accelerometric Network

Destructive boreholes were equipped with seismic accelerometers at the bottom of each borehole (except the core borehole). One accelerometer was settled at the surface. All accelerometers (Kinematics Episensor) in boreholes have 3 components. An additional rotational sensor (EENTEC R1) is located at surface. The anchorages in the boreholes are made up by glass beads. This process was validated by shaking table test (AZALEE, Saclay, France).

**Results and interpretation**

Geological interpretation

The interpretation of the geological logging and the geotechnical investigations (SPT/CH/DH), allow defining five lithostratigraphic units (Figure 6):

- Quaternary deposits (Q) : 2 meters of backfill overlying about 6 m of lagoonal deposits. For this layer the SPT values are under 10 and the Vs values are less than 250 m/s. In this unit, a recent study (Hadler, 2013) identified a possible succession of four distinct tsunamigenic layers. The ages of these deposits are validated by radiocarbon dating of about 6000 BP for the oldest event.
- (Lower?) Pleistocene (Pa) : this unit shows 3 distinct lithological sets from top to bottom : 39 m of red brown clays, 21 m of red-brown clays and 10 m of grey-blue marls with organic matter and fossils (corals, gastropods and oysters). SPT values are about 30 in average and Vs values ranges between 400 and 500 m/s. This series has been correlated with the one observed in the two previous boreholes drilled 1,5 km further N-W close to the *De Bosset* Bridge where an extensive subsurface investigation program was performed in 2005 (Rovithis et al., 2014). This series outcrops in the vicinity clay quarry as yellowish to reddish sandy clays. This formation may be correlated with the local lower Pleistocene sandy shales outcropping close to Koutavos area.
- Pliocene (Plaisancian ?) (Pb) : 15.5 meters of marly sandy limestones and marls. The Vs values range between 500 and 700 m/s. This formation was encountered also in the *De Bosset* bridge boreholes. It outcrops in the Argostoli town as an alternation of yellowish calcarenites and clays.
- In the bottom of B1 borehole, cretaceous limestones blocks have been collected suggesting that this unit may be reached at 90 m below the ground surface considering close water borehole information.

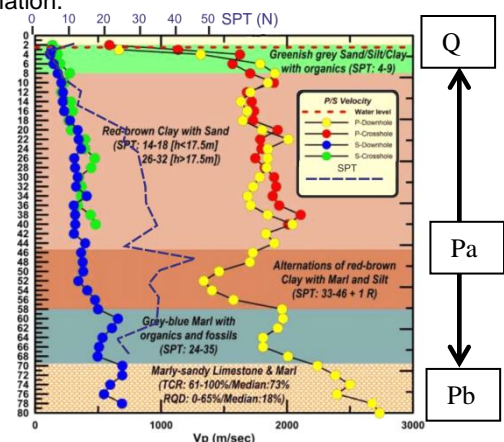


Figure 6: Joint evaluation of the derived P and S-wave velocity distribution with depth from crosshole and downhole measurements. SPT values are also presented. The simplified geological and geotechnical profile of borehole B1 is also presented (after Papazachos et al., 2015).



### First validation of the vertical network

On November 17<sup>th</sup> 2015, a Mw 6.5 earthquake occurred in the western part of the Levkada island, 50 km north of the vertical array. This earthquake was recorded by all the accelerometers on the vertical network and at surface. PGA varies between 0.03 g at the bottom (B2) to 0.15 g at surface, as illustrated in figure 7.

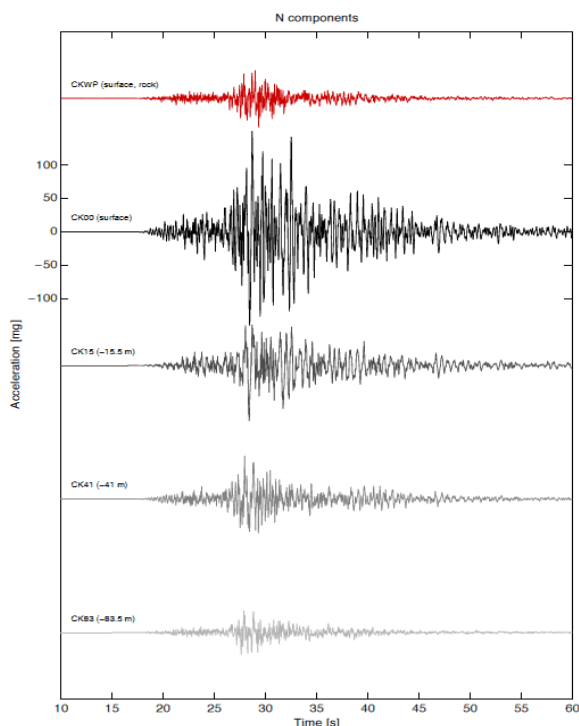


Figure 7: Variation of horizontal (North-South direction) accelerations recorded at different depth from the deepest borehole (-B2) up to the surface. The B5 has not yet been equipped. The red trace is the record of the Levkada Earthquake a few hundred meters away on a rock site.

### Conclusions

The experimental site of Koutavos is well constrained by geological and geophysical data gathered during previous different investigations (NERA, SINAPS@, post seismic campaign). Geological and geotechnical data were also collected during the drilling of boreholes confirming the previous geological interpretation of the Koutavos area.

The recording of a strong earthquake in Levkada 50 km away from the network shows that this one is operational and confirms the expected amplifications of the Koutavos Plio-Quaternary basin. The interpretation of geophysical investigations previously

performed (H/V, AVA and MASW + rotational accelerometers) and postseismic records on a large array are pending. The present network is now ready to record strong motion for non-linearity studies.

**Acknowledgements:** This project was conceived after the NERA-JRA1 et SIGMA / PRENOLIN projects then founded by French ANR in the framework of the program "Investissements d'avenir" (PIA) : SINAPS@ (ANR-11-RSNR-0022 - www.institut-seism.fr/en/). Local authorities have warmly welcomed the project and helped to obtain all necessary authorizations. Thanks also to Agis Konidaris, Chrisostomos Andreou, GEOTER co., Geophysical lab. of Thessaloniki University and many persons who participated to September 2013 and February 2014 field campaigns.

### References

- Hadler H. (2013). *Ancient Greek harbours used as geo-archives for palaeotsunami research - Case studies from Krane (Cefalonia), Lechaion (Gulf of Corinth) and Kyllini (Peloponnese)*. Ph.D.Thesis, Johannes Gutenberg-Universität in Mainz. 140 p.
- Cushing M., (1985). *Evolution structurale de la marge nord ouest hellénique dans l'île de Levkas et ses environs (Grèce nord occidentale)*. Ph.D.Thesis, University of Paris-Sud, France (in French).
- Protopapa E., Papastamatiou D. M. & G. Gazetas, (1998). The Ionian Accelerometer Array: Early Results and Analysis in: *Proceedings of the 11th European Conference on Earthquake Engineering*, Balkema, Rotterdam.
- Papazachos, C.B., Poultisidis M. & M. Anthymidis, (2015). *Performance of seismic wave velocity measurements at selected areas of Cephalonia Island*, A.U.TH., Final Report, July 2015.
- Rovithis E., Pitilakis K., Iachoulis T., Karani I., Chorafa E. & E. Zarogiani, (2014). "De Bosset" monumental stone bridge in Cephalonia: Strengthening measures and seismic response under the earthquakes of 26/01/2014 and 03/02/2014 in: *2nd International Conference on Bridges "Innovations on Bridges and Soil-Bridge Interaction*, 16-18 October, Athens, Greece.
- Saltogianni V. & S. Stiros, (2015). A Two-Fault Model of the 2003 Leucas (Aegean Arc) Earthquake Based on Topological Inversion of GPS Data. *Bulletin of the Seismological Society of America* 105, 2510-2520.
- Sorel D. (1976). *Etude néotectonique dans l'arc égéen occidental*. PhD Thesis - Paris Orsay (Paris XI).
- Sorel D. (1989). *L'évolution structurale de la Grèce nord-occidentale depuis le Miocène dans le cadre de géodynamique de l'arc égéen*. Thèse d'état. Paris Orsay (Paris XI).
- Underhill J. (1989). Late Cenozoic deformation of the Hellenide foreland, western Greece. *Geological Society of America Bulletin* 101, 613-614



## Developing a paleoseismic age model for large-magnitude earthquakes on fault segments of the Himalayan Frontal Thrust in India

Daniels, Robyn L. (1), Tina M. Niemi (1), R. Jayangondaperumal (2)

- (1) Department of Geosciences, University of Missouri-Kansas City, 5100 Rockhill Road, Kansas City, MO 64110, USA.  
Email: [rldwvf@mail.umkc.edu](mailto:rldwvf@mail.umkc.edu)
- (2) Wadia Institute of Himalayan Geology, 33 GMS Road, Dehradun 248001, India

**Abstract:** Crustal collision between Eurasia and the Indian subcontinent has produced a thrust fault system that accommodates a share of the strain associated with convergence. The foremost of these faults is the Himalayan Frontal Thrust (HFT), which has produced numerous, large-magnitude earthquakes along discrete segments of the fault throughout the last two centuries that are constrained through instrumental and historical records. Paleoseismic studies have aimed to establish comparable constraint for penultimate ruptures of the fault. Of particular interest is the segment of the fault known as the Central Seismic Gap (CSG), due to an apparent long-term quiescence that suggests the potential for impending large-scale rupture. Here we compile recent, paleoseismic findings from seven published trench sites into a coherent OxCal age model for large-magnitude ruptures along the CSG. Our results indicate that the CSG likely ruptured in the event corresponding to historical accounts of an earthquake in 1344 A.D., while the north-westernmost segment in India likely ruptured in the earthquake of 1555 A.D.

**Key words:** Himalaya thrust, historic earthquakes, paleoseismology,

### INTRODUCTION

The Himalayan thrust fault system lies at the active, tectonic boundary between Eurasia and the Indian subcontinent, and accommodates a share of the strain associated with convergence and the concomitant uplift of the Himalayan Mountain Range (Fig 1). The foremost in this series of transverse thrust faults is the Himalayan Frontal Thrust (HFT), also referred to as the Main Frontal Thrust (MFT). Numerous large-magnitude earthquakes have ruptured discrete segments of the HFT in the last two centuries, as referenced in earthquake catalogues (e.g. Khattri, 1987; Iyengar et al., 1999; Ambraseys, 2000; Pant, 2002; Ambraseys and Douglas, 2004).

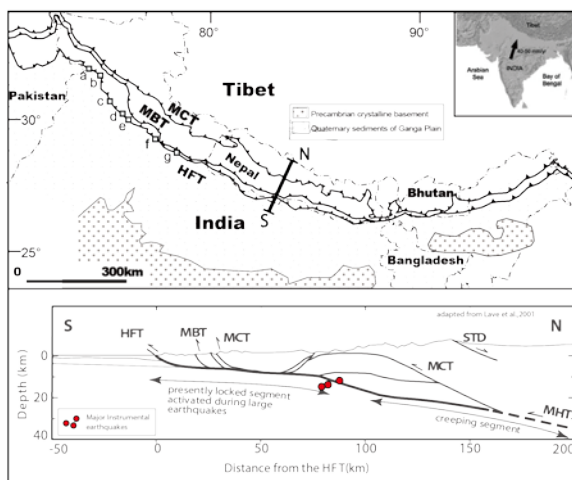


Fig. 1: Map showing the major zones of Himalayan convergence—MCT: Main Central Thrust; MBT: Main Boundary Thrust; and HFT: Himalayan Frontal Thrust. Trench site locations are labeled as in Fig. 2. Schematic cross-section through central Nepal showing the main structures and instrumental thrust earthquake foci. STD: Southern Tibet Detachment; MHT: Main Himalayan Thrust; (after Lavé et al., 2001).

Incomplete historical records and inferred rupture locations leave many unanswered questions surrounding the timing and nature of these events that can be addressed through paleoseismic investigation. The need for additional paleoseismic data is particularly critical along segments of the HFT that lack a 20<sup>th</sup> century rupture, such as the Central Seismic Gap (CSG), which lies between the areas affected by the 1905 A.D. and 1934 A.D. earthquakes. Establishing the timing of earthquakes along the CSG is critical in assessing seismic hazards for areas proximal to the fault that have both large populations and inadequate infrastructures. While several paleoseismic studies have been conducted across the HFT, along and adjacent to the CSG; a comprehensive analysis of the radiocarbon ages associated with these studies has not previously been completed. In order to better constrain the timing of paleoearthquakes on the northwest, Indian section of the HFT, we have evaluated trench data and compiled recent, radiocarbon age results from seven sites including (from northwest to southeast): Hajipur, Bhatpur, Chandigarh, Kala Amb, Rampur Ganda, Lal Dhang, and Ramnagar (Fig. 1) (Kumahara and Jayangondaperumal, 2013; Malik et al., 2010; Kumar et al., 2001 and Kumar et al., 2006). Review articles by Mugnier et al. (2013) and Bollinger et al. (2016) provided a synopsis of earthquakes along the central Himalaya and Nepal sections of the HFT, respectively.

An age model was developed for each of the seven trench sites based on published radiocarbon results, with consideration given to the stratigraphic context of each trench, using the OxCal software program (Bronk Ramsey, 2009) with the IntCal13 atmospheric calibration curve (Reimer et al., 2013). These models are presented here, alongside published trench logs, in a panoptic illustration (Fig. 2) that offers a coherent chronology for



## INQUA Focus Group on Paleoseismology and Active Tectonics



paleoseismicity.org

large-scale ruptures of the CSG. Calendar date ranges at one- and two-sigma confidence intervals are shown adjacent to probability distribution functions for earthquakes identified at each of the sites. The data reveal collective evidence for a rupture of the CSG corresponding to the historical earthquake of 1344 A.D.

### PALEOSEISMIC DATA

A short description of each of the trenches follows, beginning with the Hajipur site, which lies outside of the CSG to the northwest. Four stratigraphic units were identified in the trench at Hajipur (Malik et al., 2010), which measured approximately 18 meters long, 2-2.5 meters wide and 1-4.5 meters in depth. The oldest layer, Unit A, is a gravel layer with sand lenses. Unit B is a medium to coarse sand, and is the youngest faulted unit. Units A and B are thrust over Unit B in the footwall along a low-angle fault strand in a single event. Units C and D are colluvium layers capping the faulted sequence. Charcoal samples included in the model were collected from Unit B in the hanging wall (H5) and at the interface between Unit B in the footwall and the colluvium layer, Unit D (H2a). The age model gives a two-sigma confidence interval for the event occurring within the range of 1336 A.D. – 1771 A.D., and a one-sigma confidence interval for occurrence in the range of 1406 A.D. – 1628 A.D.

The Bhatpur trench (Kumahara and Jayangondaperumal, 2013), located 80 km southeast of Hajipur and also to the northwest of the CSG, measured 22 meters long and 5 meters deep, and revealed six stratigraphic units. The oldest of these, Unit 1, is a matrix-supported pebble-gravel. Unit 2 is also a matrix-supported pebble-gravel that is faulted in the hanging wall, and repeated as a sub-horizontal layer with some folding in the footwall. The base of Unit 2 is a fine-grained sand. Unit 3 is a sand and silt layer with gravel lenses, with interbedded, organic-rich layers that are interpreted to be buried paleosols. Units 1-3 are faulted and displaced over Unit 3 in the footwall. Units 4 and 5 are capping colluvium layers and Unit 6 is interpreted as an active fan deposit. Four charcoal samples were collected from the faulted Unit 3 (BHA-004, BHA-103, BHA-114, and BHA-118) and one from the Unit 5 colluvium layer (BHA-117). The age model gives a two-sigma confidence interval for occurrence in the range of 1341 A.D. – 1460 A.D., and a one-sigma confidence interval for occurrence in the range of 1399 A.D. – 1445 A.D.

The trench at Chandigarh (Kumar et al., 2006), located approximately 90 km southeast of the Bhatpur site, was excavated to 40 meters in length and 4-5 meters in depth. Seven distinct units were exposed on excavation. Units 1-3 are gravel layers and Unit 4 is described as a sandy, silty clay. Units 1-4 are faulted and overlie Unit 4 in the footwall. Unit 5 is interpreted as a cut and fill channel that caps the fault strand, and Unit 6 is colluvium. Unit 7 is a young, overbank deposit of silty sand. Charcoal samples were collected from Unit 4 in the footwall (PAN-05, PAN-

08, PAN-23, and PAN-26), from the colluvium layer, Unit 6 (PAN-01, PAN-02, PAN-03, and PAN-27) and from Unit 7 (PAN-09, PAN-11, and PAN-17). The age model gives a two-sigma confidence interval for this rupture occurring in the range of 1325 A.D. – 1390 A.D. and a one-sigma confidence interval for occurrence in the range of 1340 A.D. – 1374 A.D.

The trench at Kala Amb (also known as Black Mango) (Kumar et al., 2001), located 50 km to the southeast of Chandigarh, measured 55 meters in length and 5-10 meters in depth. Four fault strands were identified in this trench. For the purpose of this model, we focus on the strand labeled F3, as it is suggested that the upper strands may have occurred in a second event with much less co-seismic slip. The F3 fault strand marks the displacement of a gravel layer, Unit 2, and a silty sand layer, Unit 3, in the hanging wall over Unit 3 in the footwall. Unit 1 is identified as Siwalik bedrock, but this layer is not exposed adjacent to F3. Although it is apparent that colluvium layers have developed above Unit 3, these are not differentiated from Unit 3. Radiocarbon ages for charcoal samples collected from Unit 3 in the footwall of F3 are included (C-14, C-18, C-19, and C-21) and from colluvium layers in Unit 3 that cap the faulted sequence (C-13, C-15, and C-22). The age model gives a two-sigma confidence interval for occurrence in the range of 1304 A.D. – 1393 A.D. and a one-sigma confidence interval for occurrence in the range of 1327 A.D. – 1380 A.D.

Rampur Ganda is located just 20 km southeast of Kala Amb. The trench excavated at this location (Kumar et al., 2006) measured 58 meters in length and exposed 3 distinct stratigraphic units. The oldest of these, Unit 1, is sheared, Siwalik sandstone bedrock. Unit 1 together with Unit 2, a fluvial sand and gravel layer capped by a succession of soils, are displaced over Unit 2 in the footwall. The fault is capped by Unit 3, which consists of aeolian fill abutting the newly formed scarp underlying a layer of colluvium. Charcoal samples were collected from Unit 2 in the hanging wall some distance from the fault (AB-18) and at the interface between Unit 2 and Unit 3 in the footwall (AB-07). Unit 3 was also dated above Unit 2 in the footwall (AB-08). A two-sigma confidence interval is given for the event occurring within the range of 1265 A.D. – 1417 A.D. and a one-sigma confidence interval for the range of 1275 A.D. – 1400 A.D.

The trench at Lal Dhang (Kumar et al., 2006) measured 25 meters in length and 4-6 meters deep and exposed seven stratigraphic units. From oldest to youngest: Units 1 and 2 are gravel layers, Unit 3 is a poorly compacted sand layer, Unit 4 is a compact, silty clay and Unit 5 is a sandy loam. Units 1-5 are thrust over and plowed into Unit 5 in the footwall. Both Unit 6, a basal colluvium layer, and Unit 7, a scarp-derived colluvium layer, are unfaulted. Charcoal samples were collected from Unit 3 in the footwall (LDT-02) and in the hanging wall (LDT-15), and from Unit 4 in the footwall (LDT-11). Additional samples were collected just above the contact between Unit 5 in the footwall and

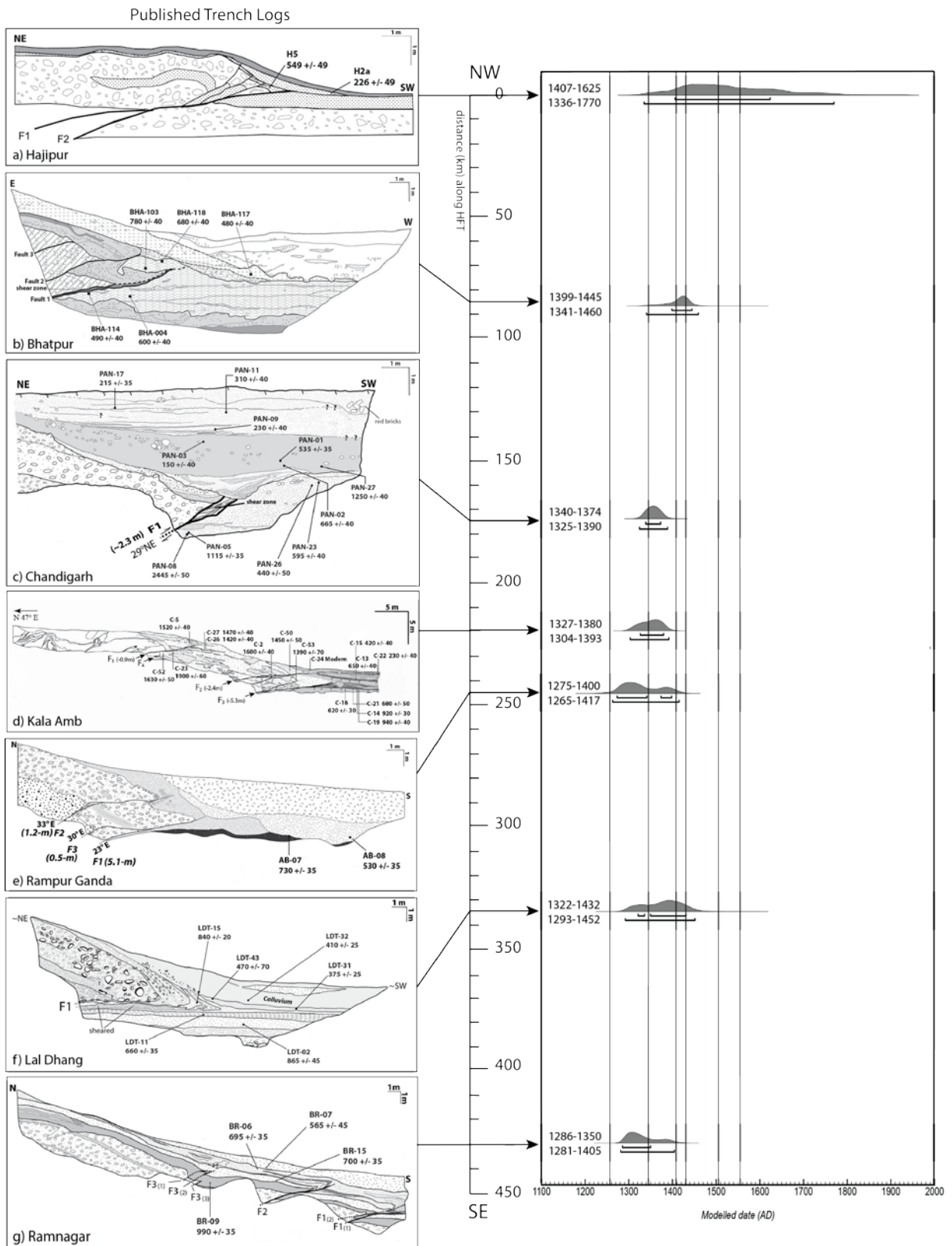


Fig. 2: Evidence of paleoearthquakes at seven trench sites along the HFT based on published, paleoseismic trench data (Kumahara and Jayagondaperumal, 2013; Malik et al., 2010; Kumar et al., 2001 and Kumar et al., 2006). One- and two-sigma confidence intervals are given for rupture dates at each site, alongside probability distribution functions developed from radiocarbon age results using the OxCal software program (Bronk Ramsey, 2009). Vertical lines indicating dates of putative earthquakes in 1255, 1344, 1408, 1430, 1505 and 1555 are superimposed. Radiocarbon sample collection locations are shown on each trench log and trench sites are labeled alphabetically, corresponding to labeled locations in Fig. 1.



## INQUA Focus Group on Paleoseismology and Active Tectonics



paleoseismicity.org

the colluvium layer, Unit 6 (LDT-31), near the hanging wall in Unit 6 (LDT-43) and from the Unit 7 colluvium layer (LDT-32). The age model gives a two-sigma confidence interval at this site for an event occurrence in the range of 1293 A.D. – 1452 A.D. and a one-sigma confidence interval for occurrence in the range of 1322 A.D. – 1432 A.D. A new trench was excavated at this site in late September 2015 and is presented at this conference (Niemi et al., 2016).

The southernmost trench site included in our study was excavated near Ramnagar (Kumar et al., 2006), approximately 90 km southeast of the Chandigarh site, and measured 32 meters in length. Five stratigraphic units and three fault strands were identified, and all displacement is attributed to a single event. Faulted units include: Unit 1, a gravel layer; Unit 2, a silty, sandy clay; Unit 3, a clayey, medium to coarse sand with gravel stringers and Unit 4, a clayey silt to coarse sand layer. Unit 5 is unfaulted, scarp-derived colluvium of dark, clayey sand with weak soil development. Charcoal samples were collected from Unit 3 between the F2 and F3 fault strands (BR-09), Units 3 and 4 in the hanging wall of F2 (BR-06 and BR-15) and the colluvium layer, Unit 5 (BR-07). A two-sigma confidence interval is given for an occurrence date range between 1281 A.D. – 1405 A.D., and a one-sigma confidence interval for 1286 A.D. – 1350 A.D.

### DISCUSSION

Dating paleoseismic events using radiocarbon data can be problematic due to the potential for reworking of charcoal samples during the post-seismic erosion of fault scarps. For this reason, it is critical that a sufficient number of samples be collected, and that collection from colluvium layers be avoided. Modelling these data using a Bayesian statistical program such as OxCal that incorporates stratigraphic relationships greatly increases the accuracy of these results.

The OxCal model presented here indicates one event, coeval across the five southernmost sites, corresponding to the historically documented earthquake of 1344 A.D. The two-sigma confidence interval for the Lal Dhang site includes probability for putative events in 1408 A.D. and 1430 A.D.; however preliminary data from a new study at this site (Niemi et al., 2016) indicates a two-sigma range ending prior to 1408 A.D., which suggests greater agreement with the 1344 A.D. event. To the northwest of the CSG, results are less clear. The two-sigma confidence interval for Bhatpur also includes probability for rupture in 1344 A.D., however the distribution for this site does not rule out the possibility of rupture in 1408 A.D. or 1430 A.D. It is worth noting, however, that evidence for purported earthquakes along the northwestern section of the HFT in the 15<sup>th</sup> century is scarce. The northernmost site at Hajipur is poorly constrained due to a dearth of radiocarbon data for this site, and therefore some probability exists for ruptures corresponding to any of several historical earthquakes. However, the earthquake of 1555 A.D. is a probable candidate, due to the close proximity to the affected area for that event.

Preliminary estimates of recurrence intervals for the segment to the northwest of the CSG can be calculated as 1905 A.D.–1555 A.D., or 350 years; and southeast of the CSG as 1934 A.D.–1255 A.D. or 679 years (Mugnier, et al., 2013). Based on an inferred rupture date of 1344 A.D. as suggested by our model, the CSG has not ruptured in 672 years, which reinforces the concern for an impending large-scale event.

**Acknowledgements:** Special thanks to the University of Missouri-Kansas City Women's Council, School of Graduate Studies, College of Arts & Sciences and Department of Geosciences, and the Wadia Institute of Himalayan Geology.

### References

- Ambraseys, N., 2000, Reappraisal of north-India earthquakes at the turn of the 20th century: *Current Science*, v.70, p. 1237-50.
- Ambraseys, N., and Jackson, D., 2003, A note on early earthquakes in northern India and southern Tibet: *Current Science*, v. 84, no. 4, p. 570-582.
- Ambraseys, N., and Douglas, J., 2004, Magnitude calibration of north Indian earthquakes: *Geophysical Journal International*, v. 158, p. 1-42.
- Bollinger, L., and 3 others, 2016, Slip deficit in central Nepal: omen for a repeat of the 1344 AD earthquake?: *Earth, Planets and Space*, v. 68, no. 12, DOI 10.1186/s40623-016-0389-1.
- Bronk Ramsey, C., 2009, Bayesian analysis of radiocarbon dates. *Radiocarbon*, v. 51, no.1, p. 337-360.
- Iyengar, R.N., Sharma, D., and Siddiqui, J.M., 1999, Earthquake history of India in Medieval times: *Indian Journal of History of Science*, v. 34, no. 3, p. 181-237.
- Jayangondaperumal, R., Mugnier, J.-L., and Dubey, A.K., 2013, Earthquake slip estimation from the scarp geometry of Himalayan Frontal Thrust, western Himalaya: Implications for seismic hazard assessment: *International Journal of Earth Sciences*, v. 102, p. 1937-1955.
- Khattri, K.N., 1987, Great earthquakes, seismicity gaps and potential for earthquake disaster along the Himalaya plate boundary: *Tectonophysics*, v. 138, P. 79-92.
- Kumahara, Y., Jayangondaperumal, R., 2013, Paleoseismic evidence of a surface rupture along the northwestern Himalayan Frontal Thrust (HFT), *Geomorphology*, <http://dx.doi.org/10.1016/j.geomorph.2012.09.004>.
- Kumar, S., and 5 others, 2001, Earthquake recurrence and rupture dynamics of Himalayan Frontal Thrust, India: *Science*, v. 294, p. 2328-2331.
- Kumar, S., and 5 others, 2006, Paleoseismic evidence of great surface rupture earthquakes along the Indian Himalaya: *Journal of Geophysical Research*, v. 111, B03304, doi:10.1029/2004JB003309.
- Lave, J., and 6 others, 2005, Evidence for a great medieval earthquake (1100 AD) in the Central Himalayas, Nepal: *Science*, v. 307, p. 1302-1305.
- Malik, J.N., and 5 others, 2010, Active faults and related Late Quaternary deformation along the northwestern Himalayan Frontal zone, India: *Annales Geophysics*, v. 46, p. 917-936.
- Mugnier, J.L., and 5 others, 2013, Structural interpretation of the great earthquakes of the last millennium in the central Himalaya: *Earth Science Reviews*, v. 127, p. 30-47.
- Niemi, T.M., Daniels, R.L., and Jayangondaperumal, R., 2016, New paleoseismic data from the Lal Dhang trench site across the Himalayan Frontal Thrust in India: This meeting.
- Pant, M.J., 2002, A step towards a historical seismicity of Nepal: *Adarsa*, no. 2, p. 29-60.
- Reimer, P. J., and 25 others, 2013, IntCal13 and Marine13 Radiocarbon Age Calibration Curves 0-50,000 Years cal BP. *Radiocarbon*, 55(4).



## Paleoliquefaction and possible surface deformation along New Madrid Seismic Zone in Yarbro, Arkansas

Dunahue, J.C. (1), Niemi, T.M. (1), Tuttle, M.P. (2) Haynes, M. (3) Torgashov, E.V. (4)

- (1) Department of Geosciences, University of Missouri – Kansas City, Kansas City, MO. James.dunahue@gmail.com
- (2) M. Tuttle & Associates, Georgetown, ME. United States 04548.
- (3) Arkansas Archeological Survey, Fayetteville, AR. United States 72315
- (4) Department of Geological Sciences & Engineering, Missouri University of Science and Technology, Rolla, MO.

**Abstract:** From interpretation of historical aerial photography and LiDAR imagery of northeast Arkansas, we identified a northeast-striking topographic lineament coincident with the southwestern trend of modern seismicity in the New Madrid seismic zone. The lineament extends 7.0 km across the landscape, is approximately 1 – 2 m higher than the adjacent topography, and has an echelon segments. We collected geophysical data including electrical resistivity and ground penetrating radar across the lineament at three locations, and excavated three paleoseismic trenches (0.75-2.25 m deep) to try to determine whether the feature was depositional or tectonic in origin. The anomalous geomorphology, seismicity trend, and the geophysical imaging of a large, abrupt discontinuity suggest that the lineament may be fault controlled. However, the trenches revealed no unequivocal evidence of faulting. Instead, they uncovered earthquake-induced liquefaction features and a channel margin. Both may be fault controlled but deeper trenches will be required to adequately test the hypothesis.

**Key words:** Paleoseismology, geophysics, geomorphology, near-surface faulting, New Madrid seismic zone

### Introduction

Despite the occurrence of large magnitude earthquakes in the New Madrid seismic zone (NMSZ), the current body of research can only confirm monoclinial folding above the reverse Reelfoot fault (Russ et al., 1978; Russ, 1979; Kelson et al., 1996; Schweig and Van Arsdale, 1996; Purser and Van Arsdale, 1998; Champion et al., 2001; Guccione et al., 2002) and right-lateral displacement along the New Madrid North fault (Baldwin et al., 2002). These faults provide valuable data on the Reelfoot step-over structure and the associated strike-slip North New Madrid fault continuing to the northeast. However, similar fault-related data are lacking for the southwestern portion of the NMSZ. Paleoliquefaction studies have provided valuable information about timing, source area, and magnitudes of paleoearthquakes in this area (e.g., Tuttle et al., 2002 and 2005), but fault studies could help to reduce uncertainties associated with the sources and magnitude of past earthquakes. Uncovering a surface rupture of an active fault would allow direct measurement of the direction and amount of slip. In order to reduce these uncertainties, we are searching for surficial, tectonic deformation above strike-slip faults inferred from seismicity and seismic reflection studies.

The Cottonwood Grove fault (CGF), associated with the Reelfoot Rift in the vicinity of Blytheville and terminating at the Reelfoot fault structure to the northeast, is a predominantly right-lateral strike-slip fault and is interpreted to be the segment that ruptured in 1811 to produce the December 16<sup>th</sup> mainshock (Johnston and Schweig, 1996; Tavakoli et al., 2010). Mini-Sosie (Sexton

and Jones, 1992) and Vibroseis reflection geophysics (Hamilton and Zoback, 1982; Zoback and others, 1980) across the CGF indicate ~75 m of middle-Eocene uplift with very little to no vertical deformation above the Eocene strata. However, recent interpretation of seismic reflection data collected on the southwestern portion of the Blytheville Arch, a strike-slip, pop-up structure coincident with the CGF trace, shows ~20 m of uplift in Eocene to Quaternary sediments (Williams et al., 2010; Pratt et al., 2012). This suggests active Quaternary faulting along the CGF that may be expressed in the geomorphology.

The location of microseismicity south of the Reelfoot fault appears to align with the CGF (or what is sometimes referred to as the Blytheville fault). However, the surface trace of this fault has not been located and may be partially destroyed or buried by fluvial processes. Newly acquired airborne LiDAR data from the U.S.G.S. shows a NE-trending topographic lineament in the vicinity of microseismicity near Yarbro, north of Blytheville (Fig. 1). The linear ridge is approximately 1-1.7 m higher than the topography to the east and west and apparently has an *en echelon* trend with right-stepping segments. The anomalous topography appears to cross cut scroll bars, meander loops, and other geomorphic features along this portion of the Mississippi River flood plain. Our preliminary interpretations are that the topographic lineament represents the surface expression of an underlying fault, and therefore may be a fault scarp, and that the geomorphic features crosscut by the fault may provide piercing points for measuring fault displacements.

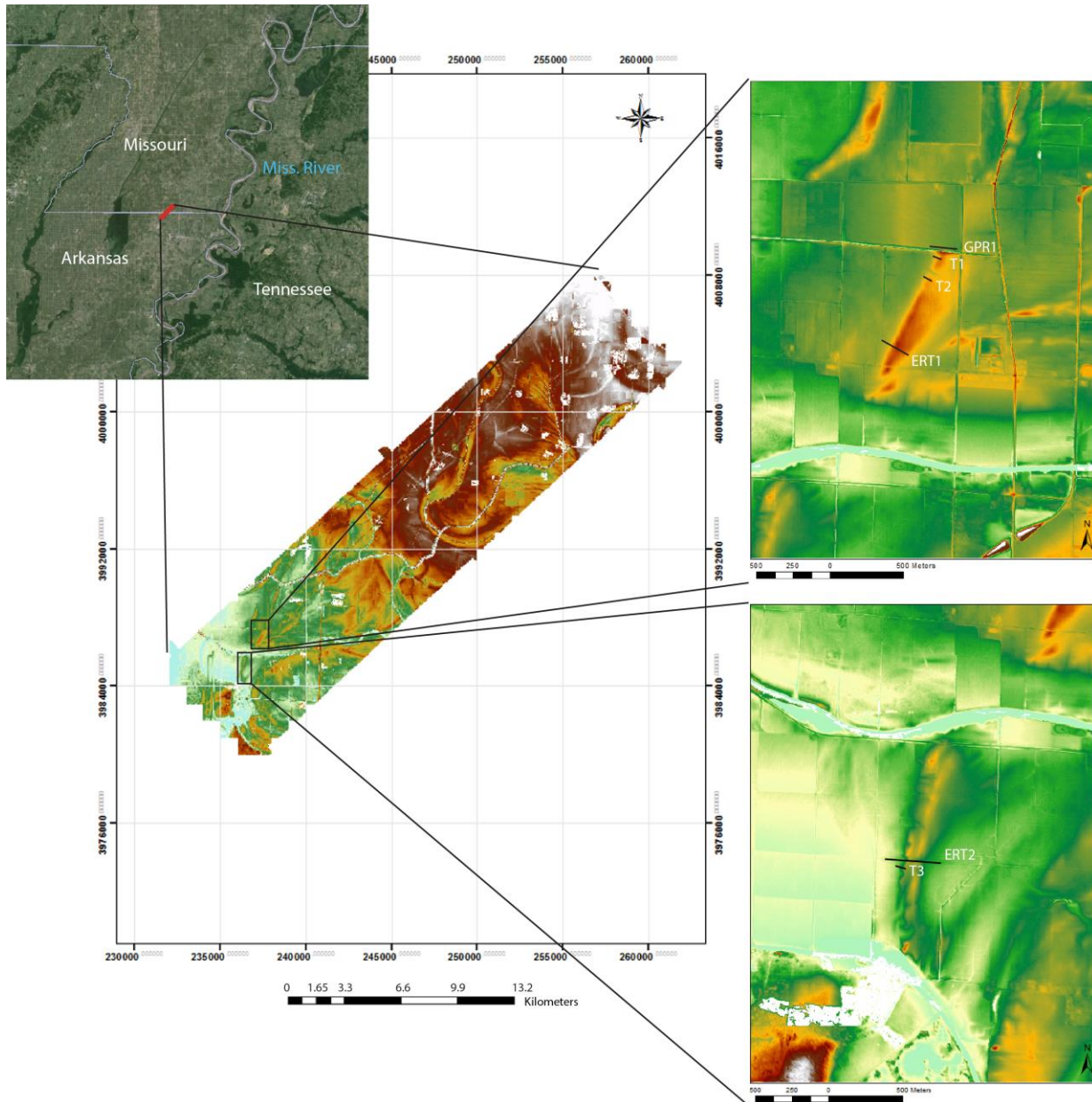


Fig. 1: Map of geophysical surveys (ERT1, ERT2, GPR1) and paleoseismic trenches (T1, T2, T3) using LiDAR data provided by the USGS. Warm colors represent higher elevation; cool colors represent lower elevation.

### Geophysical Surveys

To determine if the linear, NE-trending ridges in the Yarbro area showed evidence of subsurface faulting, we conducted geophysical surveys of the area along the anomalous “topographic high”. We used a variety of geophysical methods in collaboration with Prof. Neil Anderson’s research group at Missouri University of Science and Technology (MS&T) in Rolla, MO including ground-penetrating radar (GPR), electrical resistivity tomography (ERT), and seismic refraction.

A 160 m GPR (400MHz) profile across the northern lineament reveals a depression-like structure that spans

1.5 m and extends 1.0 m below the surface. In the image, a reflector gently dips into the structure as it approaches from either side of the profile and dips steeply as it enters the depression. Such a depression could be interpreted in various ways. In a region of large-scale liquefaction, the apparent depression and dipping beds could be related to subsidence caused by earthquake-induced liquefaction and lateral spreading. An alternative interpretation is that the depression is a filled graben at the margin of a fault. The presence of liquefaction features, as they are prone to take any advantageous route to the surface including faults, can increase uncertainty in geophysical interpretations.



To image deeper structures across the lineaments, Two ERT profiles were run, one 175 m with 1.5 m electrode spacing across the north lineament, and one 350 m with 3 m electrode spacing across the south lineament. In both profiles the data show an abrupt discontinuity between higher and lower resistivities across the margin of the ridge. Resistivities on the eastern sides of the lineaments have the values and form consistent with a broad, abandoned channel, while across the discontinuity, the resistivity values increase and are higher in the section relative to the sediments in the east. A high resistivity discontinuity at a channel margin could be due to the juxtaposition of different materials across a fault or to a large sand dike emplaced during an earthquake. The interpretation of the seismic refraction line shows similar results. We tested these hypotheses by excavating paleoseismic trenches across the western flank of the ridges at both locations.

### Paleoseismic Trench Investigation

Three trenches, 0.75-2.25 m deep, were excavated across the proposed fault scarp, two crossing the north lineament and one crossing the southern lineament. The northernmost trench (T1) revealed a silty clay soil developed on massive fluvial deposits of clayey silt, silt and fine sand. East of the ridge where elevation is higher, the soil is interrupted by a 6.5 m wide and 1.0 m deep channel fill of organic-rich clay with many fractures along which root casts have formed and small (< 3 cm) sand dikes have intruded (Fig. 2). To the west of the ridge, the soil dips westward toward the same discontinuity noted in the GPR and ERT data and the sediment in which the soil developed gradually changes from silt to clayey silt.

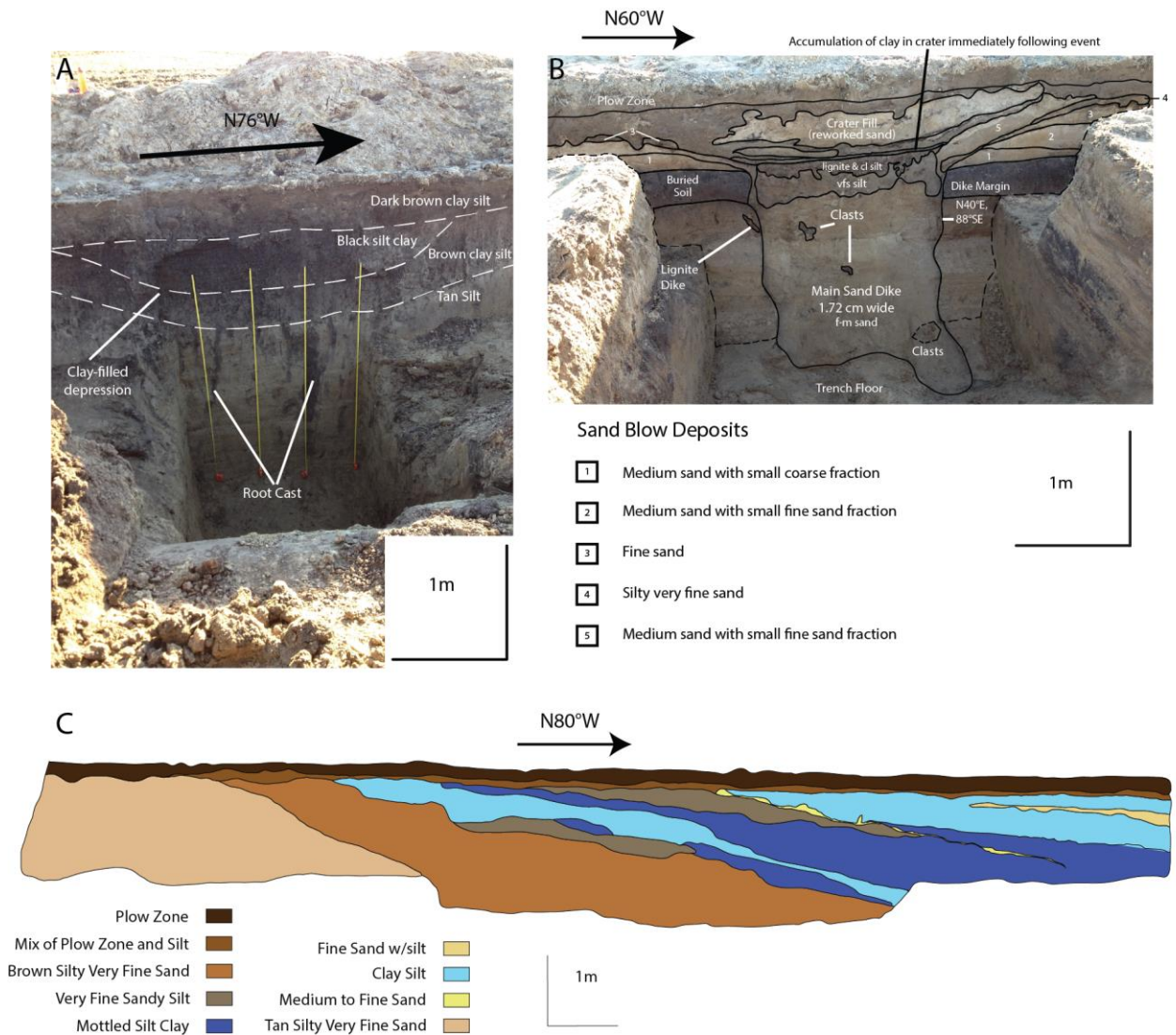


Fig. 2: Annotated photographs of clay depression in T1 (A) and main feeder dike and related sand blow deposits in T2 (B). Trench log of channel margin in T3 (C).



At 45 m west of the clay-filled depression, the soil is buried by a sandblow of five, fining-upward, depositional units of mostly medium sand with no soil development between layers; they originate from a 1.80-m-wide feeder dike (Fig. 2). Both the sand dike in the west and the clay-filled depression in the east of T1 are also present in T2, roughly 100.0 m to the south (Fig. 1). This suggests that the features are continuous and subparallel to the trend of the lineament.

The third trench (T3) transects the southern lineament which has been proposed to be an *en echelon*, right-stepping segment of a fault in a strike-slip system (Fig. 1). East of the ridge, a layer of silty clay dips eastward, away from the apex of the ridge, and is underlain by silty, very fine sand. The silty clay unit pinches out at the surface 20 m from the east end of the trench. The massive silt and fine sand fluvial deposits continue west, extending beyond the apex of the ridge where they are overlain by westward-dipping layers of clay and silty clay (Fig. 2). Several domains of mixed silt and silty clay occur along the contact. The contact is interpreted as a channel margin and the overlying fine-grained sediment as a channel-fill deposit. The domains of mixed material may be colluvium or slope wash. Within the channel-fill deposit, there are three lenses of weathered and mottled, silty sand and fine sand that in general fine upward. Although a feeder dike does not occur in the trench, we suspect that these are sand blows because they fine upward and are capped by a layer of lignite, like many other sand blows in the region. The feeder dike most likely occurs to the north or south of the thickest portion of the sand deposits and parallel to the flank of the channel margin. ERT imaged a possible sand dike about 50 m to the north along the flank of the scarp, which could be the feeder dike of this compound sand blow.

## Conclusions

The results of the geophysical surveys and subsequent paleoseismic trenches neither prove nor refute the existence of neotectonic deformation in the sediments above the CGF. While the ERT image suggests a large, inclined discontinuity at the margin of the lineament, no unequivocal evidence of faulting was discovered in the trenches. Instead, the trenches revealed a small clay-filled channel and compound sand blow and related feeder dikes in T1 and T2 and a channel margin and likely compound sand blow in T3. These features may be fault controlled; however, in this dynamic depositional environment, deeper excavations are required to reveal any tectonic structures that may have influence their formation.

## Acknowledgements

This study was made possible from funding provided by the USGS National Earthquake Hazards Reduction Program. It also benefited from the enthusiastic cooperation of the landowner John Nelson and UMKC undergraduate students enrolled in the GEOL 472

Earthquake Geology class. We thank MS&T graduate student, Faraj Eljabir for seismic refraction and Aleksey Khamzin for GPR acquisition and processing.

## References

- Baldwin, J.N., Barron, A.D., Kelson, K.I., Harris, J.B., and Cashman, S. (2002). Preliminary paleoseismic and geophysical investigation of the North Farrenburg lineament: Primary tectonic deformation associated with the New Madrid North Fault? *Seismological Research Letters* **73**, 393–413.
- Champion, J., Mueller, K., Tate, A., and Guccione, M.J. (2001). Geometry, numerical models and revised slip rates for the Reelfoot fault and trishear fault-propagation fold, New Madrid seismic zone, *Engineering Geology* **62**, 31–49.
- Guccione, M.J., Mueller, K., Champion, J., Shepherd, S., and Odhiambo, B. (2002). Stream response to repeated co-seismic folding, Tiptonville dome, western Tennessee, *Geomorphology* **43**, 313–349.
- Hamilton, R. M., and Zoback, M. D. (1982). Tectonic features of the New Madrid seismic zone from seismic-reflection profiles, in *Investigations of the New Madrid, Missouri, Earthquake Region*, F. A. Mckeown and L. C. Pakiser (Editors), *U.S. Geol. Surv. Profess. Pap.* **1236**, 55–82.
- Kelson, K.I., Simpson, G.D., Van Arsdale, R.B., Haraden, C.C., and Lettis, W.R. (1996). Multiple late Holocene earthquakes along the Reelfoot fault, central New Madrid seismic zone, *Journal of Geophysical Research* **101**, no. B3, 6151–6170.
- Pratt, T.L., Williams, R.A., Odum, J.K., Stephenson, W.J. (2012). Origin of the Blytheville arch, and long-term displacement on the New Madrid seismic zone, central U.S. In: Cox, R.T., Tuttle, M.P., Boyd, O.S., Locat, J. (Eds.), *Recent Advances in North American Paleoseismology and Neotectonics East of the Rockies. Geological Society of America Special Paper 493. Geological Society of America, Boulder, CO*, 1–15.
- Purser, J.L., and Van Arsdale, R.B. (1998). Structure of the Lake County uplift: New Madrid seismic zone, *Bulletin of the Seismological Society of America* **88**, 1204–1211.
- Russ, D.P. (1979). Late Holocene faulting and earthquake recurrence in the Reelfoot Lake area, northwestern Tennessee, *Geological Society of America Bulletin* **90**, 1013–1018.
- Russ, D.P., Stearns, R.G., and Herd, D.G. (1978). Map of exploratory trench across Reelfoot scarp northwestern Tennessee, *U.S. Geological Survey Miscellaneous Field Studies Map MF-986*, scale 1:254.
- Schweig III, E.S., and Van Arsdale, R.B. (1996). Neotectonics of the upper Mississippi embayment: *Engineering Geology* **45**, p. 185–203.
- Sexton, J.L., Henson Jr., H., Dial, P., and Shedlock, K.M. (1992). Mini-Sosie high resolution seismic reflection profiles along the Bootheel lineament in the New Madrid seismic zone, *Seismological Research Letters* **63**, 297–308.
- Tavakoli, B., Pezeshk, S., and Cox, R.T. (2010). Seismicity of the New Madrid seismic zone derived from a deep-seated strike-slip Fault, *Bulletin of the Seismological Society of America* **100**, 1646–1658.
- Tuttle, M. P., Schweig, E. S., Sims, J. D., Lafferty, R. H., Wolf, L. W., Haynes, M. L., 2002, The earthquake potential of the New Madrid seismic zone, *Bulletin of the*



INQUA Focus Group on Paleoseismology and Active Tectonics



paleoseismicity.org

Seismological Society of America, v. 92, n. 6, p. 2080-2089.

- Tuttle, M. P., Schweig, E., III, Campbell, J., Thomas, P. M., Sims, J. D., and Lafferty, R. H., III, 2005, Evidence for New Madrid earthquakes in A.D. 300 and 2350 B.C., *Seismological Research Letters*, v. 76, n. 4, p. 489-501.
- Williams, R.A., Stephenson, W.J., Pratt, T.L., and Odum, J.K. (2010). Recurrent Eocene and Quaternary uplift across the southwestern Blytheville Arch, Arkansas: Is it contributing to the formation of Lake St. Francis? *Seismological Research Letters* **81**, no. 2, p. 323.
- Zoback, M. D., Hamilton, R. M., Crone, A. J., Russ, D. P., McKeown, F. A., and Brockman S. R. (1980). Recurrent intraplate tectonism in the New Madrid seismic zone, *Science* **209**, 971–976.



## Late Pleistocene deformation at Aljezur fault system, SW Portugal: Seismicity triggering within a low tectonic rate setting and relationship with sea-level rise

Paula M. Figueiredo (1,2), Tom Rockwell (3), João Cabral (1), Maria C. Neves (1,4)

- (1) Instituto Dom Luiz & Geology Department, Lisbon University, Portugal
- (2) now at Quaternary and Anthropocene Research Group, University of Cincinnati, USA paula.figueiredo@uc.edu
- (3) Department of Geological Sciences, San Diego State University, USA
- (4) Algarve University, Portugal

**Abstract:** The southwest of Portugal is located close to the Eurasia – Nubia plate boundary, characterized by an NW-SE to WNW-ESE oblique convergence at a rate of 4-6 mm/yr. Inland, this convergence is accommodated by several active structures with low tectonic rates ( $< 0.5$  mm/yr). The São Teotónio – Aljezur - Sincera Fault system (STASFS) is a 50 km long left-lateral strike-slip fault system, trending NNE-SSW, approximately parallel and close to the SW Portuguese coastline, with an estimated horizontal slip rate of 0.16 mm/yr. Holocene deformation was not recognized. Recent paleoseismological studies demonstrated that STASFS fault segments may have been subjected to an increase in Coulomb stress during periods of sea level rise. We suggest that late Pleistocene seismicity along STASFS might be related to periods of rapid sea-level rise, such as the one that occurred immediately after Last Glacial Maximum, thereby releasing accumulated strain and allowing for ~15 ka of inactivity.

**Key words:** Portugal, active tectonics, Pleistocene, seismic triggering, sea level rise.

### INTRODUCTION

The study area (SW Portugal) is located in the southwestern region of Iberia, at the northern edge of the Gulf of Cadiz, and near the SW Iberian continental margin. In this region of the Atlantic, the Eurasia and Nubia plates converge obliquely along a NW-SE to WSW-ESE direction at a average rate of 4-6 mm/yr (Fernandes *et al.*, 2007, Serpelloni *et al.* 2007 among others) (Fig. 1).

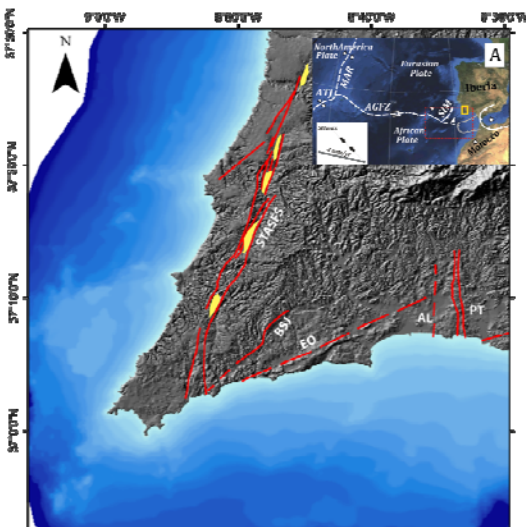


Fig.1- Quaternary tectonic structures at the SW Portugal. STASFS is marked in the map. Tectonic basins are indicated by yellow color. Bathymetry for 0-200 meters (A). Localization of Gulf of Cadiz and South Iberia Margin, and SW Portugal in the context of Eurasia-Nubia plate boundary (adapted from Figueiredo *et al.*, 2013)

The plates convergence is distributed through several folds and faults which define a wide plate boundary zone partially encompassing the Southwest Portuguese Continental Margin. Major offshore NNE-SSW to NE-SW striking thrust systems are thus present, such as the Marquês de Pombal, Horseshoe and Goringe Bank faults, inferred as likely sources of high magnitude seismicity, as the 1755 ( $M_w \geq 8$ ) (Baptista *et al.*, 2009) and the 1969 ( $M_w 7.9$ ) earthquakes. Inland, several active structures with low tectonic rates ( $< 0.5$  mm/yr) accommodate the ongoing deformation (Cabral, 1995; Dias, 2001). From these the most significant is the NNE-SSW 50 km long São Teotónio–Aljezur–Sincera left-lateral fault system (STASFS), which trends parallel to the western coast (Fig. 1).

Significant regional historical seismicity with high intensities is reported, probably related as well with the offshore generated seismicity. Paleoseismological trenches across the STASFS exposed evidence for Pleistocene seismic activity but not for the Holocene (Figueiredo *et al.* 2010; Figueiredo, 2015).

Recent studies demonstrated that during periods of fast sea level rise and consequent loading at the continental platform, changes in the Coulomb stress for specific faults in Portugal might occur with implication in the seismic triggering (Neves *et al.*, 2015). In this abstract we discuss this relationship for the STASFS.

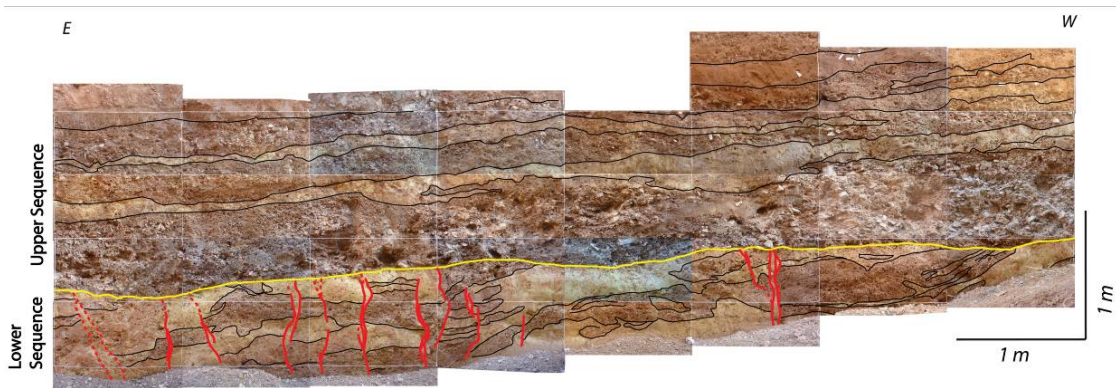


Fig. 2- Photo-mosaic of Alfambras trench: lower and upper alluvial fan deposits are identified; yellow trace indicates the top of the lower sequence. Faults in red, bedding in black.

## DISCUSSION

### The São Teotónio – Aljezur - Sinceira Fault System

Active faults in SW Portugal are characterized by low tectonic rates, although capable to generate medium to large magnitudes earthquakes. A slow deformation rate also implies large average recurrence periods and infrequent large earthquakes. The SW Portugal is also characterized by high drainage incision rates favored by a regionally high uplift rate of circa 0.1 mm/yr (Figueiredo et al., 2013), which also promotes erosion and the removal of the Pleistocene and older cover sediments. Thus, the recognition of paleo-earthquakes is difficult and the likelihood to constrain the seismic cycle record is very low.

The STASFS is an *en echelon* left lateral fault system, deforming an inherited Miocene regional abrasion platform which was re-trimmed during the Plio-Pleistocene. Along the STASFS exist 4 small elongated tectonic basins filled with sediments dating from the Miocene (marine sediments) to the Pleistocene (fluvial and colluvial). When the main fault crosses the regional platform stepping out of the tectonic basins, it does not evidence any significant vertical offset and the horizontal slip component is difficult to track in the smoothed regional topography. Thus, apparently the main fault trace does not control significantly the morphology of the regional planation surface, except for the basins. The largest of these basins is the Aljezur basin which is almost in continuity with the smaller Alfambras basin to the south, separated by a small push-up structure.

A detailed morphotectonic analysis aiming to recognize Quaternary deformation was conducted along the Aljezur and Alfambras basins. Several morphometric indexes were also applied to the drainages and to the relief. All tectonic basins have the main drainage running approximately parallel to the main fault, sometimes crossing it; the basins are elongated parallel to the fault system, but with an asymmetrical drainage pattern, with longer tributaries

to the E and shorter to the W. Several indexes were calculated to analyse the streams, such as the stream channel sinuosity (S), stream gradient index (SL) and channel steepness (K<sub>sn</sub>), and to characterize the basins shape, as the basin relief ratio (Rh), elongation ratio, and basin asymmetry factor (AF). Valley floor width to height ratio (V<sub>i</sub>) and mountain front sinuosity (S<sub>mf</sub>), which are applied to mountain fronts, were applied in this study to the relief generated by the development of the strike-slip basins. Although not all of the geomorphic indexes were adequate to apply to strike-slip kinematics, and the deformation rates of the STASFS are very low, a cross correlation of analysis conducted through different approaches lead to the identification of fault activity (Figueiredo, 2015).

These analyses along with field surveys and geoelectric tomography measurements, allowed identifying not previously recognized active segments of the STASFS. Based upon the interpretation of geomorphic features, a long term Pleistocene activity was recognized for the STASFS along the Aljezur and Alfambras basins. A landform interpreted as a shutter ridge was used to estimate a horizontal slip rate in the range of 0.1-0.2 mm/yr.

Based upon fault length and other characteristics, the presence of distinct fault segments, and assumptions about failure scenarios, we estimated a maximum expectable earthquake on this fault system to be in the range of Mw 6.0 to 7.1, with average displacements per event smaller than 1 m, and average recurrence intervals ranging from 8 to 20 ka (Figueiredo, 2015).

Several paleoseismological trenches were opened in an effort to recognize paleo-earthquakes as well as evidence for the last significant event. Pleistocene deformation was identified and the trench sections exposed sediments that were folded and dragged into a narrow fault zone, which restricted the individualization of paleo-events (Figueiredo et al., 2010; Figueiredo, 2015). No Holocene surface ruptures were recognized.



Recent trenching at the Alfambras segment (Fig.2) revealed deformation within weathered alluvial fan sediments (Lower Sequence), covered by a younger alluvial fan sequence (Upper Sequence). Carbon 14 dating of detrital charcoal recovered from the base of this younger sequence yielded uncorrected ages of  $13930 \pm 610$  yr and  $13320 \pm 180$ yr, supporting the absence of Holocene surface ruptures for this strand of the fault system.

Although the fault zone was not fully exposed at the trench and further work needs to be conducted, at this site, it exposed a sequence of older and weathered alluvial fan sediments with embedded channels which was deformed, with minor folding and displacements as expected along a strike-slip fault. It is our reasoning that both alluvial fan deposits (Lower and Upper Sequences) are related with a local transverse drainage. We interpret that the Lower sequence might be late Pleistocene in age, probably corresponding to MIS 5 high-stand. To support this evidence, samples for OSL dating were collected.

#### LGM Sea level rise and Stress Loading

The concept of ocean loading as a mechanism to promote small static stress variations and Coulomb stress changes at active faults, which could favor or inhibit seismic failure on near-shore fault systems, was developed by Luttrell & Sandwell (2010). It is based on the assumption of the bending of the lithosphere in response of the increase of the water load on the continental shelf due to eustatic sea-level rise. Depending on the elastic plate thickness, the platform morphology and the location, geometry and kinematics of the faults, distinct increases or decreases in the Coulomb stress could be calculated.

This concept was recently modeled for Portugal considering the sea-level rise after the Last Glacial Maximum (LGM), which was of circa 120 m (Neves et al., 2015). Neves et al. have modeled the flexural effects of ocean loading for several fault systems and locations in Portugal assuming an elastic plate thickness of 25 and 45 km. Results evidence that the sea level rising might have contributed as much as 0.05 kPa/yr, which may be larger than the tectonic loading in most faults for Portugal and thus significant for seismic triggering in such a low tectonic rate setting. These stress increases were verified along faults with favorable location, geometry and kinematics. Although the STASFS was not considered in the previously published work, it was also tested. Results indicate that STASFS fault segments located east of longitude -8.85 may have been subjected to an increase of the Coulomb stress during periods of sea level rise (Fig.3). These fault segments are the ones present at the Alfambras and Aljezur basins, corresponding as well to those with clearer geomorphic expression and evidence for Pleistocene deformation relatively to other fault segments located southwards and west of longitude -8.85, at the Sinceira basin.

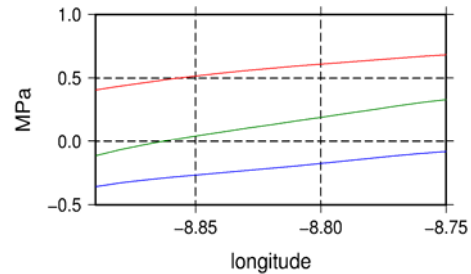


Fig. 3 - Normal (red,  $\Delta\tau_n$ ) and Coulomb (green,  $\Delta\sigma_c$ ) stress changes resolved for the STASFS.

Additional results for the SW Portugal are that for an elastic plate thickness of 40 km and modelled for a shallow observation (3km depth) positive Coulomb stress changes can occur and consequently favoring fault rupture at shallow depths (Fig.4). STASFS is located within the area where increases of circa 1.0 to 1.2 MPa might be promoted by a sea leve rise.

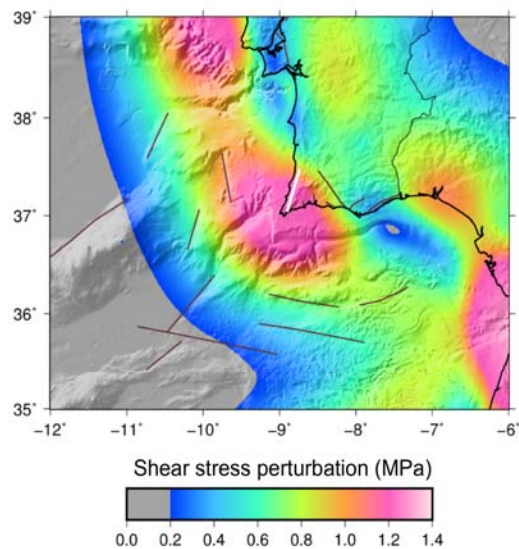


Fig.4 - Maximum shear stress due to the elastic deflection in response to 120mof sea level rise. The stress perturbations are particularly sensitive to the elastic plate thickness ( $T_e$ ) and to the geometry of the coastline. Here it is presented the computing results for a  $T_e$  of 40 km and shallow depths of 3 km. STASFS is highlighted by the white color trace.

#### Stress Loading vs. Late Pleistocene Seismicity

At the above referred Alfambras trench, alluvial fan deposits older than circa 13-14 ka are deformed, evidencing bedding disruptions, minor folding and offsets. This older unit, (Lower Sequence), is at the moment of unknown age but its similarity with the Upper Sequence leads to the interpretation that they both have the same provenience under similar conditions. The top of the Lower Sequence unit evidences erosion and a deposition hiatus, eroding



also some of the deformation (see yellow line in Fig.2). Upper Sequence unconformably overlies the Lower Sequence, both lying approximately horizontally. Since the base of the Upper Sequence is 13-14 ka we may assume that Lower Sequence is late Pleistocene in age, to be confirmed by OSL dating..

The Upper Sequence is not deformed; therefore we know that seismicity has occurred before 13-14 ka and possibly not much before that. We thus raise the hypothesis of this late Pleistocene deformation being related with the fast sea level rise that started after the LGM, 16 ka ago. Such a correlation between seismicity and sea level rise after the LGM has been previously identified in NE Portugal (Rockwell et al. 2009) (Fig.5) and it is in good agreement with the modelled sea level rise effects by Neves et al. (2015).

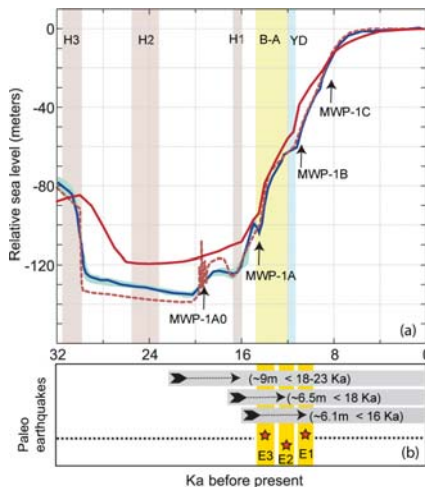


Fig.6.- (a) Relative sea level curves according to several authors overlapped with significant Melting Water Pulses [(MWP) and climatic events; (b) Cluster of large magnitude events (E1, E2 and E3) that occurred at the Vilarica fault (NE Portugal) in the period between 14.5 and 11 ka). Amount of displacement and age of deformation is indicated. (adapted from Neves et al. 2015).

We then suggest that STASFS fault segments may have been subjected to an increase in Coulomb stress, and that late Pleistocene seismicity along the STASFS may be related to periods of rapid sea-level rise, such as the one that occurred immediately after the LGM, thereby releasing accumulated strain and allowing for ~15 ka of inactivity up to the present.

**Acknowledgements:** This work was funded by Fundação da Ciência e Tecnologia, through a PhD scholarship (SFRH/BD/36892/2007) and Research Project FASTLOAD (PTDC/GEO-GEO/2860/2012).

## References

- Cabral, J., (1995). *Neotectónica em Portugal Continental*, Memória 31, Instituto Geológico e Mineiro, 265 p.
- Dias, R. (2001). *Neotectónica da Região do Algarve*, Doctoral Thesis, Lisbon University.
- Fernandes, R.M.S., Miranda, J.M., Meijninger, B.M.L., Bos, M.S., Bastos, L., Ambrosius, B.A.C. and Riva, R.E.M., (2007). Surface velocity field of the Ibero-Maghrebien segment of the Eurasia-Nubia plate boundary. *Geoph. J. Int.*, 169 (1), 315-324.
- Figueiredo, P.M., Cabral, J., Rockwell, T.K. (2010). Neotectonics and paleoseismic studies at SW Portugal mainland: The S. Teotónio – Aljezur – Sinceira Fault System, *VIII Portuguese Geology Congress, Geosciences On-line Journal*, Vol. 11 – n. 8, ISSN 1645-0388
- Figueiredo, P.M., Cabral, J. and Rockwell, T.K. (2013). Recognition of Pleistocene marine terraces in the Southwest of Portugal (Iberian Peninsula): Evidences of regional Quaternary uplift. *Annals of Geophysics*, 56 (6), *Special Issue Earthquake Geology*, S0672, doi:10.4401/ag-6276.
- Figueiredo, P.M. (2015). *Neotectonic and Seismotectonic Studies along the Southwest Portugal sector: Implications for the regional seismicity*, Doctoral Thesis, Lisbon University.
- Luttrell, K. & Sandwell, D. (2010). Ocean loading effects on stress at near shore plate boundary fault systems. *J. Geophys. Res.* 115, B08411.
- Neves, M.C., Cabral, J., Luttrell, K., Figueiredo, P.M., Rockwell, T. Sandwell, D. (2015). The effect of sea level changes on fault reactivation potential in Portugal, *Tectonophysics*, 658, 206-220.
- Rockwell, T., Fonseca, J., Madden, C., Dawson, T., Owen, L., Vilanova, S. and Figueiredo, P., (2009). Paleoseismology of the Vilarica Segment of the Manteigas-Bragança Fault in Northeastern Portugal. Reicherter, K., Michetti, A.M. and Silva, P.G. (eds) *Paleoseismology: Historical and Prehistorical Records of Earthquake Ground Effects For Seismic Hazard Assessment*. The Geol. Soc. of London Sp. Publ., 316, pp.237-258. DOI: 10.1144/SP316.15
- Serpelloni, E., Vannucci, G., Pondrelli, S., Argnani, A., Casula, G., Anzidei, M., Baldi, P. and Gasperini, P., (2007). Kinematics of the Western Africa-Eurasia plate boundary from focal mechanisms and GPS data. *Geoph. J. Int.*, 169(3), 1180-1200.
- Wells, D., Coppersmith, K. (1994). New empirical relationships among magnitude, rupture length, rupture width, rupture area and surface displacement. *Bulletin of the Seismological Society of America*, 84 (4), 974-1002.



## COSEISMIC STRATIGRAPHY: A USEFUL APPROACH IN THE STUDY OF ACTIVE TECTONIC BASIN SCENARIOS IN CENTRAL MEXICO

Garduño-Monroy V.H<sup>1</sup>, Soria-Caballero D<sup>2</sup> and Vázquez-Bucio M.M<sup>3</sup>

<sup>1</sup>[INICIT-UMSNH-MGPT-vhgardunom@gmail.com](mailto:INICIT-UMSNH-MGPT-vhgardunom@gmail.com)

<sup>2</sup>Postgraduate in Earth Sciences-UNAM

<sup>3</sup>Postgraduate of the CIGA-UNAM

**Abstract:** We propose the concept of coseismic stratigraphy, an approach that could be highly useful for studying lacustrine basins in zones with important tectonic activity. Extant and past lakes have been studied in many parts of the world with paleolimnological objectives, for knowing climate evolution, or for detecting anthropogenic effects. Our research team working in lakes of the Trans Mexican Volcanic Belt has noticed that many of the secondary effects of important earthquakes (>5) have been either omitted or interpreted as effects of climate and human processes. Through the analysis of stratigraphy and the examination of secondary structures generated by earthquakes or by coseismic ruptures, we propose the term coseismic stratigraphy in order to call the attention of students of sediments in basins within scenarios that have been modified by seismic events that changed the conditions of sediment deposition and sediment structure.

**Key words:** lakes, seism and stratigraphy

### INTRODUCTION

Making strict sense paleoseismic studies in active volcanic zones like the Trans Mexican Volcanic Belt (TMVB) – particularly in central Mexico– becomes a complex task. While several fault systems have been defined and their historical activity has been documented to some extent, because the rupture occurs in either lava blocks or in volcanic scoria, the study of a given coseismic rupture is complicated by their coexistence until recent time with highly active volcanic fields and other factors. However, scenarios are known in which paleoseismic analysis is favored.

The age and permanence of sediments of paleobasins and present lacustrine basins in central Mexico –directly or indirectly originated and influenced by regional tectonic activity– have made them focal to paleoenvironmental and anthropological studies because of their physical capacity of preserving a continual sedimentary record (reference please). More recently, these sediments have been proven to be effective for recording important earthquakes by a combination of direct (synsedimentary faults) or secondary effects (liquefaction, underwater slumps, slumps on slopes), and of geometric modifications of either the basin or the sedimentary sequence. In studies of sedimentary sequences of surface coseismic ruptures, one must also account for the possible effects of erosive processes in the seismic record. Nevertheless, seismic records in lacustrine sequences have received little attention (Langridge et al 2000 Garduño-Monroy et al., 2010; Rodríguez-Pascua et al., 2003; Israde-Alcántara et al., 2005, Rodríguez-Pascua et al., 2009).

The review of research reports of basins in central Mexico, and the thorough stratigraphic survey and initial paleoseismological studies made in some of these basins,

showed us the need to introduce a new approach for the study of lacustrine sequences evolving in active tectonic scenarios. Such new approach is needed as an aid for distinguishing the effects of climate, anthropogenic activity, and earthquakes in the variations observed in the sedimentary record, for improving paleoenvironmental interpretations, and for strengthening paleoseismological studies made with conventional methodologies. We herein define *Coseismic Stratigraphy* (CS) as a branch of Stratigraphy focused on the study of marine, lacustrine or fluvial sequences in which the direct or indirect effects of earthquakes have modified the facies, the sedimentary and erosion rates, and in some cases also the geometry of the deposition center (Fig. 1). Applying CS requires previous knowledge about the geotectonic framework of the studied area and of the dominant sedimentary processes occurring in it, which allows for inferring the existence of tectonic effects and analyzing *in situ* sedimentary sequences, while also considering major environmental and sedimentary processes.

Paleoseismology has proved the importance of considering local or regional seismic activity for studying the evolution of sedimentary basins affected by segments of active faults (Rodríguez-Pascua, et al., 2009), but paleoseismological studies are limited to a few columns and these columns rarely take into account changes in the exogenous processes of the basin generated by the earthquakes themselves.

Assuming a lacustrine basin whose sediments were deposited within an active tectonic scenario, the CS approach would allow for generating a conceptual study framework that improves the selection and application of conventional limnological, stratigraphic, paleoenvironmental or paleoseismological methods in



order to reach more comprehensive results. The ultimate objectives of CS would then be to obtain a better interpretation of the evolution of a sedimentary basin in an active seismotectonic, and sometimes volcanic, scenario, and to generate additional information contributing to the extension of existing earthquake catalogs.

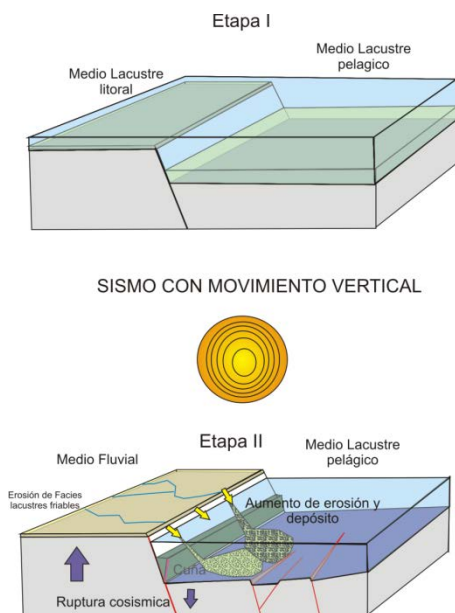


Figure 1. Example of the effects of a coseismic rupture in a lake: the vertical movement of the rupture will modify the rate of erosion of uplifted unconsolidated sediments, modifying the sedimentation rates and the local distribution of facies.

The effect on a lake of a coseismic rupture in an active tectonic scenario, schematized in Figure 1, has been inferred for Lake Pátzcuaro, Michoacán, because of available documentation of variations in its facies, sedimentation rates, and deformations that were caused by seismic events (Garduño-Monroy et al., 2010), and not only by climatic or anthropogenic variations. When an earthquake affects underwater lacustrine sequences in the process of consolidation, underwater slumps, microfaulting or liquefaction processes (Fig. 2) can take place, which corresponds to the scenario inferred for the Acambay paleobasin in the state of México (Rodríguez-Pascua et al., 2009).

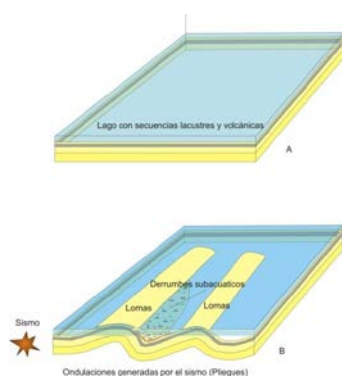


Figure 2. Schematic representation of undulation/folding generated in lacustrine sediments during the displacement in these of seismic waves from moderate or high intensity earthquakes. Rising of water-saturated sediments above their resting angle can generate underwater slumps.

The CS approach can be applied to all sedimentary basins developing in an active fault context similar to that in central Mexico. Few lacustrine sequences have continual (in time and space) seismic records and visible surface coseismic ruptures, because of which incorporation of CS to their study would allow for supplementing their seismic records. Additionally, the alterations in deposition due to seismic events can be studied by combining the use of CS, analysis of sedimentary records from seismic reflection profiles, and analysis of sediment core samples, in order to improve the estimated values of intensity, distance to epicenter, and recurrence intervals of historical earthquakes. Similar studies have been successfully made in the East African Rift (reference please) and in the Chilean Lake District (Moernaut et al., 2000). We expect that the inclusion of CS to future studies of sedimentary sequences from bodies of water in seismically active fault scenarios will make these to be conceived not only as records of climate and anthropic activity, but also as seismic records.

### LAKE PÁTZCUARO, MICHOACÁN, A CASE STUDY

**Local geological framework.** –The Lake Pátzcuaro basin (19°35'N, 101°39'W; 2035 m a.s.l.) belongs to the Michoacán-Guanajuato Volcanic Field (MGVF) in the central TMVB and has tectonic and volcanic origins. Two main fault systems affect the basin with NE-SW and E-W directions. The basin encloses domes, shield and semi shield volcanoes, and scoria cones, some of which (e.g., El Metate, Janitzio, El Estribo) exhibit the effects of gravitational or tectonic collapse (Garduño-Monroy et al 2010).

The older sediments in the region are pyroclastic products mixed with breccia, basaltic-andesitic lavas, and pyroclastic flows from the Miocene volcanic range Sierra de Mil Cumbres. This sequence is overlain by a series of volcanoclastic units and lacustrine Quaternary sediments which, according to Israde-Alcántara et al. (2005) consist of three units:

1. Open water lacustrine deposits alternating diatomites and clay layers, silts and tephras with a probable age of 45,000 years (Fig. 3).
2. Exposed lacustrine sediments due to a recent regression of the lake including a series of swamps, paleosols, and fluvial deposits of the Late Holocene with signs of the effect of human activity.
- 3.



INQUA Focus Group on Paleoseismology and Active Tectonics



paleoseismicity.org

Figure 3. Diagram showing a selection of the studied columns in the Lake Pátzcuaro basin that display the effects of earthquakes. Lacustrine sequences with ages older than 20,000 years are strongly deformed (yellow).

- Over 2 m thick paleosols and modern soils classified as Andosol and Luvisol.

The most recent volcanic activity is seen in the scoria cone and lavas of the La Taza volcano, which lifted the basin's southern lacustrine sequences. Sediments show strong deformation and normal faulting, the top layers contain archaeological materials younger than 3000 years.

**Stratigraphy.** –Figure 4 shows the location of several stratigraphic columns from different authors and the two more relevant sequences are described below.

**Jarácuaro 4.** – Located in the island of Jarácuaro in the south of the basin, displays a ca. 3 m thick sequence of clayey slime sediments intercalated with at least four centimetric thickness layers of black and white volcanic ashes. The sequence is strongly deformed by faulting and folding with layers tilting to the south. Overlying this sequence with an erosive and angular discordance is a fine 10 cm thick sand layer with low textural maturity and angular and accidental lithic, containing abundant ostracods, bivalves, fish and plant remains, and pottery from the Purépecha Postclassic period. This layer was associated to a tsunami deposit linked to the 1858 earthquake. The sequence is topped by a series of clayey slime layers deposited during the regression of the lake and by recent soil formation. Its older age was determined at 23,550 years BP

**Column I.** – Described by Metcalfe et al. (1994) and located inside the lake in the northern part of the basin, it shows a series of organic matter rich deposits dated at their base to 23,000 years BP, followed by a series of diatomite and slime layers intercalated by three strata containing abundant ostracods, and finally, by reworked deposits of recent age.

**Application of Coseismic Stratigraphy**

Two large deformed lacustrine sequences are obvious along the southern sector of Lake Pátzcuaro (Uranderes, Uricho, and Jarácuaro). The oldest of these sequences – over 20,000 years old– display a severe deformation style of listric faults, inverse faulting, and reclined folds, all structures that may be associated to the lifting of the island

of Jarácuaro and in correspondence with the 28,000 years old landslide of the El Estribo volcano (Garduño-Monroy et al 2010). The uplift caused the unconsolidated littoral lacustrine sequences to become exposed to meteoric agents, therefore presenting high erosion and sedimentation rates. Uplift of the Jarácuaro block changed the geometry of facies in the south of the lake (Fig. 1). Sequences from the Holocene and Recent were affected by normal faulting – in Jarácuaro forming the Jarácuaro-Pátzcuaro graben that generated relative uplift during the Postclassic period (900-1325) – cutting through sediments containing Pre-Hispanic pottery. Such uplift has been associated with the Purépecha word *jarácuaroque*,

meaning *place that appears*. In consequence, a mere stratigraphic approach as commonly applied until our proposal of the CS approach is shown to be insufficient for interpreting the geological and environmental history of the basin.

In Figure 4 we schematize the interpretations of a conventional stratigraphic and sedimentological study using sediment core samples, and a study applying Coseismic Stratigraphy (CS). In the first stratigraphic unit, inverted ages would be observed when dating reclined folds. If deformation of unconsolidated sequences exposed these friable sediments, an important angular discordance and a change in erosion and deposition rates would be appreciated. In the upper part of the column, sequences became tilted by the normal faults of an earthquake that occurred after the Classical period, so that the younger sequences in the lake would exhibit changes in erosion and deposition rates, reworked facies, sediments, and microfauna, and, in some cases, inverted ages. Interpretation of a core based only on conventional stratigraphy is partial, while an interpretation using data from a paleoseismic trench and the CS approach reveals a more complete record.

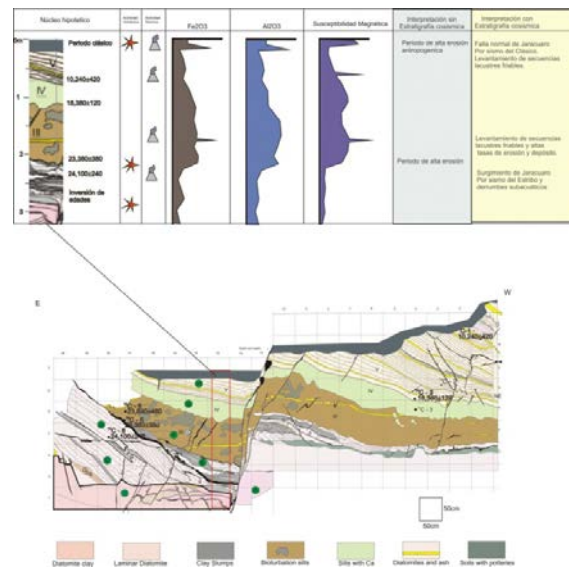


Figure 4. Schematic representation of a hypothetical core and possible interpretations using conventional and coseismic stratigraphic approaches (A) using data from a paleoseismic trench dug in the island of Jarácuaro (B). A single core would provide a partial history of events in the basin; for example, horizontal slumps and normal faults are not evident in the hypothetical core.

**Discussion**

Application of the CS approach allowed for a more comprehensive reinterpretation of the evolution of Lake Pátzcuaro basin in a scenario combining high volcanic and tectonic activities. Based on paleoseismological, stratigraphical, archaeological, and geophysical data from the basin, we clearly recognized lacustrine sequences



INQUA Focus Group on Paleoseismology and Active Tectonics



paleoseismicity.org

dated between 10,000 and 45,000 years BP that were affected by seismic events. These data provided stratigraphic columns evidencing in time and space the occurrence of a series of seismic events, the most recent of which was dated after the Classical period, and a later one possibly associated with the 1858 earthquake. A reconstruction based on paleolimnology, climate changes, or other proxies would fail to reveal in its columns the effects of endogenous events (earthquakes). For instance, liquefaction could be wrongly interpreted as bioturbation or as deposition of coarser structures, variations in deposition rate could be due to seismic ruptures (e.g., lifting in Jarácuaro exposed to erosion an extensive area of lacustrine sediments), and normal faulting is difficult to identify in conventional studies based on obtaining cores because they are vertical processes in parallel with the plane of faults.

The CS approach can be applied to lakes in other parts of the TMVB (e.g., Juanacatlán, Zacoalco, and Chapala in Jalisco, Santa María in Nayarit, Ixtlahuaca and Chalco in State of México, etc.), or to basins in active tectonic regimes in other countries and continents (e.g., Venezuela, Ecuador, Colombia, Bolivia, Peru, and Chile in South America, and the East African Rift), even if they were alpine. CS application is supported by its proven potential for improving interpretations of sedimentary records in tectonically affected basins (Langridge, 1998), which is due to not only considering climatic and anthropogenic factors as responsible of variations in erosion and deposition rates, in facies, or in geochemical conditions, but also considering the primary and secondary effects of earthquakes.

Our research team believes that it is now important to make future studies in the opposite direction, i.e., to prove that deformations and primary structures can occur that are unrelated to earthquakes, but rather to sedimentary, climatic or anthropological processes.

#### Acknowledgements

The authors acknowledge CONACyT for financing the present work (Research project no. 37334-T: “*Estudio de Paleosismología de los segmentos orientales del sistema de falla Morelia-Acambay, Michoacán, México*”).

#### References

Garduño-Monroy, V.H., Pérez-Lopez R., Israde-Alcantara, I., Rodríguez-Pascua M.A., Szykaruk E., Hernández-Madrigal V.M., García-Zepeda M.L., Corona-Chávez P., Ostroumov M., Medina-Vega V.H., García-Estrada G, Carranza O., López-Granados E. (2010). Paleoseismology of the Southwestern Morelia-Acambay Fault System, Central Mexico. *Geofísica Internacional* 48(3): 319-335.

Israde-Alcantara, I., Garduño-Monroy, V. H., Fisher, Pollard H.P. (2005). Lake level change, climate, and the impact of natural events: the role of seismic and volcanic events in the formation of the Lake Patzcuaro Basin, Michoacan, Mexico. *Quaternary International*. 135: 35-46.

Langridge, R.M. (1998). Paleoseismic deformation in behind-arc lacustrine settings: Acambay, Mexico and Ana River, Oregon. Unpublished Ph.D. dissertation, University of Oregon, Eugene, Oregon. 188 p.

Langridge R., Waldon R.J., Moya JC. Suarez G. (2000). Paleoseismology of the 1912 Acambay earthquake and the Acambay-Tixmadejé fault, Trans-Mexican Volcanic Belt OJour Geoph. Res., 105, 3019–3037.

Metcalfe S.E., F.A. Street – Perrott, S.L. O’Hara, P.E. Hales y R.A. Perrott. (1994). The Paleolimnological Record of Environmental Change: Examples from the Arid Frontier of Mesoamerica. En: *Environmental Change in Drylands: Biogeographical and Geomorphological Perspectives*. A.C. Millington y K. Pye (eds.). 131 – 145.

Moernaut J., M. De Batist, F. Charlet, K. Heirman, E. Chapron, M. Pino, R. Brümmer y R. Urrutia. (2007). Giant earthquakes in South-Central Chile revealed by Holocene mass-wasting events in Lake Puyehue. *Sedimentary Geology*. 195: 239 – 256.

Rodríguez-Pascua, M.A., Garduño-Monroy, V.H., y Alcántara-Israde, I. (2003). Paleosismología y efectos de licuefacción en la región de Acambay, México. *GEOS*. 23 (2): 121-122.

Rodríguez-Pascua, M.A., V.H. Garduño-Monroy, I. Alcántara-Israde y R. Pérez-Lopéz. (2009). Estimation of the epicentralárea from the spatial gradient of deformation in lacustrine seismites (TierrasBlancas Basin, Mexico). *Quaternary International*.



## Tectonic geomorphic and paleoseismic investigation of the Gatún fault in central Panamá

Gath, Eldon (1), Tania Gonzalez (1), Thomas Rockwell (1), and Pastora Franceschi (2)

- (1) Earth Consultants International, 1642 E. 4<sup>th</sup> St., Santa Ana, CA 92701, USA; [gath@earthconsultants.com](mailto:gath@earthconsultants.com)
- (2) Autoridad del Canal de Panamá, Department of Geotechnical Engineering, Bldg 721, Corozal, Panamá

**Abstract** The Gatún fault, a primary east-west structural feature in central Panamá, has a strong geomorphic signature that can be readily observed in aerial photographs and digital elevation models. The fault forms an abrupt southern margin to the Sierra Maestra Mountains, and all rivers and streams that cross the fault are affected at the fault crossing. Most large rivers are left-laterally deflected, and all streams that cross the fault have a 1- to 2-meter, and locally as high as 5-meter near-vertical nickpoint at or immediately upstream of the fault. Paleoseismic trenching of the Gatún fault east of Gatún Lake has shown that this fault has experienced at least two, and possibly three, surface-rupturing earthquakes since 1490 AD. Based on 3-D trenching of a 3 ka channel thalweg that is offset 19-20 m, the left-lateral slip rate on the Gatún fault is 6-9 mm/yr with a maximum of 20% north-side up normal slip, and the most recent earthquake (possibly in 1849 AD) generated at least  $0.7 \pm 0.2$  meters of left-lateral surface offset that apparently went unnoticed at the time. Our best estimate is that this 40 km segment of the Gatún fault has a recurrence interval of ~M6.8 earthquakes every 100-170 years based on the last three events, but if the fault is capable of multi-segment, less-frequent ruptures, the earthquakes could potentially be as large as M7.4 if the entire 120 km fault were to rupture. We suspect, but cannot prove, that triggered slip resulted in soil fracturing on the Gatún fault during the 1991 M7.6 earthquake on the North Panamá Deformed Belt off of Bocas del Toro. These findings are important for the seismic stability analysis of the AD 1913 Gatún Dam across the Chagres River, one of the most critical structures in the Panamá Canal.

**Key words:** Paleoseismology, neotectonics, Panamá, seismic hazard

### INTRODUCTION

As part of studies for the seismic hazard assessment for the Panamá Canal Expansion Project, extensive geological studies were completed for several prominent faults within the east-central part of the Canal watershed (ECI 2005, 2006, 2007, & 2008). These faults (Fig. 1), previously assumed to be inactive, were instead all confirmed to have experienced multiple, Holocene-age, surface-rupturing earthquakes.

The Limón and Pedro Miguel faults were both shown to have produced three large earthquakes in the last 1500 years, and ruptured together in a 3 m event as the 1621 AD Panamá Viejo earthquake (Rockwell et al., 2010b). The Azota and Miraflores faults were also both confirmed as Holocene structures (ECI, 2006). This paper summarizes the geomorphic mapping and paleoseismic trenching investigation for the Gatún fault at the location shown on Fig. 1.

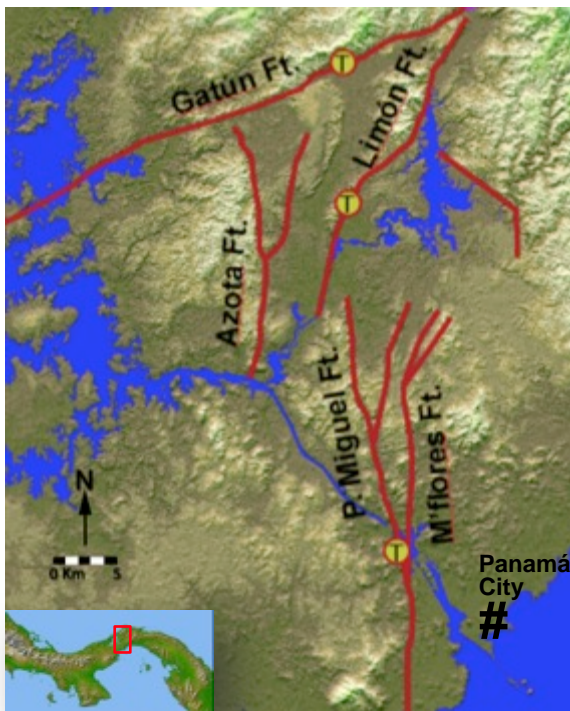


Fig. 1: Holocene fault map of Central Panamá and the Panamá Canal area, based on recent investigations (ECI 2005, 2006, 2007, & 2008). The circled T indicates sites where 3-D paleoseismic studies have been conducted.

The Gatún fault trends generally east-west across the southern margin of the Sierra Maestra mountain range separating the dominantly Mesozoic igneous rocks to the north from Cenozoic sedimentary strata to the south (Fig. 2). The fault extends east as far as the San Blas Islands for a total length of 100-120 km, and may extend another 100 km west of Gatún Lake along a prominent lineament. No historical earthquakes are associated with the Gatún fault, but its westward extension places it less than 10 km from Gatún Dam and Locks, the major structure across the Chagres River that allows the Canal to function. As such, understanding and mitigating its seismic hazard is critical to the Canal's future operations.

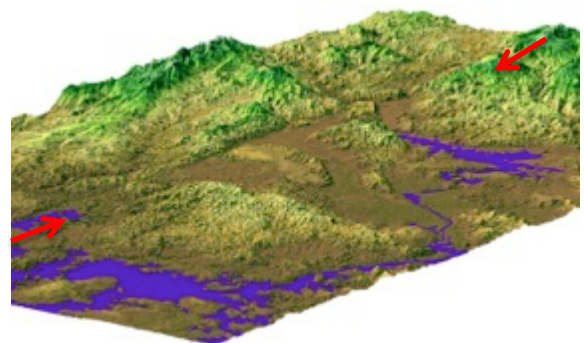


Fig. 2: DEM terrain model showing the spectacular geomorphic expression of the ~E-W trending Gatún fault



(red arrows) across the southern front of the Sierra Maestra range.

A tectonic geomorphic strip map was prepared of the 40 km segment of the fault between Gatun Lake, east to the Chagres River (Fig. 1) (ECI, 2005). On the ground, the surficial geomorphology is equally spectacular with all drainages across the fault left-laterally deflected, stream knickpoints, and small scarps across fan surfaces. The smallest left-lateral deflection observed was ~2 m, with a 0.5 m vertical scarp, while the largest was ~150 m with a scarp over 10 m high (Figs 3, 4, & 5).

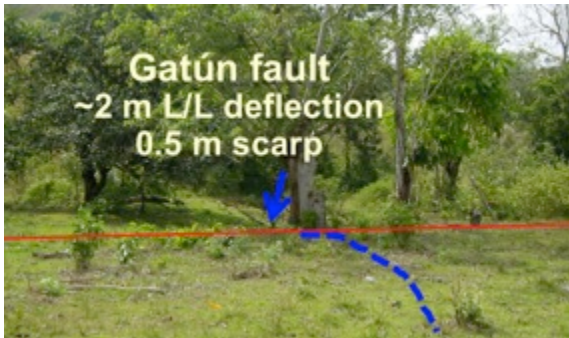


Fig. 3: Stream deflection of ~2 m left-lateral across the Gatun fault. This deflection is uphill to the regional drainage (to the left in the photo).



Fig. 4: Left-lateral stream deflection of ~150 m (well outside the photo view) across the Gatun fault east of Gatun Lake. An increased deflection of larger rivers is an indicator of progressive tectonic offsets.



Fig. 5: Sharp stream deflection (blue lines) of ~10 m left-lateral across the Gatun fault east of Gatun Lake. Terrace risers (purple lines) are offset 15 m. Exposed in the terrace deposits is a piece of pottery (Fig. 6).



Fig. 6: Large pottery fragment exposed ~1 m below the surface, lying on top of a buried paleosol within the offset terrace deposits. Assuming that such pottery was first found in Panamá <2500 years ago, its presence incorporated into the abandoned terrace surface indicates that it has been offset equivalently to the terrace riser, yielding a 6-9 mm/yr slip rate.

The clear presence of youthful tectonic geomorphic features, the increased deflections of larger rivers over smaller streams indicating a temporal progression of offsets, and the potential for a 6-9 m/yr slip rate were dramatic findings for an assumed inactive fault. A paleoseismic trenching study was authorized to confirm the geomorphic observations and collect data on slip rate, event recurrence, displacement magnitudes, and slip kinematics.

#### INVESTIGATION

Based on the strip map and field reconnaissance, several locations were considered for the trenching study. Shallow groundwater was a constraint at the site in Fig. 3, while site access was a constraint at the pottery site (Figs. 5 & 6). A site about 300m east of Fig. 4, and geomorphically similar to the Fig. 5 site, was chosen for the trenching study (Figs. 7 & 8). At this site, the primary objective was to determine a Holocene slip rate by accurately measuring the offset and determining the age of a channel that had been left-deflected ~20 m across the fault.

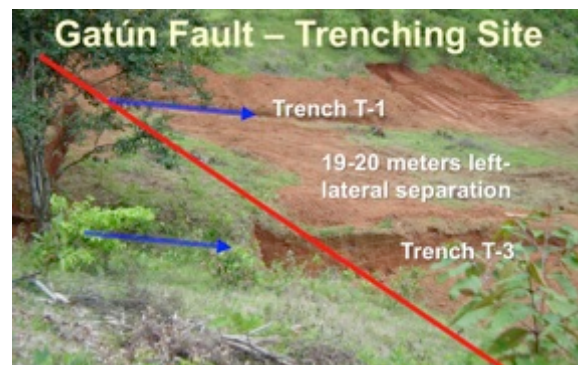


Fig. 7: Site of the 3-D trenching study of the Gatun fault. A stream enters the fault from the left of the image, and its former channel margin (rising from the T-1 location) has been translated 19-20 m leftward across the fault. The modern channel exposed in T-3 has recently been captured to the right, into the large river system shown in Fig. 4.

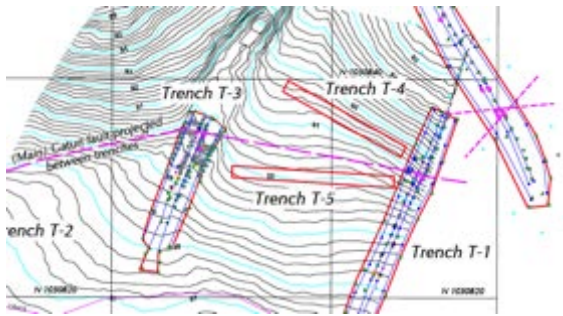


Fig. 8: Map of the principal trenches. T-1 was emplaced to constrain the long-term slip rate, T- 4 & 5 were dug to look for secondary entry and exit channels, and T-3 focused on the youngest event chronology and kinematics. Primary (blue) contours are meters.



Fig. 9: Trenching parallel to the fault (red line) to look for younger channels that would indicate smaller offsets to help confirm the long-term slip rate calculated from the Trench T-1 offset of the ~3 ka basal sediments (Fig. 10). No additional channels were found.

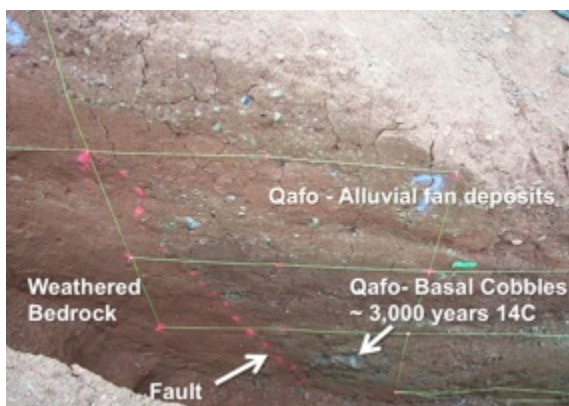


Fig. 10: Offset alluvial deposits against the weathered bedrock as exposed in Trench T-1. Undated colluvial and alluvial units cap the fault within the uppermost 75 cm of the trench exposure, but upslope fractures (not shown) penetrate to the original ground surface. Grids are 1.0 m horizontal and vertical.

A charcoal sample collected from within the basal cobbles of T-1 (Fig. 10) yielded an age of  $3155 \pm 35$  ybp and a second sample  $2730 \pm 35$  ybp was obtained 1.5 m higher. We interpret these cobbles to represent when the stream first penetrated across the fault, and thus this represents the total fault offset since that time. Based on the 19-20 m left-lateral offset of the channel margin from its piercing point entry across the fault, and the absence of any other entry or exit channels, we conclude that the entire separation is due to fault offset.

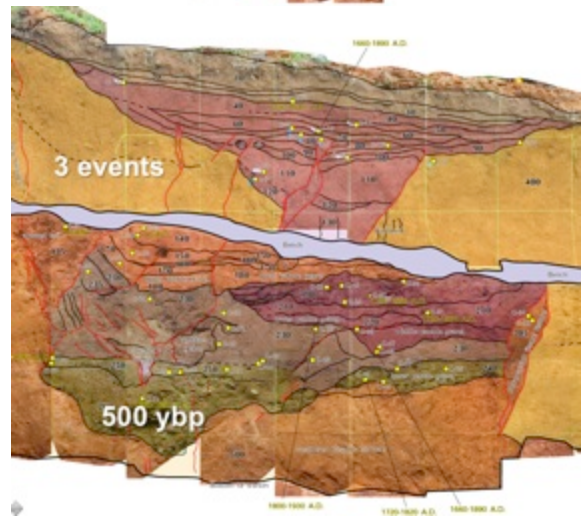
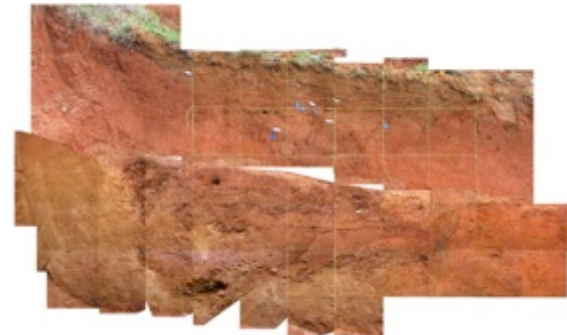


Fig. 11: Photo mosaic (upper) and graphic log (lower) of the eastern wall of Trench T-3 (see Fig. 11) showing the youngest alluvial deposits incised post-capture into the older (1-3 ka) deposits. Based on stratigraphic fault terminations, we interpreted 3 events within these 500-year deposits, with the last event potentially in 1849 AD. Charcoal within fractures that penetrate almost to the ground surface yielded post-1950 AD radiocarbon dates, from which we infer a potential (small) triggered slip event from the M7.6 1991 Limón (Costa Rica) earthquake on the North Panama Deformed Belt.



Fig. 12: Hand excavation of small trenches into the eastern bench of Trench T-3 allowed us to define and measure the fault displacement for the most recent (blue flags) and penultimate (yellow flags) events based on the offset of discrete channel margins. The MRE was measured at  $0.7 \pm 0.2$  m and the penultimate event a cumulative  $1.4 \pm 0.3$  m. The ~500 year third event was displaced beyond the 2 m exposure afforded by the bench.



Based on the geomorphic expression of the terrace riser, and the elevation of the base of the alluvial cobbles and the upstream channel thalweg, the vertical separation across the fault is about 3-4 m in 3 ka, or 15-20% of the ~20 m left-lateral horizontal displacement.

An event chronology was obtained from the youngest sediments exposed in T-3, incised into the 3 ka older alluvium. These deposits were radiocarbon dated at ~1460 AD at the base, up to about the mid-1800s. Three events were interpreted based on stratigraphic terminations of fault tips, with the last two events accurately measured at ~0.7 m left-lateral per event, and the most recent event possibly 1849 AD. Modern-dating charcoal was obtained from a fissure that cut across all other strata, from which we infer a more recent small surface cracking, potentially triggered slip from the 1991 Limón event on the North Panama Deformed Belt.

### DISCUSSION

The Gatún fault has been shown to be a significant seismic hazard to central Panamá and the Panamá Canal. Based on detailed paleoseismic investigations, it has a late Holocene (3 ka) slip rate of 6-9 mm/yr, and has generated three surface-rupturing earthquakes of ~0.7 m left-lateral offset each in the past 500 years. Three events in 500 years averages 167 years. But, the most-recent event is clearly historic, possibly 1849 AD, or 166 years ago. Subtracting that time since the 1849 AD event from the ~500 year oldest determined event, leaves 334 years into which to squeeze three events. Assuming the oldest event occurred exactly 500 years ago leaves two additional events in 334 years, or 167 years between events.

But, for a 40 km fault, 0.7 m displacements (M6.8) seem small. It is possible that these last three events are the tip of a seismic cluster, and the 166-year recurrence interval is abnormally short. Using the 20-meter displacement of the 3 ka channel in T-1, and 0.7 m events, requires ~30 similar events with a recurrence of 100 years, or a few larger events. No matter how the numbers are examined, this is a fault that is near its seismic recurrence, based on the last three ruptures.

Lastly, it is not yet clear how significant a role the Gatún fault plays in the overall tectonic deformation of Panamá, but Fig. 13 shows a possible 20 km reconstruction of the principal mountain ranges of central Panamá along the Gatún fault and an additional 80+ km westerly extension. This model, incorporated by Rockwell et al., (2010a), restores the two mountain ranges, explains the lowlands now forming Gatún Lake, fills in the basin now bounded by the Limón fault, and extends the Gatún fault well to the west into the interior of Panamá. Obviously earthquake ruptures larger than a M6.8 are a possibility.

**Acknowledgements:** This work was made possible by a consulting contract from the Autoridad del Canal de Panamá. Tim Dawson and Ana Cadena were heavily involved in the fieldwork, as were several ACP geologists.

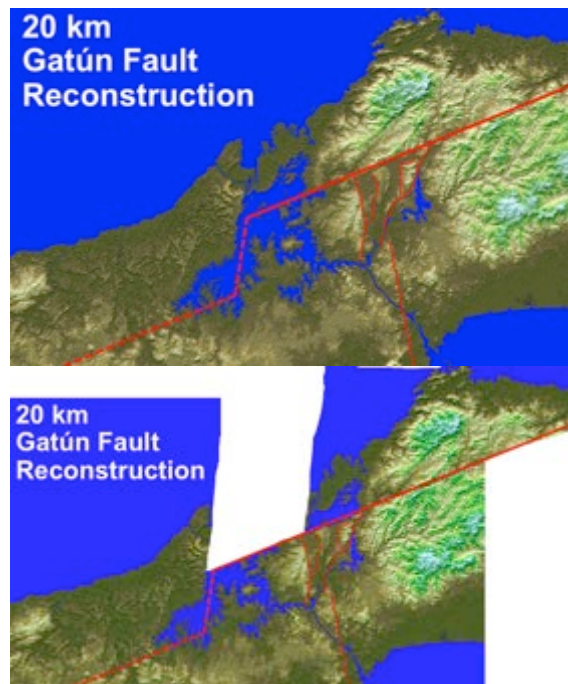


Fig. 13: 20 km displacement reconstruction of central Panamá by retro-deforming along the Gatún fault. At 6-9 mm/yr, this displacement would require 2-3 Ma, almost exactly when Panamá is thought to have sealed the gap between the Pacific and the Atlantic Oceans at the beginning of the Pleistocene.

### REFERENCES

- Earth Consultants International, (ECI), 2005, Paleoseismic investigation of the Gatún and Limón faults in Central Panamá, ECI Project No. 2505; unpublished consulting report prepared for the Autoridad del Canal de Panamá, Project No. 2505, September 2005, 89p. + figures and appendices.
- ECI, 2006, Geomorphic Evaluation of the Miraflores, Pedro Miguel, Azota, and Caballo Faults, Central Panamá; unpublished consulting report prepared for the Autoridad del Canal de Panamá, Project No. 2614.01, November 2006, 36p. + figures and appendices.
- ECI, 2007, Paleoseismic Trenching of the Pedro Miguel Fault in Cocolí, Located Immediately Southwest of the Panamá Canal, Panamá; unpublished consulting report prepared for the Autoridad del Canal de Panamá, Project No. 2614.02, February 2007, 31p. + figures and appendices.
- ECI, 2008, Quantitative Characterization of the Pedro Miguel Fault, Determination of Recency of Activity on the Miraflores Fault, and Detailed Mapping of the Active Faults Through the Proposed Borinquén Dam Location; unpublished consulting report prepared for the Autoridad del Canal de Panamá, Project No. 2708.05, January 2008.
- Rockwell, T.K., Bennett, R.E., Gath, E., and Franceschi, P., 2010, Unhinging an Indenter: A New Tectonic Model for the Internal Deformation of Panamá; *Tectonics*, v. 29, TC4027, doi: 10.1029/2009TC002571.
- Rockwell, T., E. Gath, T. Gonzalez, C. Madden, D. Verdugo, C. Lippencott, T. Dawson, L.A. Owen, M. Fuchs, A. Cadena, P. Williams, E. Weldon, and P. Franceschi, 2010, Neotectonics and paleoseismology of the Limón and Pedro Miguel faults in Panamá: Earthquake Hazard to the Panamá Canal; *Bulletin of the Seismological Society of America*, Vol. 100, No. 6, pp. 3097-3129, doi: 10.1785/0120090342.



## Re-evaluation of late Quaternary deformation in the northern Wind River Basin, Wyoming

Francisco Gomez (1), Alzubair Abousaif (1,2), Eric Sandvol (1)

- (1) Dept. Geological Sciences, University of Missouri, Columbia, MO 65211 USA. Email: fgomez@missouri.edu  
(2) Geology Dept., Omar Al Mukhtar University, El Beida, Libya.

**Abstract:** At the northern boundary of the Wind River basin, the Stagner Creek fault is one of several ENE-WSW striking Quaternary faults in central Wyoming. In order to understand the structural context of this fault, this study combines a reassessment of the morphology of the Stagner Creek scarp along with an initial view of its shallow subsurface structure. New geomorphic analyses were facilitated by micro-topographic surveying using RTK GPS that provides higher resolution constraints on the scarp morphology. Apparent correlation of scarp slope and relative age suggests that the scarp results from folding, rather than surface faulting. Shallow seismic reflection profiling suggests a steep, north-dipping fault coincident with the surface scarp. Throw across the fault is approximately 10-15 meters, and the tip line of the fault is at 60-100 meters depth. These results suggest a new tectonic scenario involving possible reactivation of an inherited, Laramide-age structure.

**Key words:** Wind River Basin, neotectonics, seismic reflection profile, fault scarp

Although intraplate seismicity is typically less prominent than along plate boundaries, moderate earthquakes within these regions often pose risk to infrastructure that were not necessarily designed with the hazard in mind. In recent times, the hazard is further complicated by anthropogenic activities such as waste water injections that can induce seismicity in relatively seismically quiescent areas (e.g., Seeber et al., 2004; Keranen et al., 2014). To that end, understanding styles and kinematics of intraplate deformation such as the role of inherited structures, is needed for refining and improving our understanding of continental tectonics and associated intraplate earthquake hazard. This study presents a reassessment of late Quaternary deformation along the northern margin of the Wind River basin of Wyoming.

The Wind River Basin encompasses an area of about 13,600 km<sup>2</sup> in central Wyoming. Major structural elements in central Wyoming include broad and deep basins and asymmetric anticlinal uplifts that formed primarily during the late Cretaceous-early Tertiary Laramide Orogeny. The basin has a long history of hydrocarbon production (e.g., Nelson et al., 2008). The basin is bounded on the west by the Wind River Range, along the north by the Owl Creek Mountains, along the east by the Caspar Arch, and on the south by the Granite Mountains (Figure 1).

Active seismicity demonstrates that the region is tectonically active, and prior neotectonic studies have identified active and suspected active faults located within central Wyoming, capable of generating magnitude 6.5 – 7.1 earthquakes (Geomatrix, 1988). Around the Wind River basin, Quaternary faults are

expressed as discontinuous scarps often within late Pleistocene alluvial surface and typically aligned with the Owl Creek Mountains to the north and the Granite Mountains in the south (Machette et al., 2001).

Field work for this study focused on a section of the Stagner Creek Fault, bounding the northern Wind River Basin and the Owl Creek Mountains proximal to the Boysen Reservoir (Figure 1). In the study area, 6 late Quaternary alluvial surfaces are identified, all lying at elevations between 1,510 m and 1,540m. Alluvium is relatively thin, and locally, Paleogene Wind River Formation outcrops. The alluvial surfaces have regional slopes of 1.5 – 2 degrees and the scarp faces have modestly shallower slopes of 2.5 - 7 degrees. Preliminary age constraints are provided by correlation of soil development with late Pleistocene interglacial periods (Geomatrix, 1988). The Stagner Creek scarp is well expressed on Q1 through Q4 and not clear on Q5 and Q6 (Figure 1).

Topographic mapping and measurement were accomplished using a real time kinematic (RTK) Global Position System (GPS) surveying. In particular, an area 350 meters long and 500 meters wide was mapped for general topography with points acquired approximately every 2 meters. More detailed profiles were measured across the scarps with 1 meter posting on alluvial surfaces and half meter spacing across the scarp faces. Across each surface, at least two profiles were measured. Example profiles for each of the surfaces are shown in Figure 2.

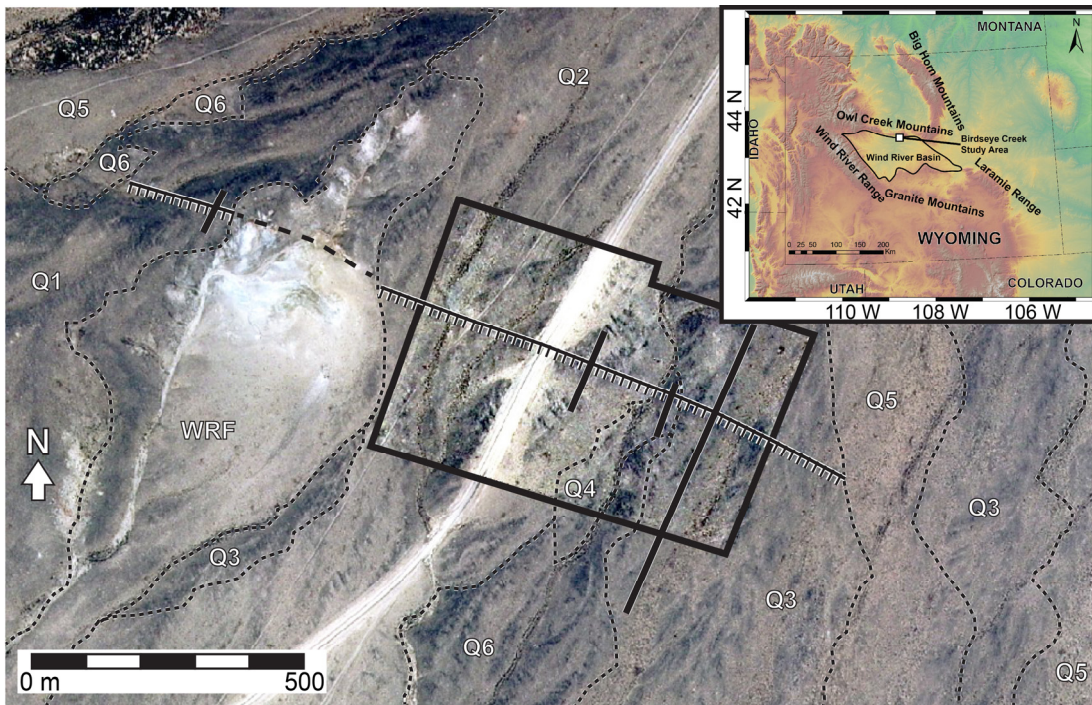


Fig. 1: Map of the Birdseye Creek area along the Stagner Creek fault. Q1-6 denote alluvial surfaces. WRF = Wind River Formation. Black box outlines area of detailed topographic mapping. Heavy black lines indicate topographic profiles shown in Figure 2. Seismic profile coincides with topographic profile in Q3 surface. Hachured line denotes the scarp.

Scarp morphologic parameters were calculated from the profiles (Table 1). Consistent with the relative age, older profiles demonstrate progressively higher scarps. This suggests that scarps in older surfaces are likely composite features formed by multiple events. Longer scarp faces also correspond with older surfaces, and the scarp profile in the Q1 surface shows possible indications of a segmented face. Additionally, the scarp inflection (i.e., the angle between the alluvial slope and scarp face) also increase with age.

Initial interpretations of the scarps as results of surface faulting permit quantitative assessment using fault scarp degradation models (e.g., Colman & Watson, 1983; Hanks, 2000). Such degradation models assume diffusive mass transport (e.g., sheet wash) and predict that the maximum slope angle, which ideally occurs at the inflection point in the scarp profile, will decrease with age. Increased scarp face length is also predicted by these models. One relatively straightforward approach involves the scarp height, regional surface slope, and the maximum scarp angle -- the analytic solution is derived by solving a 1-dimensional diffusion equation (Colman & Watson, 1983). A mass diffusivity parameter is required to calculate a numerical age; such parameters typically reflect a combination of erodibility of the surficial material and climatic constraints on mass transport. Lacking local constraints, a mass diffusivity value of  $1.1 \text{ m}^2/\text{ka}$  reported for the Basin and Range (Hanks, 2000) may be appropriate for the study area.

Regardless, an incorrect diffusion term will result in a systematic error for the absolute ages -- the relative ages should still be valid.

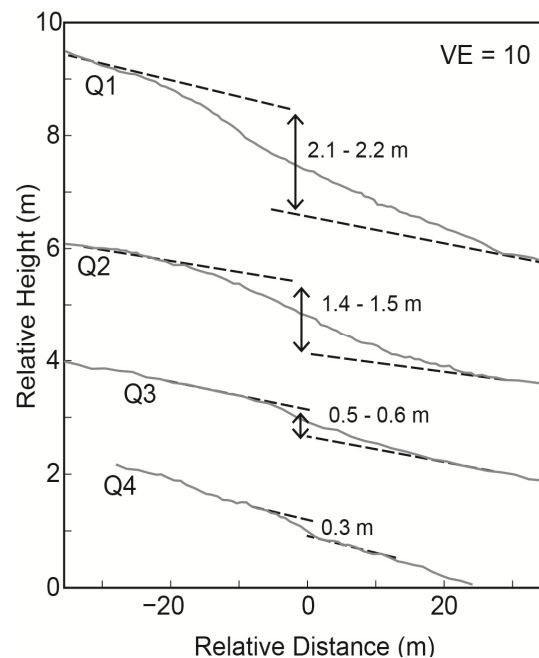


Fig. 2: Topographic profiles across the Stagner Creek fault scarp (see Figure 1 for locations). Horizontal position denotes distance relative to scarp midpoint.



	Age (kybp)	Slope (deg.)	Scarp Angle (deg.)	Scarp Height (m)	Inflection (deg.)
Q1		2.0	6.5 – 7.0	2.1 – 2.2	4.5 – 5.0
Q2	30 - 60	1.5 – 2.0	4.5 – 5.0	1.4 – 1.5	3.0 – 3.5
Q3	15 -40	2.0	3.0	0.5 – 0.6	1.0
Q4	8 - 20	2.0	2.5	0.25 - 0.3	0.5
Q5	1 – 7	n/a	n/a	n/a	n/a
Q6	< 1	n/a	n/a	n/a	n/a

Table 1. Alluvial surface ages (Geomatrix, 1988) and corresponding scarp parameters from topographic profiles:

The applicability of fault scarp degradation models to the scarps along the Stagner Creek fault is called into question by the observation of increasing scarp face inflections for older alluvial surfaces – this is counter to predictions of the models, even if one considers more complicated fault scarp degradation models that account for multiple faulting events. Consequently, ages calculated from diffusion modelling predict a relative order that is inconsistent with geomorphic positions:

- The Q1 scarp (the oldest and highest surface) demonstrates the youngest degradation-based age of 35 – 55 ka.
- The Q2 scarp has a degradation age of 45 – 65 ka.
- The Q3 & Q4 scarps exhibit degradation ages of 65 – 90 ka.

Given the inconsistency between landscape position and modeled relative scarp ages, we, thus, conclude that the fault scarp degradation modelling is probably inappropriate for this case.

Owing to the relationship between age and scarp angle, we suggest an alternative interpretation that the scarps result from folding of the alluvial surfaces rather than faulting and displacement. Such a fold scarp model suggests that older surfaces have steeper faces than the younger, owing to the progressive amount of tilting. Using the previously reported soil-correlation ages suggests that rates of surface warping range from 0.03 to 0.1 degree/ka.

A shallow seismic reflection profile was acquired across the scarp with the aim of constraining the shallow geometry of the controlling fault. In order to insure the fault geometry was captured in the seismic imaging across, the seismic line was ~420 meters long, trending NNW on the Q3 alluvial surface. The spacing between geophones was 2 meters, and 104 geophones moved four separate times along the seismic line in a ‘rolling spread’ configuration. A Betsy gun provided the seismic source (single shot load of 400 grains of black powder), with a total number of 36 shots and 6 meters spacing between each shot.

Data processing was accomplished using Visual-SUNT (<http://www.wgeosoft.ch>). Raw waveforms were filtered using a bandpass filter with cut-off frequencies at 15 Hz

and 25 Hz. Additionally ground roll was muted after identifying it with velocities around 100 m/s and linear move-out. Seismic stacking velocities were estimated by analyzing travel-time plots for selected shot locations at the beginning, middle, and end of the profile. From the first breaks in slopes of the travel-time plots, the depth to the alluvium-bedrock (Wind River Formation) interface was estimated based on the offset. Using the dip of the interface (estimated at 8 degrees), the true seismic velocity was then calculated from dip move-out to be approximately 2,500 m/s. This seismic velocity was used to stack the seismic sections and depth-convert the final seismic reflection profile (Figure 3).

The seismic line crosses the scarp around CDP 140 (Figure 3), where the seismic profile also shows discontinuous reflectors at depth. This break in reflectors is interpreted to be a fault dipping approximately 70 degrees toward the north (high angle reverse fault). Furthermore, the fault appears to be blind, as it does not offset the uppermost reflector in the seismic profile. Throw across the fault is estimated to be 11-15 meters, with a fault tip located at depth approximately 60-100 m. In addition to the fault that projects to the surface scarp, other faults are visible in the subsurface. Since these lack apparent surface expressions, we believe these are likely relict, Laramide-age structures.

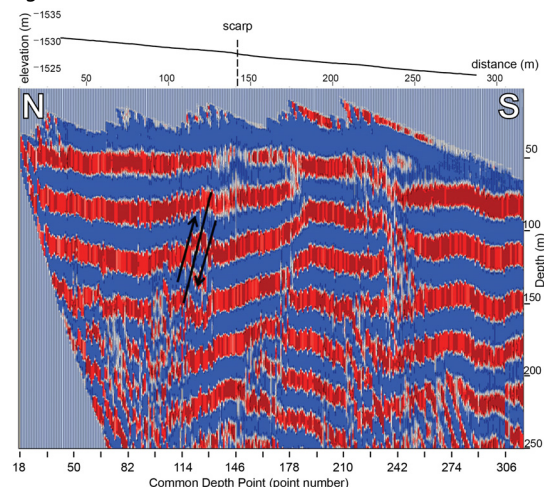


Fig. 3: Shallow seismic reflection profile. The surface scarp corresponds with CDP 146.



Combining the interpretation of the fold scarp with the associated fault imaged by seismic reflection profiling, we thus suggest that the scarp along the Stagner Creek fault near Boysen Reservoir is a consequence of folding above a shallow, but blind, reverse fault dipping toward the north (Figure 4). Surface morphology and seismic reflection imaging document that the fault has a component of reverse slip, but we are unable to ascertain whether or not there is a component of strike-slip. Currently, there is a paucity of geodetic and seismological indicators of present-day strain in the Wind River Basin for comparison. The scarp trend is similar with Laramide structures in the Owl Creek Mountains (Keefer, 1970). Therefore, we suggest that the active fault likely represents a reactivated, inherited structure.

This interpretation of blind faulting suggests that the scarp is more warped than degraded – consequently, this site is not ideal for paleoseismic trench investigations owing to minimal deposition along the fault. Despite that limitation, the scarp morphology provides some approximate constraints on the local earthquake potential. In particular, if the uplift and warping of the Q4 scarp is assumed as a consequence of a single earthquake event, then the composite scarps in the Q1 surface and Q2 surfaces may represent the effects of 8 and 5 paleo-earthquakes, respectively, assuming a characteristic earthquake recurrence model. Using the approximate age of the Q2 surface (30 ka to 60 ka) would imply an average recurrence time of 6,000 to 12,000 years. Owing to the very shallow depth of the fault tip, uplift of 0.3 m is approximately equivalent to the throw on the fault. Using earthquake magnitude scaling relations (Wells & Coppersmith, 1994), the possible, single-event uplift of 0.3 m corresponds with an earthquake of approximate magnitude 6.4 – 6.7 -- this is also consistent with the 27 km length of the Stagner Creek fault. These interpretations of earthquake potential are similar to prior assessments of the Stagner Creek fault (Geomatrix, 1988).

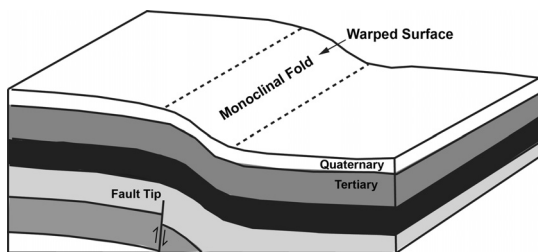


Fig. 4: Schematic model of a monoclonal warping above a blind fault.

It is important to note that this is a single location along the 27-km-long Stagner Creek fault, and it is possible the fault may daylight at other locations. Future directions for study of the Stagner Creek fault should include more geophysical investigations to improve the seismic

velocity control (e.g., using seismic refraction methods), as well as additional seismic reflection profiling to constrain the subsurface fault geometry in both strike and dip (is it consistent with the surface scarp trend?). Furthermore, advances in Quaternary geochronology (e.g., exposure dating) have the potential to refine the ages of the geomorphic surfaces considerably.

In conclusion, these preliminary results do not substantially change the earthquake potential from previous estimates. On the other hand, the new structural interpretation related to the Stagner Creek scarp may contribute to future earthquake hazard assessments, particularly for efforts in which existing geometry may play a role in considering the effects of changes in crustal stress that may result from other earthquakes or anthropic activities.

**Acknowledgements:** This research was partly supported by MU Geology Departmental Scholarship for Z. Abousaif during his M.S. studies. Field assistance was provided by William Cochran, John Corley, Bjorn Held, Nathan Hinrichs, and Wang Hu. Additional support was provided by the University of Missouri Field Camp.

#### References

- Colman, S.M., and K. Watson, (1983). Ages Estimated from a Diffusion Equation Model for Scarp Degradation. *Science* 221 (4607), 263-265.
- Geomatrix Consultants, Inc., (1988). *Seismotectonic evaluation of the northwestern Wind River Basin*. Final Report prepared for the U.S. Bureau of Reclamation, Contract No. 6-CS-81-07310, p.116.
- Hanks, T., (2000). The age of scarplike landforms from diffusion-equation analysis. In: *Quaternary Geochronology: Methods and Applications* (Noller, J. S., Sowers, J. M., Lettis, W. R. eds). AGU Reference Shelf #4, 313-338.
- Keefer, W.R., (1970). Structural geology of the Wind River Basin, Wyoming. *United States Geological Survey Professional Paper* 495-D, 35 p.
- Keranen, K. M., M. Weingarten, G. A. Abers, B. A. Bekins, & S. Ge, (2014). Sharp increase in central Oklahoma seismicity since 2008 induced by massive wastewater injection. *Science*, 25 July 2014: Vol. 345 no. 6195, pp. 448-451, doi: 10.1126/science.1255802.
- Machette, M.N., K. L. Pierce, J. P. McCalpin, K. M. Haller, & R. L. Dart, R, (2001). Map and data for Quaternary faults and folds in Wyoming. U.S. *Geological Survey Open File Report* 01-461, 155 p.
- Nelson, P. H., P. K. Tainor, & T. M. Finn, (2008). Gas, oil, and water production in the Wind River Basin, Wyoming. *United States Geological Survey Scientific Investigations Report* 2008-5225, 23 p.
- Seeber, L., J. G. Armbruster, & W.-Y. Kim, (2004). A Fluid-Injection-Triggered Earthquake Sequence in Ashtabula, Ohio: Implications for Seismogenesis in Stable Continental Regions. *Bulletin of the Seismological Society of America* 94, 76-87, doi:10.1785/0120020091.
- Wells, D. L., & K. J. Coppersmith, (1994). New empirical relationships among magnitude, rupture length, rupture width, rupture area, and surface displacement. *Bulletin of the Seismological Society of America* 84, 974-1002.



## Seismic hazard analysis and active fault slip-rates in the Tongariro Graben, southern Taupo Volcanic Zone, New Zealand.

Martha Gabriela, Gómez-Vasconcelos (1), Pilar, Villamor (2), Jon, Procter (1), Alan, Palmer (1), Shane, Cronin (1,3), Clel Wallace (1), Dougal, Townsend (2), Graham Leonard (2).

- (1) Volcanic Risk Solutions, Institute of Agriculture and Environment, Soil and Earth Sciences, Massey University, Private Bag 11 222, Palmerston North 4442, New Zealand. Email: ga8ygomez@yahoo.com
- (2) GNS Science, PO Box 30-368, Lower Hutt, New Zealand.
- (3) School of Environment, The University of Auckland, Private Bag 92019, Auckland 1142, New Zealand.

**Abstract:** In the central North Island of New Zealand lies the intra-arc Taupo Rift, where crustal extension is achieved through a combination of dike intrusion and normal faulting. In the southern Taupo Volcanic Zone, the Tongariro volcanic complex lies in the here defined Tongariro Graben, between two regional and parallel NNE-oriented active normal fault sets; the Waihi and Poutu fault zones. This study presents an analysis of the movement associated with the Waihi and Poutu faults between 200 and 1.72 ka. We evaluated the time-variant movement associated with these fault zones by measuring vertically displaced geomorphic surfaces over 227 strands and field exposures. The Waihi and Poutu faults have a mean slip-rate of 2.6 and 2.3 mm/yr, respectively, and are capable of producing a  $M_w$  7 earthquake. A better understanding of the kinematics and evolution of these faults will help improve the seismic and volcanic hazard assessment in the Central North Island.

**Key words:** Paleoearthquake history, Waihi and Poutu fault zones, slip-rates, Tongariro Volcanic Centre, New Zealand.

### INTRODUCTION

Extension in volcanic rift zones is reflected by a combination of normal faults, extensional fissures and dike intrusions (McCalpin, 1996). In the here defined Tongariro Graben, crustal extension started at  $\sim 0.5$  Ma (Villamor and Berryman, 2006). Two NNE-oriented parallel fault zones in the rift axis accommodate most of the extension in this area, and bound the western and eastern flanks of Tongariro volcano; the Waihi and Poutu faults, respectively.

We aim to quantify the spatial and temporal variability of extension of these fault systems. We further aim to improve seismic and volcanic hazard assessments in the region, since the Waihi and Poutu faults represent a significant component of the present seismic potential of active faults in the region (Lecointre et al., 2004; Villamor and Berryman, 2006).

### GEOLOGICAL AND STRUCTURAL SETTING

The Taupo Volcanic Zone is a NNE-trending Quaternary volcanic arc located in the North Island of New Zealand and associated with a crustal extension regime created by slab rollback (Seebeck et al., 2014) and fore-arc clockwise rotation of the NNE-SSW Hikurangi Trench, where the Pacific Plate subducts below the Australian Plate (Wallace et al., 2004). Faults within the volcanic arc define the intra-arc Taupo Rift (Acocella et al., 2003; Fig. 1).

The Tongariro volcanic complex is a NNE-aligned andesite volcano complex, with vents aligned along the same strike as the Tongariro Graben axis (Topping, 1973; Rowland and Sibson, 2001; Villamor and Berryman, 2006; Fig. 1). The complex includes more than 17 overlapping

vents that have produced hundreds of eruptions over the last  $\sim 300$  ka (Topping, 1973; Cole, 1978; Hobden et al., 1996; Gamble, et al., 2003). Extension (strain) direction in the Tongariro area has an ESE-WNW direction (ca.  $110^\circ$ ), as suggested by the trend of active faults and dikes (Rowland and Sibson, 2001).

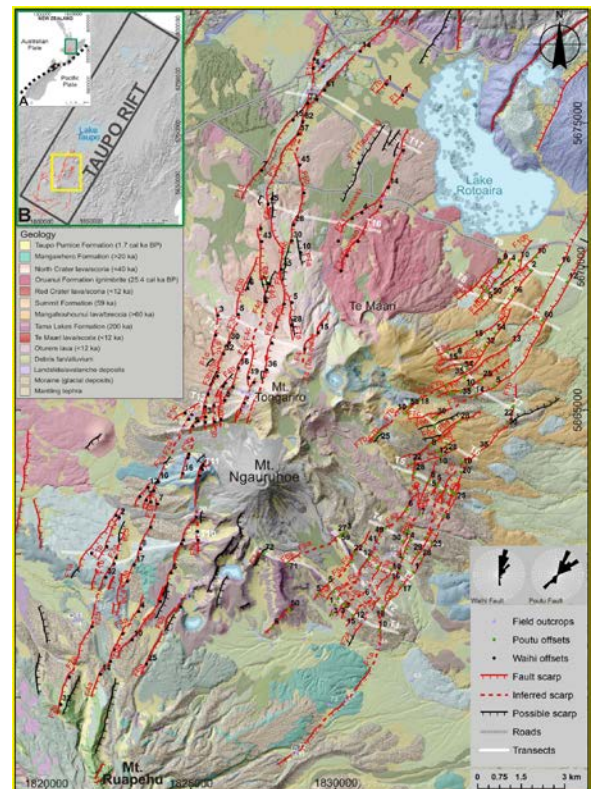


Fig. 1: Location map of the Tongariro Graben in the southern Taupo Rift (B) in the North Island of New Zealand (A) showing the



INQUA Focus Group on Paleoseismology and Active Tectonics



paleoseismicity.org

regional geology, main volcanic vents and the Waihi and Poutu fault zones (offsets marked with black and green dots). Active fault scarps marked in red, inferred scarps marked with red dashed lines and possible scarps marked in black. 17 transects are marked with white lines. Field points marked with purple dots. The fault planes are plotted in stereographic (lower hemisphere) projection and superimposed rose diagrams of fault strike frequency (right-hand rule).

**METHODOLOGY**

We measured fault geometry (azimuth and dip), movement sense, fault displacements with field measurements (Fig. 2), and geomorphic analysis of the faults using ArcGIS on a 2 m resolution Digital Surface Model (S. Ashraf, methodology described in Gómez-Vasconcelos et al., 2016). We traced 117 profiles across the Waihi Fault zone and 110 across the Poutu Fault zone, perpendicular to the fault strands, at locations where the faults displace geomorphic surfaces of known ages. The age of stratigraphic markers and geomorphic surfaces provided a broad age control of vertical fault motion. Vertical displacements were converted to net-displacement to calculate net faults slip-rates, following the methods described by Villamor and Berryman (2001 and 2006).

In order to calculate seismic hazard, earthquake moment magnitudes ( $M_w$ ) were calculated using a fault-scaling relationship developed for the Taupo Volcanic Zone (Villamor et al., 2007; Stirling et al., 2012), based mainly on the surface-rupture length ( $M_w = 4.80 + 1.33 \times \log$  [subsurface rupture length]). Fault lengths were measured in this work, based on fault displacements, geomorphology and field observations. For fault width we assumed a 15 km-thick seismogenic crust, as suggested on previous seismic studies (Hurst & McGinty, 1999; Hayes et al., 2004; Stirling et al., 2012).

**THE WAIHI AND POUTU FAULT ZONES**

The Waihi Fault Zone is an active NNE-oriented normal fault set at the western side of the Tongariro complex, downthrown to the ESE (Grindley, 1960; Van Dissen et al., 2003). The zone comprises 19 parallel fault strands and 1

antithetic fault, with an average strike of 055. The Poutu Fault Zone, at the eastern side of the Tongariro complex, is downthrown both to the SE and to the NW (Van Dissen et al., 2003), and comprises 23 fault strands, with an average strike of 041 (Fig. 1).

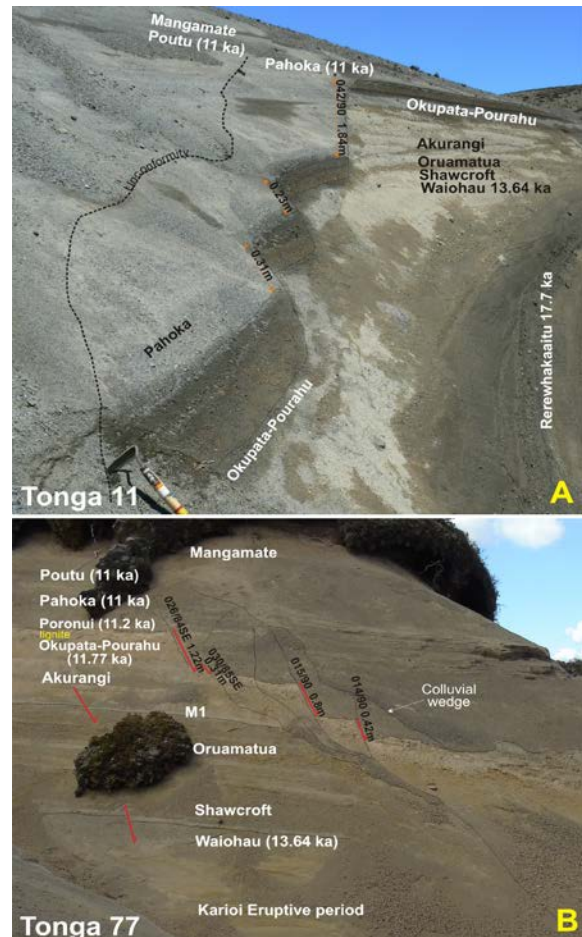


Fig. 2: Field outcrops from the Poutu Fault. A, Tonga 11: normal fault displacing the Pahoka and Okupata-Pourahu tephras. B, Tonga 77: Normal fault (F2b) displacing the Okupata-Pourahu tephras (11.77 cal ka BP; Hajdas et al., 2006).

Table 1. Waihi and Poutu faults transects

Waihi Fault Transect # (age)	Vertical displacement (Fault) (m)								Total offset* (sum all)	Vertical Slip-rate (mm/yr)	Total offset* (sum all except antithetic)	Vertical slip-rate (mm/yr)	
Transect 15 (12 ka)	3±1.3 (1c)	5±1.5 (3b)	5±1.5 (4d)	11±2.1 (6b)					24±3.5	2±0.4	24±3.5	2±0.4	
Transect 10 (20 ka)	3±1.3 (1a)	4±1.4 (1b)	5±1.5 (2a)	8±1.8 (3a)	55±6.5 (5a, 200ka)	22±3.2 (6b, 200 ka)			28±3.6	1.39±0.2	28±3.6	1.39±0.2	
Transect 12 (22 ka)	3±1.3 (2a)	5±1.5 (3b)	15±2.5 (3b)	12±2.2 (4b)	13±2.3 (4c, 30.6ka)	65±7.5 (5a, 59 ka)			69±5.6	3.12±0.25	69±5.6	3.12±0.25	
Transect 11 (25 ka)	10±2 (2a)	16±2.6 (3b)	20±3 (5a)	15±2.5 (5a)					61±5.1	2.44±0.32	61±5.1	2.44±0.32	
Transect 16 (40 ka)	16±2.6 (1d)	45±5.5 (3b)	28±3.8 (6b)	33±4.3 (6c)	11±2.1 (2)	27±3.7 (3)			160±9.4	4.0±0.32	160±9.4	4.0±0.32	
Transect 13 (52.6 ka)	37±4.7 (3b)	5±1.5 (4b)	8±1.8 (4c)	40±5 (5a, 40 ka)					102±8.1	1.95±0.2	102±8.1	1.95±0.2	
Transect 14 (59 ka)	22±3.2 (1c)	30±4 (3b)	16±2.6 (4c, 25ka)	19±2.9 (5b, 25ka)	36±4.6 (6b, 40 ka)				173±10.9	3.18±0.3	173±10.9	3.18±0.3	
Transect 17 (85 ka)	73±8.3 (1d)	61±7.1 (3b)	15±2.5 (1T, 25ka)	14±2.4 (3, 25 ka)	±1.1 (7b, 3 ka)				206±12.8	3.07±0.5	149±11.5	2.47±0.47	
Mean slip-rate										2.6±0.9		2.6±0.8	
<b>Poutu Fault</b>													
Transect 5 (15 ka?)	25±3.5 (1a)	25±3.5 (1b)	12±2.2 (1b)	10±2 (2c)	12±2.2 (2c)	5±1.5 (3b)	5±1.5 (3b)	8±1.8 (3b)	28±3.8 (4a, 60ka)	110±6.1	7.27±0.6	79±4.7	5.3±1.8
Transect 9 (17.7 ka)	12±2.2 (7c)	16±2.6 (7b)	2±1.2 (9a)	10±2 (10a)	10±2 (10b)	4±1.4 (11a, 10 ka)	9±1.9 (12a)		66±5.2	3.7±0.33	40±4.1	2.3±0.24	
Transect 1 (20 ka)	10±2 (1a)	12±2.2 (2a)	15±2.5 (3a)	3±1.3 (3b)	3±1.3 (3b)	5±1.5 (4a)	5±1.5 (4b)	5±1.5 (5a)	58±5.6	2.9±0.7	37±3.9	1.9±0.27	
Transect 2 (20 ka)	10±2 (1a)	9±1.9 (2a)	6±1.6 (3a)	13±2.3 (3b)	6±1.6 (4a)	38±4.8 (5a, 128ka)			50±4.8	2.5±0.34	38±3.9	1.9±0.5	
Transect 3 (20 ka)	17±2.7 (1a)	16±2.6 (2b)	10±2 (3a)	11±2.1 (3b)	12±2.2 (4a)	22±3.2 (5a, 60 ka)			72±5.7	3.6±0.46	38±4	1.9±0.5	
Transect 7 (20 ka)	22±3.2 (1b, 36.1ka)	14±2.4 (7c)	10±2 (7d)	35±4.5 (7b, 60 ka)	4±1.4 (8a)	5±1.5 (8b)	6±1.6 (8c)	15±2.5 (8d)	78±5.7	3.9±0.42	41±4.2	2.1±0.29	
Transect 4 (60 ka)	25±3.5 (1a)	27±3.7 (2c)	12±2.2 (2b)	30±4 (3b)	49±5.9 (4a, 97 ka)				124±7.9	2.1±0.15	82±6.5	1.4±0.16	
Transect 6 (60 ka)	38±4.8 (1b)	29±3.9 (6b)	28±3.8 (6c)	60±7 (6d)	10±2 (6e)	30±4 (7c)	2±1.2 (7b, 3 ka)	50±6 (7b, 110 ka)	232±11.8	4.4±0.64	95±7.3	1.6±0.18	
Transect 8 (100 ka)	60±7 (7c)	13±2.3 (7b, 17.7ka)	56±6.6 (9a)	50±6 (10a)	10±2 (11a)	9±1.9 (12a, 17.7ka)			291±15	3±0.21	181±12.2	1.8±0.22	
Mean slip-rate										3.7±1.38		2.3±1.9	

\* Displacement values were converted to transect ages when the existing values were of a different age. Antithetic fault strands



### FAULT GEOMETRY AND SLIP-RATE

The Waihi and Poutu fault zones show a complex geometry (e.g., en-echelon fault traces, horsetail fault splaying and non-parallel fault strands). The two fault systems trend slightly closer together towards the south, creating a narrower graben at the axis of the rift, parallel to, but offset from, the modern volcanic vent complex. In the northern part of the Tongariro Graben the fault strands splay outward from the volcanic vent alignment (Fig. 2).

We infer that these multiple surface fault strands splay and merge into a single fault plane at depth, as also suggested elsewhere in the rift by Villamor and Berryman (2001) and Nicol et al. (2010). Based on this interpretation, we traced eight transects across the Waihi Fault strands and nine transects across the Poutu Fault strands (Fig. 1), which we summed and analysed as the best representation of the total deformation accommodated by these faults. Fault slip-rates were calculated from these transects: the Waihi Fault has a mean slip-rate of  $2.6 \pm 0.8$  mm/yr and Poutu Fault of a mean slip-rate of  $2.3 \pm 1.9$  mm over the last 200 ka (Table 1).

### MAGNITUDE AND RECURRENCE INTERVAL OF POTENTIAL EARTHQUAKES

The seismic parameters for the Waihi and Poutu faults, such as earthquake magnitudes and recurrence times for segments of different surface lengths, have been derived from slip-rate calculations and different models of fault rupture length (Hurst & McGinty, 1999; Hayes et al., 2004; Stirling et al., 2012; Table 2).

The complexity of the surface fault expression and the lack of historic fault surface ruptures in this region make the fault segmentation uncertain. Nevertheless, we suggest different possible scenarios for segment surface-length rupture for each of the fault zones, mainly based on the fault strands geometry (morphometry and distribution; Fig. 3). Although we suggest a minimal segment surface length of 12 km, we expect it to be at least as long as the thickness of the seismogenic crust; c. 15 km (Hurst & McGinty 1999; Hayes et al. 2004), as suggested by previous seismic hazard studies (Stirling et al. 2012).

Waihi Fault is at least 38 km in length (up to 52 km if it extends to the SW boundary of Lake Taupo). Waihi South segment (18 km) is based on relatively continuous ~025-trending parallel fault strands; it could finish against ~N-trending fault strands. Waihi North segment (20 km) starts with ~N-trending fault strands, changing again to ~025-trending rift-parallel fault strands. Poutu Fault is at least 30 km in length. Poutu South segment (12 km) is based on relatively continuous ~025-trending parallel fault strands; it could finish against ~060-trending fault strands. Poutu North segment (18 km) starts with ~060-trending fault strands, changing again to ~025-trending rift-parallel fault strands.

If the entire length of the Waihi Fault Zone were to rupture (38 km-long) we calculated a  $M_w$  7.0 earthquake with an average single-event displacement of 2 m. For the whole Poutu Fault Zone rupture (30 km-long) we calculated a  $M_w$  6.9 earthquake with an average displacement of 1.6 m. The worst case scenario would be a 52 km-long rupture, including the whole Waihi Fault Zone and the SW boundary of Lake Taupo, generating a  $M_w$  7.2 earthquake with an average single-event displacement of 2.9 m (Fig. 3; Table 2).

When slip-rates are combined with the derived average displacements we obtain a recurrence interval of 1.0 ka and 0.9 ka for Waihi and Poutu faults, respectively.

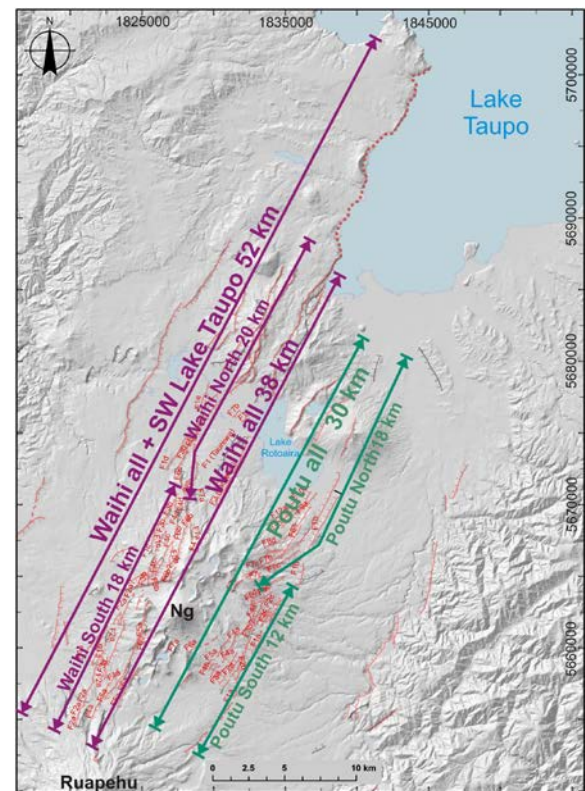


Fig. 3. Potential segment surface length rupture models for the Waihi and Poutu faults, marked with purple and green lines, respectively. Ng= Ngauruhoe volcano

Table 2. Moment magnitude and single-event displacement for different fault lengths. Estimated average single-event displacement in meters and earthquake moment magnitude ( $M_w$ ) based on Webb's equation, for a certain segment surface length (km) and fault area (as described in Villamor et al. 2007; Stirling et al. 2012).

Fault	Segment surface length (km)	Sub-surface length (m)	Average displacement (m)	$M_w$
Poutu South segment	12	14	0.7	6.3
Waihi South/Poutu North	18	21	1	6.6
Waihi North segment	20	23	1.1	6.7
whole Poutu Fault	30	35	1.6	6.9
whole Waihi Fault	38	44	2	7.0
whole Waihi + SW Lake Taupo	52	61	2.9	7.2

### PRELIMINARY CONCLUSIONS



## INQUA Focus Group on Paleoseismology and Active Tectonics



paleoseismicity.org

Earlier studies on the Waihi and Poutu fault zones (GNS science, unpublished data) estimated mean slip-rates of 1.3 and 1.85 mm/yr, respectively. Our data show that the Waihi Fault mean slip-rate value could be  $2.6 \pm 0.8$  mm/yr and the Poutu Fault mean slip-rate could be  $2.3 \pm 1.9$  mm/yr, increasing the seismic hazard potential. Consequently, our study would provide an update to the National Seismic Hazard Model for New Zealand (Stirling et al., 2012; Litchfield et al., 2014).

Available vertical slip-rates will aid calculation of the extension rates for the Waihi and Poutu fault zones. Future studies involve a comparison between tectonic and volcanic extension and insights of volcano-tectonic interactions.

**Acknowledgements:** This project was funded by a Massey University doctoral scholarship and GNS Science CORE Funds. We thank Anja Moebis, Diana Cabrera, Agnes Samper, Denis Avellán, Alderik, Kate Arentsen, Nicola Litchfield and Ivan Martin for their support during field work, laboratory analysis and stratigraphic identification. We also want to acknowledge the Volcanic Risk Solutions group in Massey University and the Department of Conservation staff of Tongariro National Park.

### References

- Acocella V, Spinks K, Cole J, Nicol A 2003. Oblique back arc rifting of Taupo Volcanic Zone, New Zealand. *Tectonics*, 22(4)
- Cole JW 1978. Andesites of the Tongariro Volcanic Centre, North Island, New Zealand. *Journal of volcanology and geothermal research*, 3(1): 121-153.
- Gamble JA, Price RC, Smith IE, McIntosh WC, Dunbar NW 2003. <sup>40</sup>Ar/<sup>39</sup>Ar geochronology of magmatic activity, magma flux and hazards at Ruapehu volcano, Taupo Volcanic Zone, New Zealand. *Journal of Volcanology and Geothermal Research*, 120(3): 271-287.
- Gómez-Vasconcelos MG, Villamor P, Cronin SJ, Procter J, Kereszturi G, Palmer A, Townsend D, Leonard G, Berryman K, Ashraf S 2016. Earthquake history at the eastern boundary of south Taupo Volcanic Zone, New Zealand. *New Zealand Journal of Geology and Geophysics*. In press.
- Grindley GW 1960: Sheet 8—Taupo. Geological map of New Zealand 1:250 000. Wellington, New Zealand. Department of Scientific and Industrial Research.
- Hajdas I, Lowe DJ, Newnham RM, Bonani G 2006. Timing of the late-glacial climate reversal in the Southern Hemisphere using high resolution radiocarbon chronology for Kaipo bog, New Zealand. *Quaternary Research* 65: 340-345.
- Hayes G, Reyners M, Stuart G 2004. The Waiouru, New Zealand, earthquake swarm: persistent mid crustal activity near an active volcano. *Geophysical research letters*, 31(19).
- Hurst AW, McGinty PJ 1999. Earthquake swarms to the west of Mt Ruapehu preceding its 1995 eruption. *Journal of Volcanology and Geothermal Research*, 90(1): 19-28.
- Lecoindre JA, Neall VE, Wallace RC, Elliot MB, Sparks R 2004. Late Quaternary evolution of the Rotoaira Basin, northern Tongariro ring plain, New Zealand. *New Zealand Journal of Geology and Geophysics*, 47(3), 549-565.
- McCalpin JP 1996. Paleoseismology in extensional tectonic environments. *International Geophysics*, 62, 85-146.
- Nicol A, Walsh JJ, Villamor P, Seebeck H, Berryman KR 2010. Normal fault interactions, paleoearthquakes and growth in an active rift. *Journal of Structural Geology*, 32(8), 1101-1113.
- Rowland JV, Sibson RH 2001. Extensional fault kinematics within the Taupo Volcanic Zone, New Zealand: soft-linked segmentation of a continental rift system. *New Zealand Journal of Geology and Geophysics*, 44(2): 271-283.
- Topping WW 1973. Tephrostratigraphy and chronology of late Quaternary eruptives from the Tongariro Volcanic Centre, New Zealand. *New Zealand journal of geology and geophysics*, 16(3): 397-423.
- Seebeck H, Nicol A, Giba M, Pettinga J, Walsh J 2014. Geometry of the subducting Pacific plate since 20 Ma, Hikurangi margin, New Zealand. *Journal of the Geological Society*, 171(1): 131-143.
- Stirling M, McVerry G, Gerstenberger M et al. 2012. National seismic hazard model for New Zealand: 2010 update. *Bulletin of the Seismological Society of America*, 102(4): 1514-1542.
- Van Dissen RJ, Berryman K, Webb T, Stirling M, Villamor P, Wood PR, Pace B 2003. An interim classification of New Zealand's active faults for the mitigation of surface rupture hazards. In proceedings, Pacific Conference on Earthquake Engineering.
- Villamor P, Berryman K 2001. A late Quaternary extension rate in the Taupo Volcanic Zone, New Zealand, derived from fault slip data. *New Zealand Journal of Geology and Geophysics*, 44(2): 243-269.
- Villamor P, Berryman KR 2006. Late Quaternary geometry and kinematics of faults at the southern termination of the Taupo Volcanic Zone, New Zealand. *New Zealand journal of geology and geophysics*, 49(1), 1-21.
- Villamor P, Van Dissen R, Alloway BV, Palmer AS, Litchfield N 2007. The Rangipo fault, Taupo rift, New Zealand: An example of temporal slip-rate and single-event displacement variability in a volcanic environment. *Geological Society of America Bulletin*, 119(5-6), 529-547.
- Wallace LM, Beavan J, McCaffrey R, Darby D 2004. Subduction zone coupling and tectonic block rotations in the North Island, New Zealand. *Journal of Geophysical Research: Solid Earth* (1978–2012), 109(B12).



## Quaternary deformation in the Atacama Fault System in northern Chile: new discoveries from trenching and OSL dating of colluvial wedges

Gabriel González<sup>1,2</sup>, Luis Astudillo<sup>1</sup>, Isabel Santibañez<sup>1,3</sup>, Ian del Rio<sup>1</sup>, Richard Allmendinger<sup>4</sup>, Ruth Robinson<sup>5</sup>, Steven Binnie<sup>6</sup> and José Cembrano<sup>1,3</sup>

- (1) National Research Center for Integrated Natural Disaster Management, Chile
- (2) Universidad Católica del Norte, Antofagasta, Chile
- (3) Pontificia Universidad Católica de Chile, Chile
- (4) Department of Earth and Atmospheric Sciences, Cornell University, Ithaca, New York, USA.
- (5) Institute of Geography, University of Edinburgh, Edinburgh, UK.
- (6) Institut für Geologie und Mineralogie, Universität zu Köln, Cologne, Germany

**Abstract:** The Atacama Fault System (AFS) is an ancient trench parallel fault system in northern Chile, which has been reactivated during the Neogene producing a conspicuous mountain and range topography in the Coastal Cordillera. NS-striking fault scarps affecting Quaternary alluvial fans are common in the piedmont of the mountain fronts. Direct dating of single events along these faults is still needed. In this contribution we presented the results of a detailed geological analysis of two main faults of the AFS, including the Salar del Carmen Fault and the Mititus Fault. Twenty-four trenches were geologically mapped to characterize the fault scarp morphology; 2 cm resolution digital elevation models by UAV-based photogrammetry were built. The following aspects were resolved: 1) the temporal relationship between previously documented reverse and normal faulting along these faults, 2) the age of the latest faulting on the Salar del Carmen Fault, and 3) the paleoseismological significance of fault reactivation

**Key words:** Atacama Fault System, northern Chile, Paleoseismology, upper plate faulting

### INTRODUCTION

The Atacama Fault System (AFS) in northern Chile exerts a strong control on the morphology of the Coastal Cordillera near Antofagasta (24° Latitude S). This control is primary expressed by kilometer-long mountain fronts limited by large subsiding alluvial basins (Fig.1). Long-term fault displacements have produced cumulative vertical offsets of up to 500 m. Miocene and Pliocene ages from volcanic ash layers interbedded in the alluvial infill of the structurally controlled basins attest to a prolonged period of faulting. NS-striking sharp fault scarps affecting Quaternary alluvial fans are common in the piedmont of the mountain fronts. These fault scarps are the most recent reactivation features of the faults. The faults are expressed from the western side of the Mejillones Peninsula to the eastern border of the Coastal Cordillera, covering a 45 km wide transect where half-graben structures dominate. In this section the most important upper plate structures are the Mejillones Fault (MF), the Mititus Fault (MIF) and the Salar del Carmen Fault (SCF).

The Quaternary kinematics of the main faults has been intensively studied during the last few decades (Armijo and Thiele, 1990, Delouis et al., 1998; Gonzalez and Carrizo, 1996; Allmendinger and Gonzalez, 2011). According to these studies the fault kinematics are dominated by normal faulting. However Armijo and Thiele (1990) described sinistral strike slip faulting in the northernmost part of the AFS and Allmendinger and González (2011) reported 2-1 m of piedmont uplift due to reverse fault reactivation along the main fault of the AFS. Therefore the kinematics of these upper plate structures shows some controversial aspects, which is resolved in this study. The ages of the Quaternary faulting have been constrained in a general way by

dating faulted-abandoned alluvial surfaces (González et al., 2006) and by dating gypsum veins hosted in the fault planes of the AFS (Vargas et al., 2010). However, direct dating of single events along the upper plate faults of the AFS are still needed.

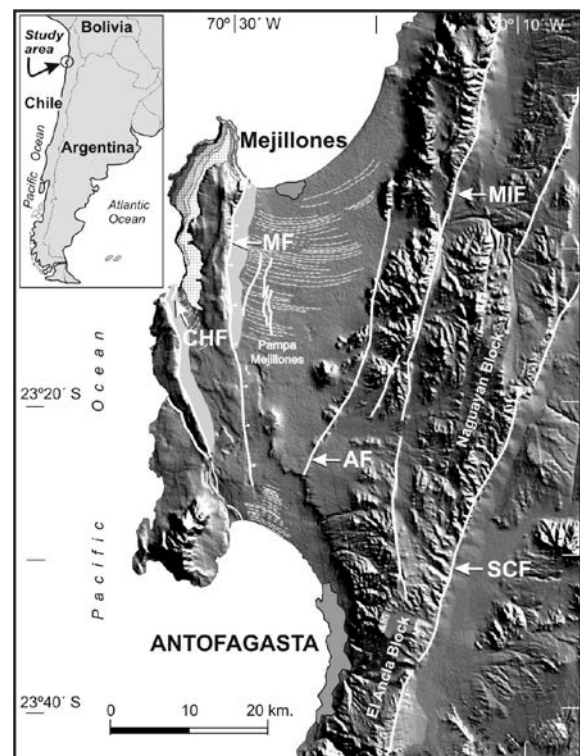
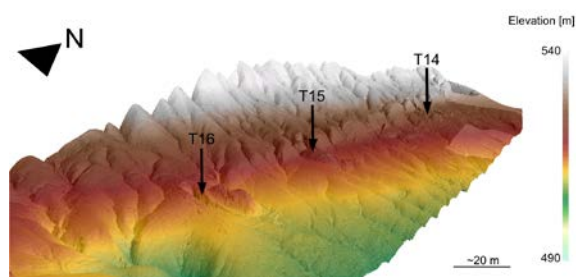


Figure 1. Hill shade model extracted from STRM 90 data. White lines represent major fault of the area. MIF= Mititus Fault, SCF= Salar del Carmen Fault. Segmented white lines are Quaternary paleo-shore lines



In this contribution the results of a detailed geological analysis of two main faults of the Atacama Fault System, including the Salar del Carmen Fault and the Mititus Fault, are presented. In our analysis we mapped 24 trenches excavated along these two faults. In order to characterize fault scarp morphology we used 2 cm resolution digital elevation models generated by UAV-based photogrammetry (Fig. 2). We resolved the following geological problems: 1) the temporal relationship between previously documented reverse and normal faulting along these faults, 2) the age of the latest fault faulting on the Salar del Carmen Fault and 3) the paleoseismological significance of the late fault reactivation of the AFS.

a)



b)

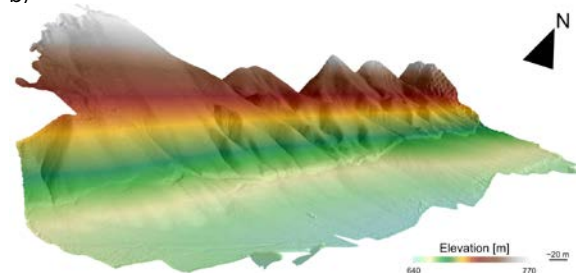


Figura 2. High-resolution digital elevation models based on UAV photogrammetry. a) fault-scarp of Mititus Fault and b) fault-scarp of Salar del Carmen Fault, vertical exaggeration  $\times 2$ .

Optically stimulated luminescence (OSL) for age constrain of sediments derived from fault scarp degradation was used. It included colluvial wedges and hill-slope deposits exposed in trench walls, as well as sediments from fluvial beds affected by faulting. The OSL dating is based on quartz single aliquot regeneration methods (Murray and Wintle, 2000). The burial ages are modeled using minimum age model and finite age model (Arnold et al., 2009). The OSL dating targets were medium-grained lithic arenite.

## TECTONIC SETTING

Convergence between the Nazca and South America along the Chilean margin occurs at a rate of 66 mm/yr (Angermann et al., 1999) and thus generates one of the most active subduction zones on Earth. This margin has generated the largest earthquake ( $M^w$  9.4, Valdivia earthquake in 1960) ever recorded in the human

history (Lomnitz, 2004). Despite this relatively high convergence rate, no destructive earthquakes have been historically documented in upper plate faults. Therefore there is a widespread belief among scientists that plate interaction is mainly elastic and driven fundamentally by sudden slip of the megathrust and no upper plate reactivation is driven by plate interaction at this continental margin. However, a close view of the continental margin overlying the seismogenic zone shows a strongly segmented topography controlled by large upper plate faults.

A suite of trench parallel faults located along the Coastal Cordillera forms the AFS. It is possible to identify the system in satellite images from 21°S to 29°S. The AFS formed during the Early Cretaceous as a trench linked strike slip fault system (Scheuber and Andriessen, 1990). During the Neogene the AFS reactivated as a normal fault producing the strong-segmented topography of the Coastal Cordillera in northern Chile (Allmendinger and Gonzalez, 2011).

## THE SALAR DEL CARMEN FAULT

The fault is highly segmented and located along the eastern side of the Coastal Cordillera (Fig. 1). Fault activity has constructed an eastward facing scarp with an average height of  $\sim 5$  m. A detailed inspection of the topography of the scarp indicates that it was formed by at least two or three events. Trenches excavated in the northernmost segment expose two colluvial wedges which grade laterally into slope wash deposits (Fig. 3). The oldest colluvial wedge and hillslope deposits are deformed and rotated by normal faults, whereas the youngest colluvial and hillslope deposits show minor effects by faulting. An OSL sample from the oldest slope wash deposit has a burial age of  $4.91 \pm 0.32$  ka, indicating that the colluvial wedge formed shortly before this age. Two OSL ages of  $2.65 \pm 0.17$  ka and  $2.03 \pm 0.23$  ka, with a mean of  $2.34 \pm 0.12$  ka, from the base of the youngest colluvial wedge put constraints for the youngest event in this fault. Undeformed hillslope deposits have OSL burial ages of  $0.40 \pm 0.03$  ka and  $0.46 \pm 0.08$  ka, respectively. Across this trench we determined a net fault slip of 4.2 m since deposition of oldest colluvial wedge/wash slope deposit. Using the age of this sediment a minimum slip rate of  $0.37 \pm 0.07$  m/ka can be estimated.

We measured a cumulative vertical slip of  $4.2 \pm 0.1$  m since deposition of the lower colluvial wedge. This cumulative vertical slip is the same order of magnitude of the fault scarp height itself, suggesting that the scarp was formed by two faulting events. Following the standard convention that colluvial wedge thickness is equivalent to roughly the half of the average normal fault displacement (McCalping, 1996) and by using the relationship between average displacement and moment magnitude (Wells and Coopersmith, 1994), we estimated the paleo-earthquake magnitude in the SCF. The average thickness of the colluvial wedges in the trenches is  $1.1 \pm 0.45$  m. By using this average thickness



we estimated an average coseismic vertical slip of  $2.2 \pm 0.9$  m inferring that the magnitude of paleo-earthquakes in the SCF were in the order of  $M_w 7.1 \pm 0.2$ .

The data demonstrate that there is a significant active faulting expressed as reactivation of some branches of the AFS directly overlying the coupling zone of the Nazca and South American plates.

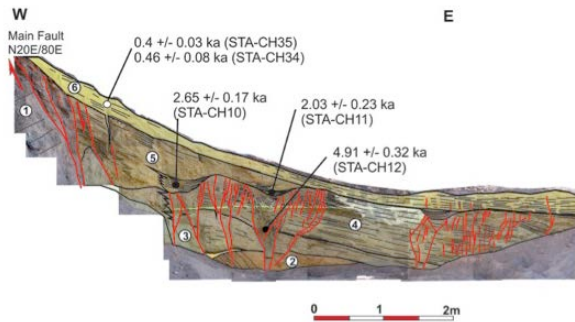


Figure 3. Photo-mosaic and stratigraphic log of trench dug in the Salar del Carmen Fault. Black dots location of OSL samples, white dots approximately location of OSL samples from neighbour trenches. Red lines represent faults. Black lines show bedding in the hillslope and colluvial wedge deposits.

### THE MITITUS FAULT

Trench descriptions along this fault are currently ongoing and OSL dating of colluvial wedges are still in progress. The associated fault scarp is also an eastward facing scarp formed in alluvial fan deposits. The surface offset measured along 10 transects crossing the fault scarp has an average of 2.84 m. One of the most relevant aspects documented in the trenches is the occurrence of a west vergence reverse fault, which is cut by a  $75^\circ$  east dipping normal fault that forms the fault scarp. The reverse fault folded and thrust an old gypsum soil formed on top of alluvial fan deposits over Mesozoic volcanic rocks. The stratigraphy of the trenches allows identifying two faulting events related to normal fault-scarp formation. These events are deduced from the occurrence of two colluvial wedge deposited on top of the intense broken gypsum soil. Using the 1.1 m average thickness of the displaced colluvial wedge we infer a paleo-earthquake of  $M_w 7.0$  for the first normal event registered in the trenches.

The detailed mapping of the trench walls in the Salar del Carmen and Mititus faults reveals that normal faulting is the dominant mechanism of fault scarp formation. Reverse faulting documented in previous studies (Allmendinger and González, 2010) is also expressed in the trenches dug in the Mititus Fault. The geometry of the reverse fault displacement showing “young unit thrust on older units” indicates that reverse faulting resulted from the reactivation of an older normal fault. Then, it can be interpreted that the change from normal faulting to reverse faulting represents a major change in the kinematic regime of the Mititus Fault. Because the fold exposed in the trenches of the Mititus Fault is cut by the youngest normal faulting event we suggest that normal faulting and reverse faulting have alternated through time. Nevertheless, it should be noted that the dominant process in the topographic configuration is normal faulting.

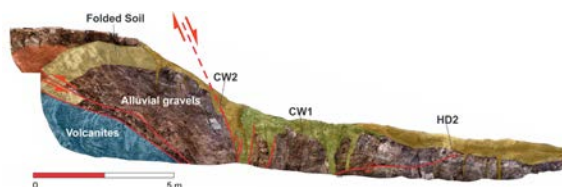


Figure 4. Photo-mosaic and stratigraphic log of trench dug in the Mititus Fault. Red lines represent faults. CW2= Young Colluvial wedge, CW1= Old Colluvial wedge. HD2= Young hillslope deposit (Wash slope deposit).

Systematic trench mapping shows that upper plate fault activity has been seismogenic. It is deduced from the occurrence of colluvial wedges. The estimation of Paleo-earthquake magnitudes shows the occurrence of  $\sim M_w 7.0$  event(s) in the main branches of the AFS. OSL data indicate that fault reactivation occurred during the Holocene. The occurrence of two colluvial wedges in the AFS put constraints on the number of events that formed the fault scarp preserved in alluvial sediments. The temporal distribution of ages in individual faults shows that the recurrence of  $M_w 7.0$  earthquake(s) that are capable to rupture the topographic surface, is in the order of thousands of years. This can be clearly demonstrated for the Salar del Carmen Fault, where deposition of the two colluvial wedges is separated for a minimum of 2.06 ka. The 0.37 m/ka slip rate and the average coseismic displacement also imply a recurrence of thousand years for this fault.

In northern Chile  $M_w > 7.0$  subduction earthquakes have a recurrence of approximately 50 years (Comte et al., 1988) and  $M_w 8.8$  subduction earthquakes have a return period of 128 years (Comte y Pardo, 1999). Firstly, it may be concluded by comparison with the return period of paleo-earthquakes in the AFS that intermediate to large subduction earthquakes are not synchronized in occurrence with the  $M_w 7.0$  earthquakes documented in the AFS. Secondly, over the time scale of decades, upper plate faulting does not contribute significantly to the bulk deformation in the margin, but it is relevant at the time scale of thousands of years reflecting the long-term geological component of upper faulting.

### DISCUSSIONS

How normal faulting and reverse faulting alternate through the time is still not very clear. Normal



## INQUA Focus Group on Paleoseismology and Active Tectonics



paleoseismicity.org

faulting seems to be related to upper plate relaxation following major subduction earthquakes (Cortes et al., 2013). Reverse faulting could result of unusual long periods of interseismic phase of subduction earthquake cycle. During this period compressive stresses emerging from plate interaction could be effectively transmitted to the upper plate and thus cause compression near the topographic surface.

**Acknowledgements:** The authors thank to CONICYT for the grants FONDECYT 1140846 and FONDAPE 15110017 (Excellence Center CIGIDEN).

### References

- Allmendinger, R., and González, G., (2010). Invited Paper: Neogene to Quaternary Tectonics of the Coastal Cordillera, northern Chile. *Tectonophysics*, 2010, v. 495, p. 93-110.
- Angermann, D., Klotz, J., and Reigber, C., 1999, Space-geodetic estimation of the Nazca-South America Euler Vector. *Earth and Planetary Science Letters*, v. 171, p. 329-334.
- Armijo, R., and Thiele, R., (1990). Active faulting in northern Chile: ramp stacking and lateral decoupling along a subduction plate boundary? *Earth and Planetary Science Letter*, v. 98, 40-61.
- Arnold, L. J., Roberts, R. G., Galbraith, R. F. & DeLong, S. B. A (2009). Revised burial dose estimation procedure for optical dating of young and modern-age sediments. *Quaternary Geochronology* 4, 306-325, doi:10.1016/j.quageo.2009.02.017
- Comte, D. Eissenberg, A. and Pardo, M. (1988). Sismicidad y Riesgo Sísmico en el margen occidental de Sud-América entre los 16 y 22° Sur. Tomo II F 227-F246. Primeras Jornadas de Geofísica, V Congreso Geológico Chileno Santiago 8-12 de Agosto de 1988.
- Comte, D., and Pardo, M., 1991, Reappraisal of great historical earthquakes in the northern Chile and southern Peru seismic gaps. *Natural Hazards*, v. 4, p. 23-44.
- Cortés-Aranda, J. González, G., Rémy, D., Martinod, J. (2015). Normal upper plate fault reactivation in northern Chile and the subduction earthquake cycle: From geological observations and static Coulomb Failure Stress (CFS) change. *Tectonophysics* 639, 118-131.
- Delouis, B., Philip, H., Dorbath, L., Cisternas, A., (1998). Recent crustal deformation in the Antofagasta region (northern Chile) and the subduction process. *Geophysical Journal International*, v. 132, p. 302-338.
- González, G. & Carrizo D. (2003). Segmentación, cinemática y cronología relativa de la deformación tardía de la Falla Salar del Carmen, Sistema de Fallas de Atacama, Cordillera de la Costa de Antofagasta. *Revista Geológica de Chile*. Vol. 30, N°2, 223-244.
- González, G. Dunai, T, Carrizo, D. and Allmendinger, R. (2006). Young displacements on the Atacama Fault System, northern Chile from field observations and cosmogenic <sup>21</sup>Ne concentrations. *Tectonics* 25 (3), TC3006, doi:10.1029/2005TC001846.
- Lomnitz, C. 2004, Major Earthquakes of Chile: A Historical Survey, 1535-1960. *Seismological Research Letters*, v. 75 , 368-378.
- Murray, A. S. & Wintle, A. G. (2000), Luminescence dating of quartz using an improved single-aliquot regenerative-dose protocol. *Radiation Measurements* 32, 57-73, doi:10.1016/s1350-4487(99)00253-x (2000).
- McCalpin, J. (1996), *Paleoseismology*, 588 pp., Academic, San Diego, Calif.
- Vargas, G.; Palacios, C.; Reich, M.; Luo, S.; Shen, Ch. González, G. Wu, Ch. 2011, U-series dating of co-seismic gypsum and submarine paleoseismology of active faults (23°S). *Tectonophysics*. Volume 497, Issues 1-4, 2 January 2011, Pages 34-44.
- Wells, D. L., and Coppersmith, K. J., New empirical relationships among magnitude, rupture length, rupture width, rupture area, and surface displacement, *Bull. Seismol. Soc. Am.*, 84, 974-1002 (1994).
- Scheuber, E. & Andriessen, P.A.M. (1990): The kinematic and geodynamic significance of the Atacama Fault Zone, northern Chile.- *J. Struct. Geol.*, 12: 243-257.



## Accelerated upper crustal uplift since MIS3 at the southern edge of the northern Chile megathrust seismic gap

José González-Alfaro (1), Gabriel Vargas (1), Gabriel González (2), Luc Ortlieb (3)

(1) Departamento de Geología, Facultad de Ciencias Físicas y Matemáticas, Universidad de Chile, Plaza Ercilla 803, Santiago, Chile. Email: josgonal@uchile.cl

(2) Departamento de Ciencias Geológicas, National Research Center for Integrated Natural Disaster Management (CIGIDEN), Universidad Católica del Norte, Avenida Angamos 0610, Antofagasta, Chile

(3) LOCEAN, URM 7159 (IRD, CNRS, UPMC, MNHN), Institute Pierre Simon Laplace, Bondy, France

**Abstract:** *The Mejillones Peninsula – located at the continental active margin of the Central Andes, northern Chile – is a first order geomorphic feature characterized by uplifted Pleistocene marine terraces and beach-ridges. Based on radiocarbon and Optically Stimulated Luminescence results, we dated marine deposits located up to 21 m a.s.l. as 31 – 46 ka, which corresponds to the Marine Isotope Stage 3, globally defined between 60 and 25 ka. Consequently, for the last 40 ka we estimate an uplift rate of  $2.1 \pm 0.7$  m/ka, evidencing an acceleration of the tectonic uplift of this peninsula if we consider previous estimates of 0.5 m/ka for the last 400 ka. We propose that this acceleration resulted from coseismic vertical deformation and rupture propagation which breaks beneath the northern Mejillones Peninsula along the subduction zone during megathrust earthquakes. Each earthquake would result in large permanent uplift unlike other coastal areas since the late Pleistocene-Holocene.*

**Key words:** *Marine isotope stage 3 (MIS 3), uplift, coseismic deformation, paleoseismology*

### INTRODUCTION

The Mejillones Peninsula is a first order characteristic feature in the Central Andes forearc of northern Chile, which is part of the continental shelf that has been uplifted since  $\sim 3$  Ma (Marquardt, 2005), due to crustal deformation linked to subduction of the Nazca plate beneath the South American plate. Geologically, Mejillones Peninsula is formed by Paleozoic-Triassic metamorphic rocks, Jurassic-Cretacic igneous intrusive and late Neogen-Pleistocene semi-consolidated sediments (Cortés et al., 2007). Geomorphologically, the peninsula displays marine terraces, paleo-coastal ridges, escarpments and coastal cliffs. From a morpho-structural point of view, it comprises horst and half-grabens linked to active normal faults with subaerial and submarine expression (Vargas et al., 2011a; Cortés et al., 2012), as well as long-wavelength folds recognized in the submarine substratum and superficial tensional cracks. Moreover, geomorphological analyses have determined that the Mejillones Peninsula records evidence for uplift at relatively high rates (Ortlieb et al., 1996a; Marquardt, 2005; Victor et al., 2011). In addition, it has been postulated that Mejillones Peninsula behaves as a tectonic boundary for seismic megathrust rupture propagation for earthquakes that nucleates both from north and south of it (Victor et al., 2011). The last great subduction earthquake  $\sim M_w$  8.8 was in 1877 and the rupture length could have spanned about at least 300 km between Iquique and Mejillones city (Metois et al., 2013).

Through geomorphological and paleontological analysis, previous works have correlated the distribution of paleo beach-ridges and paleo coastal escarpments, located in Pampa Mejillones and Pampa Aeropuerto, with the last marine isotope stages (MISs), corresponding to the time span encompassing from Middle to late Pleistocene. From these correlations uplift rates for the last 400 ka have been estimated, which vary between 0.2 – 0.5 m/ka. These uplift rates are high if we consider that the coastal northern Chile is characterized by an uplift rate about 0.1 – 0.2 m/ka (Ortlieb et al., 1996a; Marquardt et al., 2005; Victor et al., 2011). Nevertheless, the work we present here leads us to rethink the chronostratigraphy associated with the beach ridges and their previously-assumed ages. Particularly, we report for the first time consistent MIS 3 ages, globally defined between 60 – 25 ka and characterized by with few outcrops above the current sea level (Siddall et al., 2008). In addition, we discuss the linking between the new uplift rate estimates and the occurrence of megathrust earthquakes triggered at the southern edge of the northern Chile seismic gap.

### METHODS

The study area extends from the northern part of the Mejillones Peninsula, specifically the littoral coast that includes the coastal escarpment of the Mejillones Bay, between the Punta Chacaya and Rinconada Beach (Figure 1).



INQUA Focus Group on Paleoseismology and Active Tectonics



paleoseismicity.org

To quantify the deformation of Pampa Mejillones linked to both Mejillones Peninsula uplifting and Mejillones Fault Quaternary activity, we carried out measurements on the littoral zone corresponding to trigonometric profiles transverse to the Mejillones Bay's coastal escarpment, between Punta Chacaya and Rinconada Beach (Figure 1), including a sea level average determination considering tidal measurements and GPS positioning observations. The profiles located on Mejillones Bay's coastal cliff (Figure 1) show a height scarp that decreases from east to west, from 22 to 9 m a.s.l., respectively.

abrasion terrace carved on semi-consolidated silt corresponding to the Neogene La Portada Formation. From a tectonic point of view, this bed is situated at 21 and 1 m a.s.l. and has been displaced vertically 20 m by the Mejillones Fault, hence the samples were taken from both the hanging wall and the foot wall. The shell samples were dated through radiocarbon method which yielded consistent ages between 31 – 47 ka, with a high frequency concentration ~38 – 40 ka. All the radiocarbon conventional ages were calibrated using the marine Delta R (Vargas et al., 2007; Ortlieb et al., 2011). Moreover, OSL results from sediment sand samples from the stratigraphic sequence overlying the conglomerate with abundant shells yielded an age of 38 ka age. Most of the shell and sediment samples were taken from the stratigraphic sequence that is located on the coastal escarpment of the Mejillones Bay, immediately eastward of the Mejillones Fault (Figure 2).

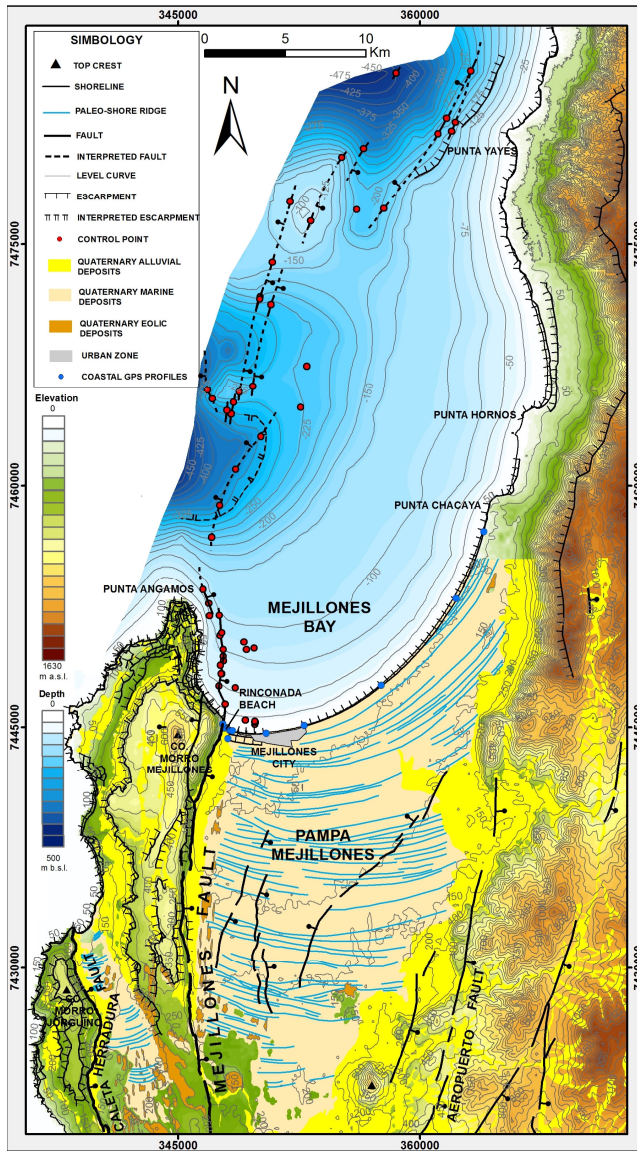


Fig. 1: Northern Mejillones Peninsula, showing geomorphological and structural features present in the study area.

We observed marine sedimentary layers with abundant mollusc shells in Rinconada Beach (Figure 2), from a semi-consolidated conglomerate overlying in angular unconformity a marine

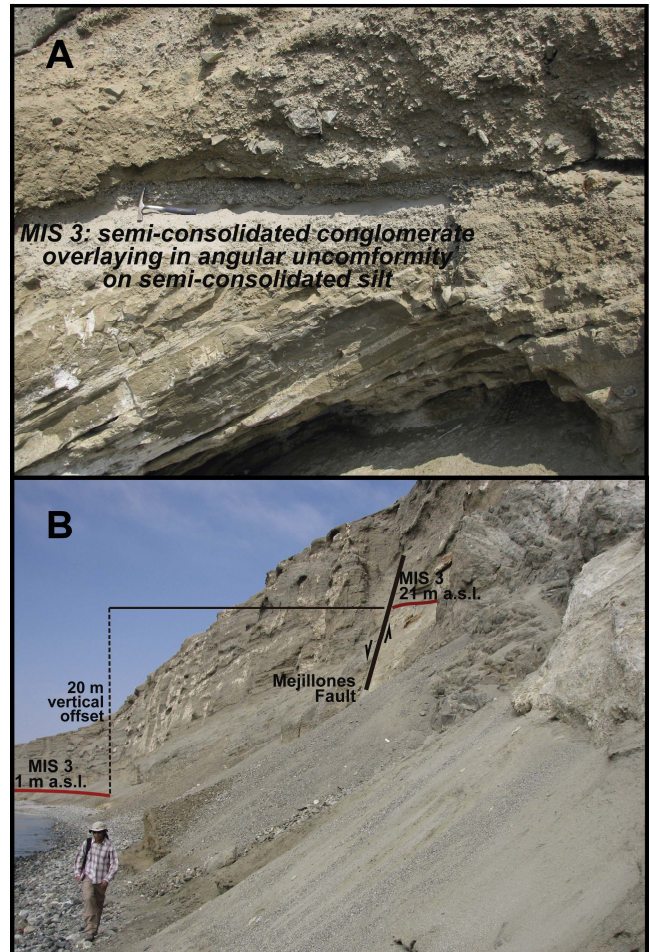


Fig. 2: A) Bioclastic conglomerate corresponding to MIS 3, overlaying Neogene marine silts from La Portada Formation. B) MIS3 deposits offset by the Mejillones Fault.

In order to interpret the sedimentary environments of the deposits outcrops arranged in the free face of the coastal



## INQUA Focus Group on Paleoseismology and Active Tectonics



paleoseismicity.org

escarpment on Rinconada Beach, we dug pits to expose the facies of the stratigraphic sequence. The marine fossil fauna and sedimentary facies indicate that the marine sequence was deposited near sea level during MIS 3. In the higher part of the stratigraphic column a marine to continental transition can be deduced from alluvial sediments overlying supra-littoral sands with remains of shells. The latter is overlain by 3 m of alluvial fan deposits that coarsen upward.

In the western Mejillones Peninsula foot wall block (Figure 1), we also identified MIS 3 deposits. These deposits comprise a conglomerate and a sandy layer with shells from which we obtained a radiocarbon age  $\sim 37$  ka. Deposits of MIS 3 age are located over a marine escarpment of 12.5 m a.s.l. that corresponds to an uplifted marine terrace strath. At the foot of this marine escarpment we found an uplifted marine deposit constituted by boulders, sand, shells, seaweed and archeological remains. This is located at 4.5 m a.s.l. and radiocarbon analyses yielded a calibrated age between CE 1665 – 1949. Slightly further below of these deposits, we found, close to the present shoreline, an uplifted marine terrace located 1.5 m a.s.l. We interpret that both the marine deposit and the terrace are associated and represent the coastline previous to the last large 1877  $\sim M_w$  8.8 megathrust event.

To achieve the best representation of the sea level during the MIS 3, we developed a sea level compilation based on Siddall et al. (2008) and others authors as Cabioch & Ayliffe (2001), with emphasis in the sea level curve of Arz et al. (2007), mostly based on a water input from the ice sheet retreat at the Northern Hemisphere. Thus, we considered a range of 42 – 96 m b.s.l. for  $\sim 40$  ka. Taking this, we estimated an uplift rate of 1.6 – 2.9 m/ka from the MIS 3 deposits that lie 21 m a.s.l. on the Mejillones Fault foot wall, and 1.2 – 2.6 m/ka from deposits in the Mejillones Fault hanging wall or  $2.1 \pm 0.7$  m/ka for the northern Mejillones Peninsula in the last 40 ka. These new uplift rates are one order of magnitude higher than previous estimations (Ortlieb et al 1996, Marquardt et al 2005, Victor et al, 2011).

### DISCUSSION

Deposits of MIS 3 are present along the coastal escarpment of Rinconada Beach, with 1 – 7m thickness, either in the hanging wall and foot wall of the Mejillones Fault. Southward of the Mejillones Peninsula MIS 3 outcrops, may not be subaerially exposed because the northern part of this peninsula shows higher uplift rates than the southern part (Ortlieb et al., 1996; Victor et al., 2011). Most workers agree that higher slip rates are located near Morro Mejillones horst (Ortlieb et al., 1996a; Marquardt, 2005, Victor et al, 2011), which is located immediately to the west of the MIS 3 outcrops. Moreover, through subbottom profiles analysis (Figure 1), González et al. (2012) determined a syncline fold characterized by wide wavelength, which is present in the whole Mejillones Bay and that would transfer strain from the Mejillones Fault through the hanging wall. This fold has a NS axis with an asymmetrical wavelength from south to north, with a maximum wavelength

spreading beneath the coastal edge of the Mejillones Bay near to Mejillones city. The MIS 3 deposits located on Punta Chacaya (20 m a.s.l.), on the hanging wall block, can be correlated with the MIS 3 deposits located on Rinconada beach (21 m a.s.l.), on the foot wall block (Figure 1). Thus, the differences in MIS 3 heights between the hanging wall and the foot wall blocks resulted from the slip along the Mejillones Fault, which is a structure that accommodates localized uplift at the northern Mejillones Peninsula, with major fault slip increasing from south to north, as is evidenced from geomorphologic and seismostratigraphic observations (Cortés et al., 2012, Victor et al., 2011, Vargas et al., 2011a), and by geomorphological coastal evidence like decreasing elevation of the coastal escarpment of the Mejillones Bay from east to west, from 20 to 9 m a.s.l., respectively (Chacaya Beach-Rinconada Beach) (Figure 2).

The uplift rate estimated since MIS 3 at northern Mejillones Peninsula is similar to those reported around the Circum-Pacific region like Huon Peninsula, New Zealand, Vanuatu, Panama and California (Siddall et al., 2008). Also it is similar to the uplift rates estimated for Santa María Island in Central Chile, where uplift rates of  $1.5 \pm 0.3$  m/ka since the MIS 3 have been reported (Jara-Muñoz et al., 2015).

Uplift along the Chilean coastal edge has been observed as a consequence of elastic rebound from subduction megathrust earthquakes (Delouis et al., 1998; Vargas et al., 2011b; Wesson et al., 2015). Previous works determined that during the 1995  $M_w$  8.1 Antofagasta earthquake, the coastal edge of the southern part of the Mejillones Peninsula had a coseismic uplift in the range of 0.15 – 0.8m (Ruegg et al., 1996; Ortlieb et al., 1996b; Delouis et al., 1998). The 2007  $M_w$  7.7 Tocopilla earthquake produced a coseismic uplift about 0.35 m in Mejillones city (Schuur et al., 2013), which has not been recovered in the last 8 years. From these examples it is possible to assume that the Mejillones Peninsula uplift represents permanent vertical deformation associated to megathrust earthquakes. This implies that to uplift the northern Mejillones Peninsula requires megathrust earthquakes with seismic rupture propagation beneath the peninsula, like the 2007 Tocopilla earthquake (Fuenzalida et al., 2013).

The 2010  $M_w$  8.8 Maule earthquake, that hit the central part of Chile, uplifted the coast around  $1.3 \pm 0.2$  –  $2.6 \pm 0.6$  m, with an average of  $1.95 \pm 0.4$  m in Arauco Peninsula, located at the southern edge of the seismic rupture (Vargas et al., 2011b). Wesson et al. (2015) using geomorphological and bathymetric data from Santa María Island (located immediately to the north of Arauco Peninsula) estimated an interseismic subsidence rate of 10 mm/yr from the 1837  $\sim M_w$  8.8 to the 2010  $M_w$  8.8 Maule earthquake, which represents a complete seismic cycle. This implies that each mega-earthquake result in permanent uplift. The strong evidence collected on Arauco Peninsula suggests that it would act as a seismic barrier for ruptures that propagate from the south (1960  $M_w$  9.5 Valdivia Earthquake) and the north (1837 and 2010  $M_w$  8.8 Maule earthquake) (Jara-Muñoz et al., 2015). The seismotectonic, geomorphological and geological



## INQUA Focus Group on Paleoseismology and Active Tectonics



paleoseismicity.org

settings that the Arauco Peninsula shares with the Mejillones Peninsula are very similar for the late Pleistocene-holocene. Therefore, we propose that the mega-earthquakes that hit the Arauco Peninsula with permanent deformation effects are comparable with the 1877  $\sim M_w$  8.8 earthquake that ruptured beneath the northern part of the Mejillones Peninsula (Vargas et al., 2011b; Metois et al., 2013).

The long-term uplift that has affected the Mejillones Peninsula, since  $\sim 40$  ka, has been  $94 \pm 30$  m. The mean issue is discriminate the uplift contribution for both the 2007  $M_w$  7.7 Tocopilla and the 1877  $\sim M_w$  8.8 earthquakes. The first had a deeper seismic rupture ( $<40$  km depth) (Schuur et al., 2012), and the latter was a tsunamigenic earthquake (Vargas et al., 2005 and 2011b). Considering the 0.35 m of the 2007 Tocopilla earthquake coseismic uplift, the long-term uplift in Mejillones Peninsula could be easily explained by this kind of deep earthquakes, even more if we consider that the recurrence of a  $M_w$  7.7 is lower than a  $M_w$  8.8 earthquake taking a simple Gutenberg-Richter's law approach. This implies that together the 1877 and 2007-type earthquakes would contribute more than the  $94 \pm 30$  m estimated for the last  $\sim 40$  ka. The interseismic elastic subsidence rate for the Mejillones Peninsula would be of the order calculated by Wesson et al. (2015) for the 2010 Maule earthquake, in Santa María Island, and could even be lower.

### CONCLUSION

New observations of MIS 3 age deposits along the Mejillones Peninsula and their implications for uplift rates over the last 40 ka might require rethinking MIS assignments for the last 400 ka. Aside from these implications, the highest uplift rate for the last 40 ka indicates a non-constant uplift rate for the entire Mejillones Peninsula block and an accelerating uplift process during the late-Pleistocene associated with subduction megathrusts. This could suggest that the recurrence of subduction earthquakes might be non-linear in the long-term and that it has accelerated at least since 40 ka.

**Acknowledgements:** This work was funded through the financial contributions made by the FONDECYT project N° 1140846. The work is part of a doctoral thesis, which has been supported through the national doctoral grant provided by CONICYT.

### References

- Cortés, J., G. González, S. Binnie, R. Ruth, S. Freeman & G. Vargas, (2012). Paleoseismology of the Mejillones Fault, northern Chile: insights from cosmogenic  $^{10}\text{Be}$  and optically stimulated luminescence determinations. *Tectonics* 31, 21 p.
- Cabioch, G., Ayliffe, L.K. (2001). Raised coral terraces at Malakula, Vanuatu, Southwest Pacific, indicate high sea level during marine isotope stage 3. *Quaternary Research* 56, 357-365.
- Cortés, J., C. Marquardt, G. González, H.-G. Wilke & N. Marinovic, (2007). Cartas Mejillones y Península de Mejillones. Región de Antofagasta. Servicio Nacional de Geología y Minería, escala 1:100.000, N° 103-104, 58 p.
- Delouis, B., H. Philip, L. Dorbath & A. Cisternas, (1998). Recent crustal deformation in the Antofagasta region and the subduction process. *Geophysics Journal International* 132, 302-338.
- Fuenzalida, A., B. Schuur, M. Lancieri, M. Sobiesiak & R. Madariaga, (2013). High-resolution relocation and mechanism of aftershocks of the 2007 Tocopilla (Chile) earthquake. *Geophysical Journal International* 194 (2), 1216-1228.
- González, J., G. González & G. Vargas, (2012). Cartografía de fallas submarinas activas en la Península de Mejillones. In Congreso Geológico Chileno 13, Sesión T2, Universidad Católica del Norte, Antofagasta, 5-9 august.
- Jara-Muñoz, J., Melnick, D. (2015). Unraveling sea-level variations and tectonic uplift in wave-built marine terraces, Santa María island, Chile. *Quaternary Research* 83, 216-228.
- Jara-Muñoz, J., Melnick, D., Brill, D., Strecker, M.R., (2015). Segmentation of the 2010 Maule Chile earthquake rupture from a joint analysis of uplifted marine terraces and seismic-cycle deformation patterns. *Quaternary Science Reviews* 113, 171-192.
- Metois, M., A. Socquet, C. Vigny, D. Carrizo, S. Peyrat, A. Delorme, E. Maureira, M. Valderas-Bermejo & I. Ortega, (2013). *Geophysics Journal International* 194 (3), 1283-1294.
- Marquardt, C. 2005. Deformations néogènes le long de la côte nord du Chili ( $23^\circ$ - $27^\circ$  S), avant-arc des Andes centrales. Thèse pour obtenir le grade de Docteur (Unpublished), Université Toulouse III.
- Ortlieb, L., C. Zazo, J. Goy, C. Hillaire-Marcel, B. Ghaleb & L. Cournoyer, (1996a). Coastal deformation and sea-level changes in the northern Chile subduction area ( $23^\circ\text{S}$ ) during the last 330 ky. *Quaternary Science Reviews* 15, 819-831.
- Ortlieb, L., S. Barrientos & N. Guzmán, (1996b). Coseismic coastal uplift and coralline algae record in northern Chile: the 1995 Antofagasta earthquake case. *Quaternary Science Reviews* 15: 949-960.
- Ruegg, J., J. Campos, R. Armijo, S. Barrientos, P. Briole, R. Thiele, M. Arancibia, J. Cañuta, T. Duquesnoy, M. Chang, D. Lazo, H. Lyon-Caen, L. Ortlieb, J.C. Rossignol & L. Serrurier, (1998). The  $M_w = 8.1$  Antofagasta earthquake of July 30, 1995: First results from teleseismic and geodetic data. *Geophysical Research Letters* 23 (9), 917-920.
- Siddall, M., E.J. Rohling, W.G. Thompson & C. Waelbroeck, (2008). Marine isotope stage 3 sea level fluctuations: data synthesis and new outlook. *Reviews of Geophysics* 46 8755-1209. *Tectonophysics* 497: 34-44.
- Schurr, B., G. Asch, M. Rosenau, R. Wang, O. Oncken, S. Barrientos, P. Salazar & J.P. Vilotte, (2012). The 2007  $M_w$  7.7 Tocopilla northern Chile earthquake sequence: Implications for along-strike and down-dip rupture segmentation and megathrust frictional behavior. *J. Geophys. Res.*, 117.
- Vargas, G., L. Ortlieb, E. Chapron, J. Valdés & C. Marquardt, (2005). Paleoseismic inferences from a high-resolution marine sedimentary record in northern Chile ( $23^\circ\text{S}$ ). *Tectonophysics* 399, 381-398.
- Vargas, G., M. Fariás, C. Sebastien, A. Tassara, B. Stéphane & D. Melnick, (2011b). Coastal uplift and tsunami effects associated to the 2010  $M_w$  8.8 earthquake in Central Chile.
- Vargas, G., C. Palacios, M. Reich, S. Luo, C. Shen, G. González & Y. Wu, (2011a). U-series dating of co-seismic gypsum and submarine paleoseismology of active faults in Northern Chile ( $23^\circ\text{S}$ ). *Andean Geology* 38 (1), 219-238.
- Victor, P., M. Sobiesiak, J. Glodny, S.N. Nielsen & O. Oncken, (2011). Long-term persistence of subduction earthquake segment boundaries: evidence from Mejillones Peninsula, northern Chile. *Journal of Geophysical Research* 116.
- Wesson, R., M. Melnick, M. Cisternas, M. Moreno & L. Ely, (2015). Vertical deformation through a complete seismic cycle at Isla Santa María, Chile. *Nature Geoscience* 8, 547-551.



## On Linkage between Present Geomorphology and Substrate Geology in a Tectonically Active Terrain along the North Eastern Himalayan Foothills

Chandreyee Chakrabarti Goswami (1), Shayan Sarkar (1) B C Poddar (1),

1 Department of Geology, University of Calcutta, 35 Ballygunge Circular Road, Kolkata 700019, India  
2. BE-367, Salt Lake City Kolkata 700064, India. \*Corresponding Author, Email: chandreyee.goswami75@gmail.com

**Abstract:** The area around Itanagar-Naharlagun Capital Complex (INCC) of Arunachal Pradesh, India, anchored in neotectonically active foothills of Eastern Himalayas has been studied. Our objective is to unravel the hidden and subtle linkages between geological nuances and present geomorphology. From the analysis of satellite imageries, Digital Elevation Models (DEMs) and extensive field study it reveals that the terrain is underlain by a system of thrust-controlled asymmetric folds involving incipiently lithified fluvial sediments of unclassified late Neogene Siwaliks. These are unconformably overlain by the Quaternary sequence of unlithified and poorly sorted sediments deposited by rivers and slope processes on multiple strath terraces and extant flood plains. The Siwaliks and Quaternaries both are affected by both the ENE-WSW trending regional Himalayan thrusts as well as prominent transverse faults making the area a highly landslide prone zone. The rapid and haphazard urban growth superimposed on this natural matrix has made this area extremely vulnerable to natural hazard.

Keywords: Eastern Himalayan foothills, Neotectonics, thrusts, urbanisation.

### Introduction

The collision between the Indian and Eurasian plates leads to the formation of the great Himalayan range which trends NW-SE in the westernmost part, E-W in the central part and NE-SW in the easternmost part. The Arunachal Himalayas is part of the eastern Himalayas and it falls under the Seismic zone (IV). Itanagar-Naharlagun Capital Complex (INCC) is a growing city developing as the capital of the Arunachal Pradesh within the Siwalik Hills and its foothills (Fig. 1).

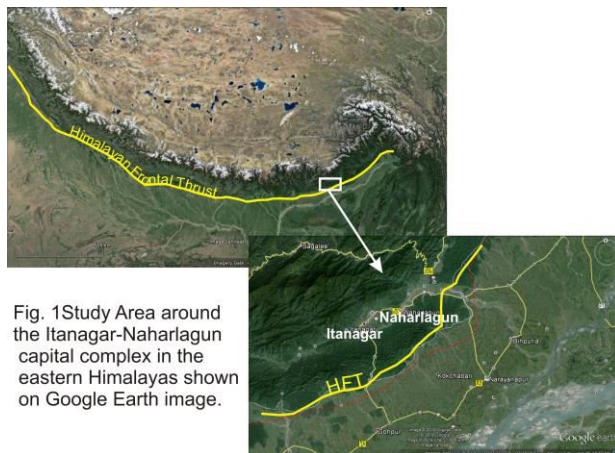


Fig. 1 Study Area around the Itanagar-Naharlagun capital complex in the eastern Himalayas shown on Google Earth image.

The area is near the edge of the meizoseismal region of the 1950 Assam earthquake and the displacement within the Quaternary boulder beds dated after 1270 AD. Kumar et al. 2010 speculates the displacement records the 1950  $M_w$  8.4 Assam earthquake. The Arunachal Himalayan geology has been studied by many workers but the Itanagar area lacks detailed geological studies. The area is anchored within the Mio-Pliocene sediments

comprising Dafla, Subansiri and Kimin formations of Siwalik group and four formations within the Quaternary sediments namely Itanagar Formation, Banderdewa Formation, Sonajuli Formation and the Pachin Formation (Singh T, 2007). From the magnetostratigraphic study of the adjacent Kameng basin the age of the Siwalik sequence is 14.6 Ma to 1.8 Ma in the Eastern Himalayan portion (Chirouze et al., 2012). Many tectonic signatures within the Siwalik sediments as well as Quaternary deposits have been reported. In this paper we have attempted to document and analyse the geomorphic framework and geology of the substrate with particular reference to interaction of episodic deep-seated tectonic processes, surficial, fluvial and slope process activities during the Neogene and Quaternary and continue in the Holocene-Anthropocene. The tectonic activity associated with Himalayan Thrust system and associated transverse normal and strike slip faults have made this area highly landslide prone. In addition to tectonic disturbances the rapid growth of population in this area causes increase in pressure on the natural resources and the consequent danger on environmental degradation. Specifically, this increase in population pressure puts a greater number of people at risk from a natural calamity. The increasing population pressure is leading to settlement expansion along with agricultural activities on the steep sided slopes mostly along the road highways through earth cutting on the hill top causing frequent landslides when it rains. The unplanned growth of settlements on hill faces, cutting and levelling of hill slopes, degradation of natural drainage system, cutting and felling of trees, especially along hill faces and increased run off due to increase in impervious areas are the main issues



and challenges that has triggered more landslide in the study area (Singh and Devi, 2006, Rupa, 2015). We have analysed the Satellite images, DEMs along with field work to understand the relationship of present day Geomorphology with the geology of the area. We have prepared the preliminary Geological-geomorphological map from all the primary and secondary data (Fig. 2).

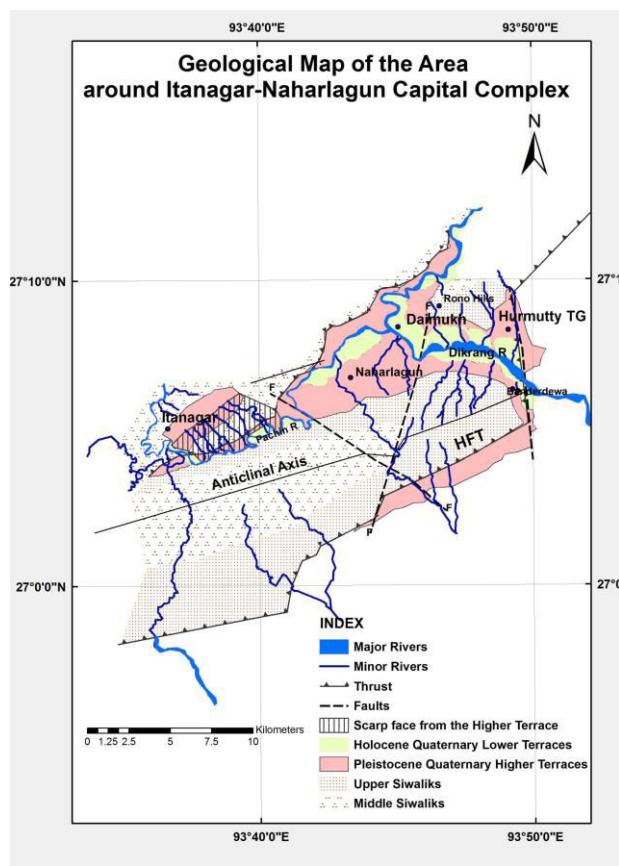


Fig. 2 Geological Map of the Study Area

### Discussion

The most important geomorphic features of this area are two river valleys: the Dikrang River valley trending NW-SE and the Pachin River valley trending E-W. The Dikrang River is a major river originating in the Lesser Himalayan crystalline region NE of the study area. It takes a sharp westerly bend and then from the central part of the area it flows south easterly to meet the Brahmaputra. The Pachin River originates in the NW part of the area from the Siwalik Hills and flows easterly to meet the Dikrang River near Daimukh (Fig. 2).

The area is characterised by ENE-WSW trending ridges and valleys. The altitude varies from ~50m in Brahmaputra plane in south to 450m in north within the Siwalik Hills. The height of the Siwalik ridges increases from the 250m in the south with

successive increase in height to 450m in the north. The southerly sloping flanks of the hills are showing more erosional features than the northern flanks of the hills.

The rocks of Subansiri formation of Middle Siwaliks characterised by mainly thick bedded sand and pepper sandstones with occasional coal blocks are folded into a slightly asymmetric open fold with nearly ENE-WSW trending fold axis. The northern limb dips 30-35° towards NW and the southern limb dips 35-40° towards SE. The sandstones are cross bedded with the average current direction towards SE and with convolute bedding indicating syndepositional deformation or seismites (Fig. 3).



Fig. 3 Convolute laminations within the Middle Siwalik thick sand beds.

The overlying Kimin Formation of the Upper Siwaliks is characterised by thick pebble beds with laminated and cross bedded sand beds with very low consolidation and diagenesis. These rocks have formed a gentle fold with the beds dipping ~10-15° towards NW and SE respectively blanketing the Middle Siwaliks folded rocks. These pebble beds are overlain by Quaternary boulder and pebble beds. The contact between the Upper Siwaliks and the Lower Quaternaries is marked by an extensive boulder bed characterised by very large granitic boulders within a clay matrix indicating rapid erosion may be due to paleo- landslide (Fig. 4).



Fig. 4 Boulder bed at the base of the Lower Quaternaries.

The Siwaliks have formed a sharp mountain front marked as Himalayan Frontal Thrust with the Quaternary flood plane in the south. The Upper Siwalik sand beds are thrusts over the Quaternary clay beds along a slip plane dipping  $\sim 10^\circ$  towards north-west (Fig.5).

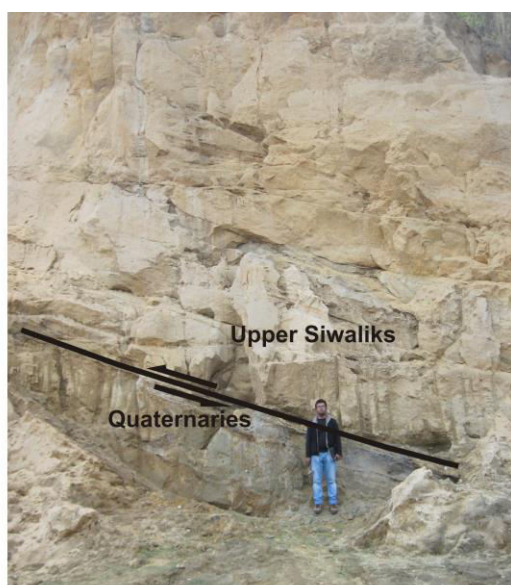


Fig. 5 The Upper Siwalik sand beds are thrusts over the Quaternaries

We have identified two Quaternary formations: the Pleistocene sediments are characterised by large

boulders and pebbles with sand lenses, highly oxidised, bedded and forming the higher terraces whereas the Holocene sediments are characterised by small pebble beds and thick loose sand beds, less oxidation confined to the lower terraces along the rivers.

Apart from the ENE-WSW trending regional thrusts the area is characterised by a number of transverse faults. One N-S trending fault has shifted the Himalayan Frontal Thrust (HFT) towards north crossing the Dikrang River near the Hurmutty tea garden, another NE-SW trending fault has shifted the Middle Siwalik anticlinal fold axis and another NNW-SSE trending fault has shifted the Pachin river course towards north along Pappu Nala between the Itanagar and Naharlagun towns.

The Pachin River flows along the south of the Itanagar. There is a ca.250m high southerly sloping scarp from the Governor House to the Pachin River and the scarp is characterised by extensive erosion with triangular facets. We interpret that this scarp is the southern limb of a north-westerly dipping thrust which has carried out the Middle Siwalik rocks over the Upper Siwaliks and the Pachin River marks the trace of this buried thrust fault (Fig.6). This thrust fault may be a splay of the Tipi thrust within the Siwaliks in the north of our study area. Aggressive erosional process has removed the hanging wall cut-off of the Siwalik sediments and filling up the Pachin River valley.

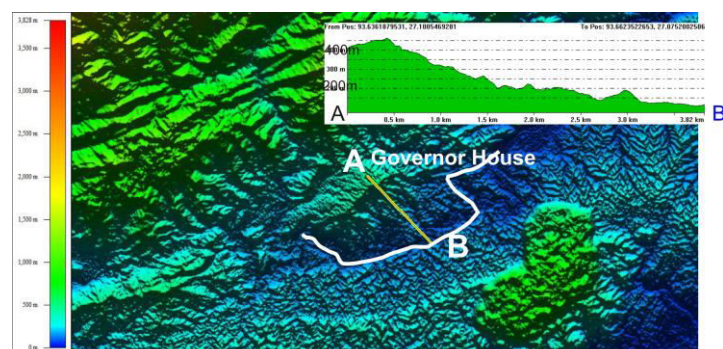


Fig. 6 The Ca.250m scarp below the Governor House and below the Pachin River .

As the gradient of the Pachin River is affected by both the normal fault and a thrust fault at a high angle to each other the river has become a meandering one due to low energy condition. These fault zones are forming loose sediments and hence these areas are vulnerable to the landslides. The high precipitation in this area triggers the landslides throughout this weak zone, which has made this area hazardous for urban living (Fig. 7).



Fig. 7 The landslide prone area behind the Governor House.

Uncontrolled human activity to sustain urban growth is making the area prone to natural hazard every day and thus needs prompt action for sustainable planning for development.

It can be summarised that the geomorphology of this area is guided by the substrate geology along with the climatic factor of recent time. The primary landscape was formed imitating the fold of the substrate rocks which afterwards modified by the late transverse faults.

**Acknowledgements** The present study is part of a Research Project funded by Department of Science and Technology, Government of India (SR/FTP/ES-47/2013) and executed at the Department of Geology, University of Calcutta. We thank the Head of the Department of Geology, University of Calcutta for infrastructural facilities for research. SS acknowledges Dr. B Goswami, Associate Professor, Department of Geology, University of Calcutta for infrastructural support and discussions.

## References

- Chirouze, F., Dupont-Nivet, G., Huyghe, P., Peter van der Beek, Chakraborti, T., Bernet, M., Erens, V., (2012). Magnetostratigraphy of the Neogene Siwalik Group in the far eastern Himalaya: Kameng section, Arunachal Pradesh, India. *Journal of Asian Earth Sciences*, 44, 117-135
- Kumar, S., Wesnousky, S.G., Jayangondaperumal, R., Nakata, T., Kumahara, Y., Singh, V., 2011. Paleoseismological evidence of surface faulting along the northeastern Himalayan front, India: timing, size, and spatial extent of great earthquakes. *Journal of Geophysical Research* 115, B12422.  
<http://dx.doi.org/10.1029/2009JB006789>

- Rupa, T., (2015), Geomorphological study with special reference to landslide in the adjoining areas of National Highway No. 52-A (Banderdewa to Itanagar), Arunachal Pradesh, *IOSR Journal of Environmental Science, Toxicology and Food Technology (IOSR-JESTFT)*, 9(4) III, 20-26.
- Singh, T. and Devi, M. (2006) Landslide Occurrences and Risk Assessment in Itanagar Capital Complex, Arunachal Himalaya. *Himalayan Geology*, 27 (2), 145-162.
- Singh, T., (2007). Geology of the Itanagar Capital Complex, Arunachal Himalaya, with special reference to the Neotectonics, *Journal Geological Society of India*, 70, 339-352.



## Manabhum Anticline: An Apparent Key to the Genesis of the Eastern Himalayan Syntaxial Zone.

Chandreyee Chakrabarti Goswami (1), Somhrita Bhattacharjee (1)

(1) Department of Geology, University of Calcutta, 35 Ballygunge Circular Road, Kolkata 700019, India  
Email: chandreyee.goswami75@gmail.com

**Abstract:** The geologically complex and logistically hostile terrain of the Assam–Arakan basin near fore deep of the Himalayan foot hills is one of the key factors to understand the Himalayan tectonics in its eastern extremity. The spectacular anticlinal structure, the Manabhum anticline in this region which is flanked by the Himalaya, the Mishmi Hills and the Naga Schuppen belts on three sides and upper Assam basin on one side has been studied. An effort has been given to document the geomorphological and geological features from the remotely sensed data and subsequent detailed field mapping. The accumulated data have been analysed to understand the tectonic scenario which has contributed to the morphological evidences of this area in recent past.

**Key Words:** Anticline, thrust, Himalayan tectonics.

### Introduction

The easternmost part of the 2500km long Himalayan Frontal Thrust (HFT) is characterised by the presence of some large tributary rivers contributing to the westerly flowing trunk channel of the river Brahmaputra with one of the biggest flood-plain and delta systems of the world. The south-eastern part of this area is a part of the Indo-Myanmar subduction zone forming the Naga-Patkoï hill ranges. The Manabhum area is situated in the south bank of the Brahmaputra, within the fore deep region of the Himalayas in the north, Mishmi Hills in the east and north east, partly in Belt of Naga Schuppen (thrust belt) to the south east, facing the Upper Assam foreland shelf in Arunachal Pradesh. It is characterised by the presence of a spectacular antiformal structure with a NNW-SSE direction of fold axis (Fig. 1).

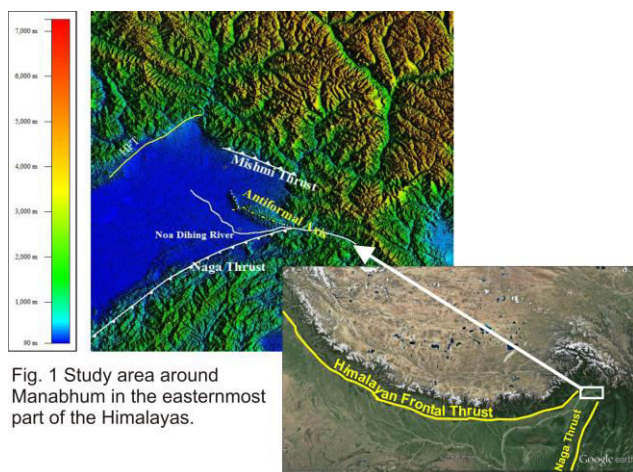


Fig. 1 Study area around Manabhum in the easternmost part of the Himalayas.

and Siwalik/Dhekiajuli (Recent) formation in the south (Mandal K L, 2013).

The Kumchai oil field in the vicinity of Manabhum was discovered in 1987, and has been producing oil and gas since then. Subsequent basin modelling, suggests the Manabhum area is within a high risk high reward category (Barathakur et al. 2013).

As the area is tectonically an unique one and vulnerable to the natural disasters like earthquake and flood but is economically important due to presence of oil we tried to document the surficial as well as substrate geology of this area to find out how the tectonism in recent past has shaped this area. These findings may also help to identify whether the easternmost part of the Himalayan range forms a syntaxial bend or if it comprises a different thrust system transverse to both of them.

The area is thickly covered by dense vegetation; one part is within the Namdapha Reserve Forest which is shelter for almost all types of big cats from Royal Bengal tiger to snow leopard, many exotic birds like hornbill and green pigeon, numerous orchids and medicinal plants and large trees of rainforests as well as high altitude conifers. The area is drained by numerous small and big rivers.

Due to thick forest cover and extremely difficult logistics we identified the drainage and the first order geomorphic features by analysing the satellite images and DEMs and consequently after a rigorous geological field work we have prepared a preliminary geological map (Fig. 2).

The area is flanked by the lesser Himalayan crystalline rocks present in Dapha Bum and Mishmi Hills to the east and north-east, the Disangs and the Barails along the Patkoï Bum in the south west part and Namsang, Girujan

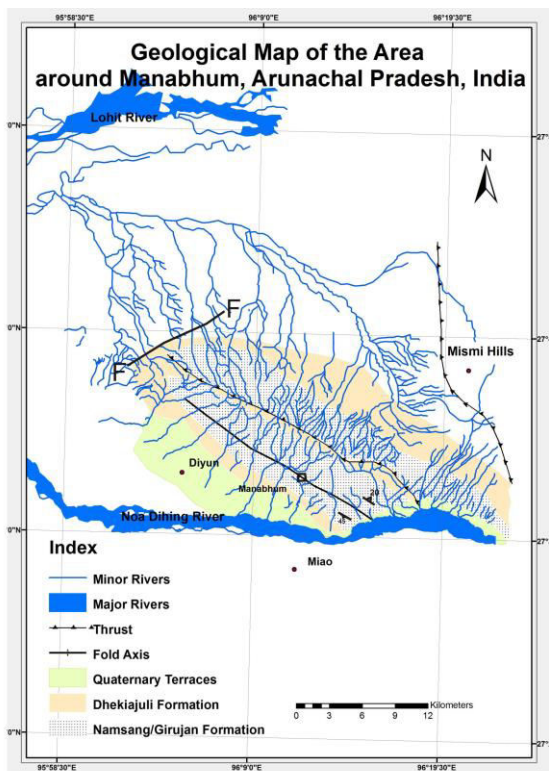


Fig. 2 Geological Map of the study area.

### Discussion

The most important river which is draining this area is Noa Dihing, which flows northerly from the Patkai Bum range in Vijaynagar and takes a sharp westerly bend from the Namdapha and flows towards west as Buri Dihing, but from Miao it again takes a northerly bend as Noa Dihing to meet the Brahmaputra.

The Noa Dihing River is shifting easterly in its northerly flowing tract abandoning earlier river courses due to tilting of the surface towards east (Ramesh, 1988).

As most of the area is thickly vegetated and due to very high precipitation it is almost impossible to find rock exposures and the only places to get a chance of viewing the substrate rocks are in the Noa Dihing river section, small nallah sections and road cuttings. These rocks are mainly grey to greenish grey colour medium to coarse grained arkosic sandstone with salt and pepper appearance with abundant coal fragments or fossilised woods associated with pebble and boulder beds. These rocks are reported as Miocene Tipam sandstone in earlier literatures (Shrivastava, R. N., Sharma, S. K.,) but according to Mandal K L (2013) these may be of Girujan and Namsang formation of Plio- Pleistocene age.

The sandstones are cross bedded, laminated and forming the core of the antiform. As the sandstones are older than the overlying pebble beds the antiform can be classified as anticline. The sandstone beds become thicker towards the core of the anticline and the pebble beds are absent in the core region.

The upper Namsang/Girujan formation is characterised by thick pebble with thin sand beds.

This older sandstones are folded into an asymmetric northerly plunging antiform with the western limb dipping 45 to 50° towards south-west and the eastern limb dipping 20 to 25° towards north-east (Fig. 3).

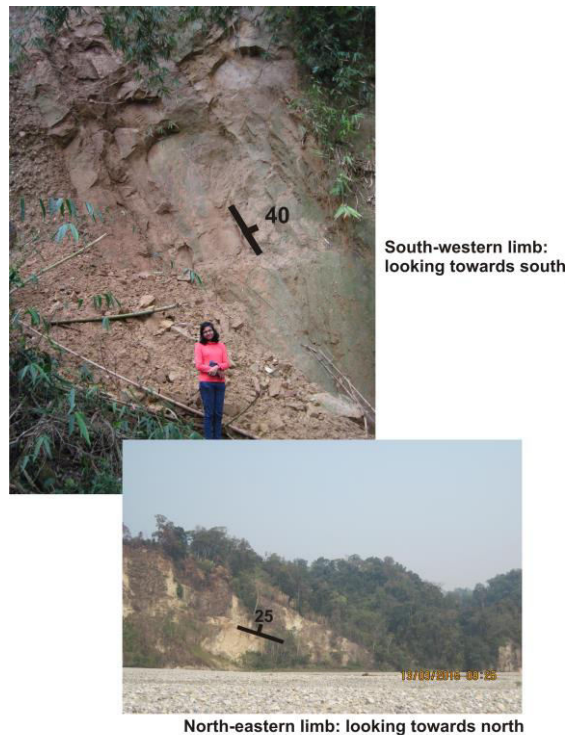


Fig. 3 The Namsang/Girujan sandstones are folded into an asymmetric fold

The upper Namsang/Girujan boulder beds imitates the same folding but the beds dip gentler than the sandstone beds. There are thinner clay beds within the sand beds which show convolute laminations which is evidence of tectonic disturbance during sedimentation (Fig. 4).



Fig. 4 Convolute lamination within the clay beds of Namsang/Girujan Formations.

These older sandstones are overlain by deformed Quaternary Dhekiajuli sediments forming higher river terraces. The oldest Quaternary formation overlying the sandstones are boulders and pebbles embedded in silt and clay matrix. It is highly oxidised and colour is deep reddish brown. It is difficult to differentiate the upper Namsang/Girujan boulders from the oldest Quaternary boulders (Fig.5).



Fig. 5 It is difficult to differentiate the upper Namsang/Girujan boulder beds from the oldest Quaternary boulder beds.

The overlying pebble and boulder beds contain less clay matrix than below. Sand and silt beds with few coarse boulders overlie the pebble and boulder beds and are capped by a clay. Though in some places there is a distinct clay horizon marked by ochre and black clay beds which differentiate the Girujan pebble beds from the older Quaternary pebble beds (Fig. 6). Due to thrusting the river which was earlier carrying the pebbles in high energy condition lost its energy and a temporary ponding of the river caused the deposition of highly carbonaceous black clay. This clay bed thus may represent a thrusting event.



Fig. 6 A distinct clay horizon marked by black clay beds which differentiate the Girujan pebble beds from the older Quaternary pebble beds

The Quaternary Dhekiajuli sediments are showing the similar folding but the dip of the beds are very gentle, 10 to 15°.

The higher river terraces are extensive and few along the northern bank of Noa Dihing River whereas the southern bank terraces are smaller but in higher number.

There are three major structural trends within this small area. The Naga thrust trend which is NE-SW in the Southern portion of the study area, the axis of the Manabhum anticline shows an offset perpendicular to it in its northern part which is nearly parallel to the HFT (Himalayan Frontal Thrust) but the major structural trend is the trend of the fold axis. The Manabhum anticline and the present course of northerly flowing Noa-Dihing River is neither parallel to the Himalayan thrusts nor the Naga thrust but parallel to the NW-SE trending Mishmi thrust. According to Barthakur et al. (2013) the anticline is growing over an easterly dipping thrust fault but it cannot

be traced at the surface. The south-western limb of the anticline is shorter and steeper but the north-eastern limb is gentler with a break in slope along a line almost parallel to the fold axis forming another distinct lineament (Fig. 2). This may be a fault propagation fold over a north-easterly dipping thrust and the eastern limb is on the hanging wall side. This area is a prospective for the hydrocarbons as Khumchai oil field is in the foot of the western limb.

There is a topographic high east of the anticline formed in the Quaternary sediments which is in a thrust contact with the north-easterly dipping gneissic rocks of the Mismi hills. The rivers are shifting westward in this region.

So the Noa Dihing River which flows towards north in the western flank of the anticline is moving eastward from its earlier course let behind many cut off meanders and the major river in the eastern flank of the anticline is moving westward. This may be an evidence of compression of the area in recent time and the compression direction is neither similar to the compression of Indo-Tibetan plate nor the Indo-Burmese plate. The tilting of the river terraces and changing of river courses suggest that the anticline is still growing. A detailed work on this anticline will definitely throw light on the genetics of the eastern Himalayan syntaxial zone.

**Acknowledgements** The present study is part of a Research Project funded by Department of Science and Technology, Government of India (SR/FTP/ES-47/2013) and executed at the Department of Geology, University of Calcutta. We thank the Head of the Department of Geology, University of Calcutta for infrastructural facilities for research. We acknowledge the immense help by B C Poddar, Deputy Director General (Retired), GSI in field work and during preparing the manuscript. SB acknowledges Dr. B Goswami, Associate Professor, Department of Geology, University of Calcutta for infrastructural support and discussions.

## Reference

- Borthakur, A.N., Ahmed, J.P., Singh, S.P. (2013). 10th Biennial International Conference & Exposition, 370p.
- Mandal, K. (2013). South East Asian Journal of Sedimentary Basin Research, 1 (1), 3-9.
- Ramesh, N.R. (1988) Journal of Engineering Geology, XVII(3&4) .
- Shrivastava, R.N., Sharma, S.K. (1986). Geological Survey of India Progress Report for the Field Season 1985-86. GSI portal.



INQUA Focus Group on Paleoseismology and Active Tectonics



paleoseismicity.org

## Seamless Photomosaic Trench Logging Using Trench-Based Photogrammetry Methods: Workflow and Case-Studies

Gray, Brian (1), Nicholas Graehl (1), Serkan Bozkurt (1), John Baldwin (1), and Kevin Clahan (1)

(1) Lettis Consultants International, Inc., 1981 N. Broadway, Suite 330, Walnut Creek, CA 94596, Email: bgray@lettisci.com

**Abstract:** Modern photo-logging methods of paleoseismic trench exposures include Structure-from-Motion (SfM) and Image-Based Modeling (IBM) techniques that reconstruct 3D surfaces to create seamless, high-resolution photomosaics designed for in-situ trench photo logging. Given the often large expense and time-critical nature of paleoseismic investigations, efficient and accurate production of seamless photomosaic trench logs is an essential component to modern paleoseismic investigations. We present our field-tested workflow, based on methods developed by Reitman and Bennet (unpublished USGS report) and Reitman et al. (2015), that includes photo acquisition techniques, software reconstruction, and post-processing methods. Techniques are illustrated to demonstrate the workflow on various types of trench excavations in remote field settings using basic equipment. Our workflow builds on experience using SfM methods in more than 25 paleoseismic trenches in various tectonic settings, trench styles, and site conditions.

**Key words:** Structure-from-Motion (SfM), Image-Based-Modeling (IBM), Paleoseismology, Photogrammetry, Photomosaic

### Introduction

Over the last few years, the development of Structure-from-Motion (SfM) and Image-Based-Modeling (IBM) techniques have revolutionized the production and improved the quality of photomosaic logs generated for paleoseismic studies. Rendered obsolete is the need for perfectly-positioned orthogonal photos taken with the aid of the "Trench-O-Matic" and gone are the sleepless nights consumed by painstaking Photoshop mosaicking sessions. Paleoseismic trenches can now be photographed in as little as a few tens of minutes and seamless trench mosaics can be generated in the time it takes to (casually) consume a couple of end-of-the-day beverages. However, efficient SfM model generation requires practical knowledge of photography, image processing, and the software-rectification development or the entire process can become cumbersome. With experience from more than 25 paleoseismic trenches, we present a field-tested workflow that builds upon the workflows outlined by Reitman and Bennet (unpublished USGS report) and Reitman et al. (2015). We specifically aim to address typical challenges associated with the use of this relatively new paleoseismic tool.

Because of the added time, expense, and logistical challenges of purchasing and bringing survey equipment to remote field sites, the majority of our recent trenches utilizing SfM-based logs have been set up without absolute survey control. The methods presented herein

are geared toward log production in the absence of Real-Time Kinematic (RTK), total station, or Light Detection and Ranging (LiDAR)-based survey control. Instead we use local grids generated for the trench exposure, averaged handheld GPS points for endpoints and corners, and trench length and orientation to place the trench in an absolute coordinate system (e.g., UTM Zone 10, WGS 84,).

### General Workflow

The goal of any photomosaic trench logging exercise is to develop an accurate, archive-quality, orthorectified image of the exposure. Efficient generation of a photomosaic log requires four basic steps: (1) trench excavation and grid preparation, (2) photography, (3) model generation, and (4) final log rectification and printing. In addition, having the proper equipment has proven critical in a number of our excavations. The following is a rundown of equipment we typically have on hand for log production. For SfM processing, we recommend using a computer with at least 16+ GB of RAM, an Intel i7 processor, and a reasonable graphics processing unit (GPU) as it may be utilized for processing power. A powerful desktop computer with a solid-state hard drive and optimized GPU is ideal (we use settings outlined in the Agisoft PhotoScan user manual), but high-powered laptops, especially those with solid-state hard-drives can be a great alternative if portability is necessary. For photography, a moderate-to-high-resolution camera



## INQUA Focus Group on Paleoseismology and Active Tectonics



paleoseismicity.org

(minimum 12 MP) with semi-manual settings to manipulate ISO (light sensitivity), aperture, exposure compensation, and white balance is ideal. A relatively wide, albeit undistorted, viewing angle, wide aperture (to allow low-light photography), and variable-angle LCD screen are important features to have in shored trenches as both space (wall to wall) and light are usually limited. Mirrored digital cameras (DSLRs) are not recommended for several reasons. First, DSLR lenses often have greater out-of-focus portions of the image at wider apertures (for low light photography) and greater edge distortion than mirrorless cameras. This will cause major headaches when the SfM software attempts to pair images. This is especially true for benched exposures where multiple planes may be represented in a single image. Second, they are typically more expensive, heavier, and less expendable than most mirrorless cameras. A high-quality point and shoot that takes a nearly undistorted photo with a wide viewing angle is preferred. Photographing a sheet of graph paper provides a simple test of lens distortion at various focal lengths. Our Canon Powershot SX50-HS (shooting RAW) has produced the most consistent results so far. Additionally, cameras that perform extensive automated in-camera post processing (i.e., enhancing color, contrast, and sharpness) may also produce images that are difficult for the SfM software to reconstruct. If necessary, post processing should be completed by the user to avoid altering the images to a point where the software can no longer match images.

For slot trenches, we have found that using a sturdy extendible paint pole with an affixed tripod adapter to attach the camera, coupled with a radio-controlled shutter switch on the camera, significantly reduces the time required to photograph the trench (Figure 1). For example, a recent trench on the Rodgers Creek fault measuring 23 m long by 3.7 m deep took approximately 50 minutes to photograph one wall with approximately half the trench requiring a small amount of additional time to manage shading. Avoiding the hassle of climbing up and down shores, moving boards, and awkward photography positions reduced photography time in half compared to what we anticipated for handheld photography. Logs are printed in the field on 11x17 photo paper using a Canon Pixma iX6820 inkjet printer which prints well and is relatively inexpensive to purchase.

For field processing of SfM logs, a portable power pack or power inverter connected to a car battery can be helpful as Agisoft PhotoScan is a power-hungry software that quickly consumes laptop batteries. Field processing is especially helpful when time is critical or the exposure location is remote. A portable power source also facilitates printing of logs directly in the field.

While often site and fault conditions limit how the trench



Figure 1: Pole photography using a sturdy paint pole with camera attachment, radio remote, and camera with a variable-position (upturned) screen.

is excavated, it is important to keep in the mind that straight trenches with vertical walls, or at the very least planar walls, are the quickest and least-problematic trenches to generate SfM-based photomosaics for. Trenches that curve and/or have irregular walls will be considerably more challenging to rectify. This is because the SfM IBM are exported as orthorectified images projected onto a single x/y plane. As the wall becomes progressively more oblique to the projection plane, the rectified image becomes progressively more distorted. Large variations in trench azimuth are best managed with multiple orthophoto exports and subsequent stitching to complete a log that appears as a single plane. If bends in the trench are required, for the sake of photomosaic development, it is best to excavate in linear sections rather than a continuous curve as each section can be exported with a single orthophoto defined by a single plane. Like other steps of the process, our photography method emphasizes efficiency. The ultimate goal is to obtain the best log with the least number of acceptable photos as model processing times increase substantially with large photo sets or if photos are difficult to align. As noted above, for slot trenches we use a paint pole and remote to systematically photograph the trench in top-to-bottom/bottom-to-top rows, maintaining a roughly



## INQUA Focus Group on Paleoseismology and Active Tectonics



paleoseismicity.org

50% vertical and side-to-side overlap (utilizing the camera's tilt screen to track movement). Benched trenches are usually easier to photograph in rows.

The standard rule is to achieve adequate coverage without overdoing it, as dealing with too many photographs consumes valuable time. Conversely, taking too few photos will result in gaps in the mosaic that may require a significant effort to fill/repair. To maintain color and exposure consistency, we lock the ISO sensitivity, white balance, and aperture before starting the photography session. As in Reitman et al. (2015), we typically take an additional row of photos at the top and bottom of the trench for completeness. Fault zones are often photographed a second time as a way to provide additional photos in case the first set does not have adequate coverage. This additional photo set generally does not increase processing time because it only used if there are gaps in the first set. Lighting should be carefully controlled to avoid bright spots or sunlight on the camera lens as this may cause problems during SfM processing. Photographing the exposure when shaded or cloudy is best and avoids high contrast exposures. We typically try to avoid taking overly oblique photos or photos that of anything outside the trench where possible as extraneous portions of photos will need to be cropped during processing. Additionally, it is important to keep loose objects stationary and to avoid change from one image to the other. Notably, flagging with important sample or kinematic labels should be nailed to the wall if wind is present.

Model processing and export closely follow the methods

outlined by Reitman and Bennett (2015) with a few exceptions noted here. We are meticulous about masking out extraneous portions of images such as excavation spoils, trees behind the trench, etc. In PhotoScan, these masked-out sections are excluded using the "constrain features by mask" toggle in the "Align Photos" window. This can dramatically improve processing times and has saved a number of our initially failed mosaics. To export orthophotos, we use the native window and define the export plane based on markers, using those pre-determined for the x and y axes. This makes the export orientation reproducible in case complete updates are necessary. For benched exposures, we commonly export one log normal to the vertical risers and a second log (typically the opposite wall) at a slightly oblique angle that results in a nice 3-dimensional base that can still be used as a trench log (Figure 2). The export file type will default to TIF format which results in images that are often times hundreds of megabytes in size. We opt for JPEG or PNG images instead and have had no issues with either.

The final steps to completing the mosaic are rectification of the log and export to a printable format. We have worked with Illustrator, Photoshop, and ArcMap to complete these final tasks and ArcMap is by far the most accurate and efficient. As in Reitman et al. (2015), we use the georeferencing tool to add control points based on grid nail coordinates. However, we use the "spline" transformation method which allows all points to snap directly to their respective grid coordinates. This transformation method is only active once a minimum of 10 points are entered. The ability to rectify the image to the exact coordinates or markers also allows for easy and



Figure 2: SfM export options for benched paleoseismic investigations. (a). Standard export orientation using grid markers for a pre-defined projection plane that is normal to the trench wall. (b). Optional oblique view of the benched exposure, provides additional context for contacts crossing benches or oblique walls, orthophoto typically exported using an arbitrary projection plane.



## INQUA Focus Group on Paleoseismology and Active Tectonics



paleoseismicity.org

seamless stitching of subsequent images. Once complete, the desired grid (typically 0.5 or 1.0 m) is overlain on the rectified mosaic. Final log export is accomplished with an 11x17 map document scaled to the desired output resolution.

### Troubleshooting Common Issues

The following section addresses common photomosaic log production issues that regularly result in significant delays and lost field time. These issues include patching in trench updates (after shore moves, additional excavation, and re-flagging), log production in trenches with bends, and lengthy model processing times.

Additional photography and model updates are often necessary during the course of a paleoseismic investigation. Reasons may include further excavation, removal of shores in a fault zone, and significant updates to interpretations and flagging. Where additional photography is necessary, care should be taken to minimize disturbance of the adjacent sections and/or overlapping tie points. The updated section should be photographed with significant overlap of the original undisturbed sections. Without proper overlap, seamlessly incorporating the new log can be problematic. Care should also be taken to mimic the original lighting conditions as best as possible using proper shading and photographing at the same time of day. Differences due to cloud cover and soil moisture and largely unavoidable but can be managed with Photoshop adjustments. Once the new photo set has been processed and exported, we incorporate the image directly into the ArcMap rectification document using the "spline" transformation method outlined above. Alternatively, the new log sections can be merged using Photoshop or directly into the existing SfM model, although these alternative methods are typically more time consuming and result in visible seams.

As discussed in the workflow section above, trenches with bends present specific challenges with respect to log production. As each orthorectified log is exported from the SfM model using a given plane normal to the exposure, trenches with walls of variable azimuth will; (a) have sections that are exported oblique to that plane (requiring significant stretching), (b) be logged in individual sections, or (c) be presented as one log comprised of multiple stitched orthophotos. Multi-azimuthal trench walls intended as one exposure will use the latter method. Each section is exported using a given set of x/y markers defining the specific export plane. Planning ahead here is helpful because determining which grid markers will be used to export each plane is more easily accomplished in the field rather than back at the office. The resulting orthophotos are cropped to

remove the unwanted sections and then rectified and merged in ArcMap using the spline interpolation (Figure 3). If done correctly, the resulting log will be seamless and distortion from sections oblique to the orthophoto projection planes will be mitigated.

### Conclusions

Paleoseismic exposures can be quickly, accurately, and seamlessly reconstructed in exceptional detail with careful planning and anticipation of common log

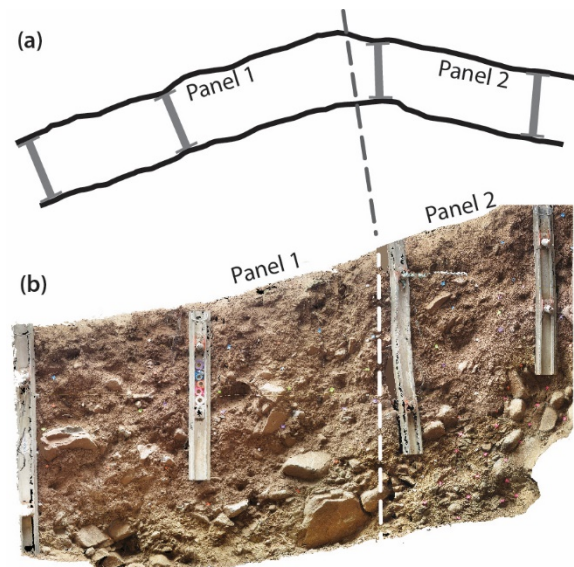


Figure 3: Working with bends in the exposure: (a) Map view of slotted trench with prominent bend. (b) Rectified mosaic created from two merged sections exported normal to the exposure, oblique distortion is eliminated and the seam is largely undetectable.

production issues. For even the most challenging of paleoseismic excavations, SfM-based photomosaics can be developed in a fraction of the time of traditional Photoshop-based methods.

### Acknowledgements:

The authors would like to thank additional LCI staff members Christopher Bloszies, Jereme Chandler, Brian Greer, Alex Remar, and Patrick Williams who have helped streamline every step of the process, and Chris Milliner for passing on his knowledge during LCI's first big run of PhotoScan logs.

### References

- Agisoft PhotoScan v. 1.2.4 [computer software]. (2016), accessed via <http://www.agisoft.com/downloads/>
- Reitman, N. and S. E. K. Bennett, Structure from Motion (SfM) photo mosaic workflow using Agisoft PhotoScan Professional, unpublished white paper, USGS Golden, CO, 8 p.



INQUA Focus Group on Paleoseismology and Active Tectonics



[paleoseismicity.org](http://paleoseismicity.org)

Reitman, N., S. E. K. Bennett, R. D. Gold, R. W. Briggs, and C. B. DuRoss, (2015), High-resolution trench photomosaics from image-based modeling: workflow and error analysis, *Bull. Seismo. Soc. Am.*, Vol. 105, No. 5



## Large strike-slip faults in a convergent continental setting - the Dzhungarian Fault in the Northern Tien Shan

Grützner, Christoph (1), Austin Elliott (2), Richard Walker (2), Kanatbek Abdrakhmatov (3), Grace Campbell (1, 4)

- (1) COMET; Department of Earth Sciences, University of Cambridge, Madingley Rise, Madingley Road, CB3 0EZ Cambridge, UK, chg39@cam.ac.uk  
(2) Department of Earth Sciences, University of Oxford, South Parks Road, OX1 3AN Oxford, UK  
(3) Kyrgyz Seismological Institute, Academy of Sciences of the Kyrgyz Republic, Asanbay str. 52/1, 720060 Bishkek, Kyrgyz Republic  
(4) now at: Arup, 13 Fitzroy St, London, Middlesex W1T 4BQ, UK.

**Abstract:** This paper presents results of field work at the Dzhungarian Fault in the northernmost Tien Shan in East Kazakhstan. This right-lateral strike-slip fault is several hundred kilometres long; a fault scarp extends for more than 30 km in the central part of the fault. We surveyed offset morphological markers such as terrace risers and river terraces with DGPS and balloon surveys to produce high-resolution digital elevation models and to measure offsets. Abandoned surfaces were dated to estimate the timing of the last large surface rupture and to measure slip rates. We show that the fault probably generated a great earthquake few hundred years ago and that folding contributes to the overall deformation. Also, we discuss the challenges involved in dating methods and geomorphological analyses in an arid intracontinental setting.

**Key words:** Tien Shan, paleoseismology, Dzhungarian Fault, surface rupture, folding

### INTRODUCTION

Large strike-slip faults are a characteristic feature of Tien Shan tectonics. Yet little is known about their role in accommodating the N-S shortening between India and Eurasia, and in most cases slip rates are only estimates from satellite geodesy and GPS. We present results from our field work at the Dzhungarian Fault, which is situated in the northernmost Tien Shan. This right-lateral strike-slip fault is several hundred kilometres long and runs NW-SE. Its strike varies and is more northerly in the southern parts. Slip rate estimates range between 0.5–3.9 mm/a for the Quaternary (Voytovich, 1965, 1969; England and Monar, 1997; Campbell et al., 2013). The fault's earthquake history is unknown.

The fault has a vertical component of motion, but the strong topographic contrast – the Dzhungarian Ala-tau in the hanging wall vs. the Dzhungarian Gate in the footwall – was most likely not solely caused by motion on this fault. Instead, E-W trending mountain ranges in the Dzhungarian Ala-tau imply that folding and faulting on E-W striking thrusts faults produced at least part of the topography (Campbell et al., 2013). England & Molnar (1997) estimate 1.4 - 0.7 mm/a shortening across the Dzhungarian Ala-tau from Quaternary slip rate data.

We conducted a field campaign in 2015 and focused on three sites along the Dzhungarian Fault (Fig. 1). Each of these study areas exhibits geomorphologic evidence for Late Quaternary fault activity. Here we present first results from the two sites labelled 2 and 3 in Fig. 1.

### BEAR RIVER – A SURFACE-RUPTURING EARTHQUAKE A FEW HUNDRED YEARS AGO?

At the Bear River site close to Lake Alakol a large NE-facing fault scarp is present, offsetting alluvial and fluvial deposits (Fig. 2). Campbell et al. (2013) reported a total

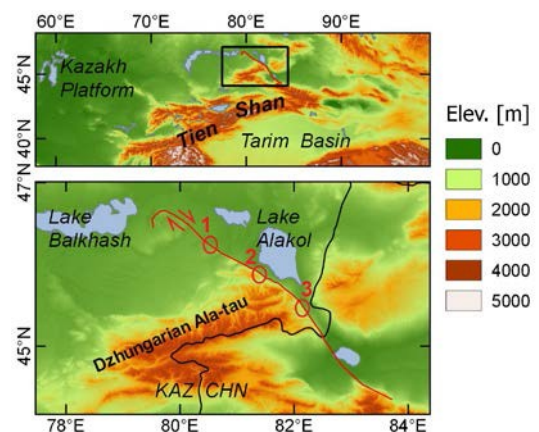


Fig. 1: The Dzhungarian Fault is a right-lateral strike-slip fault with a vertical component, marking the boundary between the Dzhungarian Ala-tau and the Kazakh Platform. Our three study sites are marked in red. Hill-shaded DEM from SRTM1 and ETOPO data.

scarp length of ~32 km and a height of ~1.6 m. We investigated a well-preserved section of the scarp where an ephemeral streams drain the mountains in flash flood events. We used a helium balloon with an attached compact camera to take more than 1000 aerial photos of the scarp. Ground control points were measured with DGPS. Structure-from Motion (SfM) was then used to



build a digital elevation model with 0.1 m resolution, and additional DGPS profiles were recorded across the scarp for comparison. The DEM is the light patch in Fig. 2a, and one representative DGPS profile is marked in black. Both DGPS and DEM data reveal ~8 m vertical and right-lateral offset at the lower scarp (Fig. 2A, lower panel, and Fig. 2B).

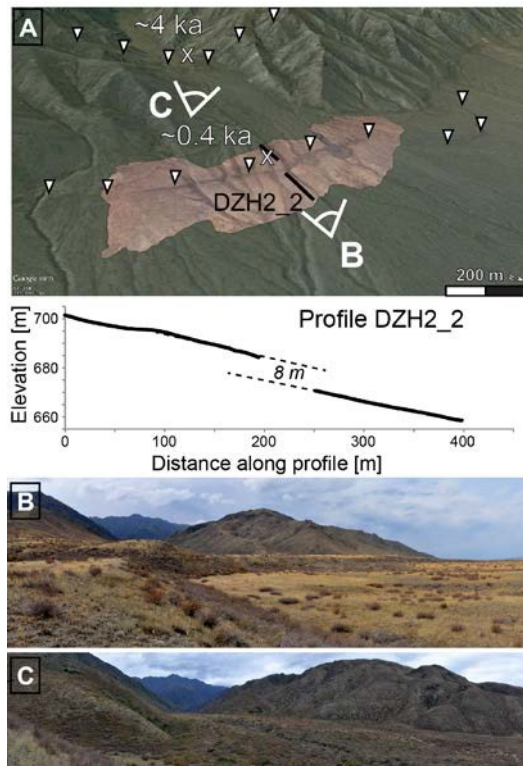


Fig. 2: Two scarps were found at location 2 and are marked by white triangles. (A) About 8 m vertical and 8 m lateral offset, respectively, are preserved at the lower scarp. About 5 m vertical offset are visible at the upper scarp. Preliminary radiocarbon dating of the abandoned surfaces gave ages of ~0.4 ka for the lower scarp and around 4 ka for the upper scarp. Note the different scales of the axes. (B) View to the lower scarp. (C) View to the upper scarp.

We dug several pits of ~1 m depth into the terraces in order to determine the age of their abandonment, which would allow us to estimate the time since the last earthquake. Flash-flood deposits consisting of coarse gravels were encountered. Unfortunately, no fine grained material for optical/infrared stimulated luminescence dating was found, and the lack of quartz cobbles did not allow us to date  $^{10}\text{Be}$  depth profiles. We found carbonate crusts at the lower sides of cobbles, which formed by carbonate precipitation during the onset of soil formation once an alluvial fan is abandoned, and the dating of these with U-Th series is underway.

In the pit at the highest terrace on the hanging wall, we found two snails and one bone in two different layers 0.7 m and 0.75 m below surface, respectively. While the bone was too small for radiocarbon dating, the shells yielded radiocarbon ages of ~300-400 years BP (Fig. 2A).

This means that the terraces became inactive shortly after this, and probably a surface-rupturing earthquake produced the observed offsets a few hundred years ago. Although there is no historical account for such an event, this isn't significant in this part of the world because the historical catalogue is notoriously short (cf. Campbell et al., 2015).

Further mapping led to the discovery of a second fault scarp ~1 km upstream in the mountains (Fig. 2A, C). This scarp also faces towards the NE, and has a vertical offset of ~5 m. No obvious lateral offset was found in the stream bed. The fault can be traced in the adjacent hills where, in addition to vertical offset, clear morphological hints for right-lateral motion were encountered. We dug another pit into an abandoned gravel terrace, and again found no suitable material for  $^{10}\text{Be}$  or OSL/IRSL dating, but the aforementioned carbonate rinds and one snail. The U-Th-series dating of the carbonate crust is currently being conducted, and the snail returned a radiocarbon age of ~4 ka BP. This implies that the offset occurred at some point after 4 ka. We also dated a recent snail specimen to test the influence of age inheritance, but found that a correction for this effect need not be applied.

Without better age control we cannot say whether the upper and the lower scarp originate from different earthquakes. Our dating results leave room for the speculation that one earthquake ruptured both strands. Such behaviour has been described for other major events from the Tien Shan (Abdrakhmatov et al., 2016) and elsewhere (e.g. Fletcher et al., 2014). However, it is also possible that we have found two independent events. A short thought experiment reveals that this possibility is well feasible: 8 m vertical and 8 m lateral slip give a total slip of ~11 m. If we assume that the slip rate of ~3 mm/a from England and Molnar (1997) is valid for our study site, then enough stress to be released in an ~11 m slip event would accumulate over ~3700 years. Interestingly, Campbell et al. (2015) report a strong surface-rupturing earthquake about 400 years ago for the Lepsy fault, the eastern end of which is only ~30 km away from the scarp that we investigated.

### TOKTY RIVER – FAULTING, FOLDING, AND THE MORPHOLOGY OF TRANSPRESSIONAL MOTION

The second site that we discuss is the Tokty River close to the border between Kazakhstan and China (Fig. 1), where the Dzhungarian Fault has a very clear surface expression. The fault trace is visible for dozens of kilometres. A linear set of springs emerges from the alluvial fans, vertically offset alluvial fans are found, and "classical" strike-slip morphology including push-up ridges and small pull-apart structures are present. However, Late Quaternary/Holocene lateral motion is not very obvious, but seems to be preserved in some places.

The most eye-catching feature is a push-up ridge SE of the Tokty River outlet (Fig. 3A, C) which rises up to 100 m above its surroundings. Directly adjacent to the NW an



elongated depression bordered by scarps facing towards each other appears to be a pull-apart feature (Fig. 3A, C). Such features within short distances are typically the result of a close-to-vertical strike slip fault with slight variations in strike that lead to local compression and extension (e.g., Hilley and Arrowsmith, 2008).

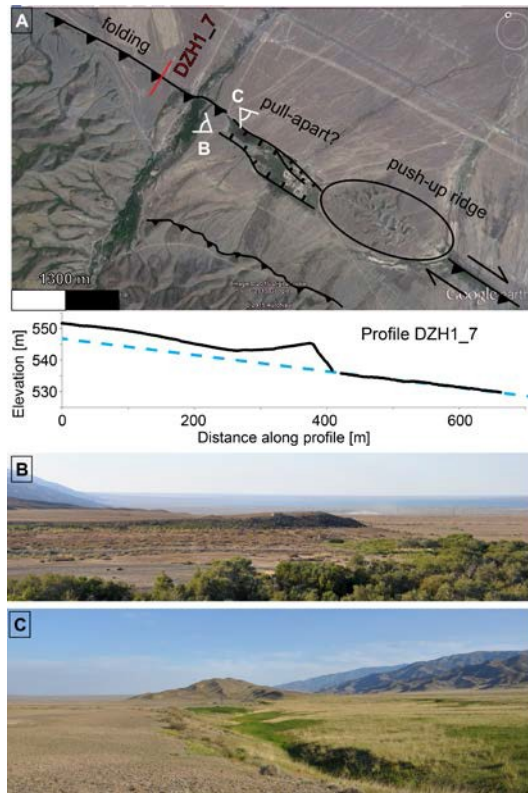


Fig. 3: Deformation features at site 3. (A) Along fault strike we observe fault/fold scarps, folded terraces, probably a pull-apart structure and a push-up ridge. A second fault strand runs along the base of the mountain front. The elevation profile exhibits short-wavelength folding and offset of the alluvial fan (blue line). Note the different scales of the axes. (B) View towards the folded terrace where profile DZH1\_7 is located. (C) View towards the push-up ridge with the graben features in front.

At our study site, however, we also found evidence of vertical motion with uplift of the SW side of the fault. An alluvial fan is offset by several metres at the fault, and we observed short-wavelength folding in DGPS profiles that cross the fault perpendicularly. Fig. 3A (lower panel) shows an example of the surface deformation. The same pattern persists in a number of additional profiles parallel to the one presented here. Our observation indicates a SW-dipping thrust fault to have caused the morphology. This is somewhat at odds with the presence of the push-up ridge and the pull-apart feature just a few hundred meters away along strike, but localised slip-partitioning and/or flower structures might explain these findings. A second, smaller fault scarp can be observed closer to the mountain front (Fig. 3A) and implies dip-slip dominated motion here.

We attempted to date the age of the abandonment of the folded terraces in order to get an idea on the deformation rate at this site. Four pits were dug into the gravels with ~1 m depth each. Unfortunately, we did not encounter material suitable for radiocarbon,  $^{10}\text{Be}$ , or OSL/IRSL dating. We did find carbonate rinds at the underside of river cobbles which are currently being processed in a lab.

## DISCUSSION

Our first study site, the Bear River, has probably recorded an earthquake with significant surface offset in very recent times. A puzzling observation is that Campbell et al. (2013) report a scarp height of around 1.6 m, while we observe up to 8 m vertical and horizontal displacement at our site. Further investigation will show if our site exhibits much higher offsets only due to some local anomalies like a deviation in fault strike. Another interesting find is that the earthquake occurred close to the one Campbell et al. (2015) reported from the nearby Lepsy Fault. Our preliminary dating suggests both quakes occurred around the same time. This gives rise to some speculation about a multiple-fault rupture. Alternatively, coulomb stress transfer from one fault to another might have caused both quakes to have happened within a short time interval. Mushketov & Orlov (1893) list a destructive earthquake that occurred in the Lake Balkhash area in the early 18<sup>th</sup> Century, which could mean that only one, but larger quake is more likely. However, the incomplete historical record has to be considered. In any case our study illustrates the limits of instrumental and historical catalogues in seismic hazard assessments.

In interpreting our results, we are currently limited to the ages from the radiocarbon samples. A future comparison to the ages obtained from the U-Th series dating of the carbonate rinds will not only enhance our age control, but will also give interesting insights as to how this latter method can be applied to paleo-earthquake dating in semi-arid environments. We found such carbonate rinds to be abundant in Central Asian gravels, and we hope to exploit them as reliable age indicators in future trenching campaigns.

Our second study site actually raises the same questions about Quaternary dating. Here we even more rely on the suitability of carbonate crusts to work as robust age control.

The Tokty River site is also interesting from a structural geology point of view. How securely does the "classical" strike-slip morphology with push-up ridges and extension zones imply a (near-) vertical fault? How does this match our observation of persistent SW-side up fault motion and short-wavelength folding? What is the relative role of folding and faulting in accommodating shortening here? How effectively can a vertical fault take up shortening at all? Did we overlook hints for slip partitioning?



## INQUA Focus Group on Paleoseismology and Active Tectonics



paleoseismicity.org

To answer these questions we will use stereo- satellite data to build a high-resolution DEM of the entire Kazakh part of the Dzhungarian Fault. These data will help us better constrain the relation between horizontal and vertical fault motion. We hope to better understand the overall deformation, and we would not be surprised if we found additional hints of young deformation away from the main fault trace. Currently, field work is somewhat limited by all the problems that come along with working close to international borders in Central Asia.

**Acknowledgements:** This study was financed by the Earthquakes without Frontiers project, and the Centre for Observation and Modelling of Earthquakes and Tectonics (COMET). We used the Generic Mapping Tool software by Wessel & Smith (1998).

### References

- Abdrakhmatov, K., Walker, R. T., Campbell, G. E., Carr, A. S., Elliott, A., Hillemann, C., Hollingsworth, J., Landgraf, A., Mackenzie, D., Mukambayev, A., Rizza, M., & Sloan, R. A. (2016). Multi-segment rupture in the July 11th 1889 Chilik earthquake (Mw 8.0-8.3), Kazakh Tien Shan, identified from remote-sensing, field survey, and palaeoseismic trenching. *In review*.
- Campbell, G. E., Walker, R. T., Abdrakhmatov, K., Schwenninger, J. L., Jackson, J., Elliott, J. R., & Copley, A. (2013). The Dzhungarian fault: Late Quaternary tectonics and slip rate of a major right-lateral strike-slip fault in the northern Tien Shan region. *Journal of Geophysical Research: Solid Earth*, 118(10), 5681-5698.
- Campbell, G. E., Walker, R. T., Abdrakhmatov, K., Jackson, J., Elliott, J. R., Mackenzie, D., Middleton, T., & Schwenninger, J. L. (2015). Great earthquakes in low strain rate continental interiors: An example from SE Kazakhstan. *Journal of Geophysical Research: Solid Earth*, 120(8), 5507-5534.
- England, P., & Molnar, P. (1997). The field of crustal velocity in Asia calculated from Quaternary rates of slip on faults. *Geophysical Journal International*, 130(3), 551-582.
- Fletcher, J. M., Teran, O. J., Rockwell, T. K., Oskin, M. E., Hudnut, K. W., Mueller, K. J., Spelz, R. M., Akciz, S. O., Masana, E., Faneros, G., Fielding, E. J., Leprince, S., Morelan, A. E., Stock, J. M., Lynch, D. K., Elliott, A. J., Gold, P., Liu-Zeng, J., González-Ortega, A., Hinojosa-Corona, A., González-García, J. (2014). Assembly of a large earthquake from a complex fault system: Surface rupture kinematics of the 4 April 2010 El Mayor-Cucapah (Mexico) Mw 7.2 earthquake. *Geosphere*, 10(4), 797-827.
- Hilley, G. E., & Arrowsmith, J. R. (2008). Geomorphic response to uplift along the Dragon's Back pressure ridge, Carrizo Plain, California. *Geology*, 36(5), 367-370.
- Mushketov, I. V., & A. P. Orlov (1893). Catalog of Earthquakes of the Russian Empire, *Imperial Academy of Sciences St. Petersburg*.
- Voytovich, V. S. (1965). Development of Dzhungar deep fault. *International Geology Review*, 7(5), 874-883.
- Voytovich, V. S. (1969). Природа Джунгарского глубинного разлома. *Труды Геол. ин-та АН СССР*, 183, 191.



## Paleoseismological challenges in Central Asia

Grützner, Christoph (1), Eleanor Ainscoe (2), Richard Walker (2), Austin Elliott (2), Kanatbek Abdrakhmatov (3)

- (1) COMET; Department of Earth Sciences, University of Cambridge, Madingley Rise, Madingley Road, CB3 0EZ Cambridge, UK, chg39@cam.ac.uk  
(2) Department of Earth Sciences, University of Oxford, South Parks Road, OX1 3AN Oxford, UK  
(3) Kyrgyz Seismological Institute, Academy of Sciences of the Kyrgyz Republic, Asanbay str. 52/1, 720060 Bishkek, Kyrgyz Republic

**Abstract:** This paper discusses paleoseismological investigations in the Tien Shan. We use two case studies to illustrate problems that confront research on active faults and seismic hazard. In the Tien Shan, large E-W striking thrust faults and conjugate strike-slip faults take up several mm/yr of distributed N-S shortening. Many of them are characterized by rather long recurrence intervals. Combined with major landscape modifications caused by Late Quaternary climatic changes, this makes the identification of active faults challenging. In our first case study we show how the geomorphological fingerprint of large, surface rupturing earthquakes can be obliterated by erosional events. In our second example we focus on a site in Kyrgyzstan where a  $M_w7.2$  earthquake produced discontinuous surface ruptures in 1992. Paleoseismological data reveal that surface ruptures on this very fault are much more complicated than thought, posing a challenge not only to understanding the active deformation, but also to evaluating seismic and surface-rupturing hazard.

**Key words:** Tien Shan, paleoseismology, erosion, surface rupture

### INTRODUCTION

Around 10-20 mm/yr of N-S shortening is accommodated in the Tien Shan (Abdrakhmatov et al., 1996). Most of this deformation is taken up by E-W striking thrust faults. Seismicity is high and earthquakes of up to ~M8 have occurred in the past 150 years, but overall only a few historical earthquakes have produced surface ruptures. Fault scarps are present in many locations, and they serve as primary evidence of fault activity.

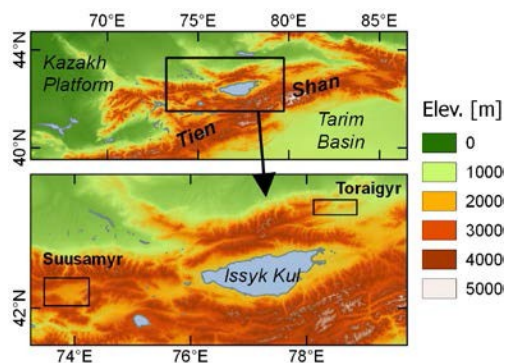


Fig. 1: Our two case study areas in the Tien Shan. Hill-shaded DEM from SRTM1 data, Mercator projection

The large number of active faults, the long earthquake recurrence intervals for individual faults, and the fast growth of population centres in Central Asia make this region an obvious target for paleoseismological studies. Earthquake geology in this region should be an easy job given the high deformation rates and the presence of climatic conditions that favour the preservation of deformation features in the landscape but, as always, it is not that simple. In this paper we highlight some possible pitfalls related to the investigation of active tectonics.

### TORAIGYR FAULT – LONG RECURRENCE INTERVALS AND THE PROBLEM OF EROSION

Our first case study is the Toraigyr Fault NW of Lake Issyk Kul (Fig. 1) in Kazakhstan. This ~50-km-long thrust fault runs E-W, dips to the south and has a 25-km-long, discontinuous fault scarp that offsets alluvial fans as much as 2 m vertically. We mapped the entire fault, measured offsets with DGPS and produced a digital elevation model (DEM) from balloon aerial imagery using the Structure-from-Motion (SfM) technique (Grützner et al., in prep.). We found that besides the faulted alluvium T1, there are few isolated remains of older offset terrace levels with up to 12 m high scarps. Remnants of T2 are heavily eroded and do not expose clear faulting morphology (T2 in Fig. 2)

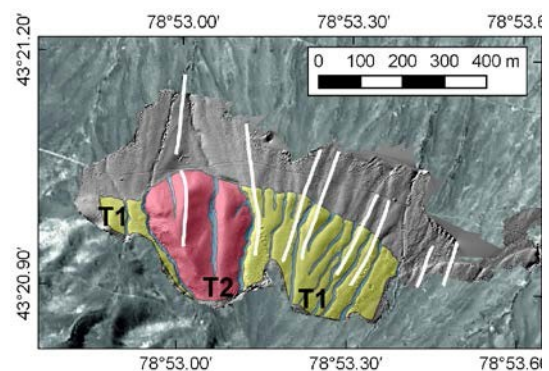


Fig. 2: Two terrace levels T1 (lower) and T2 (upper) at the Toraigyr Fault. Background imagery: 1 m Kompsat data, DEM is from our own balloon survey and SfM. White lines indicate locations of elevation profiles, which we do not show here.



We excavated a paleoseismological trench across the fault to help constrain the timing of the last earthquake that produced the 2-m-high scarp. We found evidence for two paleoearthquakes in the trench (Fig. 3) that occurred on two closely spaced surface faults. Dates from Infrared Stimulated Luminescence (IRSL) and radiocarbon samples show that the last surface-rupturing event occurred 3.5 - 7.3 ka BP. Based on the offset observed in the trench (Fig. 3) and the length of the rupture, we estimate that the earthquake had a magnitude of ~M7.

our mapping showed that the 2-m-high scarp stems from the last earthquake. This landscape reset must have taken place between the two earthquakes, that is between 3.5-37.4 ka BP. It is astonishing that along the 50 km of mapped fault, we found no morphological trace of the penultimate event. If the last surface-rupturing event had not happened, no fault scarp would have testified to the presence of an active fault, even though a large earthquake had ruptured the surface in the last 37.4 ka.

The lesson that we learn from these observations is that the absence of a fault scarp in our study area is not a sufficient condition to state that this fault is inactive.

So far we can only speculate that the widespread landscape reset that we observe is due to an abrupt climatic change at the end of the last glacial maximum (LGM), although this is commonly assumed to have had a major impact on erosion and sedimentation rates. A test for this hypothesis would be the dating of many cumulative fault scarps in the region or an extensive trenching campaign.

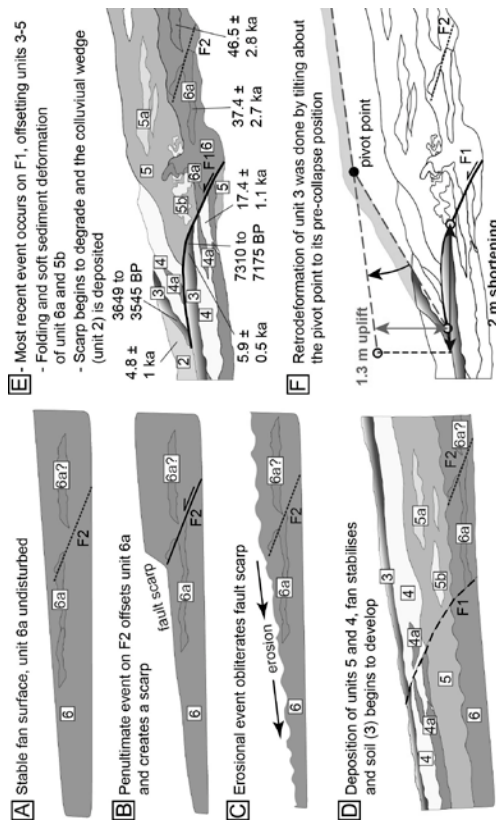


Fig. 3: Trench reconstruction and dating results. We identified two surface-rupturing earthquakes in our trench.

The penultimate event is evident from an offset gravel layer below an erosional unconformity. Our age control allows us to bracket it between 17.4 and 37.4 ka BP. We can only use the offset observed in the trench ( $\geq 0.6$  m; erosion might have erased evidence for more offset) as an input parameter to estimate a minimum magnitude for this earthquake. The paleomagnitude was probably  $> M6.5$ .

We make two important observations here. First, recurrence intervals on single faults can easily exceed 10,000 years, even in an area that is deforming as rapidly as the Tien Shan. Second, erosion has completely obliterated any surficial evidence of the penultimate event since

#### SUUSAMYR VALLEY – VARIABILITY OF THE SURFACE RUPTURE PATTERN

Our second study concerns the Suusamyr Valley in Kyrgyzstan (Fig. 1). In 1992 a crustal thrust earthquake with a magnitude of  $M_s 7.3$  shook the Suusamyr basin, and strong aftershocks occurred throughout the valley immediately after the main event (Mellors et al., 1997). The main shock or both the main shock and the aftershocks produced an interesting pattern of surface ruptures (Ghose et al., 1997; Fig. 4). Along the eastern part of the valley, ruptures were reported with less than 1 m vertical offset for more than 3 km along a N-dipping slope. Our, more accurate, measurements show that they are actually shorter than 3 km. 25 km to the east of this location, another surface rupture occurred in the Suusamyr River valley. These ruptures were more than 3 m high, but are only ~600 m long.

If these quakes had happened few hundred years ago, 21<sup>st</sup> century paleoseismologists would have an interesting puzzle to solve. Mapping and dating the ruptures would lead to results that allow for a certain degree of speculation. How many earthquakes did occur? Did erosion affect the area in between the two sets of ruptures? Should one trench there to search for the continuous rupture? What input parameters would be used for magnitude estimation à la Wells & Coppersmith (1994)? We do not aim to answer these questions here, but we present data that may help to better understand the uncertainties related to paleoseismology in such a setting.

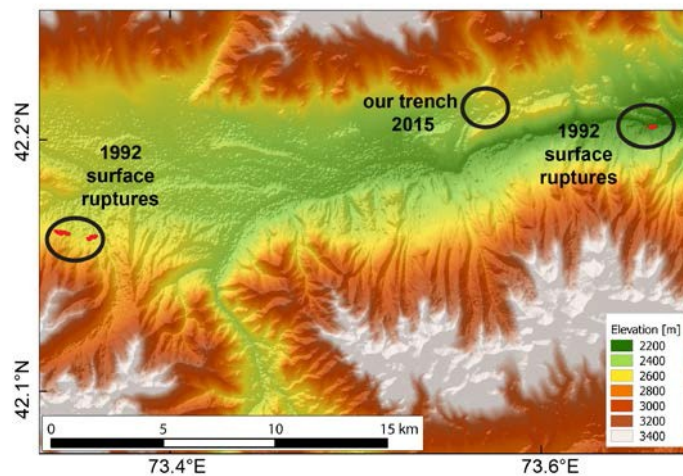


Fig. 4: The Suusamyry study area in Kyrgyzstan, hill-shaded DEM from SRTM1 data.

We mapped the area between the two surface ruptures and discovered a ~0.5 m high scarp north of an elongated ridge that parallels the Suusamyry River (Fig. 4). Large landslides were triggered along this ridge in 1992, and small grabens opened at its top, either due to coseismic shaking or due to folding. We surveyed the scarp with a drone and produced a DEM that clearly shows that the scarp is not an erosional feature (Ainscoe et al., in prep.). On a south-dipping slope the scarp faces to the north and offsets block fields that we ascribe to old flash flood events.

We opened a short trench there and found evidence for at least two surface rupturing paleo-earthquakes (Fig. 5). The older earthquake must have dammed one of the episodic streams that drain the mountain range, because fine grained, layered sediments ponded against large uplifted boulders. A later event deformed the layered, fine-grained sediments. The stratigraphically lowest of these sediments are around 5.5 ka BP. The undeformed cover is around 3.2 ka BP (both results from radiocarbon dating). This means we have evidence for two surface rupturing earthquakes within probably little more than 6,000 years, in between the surface ruptures that were observed in 1992.

These results show that the surface rupture pattern of these shallow thrust earthquakes can be highly variable in the Tien Shan. When we put together all of our data, we now have evidence for three surface rupturing events on the Suusamyry fault system – two paleoearthquakes in the last ~5.5 ka and the 1992 MS7.3 event. Our preliminary data suggest that the recurrence interval here might be less than 2 ka.

## DISCUSSION

Our first example deals with the problem of erosion vs. tectonics in a seismic-active landscape. In the Tien Shan a large

number of active faults take up the overall shortening. Relatively few individual slip rates are precisely known, but in general, they vary between a fraction and a few millimetres per year (e.g., Thompson et al., 2002; Campbell et al., 2013). The climatic conditions in large parts of Central Asia are favourable for preserving morphological evidence for active faulting over long periods, but we show that faults, which are probably rather slow, have recurrence intervals in exceedance of ten thousand years. Thus, surface offsets might be obliterated by pulses of erosion related to abrupt climatic changes. This bears an important lesson for seismic-hazard studies: Even in areas where one would commonly assume that the landscape can be easily read in terms of active fault mapping, the absence of faults scarps does not necessarily prove fault inactivity. One approach to solve this problem would be extensive trenching, but of course in an area like the Tien Shan (more than 2,000 km long and several hundreds of kilometres wide), one cannot easily trench all faults in order to find out which of them has been active in the Late Quaternary. A focus on the main faults combined with strain data from geodetic observations will help identify the fastest faults, but for seismic hazard studies this is often not sufficient.

Our second study shows that surface-rupture patterns can be very complicated. This not only concerns the spatial distribution of ruptures that occur in one particular event, but also the location of ruptures in repeated earthquakes on the same fault system. This must be taken into account when estimating recurrence intervals, the magnitude of slip and stress release, and the assessment of paleo-magnitudes. In the Suusamyry case, the 1992 earthquake event would have gone unnoticed. The fact that not all ruptures reach the surface there may mean that it is a behaviour seen on other faults in the region, too.



INQUA Focus Group on Paleoseismology and Active Tectonics



paleoseismicity.org

Another interesting question is the temporal or mechanical relationship between earthquakes on either side of the Kyrgyz Range, especially since new paleo-earthquake data are now available from that area (Landgraf et al., in review).

bright side: paleoseismic trenching can at least help to narrow down the seismic history of such faults, and modern digital topography techniques like SfM or DEMs stereo satellite data can help to identify subtle evidence of active faulting that has been overlooked in the past.

**Acknowledgements:** This study was financed by the Earthquakes without Frontiers project and the Centre for Observation and Modelling of Earthquakes and Tectonics (COMET). We used the Generic Mapping Tool software by Wessel & Smith (1998). The work in Suusamyry is part of E. Ainscoe's DPhil work.

### References

- Abdrakhmatov, K. Y., Aldazhanov, S. A., Hager, B. H., Hamburger, M. W., Herring, T. A., Kalabaev, K. B., Makarov, V. I., Molnar, P., Panasyuk, S. V., Prilepin, M. T., Reilinger, R. E., Sadybakasovstar, I. S., Souter, B. J., Trapeznikov, Yu. A., Tsurkov, V. Ye., & Zubovich, A. V., (1996). Relatively recent construction of the Tien Shan inferred from GPS measurements of present-day crustal deformation rates. *Nature*, 384, 450 – 453.
- Ainscoe et al., (in prep). Surface effects of the 1992 Suusamyry earthquake and the seismic history of the Suusamyry Basin.
- Campbell, G. E., Walker, R. T., Abdrakhmatov, K., Schwenninger, J. L., Jackson, J., Elliott, J. R., & Copley, A. (2013). The Dzhungarian fault: Late Quaternary tectonics and slip rate of a major right-lateral strike-slip fault in the northern Tien Shan region. *Journal of Geophysical Research: Solid Earth*, 118(10), 5681-5698.
- Ghose, S., Mellors, R. J., Korjenkov, A. M., Hamburger, M. W., Pavlis, T. L., Pavlis, G. L., Omuraliev, M., Mamyrov, E., & Muraliev, A. R. (1997). The Ms= 7.3 1992 Suusamyry, Kyrgyzstan, earthquake in the Tien Shan: 2. Aftershock focal mechanisms and surface deformation. *BSSA*, 87(1), 23-38.
- Grützner, C., Carson, E., Walker, R.T., Rhodes, E., Mukambayev, A., Moldobaev, A., Mackenzie, D., Elliott, J.E., Campbell, G., Abdrakhmatov, K. (in prep). Assessing the activity of faults in continental interiors: palaeoseismic insights from SE Kazakhstan.
- Landgraf, A., Dzhumabaeva, A., Abdrakhmatov, K., Macaulay, E.A., Strecker, M.R., Arrowsmith, JR., Preusser, F., Rugel, G., and Merchel, S. (in review). Repeated large-magnitude earthquakes in a tectonically active, low-strain continental interior: the northern Tien Shan, Kyrgyzstan.
- Mellors, R. J., Vernon, F. L., Pavlis, G. L., Abers, G. A., Hamburger, M. W., Ghose, S., & Iliasov, B. (1997). The Ms= 7.3 1992 Suusamyry, Kyrgyzstan, earthquake: 1. Constraints on fault geometry and source parameters based on aftershocks and body-wave modeling. *BSSA*, 87(1), 11-22.
- Thompson, S. C., Weldon, R. J., Rubin, C. M., Abdrakhmatov, K., Molnar, P., & Berger, G. W. (2002). Late Quaternary slip rates across the central Tien Shan, Kyrgyzstan, central Asia. *Journal of Geophysical Research: Solid Earth*, 107(B9).
- Wells, D. L., & Coppersmith, K. J. (1994). New empirical relationships among magnitude, rupture length, rupture width, rupture area, and surface displacement. *BSSA*, 84(4), 974-1002.
- Wessel, P., & Smith, W. H., 1998. New improved version of Generic Mapping Tools released. *EOS, Trans. Am. Geophys. Un.*, 79(47), 579.

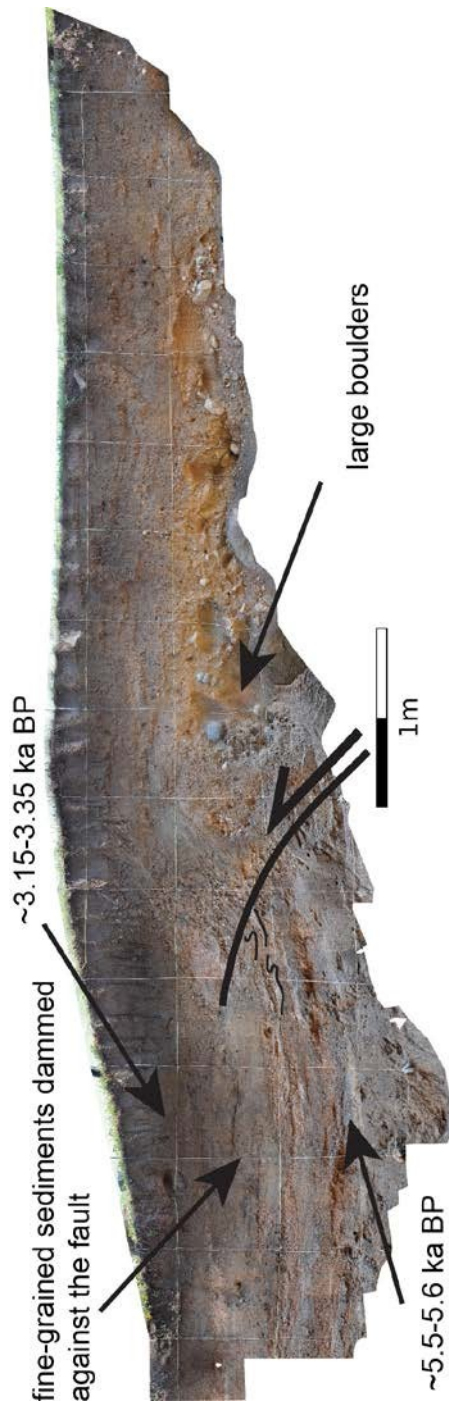


Fig. 5: Preliminary results from the trench that we opened in the Suusamyry Valley with evidence for at least two surface-rupturing earthquakes in the last 5.6 ka.

Although these findings might be rather discouraging for paleoseismological studies, our results do also have



## Fault characterization field campaign related to probabilistic seismic hazard analysis for nuclear infrastructure in the Krško Basin, Slovenia

Jamšek Rupnik, Petra (1), Jure Atanackov (1), M. Logan Cline (2), K. Michael Cline (2), Igor Rižnar (3), Bogomir Celarc (1), Anže Markelj (1), Blaž Milanič (1), Jernej Jež (1), Matevž Novak (1), Miloš Bavec (1)

- (1) Geological survey of Slovenia. Dimičeva ulica 14. SI-1000 Ljubljana, Slovenia. petra.jamsek@geo-zs.si
- (2) Rizzo Associates. 500 Penn Center Boulevard, Pittsburgh, PA 15214, USA.
- (3) Geologic expertises, Igor Rižnar, s.p. Ulica bratov Martinec 40, SI-1000 Ljubljana, Slovenia.

**Abstract:** Fault characterization field campaign is being carried out in Krško, Slovenia, to provide input for probabilistic seismic hazard analysis (PSHA) for a new nuclear power plant. Herein, we present first results from geomorphic study, field structural-geological mapping and geophysical survey targeting the Orlica Fault Zone and Artiče Structure. Orlica Fault Zone is a segmented and distributive transpressional fault zone. The Artiče Structure has been interpreted as north dipping reverse fault with fault propagation folding.

**Key words:** neotectonics, transpression, nuclear, Krško, Slovenia

### INTRODUCTION

The Krško Basin hosts critical nuclear infrastructure and is being investigated as a potential site for several engineering projects including a new nuclear power plant and a low and intermediate level radioactive waste

repository. The Krško Basin lies at the transition between two structural domains: the Sava Folds to the NW and the Mid-Hungarian Shear Zone in the SE (Fig. 1). The basin generally coincides with the post-Miocene Krško Syncline, the southernmost part of the Sava Folds. It trends WSW-ESE and comprises folded Neogene and

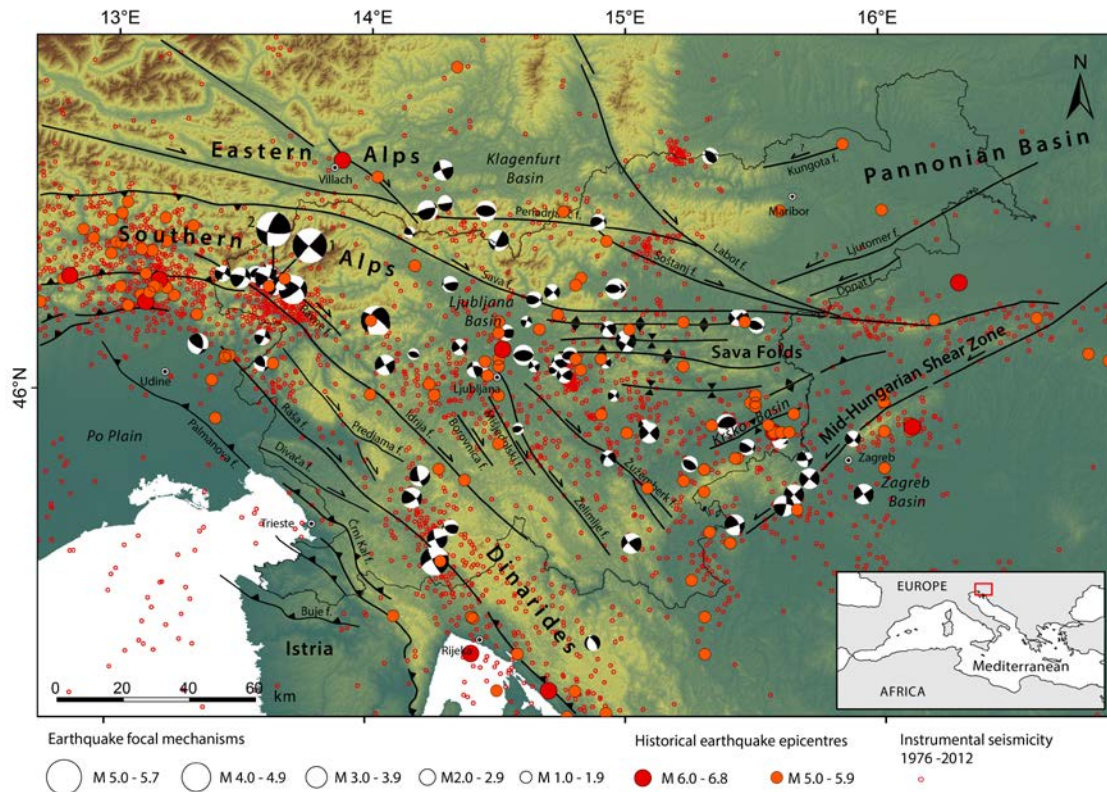


Fig. 1: Seismotectonic map of the Alps, Dinarides and Pannonian Basin contact zone. Instrumental seismicity (ANSS catalogue, 1976-2012), earthquake focal mechanisms (Bajc et al., 2001; Zupančič et al., 2001; Kastelic et al., 2006, 2008; Environmental Agency of Slovenia, yearly reports 2006-2012) and historical earthquake epicentres with estimated  $M > 5$  (Stucchi et al., 2013). Note that catalogue of focal mechanism is only complete for Slovenian territory.



Plio-Quaternary sediments overlying sedimentary Mesozoic basement rocks. Large scale N-S compression, driven by convergence between the Adriatic microplate and European plate, and complex interaction between different crustal blocks has led to a generally transpressional setting of the Krško Basin. Focal mechanisms from moderate and dispersed seismic activity demonstrate reverse to strike-slip fault motion. The strongest historical earthquake in the basin is the Mw 5.7 Brežice event in 1917 (Imax VIII EMS-98), while the strongest documented event in the region (epicenter 40 km SE) was the 1880 Zagreb earthquake, which had an estimated Mw 6.0 (Imax IX EMS-98).

In the northern limb of the Krško Syncline (also southern limb of the Orlica Anticline), two structures appear to exhibit post-Miocene faulting: the Orlica Fault Zone and the Artiče Structure (Fig. 2). These are the particular focus of a field campaign designed to characterize faults for a probabilistic seismic hazard analysis that will be carried out for the proposed NPP. Building upon numerous previous studies (e.g. Persoglia et al., 2000; Geomatrix, 2004; GeoZS, 2010; Rizzo, 2013), we performed morphotectonic analysis based on LiDAR data, field reconnaissance mapping, HRS survey, borings and shallow geophysical surveys.

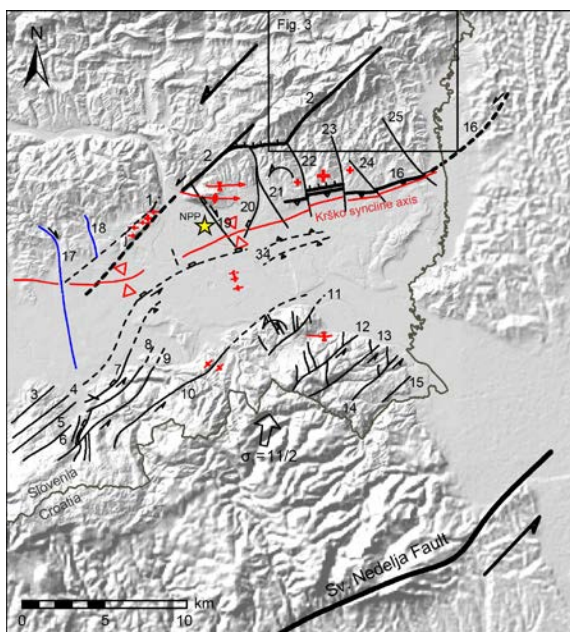


Fig. 2: Tectonic model of the Krško Basin and the extended site vicinity area (GeoZS, 2010). 1-Gric fault, 2-Orlica fault, 3-Rakovnik-Dobe fault, 4-Mali Ban fault, 5-Kocarija fault, 6-Podstrm fault, 7-Zabjek fault, 8-Studena fault, 9-Ostrc fault, 10-Poštena vas fault, 11-Čatež-Brvi structural zone, 12-Goli Cirknik fault, 13-Koritno fault, 14-Ribnica fault, 15-Jesenice fault, 16-Artiče fault/flexure, 17-Lokavec fault system, 18-Senuša fault, 19-Libna fault, 20-Močnik fault1, 21-Močnik fault2, 22-Sromljica fault, 23-Gabrnica fault, 24-Trsnjak fault, 25-Dramlja fault, 34 – Brežice flexure.

## FIELD MAPPING OF ORLICA FAULT ZONE

Detailed geomorphic analysis based on LiDAR data using a suite of techniques are presented in the accompanying contribution for this meeting (Cline et al., 2016). Together with field geomorphic and structural geological reconnaissance mapping we identified numerous fault traces with surface expressions forming the northeasternmost part of the Orlica Fault Zone (Fig. 3). Many of the mapped lineaments show strong evidence of faulting, based on field evidence that includes the presence of slickensides, brecciated rock, fault gouge, observations of displaced rock, and other tectonic indicators. Presently, these structures can only be mapped within the bedrock; thus, age determination is extremely limited. Observation of faults is limited to Miocene and older rocks.

Our results suggest the Orlica Fault Zone is a highly segmented zone running mostly within the Orlica Hills, which consists of numerous SW-NE-striking left-lateral faults, and WSW-ENE-striking reverse faults. Based on reconnaissance mapping and lineament analysis, the longest single fault segment observed at the surface is approximately 3 km long.

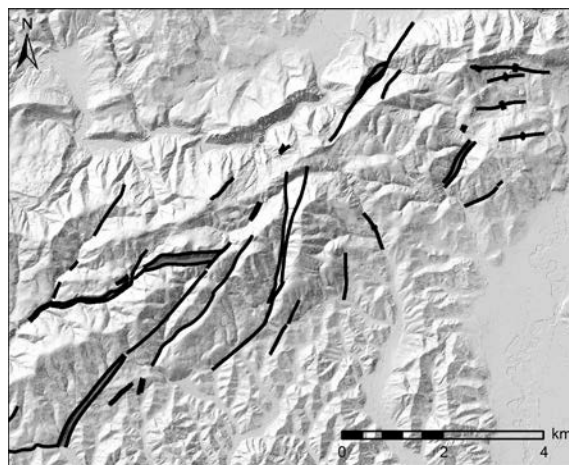


Fig. 3: Northeasternmost part of the Orlica Fault Zone.

## MOUNTAIN FRONT SINUOSITY ANALYSIS OF ARTIČE SCARP

The Artiče Structure (AS) coincides with the presence of an escarpment that forms the boundary between the Bizeljško Hills and the Krško Basin. The scarp's origin is not well understood for a number of reasons. For the scarp to be an erosional remnant that is fluvial in origin, a significant axial drainage system along the scarp front would be required, but no clear evidence of such a system exists. To provide a geomorphic context on scarp linearity, mountain-front sinuosity analysis was performed along the mapped trace of the AS to differentiate the potential roles that tectonics and climate have played in the origin of the scarp. Mountain-front sinuosity provides a proxy measurement for relative tectonic deformation rates, provided that the



mountain front is derived from a tectonic origin as opposed to other processes that may develop a straight mountain front (e.g., fluvial erosion by axial drainage). This is a quantitative geomorphic method that assesses the level of activity at the mountain front; the mountain front is defined as the transition from range to piedmont (Bull and McFadden, 1977; Silva et al., 2003; Bull, 2007). The mountain-front sinuosity index (Smf) is defined as the ratio between the length of the mountain front along its base (Lmf) and the straight-line length of the mountain front (Ls). The lateral trace of the Lmf occurs at the peak convexity of slope curvature, i.e., the slope break (Bull and McFadden, 1977).

For this study, the slope break at the base of the Artiče scarp and flood plains within the tributary valleys upstream were used to define the mountain front, MF1, which extends for 24.5 km (Fig. 4). MF1 also includes the valley floors of axial watersheds, although inclusion of the valley floors of larger tributaries can produce unnecessarily large values of mountain-front sinuosity index (Smf) if aggradation rates are high (Bull, 2007). To avoid these effects, the broad tributary valley floors (e.g., >third-order Strahler drainages) were omitted from the analysis, and only the undissected valley fronts were used. MF1 was separated into four segments ranging from 1.7 km to 5.3 km in length (Fig. 4).

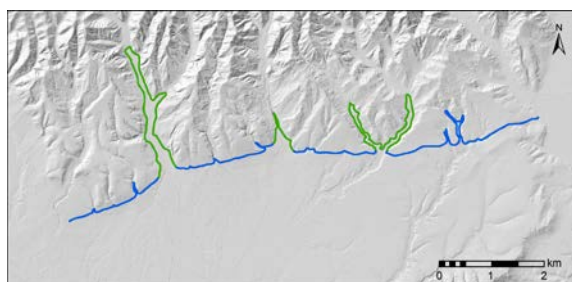


Fig. 4: Mountain front line of Artiče Scarp. Green+blue line is MF1 including valleys. Blue lines are segments of MF1.

Results are presented in Table 1. The Smf 2.68 for the whole MF1 would correspond to Bull and McFadden's (1977) Class 2 or Class 3 mountain fronts, indicating, low rates of tectonic deformation, or inactive mountain fronts, whereas particular segments of MF1 have Smf values between 1.09 and 1.80, which corresponds to Bull and McFadden's (1977) Class 1 and Class 2, active and moderate-to-slightly active mountain fronts, respectively. These results suggest that the escarpment may be of tectonic origin. However, some other geomorphological techniques applied on Artiče scarp do not necessarily support the escarpments tectonic origin (Rizzo, 2013; Cline et al., 2016).

#### HIGH RESOLUTION SEISMIC REFLECTION SURVEY

A "ultra" high-resolution seismic reflection survey was conducted on the Artiče Structure (AS), the Orlica Fault Zone (OFZ) and the minor Sromljica and Gabrnica faults. The survey was done using a 240-channel system and 40

Lmf [m]	Ls [m]	Smf	Notes	Activity Class
24540	9151	2.68	Along the whole MF1	2 or 3
2500	1873	1.33	Segment 1	1
2500	1892	1.32	Segment 2	1
1700	1561	1.09	Segment 3	1
5340	2966	1.80	Segment 4	2

Tab. 1: Results of mountain-front sinuosity analysis.

Hz or 100 Hz geophones, with a 12-gauge seismic shotgun as the primary seismic source and a weight drop as a secondary source. A field test was initially performed to demonstrate the applicability of the ultra HRS methodology to demonstrate the high resolution/quality of acquisition parameter values. All seismic lines produced high-quality data with a very broad frequency spectrum, providing high vertical resolution and high signal-to-noise ratio.

Previous deeper seismic reflection profiles (Persoglia, 2000) indicated the AS is a blind reverse fault with the fault tip at 600-800 m depth, with deformation being accommodated in a wide fault propagation fold in the softer sediments (Pannonian marls, Pontian sands, i.e. Late Miocene) closer to the surface (Rokavec and Markič, 2002). The shallow HRS survey imaged the upper 300 m of the fault propagation fold, indicating minor fracturing within Pontian strata (uppermost Miocene), particularly the coal seams, and folding of PlioQuaternary sediments (Fig. 5). The fault propagation fold is of post-Pontian inception (< 5,3 Ma).

The HRS profile on the OFZ approximately 5 km west of the NPP produced important new structural constraints. Previous deeper seismic reflection profiles (Persoglia, 2000) produced comparatively poor data in the OFZ, but hinted at the presence of a strike-slip zone with minor vertical offsets apparent in the Badenian (middle Miocene) limestone reflectors. The new HRS profile indicated a likely south-vergent reverse main fault, with the fault tip at possibly ~200 m depth and indications of a narrow fault propagation fold extending upward (Fig. 5). North of the main fault a prominent north-vergent backthrust was imaged, reaching shallower than 100 m. This geometry is only indicated at the location of HRS Mrtvi potok profile, while northeastward the OFZ consists of strike-slip and reverse segments. The near-surface extension of OFZ is being investigated with shallower geophysical methods.

#### DISCUSSION AND CONCLUSIONS

The results described here indicate that the OFZ is more segmented than previously thought and depicted on published maps. The segmented nature of the fault zone may affect how it is modelled in seismic hazard analysis.

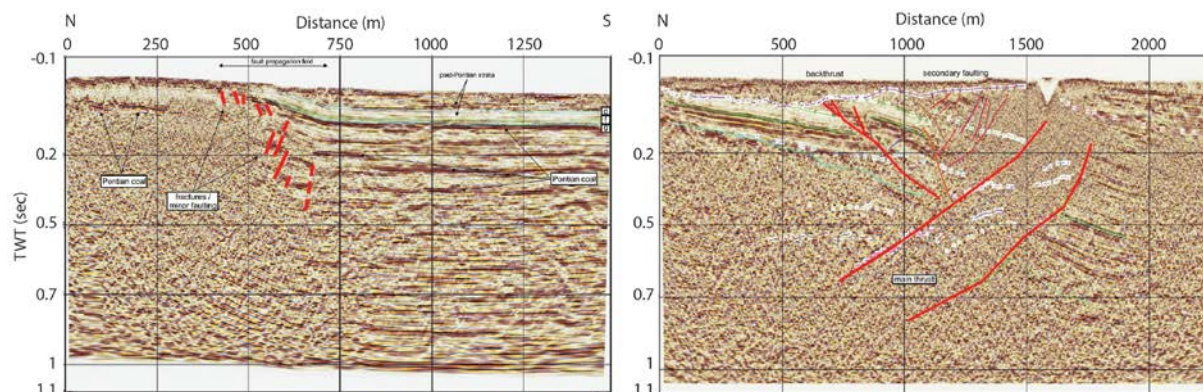


Fig. 5: HRS Artiče B across Artiče Structure and HRS Mrtvi potok across Orlica Fault Zone.

Earthquake magnitude is often estimated from the length of fault rupture. If the OFZ is modelled as a seismic source, the range of earthquake magnitudes it produces may be reduced if fault segmentation limits the extent of individual ruptures.

The results of mountain-front sinuosity analysis suggest the AS is undergoing low rates of deformation. The HRS campaign indicated the AS is a WSW-ENE-striking north-dipping reverse fault, extending into the near-surface as a fault propagation fold. Two potential paleoseismic sites were indicated, to be further targeted by shallower ERT, VES and SRT campaigns.

The HRS campaign provided important new constraints on the Orlica Fault Zone west of the NPP. Where previous geophysics hinted at a wide strike-slip zone, the HRS profile clearly indicated significant reverse components.

For both, AS and OFZ the youngest deformation is of post-Pontian age (< 5,3 Ma) and age dating campaign together with shallow geophysical campaign is ongoing to provide accurate estimation of latest movements. Moreover, morphotectonic mapping and shallow geophysical profiling (ERT, VES and SRT) identified several sites appropriate for paleoseismic trenching, which is undergoing this year.

The study presented here is part of an integrated program to identify and characterize faults in the vicinity of Krško. The integrated results and conclusions of field campaign will support the update of the seismotectonic model for the Krško Basin. The seismotectonic model will form part of the basis for a seismic source characterization model for the updated Krško PSHA.

**Acknowledgements:** This work was performed for the project Seismic hazard analysis for JEK 2, Krško, financed by GEN energija, d.o.o. OGS, Trieste is acknowledged for acquisition and processing of HRS data. Dr. Francesco Maesano provided independent review and interpretation of HRS profiles.

## References

- Bull, W. B., 2007, Tectonic Geomorphology of Mountains: A New Approach to Paleoseismology, Malden, Oxford, Blackwell Publishing, 2007, 316 p.
- Bull, W. B., and McFadden, L. D., 1977, Tectonic Geomorphology N and S of the Garlock Fault, California, A Proceedings Volume of the Annual Geomorphology Symposia Series, Vol. 8, 1977, pp. 115-138.
- Cline, M. L., Cline, K. M., Jamšek Rupnik, P., Atanackov, J., Bavec M., Tectonic geomorphology supporting a probabilistic seismic hazard analysis in the Krško Basin, Slovenia: implications for a critical infrastructure, 7th International INQUA Meeting on Paleoseismology, Active Tectonics and Archeoseismology (PATA), 30 May to 3 June, 2016, Crestone, Colorado, USA.
- Geoloski Zavod Slovenije (GeoZS), 2010, Geotechnical, Geological, and Seismological (GG&S) Evaluations for the New Nuclear Power Plant at the Krško Site (NPP Krško II): Geology – Phase 1, Rev. 1, Ljubljana, Slovenia, October 2010, Geološki Zavod Slovenije: 178 p.
- Geomatrix, 2004, Revised Seismotectonic Model of the Krško Basin, Geomatrix, Oakland, California (Reference PSR-NEK-2.7.1 [Rev. 1]), January 2004.
- Markič, M., and Rokavec, D., 2002, Geološka zgradba, Nekovinske mineralne surovine in lignit okolice Globokega (Krška kotlina), RMZ – Materials and Geoenvironment, 49, 2, 229-226.
- Persoglia, S., Cernobori, L., Gosar, A., Millhan, K., Nicolich, R., Nieto, D., Poljak, M., Terreros, M., Vesnaver, A., and Wardell, N., 2000, Geophysical Research in the Surroundings of the Krško NPP – Final Report. European Commission – DG IA – PHARE, 2000, 68 p.
- RIZZO, 2013, Final Report, Characterization of the Libna Fault and Tectonic Framework in the Krško Basin, Krško, Slovenia, 2013, 78 p., 10 Exhibits, 6 Appendices, Pittsburgh, Pennsylvania: Paul C. Rizzo Associates, Inc.
- Silva, P.G., Goy, J. L., Zazo, C., and Bardajm, T., 2003, Fault Generated Mountain Fronts in SE Spain: Geomorphologic Assessment of Tectonic and Earthquake Activity, Geomorphology, Vol. 250, 2003, pp. 203-226.
- Stucchi, M., Rovida, A., Capera, A. A. G., Alexandre, P., Camelbeeck, T., Demircioglu, M. B., Gasperini, P., Kouskouna, V., Musson, R. M. W., Radulian, M., Sesetyan, K., Vilanova, S., Baumont, D., Bungum, H., Fah, D., Lenhardt, W., Makropoulos, K., Solares, J. M. M., Scotti, O., Zivcic, M., Albini, P., Batllo, J., Papaioannou, C., Tatevossian, R., Locati, M., Meletti, C., Vigano, D., Giardini, D. 2013. The SHARE European Earthquake Catalogue (SHEEC) 1000-1899. Journal of Seismology 17: 523-544.



## Issues pertaining to active fault identification in cratonic regions: example from Peninsular India

Biju John

National Institute of Rock Mechanics, Champion Reef PO KGF, Karnataka India, Email: b\_johnp@yahoo.co.in

**Abstract:** The region around Wadakkancheri, in the province of Kerala, India, has been a site of microseismic activity. Geological studies have mapped a NW-SE trending 30 km long south dipping structure and identified a brittle fault zone having multiple fracture sets and slip planes with slicken sides and clay gouges. Four faulting episodes are recognized based on the sequential development of different structural elements in the fault rocks. The fault zone shows a possible characteristic slip of 52 cm, where the gouge records a major neotectonic event. The empirical relationships between fault length and slip show that this fault might have generated events  $M \geq 6$ . The study further identified paleoseismic evidences in the form of sand dikes in the southwestern side of the fault. The present study is a pointer for exploring the discrete active faults in slow deforming cratonic hinterlands, which is vital for seismic hazard assessment for critical infrastructural facilities.

**Key words:** Palghat Gap, Geomorphic anomaly, Brittle faulting, Episodic deformation, Paleoliquefaction.

The region around Wadakkancheri (Fig. 1), a part of Precambrian Palghat–Cauvery shear zone in the province of Kerala, India had not been affected by any major earthquakes in the historical past. However, since 1989, a number of low magnitude earthquakes occurred around Wadakkancheri area. A light earthquake (ML 4.3) occurred near Wadakkancheri on December 2, 1994 caused widespread panic as it induced slight damages (Rajendran & Rajendran, 1995). This earthquake generated minor damage to buildings around the epicentral area and is mostly confined to south of Bharathapuzha River (Fig. 1). The present studies are based on the observations from various active fault and paleoseismic investigations carried out worldwide.

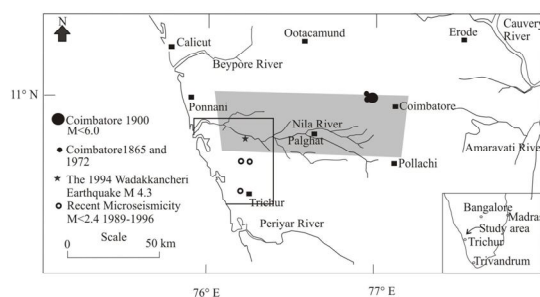


Fig. 1 Map showing locations of regional seismicity, shaded portion is Palghat Gap; study area marked with a rectangle.

The study area lies on the southern flank of the 'Palghat gap' (Fig. 1), a conspicuous E–W-trending linear valley developed within the Proterozoic granulite terrain in South India (e.g. Arogyaswami, 1962; Drury et al., 1984). The west-flowing Bharathapuzha River, occupies the central part of the Gap area (Fig. 2). Regionally, the overall compressive style of Late Proterozoic deformation (900–550 Ma) is preserved in the exhumed low-mid-crustal basement. The youngest deformation dated associated with the shear zone is around  $895 \pm 17$  Ma (Bhaskar Rao et al.,

2006). The higher levels of the crystalline basement are occasionally covered by lateritic regolith and the terraces adjoining the southern riverbank are made up of older alluvium (John, 2003).

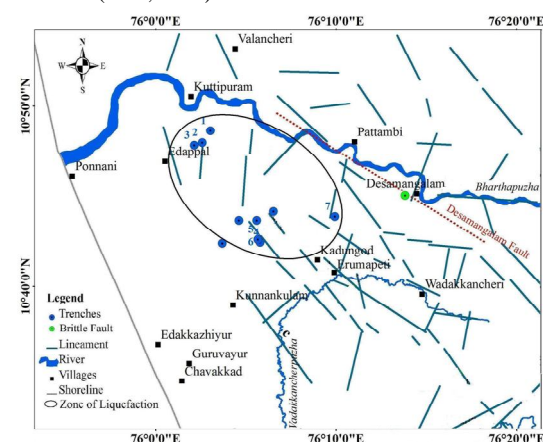


Fig. 2 Detailed view of the study area. The green dot indicate the area shown in figure 4.

The drainage system of the area is mostly controlled by the regionally dominant E–W lineaments associated with the shear zone (John & Rajendran 2008). The main reach of the river follows one such linear feature until it approaches Desamangalam, the site of the 1994 Wadakkancheri earthquake (Fig. 2), where it takes a right angled turn, and follows a NW–SE trend. Morphometric analysis shows a preferred direction of tilt in hanging wall block towards south (Fig. 3). The anomalous zones identified from the analysis of symmetry factors are consistent with the NW–SE structure. The ratio of valley floor width to valley height (Vf) calculated for different reaches indicate that the NW–SE segment of the Bharathapuzha shows relatively narrow valley in comparison to the upper reaches of the river (John & Rajendran 2008). Analysis of satellite image combined with field verification indicates



that the drainage channels in the hanging wall were shifted from their original course, forming paleochannels. There is also a waterfall observed (Fig. 4) associated with the NW-SE trending structure near the fault zone exposed at Desamangalam. Most of the aftershocks detected by India Meteorological Department network (IMD, 1995) subsequent to 1994 earthquakes are also located close to the structure (Fig. 3).

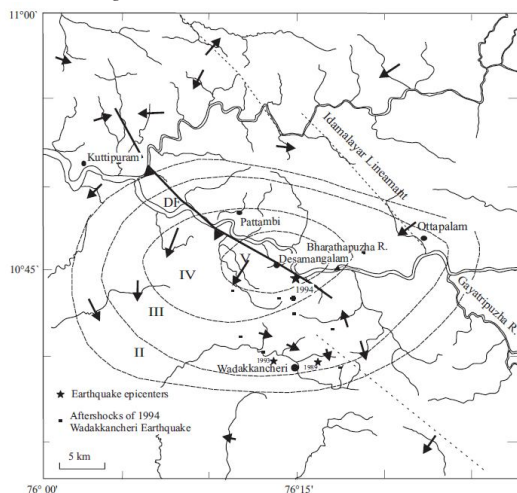


Fig. 3. Sketch showing the locations of geomorphic anomalies and the NW-SE fault. Dashed lines are isoseismals of 1994 earthquakes. Arrows (not to scale) indicate the direction of stream anomalies (shift) deduced from drainage pattern, paleochannels and morphometric analysis. (Modified after John and Rajendran 2008)



Fig. 4 Google earth image showing locations described in the text; closely spaced joint development, waterfall and fault zone (Courtesy [www.google.earth.com](http://www.google.earth.com)).

The fault zone is 6 m-wide and coincides with the foliation that strikes NW-SE with a dip of 45°S (Fig. 5). The fault zone in the bedrock consists of a major slip plane with a gouge and two sub parallel fractures.

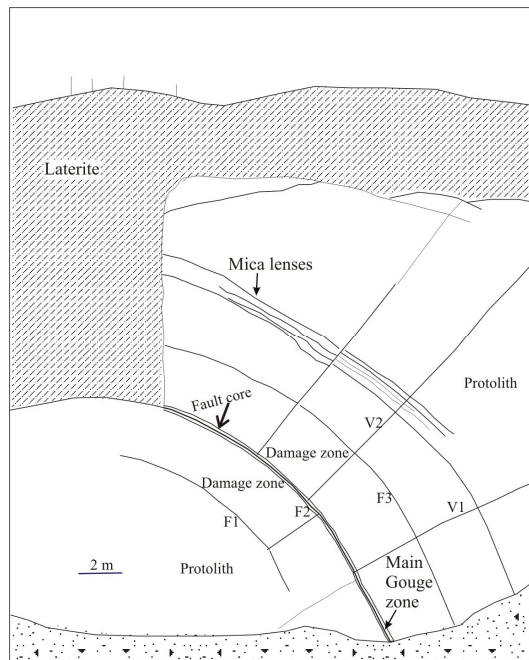


Fig.5 Schematic diagram representing the fault zone; F2: main fault; F1 and F2: fractures V1 and V2: pegmatitic veins. (Modified after John and Rajendran, 2009)

Textural and mineralogical studies identified distinct gouge zones (John and Rajendran 2009). These gouge zones show a wide range of secondary minerals namely, chlorite, muscovite, clinoptilolite and montmorillonite. It is possible that each of these minerals might have formed during the faulting events at different temperature conditions. Close to the principal slip plane, the host rock appears to have been comminuted and the original bulk fabric is completely disturbed, thus generating the gouge material. Most of the fractures within the damaged zone are in sealed condition, filled with either green colored or white colored material resulted from secondary mineralization. Detailed macroscopic examination of fracture fills reveals that there are different types of fractures (John & Rajendran 2009). The different gouge types and fracture fills can be attributed to different episodes of deformation, an inference based on the mineralogy and cross-cutting relations (John & Rajendran 2009). Electron Spin Resonance (ESR) dating of quartz grains isolated from the unconsolidated gouge yielded a Middle-Quaternary date of  $430 \pm 43$  ka for the last event (Rao et al., 2002).

A total displacement of 2.1 m along the plane of the fault is measured in the reverse direction based on the dislocation of pegmatitic veins. Based on the cross cutting relations of fractures and different gouge zones four different faulting episodes are recognised.

Several trenches were excavated in the paleochannels to find out seismogenic features, if any. Close to the sea where water accumulates in the rainy season show thick clay up to 2-3 m whereas much inland few trenches shows presence of riverine sand, some trenches shows the overlying sediments are very thin. In the present study the



dikes are formed from a deeper level (source more than 3 m below) and are abundant in 15 km wide zone (John et al., 2014). The dikes identified shows very thick tabular to thin tubular in shape (Fig. 6 & 7). All the criteria to confirm these as formed due to seismic shaking (Obermeier, 2009) were evaluated.

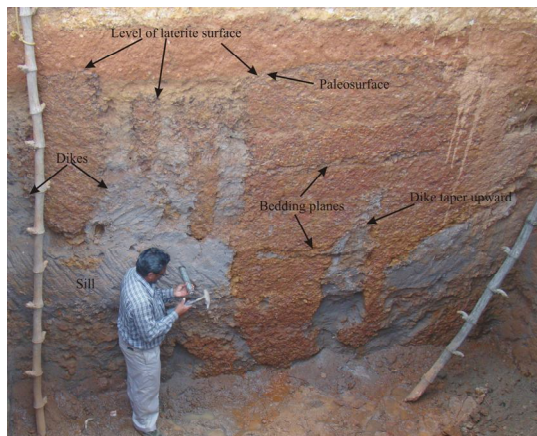


Fig. 6 The western wall of the 4 m deep well showing sand injected upwards through weathered sediments. Note the overlying material is recent dumped material.

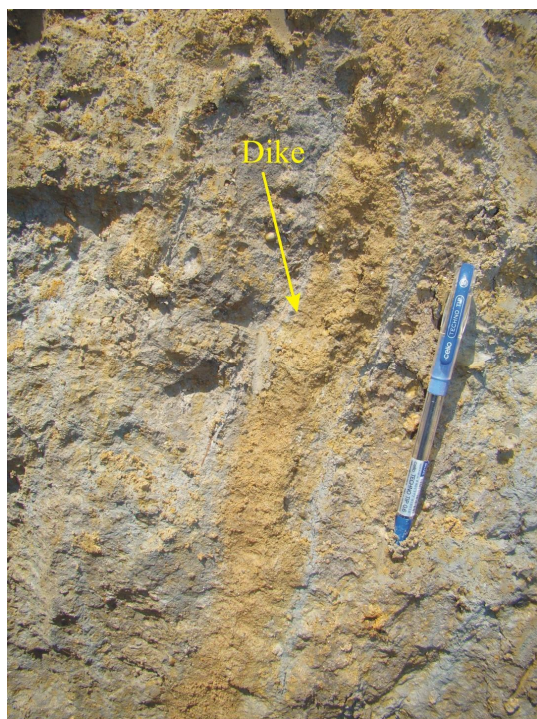


Fig. 7 close up of the sand dike observed in on of the trench

The discovery of liquefaction features is first of its kind reported from Peninsular India, other than Kutch region.

Historical and recent data suggest that a few earthquakes have occurred elsewhere in the vicinity of Palghat Gap between 1865 and 2007, including a probable moderate

event near Coimbatore in 1900 (Rajendran et al., 2009 Fig. 1). With this limited data we tried to find out the possible magnitude of earthquake that might have produced by this fault. Initially we used empirical relationship developed by Wells & Coppersmith (1994) between moment magnitude ( $M_w$ ) and surface rupture length (SRL).

$$M_w = 5.08 + 1.6 \text{ Log (SRL)}$$

Based on this relation, this fault that could rupture up to a length of 30 km may produce an earthquake of magnitude above 6.7.

For an earthquake of  $M=6.0$ , the average slip and rupture length are calculated to be 40 cm and 10 km, respectively Sibson (1989). The present study shows a cumulative displacement of 2.1 m, at the fault exposure, produced by at least four episodes of faulting. That means an approximate of 52 cm of slip in each event if we consider the fault shows a characteristic slip at this location, which according to the Sibson (1989) might have associated with an earthquake of magnitude  $M>6$ .

The Empirical relation (Wells & Coppersmith 1994), between average displacement (AD) and magnitude ( $M_w$ ) as follows.

$$M_w = 6.93 + 0.82 \text{ log (AD)}$$

Based on this relation, an average displacement of 52 cm would produce an event of magnitude  $\sim 6.6$ , which could be damaging event for the area. Investigations of the surface rupture of Peninsular India earthquake at Killari ( $M_w$  6.3) indicate a maximum near surface slip of 80 cm and an average slip of 50 cm (Rajendran et al., 1996).

The minimum earthquake magnitude to form liquefaction features in most field settings is about moment magnitude  $M$  5.5 (Ambraseys, 1988; Carter & Seed, 1988). The liquefaction features identified in the present study indicate that the dikes are cutting more than 3m thick overlying sediments. This may imply that the  $M>6$  is required to produce liquefaction of this scale near the epicentral area.

The present study shows that the subtle expressions of active faults within a discretely reactivated ancient shear zone of the Indian peninsular shield can be identified in the field using a combination of geological tools. The study initially identified a prominent NW-SE lineament and the geomorphic anomalies associated with that structure, which forced the local river to follow anomalous courses at Desamangalam, a site also known for recent spate of low magnitude earthquakes. The evidence of brittle faulting was obtained in a quarry section exposed in the NW-SE-trending hillock within the seismic source zone. The field and laboratory data show that the faulting at this site is a product of cumulative deformation episodes. Our evaluation based on the fault length and slip suggests that the failure of this fault can produce a maximum magnitude close to 6.5. Since, the local low level seismic activity can be related to this fault, the evidence of paleoliquefaction features may confirm the seismic potential of the fault.

**Acknowledgements:** Author thank the Director NIRM for his support, encouragement and the facility provided for the study. Author also thank the financial assistance from DST SERC project award no SR/S4/ES434/2009.



## References

- Ambraseys, N.N. (1988). Engineering Seismology, *Earthquake Engineering and Structural Dynamics*, Elsevier, Amsterdam 17, 1 – 105.
- Arogyaswami, R.N.P. (1962). The origin of the Palghat Gap. *Rec. Geol. Sur. India* 93, 129-134.
- Bhaskar R.Y.J., T.R.K. Chetty, A.S. Janardhan & K. Gopalan, (1996). Sm-Nd and Rb-Sr ages and P-T history of the Archaean Sittampundi and Bhavani layered meta-anorthosite complexes in Cauvery shear zone system, South India. Evidence for Neoproterozoic reworking of Archaean crust. *Contributions to Mineralogy and Petrology* 125, 237-250.
- Carter, D.P., Seed, H.B., (1988). Liquefaction Potential of Sand Deposits Under Low Levels of Excitation: Report No. UCB/EERC-81/11. *College of Engineering, Univ. of California, Berkeley*. 119 p.
- Drury, S.A, N.B.W. Harris, R.W. Holt, G.J. Reeves-Smith & R.T. Wightman, (1984). Precambrian tectonics and crustal evolution of south India. *J. Geology* 92, 3-20.
- GSI (1992). Quadrangle Geological map 58B.
- IMD (1995). Report on micro earthquake survey in Trichur District, Kerala. 18p.
- John, B., (2003). Characteristics of near surface crustal deformation associated with shield seismicity: two examples from peninsular India. *Unpublished PhD thesis*.
- John, B., Rajendran, C.P. (2008). Geomorphic indicators of Neotectonism from the Precambrian terrain of Peninsular India: A study from the Bharathapuzha Basin, Kerala. *J. Geol. Soc. India* 71, 827-840.
- John, B., Rajendran, C.P. (2009). Evidence of episodic brittle faulting in the cratonic part of the Peninsular India and its implications for seismic hazard in slow deforming regions *Tectonophysics* 471, 240-252.
- Obermeier, S.F., (2009). Using Liquefaction-induced and other soft sediment features for paleoseismic analysis. In Paleoseismology Ed. J.P McCalpin, *International Geophysical series* 95, 497-564.
- Rajendran, C.P., K. Rajendran & B. John, (1996). The 1993 Killari (Latur), Central India earthquake: An example of fault reactivation in the Precambrian crust. *Geology* 24, 651- 654.
- Rajendran, K., Rajendran, C.P. (1995). A report on the December 2, 1994 Earthquake. Technical Report, Centre for Earth Science Studies, 34p.
- Rao, T.K.G., C.P. Rajendran, G. Mathew & B. John (2002). Electron spin resonance dating of fault gouge from Desamangalam, Kerala: Evidence for Quaternary movement in Palghat gap shear zone. *Proc. Indian Acad. of Sciences (Earth and Planetary sciences)* 111, 103-113.
- Sibson, R.H., (1989). Earthquake faulting as a structural process. *J. Struc. Geol.* 11, 1-14.
- Wells, D.L., Coppersmith, K.J., 1994. New empirical relationships magnitude, rupture length, rupture width rupture area and surface displacement. *Bull. Seis. Soc. Am.* 84, 974-1002.



## Reconnaissance geologic observations along the Petersen Mountain fault zone northwest of Reno, Nevada, U.S.A

Rich D. Koehler (1)

(1) Nevada Bureau of Mines & Geology, University of Nevada Reno, 1664 N. Virginia St., MS 178, Reno, NV, USA. rkoehler@unr.edu.

**Abstract:** The Petersen Mountain fault zone is a Quaternary active, normal fault system that bounds the eastern side of Petersen Mountain between the Cold Springs and Red Rock Valleys, northwest of Reno, Nevada. In this area, a series of small fault-bounded basins extends between the Sierra Nevada frontal fault system in the west and the northern Walker Lane in the east, collectively accommodating dextral oblique extension. Evidence for late Quaternary deformation includes offset alluvial fan and lacustrine deposits, as well as abrupt range-front escarpments; however the paleoseismic history of the fault is unconstrained. Here, I compile reconnaissance-level geologic observations describing the faults geomorphic expression and age of faulted surficial deposits. The objective of this effort is to identify future paleoseismic research sites to better characterize the fault's source parameters and refine regional seismic hazard models. Preliminary observations indicate the occurrence of at least one latest Pleistocene earthquake and several viable future research sites.

**Key words:** Walker Lane, orthophoto mosaic, geomorphology, fault mapping, seismic hazards

### Introduction

The Petersen Mountain fault bounds the eastern side of the complexly faulted Petersen Mountain horst block and is the westernmost structure in a series of generally north-striking east-dipping faults which bound basins collectively known as the "North Valleys" of Reno, Nevada in the western Basin and Range province, USA (Figure 1). In this region, approximately 15-25% of the Pacific/North American plate boundary strain is accommodated east of the Sierra Nevada through a combination of normal oblique (dextral) slip on the Sierra Nevada frontal fault system and dextral slip along faults in the northern Walker Lane. The North Valleys extend between these two major tectonic elements, and late Quaternary deformation on the basin bounding faults accommodates oblique extension and vertical thinning (Faulds, 2005). Thus, the North Valleys represent a zone of strain transfer and active faulting.

Geologic and geodetic studies indicate that up to 7 mm/yr of dextral shear is distributed across the northern Walker Lane (Hammond et al., 2011; Turner et al., 2008; Gold et al., 2013). Slip rate estimates for the Sierra Nevada frontal fault system range between 0.4-1.0 mm/yr (Ramelli et al., 2003; Hammond et al., 2011). Geodetic studies of the North Valleys estimate that north striking faults collectively accommodate 0.9-1.2 mm/yr of extension and <0.3 mm/yr of dextral slip, with the Petersen Mountain fault zone accommodating ~0.4 mm/yr of extension and 0.1 mm/yr of dextral slip (Bormann, 2013). The North Valleys lack geologic estimates of slip rate and few paleoseismic studies have been conducted. These prior paleoseismic studies have been limited to poorly documented shallow trench excavations and constraints on the age of the most recent event, past event offsets, and recurrence intervals are not available. Despite the general lack of paleoseismic and slip rate constraints, the 2014 update of the National Seismic Hazard Map (NSHM) included faults of the North Valleys using modeled slip

rates ranging between 0.07 and 0.1 mm/yr (Petersen et al., 2014).

The Nevada Bureau of Mines and Geology (NBMG) has begun a multi-year regional effort to better characterize faults within the North Valleys. This effort includes

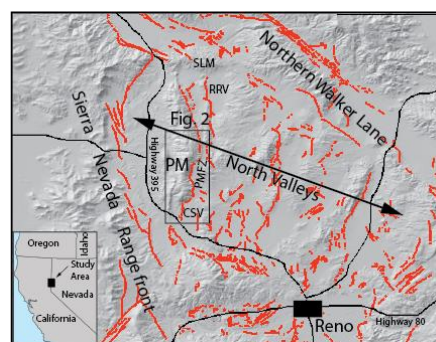


Fig. 1: Regional map showing Quaternary active faults in the North Valleys of Reno, Nevada. PMFZ, Petersen Mountain fault zone; RRV, Red Rock Valley; CSV, Cold Springs Valley; SLM, Seven Lakes Mountain.

neotectonic and geomorphic mapping, paleoseismic trenching, and dating of displaced Quaternary deposits. The ultimate goal of these studies is to provide geologic information to refine regional seismic hazard models.

Lidar data recently became available along many of the faults in the Reno area, however, only the extreme northern and southern parts of the Petersen Mountain fault zone are covered in this dataset. The utility of the lidar data along the southern part of the Petersen Mountain fault is limited due to extensive urban development and topographic modification that has obscured the geomorphic expression of the fault. Recent advances in photogrammetric image processing techniques allow for



the production of 3-dimensional photomosaics and digital elevation models from aerial imagery. A pre-development 3-dimensional photomosaic was produced using low sun angle 1:12,000 scale black and white air photos from the 1970's processed in AgiSoft photoscan software (Figure 2). This model was used to interpret the overall geomorphic expression and continuity of fault scarps and the distribution of late Quaternary deposits along the southern Petersen Mountain fault zone (Figure 3). Here, I briefly summarize previous mapping and geologic investigations along the fault and present the results of this initial reconnaissance Quaternary geologic mapping effort.

## RESULTS AND DISCUSSION

The 25-km-long, north-trending Petersen Mountain fault zone bounds the eastern flank of the Petersen Mountains and extends northward from Cold Springs Valley to Red Rock Valley where it terminates against the northwest trending Seven Lakes Mountain (Figure 1). Down to the east normal displacement along the fault has tilted the Petersen Mountains to the west and has generated over 500 m of topographic relief. Quaternary active traces of the fault were originally mapped by Soeller and Nielsen (1980) and Bell (1984). The southern part of the fault zone in the vicinity of Cold Springs Valley consists of a singular trace characterized by a prominent over-steepened range-front escarpment that juxtaposes bedrock against Quaternary alluvial deposits and basal colluvium (Figure 2). The northern part of the fault zone consists of a western and an eastern strand (Figure 1). The western strand extends across the western



Fig. 2: Orthophoto mosaic of the southern Petersen Mountain fault zone generated by AgiSoft photoscan.

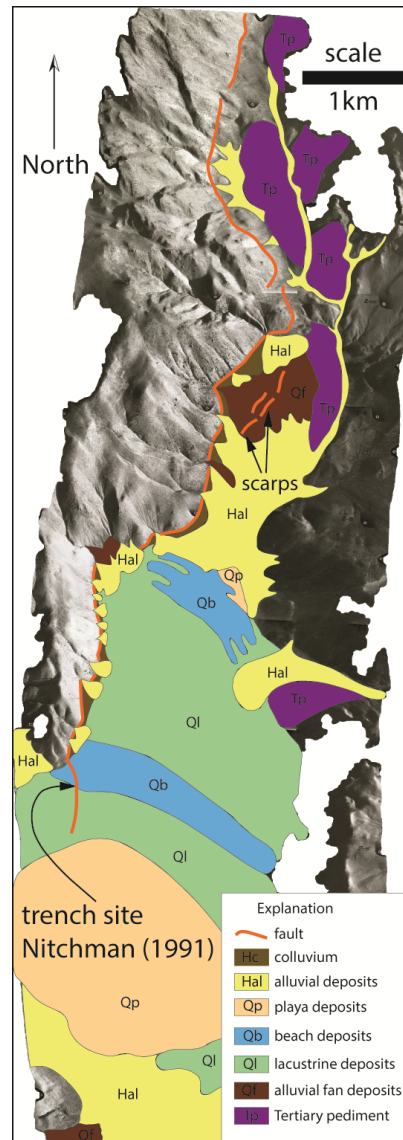


Fig. 3: Quaternary geologic map of the southern Petersen Mountain fault zone.



margin of a short linear inter-mountain valley filled by a Tertiary granitic pediment and becomes a steep faceted range-front to the north. Despite the steep range-front the western strand does not displace late Quaternary deposits along the northern end of the fault. The eastern strand bounds a smaller sub-parallel range, is characterized by discontinuous escarpments in late Quaternary alluvial fan deposits, and has created the Red Rock Valley alluvial basin.

The only previous paleoseismic investigation of the fault was conducted by Nitchman (1991). This study identified a 3-km-long scarp that cuts a late Pleistocene alluvial fan along the northern part of the fault (eastern trace). A profile measured by Nitchman across this scarp indicates that the fan surface has been displaced 5.5 to 6 meters. Nitchman (1991) also measured a profile and excavated a small trench by hand across the fault where it cuts lacustrine deposits at the southern-most extent of the fault in Cold Springs Valley along Cold Springs Road (Figure 2). There, the scarp is 2.8 meters high. The trench exposed two steeply east dipping fault planes that juxtapose sand against warped lacustrine deltaic strata (Figure 4). The results of the investigation were never formally published, but are archived at the Nevada Bureau of Mines and Geology. Information on the history of events and the age of faulted deposits was not evaluated.

The scarp investigated by Nitchman (1991) is clearly evident on 1:12,000 low sun angle aerial photographs taken during the 1970's (Figure 2), however, this scarp has been removed by housing development and is no longer available to conduct additional paleoseismic studies. To search for viable paleoseismic sites, new Quaternary geologic mapping along the southern part of the fault was conducted using a 3D orthophoto mosaic created from the 1970's low sun angle photography (Figure 3). The mapping indicates that lacustrine deposits are weakly developed around the perimeter of the Cold Springs Valley basin, and subtle beach ridges at the northern side of the basin are offset by the fault scarp trenched by Nitchman (1991). Although the age of the lacustrine deposits has not been determined, paleo Lake Laughton occupied the internally drained Cold Springs basin in the late Pleistocene and reached a maximum elevation of 1575 meters (Mifflin and Wheat, 1979). Based on comparison of the morphology and preservation of the shoreline features in Cold Springs Valley with other better studied pluvial lake deposits in western Nevada, I infer that the timing of dessiccation was similar to that of pluvial Lake Lahontan which dessicated after 13 ka (Adams and Wesnousky, 1999). Thus, the Quaternary geologic relations suggest the occurrence of at least one latest Pleistocene earthquake along the Petersen Mountain fault zone.

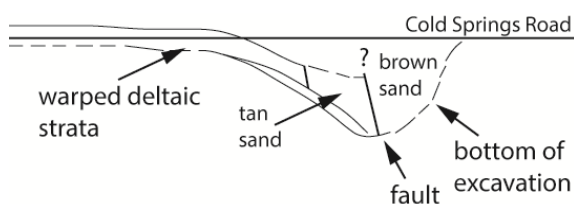


Fig. 4: Paleoseismic trench log redrafted from Nitchman (1991).

Additional mapping observations indicate that young alluvial fan deposits that cross the fault are not displaced (Figure 3). The surface trace of the fault along the range-front is sinuous and has an over-steepened basal escarpment in bedrock that appears to be of similar size to the 2.8-m-high scarp along Cold Springs Road. At one location where the range-front bends to the west, the fault projects across a late Pleistocene fan. The fault is clearly expressed on the fan surface as a dissected scarp for about a kilometer. The fan on the down thrown side of the fault has a smooth surface morphology and is buried by younger alluvial deposits. Upslope of the scarp, the fan surface is deeply incised. Although the age of this fan is unknown, the surface morphology suggests that it is at least several tens of thousands of years old and possibly much older. Due to the general lack of offset alluvial deposits along the fault, this fan represents a viable target for future investigation including fault trenching, offset measurement, and dating of the age of the surface. Future air photo interpretation and field surveys will serve to better characterize the Petersen Mountain fault zone and contribute to refining regional seismic hazard models.

## CONCLUSION

The Petersen Mountain fault zone is an active normal fault in the North Valleys area north of Reno, NV and acts to transfer oblique dextral strain from the Sierra Nevada frontal fault system to the northern Walker Lane. Quaternary geologic mapping along the southern part of the fault zone indicates the occurrence of at least one latest Pleistocene earthquake that offset beach deposits associated with pluvial Lake Laughton. The discontinuous expression of fault scarps along the range-front indicates that the fault is characterized by long recurrence times. An offset late Pleistocene alluvial fan deposit in northern Cold Springs Valley may provide a viable site for future paleoseismic research aimed at better characterizing the slip rate across the fault.

**Acknowledgements:** Discussions with Craig DePolo and Seth Dee of the Nevada Bureau of Mines and Geology helped focus this effort. A thoughtful review by Jayne Bormann of the Nevada Seismological Laboratory is greatly appreciated.

## References

- Adams, K.D., and Wesnousky, S.G., 1999, The Lake Lahontan Highstand: age, surficial characteristics, soil development, and regional shoreline correlation: *Geomorphology*, v. 30, p. 357-392.
- Bell, J.W., 1984, Quaternary fault map of Nevada-Reno sheet, Nevada Bureau of Mines and Geology Map 79, 1 sheet, scale 1:250,000.
- Bormann, J., (2013), New insights into strain accumulation and release in the central and northern Walker Lane, Pacific-North American plate boundary, California and Nevada, USA, Ph.D. dissertation, August 2013, University of Nevada, Reno.
- Faulds, J.E., Henry, C.D., and Hinz, N.H., 2005, Kinematics of the northern Walker Lane: An incipient transform fault along the Pacific-North American plate boundary, *Geology*, 33, 505-508.
- Gold, R.D., dePolo, C.M., Briggs, R.W., Crone, A.J., and Gosse, J., 2013, Late Quaternary slip-rate variations along the Warm Springs Valley fault system, northern Walker Lane, California-



INQUA Focus Group on Paleoseismology and Active Tectonics



paleoseismicity.org

- Nevada border, *Bulletin of the Seismological Society of America*, v. 103, no 1., p. 542-558.
- Hammond, W.C., Blewitt, G., and Kreemer, C., 2011, Block modeling of crustal deformation of the northern Walker Lane and Basin and Range from GPS velocities, *J. Geophys. Res. B Solid Earth Planets* 116, 1-28.
- Mifflin, M.D. and Wheat, M.M., 1979, Pluvial lakes and estimated full pluvial climates of Nevada, *Nevada Bureau of Mines and Geology Bulletin*, 94, 57 pp.
- Nitchman, S.P., 1991 (unpublished), Preliminary fault evaluation report, Nevada Bureau of Mines and Geology.
- Peterson, M.D., and 18 others, 2014, Documentation for the 2014 update of the United States national seismic hazard maps, U.S. Geological Survey Open-File Report 2014-1091, 243 p.
- Ramelli, A.R., dePolo, C.M., and Bell, J.W., 2003, Paleoseismic studies of the Peavine Peak fault, NEHRP Technical Report, 01HQGR0167, 15 pp.
- Soeller, S.A., and Nielson, R.L., 1980, Geologic map, Reno NW quadrangle, Nevada Bureau of Mines and Geology Map 4Dg, scale 1:24,000.

- Turner, R., Koehler, R.D., Briggs, R.W., and Wesnousky, S.G., 2008, Paleoseismic and slip-rate observations along the Honey Lake fault zone, northeastern California, *Bulletin of the Seismological Society of America*, 98, 4, 1730-1736.



## Assembling lidar swaths along the South Island plate boundary, New Zealand: The South Island 'b4' project

Langridge, Robert (1), William Ries (1), Nicolas Barth (2), Jamie Howarth (1), Mark Quigley (3), Tim Farrier (4)

- (1) Active Landscapes Dept., GNS Science, PO Box 30-368, Lower Hutt 5040, New Zealand. Email: [r.langridge@gns.cri.nz](mailto:r.langridge@gns.cri.nz); [w.ries@gns.cri.nz](mailto:w.ries@gns.cri.nz);
- (2) Dept. of Earth Sciences, University of California Riverside, 900 University Ave., Riverside, CA 92521, USA. Email: [nic.barth@ucr.edu](mailto:nic.barth@ucr.edu);
- (3) School of Earth Sciences, The University of Melbourne, Parkville, Victoria 3010, Australia. Email: [mark.quigley@unimelb.edu.au](mailto:mark.quigley@unimelb.edu.au);
- (4) AAM New Zealand, Level 1, 6 Ossian Street, Napier 4110, New Zealand. Email: [t.farrier@aamgroup.com](mailto:t.farrier@aamgroup.com)

**Abstract:** This paper introduces a collaborative approach to building a South Island plate boundary-scale lidar dataset that will benefit New Zealand geoscience research over the short, medium and longer term. Lidar acquisitions totalling c. 400 km of fault length have been undertaken through council, research agency and university funding along the high slip rate faults of the South Island: specifically the Alpine Fault and the main faults of the Marlborough Fault System (MFS) to form the South Island 'b4' dataset. Acquisitions along the Alpine Fault have been used to develop Fault Avoidance Zones and for use in neotectonic studies (geomorphology, shallow structure, slip rate and paleoseismology). A similar suite of research and natural hazard studies have been undertaken along the Wairau, Awatere, Clarence and Hope faults within the MFS. Lidar has proved to be an invaluable tool for mapping and studying these faults, especially in densely vegetated areas. In addition, these data have been acquired before (b4) the occurrence of future large to great earthquakes on these faults. Considering that the Alpine Fault has a conditional probability of failure of ~30% in the next 50 years it is timely to assemble such datasets now as a tool for future earthquake study.

**Key words:** lidar, active faulting, South Island, New Zealand

### INTRODUCTION

Aotearoa-New Zealand sits astride the boundary between the Australian and Pacific plates in the southwest Pacific Ocean (Fig. 1 inset). Rates of tectonic motion across the transpressive South Island portion of the plate boundary range from ~39 mm/year in the NE to ~34 mm/year in the southwest (DeMets et al. 2010; Yeats & Berryman, 1987). Strain release is dominated by large to great ( $M_w$  7 to >8) earthquakes associated with active faults across the width of the island (Wallace et al., 2007; Stirling et al., 2012) as indicated by the historical earthquake record since 1840 A.D. For example, large earthquakes have occurred in several seismo-tectonic provinces (e.g. Marlborough in 1848; NW Nelson in 1929 & 1968, offshore Fiordland in 1998-2009, and in Canterbury in 1888 & 2010) (Downes & Dowrick, 2014). However, from an active faulting perspective the vast majority of strain (in terms of fault slip rate) can be accounted for by the dextral-reverse Alpine Fault and dextral-slip faults of the Marlborough Fault System (MFS) (Fig. 1; Litchfield et al., 2014). In the central and southern South Island, where it is described as an 'isolated plate boundary fault' (Berryman et al., 2012), the Alpine Fault yields late Holocene geologic rates of  $\sim 27 \pm 5$  mm/yr, accounting for roughly 65-85 % of the plate deformation rate (Norris & Cooper, 2001). In the northern South Island the majority of plate motion is taken up by the four main faults of the MFS: the Wairau, Awatere, Clarence and Hope faults (Van Dissen & Yeats, 1991; Langridge et al., 2003) as the northern section of the Alpine Fault partitions away strain to the MFS (Fig. 1). Thus, while a significant amount of research focus is driven toward these high-slip rate faults that form the 'core' of the South Island plate boundary, the short historical record

of seismic release in New Zealand belies a mismatch between strain release in outer seismotectonic provinces versus those in the core of the plate boundary.

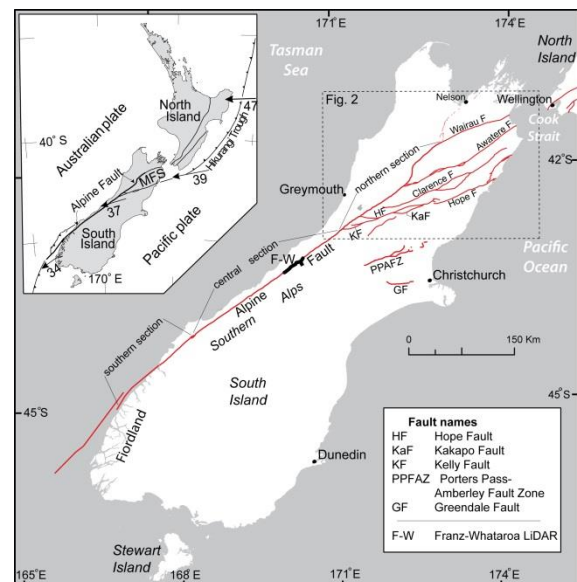


Fig. 1: Simplified active fault map of the South Island, New Zealand highlighting the Alpine Fault and faults of the Marlborough Fault System (MFS, in Inset). F-W is the Franz-Whataroa lidar (in bold) acquired along the centralmost Alpine Fault.

In recent years the adoption of airborne lidar as a viable technology for imaging the New Zealand landscape has led to the piece-by-piece development of a burgeoning South Island-wide plate boundary lidar dataset. The purpose of this paper is to introduce this collaborative



approach to building a plate boundary-scale dataset by highlighting some of its emerging examples of tectonic geomorphology and neotectonic results.

### SOUTH ISLAND LIDAR ACQUISITIONS

Local government councils were the first agencies to acquire lidar in New Zealand with the purpose of covering their territorial areas. The main reasons to acquire lidar were for mapping land-use (e.g. urban, horticulture etc.) and for defining natural hazards (e.g., flood, tsunami). Thus, these dataset areas are polygonal in shape and are typically the largest, covering large areas such as parts of the Canterbury, Wairau and Hanmer plains (Fig. 2). The first lidar acquisitions undertaken for research purposes were funded by the NZ Natural Hazards Research Platform (Hazards Platform) in 2010 (Figs. 1,2). Lidar was acquired amongst the most-densely vegetated areas along the most active faults in New Zealand: the central Alpine Fault, the western and eastern Hope Fault and the Wellington Fault in the Tararua Range (Barth et al., 2012; Beaupretre et al., 2012; Langridge et al., 2014). These studies showed the utility of lidar in bush-covered areas and the level of detail that could be attained. Significant tracts of lidar were acquired across the wider Christchurch area following the 2010-2011 Canterbury earthquake sequence to analyse differential ground and fault movement (Quigley et al., 2010; Duffy et al., 2013).

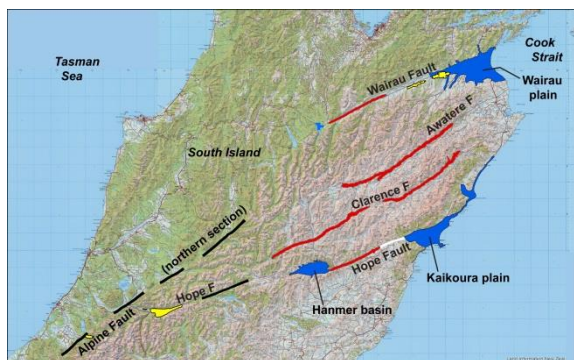


Figure 2: The northern South Island highlighting recent lidar acquisitions within the Marlborough Fault System and northern Alpine Fault. Sources: Council (blue), NSF (red), Hazards Platform (black), French (white), EQC (yellow).

The next major drive in lidar acquisition occurred in 2013. A large US National Science Foundation-funded (NSF) project acquired significant swath lengths of the four key faults within the MFS. These included the western end of the Wairau Fault, part of the eastern and central Awatere and Clarence faults, and part of the eastern Hope Fault (Fig. 2; Zinke et al., 2015). These five swaths account for a length of ~220 km with a typical width of ~1 km, centred about the major mapped trace of each fault (Langridge et al., 2016). As part of this acquisition the NZ Earthquake Commission (EQC) funded an additional 21 km of collection in the middle Wairau valley along the Wairau Fault. Thus, including the Marlborough District Council lidar across the lower

Wairau River area, coverage along the Wairau Fault totalled ~86 km or 82% of its fault length (Fig. 2).

The most recent phase of lidar acquisition in 2015 came from Hazards Platform funding with the purpose of collecting high-resolution lidar data along the northern section of the Alpine Fault (Fig. 2). In this case, four swaths totalling 90 km of length were acquired along less vegetated portions of the fault while densely-forested areas in between with poor access were overlooked. To save on flying costs, a second project piggy-backed along with the Hazards Platform acquisition. Lidar collected along the westernmost end of the Hope Fault and Kelly Fault is a joint venture between the Universities of Canterbury and Melbourne, funded by the EQC. Another research lidar acquisition is planned for the southern section of the Alpine Fault in 2016. In addition, beyond the Alpine Fault and MFS, councils and commercial concerns have acquired significant tracts of lidar in the Canterbury Plains and along the coastline.

### USES OF AIRBORNE LIDAR

Collectively, this combination of local government, research agency and university funded data has led to a semi-continuous dataset of ~400 km of (typically 1-2 km wide) lidar data along the Alpine Fault and throughout the MFS including along the Hope, Kelly, Clarence, Awatere and Wairau faults that together form the South Island 'b4' dataset.

Acquiring and collating such lidar datasets have uses for current and future active fault (neotectonic) studies, mapping to define surface rupture hazard, and in future to assess the differential ground movement from before (b4) and after large surface-rupturing earthquakes in New Zealand. In practice, to garner the best science results and outcomes for New Zealand requires a level of collaboration amongst researchers. Thus while each research dataset has its own license agreement, it is intended that all datasets would be made available for wider use at the appropriate times.

Each lidar dataset has its own intrinsic level of precision that depends upon the sensor used, acquisition conditions, and the density structure of vegetation cover. The South Island displays very large orographic gradients in both rainfall and vegetation cover from west to east. This affects the final product in terms of the pixel size or DEM quality. For example, with an average point spacing of ~7 m under the Franz-Whataroa bush a DEM with a pixel size of 3 m was justifiable (Langridge et al., 2014). In contrast DEMs of sub-1-m accuracy have been possible along the 'drier' Marlborough faults (Zinke et al., 2015).

### CASE STUDIES

So far a wide variety of studies have been undertaken using the available lidar datasets for active fault



mapping, geomorphology, geologic structure, slip rate and paleoseismic studies.

#### Central Alpine Fault

Along the central Alpine Fault on the Franz-Whataroa swath (Fig. 1) research has included documenting the surface geomorphology to develop a model of the shallow segmentation of the dextral-reverse Alpine Fault in that area (Barth et al., 2012; Langridge et al., 2014). This has in part been driven by a desire to understand the surficial structure of the Alpine Fault in proximity to the Deep Fault Drilling Project (DFDP-1 and -2; Sutherland et al., 2012). In addition, trenching studies have sought to understand the timing of the most recent faulting and Holocene slip rates along the highly-partitioned centralmost Alpine Fault (De Pascale & Langridge, 2012).

The Franz-Whataroa swath has also been used in the small tourist town of Franz Josef to assess the hazard posed by surface faulting there (Langridge et al., 2012). In this case the geomorphology of the Alpine Fault has been mapped and a Fault Avoidance Zone of 100 m width has been developed through the town (Fig. 3).



Fig. 3: The town of Franz Josef on the west coast of the South Island. The Fault Avoidance Zone (FAZ) for the Alpine Fault is the pink band that defines an area subject to ground surface fault displacement. The FAZ is 100 m wide and is asymmetrically defined about the fault traces (in red); wider on the hanging wall side. Limits of lidar acquisition are shown by the black lines.

#### Northern Alpine Fault

Lidar-based fault mapping coupled with paleoseismic studies funded through a Hazards Platform project are currently underway along the northern section of the Alpine Fault. These studies set out to document the timing and size of past earthquake rupture events both on-fault from trenching and measurement of displacement and off-fault from lacustrine records. Two surprises that have developed from lidar mapping thus far have been the complex pattern of faulting observed ubiquitously along the fault (Fig. 4), and the preservation of previously unknown large landslide deposits in highly vegetated (beech forested) landscapes.

#### Hope Fault

Studies along the western Hope Fault have included geomorphic and structural studies to understand the

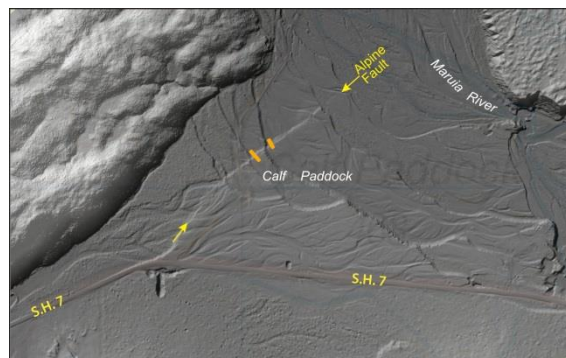


Fig. 4. The Alpine Fault (northern section; marked by yellow arrows) expressed across the Maruia River terraces. The NE-SW striking fault scarp bends toward the south in the area of State Highway 7 (S.H. 7). Recent trenches at Calf Paddock are shown in orange.

effects of topography and local stresses on the tectonic geomorphology of the fault (Khajavi et al., 2014). Environment Canterbury has acquired large lidar datasets covering the Hanmer and Kaikoura plains at either end of the Conway segment of the Hope Fault (Fig. 2). Two separate research swaths along the Conway segment have been used to assess slip along the fault (Beaupretre et al., 2012; Manighetti et al., 2015) and more recently to re-assess the Holocene slip rate at Hossack Station and the paleoseismic record at the Green Burn site (Hatem et al., 2015; Langridge et al., 2003).

#### Clarence, Awatere and Wairau faults

Two long lidar swaths have been acquired along the eastern (67 km) and central (67 km) sections of the Clarence Fault as part of a NSF-funded project to understand the collective behaviour of the four Marlborough faults (Fig. 2). In addition, a 75 km long, continuous lidar swath was also acquired along the eastern and central sections of the Awatere Fault as part of this project. Studies along these faults have thus far involved assessing the fault structure and geomorphology of the Awatere versus Wairau Fault (Zinke et al., 2015), collecting a large set of samples for optical luminescence dating toward deriving sets of slip rates, and paleoseismic studies.

Collectively, several agencies have funded lidar acquisition along much of the Wairau Fault in the Wairau valley. These data are currently being used to re-assess the fault trace mapping in the valley and to develop Fault Avoidance Zones for the Wairau Fault.

## DISCUSSION

The purpose of this paper has been to introduce a collaborative approach to building a plate boundary-scale 'b4' lidar dataset and to highlight some of its emerging examples of hazard and neotectonic studies. The South Island lidar b4 initiative is an informal, forward-thinking approach that looks to establish a set of pre-earthquake datasets that can be used in concert



## INQUA Focus Group on Paleoseismology and Active Tectonics



paleoseismicity.org

with post-earthquake lidar acquisitions to derive datasets of differential ground movement and landscape change. In this sense it follows a similar initiative across California and the western United States (e.g., Bevis et al., 2005). Differential lidar datasets have already been used to profound effect following the 2010 El Mayor-Cucupah earthquake in Baja California (Oskin et al., 2012) and the 2010-2012 Canterbury earthquake sequence in New Zealand (Duffy et al., 2013; Quigley et al., 2010).

Finally, the conditional probability of failure for the Alpine Fault is ~30 % in the next 50 years (Biasi et al., 2015), making it a reasonably likely catastrophic event. This provides the wider research community with a clear goal to continue to acquire a more comprehensive coverage along the main faults of the South Island plate boundary (e.g. more of the Alpine Fault, Kakapo Fault) so that the total surface effects of near-field co-seismic deformation can be detected post-event.

**Acknowledgements:** The authors wish to thank the agencies who have supported lidar acquisition in New Zealand, particularly the Hazards Platform. This paper has been reviewed by Kate Clark and Nicola Litchfield at GNS Science, and by Christoph Grützner from the 2016 PATA Days Scientific Program Committee. We thank them for their useful input.

### References

- Barth, N.C., Toy, V.G., Langridge, R.M., and Norris, R.J., 2012. Scale dependence of oblique plate boundary partitioning: new insights from LiDAR, central Alpine Fault, New Zealand: *Lithosphere* 4, p. 435-448.
- Beaupretre, S. and 10 others, 2012. Finding the buried record of past earthquakes with GPR-based paleoseismology: a case study on the Hope fault, New Zealand, *Geophysical Journal International*, 189, 73-100.
- Berryman, K.R., Cochran, U.A., Clark K.J., Biasi, G.P., Langridge, R.M., Villamor P., 2012. Major earthquakes occur regularly on an isolated plate boundary fault. *Science*, v. 336, 1690-1993.
- Bevis, M., and 9 others (2005), The B4 project: Scanning the San Andreas and San Jacinto fault zones, *Eos Trans. AGU*, 86(52), Fall Meet. Suppl., Abstract H34B-01.
- Biasi, G.P., Langridge, R.M., Berryman, K.R., Clark, K.J., Cochran, U.A. 2015. Maximum-likelihood recurrence parameters and conditional probability of a ground-rupturing earthquake on the southern Alpine Fault, South Island, New Zealand. *Bull. of the Seismological Society of America* v. 105, p. 94-106.
- De Pascale, G.P., Langridge, R.M., 2012. New on-fault evidence for a great earthquake in 1717, central Alpine fault, New Zealand: *Geology* 40, p. 791-794, doi:10.1130/G33363.1.
- DeMets C., Gordon R.G., Argus, D.F., 2010. Geologically current plate motions. *Geophysical Journal International* 181: 1-80.
- Downes, G.L, Dowrick, D.J. 2014. Atlas of isoseismal maps of New Zealand earthquakes – 1843-2003. (2nd edition). Institute of Geological & Nuclear Sciences Monograph 25, Lower Hutt, New Zealand.
- Duffy, B., and 7 others, 2013. Fault kinematics and surface deformation across a releasing bend during the 2010 MW 7.1 Darfield, New Zealand, earthquake revealed by differential LiDAR and cadastral surveying. *GSA Bulletin*, 125: 420-431.
- Hatem, A., Dolan, J., Langridge R, Zinke, R., McGuire, C., Rhodes, E., Van Dissen RJ, 2015. Incremental Holocene slip rates from the Hope fault at Hossack Station, Marlborough Fault Zone, New Zealand. *EOS Transactions, American Geophysical Union*, Fall Meet. 2015.
- Khajavi, N., Quigley, M., Langridge, R., 2014. Influence of topography and basement depth on surface rupture morphology revealed from LiDAR and field mapping, Hope Fault, New Zealand. *Tectonophysics* 630, 265-284.
- Langridge R. M., J. Campbell, N. Hill, V. Pere, Pope, J., B. Estrada, J. Pettinga, and K. Berryman, 2003. Paleoseismology and slip rate of the Conway segment of the Hope Fault at Greenburn Stream, South Island, New Zealand, *Annals of Geophysics*, 46: 1119-1139.
- Langridge, R.M., Traves, M., Ries W. 2011. Designing and implementing a Fault Avoidance Zone strategy for the Alpine Fault in the West Coast region. *Proceedings of the 9th Pacific Conference of Earthquake Engineering*. Paper 202.
- Langridge, R.M., Ries, W.F., Farrier, T., Barth, N.C., Khajavi, N., and De Pascale, G.P., 2014. Developing sub 5-m LiDAR DEMs for forested sections of the Alpine and Hope faults, South Island, New Zealand: Implications for structural interpretations: *Journal of Structural Geology*, doi:10.1016/j.jsg.2013.11.007.
- Langridge RM, and 14 others (2016). The New Zealand Active Faults Database. *New Zealand Journal of Geology and Geophysics* 59 (1). doi:10.1080/00288306.2015.1112818.
- Litchfield, N.J. and 19 others 2014. A model of active faulting in New Zealand. *N.Z. J. Geol. Geophys.* 57: 32-56.
- Manighetti, I., and 9 others, 2015. Recovering paleoearthquake slip record in a highly dynamic alluvial and tectonic region (Hope fault, New Zealand) from airborne LiDAR. *Journal of Geophysical Research: Solid Earth*, 10.1002/2014JB011787.
- McCalpin, J.P. 1996. Tectonic geomorphology and Holocene paleoseismicity of the Molesworth section of the Awatere Fault, South Island, New Zealand. *N.Z. J. Geol. Geophys.* 39: 33-50.
- Norris, R. J. and Cooper, A. F. 2001: Late Quaternary slip rates and slip partitioning on the Alpine Fault, New Zealand. *Journal of Structural Geology* 23: 507-520.
- Oskin ME, and 11 others 2012. Near-field deformation from the El Mayor-Cucupah earthquake revealed by differential LiDAR. *Science* 335: 702-705, doi: 10.1126/science.1213778.
- Quigley M. and 22 others 2010. Surface rupture of the Greendale fault during the Darfield (Canterbury) earthquake, New Zealand: Preliminary Findings. *Bulletin of the New Zealand Society for Earthquake Engineering* 43: 236-242.
- Stirling, M.W. and 19 others, 2012. National Seismic Hazard Model for New Zealand: 2010 Update. *Bull. Seismological Soc. America*, v. 102, p. 1514-1542, doi: 10.1785/0120110170.
- Sutherland R, and 19 others 2012. Drilling reveals fluid control on architecture and rupture of the Alpine fault, New Zealand. *Geology*, v. 40 (12): p. 1143-1146, doi:10.1130/G33614.1.
- Van Dissen, R.; Yeats, R. S. 1991: Hope fault, Jordan thrust, and uplift of the Seaward Kaikoura Range, New Zealand. *Geology* 19: 393-396.
- Wallace LM, Beavan RJ, McCaffrey R, Berryman KR, Denys P 2007. Balancing the plate motion budget in the South Island, New Zealand using GPS, geological and seismological data. *Geophysical Journal International* 168: 332-352.
- Yeats, R.; Berryman, K. R. 1987: South Island, New Zealand, and Transverse Ranges, California: A seismotectonic comparison. *Tectonics* 6: 363-376.
- Yetton, M. D., Wells, A., 2010. Earthquake rupture history of the Alpine Fault over the last 500 years. p. 881-891, in Williams, A.L., et al., (eds.) *Geologically active: delegate papers 11th Congress of the International Association for Engineering Geology and the Environment*, Auckland, Aotearoa, 5-10 September 2010. Boca Raton, Fla: CRC Press.
- Zinke R, Dolan JF, Van Dissen RJ, Grenader JR, Rhodes EJ, McGuire CP, Langridge RM, Nicol A, Hatem A 2015. Evolution and progressive geomorphic manifestation of surface faulting: A comparison of the Wairau and Awatere faults, South Island, New Zealand. *Geology* 43: 1019-1022.



## Seismic activity in SE Korea based on a trench survey (Dangu fault) and historical earthquake data around the Yangsan Fault

Jinhyun Lee (1), Sowreh Rezaei (1), Yeji Hong (1) Jin-Hyuck Choi (2), Jeong-Heon Choi (3), Weon-Hack Choi (4), Kun-Woo Rhee (5), Young-Seog Kim (1)

- (1) Department of Earth & Environmental Sciences, Pukyong National University, Busan 48513, Korea. Email: godgocogo@gmail.com.
- (2) Institute de Physique de Globe de Paris, 1 Rue Jussieu, 75005 Paris, France.
- (3) Geochronology Group, Korea Basic Science Institute, Chungbuk 28119, Korea.
- (4) Central Research Institute, Korea Hydro and Nuclear Power Co., Daejeon 34101, Korea.
- (5) Department of History, Humanities and Social Sciences & Business Administration, Pukyong National University, Busan 8513, Korea.

**Abstract:** Several Quaternary faults have been reported around the Yangsan and Ulsan Fault System in SE Korea. The Dangu fault exposed in trench is located in the northern part of the Yangsan Fault, which is a dextral oblique slip fault with minor reverse slip component. The attitude of the fault and slickenlines on the fault surface are N15°E/79°SE, 015°/15°, respectively. Three gouge bands with different colors developed along the main fault indicate at least three faulting events. We obtained OSL and radiocarbon(C<sup>14</sup>) ages of about 7.5±0.3 ka and 3990±40 B.P in layer C., respectively. Based on the analysis of historical seismicity data from earthquakes in the Gyeongsang-do region, including several big earthquakes around Gyeongju area. Some earthquakes were big enough to generate surface ruptures, although the surface ruptures were not clearly described. Based on the trench survey and historical earthquake data, Gyeongju area is seismically active and more detailed seismic and paleoseismic research is required in this area.

**Key words:** Yangsan fault system, Dangu fault, Quaternary fault, Age dating, Historical earthquake

### Introduction

The Korean Peninsula is located within the eastern part of the Eurasian plate and has been considered seismically stable region. However, since Quaternary faults were first discovered in the SE Korea, many Quaternary faults have been reported within the Korean Peninsula (Oh, 1977; Lee and Na, 1983; Kyung and Chang, 2001; Kyung and Lee, 2006; Choi *et al.*, 2014). In addition, historical earthquakes have occurred several times in SE Korea and some have caused serious damages. The Yangsan Fault system, generally trends NNE-SSW (Fig. 1), and has had at least three strike-slip faulting event and two dip-slip faulting episodes (Chae *et al.*, 1994). In the Pliocene, N-S compression affected the fault, and in the Quaternary, the fault was reactivated by a right-lateral strike-slip movement under an E-W to ENE-WSW (present stress regime in the Korean Peninsula) compression. Several Quaternary faults have been reported around the Yangsan fault system, apparently showing reverse fault geometry in general. Slickensides on fault plane, however, indicate right-lateral strike-slip based on low angle striations. The junction between the Yangsan Fault and the NNW-SSE trending Ulsan Fault is located around Gyeongju City. The Yangsan fault can be divided into northern and southern parts around Gyeongju City. Displacement on the northern part of the Yangsan Fault are younger than those on the southern part of the fault (Fig. 1; Yang, 2006). The northern part of the fault has good evidence of the characteristics of fault interaction and fault's evolution.

### Characteristics and timing of Dangu fault

Dangu fault is located along the northern part of the Yangsan Fault. A lineament analysis in Dangu area show that the dominant trend of lineaments is NNE-SSW direction. In order to study this fault, we excavated two trenches (36° 3' 35.96" N and 129° 15' 14.66" E) in Danguri area, which are almost perpendicular to the lineament. Attitude of the fault and slickenline on the fault surface are N15°E/79°SE, 015°/15°, respectively (Figs. 2, 3). Although the fault shows reverse sense in the cross-section, but the slickenlines indicates dominantly strike-slip movement, which means that the amount of displacement on this fault is possibility quite large.

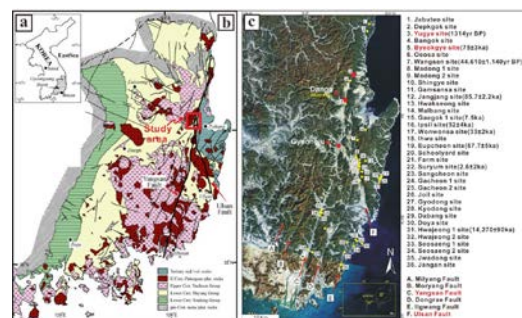


Fig. 1: (a, b) Regional geological map around the study area (modified from Lee, 2000). (c) Distribution of Quaternary fault sites in the southeastern part of the Korean peninsula. The youngest OSL or C<sup>14</sup> ages of the sediments displaced by the faults at each site (marked with numbers within white boxes) are presented in black boxes. The Yugye and Byeokgye sites, located near the studied site, are marked as the site of No. 3 and 5, respectively (modified, Yang, 2006).

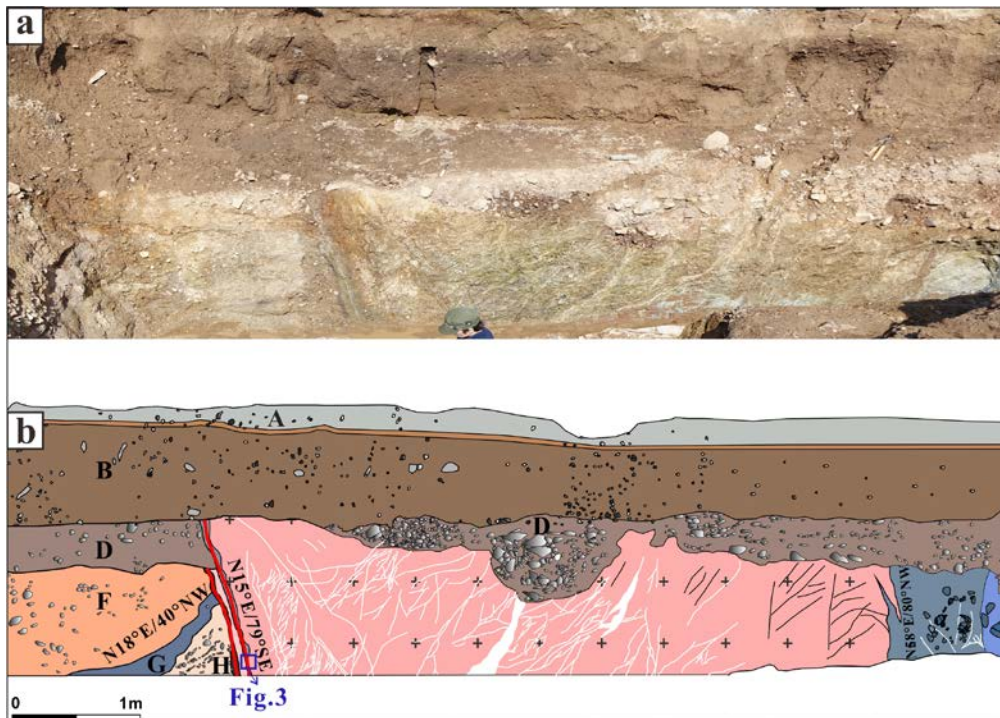


Fig. 2: Trench logs and dated stratigraphy of the trench 1. (a) View of the northern part of the first trench (T1-N), (b) Sketch of the T1-N. Dangu fault (N15°E/79°SE) contact with fine grained granite and Quaternary sediment. Three different fault gouges indicate at least three faulting events. Red line is fault and white line is Quartz vein. Unit A, B, D, F, G and H is Quaternary sediments and Unit G, H is folded by fault.

On the northern wall of the first trench (T1-N), the fault strike/dip between the Cretaceous granite in the hanging wall and the Quaternary deposits in the footwall is N15°E/79°SE, 015°/15° (Fig. 2). Based on grain size, content of matrix, roundness of pebbles, degree of sorting, color of the unconsolidated sediments, we classified the Quaternary sediments as Unit A, B, D, F, G, H. Unit G and H is folded by fault movement. In Unit F, we found some weak evidence of dragging. Three zones of different-colored gouge are present in the fault zone; a black gouge of 5-7 cm width affected Units H, G, whereas a blue gouge of 7-10cm width affected Unit H, G, F and D. Also, a dark green gouge of 10-14cm wide affects Unit H, G and F. These three different gouges may indicate at least three different faulting events.

On the northern wall of the second trench (T2-N), the fault strike/dip is almost the same (N20°E/75°SE) as that in the first trench. We classified the sediments as Unit A, B, C, D, E, F, G. Unit E is clearly cut by the fault and the amount of displacement is around 66cm (Fig. 4). Unit D is dragged by fault movement and the amount of vertical separation is around 67cm. Although the faulting affected up to Unit C, the amount of vertical separation of Unit C is relatively small compared to Unit E, D. It may indicate multiple events and a result of recent faulting event. To estimate the final faulting age, we adopted OSL, radiocarbon(C<sup>14</sup>) and archeological dating (Fig. 4). The age dating results are as follows; 7.5±0.3 ka, 7.4±0.4 ka-OSL; 3990±40yr B. P.-C<sup>14</sup>; AD 1550~1700-archeological estimation. If we trust archeological age

estimate, then the youngest faulting age is around AD1550~1700. We interpreted at least three faulting events in these trenches (Lee et al., 2015). In the first stage, faulting deformed the older sedimentary layers, which were deposited over the granitic host rock. In the second stage, the fault movement caused dragging of Unit E~H. In the third stage, Unit D and C are deposited on the Unit E. In the stage 4-1, as is distinguishable on the trench face T2-N, the fault cut the Units D, C and lower part of the Unit B. In the stage 4-2, faulting

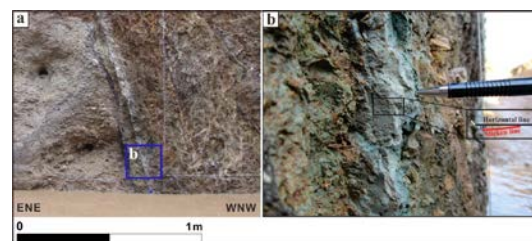


Fig. 3: Close view of T1-N. Black, dark green, green fault gouges are developed along the fault. (b) Slickensite of the Dangu fault (015°/15°) indicates dextral slip.

deformed the Unit D and C. In the last stage, remaining sedimentary layers are deposited on the Unit B or C

### Historical earthquake around the Yangsan Fault

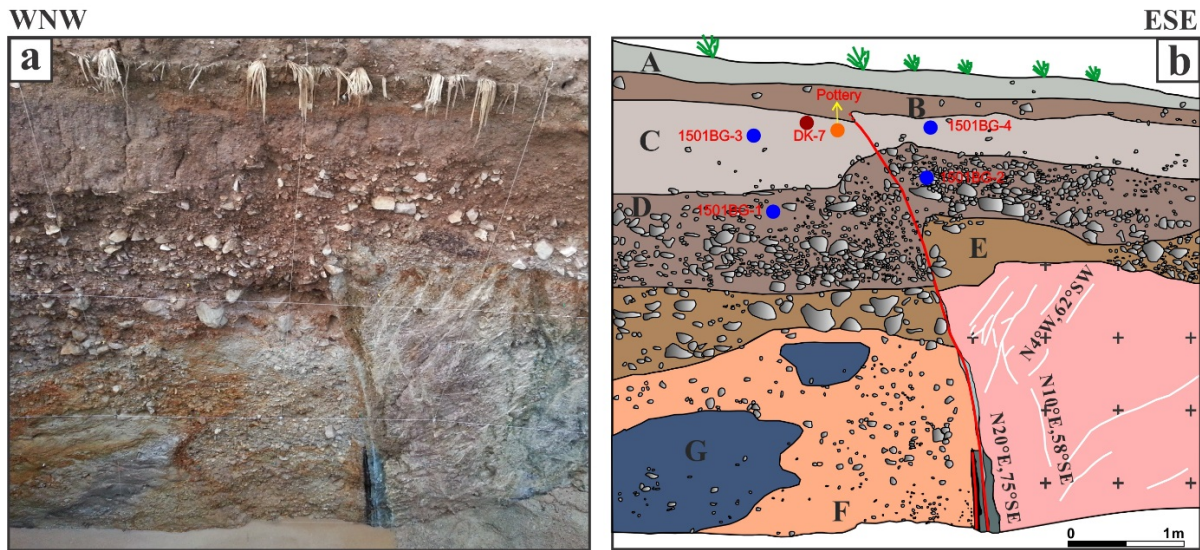


Fig. 3: Trench logs and dated stratigraphy of the trench. (a) View of the northern section of the second trench (T2-N), (b) Sketch of the T2-N. Dangu fault (N20°E/75°SE) is the contact between fine grained granite and Quaternary sediment. Fault is terminated in the upper part of Unit C. Clearly, Unit D and E are displaced by fault. Unit G is isolated inside Unit F. Blue dots are OSL dating points, orange dot represents porcelain point and reddish brown dot is radiocarbon dating point.

Based on the analysis historical seismicity data, many earthquakes occurred in the Gyeongsang-do region. Some of them were big enough to generate surface ruptures. Table 1 list major historical earthquakes occurred around the Yangsan and Ulsan fault system. Unfortunately, however, we do not know exactly where each of the historical earthquakes occurred. However, some previous researches estimated epicenters of each historical earthquakes (Lee, 1998; Kyung, 2011). Some of the historical earthquakes were remarkable; more than 100 casualties were reported from the AD 779 earthquakes in Korean history and had an estimated magnitude of about 6.7 (Lee and Yang, 2006). Another large earthquake occurred in AD 1036 in Gyungju area and destroyed many houses, ancient structures and an estimated magnitude of about 6.4 (Lee and Yang, 2006). Recent archeoseismological research argued that the collapse of a big ancient Buda statue was related with this earthquake (Jin et al, 2011). The AD 1642 earthquake in the Ulsan area might be one of the biggest earthquakes in Korea because it produced surface rupture, liquefaction, and collapse of battlements. The estimated magnitude of this earthquake is around 6.7 (Lee and Yang, 2006). Certainly, many historical earthquakes also occurred in other parts of Korea, however, most of the earthquakes larger than magnitude 6 are concentrated in Gyungju and Ulsan areas. This indicates that the

Yangsan and Ulsan Fault system is the major active seismogenic fault system in Korea.

### Discussion

Many Quaternary faults are present along the Yangsan and Ulsan Fault system (Oh, 1977; Lee and Na, 1983; Kyung and Chang, 2001; Kim and Jin, 2006; Kyung and Lee, 2006; Kee et al, 2007; Kee et al, 2009; Choi et al., 2014). We compiled age information for recent fault activity in the eastern part of the Korean peninsula (Fig. 1; Choi et al., 2012). The ages of faulting along the northern part of the Yangsan Fault are generally younger than those along the southern part of the Yangsan fault. Also, the final movement along the southern part of the Yangsan Fault is dominantly dextral, whereas the Dangu fault has reverse component (N15°E/79°SE, 015°/15°) and the Yougye fault is reverse dominant (Kim and Jin, 2006). So, based on the faulting age and final movement sense, the southern and the northern part of the Yangsan Fault is different segment showing different activities. In addition, historical earthquakes are mainly concentrated in Gyungju area and some of these earthquakes are relatively big compared with other regions in Korea. Instrumental earthquakes (since 1905) magnitude over 6 have not been reported in Korea (Korea Meteorological

Table 1. Major historical earthquake around Yangsan and Ulsan Fault. (Lee and Yang, 2006; the Annals of the Joseon Dynasty)

No.	Year/month/day	Latitude	Longitude	Rejion/description of damages	Magnitude M <sub>L</sub>
1	100/10/	35.8	129.3	Gyungju etc/collapse house and damage of human life	6.7
2	304/9/	35.8	129.3	Gyungju etc/collapse house and damage of human life	6.7
3	510/5/	35.8	129.3	Gyungju etc/collapse house and damage of human life	6.7
4	779/3/	35.8	129.3	Gyungju etc/collapse house and over 100 people dead	6.7
5	1036/7/23	35.8	129.3	Gyungju etc/collapse house, collapse ancient structure, 3 days continue	6.4
6	1643/7/24	35.8	129.3	Ulsan etc/surface rupture, liquefaction and collapse of battlement.	6.7
7	1526/8/7			Gyung etc/shaking house	
8	1525/1/5			Gyung etc/earthquake	
9	1667/4/9			Gyung etc/shaking all of house,	



## INQUA Focus Group on Paleoseismology and Active Tectonics



paleoseismicity.org

Administration, 2016). Therefore, a big earthquake can occur in Gyungju or northern part of the Yangsan fault area and a more detailed seismic and paleoseismic research is required in this area.

### Conclusion

Dangu fault is a dextral oblique slip fault with some reverse slip component. Three different bands of gouge are developed along the main fault indicating at least three faulting events. The age dating results are as follows;  $7.5 \pm 0.3$  ka,  $7.4 \pm 0.4$  ka-OSL;  $3990 \pm 40$ yr B. P.-C<sup>14</sup>; AD 1550~1700-archeological estimation. If we trust archeological age estimation, the final faulting age is around AD 1550~1700. Some remarkable earthquakes are recorded; AD 779, 1036, 1643. Therefore, this result indicates that the high possibility of reactivation exists along the northern part of the Yangsan Fault and around Gyungju city.

### References

- Choi, S.-J., Jeon, J.-S., Song, K.-Y., Kim, H.-C., Kim, Y.-H., Choi, P.-Y., Chwae, U.C., Han, J.-G., Ryoo, C.-R., Sun, C.-G., Jeon, M.S., Kim, G.-Y., Kim, Y.-B., Lee, H.-J., Shin, J.S., Lee, Y.-S., Kee, W.-S., 2012, Active faults and seismic hazard map. NEMA, Seoul, 882 p.
- Choi, S.-J., Jeon, J.-S., Choi, J.-H., Kim, B., Ryoo, C.-R., Hong, D.-G., Chwae, U., 2014, Estimation of possible maximum earthquake magnitudes of Quaternary faults in the southern Korean Peninsula. *Quaternary International* 344, 53-63.
- Jin, K., Lee, M., Kim, Y.-S., Choi J.-H., 2011, Archeoseismological studies on historical heritage sites in the Gyeongju area, SE Korea, *Quaternary International* 242, 158-170.
- Kee, W.-S., Kim, B.-C., Hwang, J.-H., Song, K.-Y., Kihm, Y.-H., 2007, Structural Characteristics of Quaternary reverse faulting on the Eupcheon Fault, SE Korea. *Journal of the Geological Society of Korea*, 43, 311-333 (in Korean with English abstract).
- Kee, W.-S., Kim, Y.-H., Lee, H.-J., Choi, D.-L., Kim, B.-C., Song, K.-Y., Koh, H.-J., Lee, S.R., Gwang, Y.Y., Hwang, S.-H., Park, K.-G., Sung, N.-H., 2009, South eastern fault variable research and DB Construction, KIGAM, Daejeon, 327 p.
- Kim, Y.-S. and Jin, K.M., 2006, Estimated earthquake magnitude from the Yugye Fault displacement on a trench section in Pohang, SE Korea, *Journal of the Geological Society of Korea*, 42, 79-94 (in Korean with English abstract).
- Korea Meteorological Administration, 2016, [http://www.kma.go.kr/weather/earthquake\\_volcano/domesticlist.jsp](http://www.kma.go.kr/weather/earthquake_volcano/domesticlist.jsp) (March 29, 2016).
- Kyung, J.B. and Chang, T.-W., 2001, The Latest Fault Movement on the Northern Yangsan Fault Zone around the Yugye-Ri Area, Southeast. *Journal of the Geological Society of Korea*, 37, 563-577 (in Korean with English abstract).
- Kyung, J.B., Lee, K., 2006, Active fault study of the Yangsan fault system and Ulsan fault system, southeastern part of the Korean Peninsula. Special Volume of the *Journal of the Korean Geophysical Society* 9, 219-230 (in Korean with English abstract).
- Kyung, J.B., 2011, Historical earthquakes catalog and DB (III) Of the Korean Peninsula, Korea Meteorological Agency, 645 p (in Korean with English abstract).
- Lee, K., Historical earthquake data of Korean, *Journal of the Korea Geophysical Society*, 1, 3-22 (in Korean with English abstract).
- Lee, K., and Yang, W.-S., 2006, Historical Seismicity of Korea, *Bulletin of the Seismological Society of America*, 96, 846-855.
- Lee, K.H. and Na, S.H., 1983, a study of microearthquake activity of the Yangsan fault. *Journal of the Geogical society of Korea*, 19, 127-135 (in Korean with English abstract).
- Lee, J., Rezaei, S., Hong, Y., Choi, J.-H., Choi, J.-H., Choi, W.-H., Rhee, K.-W., Kim, Y.-S., 2015, Quaternary fault analysis through a trench investigation on the northern extension of the Yangsan fault at Dangu-ri, Gyungju-si, Gyeongsangbuk-do. *Journal of the Geological Society of Korea*, 51, 471-485 (in Korean with English abstract).
- Oh, G.H., 1977, the geomorphic history of the south-eastern coast of the Korean Peninsula. *Geographical Review of Japan*, 50, 689-699 (in Japanese).



## Integrated InSAR Based Copernicus Ground Motion Service for Germany - Paleoseismic aspects

Thomas Lege (1), Michaela Frei (1), Andre Kalia (1)

(1) Bundesanstalt für Geowissenschaften und Rohstoffe (BGR), (Federal Institute for Geosciences and Natural Resources), Stilleweg 2, D-30655 Hannover, Germany, Email: thomas.lege@bgr.de;

**Abstract:** Though the beneficial use of InSAR methods in tectonics, earthquake analysis and other geologic and geophysical branches is widespread in the scientific community, InSAR is still almost nonexistent in the day-to-day business of federal, state and municipal work and planning. Therefore and due to explicitly expressed demand from user panels, the German government entrusted BGR (Federal Institute for Geosciences and Natural Resources) to keenly foster the integration of national space data together with scientific developments from the InSAR-community in every-day work of German administrative bodies and thus also in small and medium enterprises (SME).

In extensive reconciliation of demands and interests of concurrent technical, administrative, business and juristic responsibilities (e.g. Ministries, Mining Authorities, Geological Surveys, Geodetic Surveys and Environmental Agencies on federal and state level, SMEs, German Aerospace Center) BGR developed the concept of the German InSAR based National Ground Motion Service. The National Ground Motion Service is based on the so-called Wide Area Product (WAP), an extended Permanent Scatterer Interferometry (PSI) algorithm developed with grants from German and European research funds.

With special respect to paleoseismic versus anthropogenic aspects one of the successful implementations of the concept, a study in the area of the Northwest-German gas province, is presented here. The calibration of the WAP dataset is among others based on the integration of geologic and tectonic knowledge. Tectonically, Northern Germany is regarded to be stable, but it turned out that there might be recent slow deformation along faults that are generally assumed to be non-active. Recent slow deformation became evident through the longtime measurements of the regional GNSS-Network along the trace of the so called Aller Valley Fault. The possible interpretation of NW German faults as still active tectonic structures is supported by geological hints of paleoseismic activities in gravel pits and historical earthquake reports.

**Key words:** Remote Sensing, Persistent Scatterer Interferometry, subsidence, Copernicus Service, Sentinel-1

### Introduction

With the advent of radar satellites and the development of Differential Synthetic Aperture Radar Interferometry (DInSAR) it became possible to observe ground

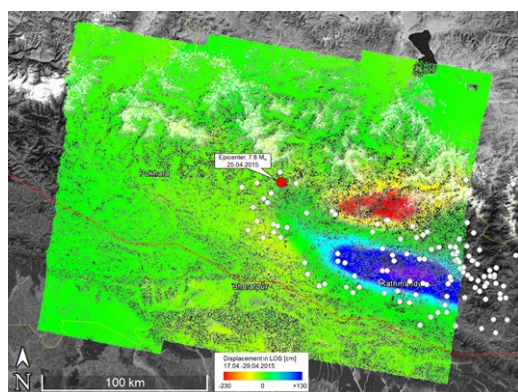


Fig. 1: Gorkha earthquake 25<sup>th</sup> Apr. 2015: Sentinel-1 based DInSAR-application; Ground motion between Apr. 17<sup>th</sup> and 29<sup>th</sup> 2015; white circles shows aftershocks between Apr. 25<sup>th</sup> and 29<sup>th</sup> 2015. Epicentre after USGS 2016.

displacements over large areas of the land surface with millimeter precision (Massonet et al., 1993, Zebker et al.

1994). The surface motion distribution gained by DInSAR allows a detailed documentation of co-seismic crustal deformation and yields important constraints to the backward modelling process of earthquakes and the understanding of the slip distribution on the ruptured fault (Kanamori & Brodski, 2004; Kobayashi et al., 2015, Briole et al., 2015). As an example our result of the Gorkha earthquake ground deformation is depicted in Fig. 1.

Since DInSAR has limitations especially regarding temporal decorrelation and tropospheric noise, several advanced DInSAR algorithms like Persistent Scatterer Interferometry (PSI) and Small Baseline Subset (SBAS) have been developed (Ferretti et al., 1999; Kampes, 2006, Berardino et al. 2002). Several European research projects, e.g. Terrafirma and GMES PanGeo (GMES: Global Monitoring for Environment and Security since 2014 renamed to "Copernicus") showed the maturity of advanced DInSAR techniques to detect surface motions with accuracies comparable to terrestrial levelling (Crosetto et al., 2008, Crosetto et al., 2011, Crosetto et al. 2016). One important result of Terrafirma was the development of the so-called Wide Area Map Product (WAP) (Adam et al., 2011).

Using the WAP a large number of single satellite footprints can be stitched together seamlessly and consistently. In addition to local effects, regional surface



## INQUA Focus Group on Paleoseismology and Active Tectonics



paleoseismicity.org

movements ( $10^5$  km<sup>2</sup>) can be captured and regional patterns can be recognized.

The German Government recognized the widely expressed demand and economic and administrative potential of these InSAR developments in the course of several national space data workshops (Lege, 2014). But how to bridge the gap between research focused project work and affordable, legally robust applications for governmental tasks such as geo-hazard assessment, spatial planning or mining administration?

### The national Copernicus ground motion service

#### National Copernicus ground motion service

For this aim, BGR as the national Geologic Survey of Germany is commissioned to implement a national ground motion service (Kalia et al., 2014). It will provide standardized and validated DInSAR derived products for end-users such as ministries, mining authorities, geological surveys, geodetic surveys and environmental agencies on European, national, state and municipal level as well as for private sector companies. With the launch of the satellite Sentinel-1A and -1B of the EU Copernicus programme in 2014 (-1B/2016) C-Band radar data sets of large parts of the world are available every 12 (6) days. The free and open data policy of the EU Copernicus program allows downloads at no costs. The national ground motion service is based on the Sentinel-1 missions and generates nationwide ground motion maps with precisions of one millimetre per year. The ground

motion data will be available on a BGR web map server in combination with existing geo-scientific maps.

The national Copernicus-service was prepared at BGR. End users, geoscientists, engineers, DInSAR experts and others from numerous institutions were involved extensively. In the following a case study from Northwestern Germany with focus on seismological aspects is discussed.

#### Case Study: Lower-Saxony

Initially the case study was focused on subsidence due to different causes (peat degradation, soft shallow sediment compaction, mining, artificial cavern operation, hydrocarbon production sites and groundwater management). The case study started before Sentinel-1A data were available and is based on ERS-1/2 data. The area of interest is located in the state of Lower-Saxony, NW Germany. A PSI-WAP was generated using five ERS-1/2 tracks, acquired in descending orbit. Each stack of SAR imagery consists of more than 50 scenes in order to enable highly reliable velocity estimates for each persistent scatterer. The SAR imagery covers the time span from 1992 until 2001 (Kalia et al, 2014). The resulting PSI-WAP was verified together with the experts from the state geodetic survey of Lower Saxony (LGLN). Their terrestrial geodetic framework consists of evenly distributed continuous GNSS-stations, gravity measurements and levelling lines (Jahn et al., 2011). The final PSI result of Lower Saxony (Fig. 2) and the GNSS data show consistency of less than a millimetre per year.

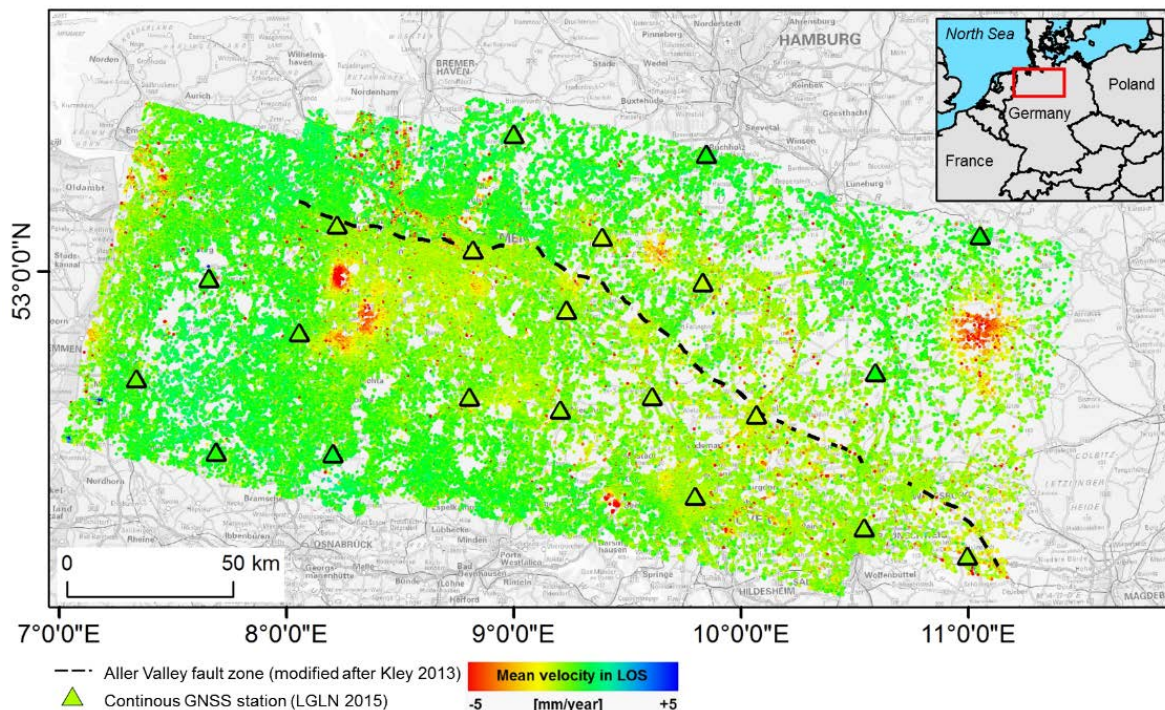


Fig. 2: PSI-WAP of NW Germany, possibly active Aller Valley fault zone and continuous GNSS stations. The color coding for the GNSS stations is the same as for the PSI-WAP. The location of the investigated area is shown by the red rectangle in the inset.



## INQUA Focus Group on Paleoseismology and Active Tectonics



paleoseismicity.org

To validate the WAP results, the processed data were discussed with the mining experts and geologists of the responsible state mining authority (LBEG). All detected local anomalies could be assigned to geological, pedological, mining or engineering-related sources.

### Subsidence on the Regional Level

In addition there are hints to regional subsidence that may be in correlation with the Aller Valley Fault zone as suggested in Fig. 2. The interpretation of the regional ground motion picture may still be subject to change when the WAP covers a bigger area and involves more GNSS stations in the future. We note in this context that preliminary results of re-levelling campaigns of the official German geodetic network (Jahn, 2015; Krickel, 2016) and a study that combined long time tide gauge data with GNSS and levelling data (IKÜS, 2008) indicate downward ground movements in NW Germany in the same order of magnitude as the WAP, though the identified subsiding regions are not congruent.

### *Seismic Hazards in Lower-Saxony*

Until recently the region was treated as an almost aseismic area. Earthquake recurrence intervals of potentially active faults are likely to be exceptionally long, and historical records have never been systematically analysed with respect to earthquakes. Seismic hazard assessment was somehow simplified following the formula: If there was no known earthquake, there will be no earthquake.

The observed subsidence can cause a stress increase at the long assumed inactive Aller Valley fault zone or at other fault zones momentarily outside the WAP-area such as the Osning Fault. Historical earthquakes in this area reached intensities between IV and VI to VII (e.g. 1612 and 1767 at the Osning thrust approximately 100 km south of the Aller Valley Fault; Leydecker, 2011). Brandes & Winsemann (2013) and Brandes et al. (2014) documented paleoseismic evidence in sandpits close to the Osning fault. Brandes et al. (2015) related the quakes to ongoing isostatic adjustments after the last glacial period. Recently Joswig et al. (2016) and Gurbisz et al. (2016) presented evidence of "singular deeper earthquakes beside the majority of shallow probably induced events at reservoir level of gas depletion" in the area of the PSI-WAP. The faint signals of the small earthquakes in depths of 25 – 30 km were recorded by a newly installed seismometer network.

It is postulated that the subsidence of the NW German area accumulates stress that was and possibly will be released by earthquakes in the way described by Kanamori & Brodski (2004). With further research more paleoseismic and historical evidence could be discovered. This information is seen as important for adequate building codes for high risk infrastructure like NPPs and nuclear waste repositories. On the other hand it will ease the discrimination between natural and anthropogenic

earthquakes. The latter can be induced by hydrocarbon production and management, geothermal energy exploitation, mining activities or storage of CO<sub>2</sub>, conventional and renewable energy.

Therefore, we like to encourage efforts to look for further paleoseismic and historical evidence of earthquakes in Lower Saxony. The research should be combined with energy computations concerning the stress build-up and release either in aseismic deformation or via earthquakes. Through the combination of terrestrial measurements and PSI observations, the size of subsiding areas and their movement rates can be better determined. Furthermore, local effects due to fluid extraction, compaction of shallow sediments, mining etc. can be separated from large area isostatic adjustments. It is expected that in NW Germany the combination of stress calculations with paleoseismic and historic earthquake research can yield more exact values of maximum magnitudes and recurrence rates of earthquakes that are characteristic for the NW German region. Eventually this will lead to a better earthquake hazard analysis for the region.

### Discussion and Conclusions

The German National Ground Motion Map generated by a combination of space borne PSI-WAP surface motion data and selected well distributed continuous GNSS stations can monitor ongoing regional movements in NW Germany that can build up stress. If the stress builds up over centuries and millenia it can be released via earthquakes at existing faults that are widely assumed to be inactive nowadays. Paleoseismic evidence (Brandes and Winsemann, 2013) coincides with sparse historical records of earthquakes in NW Germany (Leydecker, 2011). There is evidence that earthquakes with macroseismic epicentral intensities  $I_0$  between IV and VI happened close to main fault lines. Currently the data base is not sufficient to derive recurrence periods and maximum magnitudes. We recommend investigating if the stress build-up due to the large area subsidence is released aseismically or if it accumulates. Further work should be invested into the calculation of the cumulative energy balance of released stress by earthquakes and the stress built up by the measured crustal deformation. This should be correlated to the average energy release of paleoseismic and historic events to improve estimations of recurrence periods and maximum magnitudes. It is expected that with the completion of the German National Ground Motion Service similar analysis will be easier for more regions in Germany.

**Acknowledgements:** The authors like to thank C.-H. Jahn from the state geodetic survey of Lower Saxony (LGLN) for in depth discussions of geodetic accuracies, J. Fritz from the state mining authority (LBEG) for mining and geological advice and N. Adam from German Aerospace Center (DLR) for backing PSI-WAP-Processing.



## INQUA Focus Group on Paleoseismology and Active Tectonics



paleoseismicity.org

### References

- Adam, N., Rodriguez Gonzalez, F., Parizzi, A., Liebhart, W. (2011). Wide Area Persistent Scatterer Interferometry: Algorithms and Examples, *Proceedings of Fringe 2011*, 1 - 5, Noordwijk, The Netherlands.
- Berardino, P., Fornaro, G., Lanari, R. and Sanosti, E. (2002). A New Algorithm for Surface Deformation Monitoring based on Small Baseline Differential SAR Interferograms, *IEEE Transaction on Geoscience and Remote Sensing*, 40 (11), p. 2375 - 2383.
- Brandes, C., Winsemann, J. (2013). Soft-sediment deformation structures in NW Germany caused by Late Pleistocene seismicity. *Int J. Earth Sci* 102:2255-2274.
- Brandes, C., Steffen, H., Bönnemann, C., Plenefisch, T., Gesteremann, N., Winsemann, J. (2014). Aktive Tektonik in Norddeutschland: glazial-isostatische Ausgleichsbewegungen und/oder Folgen der Erdöl/Erdgas-Förderung? *ERDÖL ERDGAS KOHLE* 130. Jg. 2014, Heft 4, 138-143.
- Brandes, C., Steffen, H., Steffen, R., Wu, P. (2015). Intraplate seismicity in northern Central Europe is induced by the last glaciation. *Geology*, July 2015, v. 43; no. 7, 611-614
- Briole, P., Elias, P., Parcharidis, I., Bignami, C., Benekos, G., Samsonov, S., Kyriakopoulos, C., Stramondi, S., Chamot-Rooke, N., Drakatos, M.L., Drakatos, G. (2015). The seismic sequence of January-February 2014 at Cephalonia Island (Greece): constraints from SAR interferometry and GPS. *Geophys. J. Int.*, 203, 1528-1540.
- Crosetto, M., Crippa, B., Biescas, E., Monserrat, O., Agudo, m., Fernandez, P. (2008). Quality assessment of advanced interferometric products based on time series of ERS and Envisat SAR data. *Photogrammetric Engineering and Remote Sensing* 74(4).
- Crosetto, M., Monserrat, O., Cuevas, M., Crippa, B. (2011). Spaceborne differential SAR interferometry: data analysis tools for deformation measurement. *Remote Sens.* 3, 305-318.
- Crosetto, M., Monserrat, O., Cueva-Gonzales, M., Devanthery, N., Crippa, B. (2016). Persistent Scatterer Interferometry: A review. *ISPRS J. of Photogramm. Remote Sens.* 115, 78-89.
- Ferretti, A., Prati, C. and Rocca, F. (1999). Permanent Scatterers in SAR Interferometry. *Proceedings of IGARSS 1999*, 1528-1530, Hamburg, Germany.
- Gurbisz, Z., Mokolke, G., Walter, M., Sick, B., Blaschek, P., Joswig, M., (2016). Recent seismicity in the Rotenburg region - high-resolution monitoring and reprocessing results. In *Abstractband DGG 76. Jahrestagung*, 14.-17. Mrz. 2016 DOP-Nr: 10.2312/dgg76, Münster, Germany.
- Hooper, A., Zebker, H., Segall, P. and Kampes, B. (2004). A new method for measuring deformation on volcanoes and other natural terrains using InSAR persistent scatterers. *Geophysical Research Letters* 31, L23611.
- IKÜS (2008). Aufbau eines integrierten Höhenüberwachungssysteme in Küstenregionen durch Kombination höhenrelevanter Sensorik (IKÜS). *Final Report, TU Dresden, FKZ 03KIS055*, 172p.
- Jahn, C.-H. (2015). Aktuelle Entwicklungen im geodätischen Raumbezug Deutschlands. *FuB Flächenmanagement und Bodenordnung*, 77, 5, 201-208.
- Jahn, C.-H., Rubach, J., Elsner, C., Schenk, A., Wagenführ, P., Dick, H.-G., Brünner, A. (2011). Das SAPOS®-Qualitätsmanagement der Arbeitsgemeinschaft der Vermessungsverwaltungen der Länder der Bundesrepublik Deutschland, in *ZfV* 3/2011, S. 127-137.
- Joswig, M., Gurbisz, Z., Mokolke, G., Sick, B., Blaschek, P., Walter, M. (2016). Rezente Seismizität im Raum Rotenburg – hochauflösende Messungen und Ergebnis des Reprocessings. In *Tagungsband DGMK/ÖGEW-Frühjahrstagung 2016*, ISBN 978-3-941721-64-7, in print.
- Kalia, A.C., Frei, M., Lege, T. (2014). Preparation of a national Copernicus service for detection and monitoring of land subsidence and mass movements in the context of Remote Sensing assisted hazard mitigation. *Proc. SPIE 9245, Earth Resources and Environmental Remote Sensing/GIS Applications V*, 924508 (December 1, 2014).
- Kampes, B. (2006). Radar Interferometry: Persistent Scatterer Technique, *Springer*.
- Kanamori, H., Brodski, E.E. (2004). The physics of earthquakes. *Rep. Prog. Phys.* 67, 1429-1496.
- Kley, J. (2013). Saxonische Tektonik im 21. Jahrhundert. [“Saxonian tectonics” in the 21st century.] – *Z. Dt. Ges. Geowiss.*, 164: 295-311, Stuttgart.
- Kobayashi T., Morishita, Y., Yarai, H. (2015). Detailed crustal deformation and fault rupture of the 2015 Gorkha earthquake, Nepal, revealed from ScanSAR-based interferograms of ALOS-2, *Earth, Planets and Space*, 67:201.
- Krickel, B. (2016) Nachweis von regionalen Höhenänderungen – Ergebnisse aus den Wiederholungsmessungen des DHHN. In Niemeier, W., Riedel, B. (eds.). *GeoMonitoring 2016*, 9-20.
- Lege, T. (2014). Chapter 5.5 Detektion und Monitoring von Geofahren, Oberflächen- und Massenbewegungen, p. 21 - 22. In *Erdbeobachtung für Mensch und Umwelt. Ergebnisbericht (Version 2)*, publisher: BMVI, BMUB, BMI and DLR [http://www.d-copernicus.de/sites/default/files/dokumente/forum\\_2014/Ergebnisbericht\\_2014\\_Version2.pdf](http://www.d-copernicus.de/sites/default/files/dokumente/forum_2014/Ergebnisbericht_2014_Version2.pdf) (accessed: 29.03.2016)
- Lege, T., Frei, M., Kalia, A. (2016). Bodenbewegungsdienst Deutschland – Konzept, Pilotanwendungen und weiteres Vorgehen. In *abstracts DGG 76. Jahrestagung*, 14.-17. März. 2016 DOP-Nr: 10.2312/dgg76, Münster, Germany.
- Leydecker, G. (2011). Erdbebenkatalog für Deutschland mit Randgebieten für die Jahre 800 bis 2008. (Earthquake catalogue for Germany and adjacent areas for the years 800 to 2008). *Geologisches Jahrbuch*, E 59, 1-198; 12 Abb., 5 Tab., 9 Anh., 1 CD; BGR Hannover.
- Massonnet, D., Rossi, M., Carmona, C., Adragna, F., Peltzer, G., Feigl, K. and Rabaute, T. (1993) The displacement field of the Landers earthquake mapped by radar interferometry, *Nature*, 364, 138-142.
- USGS (2016). Earthquake Hazard Program. Epicentre of the M7.8 Gorkha earthquake. [http://earthquake.usgs.gov/earthquakes/eventpage/us20002926#general\\_region](http://earthquake.usgs.gov/earthquakes/eventpage/us20002926#general_region) (accessed: 29.03.2016).
- Zebker, H. A., Rosen, P. A., Goldstein, R. M., Gabriel, A. and Werner, C. L. (1994). On the derivation of co seismic displacement fields using differential radar interferometry: The Landers earthquake, *J. Geophys. R.*, 99, 19, 634, 617 - 19.



## **Paleoseismological techniques applied to different surface rupturing morpho-tectonic processes: case studies from tectonically active areas of the Abruzzi Region, central Apennines, Italy.**

*Lo Sardo L.<sup>1</sup>, Falucci E.<sup>2</sup>, Gori S.<sup>2</sup>; Saroli M.<sup>1</sup>; Moro M.<sup>2</sup>, Fubelli G.<sup>3</sup>, Lancia M.<sup>1</sup> and Galadini F.<sup>2</sup>*

<sup>(1)</sup> University of Cassino and Southern Lazio, Department of Civil and Mechanical Engineering, Via G. Di Biasio 43, 03043, Cassino, Italy. E-mail: l.losardo@unicas.it

<sup>(2)</sup> National Institute of Geophysics and Volcanology, National Earthquake Center, Via di Vigna Murata 605, 00143, Rome, Italy.

<sup>(3)</sup> University of Turin - Department of Earth Sciences, Via Valperga Caluso, 35 - 10125 Turin, Italy.

### **Abstract:**

*We tested the effectiveness of classical paleoseismological trenching to compare and thus achieve a better comprehension of morpho-tectonic features related to different and "tricky" geological processes able to displace the surface. We show three different case studies on the identification of capable "elements" in a tectonically active area, just based on the presence of "fault" scarps at the surface where Quaternary deposits are involved. These three selected study areas are located in the central Apennines (L'Aquila district, Abruzzi Region, Central Italy):*

*(i) a well known active fault from the Fucino basin, responsible for the 1915 Marsica earthquake (Mw7); (ii) a tectono-karstic collapse from the Prata D'Ansidonia area; (iii) the S. Stefano di Sessanio area, where several few-km-long and hundred-metres-large closed depressions are bounded by short scarps.*

*In all these cases, we have performed at least one paleoseismological trench in order to compare and to understand the differences in deformational behaviour of the structures.*

**Key words:** *Paleoseismology, capable faults, non-tectonic displacements phenomena, Quaternary geological surveys.*

### **Introduction**

In the last two to three decades, the importance of the paleoseismological approach in Italy is constantly increasing.

Nowadays, paleoseismology is one of the most effective method to understand the recent behaviour of a fault and, whenever possible, is considered one of the best methods to attribute historical earthquake to an active fault (e.g. Galli et al., 2008). This interest is also testified by the new Italian guideline (Linee guida per la gestione del territorio in aree interessate da faglie attive e capaci, 2015) that suggests paleoseismology as the best method to understand the capability of a fault. As a consequence, the surface faulting hazard related to fault activation is an even more discussed topic within the scientific community, especially after the L'Aquila 2009 earthquake, where surface faulting has affected a few urban areas, dislocating infrastructure and several buildings.

As a consequence even more attention is given to understanding the origin of a surface displacement, whether attributable to tectonic origin or not.

Paleoseismology, formerly used only to study cases of tectonic surface faulting, is now also used to understand the deformational style and the origin of different medium-large scale phenomena capable to displace the surface.

This includes Deep Seated Gravitational Slope Deformation (DSGSD) (e.g.; Gutierrez et al., 2005; Moro et

al., 2012; Carbonel et al., 2013; Gori et al., 2014), salt tectonics (e.g. McCalpin et al., 2014) and sink-holes (e.g. Carbonel et al., 2014).

So the question is, what can be the contribution of paleoseismology to address these new topics and how much can be understood from a paleoseismological excavation?

We will show the result of three paleoseismological surveys, of which only one can be ascribed to an active and capable fault, in order to characterize different surface rupturing morpho-tectonic processes and different deformational behaviours.

Three selected study areas are located in the Central Apennines (L'Aquila district, Abruzzi Region, Central Italy):

(i) a well known active fault from the Fucino basin, responsible for the 1915 Marsica earthquake (Mw7);

(ii) a tectono-karstic collapse from the Prata D'Ansidonia area;

(iii) the S. Stefano di Sessanio area, where several few-km-long and hundred-metres-large closed-depressions are bounded by short scarps.

Here we show three cases of geological processes able to displace the surface, approached by paleoseismological techniques.



Fig. 1, Wall of the "Cava Santilli" quarry showing the Fucino fault plane (white arrows)

**Three case studies: (i) Fucino Basin, (ii) Prata D'Ansidonia area and (iii) Santo Stefano di Sessanio area.**

As for the case (i), we show a rupture produced by the activation of a capable fault by the analysis of a quarry wall, known as Cava Santilli and already analyzed by Saroli et al. (2008), and visited during the field trip of the INQUA 6th International Workshop (Gori et al., 2015). The study site is located along the western flank of the basin, between the villages of Venere dei Marsi (in L'Aquila Province, AQ) and Gioia dei Marsi (AQ). The quarry hosts the expression of the surficial rupture of a main faults in the basin, the San Benedetto dei Marsi - Gioia fault (SBGF), responsible for the 1915 Marsica earthquake (Mw7). The surficial ruptures of the SBGF are reported by Oddone (1915). Here the fault plane (white arrow in Fig. 1) juxtaposes the carbonate bedrock of the footwall with the late Holocene slope-derived deposits. Refined structural/archaeological data further the late Holocene surface faulting events.

As for the case (ii), we investigate the morphogenetic significance of several linear scarps that carve the paleo-landsurface of Valle Daria, an erosional-depositional paleo-landsurface identified for the first time by Bosi & Bertini, (1970). This geomorphological features is located between Barisciano (AQ) and Prata D'Ansidonia (AQ), two villages situated in the southern termination of the L'Aquila intermountain basin (one of the largest basins of the central Apennines), close to the epicentral area of the 6th April 2009 earthquake (Mw 6.1; Chiaraluce et al., 2011). The investigated scarps, up to 3 meters high and up to 1.5 km long, define narrow/elongated flat-bottom depressions, filled by colluvial deposits. These depressions are carved into fluvial-deltaic conglomerates, dated to the lower Pleistocene (Bertini and Bosi, 1993; Giaccio et al., 2012). Even if different authors have interpreted these shapes as a paleodrainage or secondary faults (Bagnaia et al., 1992 and Bertini and Bosi, 1993, respectively), a morphometrical study of the Valle Daria paleo-landsurface provided a great deal of information, that casts doubt on both interpretations. Indeed, the depression geometry is concave, so not attributable to a

paleodrainage. At the same time the paleo-landsurface is not vertically dislocated through the depressions. A paleoseismological investigation was conducted (Lo Sardo et al., 2016) in order to better understand the contacts between the colluvial deposits and the fluvial-deltaic conglomerates. The trench was dug across one of the higher scarps (about 3 m high), as shown in Fig. 2a. From the analysis of the trench walls, five colluvial units were recognized (Fig 2b). A wide deformation zone places these units in contact with a lower Pleistocene fluvial conglomerate. The age of the colluvial deposits are correlated with upper Pleistocene-Holocene deposits in the region; these deposits are disrupted by several shear planes, synthetic and antithetic to the scarp trend (Fig 2b). The dislocation affects all stratigraphic units up to the base of the ploughed soil (E1, Fig 2b). Moreover, the shear planes, visible in the paleoseismological trench, have curvilinear and convex-upwards geometries (E2, Fig 2b). This setting is probably the result of a lowering of the involved material. The interpretation is supported by the presence of a curvilinear shear-plane that is "anastomosed" between the stratigraphic units 2/3 and 4 (Fig 2b), with the uppermost layer that progressively fell into a continuously opening fracture. We interpret this as evidence of slow and progressive deformation. The formation of the investigated landforms is thus probably due to tectono-karstic processes, related to the collapse of cavities occurring some metres below the surface. An ongoing geophysical survey, composed by ground penetrating radar (GPR), electrical resistivity tomography (ERT) and microgravimetric surveys, seems to corroborate this interpretation. We interpret the elongated shape as the coalescence of several cavities, probably aligned along inherited structural features, which determined the formation of the scarps that bound the depressions. Thus, the combined interpretation of the data seems to show a good match, pointing out the presence of localized anomalies in the subsoil. Even if it is not possible to properly define the subsoil geometry of the cavities, the available data allow to suppose the presence of a hypogeum cavity due to a process of karst dissolution with a structural control.

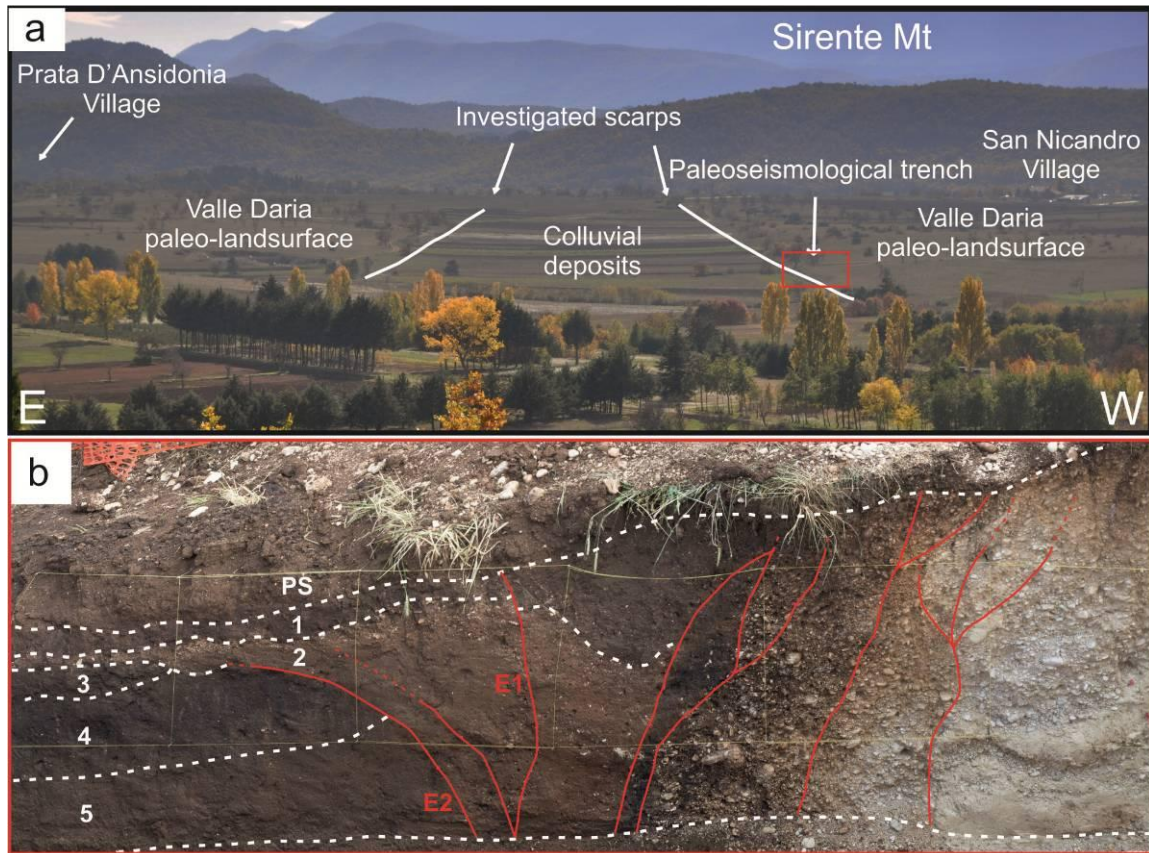


**Fig. 2 – (a)** Panoramic photo of the Valle Daria paleo-landsurface. The red square highlights the area of Fig. 2b. **(b)** Detail of one of the trench walls. The metric mesh (yellow square) measures 1m x 1m. (PS) ploughed soil. Modified from Lo Sardo et al.(2016).



**Fig. 3 – (a)** Panoramic photo of the Valle Force. The red square highlights the area of Fig. 2b. **(b)** Detail of one of the trench walls.



As for case (iii), our ongoing analyses aimed to analyze the origin of some closed depressions, up to 4 km long and up to 0.5-1 km wide, that occur along the south-western slope of the Gran Sasso Range. All these small depressions are NW-SE trending. As already described by Bertini et al. (1989), Galadini and Giuliani (1993), D'Agostino et al. (1998), and Falcucci et al. (2015), these closed depressions are bounded by scarps carved into the carbonate bedrock and, subordinately, into early Quaternary slope deposits, reaching heights of up to 5 m. These scarps are preferentially NE dipping, although in a few cases some SW dipping scarps are also present. The field work has permitted to attest that these scarps are related to shear planes that displaced two subsequent Early Pleistocene breccias formations (the Valle Valiano Fm. and Fonte Vedice Fm.; Bosi and Bertini, 1993;). A paleoseismological trench was also excavated across one of these scarps, proving the activity of these shear planes also in recent times and providing information on the deformation style.

The trench, dug across a NE dipping carbonaceous "fault" plane that borders a depression called Valle Force (Barisciano, AQ), showed a shear plane that juxtaposes calcareous bedrock of the footwall against upper Pleistocene - Holocene slope deposits. Concerning the deformational behaviour, our ongoing analysis indicates a mixed fragile-plastic deformation. Moreover, most of the deformation is localized close to shear plane. As shown, our analyses are in agreement with the recent interpretation of the origin of these shear planes as being the surface expression of Quaternary extensional structures that root at about 2-3 km depth on the presently inactive thrust plane that structured the Gran Sasso front during the Pliocene (Falcucci et al., 2015).

## References

- Bagnaia, R., A. D'Epifanio, & S. Sylos Labini, (1992). Aquila and Subequan basins: an example of Quaternary evolution in Central Apennines, Italy. *Quaternaria Nova*, 1989, 187-209.
- Bosi, C., Bertini, T. (1970). Geologia della media valle dell'Aterno. *Memorie Società Geologica Italiana*, 9(4), 719-777.
- Bertini, T., Bosi, C. (1993). La tettonica quaternaria della conca di Fossa (L'Aquila). *Il Quaternario*, 6(2), 293-314.
- Bertini, T., C. Bosi & F. Galadini, (1989). La conca di Fossa-S. Demetrio dei Vestini. CNR, Centro di Studio per la Geologia Tecnica, ENEA, PAS in Elementi di tettonica pliocenicoquaternaria ed indizi di sismicità olocenica nell'Appennino laziale-abruzzese, Società Geologica Italiana, L'Aquila, 26-58.
- Carbonel, D., F. Gutiérrez, R. Linares, C. Roqué, M. Zarroca, J. P. McCalpin, J. Guerrero, & V. Rodríguez, (2013). Differentiating between gravitational and tectonic faults by means of geomorphological mapping, trenching and geophysical surveys. The case of Zenzano Fault (Iberian Chain, N Spain): *Geomorphology*, v. 189, p. 93-10.
- Carbonel, D., V. Rodríguez, F. Gutiérrez, J.P. McCalpin, R. Linares, C. Roqué, M. Zarroca, J. Guerrero, & I. Sasowsky, (2014). Evaluation of trenching, ground penetrating radar (GPR) and electrical resistivity tomography (ERT) for sinkhole characterization. *Earth Surface Processes and Landforms*, 39(2), 214-227.
- Chiaraluca, L., L. Valoroso, D. Piccinini, R. Di Stefano & P. De Gori, (2011). The anatomy of the 2009 L'Aquila normal fault system (central Italy) imaged by high resolution foreshock and aftershock locations. *Journal of Geophysical Research: Solid Earth* (1978–2012), 116(B12).
- Commissione tecnica per la microzonazione sismica (2015). Linee guida per la gestione del territorio in aree interessate da Faglie Attive e Capaci (FAC), versione 1.0 Conferenza delle Regioni e delle Province Autonome – Dipartimento della protezione civile, Roma.
- D'Agostino, N., N. Chamot-Rooke, R. Funicello, L. Jolivet & F. Speranza, (1998). "The role of pre-existing thrust faults and topography on the styles of extension in the Gran Sasso range (central Italy)." *Tectonophysics* 292.3: 229-254.
- Falcucci, E., S. Gori, M. Moro, G. Fubelli, M. Saroli, C. Chiarabba, & F. Galadini, (2015). Deep reaching versus vertically restricted Quaternary normal faults: Implications on seismic potential assessment in tectonically active regions: Lessons from the middle Aterno valley fault system, central Italy. *Tectonophysics*, 651, 186-198.
- Galadini, F., Giuliani, R. (1993). Role of the structural geology analysis in the recent tectonic studies: an example from the area located SW of the Gran Sasso (Central Italy), *Annali di Geofisica*, Vol. XXXVI, N.1.
- Galli, P., F. Galadini, & D. Pantosti, (2008). Twenty years of paleoseismology in Italy, *Earth Sciences Review*, 88, 89-117.
- Giaccio, B., P. Galli, P. Messina, E. Peronace, G. Scardia, G. Sottili, A. Sposato, E. Chiarini, B. Jicha & S. Silvestri, (2012). Fault and basin depocentre migration over the last 2 Ma in the L'Aquila 2009 earthquake region, central Italian Apennines. *Quaternary Science Reviews*, 56, 69-88.
- Gori, S., E. Falcucci, F. Dramis, F. Galadini, P. Galli, B. Giaccio, P. Messina, A. Pizzi, A. Sposato & D. Cosentino, (2014). Deep-seated gravitational slope deformation, large-scale rock failure, and active normal faulting along Mt. Morrone (Sulmona basin, Central Italy): Geomorphological and paleoseismological analyses. *Geomorphology*, 208, 88-101.
- Gori, S., E. Falcucci & F. Galadini, (2015). Report on the INQUA 6th INTERNATIONAL WORKSHOP "ACTIVE TECTONICS, PALEOSEISMOLOGY AND ARCHAEOSEISMOLOGY" Fucino 2015. April 19-24, 2015, Pescina (AQ), Alpine and Mediterranean Quaternary, 28 (1), xi - xiii
- Gutiérrez, F., E. Acosta, S. Ríos, J. Guerrero & P. Lucha, (2005). Geomorphology and geochronology of sacking features (uphill-facing scarps) in the Central Spanish Pyrenees: *Geomorphology*, DOI:10.1016/j.geomorph.2005.01.012
- Lo Sardo L., E. Falcucci, S. Gori, M. Moro, M. Saroli, F. Galadini, G. Fubelli, M. Lancia, G. Pezzo, F. D'Ajello Caracciolo, M. Di Filippo, M. Di Nezza, I. Nicolosi, S. Urbini, (2016). Active and capable fault? The case study of Prata D'Ansiondia (L'Aquila, Central Apennine), *Rendiconti on-line della Società Geologica Italiana*, In Press.
- McCalpin, J. P. (2014). Surface faulting without earthquakes; sacking and salt tectonics., 5th PATA-Days, Busan, KOREA 2014.
- Moro, M., M. Saroli, S. Gori, E. Falcucci, F. Galadini & P. Messina, (2012). The interaction between active normal faulting and large scale gravitational mass movements revealed by paleoseismological techniques: A case study from central Italy. *Geomorphology*, 151, 164-174.
- Oddone, E. (1915). Gli elementi fisici del grande terremoto marsicano-fucense del 13 gennaio 1915. *Boll. Soc. Sismol. Ital*, 19(3/4), 71-291.
- Saroli, M., M. Moro, H. Borghesi, D. Dell'Acqua, F. Galadini & P. Galli, (2008). Nuovi dati paleosismologici dal settore orientale del bacino del Fucino (Italia centrale). *Il Quaternario*, 21, 383-394.



## Clastic dikes induced by strong earthquakes in southern Siberia and their paleoseismic significance

Oksana Lunina, Andrey Gladkov

Institute of the Earth's Crust, Siberian Branch of Russian Academy of Sciences, Lermontova street 128, Irkutsk 664033, Russia. Email: lounina@crust.irk.ru

**Abstract:** We studied clastic dikes formed by earthquakes in southern Siberia that were historically mentioned or monitored by instruments. They are the most common among all liquefaction-induced soft-sediment deformation structures (SSDSs) in the epicentral areas of the investigated seismic events. They are also the most reliable paleoseismic indicators in regions where cryogenic processes are intense. In addition to the commonly accepted criteria for the recognition of SSDSs, we suggest seven criteria that may be useful to separate the seismogenic clastic dikes from non-seismogenic SSDSs in a single outcrop. Fractures in the same outcrop may indirectly also indicate the seismogenic genesis of liquefaction-induced SSDSs. Due to the close spatial relationship of dikes with the fault structure of the investigated areas, they can be used to identify the responsible seismogenic fault, and their size can help to estimate the lower-bound magnitude/intensity of paleoearthquakes.

**Key words:** liquefaction, clastic dikes, earthquakes, southern Siberia

### INTRODUCTION

Southern Siberia is a mountainous area with alternating ridges and basins in which the Altai-Sayan and the Sayan-Baikal fold belts have the highest present-day seismic activity (Fig. 1). During 1950–2014 this area experienced more than a hundred earthquakes with magnitudes  $M \geq 5$ . Many of them have caused soil liquefaction. However, despite the widespread development of unconsolidated deposits in the intermountain basins that are favorable for seismic liquefaction, as well as numerous worldwide publications on the research topic, investigations of the soft-sediment deformation structures (SSDS) triggered by earthquakes in southern Siberia began relatively recently. These researches have shown that the commonly accepted criteria to identify the seismogenic genesis of the structures (e.g. Sims, 1975; Obermeier, 1996; Montecat et al., 2007) are not always conclusive for southern Siberia (Gladkov & Lunina, 2010), which is characterized by seasonal freezing and thawing of the ground. As a result, pseudomorphs, cryoturbation, wedge structures, involutions, drop- and mushroom-shaped sinkages and domes formed. Some of them singularly resemble the seismogenic deformation described in literature and/or can involve them. Therefore, it is necessary to define criteria for identification of seismogenic SSDS developed under cryogenic conditions in seismically active regions. To solve this problem, we chose three remarkable seismic events that affected southern Siberia and studied liquefaction-induced SSDS, mainly clastic dikes formed during these earthquakes (the September 27, 2003,  $M_s=7.5$  Chuya earthquake occurred in the Gorny Altai; the April 4, 1950,  $M_s=7.0$  Mondy earthquake in south-western flank of the Baikal rift zone; and the January 12, 1862,  $M \sim 7.4-7.5$  Thagan earthquakes on the eastern shore of Lake Baikal).

### METHODS

We used mainly standard structural and geological methods to research SSDS, following the main principals of paleoseismology (McCalpin, 2009). In the field, we dug trenches or trial pits where there were hints for liquefaction-induced soft-sediment deformation in the section. In the epicentral area of the Chuya earthquake, allogenic sediments on the surface along the seismogenic ruptures were one such sign. Sinkholes generated as a consequence of ground subsidence in the fractures or of the compensative inflow of sand and gravel after liquefaction were other features indicating clastic dikes and other types of SSDS. In the epicentral area of the Mondy earthquake, we focussed mainly on surface ruptures, sinkholes and adjacent push-ups. In the epicentral area of the Thagan earthquake, the geological and structural study was carried out mainly along a sand scarp corresponding to the Delta fault where the principal NE-SW trending surface ruptures were traceable after the catastrophic event. Upon discovering the soft-sediment deformation structures, their geometry was measured. In the case of clastic dikes, which were most distributed, we documented their width, visible height, dip direction and inclination.

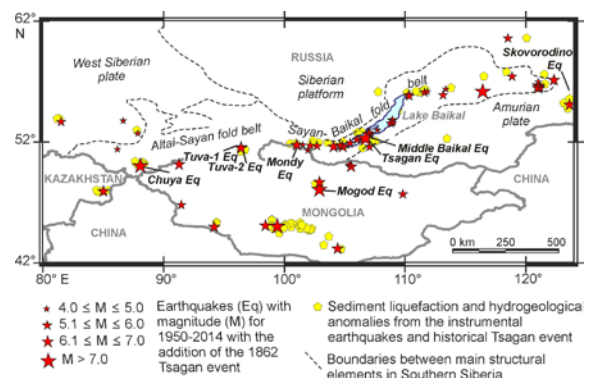




Fig.1: Earthquakes that produced liquefaction and hydrogeological anomalies in southern Siberia and the surrounding area (1950-2014).

## RESULTS AND DISCUSSION

The field study of coseismic deformations in the epicentral zones of recent earthquakes showed that clastic dikes are the most common among all liquefaction-induced SSDS in southern Siberia. Fractures often occur along with these dikes in the sequences and their dominant directions are close to the orientation of a major seismogenic fault or secondary fractures. In the case of recent earthquakes, the places where the dikes manifest can be identified at the surface by subsidence craters, the long axes of which generally coincide with the dike strikes. After thousands of years, the sinkholes may not be observed on the surface anymore due to the impact of surface processes, but they will stand out by exotic filling in sections.

The major result of our study is that in addition to the commonly accepted criteria for the recognition of earthquake-triggered SSDS, we were able to highlight several distinguishing features that can be present in the dike body or on its contacts with host sediments that indicate a seismic origin of the dike (Fig. 2):

- 1) *Pushed up sedimentary blocks within the dike body.* The rise of the layer was apparently realized due to the pressure of water flow that penetrated the deposits through the fractures. Structures with a similar attribute were found in the epicentral area of the 2003 Chuya earthquake and in Holocene sediments of the Tunka valley in the Baikal region. Comparison of these two structures gives strong grounds for the seismic genesis of the dike, which was modified by cryogenic processes later in the seismically active Tunka valley.
- 2) *Regular distorted contacts of dike with host sediments, reflecting cyclic loading during the propagation of seismic waves* (Obermeier et al., 2005).
- 3) *Turned up layers of host deposits on contacts with a dike.* It differs from ice-wedge pseudomorphs and relict frost-cracks, in which all host layers in contact with the inner zone of fill derived from above and from sides, are lowered in the direction of water movement when thawing the soil near the surface.
- 4) *Displacement along dike contacts usually in the form of a normal fault caused by subsidence that compensates for the removed sediment.* Like seismogenic features 1 and 2, this helps the recognition of an earthquake-triggered dike after an impact of cryogenic processes, when criterion 3 can be strongly shaded.
- 5) *A dike structure like a diapir.*
- 6) *Filling of an injection dike with coarser material than the host sediments.* This separates earthquake-induced dikes from loam diapirs originating from cryostatic pressure and gravitational loading of sediments, as well as from ice-wedge and frost cracks filled with more fine-grained deposits. It also allows the derivation of seismogenic SSDS after the influence of the cryogenic processes on seismically deformed sediments.

7) *A sediment layer extruded on the surface or between the strata, similar in composition to the dike.* The layer should be absent in adjacent correlated sections. In the extruded sandy-gravel-pebble bed resembling the “layer-cake”, the rock fragments show grading from large to small clasts. This is because the reduction of seismic vibrations during the earthquake decreases the size of ejected sedimentary debris on the surface.

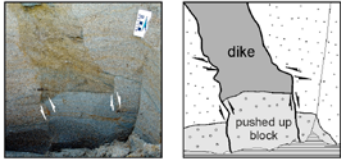
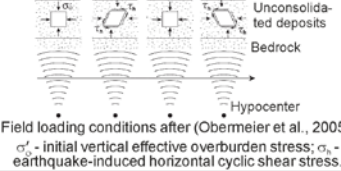
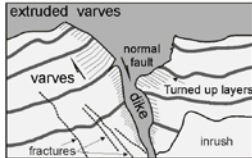
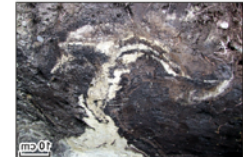
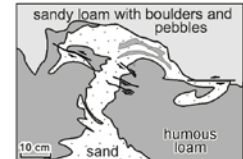
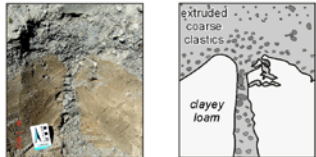
#	Criterion	Resulting seismogenic deformation
1	Pushed up sedimentary blocks within the dike body	
2	Regular distorted contacts of dike with host sediments, reflecting cyclic loading during propagation of seismic waves	
3	Turned up layers of host deposits on contacts with a dike	
4	Displacement along dike contacts usually in the form of a normal fault caused by subsidence that compensates for the removed sediment	
5	A dike structure like a diapir	
6	Filling of a clastic dike with coarser material than the host sediments	
7	A sediment layer extruded on the surface or between the strata, similar in composition to the dike; rock fragments shows upward grading	

Fig.2: Indicative criteria of seismogenic clastic dikes.

It is worth noting that one of these criteria alone may not be diagnostic but their combination is indicative to distinguish seismically-induced and cryogenic SSDS. For instance, we noted that cryogenic forms develop above the seismogenic SSDS. In our opinion, this is because the residual earthquake deformation conduces to changing conditions of heat and mass exchange as well as physical



and mechanical parameters of ground, in particular its strength properties, porosity, density and moisture. As a result, there is degradation of permafrost, increasing the depth of the seasonal freeze/thaw of soils and their migration in the deformed sediments. Therefore, it should be an integrated approach to the interpretation of structural and geological situations in the sections.

### CONCLUDING REMARKS

The research in the epicentral areas of recent earthquakes allows us to advance the identification of liquefaction-induced SSDS. The suggested criteria for revealing the earthquake-induced injection dikes make them the most reliable indicator of paleoseismicity under the conditions of intensive development of cryogenic processes characteristic for southern Siberia and other northern regions of the world. The conclusion about seismogenic origin of formation of SSDS may be based only on several criteria if visual observations are confirmed by structural measurements and analysis. Other features can be obscured by superimposed cryogenesis.

Liquefaction-induced SSDS, and in particular the clastic dikes, can be successfully used to estimate the location of the earthquake epicenter (e.g., Obermeier, 1996; Green et al., 2005; Lunina et al., 2012) and the lower-bound magnitude/intensity of paleoearthquakes (Lunina & Gladkov, 2015). A significant part of the data for the relationships between the surface-wave magnitude  $M_s$  and maximum width, visible maximum height and intensity index of clastic dikes, and local macroseismic intensity and the same three parameters was obtained when investigating the dikes in the epicentral areas of the Chuya and Mondy earthquakes. To generate similar approaches based on the fundamental knowledge of the peculiarities of development of SSDS, one needs to carry out the structural and geological work in the epicentral areas of recent and well-described historical seismic events. We see a great paleoseismic significance of such studies.

**Acknowledgements:** This work has been supported by Russian Scientific Foundation, Grant 14-17-00007.

### References

- Gladkov, A.S. & O.V. Lunina, (2010). Seismites of the Southern East Siberia: research problems and perspectives. *Geodynamics and Tectonophysics* 1 (3), 249–272.
- Green, R.A., S.F. Obermeier & S.M. Olson, (2005). Engineering geologic and geotechnical analysis of paleoseismic shaking using liquefaction effects: field examples. *Engineering Geology* 76, 263–293.
- Lunina, O.V. & A.S. Gladkov, (2015). Seismically induced clastic dikes as a potential approach for the estimation of the lower-bound magnitude/intensity of paleoearthquakes. *Engineering Geology* 195, 206–213.
- Lunina, O.V., A.V. Andreev & A.S. Gladkov, (2012). The Tsagan earthquake of 1862 on Lake Baikal revisited: a study of secondary coseismic soft-sediment deformation. *Russian Geology and Geophysics*. 53, 571–587.
- McCalpin, J.P. (Ed.). (2009). *Paleoseismology* (2nd ed.). Burlington, Mass., Academic Press, 613 p.
- Montenat, C., P. Barrier, P. Ott d'Estevou & C. Hibsich, (2007). Seismites: an attempt at critical analysis and classification. *Sedimentary Geology* 196, 5–30.
- Obermeier, S.F. (1996). Use of liquefaction-induced features for Paleoseismic analysis – an overview of how seismic liquefaction features can be distinguished from other features and how their regional distribution and properties of source sediment can be used to infer the location and strength of Holocene Paleo-earthquakes. *Engineering Geology* 44, 1–76.
- Obermeier, S.F., S.M. Olson & R.A. Green, (2005). Field occurrences of liquefaction-induced features: a primer for engineering geologic analysis of paleoseismic shaking. *Engineering Geology* 76, 209–234.
- Sims, J.D. (1975). Determining earthquake recurrence intervals from deformational structures in young lacustrine sediments. *Tectonophysics* 29, 141–152.



## Style of deformation in the Mondy active fault zone based on ground-penetrating radar and structural observations (southern East Siberia)

Oksana Lunina, Andrey Gladkov, Andrey Afonkin

Institute of the Earth's Crust, Siberian Branch of Russian Academy of Sciences, Lermontova street 128, Irkutsk 664033, Russia. Email: lounina@inbox.ru

**Abstract:** We investigated the surface deformation in the Mondy fault zone, which triggered one of the strongest earthquakes in southern East Siberia on April 04, 1950. Based on the ground-penetrating radar (GPR) and structural data, we determined the dip direction and inclination of the ruptures, types and amount of vertical offsets, as well as the width of fault zones, which varies from 2.5 to 17 m and decrease with depth within the first few meters. In addition to sinistral strike-slip, we established that normal fault offsets occurred along the nearly E–W and NW–SE trending ruptures. Based on polarization-optical modeling, we established a local change of stress field in the junction of the Mondy and Yaminshinsky faults that explains style of deformations in the investigated area.

**Key words:** Mondy fault, structure, seismogenic ruptures, ground-penetrating radar, southern Siberia

### INTRODUCTION

Several studies over the last two decades describe the geometry and kinematics of recent deformation in the Mondy-Tunka area, which is located in the south-westernmost Baikal rift zone. This deformation is associated with the Mondy fault, which triggered the  $M_w=6.9$  earthquake occurred on 4 April 1950 near the Mondy basin (Delouis et al., 2002; Arjannikova et al., 2004; Lunina et al., 2015) and perhaps the March 8, 1829  $M=7$  seismic event (Radziminovich & Shchetnikov, 2005). The active fault connects the E–W trending Tunka basin and the N–S trending Khubsugul basin (Fig. 1), being a transfer fault between two segments of the Baikal rift zone, in which the recent geodynamic regime is quite complex. Our structural and geological observations confirm left-lateral slip along the nearly E–W trending ruptures, which is consistent with the recent solution of focal mechanisms (Delouis et al., 2002) and previous geomorphologic observations (Arjannikova et al., 2004). The open question concerns the vertical component of displacement along the Mondy fault as the direct records in the excavations show both normal and reverse offsets.

The scale and the origin of surface ruptures mapped in 1950 and 1972 (Treskov & Florensov, 1952; Solonenko, 1981) are other key problems in the study of the Mondy earthquake. Arjannikova et al. (2004) proposed that these surface fractures are secondary cracks. However, recently we established that the  $M_w=6.9$  Mondy earthquake produced a surface-rupture zone at least 5.4 km long and 0.6–1.7 km wide. The rupture zone comprises northern and southern segments trending WNW–ESE (nearly E–W) and NW–SE, respectively.

In this paper we present results obtained using GPR and structural investigations performed on the four parts of the Mondy fault zone (Fig. 1), mainly across the surface ruptures of the Mondy earthquake. The aim of the work

was to study peculiarities of deformation at a depth of up to 16 m.

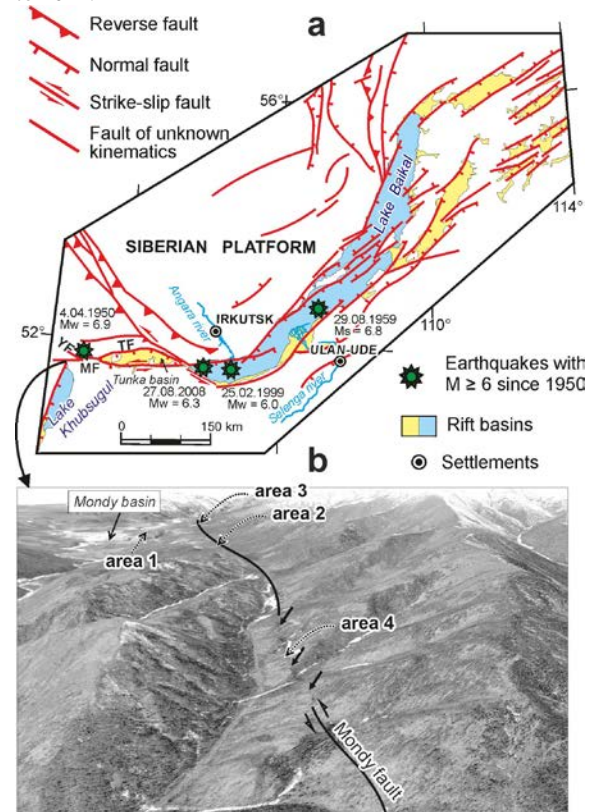


Fig. 1: a. Map of the Baikal region and location of the Mondy (MF), Yaminshinsky (YF) and Tunka (TF) faults; b. location of the area investigated with structural and GPR observation.

### METHODS



In order to study the effects of the Mondy earthquake, we first studied satellite images from the Google Earth. We subsequently verified in the field the surface deformation that we recognized. At three sites close to the village of Mondy, the seismogenic dislocations were excavated using manual method. The GPR study was performed on the four areas of the Mondy fault zone. The OKO-2 GPR equipment with three antennas ABDL Triton, AB-250 M and AB-700M, all made in Russia, were used. In the final stage, we modeled stress-deformed state in the fault zone by the polarization-optical method.

## RESULTS AND CONCLUSIONS

This GPR method is very useful for investigating deformation in sandy-gravel and boulder-pebble deposits. In many cases, we measured the width of zones of single fault planes, their azimuths and angles of dip, and types and amounts of vertical offsets on the ruptures (reverse/normal fault) that are disputable in researching the Mondy fault. The principal results and conclusions of the present work are:

1. In addition to left-lateral displacements, normal fault offsets occur along the nearly E-W and NW-SE trending fractures in southern hanging wall of the Mondy fault (Fig. 1). These offsets produce the negative flower structures in the subsurface in many places. On the ground, they are expressed as grabens on the terraces that are formed on Pleistocene fluvio-glacial sediments.

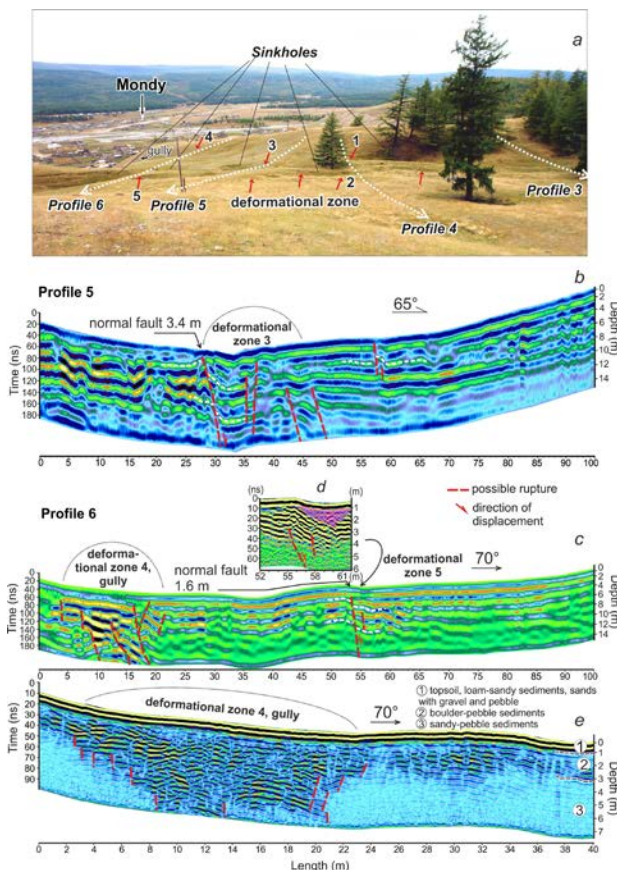


Fig.2: a. General view of the surface deformation in area 1 and location of GPR profiles; b-e. GPR profiles 5 and 6 obtained with ABDL Triton (b, c) and with AB-250M antennas (d, e).

2. The normal fault offsets measured by significant shifts of wave patterns and GPR complexes vary in different areas. The maximum normal-fault displacement of 3.4 m (Fig. 2b) is located close to the village of Mondy (area 1 in Fig. 1). The normal-fault offset of 2.2 m was measured in area 4. At the same place, the valleys of temporary streams are shifted as much as 22 m by left-lateral strike-slip. It is apparently that both vertical and horizontal displacements accumulated here during several Holocene deformational events. Judging from the data in (Lunina et al., 2015), there were at least four earthquakes, including the 1950 and 1829 events. Thus, ratio of normal slip to strike-slip is about 1:10, which corresponds to a slip vector of  $5.7^\circ$  along the Mondy fault relative to horizon.

3. The dip angles of the faults revealed by GPR are between  $75-79^\circ$ . The widths of the zones marked by low- and high frequency anomalies on the radargrams vary from 2.5 to 17 m, significantly change along the strike and decrease with a depth within few meters. This is of characteristic for seismogenic ruptures near the surface (Lunina et al., 2008).

4. Many ruptures identified on the radargrams do not reach the surface, but they are expressed by surface depressions located mainly in the hanging walls (Fig. 2d). Subsidence of clastic materials takes place at depths of up to 4–4.5 m, which coincides with a depth of seasonal frost penetration in gravel-pebble sediments of the Tunka basin (Solonenko, 1981).

5. The NW-SE trending Yaminshinsky fault, which separates two segments of the nearly E-W Mondy fault 12 km west of the village of Mondy, is a significant influence on style of deformation in the investigated area. The modeling by polarization-optical method shows that when compression is oriented in NE-SW direction, like in strike-slip focal mechanism of the 1950, Mw=6.9 Mondy earthquake (Delouis et al., 2002), a local change of stress field occurs at the junction of the two faults. As a result, the sinistral strike-slip with the extension occurs on the Yaminshinsky and Mondy faults within the area of Russia.

**Acknowledgements:** This work has been supported by Russian Scientific Foundation, Grant 14-17-00007.

## References

- Arjannikova, A., C. Larroque, J-F. Ritz, J. Deverchere, J.F. Stephan, S. Arjannikov & V.A. San'kov, (2004). Geometry and kinematics of recent deformation in the Mondy-Tunka area (south-westernmost Baikal rift zone, Mongolia-Siberia). *Terra Nova* 16, 265–272.
- Delouis, B., J. Deverchere, V. Melnikova, N. Radziminovich, L. Loncke, C. Larroque, J.F. Ritz & V. San'kov, (2002). A reappraisal of the 1950 (Mw 6.9) Mondy earthquake, Siberia, and its relationship to the strain pattern at the south-western end of the Baikal rift zone. *Terra Nova* 14, 491–500.
- Lunina, O.V., A.V. Andreev & A.S. Gladkov, (2015). The 1950 Mw = 6.9 Mondy earthquake in southern East Siberia and



INQUA Focus Group on Paleoseismology and Active Tectonics



paleoseismicity.org

associated deformations: facts and uncertainties. *Journal of Seismology* 19, 171-189.  
Lunina, O.V., A.S. Gladkov, I.S. Novikov, A.R. Agatova, E.M. Vysotskii, E.M. & A.A. Emanov, (2008). Geometry of the fault zone of the 2003 Ms=7.5 Chuya earthquake and associated stress fields, Gorny Altai. *Tectonophysics* 453, 276-294.  
Radziminovich, Y.B. & A.A. Shchetnikov, (2005). The large earthquake of March 8, 1829 in the southwestern flank of the

Baikal rift zone: updated evidence. *Volcanology & Seismology* 3, 42-50 (in Russian).  
Solonenko, V.P. (Ed.). (1981) *Seismogeology and detail seismic zoning of Pribaikal'e*. Novosibirsk, Nauka, 168 (in Russian)  
Treskov, A.A. & N.A. Florensov, (1952). The Mondy earthquake. *Bulletin Council Seismology AN USSR*, 2, 6-18 (in Russian).



## Surface rupture of a Great Himalayan 1905 Kangra earthquake (Mw7.8), NW Himalaya, India

Malik Javed N (1), Sahoo Santiswarup (2), Mohanty Asmita (3) Naik Sambit P., (3), Okumura Koji (4)

(1) Department of Earth Sciences, Indian Institute of Technology Kanpur. Kanpur 208016. Email: [javed@iitk.ac.in](mailto:javed@iitk.ac.in)

(2) Department of Geology, Utkal University, Odisha. Email: [sahoosantiswarup@gmail.com](mailto:sahoosantiswarup@gmail.com)

(3) Department of Civil Engineering, Indian Institute of Technology Kanpur. Kanpur 208016. Email: [masmita@iitk.ac.in](mailto:masmita@iitk.ac.in); [psambit@iitk.ac.in](mailto:psambit@iitk.ac.in);

(4) Department of Geography, Faculty of Letters. Hiroshima University. Higashi-Hiroshima. Hiroshima 739-8522. Japan.

Email: [kojiok@hiroshima-u.ac.jp](mailto:kojiok@hiroshima-u.ac.jp)

### Abstract:

*The 04 April 1905 Kangra earthquake (Mw 7.8) killed more than 20,000 people, caused total damage to the towns of Kangra and Dharamsala in NW Himalaya. The 1905 Kangra earthquake occurred along a newly identified the "Kangra Valley Fault" (KVF) with prominent right lateral strike-slip movement. KVF striking WNW-ESE and E-W extends for ~60 km, cutting through the Kangra and Sihunta valleys. Existence of the KVF in the Kangra Re-Entrant is indicative of oblique convergence and slip partitioning between Main Boundary Thrust (MBT) in north and Jawalamukhi Thrust (JMT) in the south and strike-slip fault in the NW Himalaya. Paleoseismic investigations revealed evidence of at least four earthquakes on KVF. Event-I (oldest) occurred before BC 900 or between BC 900-2500; Event-II between BC 100-80; penultimate Event-III occurred around AD 800-1000; and Most Recent Event (MRE) Event-IV after AD 1620 and before AD 1940, and is likely the 1905 Kangra earthquake.*

**Key words:** Active Fault, Paleoseismology, Right lateral strike-slip, Surface rupture, 1905 Kangra earthquake, Himalaya.

### Introduction

The arc-shaped mighty Himalaya, stretching east to west over a length of 2500 km, is the best example of a continent–continent collision between the Indian and Eurasian plates. In the last 100 years, four earthquakes the 1905 Kangra (Mw 7.8), 1934 Bihar–Nepal (Mw 8.1), 1950 Upper Assam (Mw 8.4), and 2005 Muzaffarabad (Mw 7.6) occurred along the Himalayan arc (Figs. 1a, b). Except the 2005 Muzaffarabad earthquake, the absence of surface rupture suggested that these earthquakes occurred on blind thrusts and that the Himalayan frontal thrust (HFT) did not rupture during recent past earthquakes. However, paleoseismic studies along the HFT revealed that the frontal fault ruptured during past earthquakes (Lavé et al., 2005; Kumar et al., 2006; Malik et al., 2008; Malik et al., 2010). Recent investigations from the Nepalese Himalaya suggest evidence of the surface rupture associated with earthquakes in 1934 Bihar–Nepal and A.D. 1255 earthquakes (Sapkota et al., 2013). The occurrence of these earthquakes along HFT implies that the accumulated strain along this part of the Himalayan arc is released periodically in large earthquakes (Rockwell, 2013).

### 1905 Kangra earthquake (Mw 7.8)

The 4 April 1905 Kangra earthquake (Mw 7.8) was the most devastating Himalayan earthquake in the recent past. This earthquake, located in Himachal Pradesh, killed more than 20,000 people and caused maximum damage in and around Kangra and Dharamsala (Ambraseys and Bilham, 2000). It was felt over a large area, extending about 300 km from Kangra to Dehra Dun (Thakur et al., 2000). The area surrounding Kangra experienced a maximum intensity of X on the Rossi–

Forel intensity scale (Middlemiss, 1910; Quittmeyer and Jacob, 1979). In the Himalaya, hazard and risk posed by active faults are not well known. An exponential increase in population along the Himalayan front and around the Indo-Gangetic Plain raises several concerns related to seismic hazard, considering the occurrence of large-magnitude earthquakes in the near future. Despite the large magnitudes of 1905 Kangra and 1950 Upper Assam earthquakes, no surface ruptures were reported (Ambraseys and Bilham, 2000). Wallace et al. (2005) suggested that slip from the 1905 Kangra earthquake was never transferred to the HFT, and it is possible that the 1905 earthquake ruptured along the Jawalamukhi thrust (JMT), located about 22 km south of the Kangra Valley. We report a newly identified active-fault trace (the KVF) from Kangra Valley showing right-lateral strike-slip movement and evidence of surface faulting during the 1905 Kangra earthquake and at least three paleoearthquakes in the last 2500–3000 years (Malik et al., 2015).

### Active fault distribution in Kangra Valley

We used high-resolution stereo pairs of Cartosat-1 (2.5 m resolution) and CORONA satellite photos (1.8–7.6 m resolution) for identification of active fault topography. The study emphasized identification of prominent geomorphic markers: vertically displaced alluvial fan surfaces and fluvial terraces, back-tilted alluvial and fluvial surfaces, offset of streams and terrace risers, pressure ridges, sag ponds, and linear valleys. Satellite data interpretation and ground truthing helped us identify a new active fault trace/traces with prominent right-lateral strikeslip movement, the KVF (Figs. 1 and 2). The KVF strikes NNW–SSE, WNW-ESE and NW-SE and cuts through the Kangra and Sihunta valleys. It extends



INQUA Focus Group on Paleoseismology and Active Tectonics



paleoseismicity.org

for ~60 km between Patka Village in the northwest (Sihunta Valley) and Tanda Village in the southeast (Kangra Valley) (Fig. 2). Prominent traces of active fault topography along the KVF were identified around the Pathiyar–Dadh–Tangroti segment in the eastern portion of the fault and around the Sihunta–Garnta–Samot segment in the western portion of the KVF (Figs. 2).

Distinct right-lateral offset of streams, offset terrace risers, north- and south-facing scarps, and pressure ridges were identified along the KVF (Figs. 3a-g). These geomorphic markers are indicators of young active tectonic deformation along the KVF.

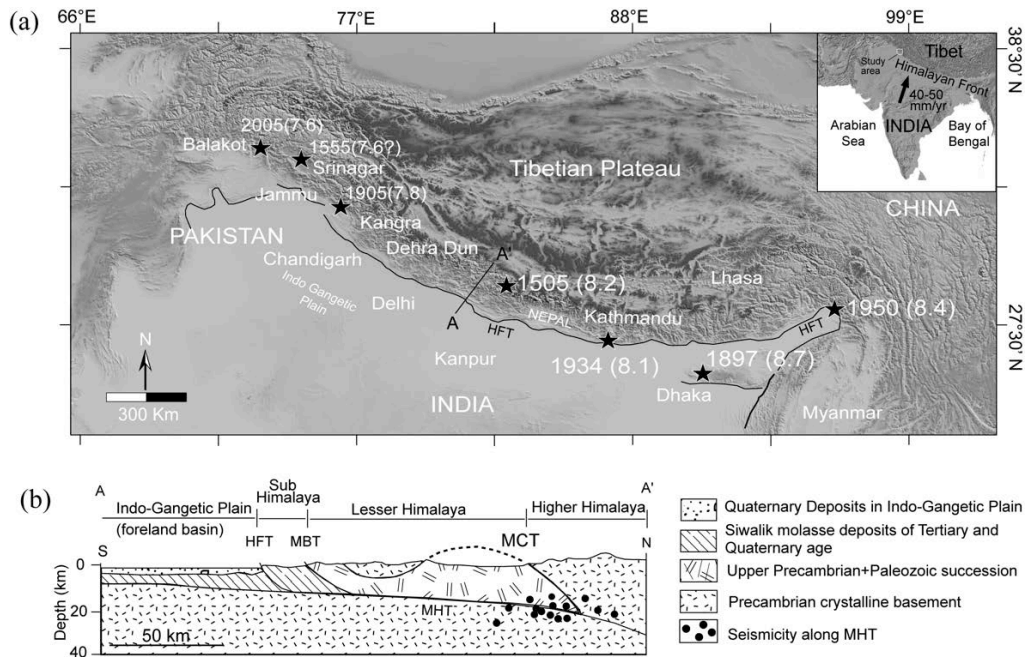


Fig. 1: (a) Locations of four major large-magnitude earthquakes: the 1905 Kangra (Mw 7.8), 1934 Bihar (Mw 8.1), 1950 Upper Assam (Mw 8.4), and 2005 Muzaffarabad (Mw 7.6) earthquakes. (b) North–south generalized geologic section across the central Himalaya, seismicity along the Main Himalayan thrust is marked by black dots (Ni and Barazangi, 1984). Location of the section is marked by the A–A' line in (a) (after Seeber and Armbruster, 1981).

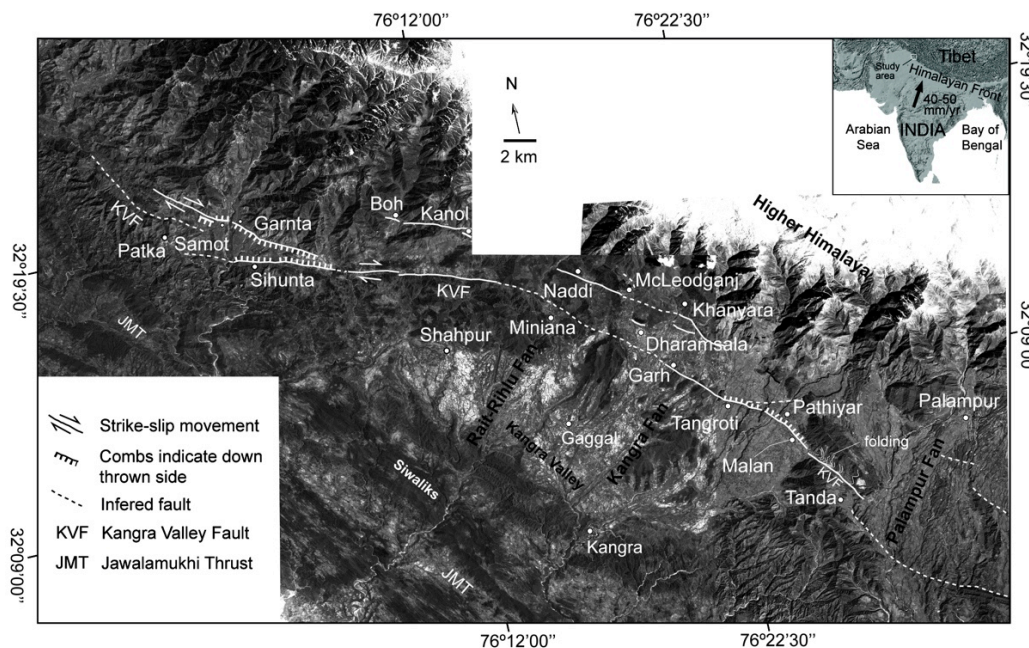


Fig. 2: Cartosat-1 photo of the area around Kangra–Dharamsala. The Kangra Valley is composed of coalesced alluvial fans (Rait-Rihlu, Kangra, and Palampur fans). The thick line marks traces of the active fault striking NNW-SSE and WNW-ESE with



prominent right-lateral strike-slip, named the Kangra Valley Fault (KVF). The fault cuts through the Kangra Valley, displacing alluvial fan surfaces and fluvial terraces. It extends for ~60 km between Patka in northwest and Tanda in southeast.

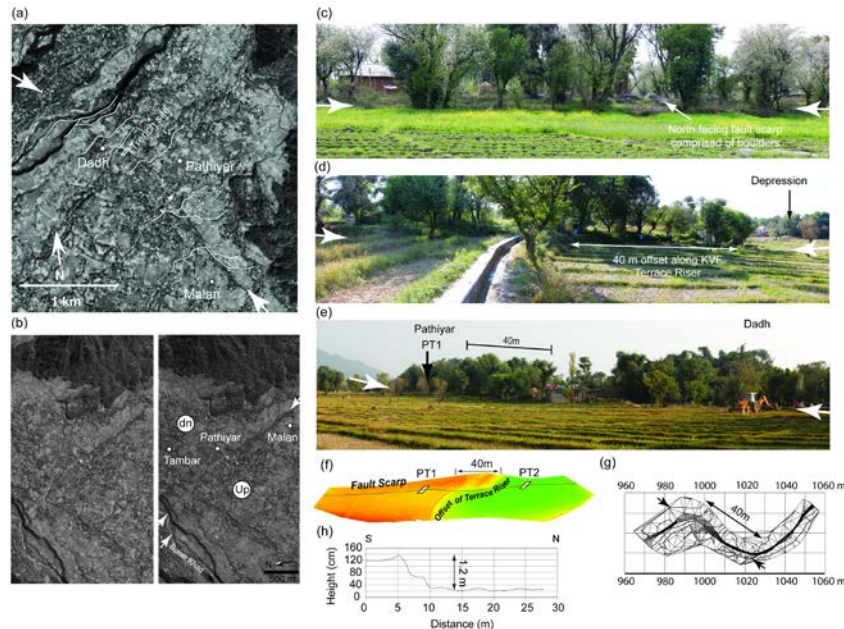


Fig. 3. (a) Cartosat-1 photo showing offset of stream along fault trace marked by white arrows, (b) Stereo photo of Cartosat-1 showing north-facing fault scarp striking NNW-SSE displacing alluvial fan surface as well as terraces, (c) North-facing active fault scarp, (d) Water aqueduct constructed along the offset terrace riser, (e) Active fault trace around Pathiyar and Dadh villages (marked by arrows) striking NNW-SSE. Total terrace riser offset measured was 40 m. PT1 mark the location of trench, (f) DEM prepared with Real Time Kinematic-integrated showing prominent offset of the terrace riser. A thin black line marks the trace of the KVF, (h) Topographic profile across the 1.2-m-high fault scarp, and (g) plan view of terrace offset obtained using total station.

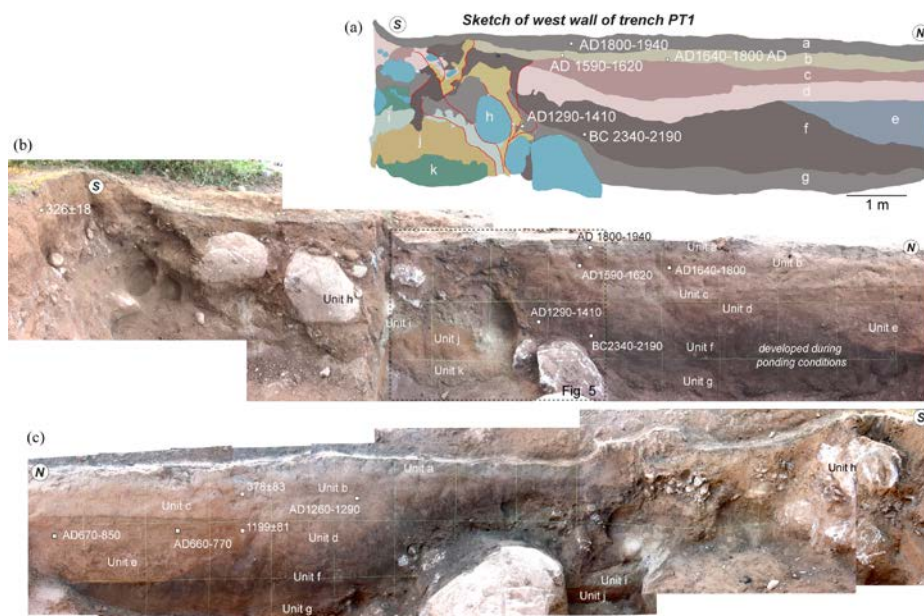


Fig. 4. (a) Sketch of west wall of trench. (b) Photomosaic of west wall of PT1 trench. The exposed sediment succession shows 11 units. Unit a (the youngest) and unit k (older) are displaced along F1 and F2 in a 0.5- to 1-m-wide fault zone. The broken line in (b) marks the location of Figure 5, (c) East wall of PT1 trench. White squares and circles mark accelerator mass spectrometry and optically stimulated luminescence ages, respectively. Unit a, grayish yellow brown clayey soil; unit b, dull yellowish red fine silty sand; unit c, dull yellowish brown silty sand; unit d, light brown silty clay soil; unit e, channel-fill deposit; unit f, brownish black medium-fine sand; unit g, dark brown clayey; unit h, matrix-supported debris; unit i, medium to coarse sand; unit j, fine silty unit; and unit k, coarse sand.

The KVF strikes NNW-SSE, WNW-ESE and NW-SE and cuts through the Kangra and Sihunta valleys. It extends for ~60 km between Patka Village in the northwest

(Sihunta Valley) and Tanda Village in the southeast (Kangra Valley) (Fig. 2). Prominent traces of active fault topography along the KVF were identified around the



Pathiyar–Dadh–Tangroti segment in the eastern portion of the fault and around the Sihunta–Garnta–Samot segment in the western portion of the KVF (Figs. 2 and 3a-g). Distinct right-lateral offset of streams, offset terrace risers, north- and south-facing scarps, and pressure ridges were identified along the KVF. These geomorphic markers are indicators of young active tectonic deformation along the KVF.

### Paleoseismic studies

Based on GPR results, trench was excavated across the eastern portion of the KVF (Figs. 4a-c and 5). Trench was excavated across a NNW–SSW-striking 1.2-m-high fault scarp near Pathiyar village. Based on upward termination of fault and unconformity four events were identified (Fig. 6). Event I occurred before 900 B.C. or between 900 and 2500 B.C.; Event II between 890 B.C. and A.D. 720; Event III between A.D. 750 and 1290; and Event IV, the MRE, was most likely the A.D. 1905 earthquake.

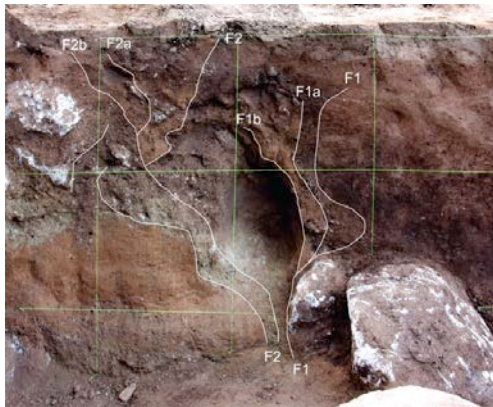


Fig. 5: Close-up view of the fault zone exposed in trench excavated across KVF.

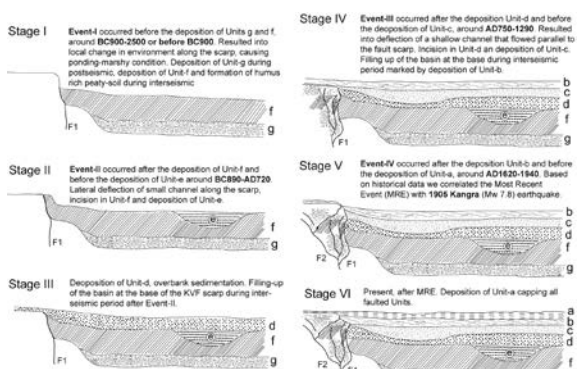


Fig. 6: Stage I-VI explaining deposition and events along KVF.

### Conclusion

The right-lateral strike-slip KVF is a clear example of oblique convergence and slip partitioning between thrust (MBT in the north and JMT in the south) and a strike-slip fault in the Kangra re-entrant. The occurrence of four paleoearthquakes along the KVF (i.e., Events I–IV) implies that the strain accumulated along the northwest

section of the collision zone is not only released periodically along the frontal faults (e.g., HFT), but also along active faults in the hinterland. It can be suggested that since 1905 event ruptured along the KVF, the potential of occurrence of larger magnitude earthquakes rupturing along the HFT still remains in the northwest Himalaya.

**Acknowledgements:** Financial support provided by Japan International Cooperation Agency (JICA) and Japan Science and Technology (JST) for funding project SATREPS-DISANET to J. N. M. and K. O. is duly acknowledged. We also knowledge the partial financial support received from the Ministry of Earth Sciences (MoES), New Delhi.

### References

Ambraseys, N., and R. Bilham (2000). A note on the Kangra Ms " 7.8 earthquake of 4 April 1905, *Current Science*, 79, 45–50.

Kumar, S., S. G. Wesnousky, T. K. Rockwell, R. W. Briggs, V. C. Thakur, and R. Jayangondaperumal (2006). Paleoseismic evidence of great surface rupture earthquakes along the Indian Himalaya, *Journal of Geophysical Research* 111, 1–19.

Lavé, J., D. Yule, S. Sapkota, K. Basant, C. Madden, M. Attal, and R. Pandey (2005). Evidence for a great medieval earthquake (1100 A.D.) in the central Himalayas, Nepal, *Science* 307, 1302–1305.

Malik, J. N., T. Nakata, G. Philip, N. Suresh, and N. S. Viridi (2008). Active fault and paleoseismic investigation: Evidence of historic earthquake along Chandigarh fault in the frontal Himalayan zone, NW India, *Journal of Himalayan Geology* 29, 109–117.

Malik, J. N., A. K. Sahoo, A. A. Shah, D. P. Shinde, N. Juyal, and A. K. Singhvi (2010). Paleoseismic evidence from trench investigation along Hajipur fault, Himalayan frontal thrust, NW Himalaya: Implication of the faulting pattern on landscape evolution and seismic hazard, *Journal of Structural Geology*, 32, 350–361.

Malik, J. N., Sahoo, S., Satuluri, S., and Okumura, K. (2015). Active Fault and Paleoseismic Studies in Kangra Valley: Evidence of Surface Rupture of a Great Himalayan 1905 Kangra Earthquake (Mw 7.8), Northwest Himalaya, India. *Bulletin of the Seismological Society of America* 105(5), 2325–2342, doi: 10.1785/0120140304.

Middlemiss, C. S. (1910). The Kangra earthquake of 4 April 1905, *Memoir Geological Survey of India* 38, 405.

Ni, J., and M. Barazangi (1984). Seismotectonics of the Himalayan collision zone: Geometry of the underthrusting Indian plate beneath the Himalaya, *Journal of Geophysical Research* 89, 1147–1163.

Quittmeyer, R. C., and K. H. Jacob (1979). Historical and modern seismicity of Pakistan, Afghanistan, northwestern India, and southeastern Iran, *Bulletin of the Seismological Society of America* 69(3), 773–823.

Rockwell, T. K. (2013). Rupture exposed, *Nature Geosciences* 6, 19–20.

Sapkota, S. N., L. Bollinger, Y. Klinger, P. Tapponnier, Y. Gaudemer, and D. Tiwari (2013). Primary surface ruptures of the great Himalayan earthquakes in 1934 and 1255, *Nature Geosciences* 6, 71–76.

Seeber, L., J. G. Armbruster, and R. C. Quittmeyer (1981). Seismicity and continental subduction in the Himalayan arc, in Zagros, Hindu-Kush Himalaya Geodynamics Series, Vol. 3, American Geophysical Union, Washington, D.C., 215–242.

Thakur, V. C., V. Sriram, and A. K. Mundepe (2000). Seismotectonics of the great 1905 Kangra earthquake



INQUA Focus Group on Paleoseismology and Active Tectonics



[paleoseismicity.org](http://paleoseismicity.org)

meizoseismal region in Kangra–Chamba, NW Himalaya, *Tectonophysics* 326, 289–298.

Wallace, K., R. Bilham, F. Blume, V. K. Gaur, and V. Gahalaut (2005). Surface deformation in the region of the 1905 Kangra Mw 7.8 earthquake in the period 1846–2001, *Journal of Geophysical Research* 32, L15307, doi:10.1029/2005GL022906.



## Investigation of uplifted marine and fluvial terraces in the Santa Rosalía basin of central Baja California, México

Martínez Gutiérrez, G.(1), Antinao Rojas, J.L.(2), Camacho Antuna, D.A.(1), Hartke, S.(3), Pugh, A.(4), Niemi, T.M.(5)

- (1) Department of Earth Sciences, UABCS, La Paz, B.C.S., 23080, México. Email: martingg@uabcs.mx
- (2) DRI-Division of Earth and Ecosystems Sciences, Reno, NV
- (3) Department of Geosciences, University of Texas, Dallas, TX
- (4) Department of Geological Sciences and Engineering, University of Nevada, Reno, NV
- (5) Department of Geosciences, UMKC, Kansas City, MO

**Abstract:** The Santa Rosalía basin in México's central Baja California peninsula records the sedimentary record of Gulf of California rifting and subsequent tectonic uplift of the basin. Gravel and calcareous fossiliferous conglomerate and sandstone defined as Santa Rosalía formation were deposited unconformably on the Infierno, Gloria, and Boleo formations. Distinct 10 m, 25-30 m, 100 m, and 190 m marine terraces were identified. Four distinct fluvial terraces were observed in the Arroyos Santa Agueda, Boleo, Montado, and Providencia with deeper and better-developed soil profiles correlating with higher elevation from modern equivalents. GIS analyses of the fluvial surfaces indicate elevation breaks and fluvial incisions between marine and fluvial terraces. Deposits from the La Reforma and Tres Vírgenes volcanic complex interfinger with terrace deposits in an area that was not studied but provide stratigraphic control of the age of terraces.

**Key words:** Baja California Sur, marine terraces, tectonic uplift.

### Introduction

The Baja California peninsula exhibits distinctive geologic and geomorphic features. Among the studies conducted in past are on marine terraces, the work realized by Ortlieb (1979, 1987, 1991) provided a extensive characterization of the main marine terraces exposed on east and west coast of Baja California peninsula. Recent work provides more information on vertical uplift rates (Simms, A.R. et al., 2016). However, there is not a detailed mapping on marine and fluvial terraces exposed at Santa Rosalía area. The purpose of this work is to provide detailed geologic and geomorphic maps (scale 1:10,000) to differentiate marine from fluvial terraces in the area and to establish a stratigraphic framework for the younger sedimentary units in the Santa Rosalía basin (Fig. 1).

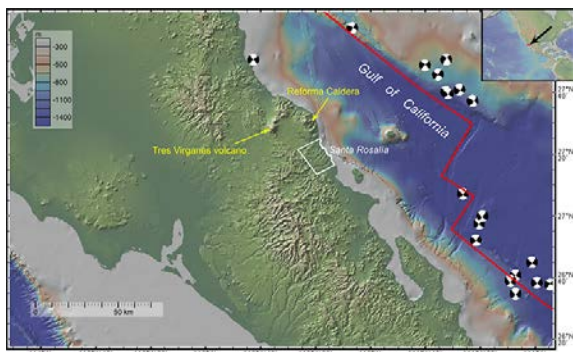


Figure 1. Location of the study area (white boundary) conducted by REU program (from Ryan et al., 2009).

### Discussion

Field activities consisted of mapping marine and fluvial terraces with the help of tablet computers and QGIS mainly in lower Arroyo Boleo, lower Arroyo Santa Agueda (including the marine terraces near ITESME and Hotel El Morro), and Santa Rosalía town for the marine terrace outcrops, using as reference GeoEye images provided by Minera Boleo Co.

Four distinct fluvial terraces were observed at both Arroyo Montado, Arroyo Boleo and Santa Agueda, with deeper and better developed soil profiles correlating with higher elevation from modern equivalents (Fig. 2; Fig. 6). The Santa Agueda soils are deeper and have better structure than the Boleo terrace soils. The soils at Santa Agueda are the only soils where a clear prismatic structure was found; we have interpreted this as reflecting a difference in clay content in the B horizon between the oldest terraces in both catchments. The Bk horizons developed on the older terraces are thicker in the Santa Agueda area than in Boleo (Fig. 6), although they appear at shallower depths in the Boleo area, mainly formed as deposition on clast surfaces (Fig. 5). Thick indurated carbonate layers appear only in the highest, uppermost terrace at Curuglu, and in the upper terrace at Santa Agueda, with almost one meter of an indurated duripan (Bk1 in Fig. 6).

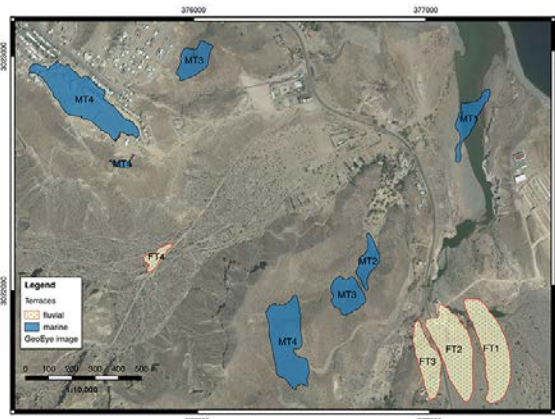


Figure 2. Marine and fluvial terraces mapped along the Santa Agueda and Montado arroyos. Four distinctive terraces were identified.

Sections described in the Curuglu quarry outcrop and a small creek draining into the old airport terrace were used to describe contacts between Quaternary units and the Infierno Formation (Fig. 3).

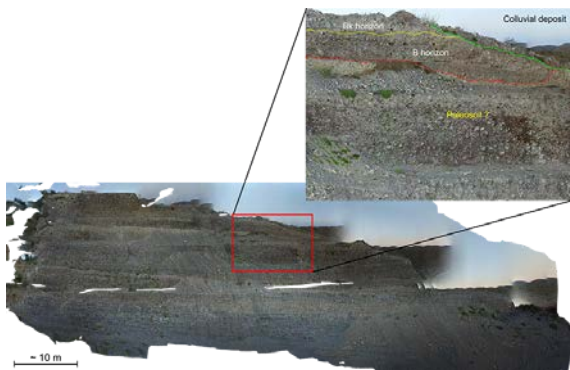


Figure 3. Photomosaic of Curuglu quarry, poor soil development in the conglomeratic deposit helped to differentiate between Pliocene?-Pleistocene deposits.

Fifteen soil profiles were described in the field for texture (estimating silt content), structure, color, carbonate stage development (e.g., examples in Fig. 6), and put them in a stratigraphic and sedimentology context. Soil horizons were sampled for laboratory grain-size analysis, pH, Fe-oxides, density, and carbonate content. A few gravelly horizons were tested for density in the field. In the thick (~50 m) section at the Curuglu quarry, we were able to describe contacts between older Pliocene?-Pleistocene units and younger capping terraces, with an interbedded tuff layer that was sampled.

Two topographic profiles were constructed using digital elevation model data from INEGI (2016) and QGIS (Fig. 4). The profiles show the trends of the terraces in spite of the low vertical and horizontal resolution of the DEM.

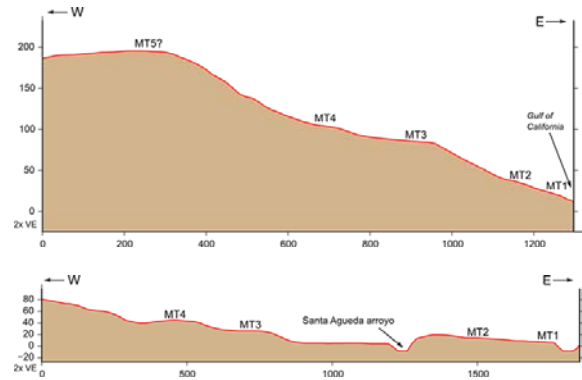


Figure 4. Topographic profiles derived from INEGI DEM (2016).

The topographic profiles show differences in terraces elevation, indicating apparently no correlation between them. More detailed survey is required to distinguish the different terraces that occur in short distances. There is a difference in elevation from north to south, in the north the marine terraces are more elevated than the south, no fault occurs but a differential uplift is assumed in the area.

Fluvial terraces occur in Boleo arroyo, at least three terraces are exposed, grading in clast size towards the Gulf of California (Fig. 5). Some of these terraces are at the same elevation as marine terraces in near of downtown Santa Rosalía (Ortlieb, 1991). The upper terraces could correspond to Upper Mesa remnants (oldest marine platform) (Ortlieb, 1981, 1991).



Figure 5. Fluvial terrace exposed on the northwestern margin of the Boleo arroyo sitting on Infierno Formation. Carbonate



precipitation is less developed in this profile compared to Curuglu section, indicating different age of formation.

**Acknowledgements:** We would like to thank to Minera Boleo Co. for allowing working in their property and providing data and satellite imagery. The work was supported by REU program funded by NSF.

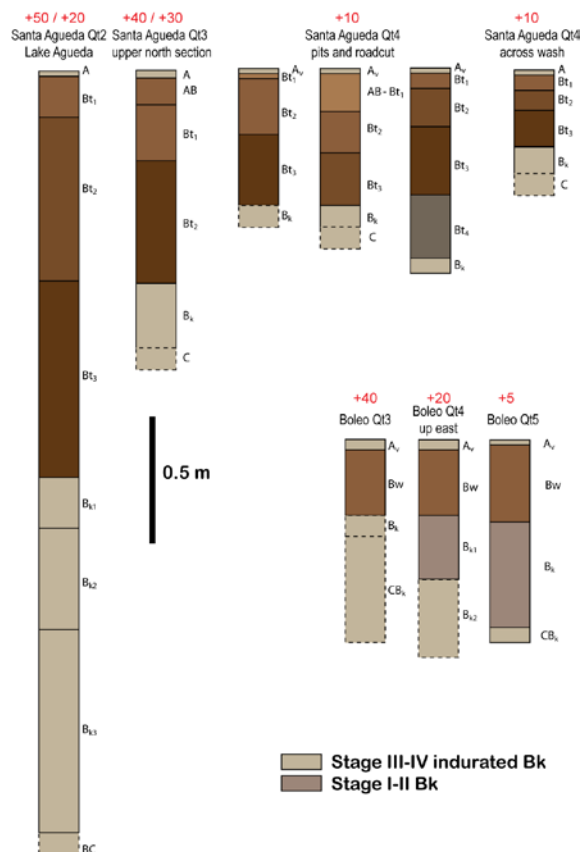


Figure 6. Simplified soil profiles for Santa Agueda (upper panel) and Boleo (lower panel) fluvial terraces. The red numbers indicate elevation of terrace relative to modern channel. Note deeper and better developed profiles in higher terraces, suggesting a significant time of stability in the surfaces. The Santa Agueda profiles are also organized from west (left) to east (right). At the same elevation of the surface (Qt4), eastern profiles seem less developed. Influence of the sea could be a factor in inhibiting development of a strong Bt both here and in the Boleo area (closer to the Gulf of California). Note for location in map: FT1=Qt2, FT2=Qt3, FT3=Qt4.

## References

- INEGI (2016). Continuo de Elevaciones de Elevaciones Mexicano 3 (CEM 3). online [http://www.inegi.org.mx/geo/contenidos/datosrelieve/continuoelevaciones.aspx], March 2016.
- Ortlieb, L. (1979). Quaternary marine terraces in southwestern Vizcaino Peninsula, Baja California, Mexico. In: Baja California Geology, Field Guides and Papers (Abbott, P.L. & Gastil, R. G. eds.). San Diego State University, 89-93.
- Ortlieb, L. (1981). Sequences of Pleistocene marine terraces in the Santa Rosalía area, Baja California Sur, Mexico. In: Geology of Northwestern Mexico and Southern Arizona : field guides and papers (Ortlieb, L. & Roldan, Q.J. eds.). Geology of Northwestern Mexico and Southern Arizona : Annual Meeting of the Geological Society of America Cordilleran Section, Hermosillo, 275-294.
- Ortlieb, L. (1987). Early middle and late Pleistocene sea levels in Baja California Mexico; chronostratigraphy and neotectonic implications, *Congress of the International Union for Quaternary Research*, 12, 235.
- Ortlieb, L., (1991). Quaternary vertical movements along the coasts of Baja California and Sonora. In: The Gulf and Peninsular Province of the Californias (Dauphin, J.P. & Simoneit, B.T. eds). Amer. Assoc. Petrol. Geol. Mem., 47, 447-480.
- Ryan, W.B.F., S.M. Carbotte, J.O. Coplan, S. O'Hara, A. Melkonian, R. Arko, R.A. Weissel, V. Ferrini, A. Goodwillie, F. Nitsche, J. Bonczkowski, and R. Zensky (2009). Global Multi-Resolution Topography synthesis, *Geochem. Geophys. Geosyst.*, 10, Q03014, doi:[10.1029/2008GC002332](https://doi.org/10.1029/2008GC002332).
- Simms, A. R., Rouby H. & Lambeck K, (2016). Marine terraces and rates of vertical tectonic motion: The importance of glacio-isostatic adjustment along the Pacific coast of central North America. *Geological Society of America Bulletin* 128(1/2), 81-93.



## Neogene Tectonism in Colorado

Matthews, Vincent (1)

(1) Author address. Leadville Geology LLC, 519 West 7th Street, Leadville CO 80461 USA. Email: LeadvilleGeology@gmail.com

**Abstract:** The catalogue of Quaternary faults in Colorado increased from 0 in 1969 to 87 in the latest inventory, and more than 350 faults that displace Miocene strata. Because of the large expanse of Proterozoic crystalline terrane, these figures are probably quite minimal. Neogene faulting is related to post-Laramide extension that is active today as the Rio Grande Rift. The rift trends ~N20W throughout the southern 2/3 of the state, but changes strike to N75W in the northern part of the state. GPS and stress indicators demonstrate these two fault trends are normal to extension in each area. These disparate stress orientations are consistent with a clockwise rotation of the Colorado Plateau away from the stable craton. The physiographic boundaries of the Colorado Plateau are not coincident with its structural boundaries on the east and northeast.

*Distinguishing natural seismicity from triggered seismicity in Colorado has become increasingly important for seismic-hazard analysis, as well as design of oil and gas, injection operations.*

**Key words:** Neogene Tectonics, Rio Grande Rift, Colorado Plateau, Triggered Seismicity

### INTRODUCTION

The dogma in Colorado during the 1960s was that the youngest deformation in the state was Laramide in age (80-40 mya). Hence, all of the faults were considered to have been dead for 40 million years, and thus there would be no natural earthquake hazard in the state. The high topography was considered a remnant of the Laramide orogeny.

In the intervening half century, an abundance of data shows that this is not accurate. Instead, Colorado is a center of active rifting with the potential for a major earthquake that could adversely affect an under-designed building stock. The high, mountainous topography of Colorado (average elevation is 2073 m and 58 peaks exceed 4,267 m) is a result of rift-flank uplift.

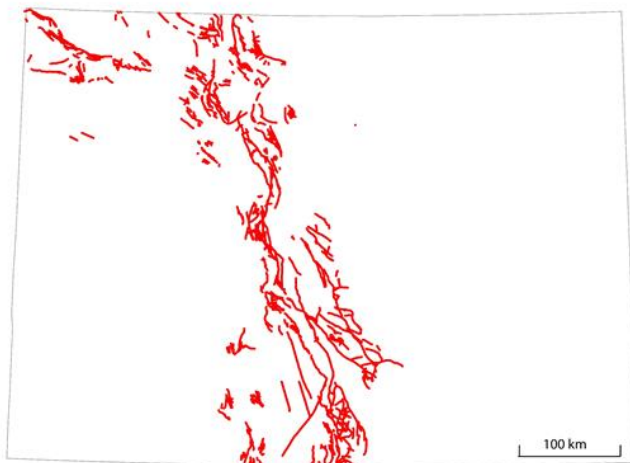


Fig. 1: Distribution of faults that displace Miocene or younger strata in Colorado associated with the Rio Grande Rift (Widmann et al, 2002). State of Colorado outline shown.

Prior to 1970, no Quaternary faults were reported in Colorado. The most recent survey of the literature (Kirkham et al, 1998) lists 87 faults and 5 folds that deform Quaternary sediments. Figure 1 shows the number (~350) and distribution of Late Cenozoic faults that displace Miocene, or younger, strata in Colorado (Widmann et al, 2002; Morgan et al 2012).

#### Late Cenozoic Faulting

The faults shown in Figure 1 are probably a minimal representation of the actual number of Late Cenozoic faults in Colorado. The state has the largest exposure of Proterozoic crystalline rocks in the Continental United States, which provides challenges for mapping Late Cenozoic faults (Matthews, 2003). Within the Proterozoic terrane are several places where Oligocene igneous rocks occur and are offset by normal faults of kilometer-scale magnitude (Figure 2). Therefore, it is quite likely that Late Cenozoic faults deform much of the Proterozoic terrane, but are as yet unverifiable (Matthews, 2003).



Figure 2 illustrates some challenges with determining the actual extent of Neogene faulting in the state of Colorado. In areas within the Proterozoic terrane where workers have concentrated on mapping faults (e.g., Boos & Boos, 1955), faulting is shown to be extensive (purple faults, Figure 2). Mapping at 1:250,000-scale (white faults, Figure 2) does not show nearly as many faults in the same areas. Moreover, the lack of Phanerozoic units within the Proterozoic terrane means that usually all we know about the age of faults that are mapped, is that they are younger than about 1.3 billion years. Several circumstances lead to the conclusion that young faulting in Proterozoic terrane is probably underestimated in published maps: 1. there are very few places in the Proterozoic terrane where Late Cenozoic units occur, 2. many workers in the Proterozoic terrane were focusing on the crystalline geology, rather than looking for evidence of Late Cenozoic faulting, so many older maps do not record the real extent of brittle faulting in the Proterozoic terrane, and 3. until the last quarter of the 20<sup>th</sup> Century, workers in Colorado were not entertaining the possibility of Late Cenozoic faulting being present, so even glacial deposits were not examined for offset.

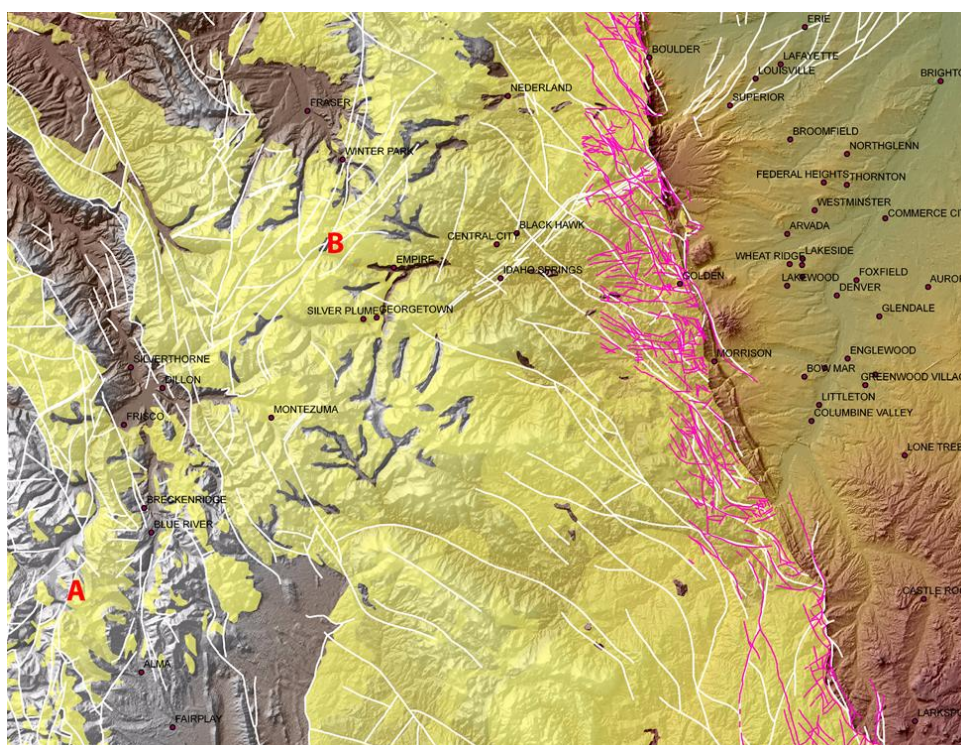


Fig.2: Extent and distribution of Proterozoic crystalline rocks (yellow shading) marginal to the Rio Grande Rift in north central Colorado. A. Location of 28 mya, Climax ore body. B. Location of 28 mya, Henderson ore body. The two intrusions are 50 km apart. White lines are faults from 1:250,000 USGS sheets. Purple lines are faults from Boos & Boos (1957).

However, two molybdenum mines within the Proterozoic terrane reveal major Late Cenozoic faulting. The Climax ore body (A in Figure 2) is displaced about 3,000 meters by a normal fault (Wallace et al, 1968). The Henderson ore body (B in Figure 2) is cut by faults totalling 2,300 meters of displacement (Geraghty et al, 1988). One other, Late Cenozoic, igneous occurrence is found in Rocky Mountain National Park, 75 kilometers north of the Henderson locale. Here 28 mya volcanic strata are displaced more than 2,000 meters by normal faulting (Braddock and Cole, 1990). It does not seem reasonable that these three, widely-separated, marker units would have been so extensively faulted without much of the surrounding Proterozoic terrane also having been faulted during the Late Cenozoic.

#### *Rio Grande Rift and Colorado Plateau*

Figure 1 illustrates the disparate, but connected, nature of Late Cenozoic, normal fault trends in the lower 2/3 of the state relative to the northern part of the state. Matthews (2013) proposed that stress, geological, and GPS data indicate that the Late Cenozoic rift trends N20W through the southern 2/3 of the state to the vicinity of Steamboat Springs, where it makes a 55° bend to the west-northwest.

GPS data show that the north-trending part of the rift in the southern 2/3 of Colorado is spreading from 1.05 to 1.39 nanostrains per year (Bergrlund et al, 2012) in a ~S75W direction (red arrows, Figure 3). Their data also show a SSW spreading direction in the northern part of the state (red arrows, Figure 3). Stress data are consistent with the directions of extension shown by the GPS data (Heidbach et al, 2008).

Geologically, the Colorado Plateau is a relatively rigid block of crust that is mildly deformed by block uplifts of the Proterozoic basement with associated, monoclinial folding of Laramide age (80-40 mya). Figure 3 shows the outlines of the



physiographic Colorado Plateau versus the structural plateau. The structural Colorado Plateau is bounded by Late Cenozoic, normal faulting on the north, east, south, and west.

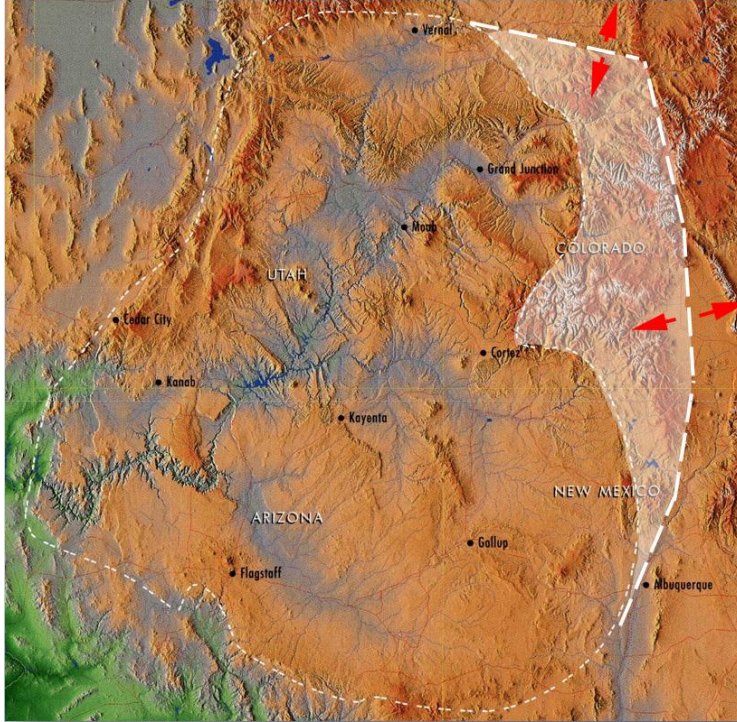


Fig. 3: Outline of Colorado Plateau Physiographic Province shown in thin white dashes. Rio Grande Rift shown in heavy white dashes. Shaded area is part of the structural Colorado Plateau, but not the Colorado Plateau Physiographic Province. When explaining the geologic history of the region, one must use the structural Colorado Plateau, not the physiographic region. The two sets of red arrows show directions of extension from geology, GPS, and stress analysis.

Matthews (2013) demonstrated how the distribution and orientation of rifting in Colorado could be explained by a clockwise rotation of the Colorado Plateau away from the stable craton. Kreemer's et al (2010) analysis of GPS data in the western USA showed that the Colorado Plateau is indeed rotating in a clockwise motion relative to the stable craton.

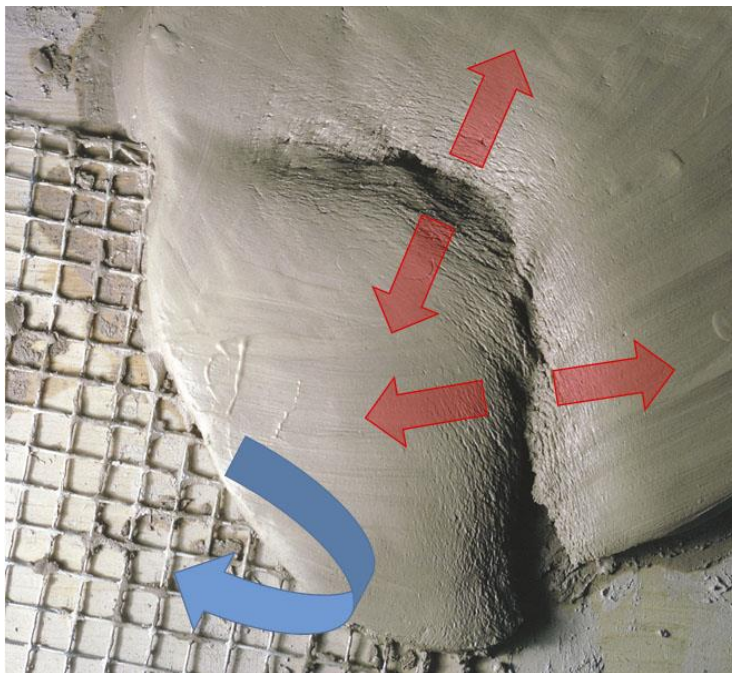


Fig. 4: Experiment demonstrating how a rigid wire mesh beneath a clay cake can create two diversely-oriented sets of faults (and rifts) (red arrows) when the wire mesh is rotated in a clockwise direction (blue arrow). These directions agree well with the Late Cenozoic fault patterns in Colorado shown in Figure 1 (modified from Matthews and Anderson, 1973).

#### Seismic Hazard and Triggered Earthquakes

An historic lack of seismographs, lack of adequate funding for geologic mapping, lack of funding for paleoseismic studies, and general attitude that Colorado is aseismic (except for triggered earthquakes); has led to a seismic-risk classification that



INQUA Focus Group on Paleoseismology and Active Tectonics



paleoseismicity.org

is quite low. Only three Quaternary faults from Colorado are used in the National Earthquake Hazard Map. Deterministic HAZUS evaluations of a number of Maximum Credible Earthquakes (MCE) for various faults around the state show the potential for multi \$billions of economic loss because of the low, design criteria in the building codes (Matthews et al, 2005).

Colorado is world famous for the numerous earthquakes at the Rocky Mountain Arsenal during the 1960s that were triggered by waste fluid injection. Since then, the state has experienced triggered earthquakes from reservoir filling; oil-field, water-flood operations; brine injection; and coal mining. It is alleged that hydraulic fracturing from unconventional oil and gas production causes earthquakes, but no evidence of this has been verified. It is also alleged that waste-water injection from oil and gas operations has caused earthquakes. One earthquake in the Denver Basin (M 3.2) had a consensus that it was triggered by an injection well. No more earthquakes have occurred in this area after modification of the injection protocol. It is alleged that two earthquakes in the Raton Basin (M 5.3 and M4.6) were also triggered by waste water injection. There is no consensus on the validity of these claims.

The Colorado Oil and Gas Conservation Commission is responsible for issuing permits for Class II injection wells for oil and gas operations. For the past five years, the Commission has required reviews of all new, injection wells as to their potential to trigger earthquakes. At present, there is no manual for this.

A much greater knowledge base of Neogene tectonics in Colorado is needed to aid society in designing safe building stock and prevent triggering of earthquakes by oil and gas operations. Much work has been done on understanding the Neogene tectonic history of Colorado since 1969. However, given what is at risk, it appears quite inadequate. The standard comment is, "What you need is a major earthquake; then you will get funding". Given the low level of seismic design criteria in the building codes, that is definitely not what we need.

## References

- Berglund, H. T., A. F. Sheehan, M. H. Murray, M. Roy, A. R. Lowry, S. Nerem, and F. Blume, Distributed deformation across the Rio Grande Rift, Great Plains, and Colorado Plateau, *Geology*, 40, 23-36, doi:10.1130/G32418.1, 2012
- Boos, C. M., and M. F. Boos, 1957, Tectonics of eastern flank and foothills of Front Range, Colorado: *Am. Assoc. Petroleum Geologists Bull.*, v. 41, p. 2603-2676.
- Braddock W.A. and J.C. Cole, 1990, *Geologic Map of Rocky Mountain National Park and Vicinity, Colorado*: USGS Miscellaneous Investigations Series Map I-1973.
- Geraghty, E.P., Carten, R.B., and Walker, B.M., 1988, Tilting of Urad-Henderson and Climax porphyry molybdenum systems, central Colorado, as related to northern Rio Grande rift tectonics: *Geological Society of America Bulletin*, v. 100, p. 1780-1786.
- Heidbach, O., Tingay, M., Barth, A., Reinecker, J., Kurfeß, D., and Müller, B., The World Stress Map database release 2008 doi:10.1594/GFZ.WSM.Rel2008, 2008
- Kreemer, C., G. Blewitt, and R.A. Bennett, 2010, The present-day motion and deformation of the Colorado Plateau, *Geophysical Research Letters*, v. 37, L10311, doi:10.1029/2010GL043374.
- Matthews, V., and Anderson, C. E., 1973, The Yellowstone convection plume and the breakup of the western United States; *Nature*, v. 243, p. 158-159.
- Matthews, Vincent III, M. L. Morgan, J. L. McHarge, L. Heerschap, 2005, Deterministic Hazus Damage Estimates For Earthquakes On Selected Faults In Colorado And The Importance Of Q (Attenuation Factor): *Geological Society of America Abstracts with Programs*, Vol. 37, No. 6, p. 14.
- Matthews, Vincent III, 2013, Whither the Rio Grande rift?: *Geological Society of America Abstracts with Programs: Prog. Ann. Mtg. Geol. Soc. Amer.*, Denver, CO
- Matthews, V. 2003, The Challenges of Evaluating Earthquake Hazard in Colorado in Boyer, D.B, Santi, P.M. Rogers, W.P., *Engineering Geology in Colorado- Contributions, Trends, and Case Histories*, Association of Engineering Geologists Special Publication No. 15, 22 p.
- Morgan, M. L., Matthews, V., and Heerschap, L. 2012, Colorado Earthquake Map Server: : <http://dnrwebcomapg.state.co.us/CGSOnline/>
- Wallace, S.R., Muncaster, N.K., Jonson, D.C., MacKenzie, W.B., Bookstrom, A.A., and Surface, V.E., 1968, Multiple intrusion and mineralization at Climax, Colorado, in Ridge, J.D., ed., *Ore deposits of the United States, 1933-1967* (Graton-Sales volume): New York, American Institute Mining Metallurgy and Petroleum Engineers, v. 1, p. 605-640.
- Widmann, B. L., Kirkham, R. M., Morgan, M. L., and Rogers, W. P., with contributions by Crone, A. J., Personius, S. F., and Kelson, K. I., and GIS and Web design by Morgan, K. S., Pattyn, G. R., and Phillips, R. C., 2002, *Colorado Late Cenozoic Fault and Fold Database and Internet Map Server: Colorado Geological Survey Information Series 60a*.
- Widmann, B.L., Kirkham, R.M., and Rogers, W.P., 1998, Preliminary Quaternary fault and fold map and database of Colorado: *Colorado Geological Survey Open- Report 98-8*, 331 p.



## Paleoseismology of the Northern Sangre de Cristo and Villa Grove Fault Zones, Rio Grande Rift, Colorado

McCalpin, James P.

GEO-HAZ Consulting, Inc., Crestone, CO 81131 USA. Email: [mccalpin@geohaz.com](mailto:mccalpin@geohaz.com)

**Abstract:** The Sangre de Cristo fault forms the eastern boundary of the Rio Grande rift over a length of 260 km, spanning the Colorado-New Mexico border. Since 1980 eight paleoseismic trenches have been dug in the Crestone section and four in the Zapata section, making this the most-trenched fault in the Colorado part of the Rio Grande rift. Despite that, there are still uncertainties about how many rupture segments exist and exactly where their boundaries are. This is partly due to poor dating control, caused by the coarse-grained sediments at the range-front.

**Key words:** paleoseismology; normal fault; rupture patterns

### INTRODUCTION

The Sangre de Cristo fault forms the eastern boundary of the Rio Grande rift over a length of 260 km, spanning the Colorado-New Mexico border. It is a west-side-down normal fault that separates the Sangre de Cristo Mountains (horst) from the San Luis Valley and Taos Plateau (grabens) in Colorado and New Mexico, respectively. Ruleman and Machette (2007) divide the fault into the Northern (NSCF) and Central (CSCF) Sangre de Cristo faults in Colorado (106 and 59 km long, respectively). The NSCF is divided into two sections (Crestone, 79 km; Zapata, 28 km) and the CSCF, divided into two sections; (Blanca, 2 km; and San Luis, 59 km). Additionally we describe the 19 km-long Villa Grove fault zone (VGF) which splays off the NSCF into the northern San Luis Valley.

The NSCF and VGF were among the first faults subjected to paleoseismic studies in Colorado, which began in the late 1970s with the statewide fault compilation of Kirkham and Rogers (1981).

### 1970s STUDIES

The first detailed study (1979-1980) covered the Crestone, Zapata, and Blanca sections (McCalpin, 1981, 1982). The Quaternary geology of the piedmont and mountains was mapped at 1:24,000 scale and fault scarps were mapped from aerial photographs at 1:20,000 scale. 77 fault scarp profiles were measured on the NSCF and 30 profiles on the VGF. One trench was excavated on the VGF and four on the NSCF (circled on Fig. 2).

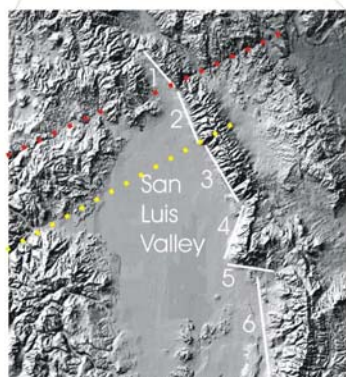
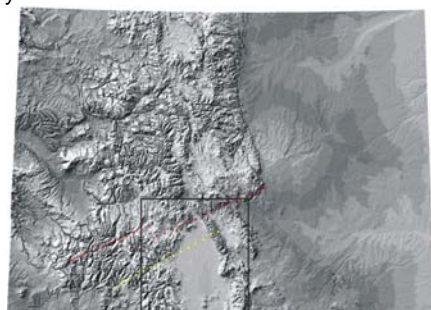


Fig. 1. Top; State of Colorado with San Luis Valley in box. Bottom; Segments of the NSCF; 1-Hayden; 2-Major; 3-Crestone; 4-Zapata; 5-Blanca. 6 is the CSCF. Dotted lines are lineaments in Precambrian rocks.

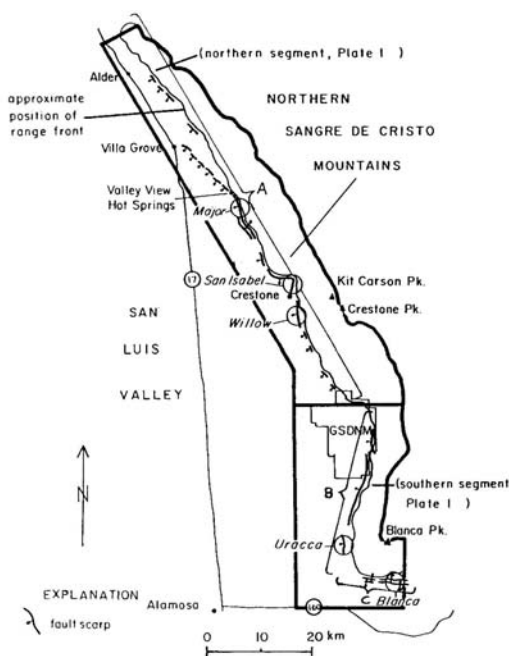


Fig. 2. Scarps (hachured) and interpreted segments of the NSCF: A, Crestone; B, Zapata; C-Blanca. Trench sites from 1980 are circled. GSDNM, Great Sand Dunes National Monument (now National Park).

**Major Creek site:** This trench crossed the fault at Major Creek (Fig. 3) and displayed evidence of two



fault movements that were constrained in time by two  $^{14}\text{C}$  dates. The latest rupture occurred shortly before  $7,600 \pm 120$  C14 yr BP, and the earlier movement occurred between  $10,100 \pm 110$  C14 yr BP and ca. 15-20 ka.



Fig. 3. The 3.8 m-high fault scarp across late Pinedale alluvium at the Major Creek site. The trench was excavated at left center, but has now been backfilled and revegetated.

Willow Creek site: This trench was excavated on a small Holocene terrace near Willow Creek and contained evidence of one fault rupture with 2.3 m of displacement.

Willow Creek site: This trench was excavated in Bull Lake fan alluvium near Willow Creek and exposed evidence of perhaps three rupture events. Age control was only from soil profile development; no datable charcoal was found.

McCalpin (1981, 1982) suggested that the part of the Crestone section south of the Major Creek/Kerber Creek fault zone has a recurrence interval of 5.0-11.7 k.y. during post-early Pinedale time (ca. <70 ? ka), whereas the fault farther north has a slower uplift rate and longer recurrence interval.

Uracca Creek site: This trench was excavated across a Holocene scarp near Uracca Creek that is about 1.2 km west of the range front. The fault exposed in this trench moved about 2.0 m during a single event between 8.0 and 5.64 ka (McCalpin, 1981, 1982), which is similar in time and perhaps contemporaneous with the last fault event at the Major Creek site on the Crestone section.

### 1980s STUDIES

Colman et al. (1985) compiled McCalpin's mapping of the northern three sections of the NSCF, but no new mapping was done.

### 1990s STUDIES

Jack Benjamin & Associates and Geomatrix Consultants (1996) suggested the Crestone section used herein should be further divided into a 38-km-long segment north of the Major Creek/Kerber Creek thrust fault zone, and a 52-km-long segment south of it.

Morel and Watkins (1997), using seismic reflection and drill-hole data, reported that the NSCF in the Crestone area is a low-angle detachment fault that flattens to subhorizontal in Precambrian rocks. All previous authors had assumed that the fault is a high-angle fault all the way to seismogenic depths.

### 2000s STUDIES

In 2001 the Crestone Science Center held its first Summer Field Course in Paleoseismology, and excavated a teaching trench across a scarp in the VGFZ (Fig. 4). This trench has been used yearly since then.

The 2002 National Seismic Hazard Map assumed the fault was not segmented and a floating Mmax earthquake of M7.5 (55 km long) could occur anywhere on the 85 km-long NSCF. Slip rate was 0.208 mm/yr. The 2008 National Seismic Hazard Map assumed a floating Mmax earthquake of M7.5 on the 85 km-long NSCF, with a slip rate of 0.208 mm/yr.



Fig. 4. The paleoseismic teaching trench on the VGFZ soon after excavation in June, 2001

In 2003 GEO-HAZ received a USGS-NEHRP grant to excavate a trench on the north side of the supposed segment boundary within the Crestone segment (its junction with the VGFZ). This trench was excavated at the mouth of Carr Gulch across a

The goal was to test whether the entire 79 km-long segment A (Crestone section of Widmann et al., 1998) is a single rupture segment. There were several potential segment boundaries on the NSCF within this "segment", as defined by crosscutting structures in the footwall, splay fault junctions, and stopovers in the range front. The northernmost



possible segment boundary (between segments 1 and 2 on Fig. 1) is at Hayden Pass, where a strong N65E-trending lineament exists in the footwall and aligns with a linear reach of the Arkansas River NE of the Sangre de Cristo Mountains (red dotted line on Fig. 1). We informally term this lineament the "Arkansas River lineament (ARL)." North of the ARL, range front scarps are common on the NSCF. South of the ARL range front scarps are mainly absent, and instead displacement appears to be shifted to the VGfZ. The part of the NSCF north of the ARL had not previously been trenched.



Fig. 5. Sketch map of the Carr Gulch area. Fault scarps shown by thick lines, numbers along scarp are profile locations. Pf, Pinedale fan; Bf, Bull lake fan.

Profile	H	SO	Alpha
<b>Pinedale fans</b>			
54	2.2m	1.2m	9 deg.
59	3.5m	2.1m	8 deg.
<b>Bull Lake fans</b>			
55	6.3m	3.4m	9 deg.
56	8.5m	3.8m	12 deg.
571	9.0m	4.6m	11 deg.
58	7.4m	4.4m	10 deg.

Table 1. Scarps heights (H, m) and vertical surface offsets (SO, m) on the numbered scarp profiles near Carr Gulch. Alpha is the slope of the faulted fan.

The Carr Gulch trench exposed evidence for 3 paleoearthquake displacements in the past 27.4 ka. The existence of 3 colluvial deposits (units 2, 3, 4) argues that the ca. 4.5 m of surface offset was formed during 3 surface-faulting events with an average displacement of about 1.5 m each.

In the past 27.4 ka there have been 3 paleoearthquakes but only 2 complete seismic cycles on which to compute closed-cycle slip rates. According to Fig. 6, the slip rate during the Event Y cycle was 0.3 mm/yr and in the Event Z cycle was 0.125 mm/yr.

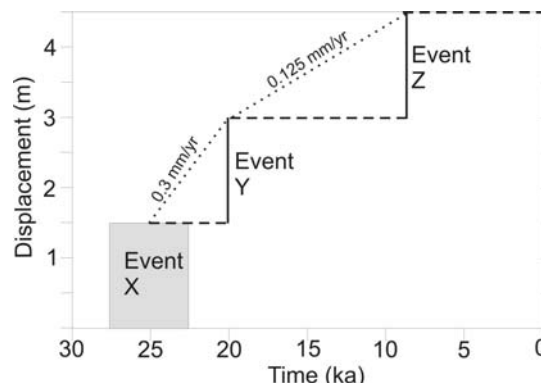


Fig. 6. Slip-history diagram of the latest 3 faulting events exposed in the Carr Gulch trench.

The averaged vertical displacement of 1.5 m is similar to the average per-event displacements computed by McCalpin (1982, p.80) elsewhere on the NSCF (1.7 m at Rock Creek, 1.4-1.8 m at Major Creek). According to Wells and Coppersmith (1994), a normal-fault displacement of 1.5 m is associated with an M7.1 earthquake if it is the average surface displacement, and with an M6.9 earthquake if it is the maximum displacement.

### 2010s STUDIES

In 2012 GEO-HAZ excavated a small trench on a 2 m-high scarp at the range front, about 500 m north of Valley View Hot Springs. This scarp revealed a single displacement event, and C14 dates are pending.

### DISCUSSION

At the Carr Gulch site there has been a maximum of 4.5 m of displacement in the past 27.4 ka. In contrast, at the Major Creek site there has been 8.9 m of displacement in a similar time period (since early Pinedale time). The displacement-per-event, reconstructed from trenches at both sites, is similar (1.5 m at Carr Gulch; 1.4-2.2 m at Major Creek). Therefore, the difference in displacement implies that fewer events have occurred at Carr Gulch than at Major Creek.

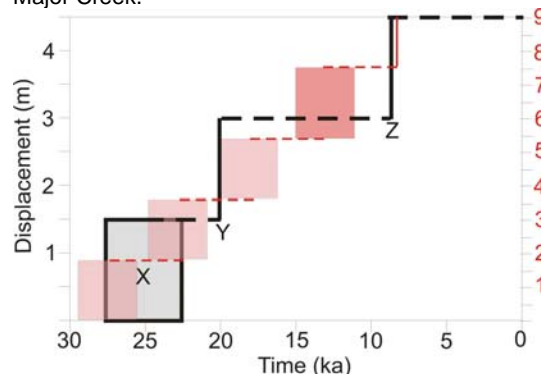


Fig. 7. Slip-histories of the Carr Gulch trench (black lines, letters, and numbers) and the Major Creek site (red lines and numbers). The time scale (bottom) is the same for both sites, but the displacement scales are different.



The latest event at both sites occurred at nearly the same time (Fig. 7). The penultimate event at Major Creek, however, occurred between about 11 ka and 15 ka, much younger than the penultimate event at Carr Gulch (ca. 20 ka). At Major Creek we have no direct dating control on the earlier events, so Fig. 7 shows three hypothetical events of average displacement (pink) spread equally in time back to ca. 30 ka. The youngest of these 3 events could conceivably correlate with the penultimate event at Carr Gulch. The oldest event at Carr Gulch could correlate with either the oldest or second-oldest event at Major Creek.

Despite the ambiguities of event-matching with such fragmentary dating control, it is clear that there have been 5 inferred faulting events at Major Creek since early Pinedale time, but only 3 events at Carr Gulch. Only the latest event appears to be a possible simultaneous rupture at both sites. The penultimate events at Carr Gulch and Major Creek cannot be the same event, if the age constraints at each site are correct. Some of the earlier events may have ruptured at both sites, but all of them could not have.

This pattern of fault behavior suggests that there is a *nonpersistent* segment boundary between the Major Creek and Carr Gulch sites. We propose that this segment boundary lies at the junction of the Villa Grove fault zone and the NCSF. Based on the record at Carr Gulch, about half of the range-front ruptures south of the VGFZ will continue north past the segment boundary. The other half of the ruptures will be deflected out onto the VGFZ. Therefore, we propose to subdivide the Crestone section into two rupture segments, with a common boundary where the VGFZ joins the NCSF. This subdivision is identical to the suggestion of Jack Benjamin and Associates and Geomatrix Consultants (1996), that the Crestone section should be subdivided into a 38-km-long segment north of the Major Creek/Kerber Creek thrust fault zone, and a 52-km-long segment south of it. We propose the name Hayden Segment for the northern segment and Major Segment for the southern segment. However, at this point we do not know exactly where the southern end of the Major segment is.

One possibility is that there is another nonpersistent segment boundary just north of San Isabel Creek, where the range front steps valleyward by more than 2 km, and where a lineament intersects the NSCF (see Fig. 1). To test this hypothesis we would need to trench somewhere between San Isabel Creek and the Great sand Dunes to derive a paleoseismic chronology to compare to that at Major Creek. The

two 1980 trenches near Willow Creek south of Crestone did not yield any C14-datable material, so they cannot be used for such a comparison. Any new trench to be dug would have to be carefully sited to avoid the extremely coarse boulder gravels typical in that area. A good location would be where a graben lies at the base of the trench that would trap eolian sediments. The best location would be where such a graben was kept moist by shallow groundwater and springs, such that organic material and well as luminescence-datable sediments might be found.

**Acknowledgements:** This research was supported by USGS-NEHRP grant 03HQGR0076 to Pls McCalpin and Kirkham, and by GEO-HAZ Consulting, Inc. and the Crestone Science Center. Thanks to Neil and Terry Seitz and the Orient Land Trust for continuing access to the teaching trench, and to the US Bureau of Land Management and the Colorado State Land Board for permission to trench at Carr Gulch and near Valley View Hot Springs. Field assistance has been provided through the years by attendees of the Summer Field Course in Paleoseismology and Neotectonics taught at the Crestone Science Center, including the French team from IRSN who logged the 2012 trench.

#### References

- Colman, S.M., McCalpin, J.P., Ostenaar, D.A., and Kirkham, R.M., 1985, Map showing upper Cenozoic rocks and deposits and Quaternary faults, Rio Grande Rift, south-central Colorado: U.S. Geological Survey Miscellaneous Geologic Investigations I-1594, 2 sheets
- Jack Benjamin & Associates and Geomatrix Consultants, 1996, Probabilistic seismic hazard assessment for the U.S. Army chemical disposal facility, Pueblo Depot Activity, Colorado: Technical report to Science Applications International Corporation, Maryland, under Contract JBA 148-130-PU-002.
- Kirkham, R.M., and Rogers, W.P., 1981, Earthquake potential in Colorado: Colorado Geological Survey Bulletin 43, 171 p., 3 pls.
- McCalpin, J., 1981, Quaternary geology and neotectonics of the west flank of the northern Sangre de Cristo Mountains, south-central Colorado: Golden, Colorado School of Mines, unpublished Ph.D. dissertation, 287 p.
- McCalpin, J.P., 1982, Quaternary geology and neotectonics of the west flank of the northern Sangre de Cristo Mountains, south-central Colorado: Colorado School of Mines Quarterly, v. 77, no. 3, p. 1-97.
- McCalpin, J.P. and Kirkham, R.M., 2006, Refine slip rates and segmentation of the northern Sangre de Cristo fault, Colorado's most active fault: Final Technical Report, Contract 03HQGR0076, National Earthquake Hazards Reduction Program, U.S. Geological Survey, 20-AUG-2006, 41 p.
- Ruleman, C. and Machette, M., 2007, An overview of the Sangre de Cristo fault system and new insights to interactions between Quaternary faults in the northern Rio Grande rift: Chapter J in USGS Open-File Report 07-1193, p. 187-197.



## Paleoseismic investigation of the Yunodake fault, Fukushima Prefecture, Japan

Yukari Miyashita (1)

(1) Geological Survey of Japan, AIST, Central 7, Higashi 1-1-1, Tsukuba, Ibaraki 305-8567, Japan. Email: yukari-miyashita@aist.go.jp

**Abstract:** The 2011 off the Pacific coast of Tohoku Earthquake occurred along the Japanese trench. The earthquake affected static stress changes to inland active faults in Northeast Japan, and induced the Fukushima-ken Hamadori earthquake ( $M_{JMA}7.0$ ). Remarkable surface ruptures appeared along the NW-trending Yunodake fault. Although the Yunodake fault was previously mapped with a normal down-to-the-SW sense of slip, its paleoseismic history is not clear. I conducted a trenching survey on the north-western part of the Yunodake fault to investigate its paleoseismic history. On the trench wall beneath the 2011 ruptures, a set of fissures and apparent reverse faults with positive flower structures were exposed. Detailed trench wall observation and radiocarbon dating revealed that the penultimate surface-rupturing earthquake occurred between about 1,000 and about 6,000 years ago.

**Key words:** active fault, the 2011 off the Pacific coast of Tohoku Earthquake, Yunodake fault, Itozawa fault, Fukushima Prefecture

### INTRODUCTION

The 2011 off the Pacific coast of Tohoku Earthquake ruptured a 450-km long and 200-km wide plate boundary between the North American and Pacific plates along the Japanese trench. The Tohoku area, northeast Japan, is located in the E-W compressional stress field. The Tohoku earthquake affected static stress changes to inland active faults in Northeast Japan, and induced the Fukushima-ken Hamadori earthquake ( $M_{JMA}7.0$ ) on 11<sup>th</sup> April 2011. This earthquake ruptured two previously mapped faults: the Yunodake fault and the Itozawa fault (Fig. 1). The NW-trending Yunodake fault exposed 16-km-long surface rupture with normal sense of slip during the 2011 earthquake, until before the earthquake the length of the fault recognised as 6-km-long. Although the Yunodake fault was previously mapped with a normal down-to-the-SW sense of slip, its paleoseismic history is poorly understood. I conducted a trenching survey on the north-western part of the Yunodake fault to evaluate the timing of paleoseismic event.

### TRENCH SITE

I conducted a trench investigation at Orimatsu, Tono town, Iwaki City, located on the northeastern part of the Yunodake fault (Fig. 1). Surficial deformation generated by the Fukushima-ken Hamadori earthquake included 1.0-1.5 m high scarps, as well as flexural folds and fissures, which were widely distributed in the Orimatsu area (Figs. 2 and 3). A small trench was excavated across the fissures and flexural scarps to sample fault gouges in the granitic rocks. The trench was then extended in size to characterize

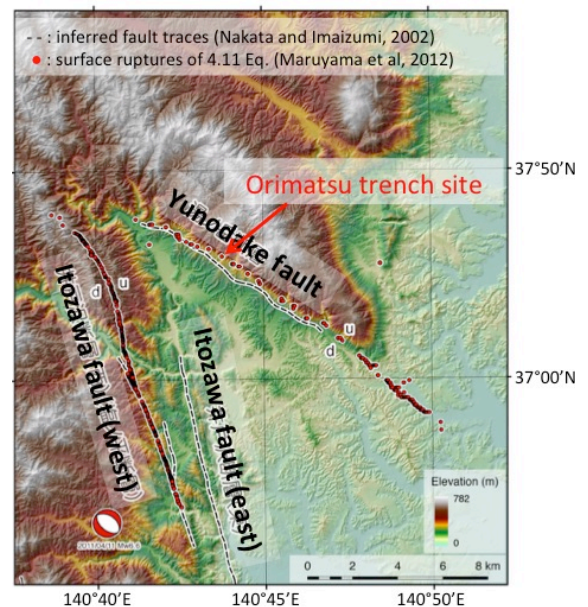


Fig. 1: Distribution of the Yunodake fault. Trench site is also shown. Base map is from Maruyama et al. (2012).

faulted humid sediments exposed in the trench walls to evaluate paleoseismic parameters.

### TRENCH WALL OBSERVATION AND INTERPRETATION

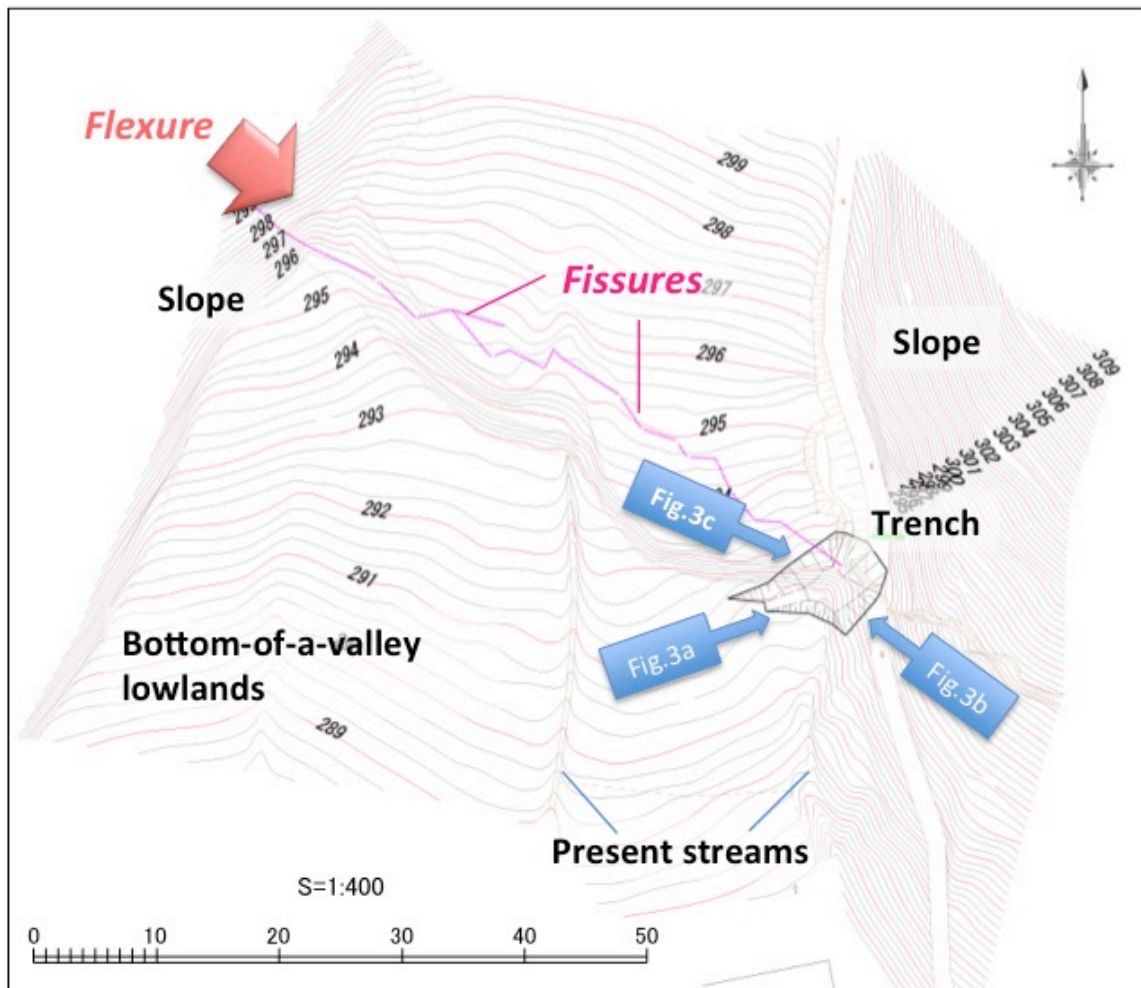


Fig. 2: Detailed contour map of the Orimatsu trench site, Tono town, Iwaki City, Fukushima Prefecture.

Geologic units exposed in the NW-wall of trench included artificial soil (1), humic sand (2a), Humic soil (2b and 2d), sand and gravel (2c and 2f), sand with gravel (2e), humic sand (4), silty sand (5), silty sand with gravel (6) and granite (Figs. 3b and 4a). The SE-wall of trench exposed a sharp normal fault plane with 1.5 m throw (Fig. 3c). The NW-wall of trench also exposed a set of fissures and apparent reverse faults with positive flower structures (fig. 3b and 4a). A main fault plane, which slipped during the 2011 event, was easily observed by crosscutting between the fault plane and the Holocene sediments. The main fault trace extends through bedrock at the base of the trench where it is associated with 10 cm of fault gouge within 1-m-wide cataclastic-damaged zone. This fault trace extends through Units 6-5 and into Unit 2d, however it becomes unclear in the upper units. Another evidence for the 2011 event is a fissure that extends through Unit 5, Units 2f-2a, although the fault traces are unclear in Unit 2a. I infer that the fissure is related to extension in the hanging wall above a blind fault with locally reverse sense of motion. Based on the stratigraphic facies change, from humic sand (4) to sand and gravel (2f), and radiocarbon ages of sediments, an unconformity is inferred at the

bottom of Units 2e and 2f. The age of the unconformity is around 1,000 yBP. Sequential radiocarbon dating of sediments from the NW-wall of the trench indicates that Units 4 and 5 were deposited before around 6,000 yBP (Figs. 4a and 4b). Fig. 4b shows the time section before the deformation caused by the 2011 earthquake. It is inferred that Units 2f and 2e deposited on moderate slope. In this case, the lower Units of Unit 4 still inclined, therefore, the penultimate earthquake event is occurred before Unit 2f sedimentation and after Unit 4 sedimentation. The penultimate event age is estimated between about 1,000 years ago and about 6,000 years ago.

#### DISCUSSION AND CONCLUSIONS

The paleoseismic trench excavation survey of the Yunodake fault revealed that the penultimate earthquake event occurred after about 6,000 years ago and before about 1,000 years ago. This result indicates that the Yunodake fault did not experience a rupture at the time of 1454 Kyotoku earthquake considered the penultimate great earthquake along the Japan Trench (Sawai et al., 2015), and imply that the fault did not activate at the time



of 869 Jogan earthquake (Sugawara et. al., 2011). As the last event of the Yunodake fault is 2011, recurrence interval of the fault is estimated as 1,000 to 6,000 years. Previously reported recurrence intervals of the Yunodake fault were 12,500 years to 40,000 years (Tokyo Electric Power Company Holdings Inc., 2011). The recurrence interval of the fault based on the result of this survey is extremely shorter than previous evaluations. However, additional trench investigations are needed to

evaluate the earthquake history farther back in time to better constrain recurrence interval, slip per event, and the long-term sense of slip.

**Acknowledgements:** I would like to thank Mr. Masahiro Miyawaki, who was working at the Dia Consultants Co. Ltd., for his great support on trenching survey.



Fig. 3: Photographs of cover shot of the Orimatsu trench (a), NW-wall (b) and SE-wall (c) of the trench.

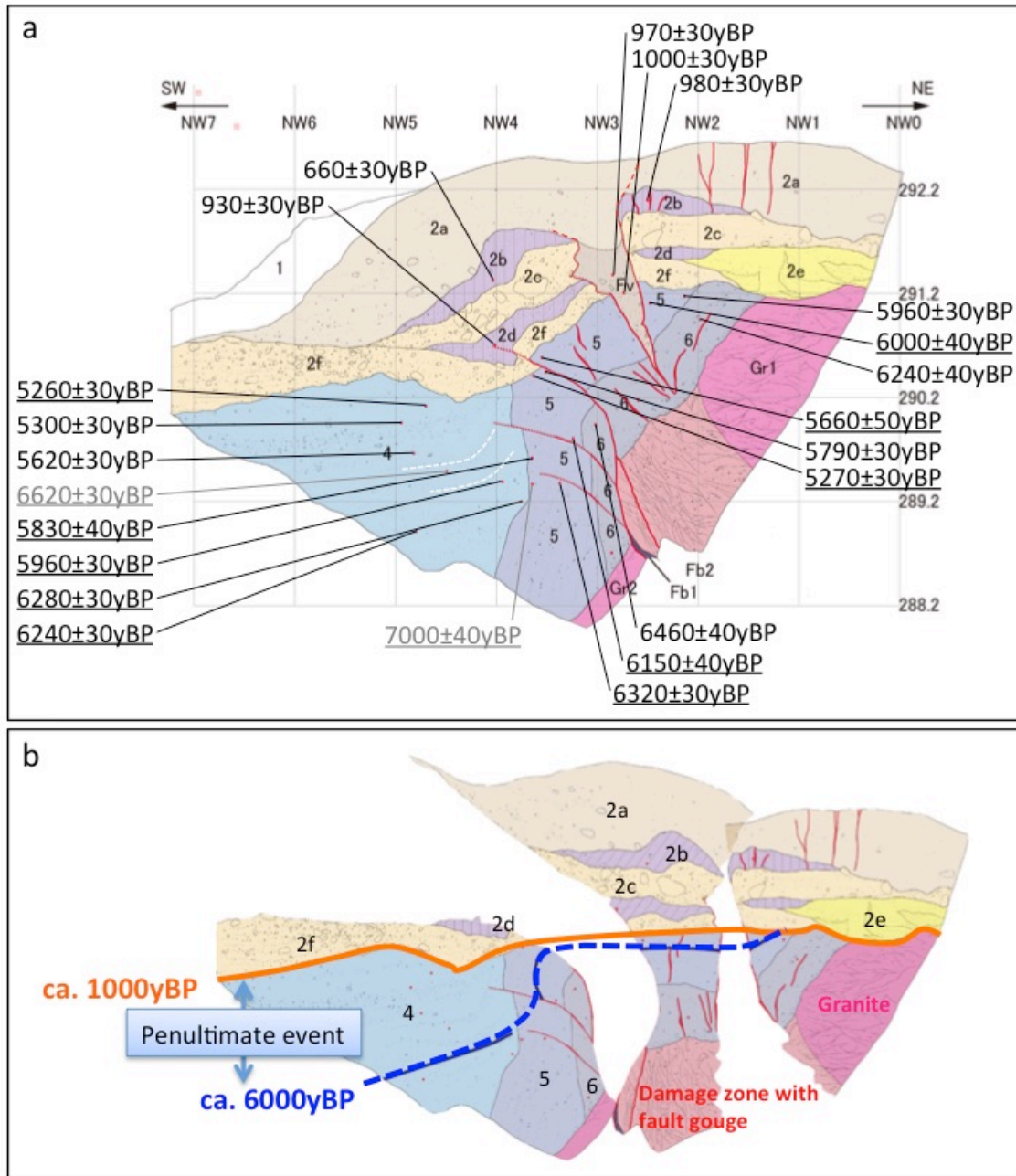


Fig. 4: Log of NW-wall of the Orimatsu trench (a) and interpretation of the penultimate event horizon (b). Radiocarbon ages are conventional ages. Underlined ages show from charcoal and others show from bulk samples.

## References

- Maruyama, T., Yoshimi, M., Saito, E. & Saito, M. (2012) Fault activities associated with the Fukushima-ken Hamadori earthquake occurred on 11<sup>th</sup> April 2011, based on tectonic-geomorphic mapping and paleoseismic investigations. *AFERC News*, 34, 1-9. (in Japanese)
- Nakata, T. & Imaizumi, T. eds. (2002) "Digital Active Fault Map of Japan", University of Tokyo Press (product serial number: DAFM0001).
- Sawai, Y., Namegaya, Y., Tamura, T., Nakashima, R. & Tanigawa, K. (2015) Shorter intervals between recent earthquakes near Sendai: Scour ponds and a sand layer attributable to A.D. 1454 overwash. *Geophys. Res. Lett.*, 42, doi: 10.1002/2015GL064167.
- Sugawara, D., Imamura, F., Matsumoto, H., Goto, K. & Minoura, K. (2011) Reconstruction of the AD869 Jogan earthquake induced tsunami by using the geological data. *J. Jpn. Soc. Nat. Disaster Sci.*, 29, 501-516. (in Japanese with English abstract)
- Tokyo Electric Power Company Holdings, Inc. (2011) Report of the additional surveys of the Yunodake fault. 82p. (in Japanese) [http://www.tepco.co.jp/cc/press/betu11\\_j/images/111227b.pdf](http://www.tepco.co.jp/cc/press/betu11_j/images/111227b.pdf)



## Tectonic geomorphology of Late Pleistocene-Holocene landscape evolution and drainage migration, NW Himalaya, India

Asmita Mohanty (1), Javed N Malik (2), Koji Okumura (3)

(1) Department of Civil Engineering, Indian Institute of Technology Kanpur, Kanpur 208016, India. Email: [masmitta@iitk.ac.in](mailto:masmitta@iitk.ac.in)

(2) Department of Earth Sciences, Indian Institute of Technology Kanpur, Kanpur 208016, India. Email: [javed@iitk.ac.in](mailto:javed@iitk.ac.in)

(3) Department of Geography, Faculty of Letters, Hiroshima University, Higashi-Hiroshima, Hiroshima 739-8522, Japan. Email: [kojiok@hiroshima-u.ac.jp](mailto:kojiok@hiroshima-u.ac.jp)

**Abstract:** The Himalayan Frontal Thrust (HFT) is the frontal most fault system of the Himalayan orogenic belt and is associated with typical foreland folded structures. The study area is located along the northwestern fringe of the Janauri anticline within the foothill zone of NW Himalaya Hajipur, Punjab, India and presents an excellent example of progressive tectonic deformation. Displacements along the two parallel faults (Hajipur faults – HF1 and HF2) have uplifted the Beas River bed, resulted in the formation of south facing fault scarps. Lateral propagation of fault and related fold growth in the fold-and-thrust belt has resulted in ~1.65 km of migration of the Beas River to the NNW. In total 6 terraces (T0-T5) and associated terrace risers were identified. Considering T0 is the part of floodplain and OSL ages obtained from terraces (T1 –  $0.96 \pm 0.07$  ka; T2 –  $2.74 \pm 0.15$  ka; T4 –  $12.29 \pm 0.7$  ka), the lateral migration would only be ~1.65 km towards northwest since 12.40 ka suggest the average migration rate of Beas River is  $\sim 13.3 \pm 0.76$  cm/yr.

**Key words:** Active Fault, fluvial terrace, lateral propagation of fold, terrace riser, Beas River, channel migration

### Introduction

The Himalayan arc is one of the most seismically active regions in the world. Geological studies, have suggested that the Himalaya was built-up by slivers of the Indian continent over-thrust to the south (Gansser, 1964; Lyon-Caen & Molnar, 1983). Due to the ongoing deformation many fault systems viz. Himalayan Frontal Thrust (HFT), Main Boundary Thrust (MBT), Barsar Thrust (BaT), Soan Thrust (SnT), Jawalamukhi Thrust (JMT), and Main Central Thrust (MCT) have developed parallel to the Himalayan arc (Fig. 1).

In last 100-150 years the Himalaya has experienced several major large magnitude earthquakes. These earthquakes are the Kangra 1905 (Mw 7.8), Bihar Nepal 1943 (Mw 8.1), Upper Assam 1950 (Mw 8.4), Muzaffarabad 2005 (Mw 7.6) and the recent Gorkha 2015 (Mw 7.8) and the Kodari 2015 (Mw 7.3) earthquakes of Nepal and Afghanistan 2015 (Mw 7.6) (Seeber and Armbruster, 1981; Yeats et al., 1997; Ambraseys and Bilham, 2000; Ambraseys and Douglas, 2004; Kaneda et al., 2008; Avouac et al., 2015). Many of these major earthquakes occurred on blind faults with no coseismic surface rupture. However, recent tectonic-geomorphic and paleoseismic studies suggest that the frontal part of the Himalayan arc is active, and is not blind that the HFT has ruptured the surface during historical past (e.g., Lave et al., 2005; Kumar et al., 2006; Malik et al., 2010 a, b; Kumahara and Jayangondaperumal, 2013; Saptkota et al., 2013; Rajendran et al., 2015; Malik et al., 2016 under review). The Himalayan frontal is considered one of the most tectonically active areas in the Himalaya (Nakata, 1989; Malik and Nakata, 2003; Thakur, 2004; Malik et al., 2010a). However, barring a few locations the overall tectonic evolution during recent geologic period is not

well understood (e.g., Delcaillau et al., 2006; Malik and Mohanty, 2007; Malik et al., 2010; Kumahara and Jayangondaperumal, 2013a). Studies in the Himalayan region emphasizing tectonic-geomorphology, active fault mapping and paleoseismic investigations have helped understand the influence of ongoing deformation in shaping of the landscape (Nakata, 1989; Wesnousky et al., 1999; Malik and Nakata, 2003; (Lavé et al., 2005; Kumar et al., 2006; Malik et al., 2008; Malik et al., 2010 a, b; Singh and Tandon, 2008; Kumahara and Jayangondaperumal, 2013; Malik et al., 2015).

This study focuses on the foothill zone of NW Himalaya around the northwest fringe of Janauri anticline with of better characterizing the influence of active tectonics on landscape evolution. The area is confined within the latitude of  $31^{\circ}44'$  to  $32^{\circ}14'$  and longitude of  $75^{\circ}26'$  to  $75^{\circ}53'$ , and falls within the mesoseismal zone of 1905 Kangra earthquake (Mw 7.8). There, the HFT marks the frontal most fault system of the Himalayan orogenic belt, and is associated with typical foreland folded structures. The forward and lateral propagation along two parallel branching out faults (Hajipur faults – HF1 and HF2) has resulted into shifting/deflection of the Beas River by about 15 km towards NNW. Displacements along the two parallel faults have uplifted the Beas River bed, resulted into the formation of south facing fault scarps.

### Methodology

We used high-resolution satellite data CARTOSAT-1 (resolution- 2.5m), CORONA (resolution 1.8-7.6 m) and LANDSAT ETM+ (resolution 28 m) and Shuttle Radar Topographic Mission (SRTM, resolution – 90m) data to generate a Digital Elevation Model (DEM) and 3D perspective views. This data helped in identifying



tectonically controlled landforms like, vertically displaced alluvial fan surfaces, fluvial terraces, back-tilted surfaces, offset streams, and active fault scarps etc.

suggests that the HF2 scarp is comparatively younger than the HF1 scarp. The height of the fault scarp along back-thrust is ~10 m and similarly, the scarp height reduces towards NNW.

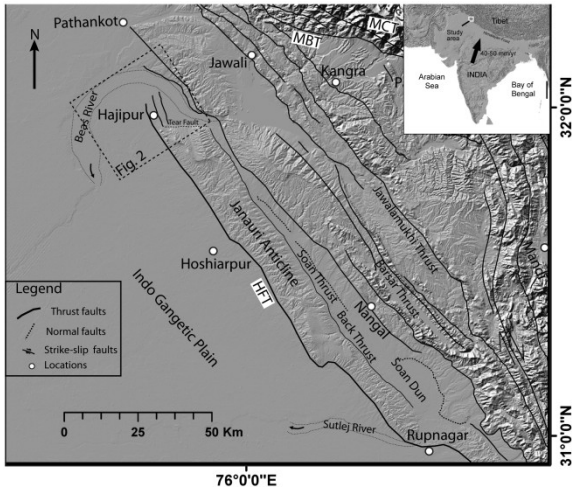


Fig. 1: Shaded relief image (USGS/SRTM data) illustrating major faults marked by continuous lines. - The rectangular box indicates the study area and its surrounding regions. The major faults are after Gansser (1964), Valdiya et al. (1984), Powers et al. (1998) and Malik and Mohanty, (2007). Inset shows DEM of India with location of study area.

### Active fault studies

The active fault mapping and paleoseismic investigation was carried out along the northwestern fringe of the Janauri anticline along the foothill zone of NW Himalaya Hajipur, Punjab. The Janauri anticline is a foreland fold, comprising the southernmost part of the Sub-Himalaya and extends for ~130 km in NNW-SSE direction. The Janauri anticline is bounded by two major rivers that flow into the Indo-Gangetic Plain – the Beas River in NNW and the Sutlej Rivers in SE. It has been suggested that this 130 km long fold structure was formed due to linkage of two smaller fold-segments (Malik and Mohanty, 2007). The segment linkage is well marked by a flat-topped uplifted surface in middle part of the anticline that represents a paleo-water gap of River Sutlej (Malik et al., 2010b). Several south facing active fault scarps were identified along the frontal part of the Janauri anticline, with the most prominent scarp along the south bank of the Beas River. Two parallel faults named as Hajipur faults (HF1 and HF2) striking NNW and SSE were identified near Hajipur and Siprian village (Fig. 2) (Malik et al., 2010a). These faults have displaced and uplifted the riverbed and terraces of the Beas River. We also identified a prominent fault trace with a north facing fault scarp, representing the evidence of a back-thrust developed parallel to the HF1 and HF2 (Fig. 2). The maximum height of the HF1 fault scarp in the SE is ~15 m near Bamonwala village and the height diminishes to 2 to 3 m towards the NNW. The height of HF2 fault scarp is about 6-8 m, comparatively lower than HF1. The fault scarp along HF1 is degraded and irregular, however HF2 fault scarp is less dissected and its relatively lower height

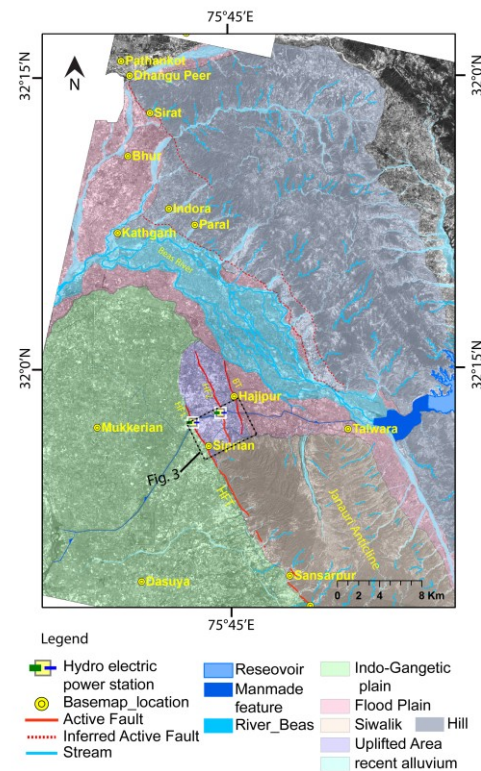


Fig. 2: Generalized geomorphic map of the study area traced on CARTOSAT-1 stereo ortho-kit satellite data. Solid red lines indicate active fault traces in Hajipur and surrounding areas.

### Fluvial terraces, terrace risers and lateral propagation of Beas River

The phenomenon of lateral propagation of faults and related fold growth is commonly observed in fold-and-thrust belts (Delcaillau et al., 1998; Burbank and Anderson, 2001). As displacement accumulates along a fault, the length and size of the surface rupture gradually increases. With each successive rupture event, the amplitude as well as breadth of the fault increase, and propagate laterally along the strike and also towards the foreland (Burbank and Anderson, 2001). Sarkar et al., 2014 suggested that Kameng River migrated towards northeast at a varying rate between ~7.5 – 13.5 cm/yr due to uplift of HFT in the Western Arunachal Himalaya.

Along the NW fringe of the Janauri anticline lateral propagation of the fault and related fold structures have resulted shift/deflection of the Beas River, during the Late Pleistocene and Holocene period. The expression of this deflection is well marked by several levels of terraces



and associated terrace risers (paleo-banks) (Figs. 3 and 4).

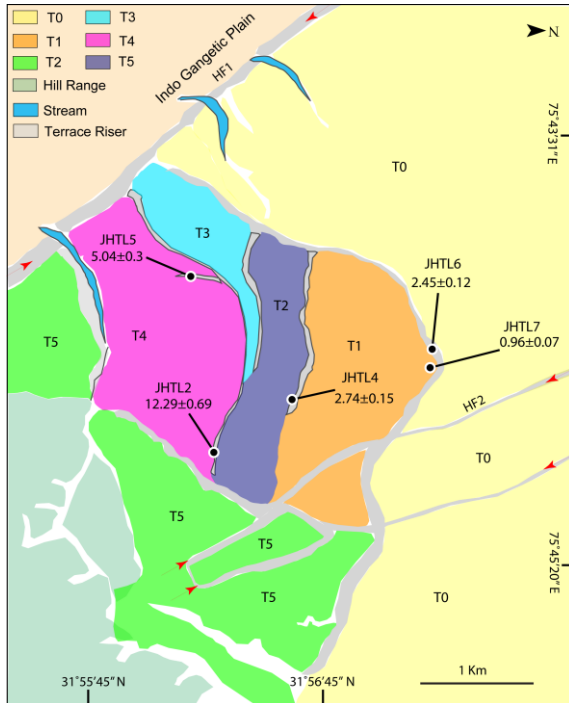


Fig. 3: Distribution of terraces on the south side of Beas River. At least six terraces (T0-T5) and five prominent terrace risers were identified. These terrace risers are indicative of shifting of Beas River channel due to lateral propagation and displacement along Hajipur Faults (HF1 and HF2). These terraces are displaced by HF1 and HF2 resulting in NNW facing fault scarps. Red arrows mark the traces of fault scarps.

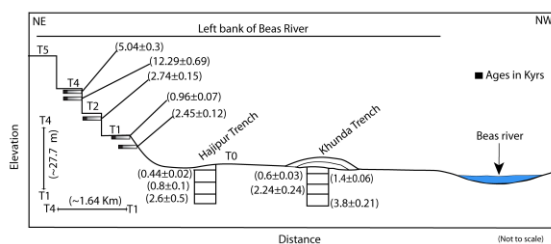


Fig. 4: Schematic diagram (Not to scale) showing the topographic profile of the T5, T4, T2, T1 and T0 terraces. Profile shows OSL sample locations from different level of terraces/terrace risers. From the OSL ages the terraces are young towards NNW. The OSL ages from Hajipur and Khunda trench are also shown.

In some areas, these terraces are vertically displaced and deformed by active faults associated with NNE and SSW facing fault scarps. In total 6 terraces/fluvial surfaces T0-T5 were identified (Figs. 3 and 4). The terraces are comprised of well-rounded pebble-cobble deposits, and finer sand+silt indicative of channel deposits and overbank deposits respectively. These deposits represent - aggradation along Beas River. We identified five paleo-banks, that indicate channel migration or

shifting of Beas River due to lateral propagation of Hajipur faults (HF1 and HF2). Ongoing tectonic movements along Hajipur fault (HF2) has displaced three terraces (T5, T1, and T0) across prominent SSW facing fault scarps with height ranging from 6 to 8 m (Fig. 3). The Optically Stimulated Luminescence (OSL) ages obtained from these terraces yielded ages ranging from 0.96 ka to 12.29 ka. T4: 12.29 ± 0.7 ka and 5.04 ± 0.3 ka; T2: 2.74 ± 0.15 ka; T1: 2.45 ± 0.12 ka and 0.96 ± 0.07 ka; T0: 0.8 ± 0.1 ka. We don't have any ages from the highest terrace (T5).

### Discussion & Summary

Existence of active faults in this region represents an excellent example of lateral propagation of faulting and related folding along the HFT. The NNE and SSW facing fault scarps, uplifted terraces and reduction in height of fault scarps along the strike towards the NNW provide evidence of successive movements along these faults and propagation of fault tip. The geomorphic relations indicate that the Beas River was not powerful enough to erode the growing fold, hence got deflected.

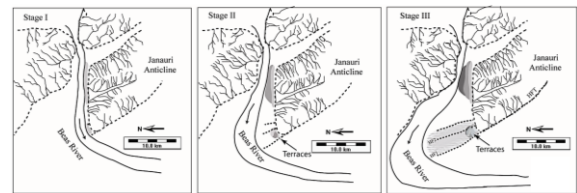


Fig. 5: Schematic diagram explaining different stages of the shifting of the Beas River. At Stage-I, in the absence of tectonic activity, the River flows close to the anticline with the development of fluvial terrace. At Stage-II, lateral propagation along HF1 and HF2 started with some deflection of the River. At stage-III, fault propagation and uplift dominates the process. It results in the development of the back-thrust and shifting of the Beas River to the present stage and formation of multiple terraces.

We propose a schematic model to explain the migration of the Beas River (Fig. 5). In Stage-I, it is presumed that prior to tectonic activity of the HFT and the two branching out faults HF1 and HF2, the Beas River was flowing close to the northwestern end of the Janauri anticline and debouching directly to the Indo-Gangetic Plain. During Stage-II, the activity of the HFT was transferred to the two newly developed faults HF1 and HF2. These faults started growing laterally by accumulating more displacement over time (Fig. 5). Movement along these faults resulted in the uplift of the floodplain of the Beas River and the development of south facing fault scarps. At this stage, the Beas River started deflecting from its original course and terraces were formed along the Beas River. Finally, in Stage-III, the continued lateral propagation and uplift in the vicinity of the faults resulted in the development of a back-thrust to the north of Hajipur fault (HF2). In this stage, the Beas River was deflected to its present position to the North



West of the Janauri anticline. Deflection and uplift resulted in the development of multiple terraces and associated terrace risers (paleo-banks). Considering the T0 is part of the floodplain and T1toT4 are the five terraces, the lateral migration would only be ~1.65 km towards northwest since 12.40 ka. This implies average lateral migration rate of  $\sim 13.3 \pm 0.76$  cm/yr. Since there are no ages available from the highest terrace, the lateral migration rate reflected is maximum. More ages from the terraces and other landforms will help towards better constrain the rate of river migration along Hajipur fault.

**Acknowledgements:** Financial support provided by Japan International Cooperation Agency (JICA) and Japan Science and Technology (JST) are duly acknowledged. We also acknowledge the partial financial support received from the Ministry of Earth Science (MoES), New Delhi, India.

## References

- Ambraseys, N. & R. Bilham, (2000). A note on Kangra Ms=7.8 earthquake of April 1905. *Current Science*, Vol. 74, 45-50.
- Ambraseys, N. N & J. Douglas, (2004). Magnitude calibration of north Indian earthquakes. *Geophysical Journal International* 158, 1-42
- Avouac, J.P., L. Meng, S. Wei, T. Wang & J. P. Ampuero, (2015). Lower edge of locked Main Himalayan Thrust unzipped by the 2015 Gorkha earthquake. *Nature Geoscience*.
- Burbank, D. W., Anderson, R. S., 2001. *Tectonic geomorphology* John Wiley & Sons.
- Delcaillau, B., B. Deffontaine, L. Floissac, J. Angelier, J. Deramond, P. Souquet, H. T. Chu & J. F. Lee, (1998). Morphotectonic evidence from lateral propagation of an active frontal fold; Pakuashan anticline, foothills of Taiwan. *Geomorphology* 24(4), 263-290.
- Delcaillau, B., J. M. Carozza & E. Laville, (2006). Recent fold growth and drainage development: the Janauri and Chandigarh anticlines in the Siwalik foothills, northwest India. *Geomorphology* 76, 241-256.
- De Sarkar, S., G. Mathew, K. Pande, P. Phukon, & A. K. Singhvi, (2014). Drainage migration and out of sequence thrusting in Bhalukpong, Western Arunachal Himalaya, India. *Journal of Geodynamics*, 81, 1-16.
- Gansser, A., (1964). *The Geology of the Himalaya*. Wiley Interscience, New York, pp.189.
- Kaneda, H., T. Nakata, H. Tsutsumi, H. Kondo, N. Sugito, Y. Awata, S. S. Akhtar, A. Majid, W. Khattak, A. A. Awan & R. S. Yeats, (2008). Surface rupture of the 2005 Kashmir, Pakistan, earthquake and its active tectonic implications. *Bulletin of the Seismological Society of America* 98 (2), 521-557.
- Kumahara Y. & R. Jayangondaperumal, (2013). Paleoseismic evidence of a surface rupture along the northwestern Himalayan Frontal Thrust (HFT). *Geomorphology* 180- 181, 47-56.
- Kumar, S., S. G. Wesnousky, T. K. Rockwell, R. W. Briggs, V. C. Thakur & R., Jayangondaperumal, (2006). Paleoseismic evidence of great surface rupture earthquakes along the Indian Himalaya. *Journal of Geophysical Research: Solid Earth* 111(B3).
- Lavé, J., D. Yule, S. Sapkota, K. Basant, C. Madden, M. Attal & R. Pandey, (2005). Evidence for a great Medieval earthquake (~ 1100 AD) in the central Himalayas, Nepal. *Science* 307(5713), 1302-1305.
- Lyon-Caen, H., & P. Molnar, (1983). Constraints on the structure of the Himalaya from the analysis of gravity anomalies and a flexural model of the lithosphere. *Journal of Geophysical Research* 88 (B10), 8171-8191.
- Malik, J. N. & T. Nakata, (2003). Active faults and related Late Quaternary deformation along the Northwestern Himalayan Frontal Zone, India. *Annals of Geophysics* 46, 917- 936.
- Malik, J. N. & C. Mohanty, (2007). Active tectonic influence on the evolution of drainage and landscape: Geomorphic signatures from frontal and hinterland areas along the Northwestern Himalaya, India. *Journal of Asian Earth Sciences* 29, 604-618.
- Malik, J. N., T. Nakata, G. Philip, N. Suresh & N. S. Viridi, (2008). Active fault and paleoseismic investigation: evidence of historic earthquake along Chandigarh Fault in the frontal Himalayan zone, NW India. *Journal of Himalayan Geology* 29(2), 109-117.
- Malik, J. N., A. A. Shah, A. K. Sahoo, B. Puhan, C. Banerjee, D. P. Shinde, N. Juyal, A. K. Singhvi & S. K. Rath, (2010a). Active fault, fault growth and segment linkage along the Janauri anticline (frontal foreland fold), NW Himalaya, India. *Tectonophysics* 483(3), 327-343.
- Malik, J. N., A. K. Sahoo, A. Shah, D. P. Shinde, N. Juyal & A. K. Singhvi, (2010b). Paleoseismic evidence from trench investigation along Hajipur fault, Himalayan Frontal Thrust, NW Himalaya: Implications of the faulting pattern on landscape evolution and seismic hazard. *Journal of Structural Geology* 32:350-361, doi:10.1016/j.jsg.2010.01.005.
- Malik, J. N., S. Sahoo, S. Satuluri & K. Okumura, (2015). Active Fault and Paleoseismic Studies in Kangra Valley: Evidence of Surface Rupture of a Great Himalayan 1905 Kangra Earthquake (Mw 7.8), Northwest Himalaya, India. *Bulletin of the Seismological Society of America*.
- Nakata, T., (1989). Active faults of the Himalaya of India and Nepal. *Geological Society of America special Paper* 232: 243-264.
- Powers, P. M., R. J. Lillie & R. S. Yeats, (1998). Structure and Shortening of the Kangra and Dehra Dun Reentrants, Sub Himalaya, India. *Geological Society of America* 110, 1010-1027.
- Rajendran, C. P., B. John & K. Rajendran, (2015). Medieval pulse of great earthquakes in the central Himalaya: Viewing past activities on the frontal thrust. *Journal of Geophysical Research: Solid Earth*, 120(3), 1623-1641.
- Sapkota, S. N., L. Bollinger, Y. Klinger, P. Tapponnier, Y. Gaudemer & D. Tiwari, (2013). Primary surface ruptures of the great Himalayan earthquakes in 1934 and 1255. *Nature Geoscience* 6(1), 71-76.
- Seeber, L. & J. G. Armbruster, (1981). Great detachment earthquakes along the Himalayan arc and long-term forecasting, in *Earthquake Prediction: an International Review*, edited by D.W. Simpson and P.G. Richards, AGU, Maurice Ewing Ser., vol. 4, 259-279.
- Thakur, V. C., (2004). Active tectonics of Himalayan Frontal Thrust and Seismic Hazard to Ganga Plain. *Current Science* 86, 1554-1559.
- Valdiya K.S., D. D. Joshi, R. Sanwal & S. K. Tandon, (1984). Geomorphologic development across the active Main Boundary Thrust, an example from the Nainital Hills in Kumaun Himalaya, *Journal of Geological Society of India* 25(12), 761-774.
- Wesnousky, S. G., S. Kumar, R. Mohindra & V. C. Thakur, (1999). Uplift and convergence along the Himalayan Frontal Thrust of India. *Tectonics* 18(6): 967-976.
- Yeats, R., Sieh, S. K., Allen, C. R. (1997). *Geology of earthquakes*; Oxford University Press, p. 568.



## AMS $^{14}\text{C}$ TESTS OF CORRELATIONS OF GREAT EARTHQUAKES ALONG THE CASCADIA SUBDUCTION ZONE, COASTAL OREGON

NELSON, Alan R., Geologic Hazards Science Center, U.S. Geological Survey, Golden, CO ([anelson@usgs.gov](mailto:anelson@usgs.gov)),

Simon E. Engelhart ([engelhart@uri.edu](mailto:engelhart@uri.edu)), Department of Geosciences, University of Rhode Island, Kingston RI,  
Robert C. Witter ([rwitter@usgs.gov](mailto:rwitter@usgs.gov)), Alaska Science Center, U.S. Geological Survey, Anchorage AK, and  
Christopher B. DuRoss ([cduross@usgs.gov](mailto:cduross@usgs.gov)) Geologic Hazards Science Center, U.S. Geological Survey, Golden CO

After three decades of debate, consensus remains elusive about the rupture lengths and frequency of megathrust earthquakes at the Cascadia subduction zone. Radiocarbon ages for earthquake evidence from coastal wetland stratigraphic sequences generally overlap broad  $^{14}\text{C}$ -age intervals for the most widely correlated marine turbidites, triggered by shaking from the greatest (~M9) earthquakes rupturing much of the 1200-km-long subduction zone. But the times and number of lesser great earthquakes (~M8-8.8), which may have ruptured only a few hundred kilometers of the megathrust, are uncertain. Along-strike correlation of coastal earthquake evidence has largely relied on position in a stratigraphic sequence and maximum-limiting  $^{14}\text{C}$  ages with errors of decades to hundreds of years.

We consider 180 (72 unpublished) AMS  $^{14}\text{C}$  ages from the 12 best-dated sequences along 350 km of the Oregon coast to test along-strike correlations of stratigraphic contacts inferred to mark subsidence during great earthquakes and(or) inundation by their accompanying tsunamis during the past 2000 years. At each coastal site we selected the highest quality (least ambiguous stratigraphic context) plant macrofossils providing the closest maximum- and minimum-limiting ages for each contact predating the ~M9 AD 1700 earthquake. Comparison of OxCal-calculated age models for contacts at each site suggests three closely spaced earthquakes from 700–1200 cal yr BP, an interval previously considered to include coastal evidence for only two earthquakes. If accurate, the comparison implies incomplete stratigraphic records for some great earthquakes at some sites. Product means (with  $2\sigma$  uncertainties) of OxCal age probability distribution functions yield great earthquakes at  $798\pm 55$ (6 sites),  $933\pm 59$ (3 sites),  $1124\pm 59$ (6 sites),  $1264\pm 26$ (5 sites), and  $1546\pm 23$ (11 sites) cal yr BP.

Keywords: paleoseismology, earthquake hazard, tsunami hazard, coastal hazards, earthquake stratigraphy, radiocarbon dating,



## New paleoseismic data from the Lal Dhang trench site across the Himalayan Frontal Thrust in India

Niemi, Tina M. (1), Robyn L. Daniels (1), R. Jayagondaperumal (2)

(1) Department of Geosciences, University of Missouri-Kansas City, 5100 Rockhill Road, Kansas City, MO 64110, USA. Email: niemit@umkc.edu

(2) Wadia Institute of Himalayan Geology, Dehradun, India

**Abstract:** The Himalayan Frontal Thrust (HFT), also referred to as the Main Frontal Thrust, is the 2500 km-long fault system that marks the active southward-verging collisional boundary of the Eurasian plate with the Indian subcontinent. Defining the rupture segments for both recent and historical earthquakes has been a challenge especially in areas with long seismic gaps. In Fall 2015, a new paleoseismic trench, approximately 5-m-wide by 30-m-long and 8-m-deep, was excavated across the HFT in the Central Seismic Gap at the Lal Dhang site, where a >10-m-high fault scarp runs north-northwest along the fault. Excavation revealed evidence of faulting and folding of the depositional units of the terrace and floodplain. Two prominent, stacked, thrust faults with recumbent folded units were driven over horizontal units to the southwest. The exposed sections show heights of approximately 3-4 m for each fold, with a combined height of approximately 6.5 m, although erosion has reduced the original fold dimensions. The folded and faulted strata can be traced laterally to the flat-lying fluvial deposits that show no erosion or depositional hiatus, thus suggesting that the deformation observed in the trench occurred in a single earthquake. Radiocarbon analyses of the stratigraphic units will constrain the date of this earthquake.

**Key words:** Himalaya thrust, historic earthquakes, paleoseismology.

### INTRODUCTION

The convergence of the Indian subcontinent with Eurasia is marked by several south-verging structures including the active Himalayan Frontal thrust (HFT) fault (also known as the Main Frontal Thrust) (e.g. Yeats *et al.*, 1992) (Fig. 1). The HFT generally marks the contact of Tertiary Siwalik Sub-Himalayan sediment with Quaternary sediment. Large magnitude, twentieth century earthquakes, including the 1905 Kangra, 1934 Nepal-Bihar, and 1950 Assam earthquakes, and historically documented earthquakes (e.g. 1255, 1344, 1505, and 1555,) have likely ruptured the HFT. Defining the rupture segments of these earthquakes has been a challenge. The Central Seismic Gap (CSG) was defined as the fault segment between the proposed 1905 and 1934 earthquake damage zone (Khattari, 1987). Some researchers have suggested that the 1505 earthquake with a rupture trace of >600 km may have filled all or part of the CSG in the past (e.g. Ambraseys and Jackson, 2003; Bilham and Ambraseys, 2005). Other large-magnitude historical earthquakes (e.g. 1803 and 1833) may be similar to the 2015 Gorkha event in Nepal (Elliot *et al.*, 2016) and have only ruptured the deeper portion of the main Himalayan detachment and not the HFT.

One of the fundamental questions in seismic hazard assessment that looms over heavily populated areas in India and surrounding countries is whether a “giant,” magnitude (M) > 9 megathrust subduction zone earthquake, like those that occurred in Japan in 2011 and Indonesia in 2004, has the potential to occur along the Himalayan Frontal Thrust fault. Geological data suggest that 10- to 20-m-horizontal slip events with >10-m-high scarps are recorded at some paleoseismic

sites along the HFT active fault (e.g. Lavé *et al.*, 2005; Kumar *et al.*, 2006; 2010). Such a “mega” seismic event has not been recorded in the past 200-400 years based on historical records as compiled and presented in earthquake catalogues for India and Nepal (e.g. Seeber and Armbruster, 1981; Iyengar *et al.*, 1999; Ambraseys, 2000; Pant, 2002; Ambraseys and Douglas, 2004; Bilham and Ambraseys, 2005). Thus, some have questioned whether earthquakes as large as M>9 can occur along this tectonic boundary (e.g. Rajendran *et al.*, 2013; Gupta and Gahalaut, 2015).

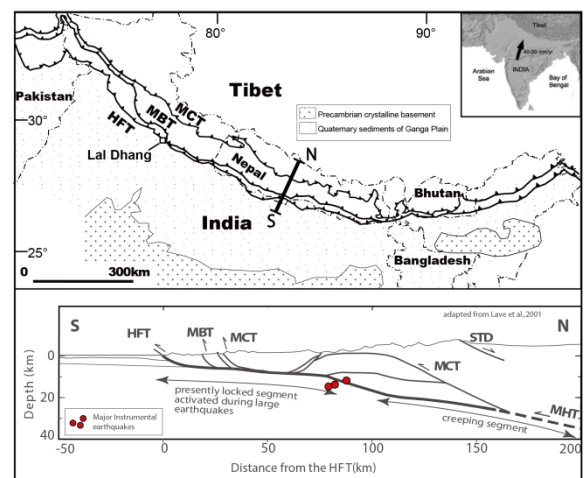


Fig. 1: Map showing the major zones of the Himalayan convergence—MCT: Main Central Thrust; MBT: Main Boundary Thrust; and HFT: Himalayan Frontal Thrust. Schematic cross-section through central Nepal showing the main structures and instrumental thrust earthquake foci. STD: Southern Tibet Detachment; MHT: Main Himalayan Thrust (after Lavé *et al.*, 2001).



Boundary-element modeling showed that a >20-m-slip event with a 1000 year strain accumulation is theoretically possible on the HFT (Feldl and Bilham, 2006) although such large fault slips are not seen in subduction zone earthquakes (Murotani *et al.*, 2013). Alternatively, the large surface scarps along the HFT may represent two or more events instead of one surface-rupturing earthquake (e.g. Kumahanra and Jayangondaperumal, 2013; Jayangondaperumal *et al.*, 2013; Rajendran *et al.*, 2015). The possibility that the Himalayan Frontal thrust could rupture in a  $M > 9$  earthquake remains controversial.

Geodetic models show that the HFT is locked from the surface down dip to a distance of approximately 100 km (Fig. 1). Given a convergence rate of 18-20 mm/yr between the Indian subcontinent and Tibet on the Main Himalayan Thrust, large amounts of strain have potentially accumulated (Aders *et al.*, 2012). Bilham and Ambraseys (2005) wrote "The absence of a well-documented earthquake cycle anywhere along the Himalayan arc is a considerable impediment to quantifying seismic risk in the Himalaya." A review of paleoseismic data by Mugnier *et al.* (2013) suggested that the pattern of great earthquakes might be random. However, recent paleoseismic data from two sites in eastern Nepal identified faulting in the 1255 and 1934 earthquakes (Sapkota *et al.*, 2013) and reported 6 to 7 earthquakes over a 4.5 ka period with a  $870 \pm 350$  year recurrence (Bollinger *et al.*, 2014; 2016) suggesting regular recurrence.

The October 8, 2005 Kashmir earthquake was a devastating example of the power that seismic events on the Himalayan fault system can unleash. An estimated 86,000 people died in the earthquake (USGS website). The earthquake can also potentially provide a modern analog for a convergent thrust event. The  $M_w$  7.6 Kashmir earthquake ruptured a 60-km-long surface fault and formed a maximum scarp height of 7 m (Kaneda *et al.*, 2008). A trench across the active fault constrained the penultimate earthquake to approximately 2,000 years ago (Kondo *et al.*, 2008). However, these authors concluded that the 2005 Kashmir earthquake did not occur on the HFT, but on an intraplate fault within the sub-Himalayan wedge.

It is evident that many issues pertaining to the historical and paleoseismic chronology of earthquakes along the HFT remain unresolved. For example, what is the rupture trace of the 1505 or other historical earthquakes and can rupture segments be defined? Deciphering the earthquake recurrence and fault segmentation of HFT historical earthquakes remains a primary research objective. In this paper, we test whether "giant" or "megathrust" earthquakes have ruptured the Indian section of the Himalayan fault system with our recent paleoseismic excavations along the HFT at a site called Lal Dhang (Fig. 1), where a high single-event scarp was previously studied by Kumar *et al.* (2006).

## PALEOSEISMIC INVESTIGATIONS

The Lal Dhang paleoseismic site is located approximately 50 km east of Dehra Dun in Uttarakhand, India. The HFT fault scarp prominently offsets Quaternary fluvial terrace deposits that were deposited at the front of the Siwalik mountains along the Rawasan River (Fig. 2). The fault scarp is at least 13 m in height based on topographic profiling (Fig. 3).

In a previous study at the Lal Dhang site (Kumar *et al.*, 2006), a trench (A1) excavated across the NW-trending fault scarp revealed folding and faulting. Radiocarbon ages of lithostratigraphic units indicate that the last faulting event occurred sometime between 1282 A.D. and 1632 A.D. Vertical separation measured on the surface scarp was measured as at least 9 m, while displacement on the horizontal fault measured a minimum of 7 m.

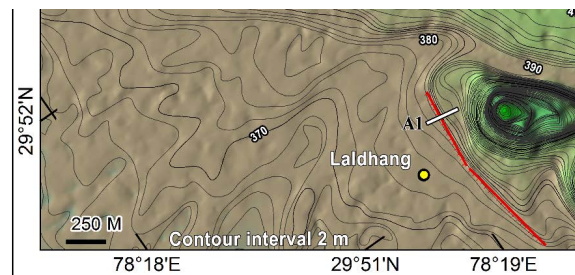


Fig. 2: Topographic map of the Lal Dhang site showing location of the paleoseismic trench investigation (A1) of Kumar *et al.* (2006).

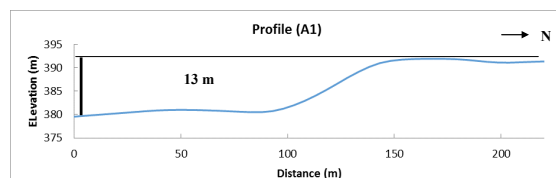


Fig. 3: Topographic profile across the HFT fault scarp at the Lal Dhang site at the A1 trench

In Fall of 2015, a new paleoseismic trench of approximately 30 meters in length, 5 meters in width and 8 meters in depth, was excavated across the fault scarp at the Lal Dhang site, just southeast of the earlier trench by Kumar *et al.* (2006). A real-time-kinematic GPS survey conducted as part of this study showed the vertical separation of the scarp to be >10 meters. Trenching at this location exposed two thrust fault strands with associated fold deformation of the units (Fig. 4). A third fault strand was also identified high in the section, but could not be verified because the hanging wall is predominately a boulder conglomerate lacking distinct stratigraphic layering. The trench clearly establishes that the one fold documented in the Kumar *et al.* (2006) paper is actually two folds and possibly three thrust faults (Fig. 4).



The stratigraphic units uncovered in our trench are analogous to those described by Kumar *et al.* (2006). This includes nearly horizontal stratigraphic units with a basal fluvial unit of rounded cobble- to boulder-sized gravel that grades to sandy gravel and sand. This is capped by fine-grained overbank sediment and a sandy loam soil. Each of the units is repeated in the hanging wall where they are folded and sheared (Fig. 4). The folds are eroded and buried by two layers of colluvium separated by a carbonaceous, silty clay layer.

In our trench, each of the two, lower faults showed dips of approximately 18° steepening to approximately 28° as the strands approached the bottom of the trench. In both cases, the depositional units of the footwall were deformed into a synclinal fold and subsequently sheared as they were dragged forward by the overriding hanging wall. The hanging wall is also deformed into an anticlinal fold. The uppermost deformed unit of the lower fault, interpreted as the ground surface at the time of rupture, exhibits the same, loading, flame structures as seen in the earlier study. The upper fault strand shows similar deformation of the footwall units, with folding and subsequent shearing evidenced here by both clastic imbrication and offset of the folded units.

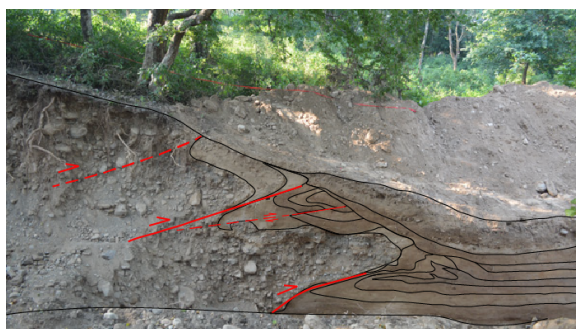


Fig. 4: Interpretation of the 2015 Lal Dhang paleoseismic trench showing multiple thrust faults displacing coarse-clastic terrace deposits over fine-grained alluvial sediment.

Because the folded strata can be traced laterally to the flat-lying fluvial deposits that show no erosion, unconformity or colluvium, the deformation observed in the trench occurred in a single earthquake. Charcoal and other organic samples were collected from key locations within each of the depositional units adjacent to each of the fault strands, in the footwall and in the overlying, unfaulted units. To date, fifteen samples have been dispatched to labs for dating by accelerated mass spectrometry, which will constrain the date of this earthquake. Although retrodeformation analysis is underway, it appears that the fault slip for the paleoseismic event at this site is very large (two to three times the previous measurement) indicating a possible megathrust magnitude earthquake.

**Acknowledgements:** This project was sponsored by a grant from the UMKC Office of Research Services to Niemi and a UMKC School of Graduate Studies grant to Daniels. Special thanks to Dr. Piyooch Rautela and the Disaster Mitigation and

Management Centre of Uttarakhand for the permissions required to complete the project, students Lauren Holt from the UMKC and Arjun Pandey and Aravind Nair from the Wadia Institute of Himalayan Geology, the city of Lal Dhang for its hospitality, and the local workers for their assistance in the field.

## References

- Ader, T., and 14 others, 2012, Convergence rate across the Nepal Himalaya and interseismic coupling on the Main Himalayan Thrust: Implications for seismic hazard: *Journal of Geophysical Research*, v. 117, B04403, doi:10.1029/2011JB009071
- Ambraseys, N., 2000, Reappraisal of north-India earthquakes at the turn of the 20<sup>th</sup> century: *Current Science*, v. 70, p. 1237-1250.
- Ambraseys, N., and Jackson, D., 2003, A note on early earthquakes in northern India and southern Tibet: *Current Science*, v. 84, no. 4, p. 570-582.
- Ambraseys, N., and Douglas, J., 2004, Magnitude calibration of north Indian earthquakes: *Geophysical Journal International*, v. 158, p. 1-42.
- Feldl, N., and Bilham, R., 2006, Great Himalayan earthquakes and the Tibetan plateau: *Nature*, v. 444, p. 165-170.
- Bilham, R., and Ambraseys, N., 2005, Apparent Himalayan slip deficit from the summation of seismic moments for Himalayan earthquakes, 1500-2000: *Current Science*, v. 88, no. 10, p. 1658-1663.
- Bollinger, L., Sapkota, S.N., Tapponnier, P., Klinger, Y., Rizza, M., Van der Woerd, J., Tiwari, D.R., Pandey, R., Bitri, A., and Bes de Berc, S., 2014, Estimating the return times of great Himalayan earthquakes in eastern Nepal: Evidence from the Patu and Bardibas strand of the Main Frontal Thrust: *Journal of Geophysical Research*, v. 119, 7123-7163.
- Bollinger, L., Tapponnier, P., Sapkota, S.N., and Klinger, Y., 2016, Slip deficit in central Nepal: omen for a repeat of the 1344 AD earthquake?: *Earth, Planets and Space*, v. 68, no. 12, DOI 10.1186/s40623-016-0389-1.
- Elliott, J.R., Jolivet, R., González, R.J Avouac, J.-P., Hollingsworth, J., Searle, M.P., and Stevens, V.L., 2016, Himalayan megathrust geometry and relation to topography revealed by the Gorkha earthquake, *Nature Geosciences*, v. 9, DOI: 10.1038/NGEO2623..
- Gupta, H.K., and Gahalaut, V.K., 2015, Can an earthquake of Mw~9 occur in the Himalayan region?, in *Tectonics of the Himalaya*, Muherjee, S. et al. (eds.): Geological Society, London, Special Publications, v. 412, p. 43-53.
- Iyengar, R.N., Sharma, D., and Siddiqui, J.M., 1999, Earthquake history of India in Medieval times: *Indian Journal of History of Science*, v. 34, no. 3, p. 181-237.
- Jayangondaperumal, R., Mugnier, J.-L., and Dubey, A.K., 2013, Earthquake slip estimation from the scarp geometry of Himalayan Frontal Thrust, western Himalaya: Implications for seismic hazard assessment: *International Journal of Earth Sciences*, v. 102, p. 1937-1955.
- Kaneda, H., Nakata, H., Tsutsumi, H., Kondo, H., Sugito, N., Awata, Y., Akhtar, S.S., Majid, A., Khattak, W., Awan, A.A., Yeats, R.S., Hussain, A., Ashraf, M., Wesnousky, S.G., and Kausar, A.B., 2008, Surface rupture of the 2005 Kashmir, Pakistan, earthquake and its active tectonic implications: *Bulletin of the Seismological Society of America*, v. 98, no. 2, p. 521-557.
- Khattri, K.N., 1987, Great earthquakes, seismicity gaps and potential for earthquake disaster along the Himalaya plate boundary: *Tectonophysics*, v. 138, P. 79-92.
- Kondo, H., Nakata, T., Akhtar, S.S., Wesnousky, S.G., Sugito, N., Kaneda, H., Tsutsumi, H., Khan, A.M., Khattak, W., Kausar, A.B., 2008, Long recurrence interval of faulting beyond the 2005 Kashmir earthquake around the northwestern margin of the Indo-Asian collision zone: *Geology*, v. 36, p. 731-734.
- Kumahara, Y., Jayangondaperumal, R., 2013, Paleoseismic



## INQUA Focus Group on Paleoseismology and Active Tectonics



paleoseismicity.org

- evidence of a surface rupture along the northwestern Himalayan Frontal Thrust (HFT): *Geomorphology*, v. 180-181, p. 47-56.
- Kumar, S., Wesnousky, S.G., Rockwell, T.K., Briggs, R.W., Thakur, V.C., and Jayangondaperumal, R., 2006, Paleoseismic evidence of great surface rupture earthquakes along the Indian Himalaya: *Journal of Geophysical Research*, v. 111, B03304, doi:10.1029/2004JB003309.
- Kumar, S., Wesnousky, S., Jayangondaperumal, R., Nakata, T., Kumahara, Y., and Singh, V., 2010, Paleoseismological evidence of surface faulting along the northeastern Himalayan front, India: Timing, size, and spatial extent of great earthquakes: *Journal of Geophysical Research*, v. 115, B12422, doi:10.1029/2009JB006789.
- Lavé, J., Yule, D., Sapkota, S., Bassant, K., Madden, C., Attal, M., and Pandey, R., 2005, Evidence for a great medieval Earthquake (1100 AD) in the Central Himalayas, Nepal: *Science*, v. 307, p. 1302-1305.
- Mugnier, J.L., Gajurel, A., Huyghe, P., Jayagondaperumal, R., Jouanne, F., and Upreti, B., 2013, Structural interpretation of the great earthquakes of the last millennium in the central Himalaya: *Earth Science Reviews*, v. 127, p. 30-47.
- Murotani, S., Satake, K., and Fujii, Y., 2013, Scaling relations of seismic moment, rupture area, average slip, and asperity size for M~9 subduction-zone earthquakes: *Geophysical Research Letters*, v. 40, p. 5070-5074.
- Pant, M.J., 2002, A step towards a historical seismicity of Nepal: *Adarsa*, no. 2, p. 29-60.
- Rajendran, C.P., Rajendran, K., Sanwal, J., and Sandiford, M., 2013, Archeological and historical database on Medieval earthquakes of the central Himalaya: Ambiguities and inferences: *Seismological Research Letters*, v. 84, no. 6, p. 1098-1108.
- Sapkota, S.N., Bollinger, L., Klinger, Y., Tapponnier, P., Gaudemer, Y., and Tiwari, D., 2013, Primary surface ruptures of the great Himalayan earthquakes in 1934 and 1255: *Nature Geosciences*, v. 6, p. 71-76.
- Seeber, L., and Armbruster, J.G., 1981, Great detachment earthquakes along the Himalayan arc and long-term forecasting, in *Earthquake Prediction: An International Review*, Maurice Ewing Series 4, edited by D. E. Simpson and P. G. Richards, AGU, Washington, D. C., p. 259-277.
- Yeats, R.S., Nakata, T., Farah, A., Fort, M., Mirza, M.A., Pandey, M.R., and Stein, R.S., 1992, The Himalayan Frontal fault system: *Annales Tectonicae*, supplement to v. 6, p. 85-98.



## Earthquake Geology of the April 14 and 16, 2016 Kumamoto Earthquakes

Koji Okumura (1)

(1) Graduate School of Letters, Hiroshima University, 1-2-3 Kagamiyama, 739-0045 Japan. Email: kojiok@hiroshima-u.ac.jp.

**Abstract:** A Mw 7.0 earthquake hit west central Kyushu Island in west Japan at 01:25 JST on April 16, 2016. Reportedly 49 were killed, 1 are missing and more than thousand are injured as of April 27. 28 hours before, at 21:26 JST on April 14 another Mw 6.1 had shook the same region severely. Intense ground shaking by two successive earthquakes caused structural damages in an extensive area. The shakings by a large number of aftershocks forced 90,000 people to evacuate from their homes no matter the homes were damaged or not. And the extensive damages to infrastructures make their lives more difficult.

Previously mapped and evaluated Futagawa and Hinagu fault zones are the sources of these two earthquakes. The Futagawa fault zone, the northeastern portion of the two fault zones, runs about 30 km ENE-WSW. The longest section of the NE portion is called Futagawa fault. The SSW-NNE trending Hinagu fault merges with the Futagawa near its west termination (F and H in figure 1). The Futagawa fault is the source of the Mw 7.0 with 2 m+ right-lateral strike-slip at the surface. The Mw 6.1 earthquake ruptured about 15 km long northernmost section of the Hinagu fault without surface ruptures. Minor surface ruptures appeared in this section during the Mw 7.0.

**Key words:** surface fault, secondary fault, foreshock, strong ground motion, earthquake forecast

### 1. Tectonics

The April 2016 earthquakes occurred on the south margin of the Central Kyushu rift. Central Kyushu is the only area of volcanic extensional tectonics in Japan, where EW compression is predominant. Unzen volcano in west of Kumamoto, Aso volcano, and Beppu-Haneyama graben in east are within this NS extending volcanic graben. In southwest, the graben is believed to continue down to the Okinawa trough, the active back-arc spreading center behind the Ryukyu island arc. In northeast, the graben terminates in Beppu Bay and the active tectonics shift to strike-slip of the Quaternary Median Tectonic Line (figure 1).

In west of the Quaternary Median Tectonic Line, there is a continuous boundary between Mesozoic subduction-related sediments in south and the Neogene volcanics and sediments in north. The Median Tectonic Line in Shikoku is a very active Quaternary transform, but the activity is replaced with normal faulting on shore Kyushu in most part of the graben. So, the geologic boundary along the south margin of the graben is mostly inactive except for the Futagawa fault.

The Futagawa-Hinagu fault zone is driven both by the EW compression derived from Philippine Sea plate subduction and by the N-S extension of the Central Kyushu rift. The slip is right-lateral strike-slip with south-side-up normal separation. That means the WSW-ENE strike Futagawa fault is dipping NNW and the NNE-SSW strike Hinagu fault is dipping WNW. The dips are within 60 to 80 degrees. On both faults, right-lateral strike-slip is predominant, but the uplift of the Kyushu Mountains

in the south is due to the normal component of the fault movement.

### 2. Earthquakes

The April 14 Mw 6.1 recorded the highest JMA intensity scale of 7 at Mashiki JMA (Japan Meteorological Agency) station. The KiK-net (Strong-motion Seismograph Network of the National Research Institute for Earth Science and Disaster Prevention: NIED) maximum peak ground acceleration at Mashiki (KMMH16) was 1580 cm/s<sup>2</sup> in the area of the JMA intensity scale of 7.

[http://www.j-risq.bosai.go.jp/report/static/R/20160414212642/0131/00001/R-20160414212642-0131-00001-RE-PORT\\_EN.html](http://www.j-risq.bosai.go.jp/report/static/R/20160414212642/0131/00001/R-20160414212642-0131-00001-RE-PORT_EN.html)

[http://www.kyoshin.bosai.go.jp/kyoshin/topics/html20160414212621/main\\_20160414212621.html](http://www.kyoshin.bosai.go.jp/kyoshin/topics/html20160414212621/main_20160414212621.html)

[http://www.fnet.bosai.go.jp/event/tdmt.php?\\_id=20160414122500&LANG=en](http://www.fnet.bosai.go.jp/event/tdmt.php?_id=20160414122500&LANG=en)

The Mw 6.1 earthquake ruptured the deeper part of the northernmost section of the Hinagu fault. Strong ground motion took place in north and northwest of the epicenter or respectively in Mashiki town and Kumamoto city. The intensity 7 at Mashiki may be due to the directivity effect of the northward rupture propagation on the Hinagu fault. The radiation of strong seismic wave perpendicular to the WNW dipping Hinagu fault plane may be the cause of the strong shaking in Kumamoto.

The Mw 7.0 earthquake on April 16 occurred during the aftershock sequence of a Mw 6.1 earthquake at 21:26 JST on April 14, 2016. Therefore the Mw 7.0 "aftershock" on



April 16 was immediately redefined as a "mainshock" after the occurrence and the Mw 6.1 "main-shock" was

which is located between the epicenter in north and the surface fault in south. Both the epicenter and the fault

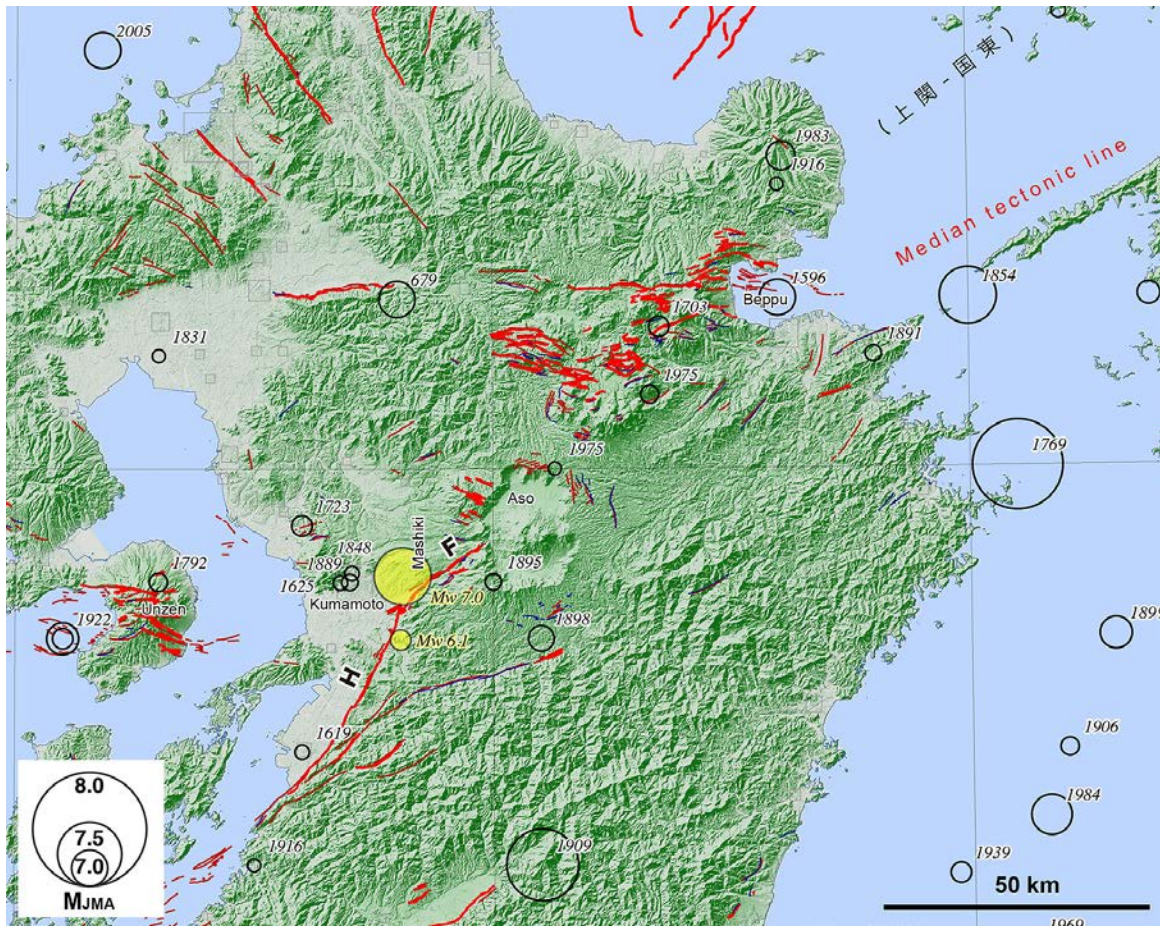


Fig. 1: Quaternary faults and earthquakes in Northern Kyushu. Quaternary faults: Nakata and Imaizumi eds. (2002), Research Group for Active Faults of Japan (1995), Historic earthquakes: Usami (1996)

redefined as a "foreshock". The Mashiki JMA station again recorded intensity 7. The Mashiki KiK-net station KMMH16 recorded  $1320 \text{ cm/s}^2$  this time, a little smaller than during the Mw 6.1.

[http://www.j-risq.bosai.go.jp/report/static/R/20160416012514/0424/00002/R-20160416012514-0424-00002-REPORT\\_EN.html](http://www.j-risq.bosai.go.jp/report/static/R/20160416012514/0424/00002/R-20160416012514-0424-00002-REPORT_EN.html)  
[http://www.kyoshin.bosai.go.jp/kyoshin/topics/html/20160416012405/main\\_20160416012405.html](http://www.kyoshin.bosai.go.jp/kyoshin/topics/html/20160416012405/main_20160416012405.html)  
<http://www.fnet.bosai.go.jp/event/tdmt.php?id=20160415162400&LANG=en>

The main-shock caused extensive structural damages along the Futagawa fault and further east and further west of the fault. The shaking was again the most intensive at Mashiki town. Many houses that were already damaged by the Mw 6.1 collapsed during the Mw 7.0. The extremely strong shaking may be due to the directivity effect of the up-dip propagation of the rupture on the Futagawa fault under Mashiki town,

are two kilometers away from the Mashiki town in opposite directions.

The fault plane dips  $60^\circ$  (by GSI: <http://www.gsi.go.jp/common/000139798.pdf>) to  $84^\circ$  (f-net moment tensor: <http://www.fnet.bosai.go.jp/event/tdmt.php?id=20160415162400&LANG=en>) NWN and hypocenter depth is 14 km. The ground acceleration spectra of NIED's KiK-net show significantly larger acceleration at 0.5 to 1.0 Hz by the Mw 7.0 than by the Mw 6.1. Though the peak ground acceleration is smaller by the Mw 7.0, this larger acceleration at 0.5 to 1.0 Hz might account for the heavier damages to Mashiki town by the Mw 7.0.

The rupture propagated toward ENE along the strike of the Futagawa fault. At the end of the rupture is the Minami-Aso village, where 14 were killed and many slope failures occurred. The source fault terminates in the east bank of the Shirakawa barranca where the fault intersects with the Aso Caldera rim. In this area, topographic relief is much larger than in other source region for the 300–700 m high caldera walls, 100–150 m



deep barranca gorge, and steeply eroded edifices or the central cone volcanoes in east. The steep slopes failed at many locations by the shaking of the mainshock, probably intensified by directivity effects. The Late Quaternary sediments filling the Aso Caldera (95,000 years old) also amplified the ground motion to cause many structural damages.

### 3. Crustal movement and surface faulting

The Geospatial Information Authority of Japan (GSI) published the GEONET (GNSS Earth Observation Network System) observation and model, and SAR (Synthetic Aperture Radar) interferometry results using the ALOS-2 (Daichi-2) satellite together with a lot of low-altitude air-photos and UAV movies.

<http://www.gsi.go.jp/BOUSAI/H27-kumamoto-earthquake-index.html>

Mw 6.1 foreshock

<http://www.gsi.go.jp/common/000139760.png>

Mw 7.0 mainshock:

<http://www.gsi.go.jp/common/000139809.png>

<http://www.gsi.go.jp/common/000139905.pdf>

The SAR interferometry results clearly demonstrate how faulting occurred and how the surface was deformed. The deformation by the Mw 6.1 is broad and as small as 10 to 20 cm over 10 km wide areas. There was no surface rupture. After the Mw 7.0 more than 10 fringe cycles appeared along the Futagawa fault corresponding to up to 2 m strike-slip offset at the surface on the fault. Along the northernmost Hinagu fault, the sharp line cutting through fringes coincides with the observation of ~25 cm offset by Tohoku University geologists (<http://irides.tohoku.ac.jp/irides-news/20160417/289>).

According to the preliminary reports from the field and the author's own survey, up to 2.0 m consistent right-lateral strike-slip is observed on the Futagawa fault. The vertical component is usually up to 0.5 m south-side-up, but up to 0.2 m north-side-up deformation is also observed. The offset along the northernmost Hinagu fault is also right-lateral strike-slip. In addition to the slip along the master strands, a 5 km long branch fault of up to 1.2 m right-lateral strike-slip appeared in the east of and under Mashiki town (Kumahara et al.: <http://jsaf.info/jishin/items/docs/20160420164714.pdf>).

There also appeared a conjugate fault with left-lateral strike-slip. These branch faults appeared on modern alluvial plain and there was no remnant of previous slips. The field report of Geological Survey of Japan by Shirahama et al. (<http://g-ever.org/updates/?p=334>) shows many offset features in the central section of the Futagawa fault. Geospatial Information Authority of Japan (GSI) report (<http://www.gsi.go.jp/common/000139911.pdf>) based on UAV survey (<https://www.youtube.com/watch?v=bS6ftodIHl&feature=youtu.be>) shows the surface rupture near the ENE termination of the Mw 7.0 fault inside the Aso Caldera just east of the barranca.

The 5 km section of the ENE termination has not been mapped previously.

Most of the Mw 7.0 surface rupture appeared along the previously mapped ~30 km strands of the Futagawa and Hinagu fault. However, the occurrence of the branch faults, south-side down dip-slip, as well as the unmapped termination section presented much more complicated faulting took place in longer than expected source fault.

### 4. Soil condition in Kumamoto--Mashiki area

Kumamoto city and Mashiki town are located north of Kumamoto alluvial plain (Heiya). Look at the area in the seamless geologic map by the Geological Survey of Japan at <https://gbank.gsj.jp/seamless/seamless2015/2d/index.html?lang=en>. Kumamoto Heiya is a Holocene alluvial plain (unit 1). The alluvial plain, especially in its southern and eastern parts are mostly too wet for developing and used as paddy fields. Northern half of Kumamoto city and Mashiki town are located north of the plain on Pleistocene fluvial terraces (170 and 171) and on early Late Pleistocene pyroclastic flow (95 and 83). The Futagawa fault cuts the lava plateau (83) and continues along the boundary between the Kumamoto Heiya (1) and Cretaceous rocks. The Hinagu fault in south juxtaposes alluvial plain (1) with bedrock and run north through bedrock to merge with the Futagawa fault.

According to Ishizaka et al. (1995), the Kumamoto Heiya is an area of active subsidence at a rate of 0.90 mm/yr near the coast and 0.45 mm/yr in south of Kumamoto city. With this subsidence rate, 900 m to 450 m sediments are to be accumulated in a million years under the Kumamoto plain. It is very likely this zone of subsidence continues toward east along the Futagawa fault in south and Mashiki town in north.

In the J-SHIS Japan Seismic Hazard Map (<http://www.jshis.bosai.go.jp/map/?lang=en>) large site amplification is expected in Kumamoto plain and intensity 6+ to 7 is forecasted in case of Futagawa-Hinagu fault zone earthquake. The Kyushu Express way (right green line) got severe damage on this alluvial plain and is closed now. An expressway bridge in the middle of the plain barely survived from collapsing with structural damages. However, the eastern part of the plain is so wet for developing there were no house to be damaged.

Mashiki town, where the severest structural damages took place, is located across the plain from the unit 100 isolated volcanic hill in the geologic map. The center of the town is on the south-facing slope above 11 m high alluvial plain and below 40 to 50 meter high upland consists of Late Quaternary sediments and pyroclastic flows. Subsurface geology is not known yet, but there should be a few hundred meters of sediments that were laid down in pace with the subsidence in south. The sediments may be deposited above south-facing bed



rock slope as there are hills of Cretaceous rocks several kilometers north.

The KiK-net 1580  $\text{cm/s}^2$  and 1328  $\text{cm/s}^2$  peak ground acceleration, as well as intensity 7 were recorded on the flat top of the upland away from the slope and the alluvial plain. The very strong ground shaking here even destroyed rather new houses on the flat top of the upland where no amplification by surface soil is expected. Therefore the effect of the deeper subsurface sediments and structures on the ground shaking are to be investigated. The significant thickness of Late Quaternary sediments as well as the shape of the basin may have affected the ground shaking on the Mashiki upland.

The author also observed a lot of gravitational slides and lateral spreading on the south-facing slope and on the slopes along incising creeks. There are many collapsed houses owing to this geotechnical cause in addition to the vibration effects. At the foot of the slope, a river runs along the boundary between the upland and the alluvial lowland. The river erodes the upland and fills its course with soft sediments. There is no clear erosional scarp along the bank, but the sediments of the upland should contact with the alluvial sediment with buried scarps. This situation may be the cause of lateral spreading and sliding in the lower part of the slope. 8 fatalities by the Mw 6.1 foreshocks were reported along the foot of the scarp.

The most intense ground shaking at Mashiki town is presumably due to the effects of seismic wave radiation pattern and of rupture directivity both for the Mw 6.1 and the Mw 7.0. The failure of slopes and possible lateral spreading are the additional cause to the shaking of the severest structural damages. There is a possibility that the branch fault in east and under the town is the cause of the localized damages. However, it is not likely because the ruptures in the sediments and shallow bedrocks generate neither strong ground motion nor directivity effect. There is no significant concentration of damages by shaking along the master strand of the Futagawa fault. This is clear and strong evidence that ruptures at and near surface have nothing to do with strong vibratory motions.

In Kumamoto city, moderate structural damages took place extensively. The southern half of the city has expanded into the Kumamoto Plain above hundreds of meter thick sediments. The northern half of the city is on Late Pleistocene terraces on Quaternary volcanics. Thick soft sediments and rocks may have amplified the ground motion. Detailed investigation on the soil condition and damages should be carried out to understand seismic risks in the cities on soft sediments.

## 5. Past earthquakes and earthquake forecast

No historic earthquake larger than M 6.5 was recorded in the source area (figure 1). In Kumamoto, M 6.0 to M 6.5 earthquake occurred every 50 to 100 years. These earthquakes killed 10s of people and damaged Kumamoto castle repeatedly. So, the 2016 shaking in Kumamoto is not an unusual event. Earthquakes larger than M 7.0 were inferred only by paleoseismological excavations on the Futagawa-Hinagu fault zone.

HERP, the Headquarters for Earthquake Research Promotion of the government of Japan, had evaluated long-term seismic potential of the Futagawa-Hinagu fault zone in 2002 and revised it in 2013. The seismic risks of the Futagawa-Hinagu fault zone was evaluated by rather limited geologic information of recurring earthquakes. For the Futagawa segment of the fault zone, an earthquake around M 7.0 with 2 m surface offset on a 19 km long rupture was forecasted. A M 6.8 earthquake was forecasted for the 16 km segment of northernmost section of the Hinagu fault, on which the Mw 6.1 occurred at depth and surface ruptured during the Mw 7.1.

The conditional probability of the earthquake in 30 years was estimated as 0 to 0.9 %. This estimate is based on two past earthquakes in paleoseismological excavations. The timing of the two events are 2200 to 6900 years before present and 23000 to 26000 years before present. One or more events were supposed to have been missing in the geologic records. Assuming 2 or 3 events since 26000 years ago, recurrence interval was estimated as 8100 to 26000 years. The large uncertainty and long interval made the probability less than 1 %. But 0.9 % 30-year probability is rather high for slow-moving intra-plate faults in Japan and the ratio between the elapsed time and the recurrence time was 0.08 to 0.85.

**Acknowledgements:** This report is a compilation of early analyses and field reconnaissance in 10 days after the events by many researchers, to whom the author is very much obliged. Takashi Azuma helped to correct and improve the manuscript.

## References

- Ishizaka, S., Y. Iwasaki, Y. Hase, K. Watanabe, A. Iwauchi, and M. Taziri, (1995), Subsidence Rate and Sediments of the Last Interglacial Epoch in the Kumamoto Plain, Japan. *The Quaternary Research*, 54, 335-334.
- Nakata, T. and T. Imaizumi eds., (2002), Digital Active Fault Map of Japan, University of Tokyo Press, 1 DVD and 68 p.
- Research Group for Active Faults of Japan, (1991), Active Faults of Japan. University of Tokyo Press, 340 p.
- Usami, T., H. Ishii, T. Imamura, M. Takemura, and R. Maatsuura, (2013), Catalog of Damaging Earthquakes in Japan, 599-2012, University of Tokyo Press, 724 p.



## Updates to the Seismic Hazard Characterization of the Cheraw Fault, Southeast Colorado

Ostenaar, Dean (1), Mark Zellman (2)

- (1) Ostenaar Geologic LLC, 25 Grays Peak Trail, Dillon, CO 80435 USA. Email: [deano3geo@gmail.com](mailto:deano3geo@gmail.com).  
 (2) Fugro Consultants, Inc., 1726 Cole Blvd., Lakewood, CO 80401 USA. Email: [m.zellman@fugro.com](mailto:m.zellman@fugro.com).

**Abstract:** The Cheraw fault is a rare, mid-continental Quaternary normal fault in North America. Crone et al., (1997) mapped a 45-km-long scarp, and based on a single trench found three surface ruptures since 20-25 ka, and suggested the prior interseismic period, extended to at least 100 ka. However, the existence of a numerous sinkholes and closed depressions in the region, and Permian evaporates below the fault trace, raised questions regarding its seismogenic potential. New constraints from mapping, shallow geophysical surveys, and boreholes, combined with interpretation of reprocessed industry 2D seismic reflection profiles, demonstrate: 1) longer fault length, 2) steeper dip, 3) planar structure from surface to basement, 4) multiple episodes of reactivation, 5) larger early Cenozoic offset, and 6) smaller Quaternary offset. The new data point to potentially greater uncertainty in the source characterization of the Cheraw fault and the limitations of single-trench characterizations.

**Key words:** Paleoseismology, Colorado, Quaternary faults.

### Introduction

The Cheraw fault is one of the few faults within the Central and Eastern United States (CEUS) of North America known to have experienced a surface rupturing earthquake in the Holocene. Despite this unique attribute, it has remained relatively under-characterized and unstudied. Crone et al. (1997) mapped a 45-km-long scarp, and based on a single trench found three surface ruptures since 20-25 ka, and suggested the prior interseismic period extended to at least 100 ka. That initial work has been the basis of seismic hazard characterization of the Cheraw fault for nearly two decades.

However, with new constraints from mapping and DEM interpretations, shallow geophysical surveys and boreholes, combined with interpretation of reprocessed industry 2D seismic reflection profiles (Zellman and Ostenaar, 2016), we can show: 1) the Cheraw fault extends an additional 16 km from its previously mapped northern termination, for a minimum total Quaternary rupture length of ~61 km, 2) the ~3 m offset of an early (?) Quaternary pediment surface along the northeast extension near the town of Haswell, is similar in magnitude to the post 20-25 ka offset of a late Pleistocene channel reported by Crone et al. (1997) along the main trace of the fault, 3) seven 2D seismic reflection lines show that the fault extends at least to depths of 2 to 3 km into lower Paleozoic strata and crystalline basement rock as a steep, discrete zone with a dip near 75°, 4) the surface fault trace is a reactivated structure, aligned within a broader and complex zone showing multiple periods of Paleozoic to late Cenozoic deformation, and 5) despite the existence of a numerous sinkholes and closed depressions in the region, and Permian evaporates below the fault trace, Quaternary surface faulting is not related to dissolution within the evaporate section, as the fault extends as a planar fault through the evaporate section to fully seismogenic depths.

### Discussion

Our new interpretations of the reprocessed seismic reflection data provide a source for vertical offset measurements on early Cenozoic units that can be compared to geomorphic scarp height and offset measurements for Quaternary surfaces along the fault. Key implications of these new data for seismic hazard models include large disparities in slip estimates derived from geomorphic vs. stratigraphic data, greater fault length and steeper dip than previously used, along with a range of new hypothesis for event behaviour and slip rate. The seismic reflection data also highlights the role of recurrent reactivation along pre-existing zones of structural weakness, with different styles of faulting resulting from changing tectonic stresses through geologic time.

Table 1 summarizes the fault characterization parameters for rupture length and fault dip from two recent national-scale seismic hazard models (CEUS-SSCn., 2012; Petersen et al., 2014) along with potential updates to these characteristics driven by new data from this research. Our basis for these updates and implications of our new data for research and uncertainty estimates are discussed briefly here and in more detail by Zellman and Ostenaar (2016).

Table 1. Comparison of Existing Seismic Source Characterization Parameters and New Data Constraints for the Cheraw Fault

Parameter	Data Source and Weighted Parameter Values			
	Petersen et al., 2014	CEUS-SSCn, 2012		New data from this research
Rupture length	45 (1.0)	46 (0.8)	62 (0.2)	61 km (minimum)
Dip	50° (1.0)	50° (0.4)	65° (0.6)	75° (to 2-3 km depth)

Our new mapping of the Cheraw fault (Figures 1A and 2) shows a geomorphic scarp expressed in the NED 10 m



INQUA Focus Group on Paleoseismology and Active Tectonics

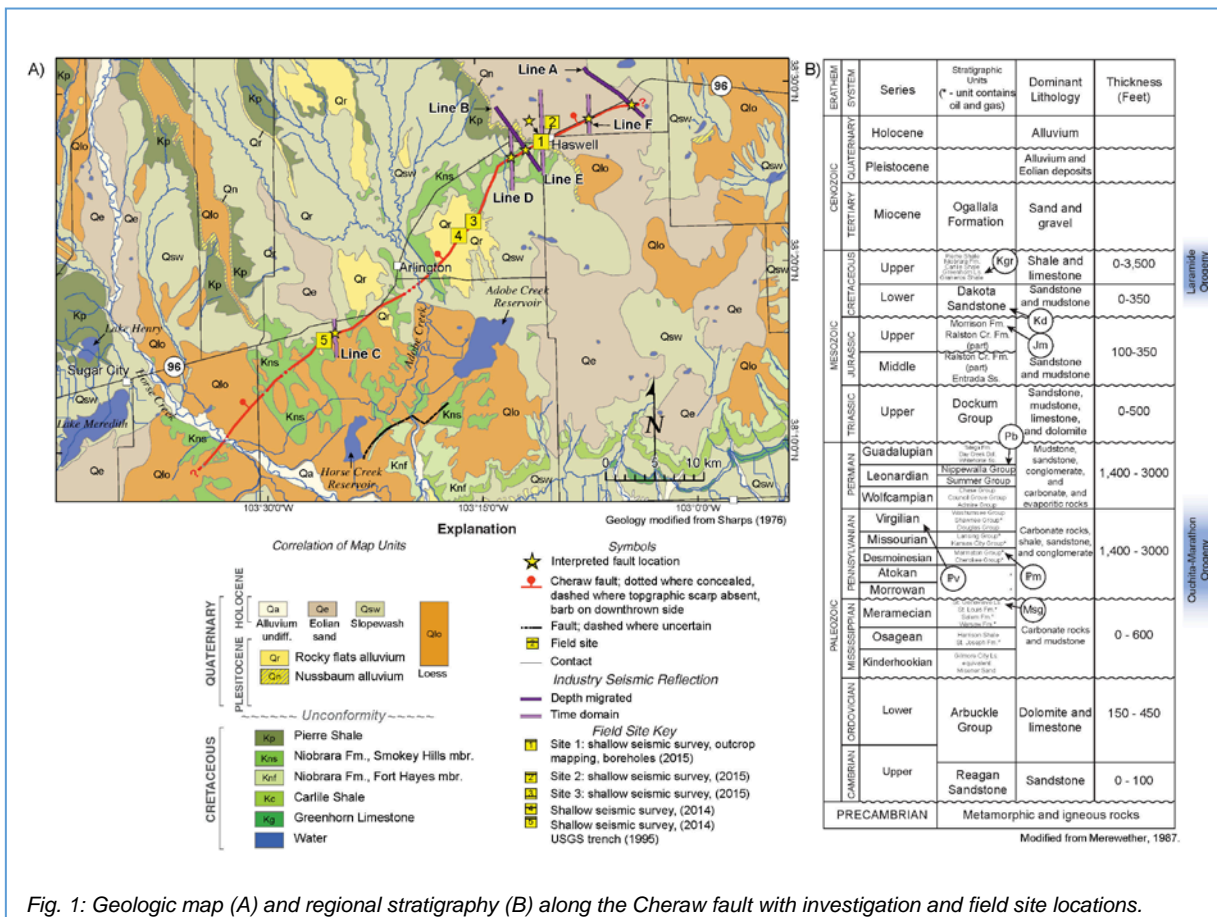


paleoseismicity.org

DEM data for at least 59 km along the Cheraw fault. This length is a minimum because both ends of the scarp terminate in areas of active or very young erosional or eolian landscapes which extend for several kilometers along the strike projection of the scarp. Multiple seismic reflection lines northeast of the mapped scarp appear to show bedrock structure consistent with that observed along the main trace of the Cheraw fault. Based on our detailed evaluation and access to one of these 2D seismic lines (Line A, Figures 1 and 3), we consider the minimum structural or rupture length of the Cheraw fault to be bounded for now at Line A, for a total length of 61 km (Zellman and Ostenaar, 2016). The strong similarity of structure and offsets between Lines A and B, suggests that both lines record the same displacement history, despite the present absence of mapped geomorphic evidence at Line A.

Because the USGS (Petersen et al., 2014) and CEUS (CEUS-SSCn, 2012) seismic hazard models pre-date the verification of northeast extension of the Cheraw fault, both solely or strongly prefer the shorter map trace (Table 1 and Figure 3) which resembles the original mapped fault length (Sharps, 1976). The CEUS model provides weighted options for the fault parameters including two options for fault length; a 46 km length which corresponds to the original mapped extent and a 62 km length which includes the original mapped extent and a northeast extension (CEUS-SSCn, 2012). The shorter fault length is given a higher weight (0.8 vs. 0.2) indicating that it is the

favoured interpretation. The USGS model uses only the shorter fault length. Both models include other logic branches and weighted options for rupture model, rate, and magnitude, which may be somewhat dependent on the fault length characterization. For example, both the CEUS and USGS fault parameters put most weight on characteristic rupture models, with a strong bias (0.7 for CEUS and 0.75 for USGS) to magnitudes of 6.8 and greater. Rupture lengths associated with these magnitudes imply nearly all events rupture the full fault length. However, the new data which indicate a minimum fault rupture length of 61 km, would now be permissive of partial ruptures along strike with magnitudes in the 6.5 to 7.0 range and associated fault rupture lengths of 25 to 40 km based on normal fault regressions of Wells and Coppersmith (1994). With the longer fault length, a recurrence rate model limited to a lower magnitude range on the longer fault length could model up to 4 to 6 earthquakes during the period since 20-25 ka. This type of model would still be consistent with the relatively small total displacement (3.2 – 4.1 m; Crone et al., 1997) ascribed to two or three events observed in the only trench along the fault to date, but effectively doubles the number of significant fault ruptures associated with the fault. This hypothesis implies differences in event timing along strike, despite the relative uniformity of the geomorphic scarp height along the entire 61 km length of the fault, and the similarity of documented Quaternary offset at the Haswell (Section 4.2) and the Crone et al. (1997) trench site.



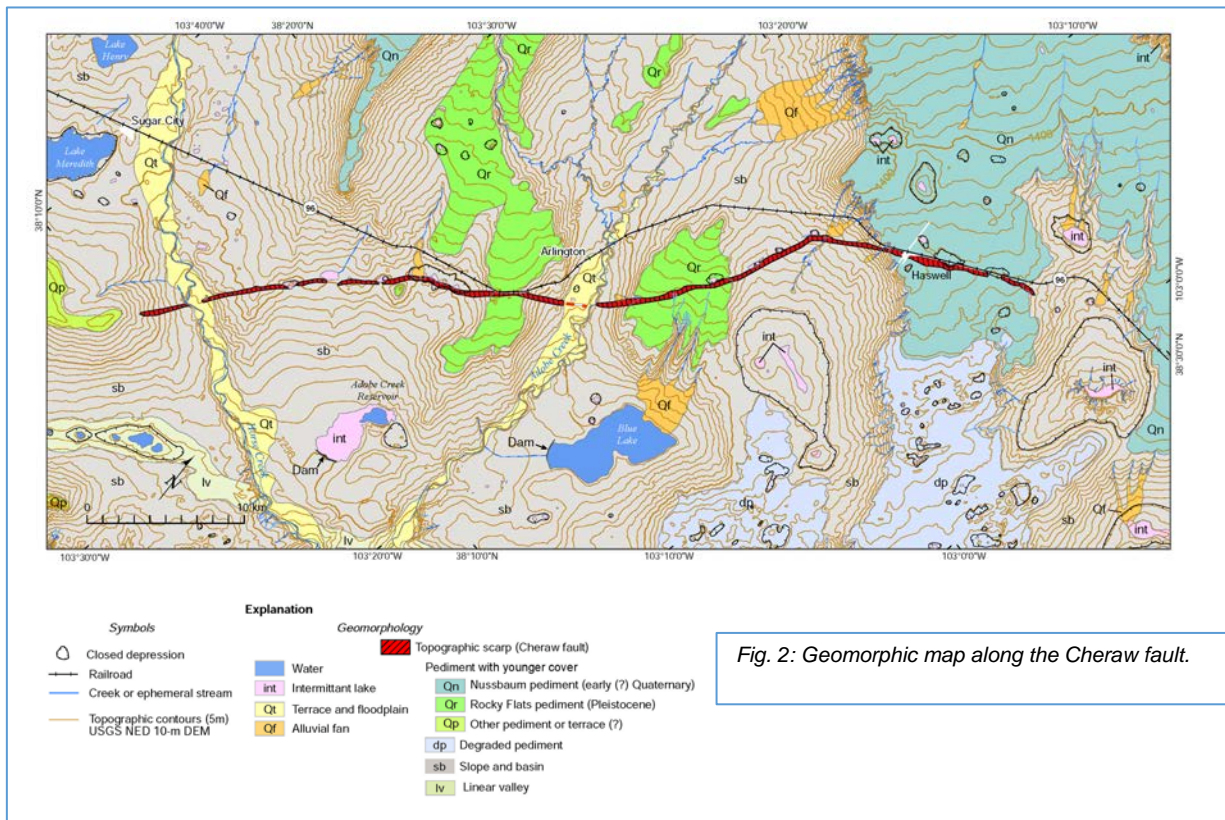


Fig. 2: Geomorphic map along the Cheraw fault.

Our interpretation of the 2D reflection lines (Zellman and Ostenaar, 2016) shows that total Cenozoic (i.e. post-Dakota SS) vertical offset on the Cheraw fault is significantly greater, by perhaps an order of magnitude, than the 6-8 m cited by Crone et al. (1997) and CEUS-SSCn (2012) based on Sharps (1976) structural contours. The 2D seismic data show that the Quaternary Cheraw fault appears to have reactivated structural features inherited from prior, early Cenozoic and older, deformational events. The earlier deformation events were primarily compressional, and likely produced structures with significant lateral or oblique offsets, and steep dips. However, as the 2D seismic data do not image upper Cenozoic units, it is not clear from that data what proportion of the total Cenozoic vertical offset derived from either near-fault or far-field projections, should be ascribed to late Cenozoic extension versus early Cenozoic compression.

Likewise, our updated estimates for dip of the Cheraw fault, which appears to extend into basement structure at depths of 2-3 km (Zellman and Ostenaar, 2016), imply a significantly steeper dip for the fault than previously modeled (Table 1). While the new data imply a much steeper dip than usually associated with ruptures on mature normal faults in the western United States, contemporary normal-fault earthquake ruptures on the Cheraw fault may be relatively new occurrences, which follow inherited structure derived from earlier tectonic stress regimes. Thus, fault ruptures are “forced” to occur on steeper than

optimal orientations. For Cheraw fault seismic hazard models, the data from our research suggest that alternatives with steeper dips may need more weight than “typical” normal faults.

We favor restricting late Cenozoic offset primarily to the narrow, discrete zone of faulting seen in the reflection data (Zellman and Ostenaar, 2016). In this interpretation, a broader zone of warping and tilting that extends 1-2 km from the main fault is viewed as related to the early Cenozoic (Laramide) compressional deformation, which may have included oblique-normal motion on the steeply dipping, discrete fault as well. In this interpretation, maximum late Cenozoic vertical offset on the Cheraw fault based on seismic Line B, southwest of Haswell, would be about 30 m (Zellman and Ostenaar, 2016). Maximum late Cenozoic offset from Line A, northeast of Haswell is 24 m, but Line A appears to be located near the end of the fault, where offset is decreasing. Note that we do not identify any Neogene or Quaternary reflectors in either seismic line, so the actual offset associated with late Cenozoic extension could be significantly less than these values. If the late Cenozoic extension faulting includes the broader zone of tilting and warping, it implies that surface offsets derived from trenching do not fully represent seismogenic fault slip, and associated seismic moment rates for the Cheraw fault need to be significantly increased to account for this unrecognized slip.

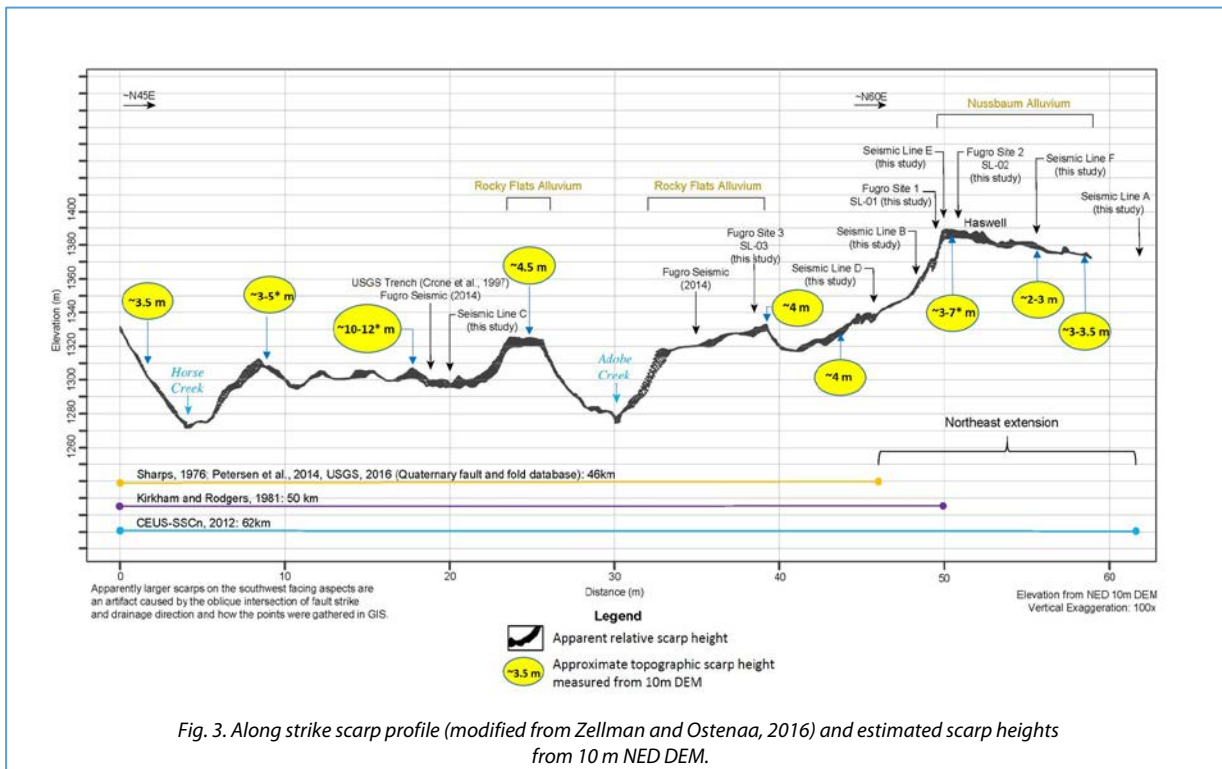


Fig. 3. Along strike scarp profile (modified from Zellman and Ostenaar, 2016) and estimated scarp heights from 10 m NED DEM.

Finally, our investigations at the Haswell site suggest that total Quaternary slip, based on the vertical offset of the base of the Nussbaum alluvium, could be no more than ~3 m (Zellman and Ostenaar, 2016). This offset is significantly less than the geomorphic offset, ~3-7 m, we would infer from topographic profiles at that site (Figure 3). If confirmed through further investigations in progress at press time, the ~3 m offset of the base of the Nussbaum alluvium could represent the entire offset history of the Cheraw fault possibly since 3 Ma. This finding could imply long hiatus between slip episodes, or that the three late Quaternary surface faulting events documented by Crone et al. (1997), which appear to drive the primary geomorphic expression of the present Cheraw fault, are indicative of the total history of a young, new extensional phase of faulting. The discrepancy of the stratigraphic versus geomorphic offsets may also suggest that the extensive active eolian processes along the Cheraw fault are overprinting the tectonic scarp in a way that slip estimates based on normal profiling approaches along the fault have greater uncertainty than previously recognized. That uncertainty is compounded by the absence of local age control for most of the Quaternary deposits and surfaces intersected by the fault.

**Acknowledgements:** Research described here was primarily supported by U.S. Geological Survey National Earthquake Hazard Reduction Program Award Number G15AP000026, the extensive support from Fugro Consultants, Inc., and inputs from numerous other colleagues and collaborators

CEUS-SSCn, 2012, Central and Eastern United States seismic source characterization for nuclear facilities: Palo Alto, California, EPRI, U.S. DOE, and U.S. NRC, [variously paged]. (Also available at <http://www.ceus-ssc.com/Report/Downloads.html>).

Colorado Oil and Gas Information System (COGIS), 2015, Oil and gas well database: <http://cogcc.state.co.us/>. Website accessed last accessed February 26, 2016.

Crone A.J., Machette, M.N., Bradley, L.-A., and Mahan, S.A., 1997, Late Quaternary surface faulting on the Cheraw fault, southeastern Colorado: U.S. Geological Survey Miscellaneous Geological Investigations I-2591, 7p. Pamphlet, 1 oversize pl.

Kirkham R.M., and Rodgers, W.P., 1981, Earthquake potential in Colorado – A preliminary evaluation: Colorado Geological Survey Bulletin 43, 171 p., 3 pls.

Merewether, E. A., 1987, Oil and gas plays of the Las Animas Arch, southeastern Colorado: U.S. Geological Survey Open-File Report 87-450D, 22p.

Petersen, M.D., et al., 2014, 2014 update to the National Seismic Hazard Map (NSHM), U.S. Geological Survey: last accessed February 26, 2016 from the USGS website: <http://earthquake.usgs.gov/hazards/2014prelim/>.

Sharps, J.A., 1976, Geologic map of the Lamar quadrangle, Colorado and Kansas: U.S. Geological Survey Miscellaneous Geologic Investigations Map I-944, scale 1:250,000.

Wells, D.L., and Coppersmith, K.J., 1994, Analysis of Empirical Relationships among Magnitude, Rupture Length, Rupture Area, and Surface Displacement, Bulletin of the Seismological Society of America, v.84, p. 974-1002.

Zellman, M., and Ostenaar, D., 2016, Geophysical and Paleoseismic Investigation of the Cheraw Fault, Southeastern Colorado: Final Technical Report submitted to U.S Geological Survey under USGS award number G15AP000026, February 2016, 29 p, 18 fig.

## References



## Earthquake-induced versus periglacially-induced load structures in clastic sediments

Pisarska-Jamroży, Małgorzata (1), Van Loon, A.J. (Tom) (2), Woronko, Barbara (3)

(1) Institute of Geology, Adam Mickiewicz University, Maków Polnych 16, 61-606 Poznań, Poland; e-mail: pisanka@amu.edu.pl

(2) Geocom Consultants, Valle del Portet 17, 03726 Benitachell, Spain; e-mail: Geocom.VanLoon@gmail.com

(3) Faculty of Geology, University of Warsaw, Żwirki i Wigury 93, 02-089 Warsaw, Poland; e-mail: bworonko@uw.edu.pl

**Abstract:** *The uplift of the earth crust after retreat of Pleistocene ice sheets was not gradual but shock-wise, causing frequent, high-magnitude earthquakes. Sufficiently strong earthquakes can be reflected in layers that are characterized by abundant soft-sediment deformation structures. Similar structures can, however, also be caused by other processes such as gravity-induced sacking, and permafrost-related processes. Some fundamental questions therefore arise because Pleistocene seismites must be ascribed to glacio-isostatic earthquakes: (1) are most Pleistocene layers that contain abundant soft-sediment deformation structures and that were ascribed earlier to periglacial processes due to periglacial processes, indeed? Or (2) were most of them due to rebound-related earthquakes? Or (3) were they formed due to both processes, and if so (3a) were the structures formed by either periglacial process or earthquakes, or (3b) can some of them result from a combination of both processes? And (4) can the origin of soft-sediment deformation structures in glacial deposits be reliably determined?*

**Key words:** *soft-sediment deformation structures, seismites, periglacial structures, glacio-isostatic rebound, Pleistocene*

Earthquakes can be reflected in layers (seismites) that are characterized by abundant soft-sediment deformation structures (SSDS) that give the affected layer (or sets of layers) a deformed – sometimes even chaotic – appearance over long distances (Van Loon, 2009; Alsop & Marco, 2011; Van Loon & Maulik, 2011; Brandes et al., 2012; Brandes & Winsemann, 2013; Tian et al., 2015, 2016). The liquefaction needed for the genesis of most SSDS requires an earthquake magnitude of at least  $M = 4.5-5$  (see, for instance, Rodríguez-Pascua et al., 2000). Such large earthquakes tend to be followed by aftershocks, which also may have magnitudes that are sufficient to transform undisturbed sediment layers into strongly deformed ones. Seismites due to earthquakes triggered by shock-wise isostatic rebound of the earth crust after the retreat of Scandinavian ice sheets have been described from several European countries, including Sweden, Denmark, Germany, Ireland, Poland and Latvia (Mörner, 1990, 1991; Knight, 1999; Muir-Wood, 2000; Kaufmann et al., 2005; Hampel et al., 2009; Brandes et al., 2012; Van Loon & Pisarska-Jamroży, 2014; Pisarska et al., 2015; Van Loon et al., 2015; Van Loon et al., *in press*).

Which types of SSDS are formed as a result of shocks has been investigated in several experiments (e.g., Owen, 1992). These experiments showed that particularly load casts and associated structures are easily formed. This is understandable, as the seismically induced shock waves that are responsible for the development of SSDS in water-saturated, unconsolidated sediments in the uppermost decimeters of the sedimentary succession are S-waves. These result in alternations of lateral pressure and tension within the sediment, thus allowing material to sink into the underlying layer, even if there is hardly any difference in density (see Rossetti, 1999). The fluidization or liquefaction that may result in the formation of load casts can, however, be caused by a

wide variety of processes, including permafrost-induced processes such as cryoturbation, and instabilities resulting from reversed density gradients.

Isostatic rebound can leave traces in the form of earthquake-induced SSDS because earthquakes of sufficient intensity trigger liquefaction. Liquefaction does, however, require not only a water-saturated state, but also a trigger. In the case of seismically-induced SSDS, a load cast can develop only if liquefaction takes place in the layer under the parent layer of the load cast or its ultimate form, a pseudonodule (Moretti & Ronchi, 2011). The type, size and complexity of SSDS in seismites are functions of the magnitude of the earthquakes (Guiraud & Plaziat, 1993) and the distance to the epicenter. The spatial distribution and lateral changes in the type, size and complexity of these SSDS can therefore be used to locate the epicenter, which is sometimes an active or reactive fault.

Under periglacial conditions, water in sediments can induce intense deformation during temperature changes around 0°C. The freezing/thawing alternations under such conditions affected many sediments during the Pleistocene glaciations, resulting in numerous SSDS. Some SSDS are considered by several authors (e.g. French, 2007) as characteristic of periglacial processes. Frost fissures, frost wedges and associated structures may, indeed, be a group (and probably the only group) that needs only periglacial processes. Cryoturbation (due to ice pressure and fluidisation of the sediment after ice melting) must, however, be considered as a result of typically periglacial processes in combination with much more common deformational processes such as loading and liquefaction. Examples of load structures formed due to periglacial processes and due to seismic shocks are presented in Figure 1.



**A. load structures developed in periglacial conditions & cryoturbations**



**B. load structures triggered by seismic shocks**



Fig. 1: Load structures triggered by periglacial features (A) and seismic shocks (B).



It should be noted in this context that load structures can develop not only due to periglacial conditions and seismic shocks, but also to various other processes and conditions, such as reversed density gradients (Dźułyński, 1965; Anketell et al., 1970). Considering the complexity of the origin of load structures and the interpretation of their genesis, these genetic types of load structures are, however, out of scope here.

The final morphology of load casts and associated structures depends largely on the initial sedimentary setting, the driving force and the duration of the deformable state, whereas the nature of the trigger mechanism seems to play a minor or negligible role (Owen & Moretti, 2011; Owen et al., 2011). In other words, SSDS can have identical morphologies, independent of whether they were formed due to a seismic shock, under periglacial conditions, or due to another process (cf. Moretti & Sabato, 2007).

As a consequence, it is commonly difficult to find out what caused the origination of a specific load structure, especially when the geological context does not provide a clue. This may easily result in incorrect interpretations. For instance, many seismically-induced and periglacial SSDS result from loading, but the trigger mechanisms are completely different. Moreover, one specific condition does not necessarily rule out other mechanisms: earthquakes may result in seismic shocks that cause loading of sediments in a periglacial environment, and thus detailed reconstruction of the deformational processes is required for a correct genetic interpretation. We present some of the main features of load casts and associated structures triggered by different processes (Fig. 1).

Our field analyses of load structures indicates that, though not always correct – periglacial load structures tend to occur in layers or sets of layers (commonly with no clearly defined lower boundaries) that tend to contain a small variety in SSDS. In contrast, seismically induced load structures are found in more clearly defined layers of sets of layers that show a wide variety of SSDS over their entire extent. We further deduce that a significant part of the layers with abundant SSDS that were considered until now as periglacial are actually seismites with earthquake-induced structures.

**Acknowledgements:** The work has been financially supported by a grant from the National Science Centre Poland (decision No. DEC-2013/09/B/ST10/00031).

## References

- Alsop G.I. & Marco, S., (2011). Soft-sediment deformation within seismogenic slumps of the Dead Sea Basin. *Journal of Structural Geology* 33, 433-457.
- Anketell, J.M., Cegła, J. & Dźułyński, S., (1970). On the deformational structures in systems with reversed density gradients. *Annales de la Société Géologique de Pologne* 40, 3-29.
- Brandes, Ch., Winsemann, J., Roskosch, J., Meinsen, J., Tanner, D.C., Frechen, M., Steffen, H. & Wu, P., (2012). Activity along the Osning Thrust in Central Europe during the Lateglacial: ice-sheet and lithosphere interactions. *Quaternary Science Reviews* 38, 49-62.
- Brandes, C. & Winsemann, J., (2013). Soft-sediment deformation structures in NW Germany caused by Late Pleistocene seismicity. *International Journal of Earth Sciences* 102, 2255-2274.
- Dźułyński, S., (1965). New data on experimental production of sedimentary structures. *Journal of Sedimentary Petrology* 35, 196-212.
- French, H.M., (2007). *The periglacial environment* (3rd ed.). Wiley & Sons, Chichester, 458 p.
- Guiraud, M. & Plaziat, J.-C., (1993). Seismites in the fluvial Bima sandstones: identification of paleoseisms and discussion of their magnitudes in a Cretaceous synsedimentary strike-slip basin (Upper Benue, Nigeria). *Tectonophysics* 225, 493-522.
- Hampel, A., Hetzel, R., Maniatis, G. & Karow, T., (2009). Three-dimensional numerical modeling of slip rate variations on normal and thrust fault arrays during ice cap growth and melting. *Journal of Geophysical Research* 114, 8406-8420.
- Kaufmann, G., Wu, P. & Ivins, E.R., (2005). Lateral viscosity variations beneath Antarctica and their implications on regional rebound motions and seismotectonics. *Journal of Geodynamics* 39, 165-181.
- Knight, J., (1999). Geological evidence for neotectonic activity during deglaciation of the southern Sperrin Mountains, Northern Ireland. *Journal of Quaternary Science* 14, 45-57.
- Moretti, M. & Ronchi, A., (2011). Liquefaction features interpreted as seismites in the Pleistocene fluvio-lacustrine deposits of the Neuquén Basin (Northern Patagonia). *Sedimentary Geology* 235, 200-209.
- Moretti, M. & Sabato, L., (2007). Recognition of trigger mechanisms for soft-sediment deformation in the Pleistocene lacustrine deposits of the Sant'Arcangelo Basin (Italy): Seismic shock vs. overloading. *Sedimentary Geology* 196, 31-45.
- Mörner, N.A., (1990). Glacioisostatic and long term crustal movements in Fennoscandia with respect to lithospheric and atmospheric processes and properties. *Tectonophysics* 176, 13-24.
- Mörner, N.A., (1991). Intense earthquakes and seismotectonics as a function of glacial isostasy. *Tectonophysics* 188, 407-410.
- Muir-Wood, R., (2000). Deglaciation seismotectonics: a principal influence on intraplate seismogenesis at high latitudes? *Quaternary Science Reviews* 19, 1399-1411.
- Owen, G., (1992). A shaking table for experiments on soft-sediment deformation. *Journal of Sedimentary Petrology* 62, 733-734.
- Owen, G., & Moretti, M., (2011). Identifying triggers for liquefaction-induced soft-sediment deformation in sands. *Sedimentary Geology* 235, 141-147.
- Owen, G., Moretti, M. & Alfaro, P., (2011). Recognising triggers for soft-sediment deformation: Current understanding and future directions. *Sedimentary Geology* 235, 133-140.
- Pisarska-Jamroży, M., Van Loon, A.J., Nartišs, M. & Krievāns, M., (2015). Seismites recording glacio-isostatic rebound after melting of the Scandinavian Ice Sheet in Latvia. *Miscellanea INGV* 27, 386-388.
- Rodríguez-Pascua, M.A., Calvo, J.P., De Vicente, G. & Gómez-Gras, D., (2000). Soft-sediment deformation structures interpreted as seismites in lacustrine sediments of the Prebetic Zone, SE Spain, and their potential use as indicators of earthquake magnitudes during the Late Miocene. *Sedimentary Geology* 135, 117-135.
- Rossetti, D.F., (1999). Soft-sediment deformation structures in late Albian to Cenomanian deposits, San Luis Basin, northern Brazil: evidence for paleoseismicity. *Sedimentology* 46, 1065-1081.
- Tian, H., Van Loon, A.J., Zhang, Z., Zhang, S., Zhang, B., Lü, M., Li, F. & Ma, X., (2015). Neogene paleoseismic events and the



## INQUA Focus Group on Paleoseismology and Active Tectonics



[paleoseismicity.org](http://paleoseismicity.org)

Shanwang biota's burial in the Linqu area, Shandong Province, China. *Acta Geologica Sinica (English Edition)* 89, 1103-1119.

Tian, H.S., Van Loon, A.J., Wang, H.L., Zhang, S.H & Zhu, J.W., (2016). Seismites in the Dasheng Group: New evidence of strong tectonic and earthquake activities of the Tanlu Fault Zone. *Science China: Earth Sciences* 59, 601-618.

Van Loon, A.J., (2009). Soft-sediment deformation structures in siliciclastic sediments: an overview. *Geologos* 15, 3-55.

Van Loon, A.J. & Maulik, P., (2011). Abraded sand volcanoes as a tool for recognizing paleo-earthquakes, with examples from the Cisuralian Talchir Formation near Angul (Orissa, eastern India). *Sedimentary Geology* 238, 145-155.

Van Loon, A.J. & Pisarska-Jamroży, M., (2014). Sedimentological evidence of Pleistocene earthquakes in NW Poland induced by glacio-isostatic rebound. *Sedimentary Geology* 300, 1-10.

Van Loon, A.J., Pisarska-Jamroży, M., Nartišs, M., Krievāns, M. & Soms, J., (2015). Frequent earthquakes recorded in a section with twelve seismites at Rakuti (SE Latvia). *Miscellanea INGV* 27, 497-499.

Van Loon, A.J., Pisarska-Jamroży, M., Nartišs, M., Krievāns, M. & Soms, J., (2016). Seismites resulting from high-frequency, high-magnitude earthquakes in Latvia caused by Late Glacial glacio-isostatic uplift. *Journal of Palaeogeography* 4, in press.



## Structural complexity and Quaternary evolution of the 2009 L'Aquila earthquake causative fault system (Abruzzi Apennines, Italy): a three-dimensional image supported by deep ERT, ground TDEM and seismic noise surveys

Pucci, S. (1), Villani, F. (2), Civico, R. (1), Di Naccio, D. (2), Sapia, V. (1), Di Giulio, G. (2), Vassallo, M. (2), Ricci, T. (1), Delcher, E. (3), Finizola, A. (3), Baccheschi, P. (2), Pantosti, D. (1)

- (1) Istituto Nazionale di Geofisica e Vulcanologia, via di Vigna Murata 605, 00143 Roma, Italy.
- (2) Istituto Nazionale di Geofisica e Vulcanologia, via dell'Arcivescovado 8, 67100 L'Aquila, Italy
- (3) Laboratoire GéoSciences Réunion, Université de la Réunion, Institut de Physique du Globe de Paris, Sorbonne Paris-Cité, CNRS, UMR 7154, Saint-Denis, La Réunion, France.

**Abstract:** We imaged the three-dimensional architecture of a tectonic basin in the epicentral area of the 2009 L'Aquila earthquake (central Italy) through a multidisciplinary approach: 1) Field survey and LIDAR analysis yield to a new structural and Quaternary continental deposits map; 2) Time domain electromagnetic soundings (TDEM), coupled with seismic noise measurements, and three 2-D Deep Electrical Resistivity Tomography (ERT) transects allowed us to study a complex Quaternary continental infill that buried a dissected Mesozoic-Tertiary substratum.

The infill grew as the interference pattern of two fault systems, occurred at the lower Early Pleistocene. The faults show a stable long-term activity with an individual leading fault splay extending to 20 km length, showing an apparent interruption that originates from the inherited basin bottom morphology. Major splays of an old fault system limit the leading fault splay and now act as segment boundaries or possibly transfer faults between stepping segments.

**Key words:** Central Apennines, extensional basin, ERT, TDEM, ambient noise.

### INTRODUCTION

The Mw 6.1 April 6, 2009 L'Aquila earthquake and its long aftershocks sequence (Valoroso et al. 2013 and references therein) struck a densely populated area in the Middle Aterno Valley (central Apennines) and caused heavy damage in the town of L'Aquila and surrounding villages, resulting in 309 fatalities and thousands of injured. As reported also by historical records (<http://emidius.mi.ingv.it/CPTI>; Tertulliani et al. 2009; Rovida et al. 2011) this region is one of the most active areas of Italy and was repeatedly hit by destructive earthquakes.

Seismological, geodetic and geological data all point to a NW-SE oriented, SW-dipping normal fault as the source of the 2009 mainshock. Its length is still a matter of debate. Different observations and models suggest values between 12 and 18 km (e.g. Atzori et al. 2009; Cheloni et al. 2010; Cirella et al. 2012; Volpe et al. 2012). Its surface expression, known as the Paganica-San Demetrio fault system (PSDFS – sensu Civico et al. 2015), belongs to a wider system of Pliocene-Quaternary, NW-SE striking normal faults affecting the whole inner central Apennines and responsible for the generation of several intermontane continental basins (Cavinato & De Celles, 1999; Ghisetti & Vezzani, 1999). The PSDFS consists of a >20km long network of Quaternary normal faults that formed a wide intermontane continental basin: the Middle Aterno basin (Fig. 1). This basin is characterized by the presence of an extensive cover of lacustrine and fluvial/alluvial deposits accumulated upon a Meso-Cenozoic carbonatic and siliciclastic

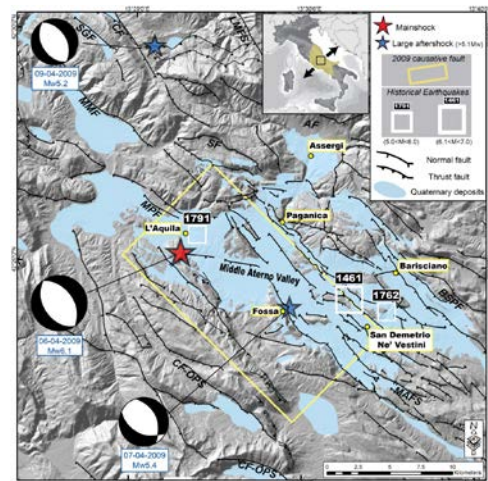


Fig. 1: Location map of the 2009 L'Aquila mainshocks ( $M > 5.0$  - stars) (Scognamiglio et al., 2010; Herrmann et al., 2011) and coseismic surface ruptures (see Civico et al. 2015 and references therein). Focal mechanisms of the mainshock and of the two largest aftershocks, historical seismicity ( $M > 5.0$ ; <http://emidius.mi.ingv.it/CPTI04>), and main active faults are shown (modified after: Galadini and Galli, 2000; Civico et al., 2015; Pucci et al., 2015).

bedrock, generally separated by unconformities and/or displaced by faulting (Pucci et al., 2015).

Prior to the 2009 earthquake, the geometry and activity of the PSDFS were only roughly known. After the event, a significant number of studies have been carried out in



the Middle Aterno Valley, in particular along the Paganica-San Demetrio Basin, focusing mainly on the coseismic geological surface effects, the structural setting, the geomorphology and the paleoseismic history (see Moro et al. 2013, Santo et al. 2014; Civico et al. 2015, Pucci et al. 2015 and reference therein;). There is a general discrepancy between the length of the seismologic-geodetic modeled fault (up to 18 km), the limited size of the primary continuous coseismic surface ruptures (3 km), and the significant morphological expression of the PSDFS. This stimulated a debate about the maximum rupture length of the PSDFS and its capability to generate earthquakes stronger than the 2009 mainshock, with much larger rupture length and displacement.

Some authors focused on the analysis of the Quaternary geological and morphological expression of PSDFS at the surface, to estimate the role and rate of long-term activity of the fault system (Giaccio et al. 2012; Civico et al. 2015).

With the same aim, a few studies focussed on the shallow subsurface of the basin, but were limited to the northwestern sector (Cesi et al. 2010; Balasco et al. 2011; Improta et al. 2012; Santo et al. 2014). Moreover, the area lacks deep boreholes, extensive deep geophysical data and commercial seismic exploration lines from oil and gas industry, thus the overall subsurface structure of the Paganica-San Demetrio Basin in its central and southeastern sectors is still uncovered.

Because of this we organized the following workflow: (1) characterization of the fault system activity through the reconstruction of its detailed geometrical organization at the surface, by means of an extensive LiDAR-based geological survey; (2) acquisition of the fault-controlled Quaternary basin image at depth, by means of a combined geophysical approach based on Time-Domain Electromagnetic Method (TDEM) coupled with seismic noise measurements, and three 2-D Deep Electrical Resistivity Tomography (ERT) transects; and (3) reconstructing the fault system's long-term evolution in order to mark the permanent fault segments boundaries and to define the expected maximum rupture length.

## METHODS AND DATA ACQUISITION

A new 1:25,000-scale high-resolution geological map of the Middle Aterno Valley basin (Pucci et al., 2015), produced by means of airborne LiDAR analysis and traditional field survey approaches was used as surficial constrain for the geophysical survey.

The outcomes of the geophysical surveys were integrated with pre-existing data and the few available boreholes, in order to produce a smooth map of the top-bedrock in the study area.

TDEM is based on the induction of a time-varying secondary magnetic field produced by a decay current in the ground. The time-decay of this magnetic field is related to the propagation of currents deeper into the ground and provides information on the conductivity of the lower layers. We used a 3-components receiver coil, in conjunction with a transmitter square loop of 50 m and 100 m size, respectively. TDEM measurements were

acquired both in central-loop and offset receiver configurations, adopting geometry file settings according to an instrument calibration performed at the Italian reference site for TDEM soundings (Sapia et al., 2015). We performed TDEM surveys avoiding high-noise sites (related to infrastructures/lifelines) and selecting data after careful noise tests for each site. Data processing was made with the SiTEM software, and the resistivity data were inverted with the SEMDI program (Effersø et al., 1999) to obtain 1-D vertical resistivity models of the subsurface.

As regards ambient noise recordings, we used the classical H/V method (Nakamura, 1989) based on the spectral ratio between the horizontal (H) and the vertical (V) components of seismograms. The resonance frequency ( $f_0$ ) was obtained from the peak of the H/V curves. The value of  $f_0$ , for 1-D structures, is closely

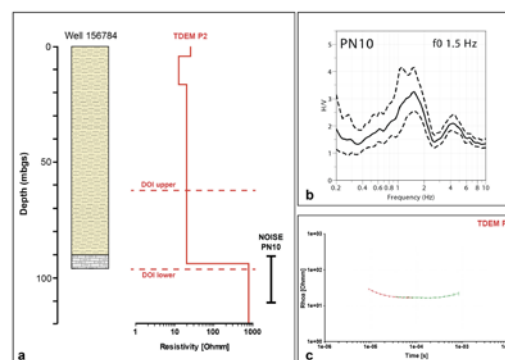


Fig. 2: a) calibration by a well log (<http://sgi.isprambiente.it/indagini/website>) of TDEM 1-D resistivity models (solid red lines) and ambient seismic noise depth-interval (solid vertical black lines). The 96 m depth of the pre-Quaternary carbonate bedrock is detected by both methods. Dashed red line indicate respectively the upper and lower depth of investigation (DOI) calculated for the TDEM output models (Christiansen et al., 2011); b) H/V curves computed from noise measurement; c) TDEM time-resistivity curve.

linked to the mean properties (thickness and shear-wave velocity  $V_s$ ) of the soft soil (Bonnetfoy-Claudet et al., 2006). Assuming the 1-D quarter wavelength approximation, we derived the seismic bedrock depth (in terms of a range of possible values) from the  $f_0$  values.  $V_s$  values of 500-700 m/s were provided by surveys carried out in the L'Aquila surroundings and in the Middle Aterno after the microzoning activity (Di Giulio et al., 2014). Seismic data were recorded using 24-bit Reftek130 data loggers coupled to Lennartz LE-3D5s velocimeters with eigenfrequency of 0.2 Hz. The sampling rate was fixed at 250 Hz with recording duration of at least 50 minutes. Data processing for computing the H/V curves was made with the Geopsy code (<http://www.geopsy.org>).

As regards electrical resistivity tomography, we acquired three deep surveys (up to > 6 km). Measurements were undertaken with a multi-electrode 2D device by means of the ABEM Terrameter™ SAS-4000 resistivity meter and an ABEM ES1064 C multiplexer. We used a 2.52 km-long



cable with a set of 64 stainless steel electrodes. Apparent resistivity data were measured with different configurations (Wenner alpha and pole-dipole): in the pole-dipole configuration we used a remote electrode (up to 10 km away from the center of the electrode array) allowing for an investigation depth > 500 m in the central portion of the profiles. Apparent resistivity data were processed using ABEM utilities software for converting data format and X2IPI software (Robain & Bobachev, 2002) for data filtering, while data inversion was carried out with RES2DINV software (Loke & Barker, 1995).

We first calibrated TDEM and ambient seismic noise data using well information. As an example Figure 2 shows the abrupt increase of resistivity within the lower depth of TDEM investigation range at 90 m depth. At the same time, the H/V curves show a peak frequency of 1.5 Hz that, assuming an average shear velocity of 550 m/s (typical of sandy clays deposits), results in a 90-100 m depth of the seismic basement. These kinds of measurements were further tested against other

### PRELIMINARY RESULTS AND DISCUSSION

The result highlights the presence of a complex basin morphology that mimics the structural complexities observed at the surface. The data illustrate the important role of the NNE- and WNW-trending conjugate extensional system in the formation of a different shaped Early Pleistocene basin.

The basin is formed by sills separating some 100-300 m-deep depocenters, with a maximum depth >500 m located at the southern end of the Middle Aterno basin (Figure 3). This deepest part of the basin has a roughly triangular shape with one side paralleling the western slope of the valley and a vertex close to the San Demetrio ne' Vestini village. As a consequence, the SE side of the depocenter is characterized by a strong topographic gradient, in coincidence with the tip of the Quaternary basin. Notably, the shape of this maximum depocenter is not coherent with the NW-trending, Quaternary normal faults affecting the eastern side of the basin. This evidence suggests that the onset of the

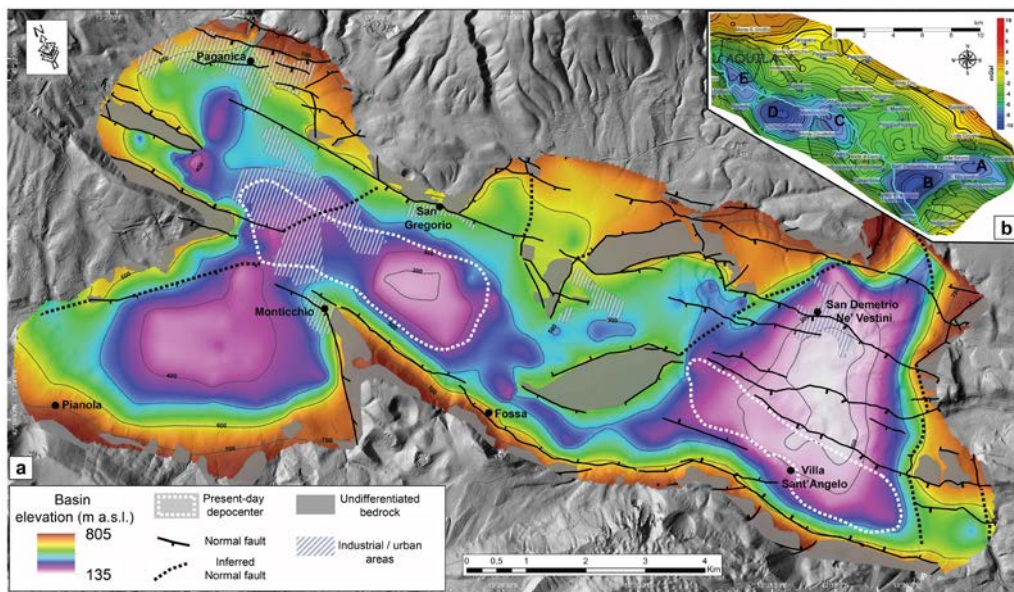


Fig. 3: a) Shape of the continental basin bottom (contour interval: 100 m). The basin architecture is compared with the fault system at the surface and the present-day depocentre. b) Gravimetric anomaly map of Cesi et al. 2010.

available geophysical and well data (Improta et al., 2012; Porreca et al. 2016), showing a consistent match with independent estimates of the basin substratum depth, within a <10% uncertainty window.

We finally obtained 77 TDEM 1-D resistivity models and 133 H/V curves. This point database, implemented with bedrock depth values recovered from boreholes and from electrical resistivity tomography served as input for a 2-D minimum curvature spline interpolation (70-m grid size). We then show two different kinds of maps: 1) the depth of the top-bedrock from the ground surface (corresponding to an isopach map of the continental infill); 2) the absolute elevation of the top-bedrock, representative of the true topography of the basin bottom under the continental cover (Fig. 3).

Middle Aterno Quaternary basin was controlled by the long-term activity of a differently oriented fault system that could have played a key role before or together with the PSDFS segments through time, and that now act as segment boundaries.

The data of the present work yield new insight to reconstruct the 3D image of the Middle Aterno basin. Indeed, our study emphasizes the utility and flexibility of combining two different methods (TDEM and ambient noise) in reconstructing the 3D geometry of the Middle Aterno Basin bottom.

The reconstruction of the physiography of the tectonic-related Quaternary basin bottom represents a critical contribution to the estimation of the fault system evolution and thus to the evaluation of the seismogenic potential of the active structures.



## INQUA Focus Group on Paleoseismology and Active Tectonics



paleoseismicity.org

**Acknowledgements:** FIRB Abruzzo project, "High-resolution analyses for assessing the seismic hazard and risk of the areas affected by the 6 April 2009 earthquake" (<http://progettoabruzzo.rm.ingv.it/en>; funding codes: RBAP10ZC8K\_005, RBAP10ZC8K\_003, RBAP10ZC8K\_007).

### References

- Atzori, S., I., Hunstad, M., Chini, S., Salvi, C., Tolomei, C., Bignami, S., Stramondo, E., Trasatti, A., Antonioli, & E., Boschi (2009). Finite fault inversion of DInSAR coseismic displacement of the 2009 L'Aquila earthquake (central Italy), *Geophys. Res. Lett.*, 36, L15305, doi:10.1029/2009GL039293.
- Balasco, M., P., Galli, A., Giocoli, E., Gueguen, V. Lapenna, A., Perrone, S., Piscitelli, E., Rizzo, G., Romano, A., Siniscalchi, & M., Votta (2011). Deep geophysical electromagnetic section across the middle Aterno Valley (central Italy): preliminary results after the April 6, 2009 L'Aquila earthquake. *Boll. Geofis. Teor. Appl.*, doi: 10.4430/bgta0028
- Bonnefoy-Claudet, S., C. Cécile, B. Pierre-Yves, C. Fabrice, M. Peter, K. Jozef, & D. Fäh, (2006). H/V ratio: a tool for site effects evaluation. Results from 1-D noise simulations. *Geophysical Journal International*, 167, (2), 827-837.
- Cavinato, G. P., & De Celles, P. G., 1999. Extensional basins in the tectonically bimodal central Apennines fold-thrust belt, Italy: response to corner flow above a subducting slab in retrograde motion, *Geology*, 27 (10), 955-958.
- Cesi, C, Di Filippo, M., Di Nezza, & M., Ferri, F., 2010. Caratteri gravimetrici della media Valle del Fiume Aterno, in *Microzonazione sismica per la ricostruzione dell'area aquilana*, Gruppo di Lavoro MS-AQ Ed., Regione Abruzzo – Dipartimento della Protezione Civile, L'Aquila, 3 vol. e Cd-rom.
- Cheloni, D., D'Agostino, N., D'Anastasio, E., Avallone, A., Mantenuto, S., Giuliani, R., Matton, M., Calcaterra, S., Gambino, P., Dominici, D., Radicioni, F., & Fastellini, G., 2010. Coseismic and initial post-seismic slip of the 2009 Mw 6.3 L'Aquila earthquake, Italy, from GPS measurements, *Geophys. J. Int.*, 181 (3), 1539-1546, doi:10.1111/j.1365-246X.2010.04584.x
- Christiansen, A.V., E. Auken and A. Viezzoli, 2011. Quantification of modeling errors in airborne TEM caused by inaccurate system description, *Geophysics*, 76, 43-52.
- Cirella, A., Piatanesi, A., Tinti, E., Chini, M., & Cocco, M., 2012. Complexity of the rupture process during the 2009 L'Aquila, Italy, earthquake: *Geophysical Journal International*, 190, 607–621, doi:10.1111/j.1365-246X.2012.05505.x.
- Civico, R., Pucci, S., De Martini, P. M., & Pantosti, D., 2015. Morphotectonic analysis of the long-term surface expression of the 2009 L'Aquila earthquake fault (Central Italy) using airborne LiDAR data. *Tectonophysics*, 644-645, 108-121, doi: 10.1016/j.tecto.2014.12.024
- Di Giulio, G., I. Gaudiosi, F. Cara, G. Milana, & M. Tallini, (2014). Shear-wave velocity profile and seismic input derived from ambient vibration array measurements: the case study of downtown L'Aquila. *Geophysical Journal International*, 198, (2), 848-866.
- Effersø, F., Auken, E., & Sørensen, K. I. (1999). Inversion of band-limited TEM responses. *Geophysical Prospecting*, 47(4), 551-564.
- Galadini, F., and Galli, P., 2000. Active tectonics in the central Apennines (Italy)–input data for seismic hazard assessment. *Natural Hazards*, 22(3), 225-268.
- Galli, P., Giaccio, B., Messina, P., Peronace, E., & Zuppi, G. M., 2011. Palaeoseismology of the L'Aquila faults (central Italy, 2009, Mw 6.3 earthquake): implications for active fault linkage. *Geophysical Journal International*, doi 10.1111/j.1365-246X.2011.05233.x.
- Ghisetti, F., & L., Vezzani (1999). Depths and modes of Pliocene-Pleistocene crustal extension of the Apennines (Italy). *Terra Nova*, 11, 67-72.
- Giaccio, B., Galli, P., Messina, P., Peronace, E., Scardia, G., Sottili, G., Sposato, A., Chiarini, E., Jicha, B., & Silvestri, S., 2012. Fault and basin depocentre migration over the last 2 Ma in the L'Aquila 2009 earthquake region, central Italian Apennines, *Quaternary Science Reviews*, 56, 2012, 69-88, doi: 10.1016/j.quascirev.2012.08.016.
- Improta, L., Villani, F., Bruno, P.P., Castiello, A., De Rosa, D., Varriale, F., Punzo, M., Brunori, C.A., Civico, R., Pierdominici, S., Berlusconi, A., & Giacomuzzi, G., 2012. High-resolution controlled-source seismic tomography across the Middle Aterno basin in the epicentral area of the 2009, Mw 6.3, L'Aquila earthquake (central Apennines, Italy), *Ital. J. Geosci. (Boll. Soc. Geol. It.)*, 131, 3, 373-388, doi: 10.3301/IJG.2011.35.
- Loke, M.H. & Barker, R.D., 1995. Least-square inversion of apparent resistivity pseudosections, *Geophysics*, 60, 1682-1690.
- Moro, M., Gori, S., Falcucci, E., Saroli, M., Galadini, F., Salvi, S., 2013. Historical earthquakes and variable kinematic behaviour of the 2009 L'Aquila seismic event (central Italy) causative fault, revealed by paleoseismological investigations, *Tectonophysics*, 583, 131-144, <http://dx.doi.org/10.1016/j.tecto.2012.10.036>.
- Nakamura, Y. 1989. A method for dynamic characteristics estimation of subsurface using microtremor on the ground surface. Railway Technical Research Institute, Quarterly Reports, 30(1).
- Porreca, M., Smedile, A., Speranza, F., Mochales Lopez, T., D'Ajello Caracciolo, F., Di Giulio, G., ... & Amoroso, S., 2016. Geological reconstruction in the area of maximum co-seismic subsidence during the 2009 Mw= 6.1 L'Aquila earthquake using geophysical and borehole data, *Italian Journal of Geosciences*, doi: 10.3301/IJG.2015.37
- Pucci, S., Villani, F., Civico, R., Pantosti, D., Del Carlo, P., Smedile, A., De Martini, P.M., Pons-Branchu, E., & Gueli, A., 2015. Quaternary geology of the Middle Aterno Valley, 2009 L'Aquila earthquake area (Abruzzi Apennines, Italy), *J. Maps.*, 11-5, 689-697, doi: 10.1080/17445647.2014.927128
- Robain, H., & Bobachev, A., 2002. X2IPI Tool box for 2D DC and DC-IP measurements <http://geophys.geol.msu.ru/x2ipi/x2ipi.html#boba>
- Rovida, A., Camassi, R., Gasperini, P., & Stucchi, M. (eds.), 2011. CPTI11, the 2011 version of the Parametric Catalogue of Italian Earthquakes, Milano, Bologna, last release 2011-12-23, <http://emidius.mi.ingv.it/CPTI>, doi: 10.6092/INGV.IT-CPTI11
- Santo, A., Ascione, A., Di Crescenzo, G., Miccadei, E., Piacentini, T., & Valente, E., 2014. Tectonic-geomorphological map of the middle Aterno river valley (Abruzzo, Central Italy), *J. Maps*, 10(3), 365-378.
- Sapia, V., Viezzoli, A., Menghini, A., Marchetti, M., & Chiappini, M., 2015. The Italian reference site for TEM methods, *Ann. Geophys.*, 58 (5), G0548, doi: 10.4401/ag-6805
- Tertulliani, A., Rossi, A., Cucci, L., & Vecchi, M., 2009. L'Aquila (Central Italy) earthquakes: the predecessors of the April 6, 2009 event, *Seismol. Res. Lett.*, 80(6), 1008.
- Valoroso, L., Chiaraluca, L., Piccinini, D., Di Stefano, R., Schaff, D., & Waldhauser, F., 2013. Radiography of a normal fault system by 64,000 high-precision earthquake locations: The 2009 L'Aquila (central Italy) case study, *J. Geophys. Res. Solid Earth*, 118, 1156–1176, doi:10.1002/jgrb.50130.
- Volpe, M., Piersanti, A., & Melini, D., 2012. Complex 3-D Finite Element modelling of the 2009 April 6 L'Aquila earthquake by inverse analysis of static deformation, *Geophys. J. Int.*, 188, 1339–1358 doi: 10.1111/j.1365-246X.2011.05330.



## Evidence for late Quaternary surface rupture along the Leech River fault near Victoria, British Columbia, Canada

Christine Regalla (1), Kristin D. Morell (2), Lucinda J. Leonard (2), Colin Amos (3), Vic Levson (2), Emily Rogalski (1)

- (1) Department of Earth and Environment, Boston University, Boston, Massachusetts 02215, USA. Email: cregalla@bu.edu
- (2) School of Earth and Ocean Sciences, University of Victoria, Victoria, British Columbia V8P 5C2, Canada
- (3) Geology Department, Western Washington University, Bellingham, Washington 98225-9080, USA

**Abstract:** We present results of new geomorphic and structural mapping of the Leech River fault near Victoria, British Columbia, Canada providing the first evidence for Quaternary surface ruptures on Vancouver Island. Based on new field and aerial mapping aided by 2m LiDAR DEMs, we identify >60 individual, sub-parallel, linear scarps, sags and swales in en echelon arrays that offset bedrock and late Pleistocene-Holocene deposits. Reconstruction of fault slip across an offset post-last glacial maximum (~15 ka) colluvial surface near the center of the fault zone requires ~6 m of dip displacement of the colluvial surface, and ~4 m of displacement of intervening channels. These data argue that the Leech River fault experienced at least two surface-rupturing ( $\geq M_w 6.5$ ) earthquakes since ~15ka. We interpret the mapped scarps as part of a steeply dipping fault zone that is 500-1000m wide and 30 - 60 km long that accommodates transpression across the northern Cascadia forearc.

**Key words:** Quaternary rupture, forearc faults, British Columbia

### INTRODUCTION

In the Cascadia forearc of southwestern British Columbia (Fig. 1), active forearc strain related to eastward subduction of the Juan de Fuca plate and northward motion of the Oregon block (e.g., McCaffrey et al., 2013) may be accommodated along a network of crustal faults. Microseismicity and geodetic data do not easily elucidate planar crustal faults in the region, however, (e.g., Cassidy et al., 2000; Balfour et al., 2011), and direct evidence for Quaternary faulting in British Columbia has remained ambiguous. Geomorphic, trenching, and geophysical studies have contributed to the recognition of several major active fault systems in the Cascadia forearc of Washington and Oregon (McCaffrey & Goldfinger, 1995; McCaffrey et al., 2013; Personius et al., 2014), including the Southern Whidbey Island Fault, the Utsalady Point Fault, the Darrington-Devil's Mountain Fault (Fig. 1) (Johnson et al., 1996, 2001; Sherrod et al., 2008; Personius et al., 2014), but no active structures of similar significance are currently formally recognized in southern British Columbia (e.g., Halchuk et al., 2015).

Here we focus on documenting new evidence for Quaternary ruptures along the Leech River fault (Fig. 1), an Eocene terrene-bounding fault located in southern Vancouver Island that separates schists of the Leech River complex from basalts of the Metchosin Fm. (Fig. 2) (Muller, 1977; MacLeod et al., 1977). The potential Quaternary activity of the Leech River fault has been the focus of several recent investigations because of the seismic hazard it may pose to the nearby population of Victoria, British Columbia (Fig. 1) (see Cassidy et al., 2000; Mosher et al., 2000; Balfour et al., 2011). The fault has a

strong topographic expression on Vancouver Island, facilitating the construction of several hydroelectric dams along its trace (Fig. 2). It trends into the city of Victoria and into the submarine expression of the Devil's Mountain fault zone (Fig. 2; Barrie and Greene, 2015). Some authors have suggested that the Leech River fault was last active in the Eocene, given a lack of observed offset Oligocene and younger sediments along some portions of the fault (MacLeod et al., 1977; Fairchild, 1979). However, we document new geomorphic and structural data that indicate the Leech River fault zone has been active during the late Quaternary.

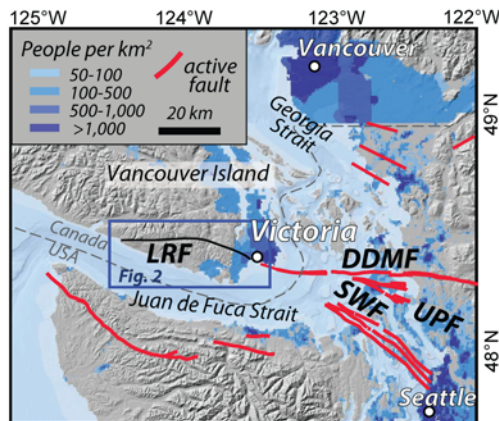


Figure 1: Tectonic setting of the Leech River fault, showing population centers (Balk et al., 2006) relative to active faults (Barrie and Green, 2015; Sherrod et al., 2008; USGS Quaternary fault and fold database for the United States, 2010; Kelsey et al., 2012; Personius et al., 2014). The Leech River fault (LRF) is shown in black. DDMF, Darrington-Devil's Mountain Fault; SWF, South Whidbey Island Fault; UPF, Utsalady Point Fault.

We use a combination of mapping of topographic scarps from a high resolution LiDAR digital elevation model (James et al., 2010), bedrock and surficial field mapping, and collection of structural, geomorphic and stratigraphic data to delineate Quaternary fault-related features along the Leech River fault. We identify several strands of the Leech River fault that displace late post-glacial (Clague and James, 2002), Pleistocene to Holocene sediments and record at least two earthquakes since ~15 thousand years ago. These data provide the first evidence for late Quaternary surface rupture along a crustal fault in the Cascadia forearc in southern British Columbia, and suggest that the Leech River fault is only one of a network of active faults that accommodate forearc transpression in southwestern Canada.

## OBSERVATIONS

We map fault-related topographic and structural features within a ~60 km long by 1 km wide region along the Leech River fault to provide evidence of Quaternary slip and reactivation of the Eocene terrane boundary fault (Fig. 2A). Individual topographic features range in length from hundreds of meters to several kilometres long, are up to five meters high, and form linear ridges, sags and scarps with both north and south facing directions (Fig. 2B). The roughly east-west oriented topographic features occur at a high angle to the southerly regional ice flow direction during the last glacial maximum, confirmed locally from glacial striae and streamlined drumlinoids (Fig 2B). Along the eastern half of the fault, where we have focused current mapping, topographic features coincide with displaced geomorphic surfaces, brittle fracture networks, and uphill facing scarps. We discuss three key sites from the eastern half of this fault system where field and LiDAR data indicate tectonic offset of bedrock and Quaternary deposits (Fig. 2B, sites A-C).

**Site A** is located on the south side of the Leech River valley, ~5 km west from the abandoned town of Leechtown (Fig. 2). Here, we identify an approximately east-west striking, >200-m-long and up to 2 m high topographic scarp that is uphill (southward) facing across a relatively steep, north-facing slope. The surface trace of this scarp is located ~100-m south of the fault contact between the Metchosin Fm. and Leech River Complex. The surficial geology at the site consists of a dense, matrix-supported subglacial till with numerous striated clasts, overlain by a ~1 m thick apron of colluvium sourced locally from bedrock exposures on the steep southern valley wall. This colluvial surface is incised by several steep, linear channels. Field and LiDAR data indicate that both the colluvial surface and the channels incising it are vertically displaced by several meters across the scarp. Scarp heights measured in the field at site A are systematically lower within the incised channels (~1m) than on the colluvial surface (~1.2 m). The vertical separation across the scarp, estimated from regressions through LiDAR-derived topographic profiles, is ~6m at interfluvial profiles but only ~4 at channel profiles. This observation requires at least two surface rupturing events at site A. The scarp at site A is nearly linear in map pattern, but deviates northward into channels and topographic lows, requiring a steeply (60-90°) north-dipping fault plane. The uphill facing scarps at Sites A and the lack of consistent lateral offset of displaced channels imply thrust-type displacement with minor to no lateral slip along this strand of the fault.

**Site B** is located approximately 5 km to the east along strike from site A, where we identify a prominent south-facing bedrock scarp that intersects the now-abandoned town of Leechtown near the confluence between the Sooke and Leech Rivers (Fig. 2). The Leechtown scarp can be traced relatively continuously for ~1.5 km along strike and is located ~100 m south of the Metchosin Fm.-Leech River Complex contact. An exposure of the fault in rock quarry near the center of this scarp exposes several steeply north-dipping sub-parallel faults cutting relatively undeformed Metchosin Fm. basalt. Faults exposed in this quarry have a 1-2-mm-wide gouge zone and one contains sub-horizontal slickenlines consistent with strike-slip. At the eastern end of site B, the scarp is defined by an ~4 m high, uphill facing bedrock scarp, where the northern (upthrown) side of the scarp consists of fractured and brittle-deformed Metchosin Fm. basalt, and the southern (downthrown) side of the scarp contains moisture-rich, fine-grained sediment. The apparent north-side-up displacement across the scarp and the northward divergence of the scarp trace into topographic lows argue for displacement along a steeply north-dipping reverse fault, and kinematic indicators at the site argue for a strong oblique component to slip.

**Site C** is located ~5 km to the east of site B, where we identify several hundred meter long linear sags, swales and benches that cut across relatively smooth, till-



mantled hillslopes. These scarps have a nearly linear trace across topography, but they do not exhibit clear upthrown fault blocks, nor a consistent increase in surface elevation across the scarps. Features at this site consist of 10-15 m wide disrupted zones that are up to ~5 m higher than the surrounding landscape, and the facing direction of scarps changes along strike. We interpret this *en echelon* stepping of topographic ridges and the lateral juxtaposition of topographic highs and lows as pressure ridges and mole tracks, developed during strike slip or oblique slip faulting.

## DISCUSSION

The topographic scarps we identify occur parallel to the mapped location of the Eocene Leech River fault (Fairchild and Cowan, 1982; Massey et al., 2005), but none of the mapped fault scarps coincide with the lithologic terrane boundary between the Leech River Complex schists and Metchosin Fm basalts (Fig. 2), nor with local lithologic contacts. Instead, individual topographic scarps occur as much as hundreds of meters north or south of the lithologic fault boundary. Thus these features cannot be explained by differential erosion across lithologic contacts. In addition, where we have mapped the lithologic contact between the basalt and schist units, we find evidence for mylonitic fabrics and foliated fault fabrics, but do not find evidence for discrete brittle structures or fault gouge. Conversely, where we identify fault planes in bedrock associated with topographic scarps, we do not identify any mylonitic fabrics, but instead observe discrete fractures and gouge-bearing fault zones. The active fault zone, therefore, does not likely exactly re-occupy the Eocene terrane boundary fault.

We suggest that the identified scarps together delineate an active fault system that is up to ~1 km wide and 30-60 km long (Fig. 2). Within this zone, we observe near vertical faults, variable scarp facing directions, laterally discontinuous surface scarps, and field evidence for strike-slip and reverse faulting. These observations of scarp morphology, fault orientations and fault kinematics suggest that the active strands of the Leech River fault accommodate strike and dip slip motion within a steeply dipping fault zone or flower structure. Such characteristics are typical of strike slip systems (e.g. Sylvester, 1988) and are similar to features observed along active oblique-reverse faults in the Pacific Northwest (e.g. Johnson et al., 2001; Sherrod et al., 2008; Personius et al., 2014).

The offset geomorphic features, faulted bedrock and surficial deposits, and prominent bedrock scarps mapped along the Leech River fault collectively argue that several strands of the fault were active since the late Pleistocene. The strongest evidence for late Pleistocene to Holocene ruptures along the Leech River fault come from Site A, where the colluvial apron overlying basal till morphologically remains both in situ

and intact. The colluvial surface and incised channels must therefore be no older than the deglaciation following the last glacial maximum (~15 ka; Clague and James, 2002), and faulting at site A must postdate ~15 ka. In addition, the difference in scarp height and estimated vertical separation between interfluvial and channel profiles implies multiple episodes of fault activity, with at least one event occurring after the formation of the colluvial apron, but before channel incision, and at least one additional event following formation of the channels. Assuming a 60-90° dipping fault plane, vertical separations across the scarp equate to approximate total dip slip magnitudes of >6.5m for interfluvial surfaces and >4.5 m for channels. These data indicate ~2m of dip displacement occurred during the first event, and ~2 to ~4m of displacement occurred during a subsequent event or events. Given minimum estimates of surface dip displacement magnitudes and surface rupture length, displacement length scaling (Wells and Coppersmith 1994) suggests that the Leech River fault has experienced at least two  $\geq M_w 6.5$  earthquakes since ~15 ka.

## CONCLUSIONS

Our observations of linear fault scarps and offset late Quaternary geomorphic features delineate a >30 km long section of the LRF that has been tectonically active since the end of the Cordilleran glaciation. This active fault zone contains numerous sub-parallel, mesoscale faults with variable orientations that together comprise a steeply-dipping ~1 km wide fault array or flower structure. While slip sense along individual fault strands is highly variable, the orientation and surface morphology of fault-related features across the entire fault zone strongly suggest that this active fault system accommodates forearc transpression. Reconstruction of an offset post-glacial colluvial landform requires at least two surface rupturing events, each with at least ~2m of dip displacement, to have occurred since ~15 Ka. These estimated displacements suggest that the Leech River fault is capable of hosting earthquakes of ~M6 within kilometers of Victoria, BC. We suggest that the Leech River fault is part of a network of active faults that accommodate forearc deformation in the northern Cascadia forearc.

**Acknowledgements:** This research was supported by an NSF EAR IRFP Grant #1349586 to Dr Regalla and an NSERC Discovery grant to Dr. Morell. We thank CRD watersheds and BC Hydroelectric Company for their assistance in accessing key field sites.

## REFERENCES

- Balk, D., Deichmann, U., Yetman, G., Pozzi, F., Hay, S., and Nelson, A., 2006, Determining global population distribution: methods, applications and data: *Advances in Parasitology*, v. 62, p. 119-156.



## INQUA Focus Group on Paleoseismology and Active Tectonics



paleoseismicity.org

- Barrie, V., and Green, G., 2015, Active faulting in the northern Juan de Fuca Strait, Implications for Victoria, British Columbia: Geological Survey of Canada Current Research 2015-6, p. 10, doi:10.4095/296564.
- Balfour, N., Cassidy, J., Dosso, S., and Mazzotti, S., 2011, Mapping crustal stress and strain in southwest British Columbia: *Journal of Geophysical Research: Solid Earth* (1978--2012), v. 116, no. B3.
- Blyth, H., and Rutter, N., 1993, Surficial geology of the Sooke area (nts 92b/5): British Columbia Ministry of Energy Mines and Petroleum Resources, Open File 1993-25.
- Cassidy, J.F., Rogers, G.C., and Waldhauser, F., 2000, Characterization of active faulting beneath the Strait of Georgia, British Columbia: *Bulletin of the Seismological Society of America*, v. 90, no. 5, p. 1188--1199.
- Clague, J.J., and James, T.S., 2002, History and isostatic effects of the last ice sheet in southern British Columbia: *Quaternary Science Reviews*, v. 21, no. 1, p. 71--87.
- Fairchild L.H., 1979, The Leech River Unit and Leech River Fault, Southern Vancouver Island, British Columbia [MS Thesis], University of Washington.
- Fairchild, L., and Cowan, D., 1982, Structure, petrology, and tectonic history of the Leech River complex northwest of Victoria, Vancouver Island: *Canadian Journal of Earth Sciences*, v. 19, p. 1817--1835.
- Halchuk, S., T. Allen, J. Adams, and G. Rogers (2015), Fifth generation seismic hazard model input files as proposed to produce values for the 2015 national building code of Canada, Geological Survey of Canada Open File 7576, doi:10.4095/293907.
- James, T., Bednarski, J., Rogers, G., and Currie, R., 2010, LiDAR and digital aerial imagery of the Leech River Fault Zone and coastal regions from Sombrio Point to Ten Mile Point, southern Vancouver Island, British Columbia: Geological Survey of Canada, Open File 6211, doi:10.4095/285486.
- James, T., Bednarski, J., Rogers, G., and Currie, R., 2010, LiDAR and digital aerial imagery of the Leech River Fault Zone and coastal regions from Sombrio Point to Ten Mile Point, southern Vancouver Island, British Columbia: Geological Survey of Canada, Open File 6211, doi:10.4095/285486.
- Johnson, S., Dadisman, S., Mosher, D., Blakely, R., and Childs, J., 2001, Active tectonics of the Devil's Mountain Fault and related structures, Northern Puget Lowland and Eastern Strait of Juan de Fuca Region, Pacific Northwest: U.S. Geological Survey Professional Paper 1643.
- Johnson, S., Potter, C., Miller, J., Armentrout, J., Finn, C., and Weaver, C., 1996, The southern Whidbey Island fault: An active structure in the Puget Lowland, Washington: *Geological Society of America Bulletin*, v. 108, p. 334--354.
- Kelsey, H.M., Sherrod, B.L., Blakely, R.J., and Haugerud, R.A., 2012, Holocene faulting in the Bellingham forearc basin: Upper-plate deformation at the northern end of the Cascadia subduction zone: *Journal of Geophysical Research: Solid Earth* (1978--2012), v. 117, no. B3, doi:10.1029/2011JB008816.
- MacLeod, N., Tiffin, D., Snavely Jr, P., and Currie, R., 1977, Geologic interpretation of magnetic and gravity anomalies in the Strait of Juan de Fuca, US-Canada: *Canadian Journal of Earth Sciences*, v. 14, no. 2, p. 223--238.
- Massey, N.W.D., MacIntyre, D., Desjardins, P., and Cooney, R., 2005, Digital geology map of British Columbia: BC Ministry of Energy and Mines, Geological Survey Branch.
- McCaffrey, R., and Goldfinger, C., 1995, Forearc deformation and great subduction earthquakes: Implications for Cascadia offshore earthquake potential: *Science*, v. 267, no. 5199, p. 856--859.
- McCaffrey, R., King, R.W., Payne, S.J., and Lancaster, M., 2013, Active tectonics of northwestern U.S. inferred from GPS-derived surface velocities: *Journal of Geophysical Research: Solid Earth*, v. 118, p. 709--721, doi:10.1029/2012JB009473.
- Mosher, D.C., Cassidy, J.F., Lowe, C., Mi, Y., Hyndman, R.D., Rogers, G.C., and Fisher, M., 2000, Neotectonics in the Strait of Georgia: first tentative correlation of seismicity with shallow geological structure in southwestern British Columbia: *Current Research*, p. A22.
- Muller, J.E., 1977, Evolution of the Pacific Margin, Vancouver Island, and adjacent regions: *Canadian Journal of Earth Sciences*, v. 14, no. 9, p. 2062--2085.
- Muller, J., 1983, Geology of Victoria map-area: Geological Survey of Canada. Map A, v. 1553.
- Personius, S.F., Briggs, R.W., Nelson, A.R., Schermer, E.R., Maharrey, J.Z., Sherrod, B.L., Spaulding, S.A., and Bradley, L.A., 2014, Holocene earthquakes and right-lateral slip on the left-lateral Darrington--Devils Mountain fault zone, northern Puget Sound, Washington: *Geosphere*, v. 10, no. 6, p. 1482--1500.
- Sherrod, B., Blakely, R., Weaver, C., Kelsey, H., Barnett, E., Liberty, L., Meagher, K., and Pape, K., 2008, Finding concealed active faults: Extending the southern Whidbey Island fault across the Puget Lowland, Washington: *Journal of Geophysical Research*, v. 113, no. B05313, doi:10.1029/2007JB005060.
- Sylvester, A.G., 1988, Strike-slip faults: *Geological Society of America Bulletin*, v. 100, no. 11, p. 1666--1703.
- USGS Quaternary fault and fold database for the United States, 2010, accessed April 2015: <http://earthquakes.usgs.gov/hazards/qfaults/>.
- Wells, D.L., and Coppersmith, K.J., 1994, New empirical relationships among magnitude, rupture length, rupture width, rupture area, and surface displacement: *Bulletin of the Seismological Society of America*, v. 84, no. 4, p. 974--1002.

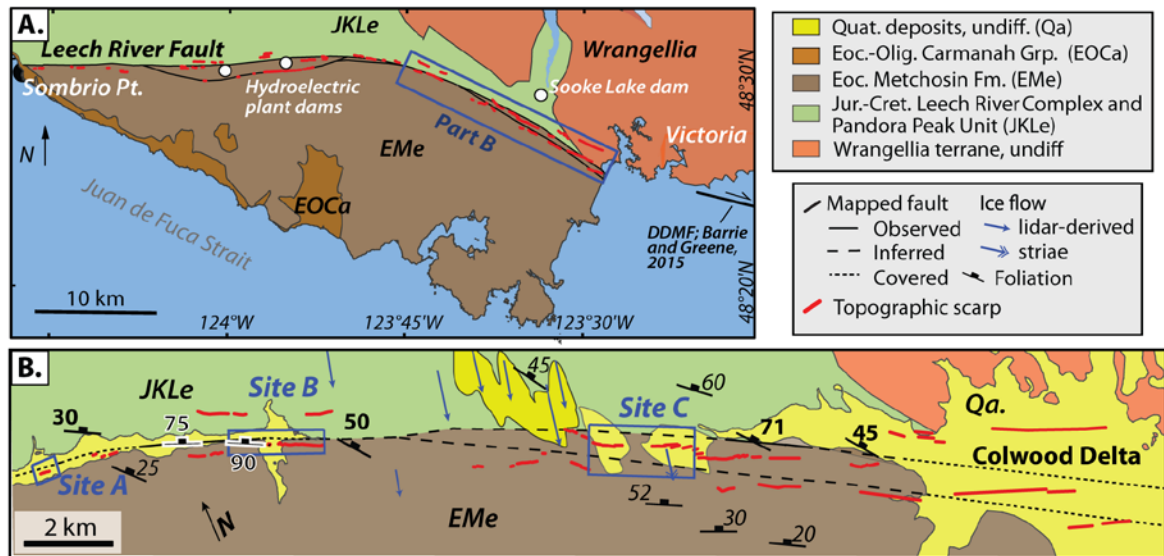


Figure 2. A. Simplified geologic map of the Leech River fault and surroundings (after Massey et al., 2005). Red lines denote topographic scarps, pressure ridges, topographic benches and linear swales and sags identified in this study. B. Map showing trace of identified features relative to bedrock (Massey et al., 2005), surficial deposits (Blyth and Rutter, 1993) and local ice flow indicators (blue arrows, this study). Foliation measurements from this study are shown in bold and those from Muller (1983) are shown in italics. Foliation data outlined in white are at the lithologic contact (this study).



## Is the Southern San Andreas Fault Really Overdue For a Large Earthquake or Just Late in the Cycle?

Thomas Rockwell

Department of Geological Sciences, San Diego State University, San Diego, CA, USA. trockwell@mail.sdsu.edu

**Abstract:** Compilation of paleoseismic data from several dozen trench sites in the southern San Andreas fault system allows for sequencing of the past 1100 years of large earthquakes for the southern 160 km of the main plate boundary. At least three generalizations are clear: 1) M7 and larger earthquakes account for most of the moment release in the southern San Andreas fault system over the past 1100 years; 2) large earthquakes on individual faults are quasi-periodic but display a relatively high coefficient of variation in recurrence time, similar to most long California records; and 3) moment release has temporally varied during the past 1100 years but within potentially predictable bounds. Together, the record suggests that the southern San Andreas fault is late in the cycle but not necessarily “overdue”, and that a systems level approach may be more accurate in long term earthquake forecasting than estimates made from individual faults.

**Key words:** San Andreas fault system, earthquake cycles, plate margin moment release, earthquake recurrence forecasts

### INTRODUCTION

Understanding the occurrence of earthquakes in space and time is key to correctly forecasting future large earthquakes. Thus far, attempts to use forecast statistics with various recurrence distributions (Weibull, Brownian Passage Time (BPT), log-normal) (Nishenko and Buland, 1987; WGCEP, 1988; Ellsworth et al., 1999; Biasi et al., 2002) only gain a factor of two increase in predictability over random (Poissonian) because the coefficient of variation (CoV) on earthquake recurrence for a fault segment or paleoseismic site is relative high, averaging about 0.6 in California (Biasi and Scharer, 2015). In this paper, I compile and analyse all published and unpublished paleoseismic data for the southern 160 kms of the San Andreas fault system from the Brawley Seismic Zone north to the Banning Pass region, including all strands of the San Andreas, San Jacinto and Elsinore faults.

**The Dataset** - Paleoseismic data from the San Andreas fault (Sieh, 1986; Sieh and Williams, 1990; Fumal et al., 2002; Philipbosian et al., 2011; Yule and Sieh, in progress), the San Jacinto fault (Rockwell et al., 2015; Onderdonk et al., 2013; Buga, 2012; Hudnut et al., 1989; Hudnut and Sieh, 1989; Gurrola and Rockwell, 1996; Rockwell et al., 2000; Faneros, 2004) and the southern Elsinore fault (Rockwell, 1990; Rockwell and Pinault, 1986; Thorup, 1998; Vaughan et al., 1999; Rockwell et al., 2013) are used to compile the rupture history of 160 km of the southern San Andreas fault system in southern California (Figure 1). In addition to timing of paleoearthquakes from these studies, we used offset data from geomorphic and 3D trenching studies to estimate average displacement per event (Salisbury et al., 2012; Williams, 2009; Pandey and Rockwell, unpublished data; Faneros, 2004). Depth of rupture is estimated from both depth of seismicity and geodetic inversion (Smith-Konter et al., 2011), which together with the displacement data, can be used to

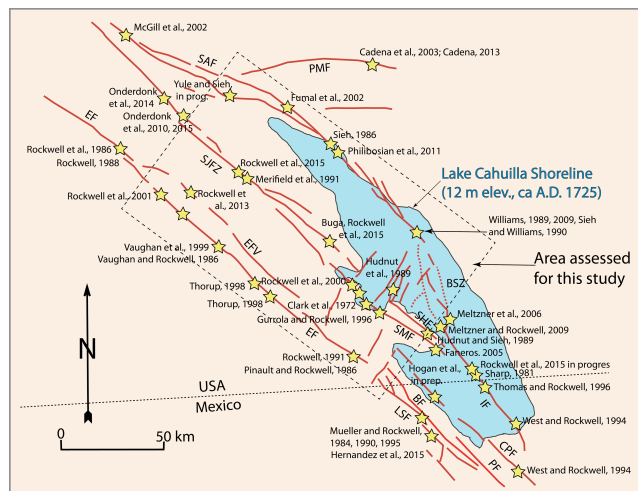


Fig. 1: Map of the major elements of the southern San Andreas fault system. The dashed box defines the area of consideration. Yellow stars are paleoseismic sites used in this analysis.

estimate moment release for individual earthquakes (Table 1).

A potential problem arises with dating of events at nearby sites on the same fault when the event ages do not agree well. This is the case for the southern San Andreas fault, where Fumal et al. (2002) recognized only 5 events in the past 1200 years at the Thousand Palms site whereas Philipbosian et al. (2011) recognized up to 7 events at the Coachella site in the past 1100 years. Part of the problem may be that the Fumal et al. (2002) study was on the Mission Creek strand of the fault zone, whereas the Philipbosian et al., (2011) study was on the combined Mission Creek-Banning fault south of their juncture, so the Thousand Palms site may not record all events. However, a larger problem is likely due to  $^{14}\text{C}$  dating of individual events, which is limited by the material that is present to be dated; this problem can be exacerbated in arid regions. There is a poor match in



INQUA Focus Group on Paleoseismology and Active Tectonics



paleoseismicity.org

Fault	EQ date (AD)	uncertainty range (95%)	Magnitude Estimate	Inferred Avg Slip (m)	Rupture length (km)	Rupture depth (km)	Seismic Mo (dyn-cm)
<b>San Andreas F</b>							
Event 1	1715	1710-1720	7.4	3	150	12	1.53E+27
event 2	1650	1640-1660	7.4	3	150	12	1.53E+27
event 3	1555		7.4	3	150	12	1.53E+27
event 4	1410	1440-1520	7.4	3	150	12	1.53E+27
event 5	1240		7.4	3	150	12	1.53E+27
event 6	1051	950-1250	7.4	3	150	12	1.53E+27
event 7	965		7.4	3	150	12	1.53E+27
						sum	1.07E+28
<b>*Clark strand, SJF*</b>							
Event 1	1918		6.7	1.25	26	13	1.30E+26
Event 2	1800		7.3	2.5	90	14	9.76E+26
event 3	1577	1535-1627	7.3	2.5	90	14	9.76E+26
event 4	1357	1303-1389	7.3	2.5	90	14	9.76E+26
event 5	1311	1280-1362	6.7	1.25	26	13	1.30E+26
event 6	1289	1267-1315	6.7	1.25	26	13	1.30E+26
event 7	1193	1118-1267	7.3	2.5	90	14	9.76E+26
event 8	1080	1028-1144	6.7	1.25	26	13	1.30E+26
event 9	947	842-1020	7.3	2.5	90	14	9.76E+26
						sum	5.40E+27
<b>*Casa Loma strand, SJF*</b>							
Event 1	1899		6.5	0.6	20	18	6.70E+25
Event 2	1800 or 1812?		6.5	0.6	20	18	6.70E+25
event 3	1577	1535-1627	6.5	0.6	20	18	6.70E+25
event 4	947	842-1020	6.5	0.6	20	18	6.70E+25
						sum	1.34E+26
<b>Superstition Mtn - Coyote Creek F</b>							
CCF-1	1968		6.3	0.3	30	12	3.35E+25
CCF-2	1795	1720-1850	6.7	1.1	35	12	1.43E+26
CCF-3	1675	1640-1710	6.3	0.3	30	12	3.35E+25
SMF-CCF-4	1535	1470-1600	7.1	1.7	90	12	5.70E+26
SMF-CCF-5	1378	1320-1430	7.1	1.7	90	12	5.70E+26
SMF-CCF-6	1090	1000-1120	7.1	1.7	90	12	5.70E+26
SMF-CCF-7	920	900-1000	7.1	1.7	90	12	5.70E+26
						sum	2.49E+27
<b>Carrizo Mtn cross fault</b>							
	1942		6.5				6.70E+25
<b>Superstition Hills F.</b>							
Event1	1987		6.5	0.7	26	12	6.77E+25
Event2	1790	1680-1892	6.5	0.7	26	12	6.77E+25
						sum	3.38E+26
<b>Southern Elsinore F</b>							
Event 1	1750	1680-1800	6.9	1.8	34	12	2.28E+26
Event 2	1000	800-1200	6.9	1.8	34	12	2.28E+26
						sum	4.56E+26
<b>Central Elsinore F</b> No ruptures in past 1200 years							
<b>Northern Elsinore F.</b>							
Event 1	1750	1680-1810	7.1	2.1	80	12	6.25E+26
Event 2	1375	1274-1474	7.1	2.1	80	12	6.25E+26
event 3	1050	1015-1104	7.1	2.1	80	12	6.25E+26
						sum	1.88E+27
						Sum of moments on major faults	2.15E+28

Table 1. Catalog of Paleoseismic Events in the Southern 160 km of the San Andreas Fault System.

event ages between the two sites, and it is unlikely that the 5 Thousand Palm events do not have correlations at the nearby Coachella site, so the likely explanation is age inheritance in the <sup>14</sup>C dates that were used to construct the chronology at each site. This issue is likely to be a factor at many or most of the sites around the Salton Trough due to the regions aridity and the fact that most charcoal is likely derived from Native American burning of wood and not from range fires.

Many or most of the problematic sites lie below the shoreline of ancient Lake Cahuilla, a freshwater lake that periodically inundated the Salton Trough when the Colorado River spills north, rather than to its current course to the head of the Gulf of California. To circumvent the detrital charcoal age issue, a preliminary common chronology for Lake Cahuilla has been constructed for the last six lake stands that have occurred during the past 1100 years (Figure 2). The ages of earthquakes at the various paleoseismic sites that lie within the lake have been recalculated based on this common lake-age model.

The central and part of the southern San Jacinto fault lie beyond the extent of Lake Cahuilla and the chronology of large earthquakes is independent from that of the lake. Nevertheless, the Hog Lake chronology is very well resolved with dates on seeds (single year growths)(Rockwell et al., 2015). The timing of earthquakes on the central and southern Elsinore fault

are not well-resolved, but the slip rate is much lower than that of the San Andreas or San Jacinto fault so does not account for much of the total moment release. For incomplete records, such as the Superstition Hills and Casa Loma strands of the San Jacinto fault, additional paleoevents are randomly inserted into the moment summation to account for expected moment release based on the faults' slip rate.

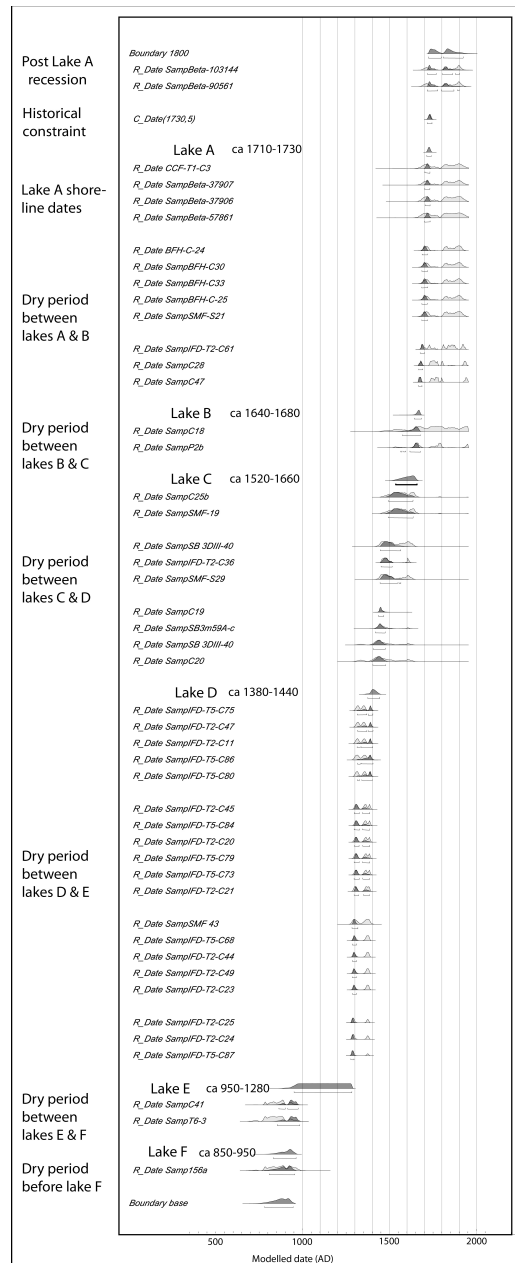


Fig. 2: Age dating of Lake Cahuilla highstands. A large part of the dataset is charcoal and Wood, including *in situ* stumps, that grew between lake intervals.

**Discussion**

Figure 3 plots the moment release for all recognized earthquakes  $\geq M 6.5$  for the faults in the dashed box in



Figure 1. There have undoubtedly been some additional moderate earthquakes that are not captured in Table 1; there are northeast-striking cross-faults, such as those that ruptured in 1942 and 1987, that have not been adequately characterized. Nevertheless, the moment contribution of these smaller events is small compared to the San Andreas and San Jacinto faults.

events below M6. We test that by compiling all M5 to M6.3 earthquakes in the area of the dashed box in Figure 1 and plot moment release from these smaller events in Figure 4. Earthquakes in the range of M5 to M6.3 account for about 6.7% of the total expected moment release, which is about 2.7 mm/yr of the plate boundary slip. Combined with the larger earthquakes from the

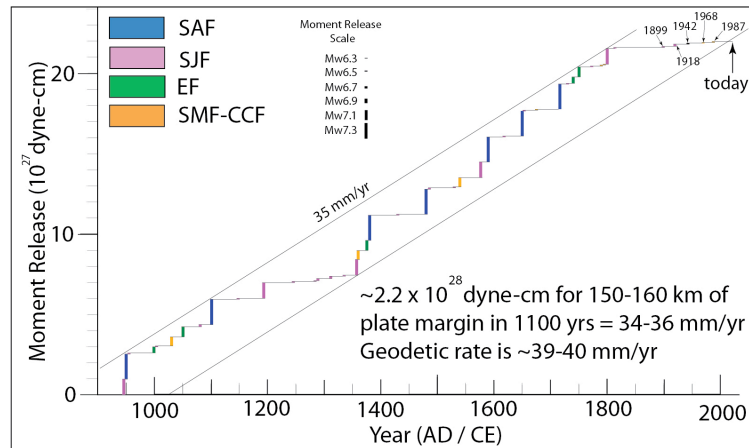


Fig. 3: Plot of seismic moment release in the southern San Andreas fault system over the past 1100 years, based on data in Table 1.

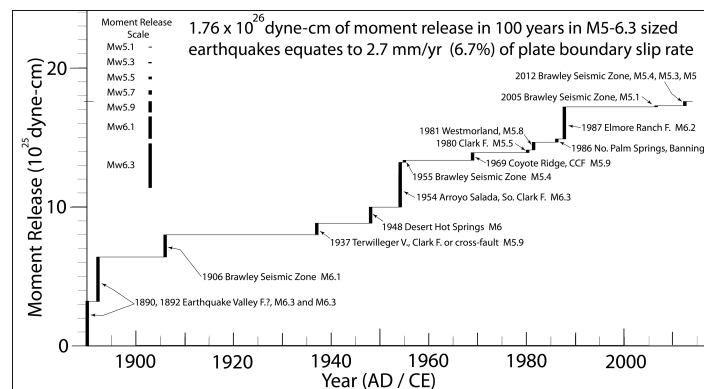


Fig. 4: Plot of moment release from moderate earthquakes ( $M < 6.5$ ) for the past 125 years.

A first order observation is that about 90% of the expected moment release can be accounted for by the known paleoseismic events. Figure 3 shows that about 35 mm/yr of the plate margin displacement has been accommodated by these known events, whereas the geodetic rate is estimated at about 39-40 mm/yr (Fialko, 2006).

The moderate earthquake history for this region is well-constrained by the historical record back to about 1890, after which there are excellent newspaper accounts, diaries, and other sources to examine the historical earthquake record, including the introduction of instrumental seismology. Youngs and Coppersmith (1985) suggest that about 6% of seismic moment is released in the smaller magnitude range and can be characterized by a Gutenberg-Richter relationship for

paleoseismic record, it appears that nearly all of the plate motion is seismic and can be accounted for by historical and paleoseismic events for the past 1100 years or so.

Two important observations can be made from the moment release record presented in Figure 3. First, although the southern San Andreas fault itself has an open interval that is longer than any other interval in the past 1100 years, from a system level view, there may have been other long periods of suppressed seismicity, such as between about 1100 and 1350 AD, when only one large earthquake occurred in the system. Thus, the relative quiescence of the largest earthquakes in the past 1100 years is not that anomalous when viewed over the past 1100 years, and considering the entire system of faults.



## INQUA Focus Group on Paleoseismology and Active Tectonics



paleoseismicity.org

That said, the second major observation supports the generally held view that the southern San Andreas fault appears to be very late in the earthquake cycle. In fact, the entire fault system appears to be late in the cycle. In the previous long open interval, nearly every major fault appears to have ruptured in a relatively short period of time, perhaps as a cluster due to stress triggering from nearby faults.

### Conclusions

Compilation of paleoseismic and historical earthquakes for the southern San Andreas fault system indicate that although the San Andreas fault is 50% beyond its average recurrence interval, the plate boundary system of faults as a whole can be argued to be very late in a regional cycle but not necessarily "overdue". This study demonstrates the need to take a systems level approach to understanding earthquake recurrence on complex fault systems.

**Acknowledgements:** This work was supported by the Southern California Earthquake Center (SCEC) and National Earthquake Hazards Reduction Program (USGS NEHRP) through many grants over many years. Much of the unpublished work is derived from work conducted during class fieldtrips at SDSU, and I thank the numerous students who participated in this work.

### References

- Biasi, G.P., R.J. Weldon II, T.E. Fumal, and G.G. Seitz (2002). Paleoseismic event dating and the conditional probability of large earthquakes on the southern San Andreas fault, California. *Bull. Seismo. Soc. Am.* 92 (7), 2761-2781.
- Biasi, G. P. and K. Scharer (2015). Coefficient of Variation Estimates for the Plate Boundary Fault System of California, American Geophysical Union 2015 Annual Meeting, S23A-2696. (December 2015).
- Buga, M. (2012) Holocene earthquake history of the southern Clark fault at Clark Lake, eastern San Diego County, California. Unpublished MS thesis, San Diego State University.
- Ellsworth, W.L., M.V. Matthews, R.M. Nadeau, S.P. Nishenko, P.A. Reasonberg, R.W. Simpson (1999). A physically-based earthquake recurrence model for estimation of long-term earthquake probabilities. Workshop on EARTHQUAKE RECURRENCE: STATE OF THE ART AND DIRECTIONS FOR THE FUTURE Istituto Nazionale de Geofisica, Rome, Italy.
- Faneros, G. (2004). Structure and neotectonics of the Superstition Mountain fault, Imperial County, California. Unpublished MS thesis, San Diego State University, 199 p.
- Fialko, Y. (2006). Interseismic strain accumulation and the earthquake potential on the southern San Andreas fault system. *Nature*, 441, 968-971.
- Fumal, T. E., M. J. Rymer, and G. G. Seitz (2002). Timing of large earthquakes since A.D. 800 on the Mission Creek strand of the San Andreas fault zone at Thousand Palms Oasis, near Palm Springs, California, *Bull. Seismol. Soc. Am.* 92, 2841-2860.
- Gurrola, Larry D. and Rockwell, Thomas K. (1996). Timing and slip for prehistoric earthquakes on the Superstition Mountain fault, Imperial Valley, southern California: *J. Geophys. Res.*, 101 (B3), 5977-5985.
- Hudnut, K.W., Seeber, L., and Rockwell, T. (1989). Slip on the Elmore Ranch fault during the past 330 years and its relation to slip on the Superstition Hills fault: *Bull. Seismo. Soc. Am.*, 79, (2), 330-341.
- Hudnut, K.W. and K.E. Sieh (1989). Behavior of the Superstition Hills fault during the past 330 years. *Bull. Seismo. Soc. Am.* 79, 304-329.
- Lindvall, S.C., Rockwell, T.K., and Hudnut, K.W. (1989). Evidence for prehistoric earthquakes on the Superstition Hills fault from offset geomorphic features: *Bull. Seismo. Soc. Am.* 79 (2), 342-361.
- Nishenko, S. P., and R. Buland (1987). A generic recurrence interval distribution for earthquake forecasting, *Bull. Seismo. Soc. Am.* 77, 1382-1399.
- Onderdonk, N., Rockwell, T.K., McGill, S., and Marliyani, G. (2013). Evidence for seven surface ruptures in the past 1600 years on the Claremont fault at Mystic Lake, northern San Jacinto fault, California. *Bull. Seismo. Soc. Am.* 103 (1), 519-541.
- Philibosian, B. T. Fumal, R. Weldon (2011). San Andreas fault earthquake chronology and Lake Cahuilla history at Coachella, California. *Bull. Seismo. Soc. Am.* 101 (1), 13-38.
- Rockwell, T.K. and Pinault, C.T. (1986). Holocene slip events on the southern Elsinore fault, Coyote Mountains, southern California: in Guidebook and Volume on Neotectonics and Faulting in Southern California (P. Ehlig, ed.), *Cordilleran Section, Geol. Soc. Am* 193-196.
- Rockwell, T. (1990). Holocene activity of the Elsinore fault in the Coyote Mountains, southern California: in *Western Salton Trough Soils and Tectonics, Friends of Pleistocene Guidebook*, p. 30-42.
- Rockwell, T.K., J.A. Dewhurst, C.W. Walls, W.J. Pollard, A. Orgil, G. Faneros, and T.E. Dawson (2000). High-resolution paleoseismology in southern California: Investigation of segment controls on the rupture history of the southern San Jacinto fault: in *Active Fault Research for the New Millenium, Proceedings of the Hokudan International Symposium and School on Active Faulting*, (K. Okumura, K Takada, and H. Goto, eds.), Letter Press Ltd., Hiroshima, Japan, p. 413-419.
- Rockwell, T., Akciz, S., and Gordon, E., 2013. Paleoseismology of the Aqua Tibia - Earthquake Valley fault, eastern strand of the Elsinore Fault Zone. *Seismo. Research Letters*, 84, 332.
- Rockwell, T.K., T.E. Dawson, J. Young-Ben Horton, and G. Seitz, 2015, A 21 event, 4,000-year history of surface ruptures in the Anza Seismic Gap, San Jacinto Fault and implications for long-term earthquake production on a major plate boundary fault. *Pure and Applied Geophysics*, 172, (5) 1143-1165.
- Salisbury, J.B., Rockwell, T.K., Middleton, T.J., and Hudnut, K.W. (2012). LiDAR and Field Observations of Slip Distribution for the Most Recent Surface Ruptures Along the Central San Jacinto Fault. *Bull. Seismo. Soc. Am.*, 102 (2), 598-619.
- Sieh, K. E. (1986). Slip rate across the San Andreas fault and prehistoric earthquakes at Indio, California, *Eos Trans. AGU* 67, 1200, Abstract T1222C-1201.
- Sieh, K. E., and P. L. Williams (1990). Behavior of the southernmost San Andreas fault during the past 300 years, *J. Geophys. Res.* 95, 6629-6645.
- Smith-Konter, B.R., D.T. Saqndwell, and P. Shearer (2011) Locking depths estimated from geodesy and seismology along the San Andreas fault system: Implications for seismic moment release. *J. Geophys. Res.* 116, B06401.
- Thorup, K.M. (1998) Paleoseismology of the central Elsinore fault in southern California: results from three trench sites, unpublished MS thesis, San Diego State University, 94 p.
- Vaughan, P.R., Thorup, K.M., and Rockwell, T.K., 1999, Paleoseismology of the Elsinore fault at Agua Tibia Mountain, southern California: *Bull. Seismo. Soc. Am.*, 89 (6), 1447-1457.
- Williams, P. (2009). Paleoseismic displacement history: Coachella Valley segment, San Andreas fault, 2009 SCEC Annual Meeting.
- Working Group on California Earthquake Probabilities (WGCEP) (1988). Probabilities of large earthquakes occurring in California on the San Andreas fault, U.S. Geol. Sur. Open-File Rep. 88-398.
- Youngs, R.R. and K.J. Coppersmith (1985). Implications of fault slip rates and earthquake recurrence models to probabilistic seismic hazard estimates. *Bull. Seismo. Soc. Am.* 75 (4), 939-964.



## Testing geomorphology-derived rupture histories against the paleoseismic record of the southern San Andreas Fault

Scharer, Katherine (1), Ray Weldon (2), Sean Bemis (3)

- (1) U.S. Geological Survey, 525 S. Wilson Ave., Pasadena, CA, USA. Email: kscharer@usgs.gov  
(2) University of Oregon, Eugene OR, USA. Email: ray@uoregon.edu  
(3) University of Kentucky, Lexington, KY, USA. Email: sean.bemis@uky.edu

**Abstract:** Evidence for the 340-km-long Fort Tejon earthquake of 1857 is found at each of the high-resolution paleoseismic sites on the southern San Andreas Fault. Using trenching data from these sites, we find that the assemblage of dated paleoearthquakes recurs quasi-periodically (coefficient of variation, COV, of 0.6, Biasi, 2013) and requires ~80% of ruptures were shorter than the 1857 rupture with an average of Mw7.5. In contrast, paleorupture lengths reconstructed from preserved geomorphic offsets extracted from lidar are longer and have repeating displacements that are quite regular (COV=0.2; Zielke et al., 2015). Direct comparison shows that paleoruptures determined from geomorphic offset populations cannot be reconciled with dated paleoearthquakes. Our study concludes that the 1857 rupture was larger than average, average displacements must be < 5 m, and suggests that fault geometry may play a role in fault behavior.

**Key words:** paleoearthquake, rupture length, San Andreas Fault

### INTRODUCTION

The last major earthquake on the southern San Andreas Fault (SSAF), the M7.9 Fort Tejon earthquake of 9 January 1857, ruptured the Carrizo, Big Bend, and Mojave sections for a total length of 340 km (Sieh, 1978; Zielke et al., 2012; Figure 1). In the ensuing 159 years, no earthquake larger than M6 has occurred on these fault sections, yet average intervals between ground-rupturing earthquakes at individual paleoseismic sites on these sections range from 90 to 140 years. Since Sieh (1978) first published a study of the 1857 rupture, several efforts have been made to document the extent, and thus size, of previous earthquakes on the San Andreas Fault in order to answer critical questions: what is the typical rupture length for the San Andreas Fault? What is the average displacement? We compare two approaches to these questions using (1) the age of ground-rupturing earthquakes from paleoseismic investigations and (2) catalogues of small (1-20 m) offsets on the fault determined from field and lidar investigations.

### PALEOSEISMIC DATA

There are six paleoseismic sites along the 1857 rupture that provide key data on the recurrence of large earthquakes on the 1857 stretch of the SSAF. From northwest to southeast, these are Bidart Fan on the Carrizo section, Frazier Mountain on the Big Bend section, and Elizabeth Lake, Littlerock, Pallett Creek and Wrightwood on the Mojave section. The Pitman Canyon site on the San Bernardino section does not show evidence of the 1857 rupture, but can be used to examine continuity of earthquakes to the southeast. Each site is characterized by fast sedimentation rates (~5 mm/yr) and abundant organic material suitable for radiocarbon dating, thus providing a high-resolution record of ground rupturing earthquakes. The records

vary in length: the shortest is Littlerock, which has evidence of three earthquakes since 1530 A.D., and the longest record is Wrightwood, with a record of 29 earthquakes in 3000 years. Average lognormal intervals are about 100 years but vary from as short as 90 years at Bidart Fan to 120 years at Pallett Creek (Biasi, 2013; Weldon et al., 2013). As each site is a point measurement that samples behavior at separate locations along the fault, variation of the average intervals could stem from location of each site relative to common endpoints of ruptures and limited sampling in the shorter records (Biasi, 2013). Despite these variations, each site has a coefficient of variation (COV) of ~0.6, indicating quasi-periodic behavior (i.e. between a COV of 0 indicating periodic behavior and COV of 1 indicating random behavior). At a site, individual earthquake intervals can be separated by just a single flood deposit (representing a few years) to as many as 305 years (Pallett Creek), but tests for clustering show that these periods are not significant enough to push the variability past random and into clustered behavior (Scharer et al., 2011).

The paleoearthquake ages from each site can be used to estimate the rupture length of individual earthquakes through time on the SSAF since 1300 A.D. (i.e., a rupture history). We modify a SSAF rupture history model from Scharer et al. (2014) (Figure 2A) to include earthquakes at Elizabeth Lake since 1300 A.D (Bemis et al., this meeting). The model was designed to maximize rupture lengths, in search of prehistoric earthquakes that could be as large as the 1857 earthquake. The most notable pattern since 1300 A.D. is the greater number of earthquakes at Bidart Fan and Frazier Mountain (n=6-7) compared to Elizabeth Lake, Littlerock, and Pallett Creek (n=3-4). This requires more frequent, shorter ruptures on the Carrizo and Big Bend sections of the fault. Despite age overlap, the



oldest earthquakes at Frazier Mountain (FM7) and Pallett Creek (PCT) are interpreted as separate earthquakes because paleoenvironmental observations of a wet period around 1350 A.D. preserved at both sites provides evidence these are not the same rupture. Specifically, FM7 occurred stratigraphically above whereas the PCT occurred stratigraphically below the wet period. The model indicates that only one 1857-like earthquake in the last 700 years is permitted, ca. 1550 A.D. Based on empirical relationships in Wesnousky (2008), the rupture lengths in *Figure 2A* (70-350 km) translate to Mw7.2-7.7 earthquakes, with an average of Mw7.5; alternate models can be made that split these long ruptures into more but smaller events. For comparison, the average magnitude for earthquakes on these sections forecast in the UCERF3 model is larger than our estimates (Mw7.8; Field et al., 2013).

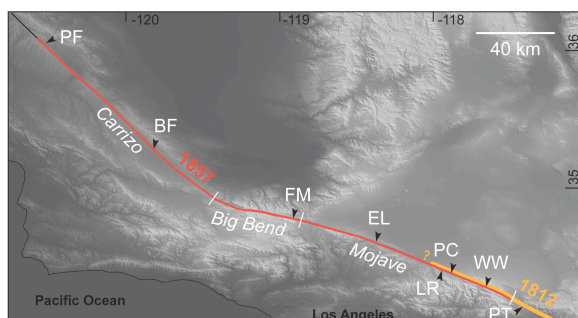


*Figure 1. Map of southern San Andreas Fault showing Carrizo, Big Bend and Mojave sections and extent of historic ruptures. The 1857 earthquake is observed at the Bidart Fan (BF), Frazier Mountain (FM), Elizabeth Lake (EL), Littlerock (LR), Pallett Creek (PC) and Wrightwood paleoseismic sites. PF=Parkfield, CA, PT=Pitman Canyon site. Base map produced from 10-m NED data.*

### GEOMORPHIC OFFSETS

An alternate approach for unraveling rupture histories utilizes small geomorphic features such as narrow gullies that are offset along the fault. As long as gullies are formed more frequently than large earthquakes occur, the cumulative displacement of gullies with each large earthquake should produce populations of displacements that reveal the rupture extent and displacement along strike for each earthquake (e.g., Sieh, 1978; Zielke et al., 2010; Klinger et al., 2011). For this study, we focus on the analysis presented by Zielke et al. (2012) for the 1857 stretch of the SSAF. That study used 0.5-m-resolution lidar data to determine the offset between pairs of gully-perpendicular profiles, incorporating the trend of each gully relative to the fault. Each of their ~450 offsets was determined by a goodness of fit measure that provides a best-fit offset estimate based on the shape of the profiles and each was qualified based on the shape of the gullies and the relative orientations of the gullies and the fault. When the moderate- to high-quality offsets were evaluated, the combined probability distributions exhibited pronounced offset populations at ~5 m intervals on the Carrizo section (Zielke et al., 2010). To construct a

possible rupture history for the 1857 stretch of the SAF, Zielke et al. (2012) binned measurements in 10-km-long, along-fault increments, thereby highlighting portions of the fault with common offset populations (*Figure 2B*). When these populations are connected along strike to produce cumulative displacement curves, a possible model of the sequence of earthquakes emerges.

### MODEL COMPARISON

We apply the rupture history determined from the dated paleoearthquakes (*Figure 2A*) to the displacement curves determined from geomorphic offsets (*Figure 2B*). In this approach, application of the sequence of dated earthquakes at each site (coded by color in 2A) to the sequence of displacements produces problems in the sequence and possible extent of individual earthquakes. For example, if the second displacement curve from Bidart Fan (green line, ca 1750 A.D.) is continued along strike, the model requires it pre-dates earthquakes at Pallett Creek and Wrightwood that are known from stratigraphic relationships to have occurred *earlier* (the 1550 and 1700 earthquakes). Thus, the rupture histories determined from these methods are not compatible and leave two possibilities: (1) either not all offsets are preserved in the geomorphic record, or (2) the paleoearthquake records are missing events. We argue that the amount of data leading to the paleoearthquake rupture history (*Figure 2A*) makes it the more robust of the two models for the following reasons: (1) At each site, each paleoearthquake is observed in multiple trench exposures and occurs at a unique stratigraphic interval that records the ground surface at the time of the earthquake. (2) Each earthquake is radiocarbon dated. (3) There is a similarity of the records at neighboring sites even though a different group of investigators completed each site. In contrast, the geomorphic displacements are not dated, and require that gully-forming events occur along the fault at least every 100 years.

The results of this comparison imply that average displacements for the SSAF are < 5 m, and that the regular 5 m-spacing for the Carrizo section is a consequence of measurement approach, limited data, or chance. There have been several studies on the uncertainties associated with geomorphic offset measurements (e.g., Gold et al., 2013; Scharer et al., 2014; Salisbury et al., 2015; Zielke et al., 2015); each illustrates that interpretations about gully width, how this width evolves over time, and how geomorphic features are projected to the fault can contain important epistemic uncertainties. We further note that the assumed form of the measurement uncertainty can make the results appear more regular. For example, we recalculated the COV for the Carrizo section replacing the quasi-normal distributions produced in the goodness of fit approach used by Zielke et al. (2010) with uniform distributions that spanned the width limits of each measurement. This approach assumes less knowledge about the pre-offset shape of each gully and allows for more post-offset modification of the gully. The resultant COV (0.6) using



these uniform distributions permits far less regular behavior.

**DISCUSSION**

We focus on two characteristics of the SSAF geomorphic displacement curves that are inconsistent with observations of modern ruptures. First, the long, smooth profiles developed from the displacement curves (Figure 2B) are dissimilar to irregular and often asymmetric profiles measured in modern strike-slip ruptures (Wesnowsky, 2008) in which significant along-strike variation is seen in field offset measurements. Second, the regular 5-m spacing between offsets (Zielke et al., 2010) is difficult to reconcile with the more irregular

and fast pace of earthquakes determined through trenching investigations. Zielke et al. (2015) computed the COV for the Carrizo section geomorphic offsets (0.2) and recognized an incompatibility with the Bidart Fan paleoearthquake record that is less regular (COV 0.6). They propose that diminished slip expected near rupture barriers such as step-overs or multi-stranded sections would not be large enough to be preserved in the geomorphic record. This idea is supported by analysis of historic ruptures that finds distributed deformation increases at these barriers thus reducing on-fault offset measurable in the gross geomorphology (e.g., Milliner et al., 2015).

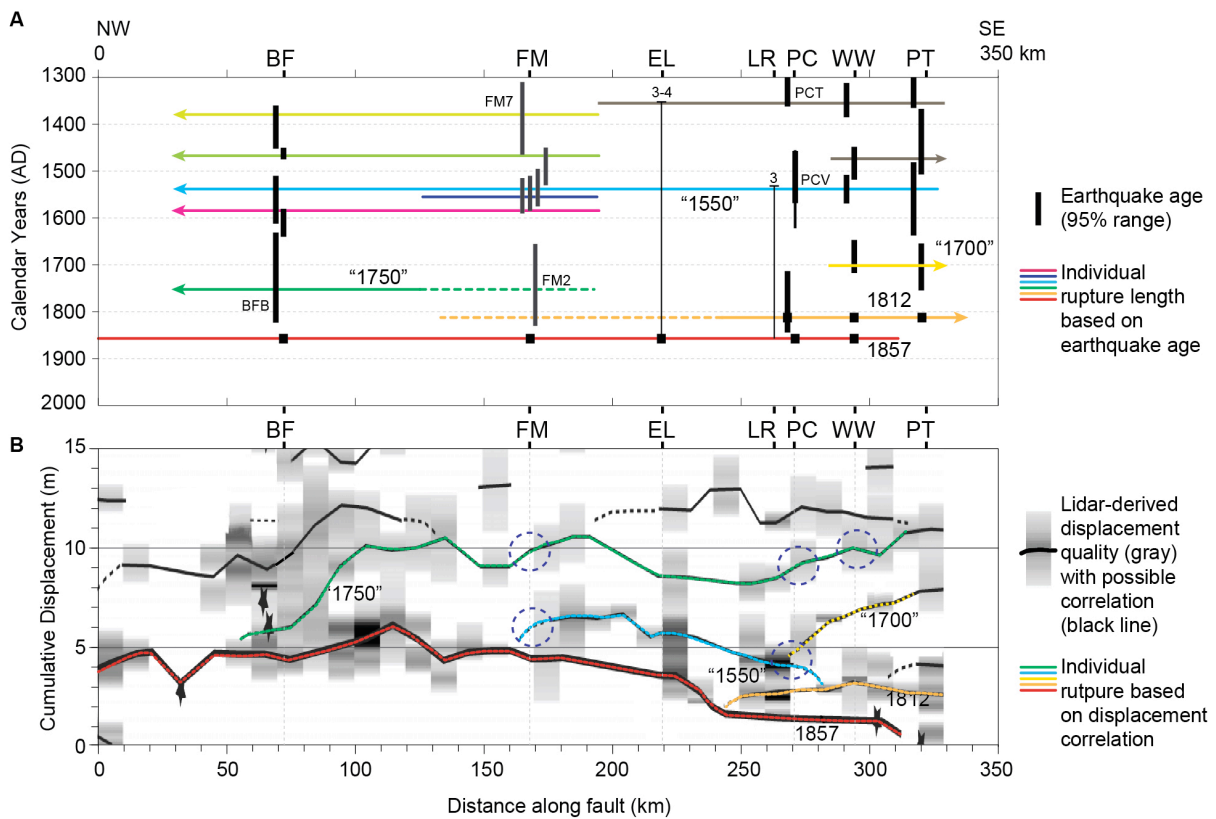


Figure 2. Comparison of earthquake ages and lidar-derived rupture histories. A. Plot of earthquake ages and interpreted rupture lengths along 1857 stretch of the SSAF. Vertical black bars show possible range of earthquake ages at each site staggered to show sequence of events. Thin vertical lines show age range for 3 to 4 earthquakes at Elizabeth Lake since 1350 A.D. and 3 earthquakes since 1530 A.D. at Littlerock. Rupture lengths (colored lines) connect sites with compatible earthquake ages to determine a model of maximum rupture lengths utilizing the age data. Ruptures are terminated midway between sites when no correlative earthquake exists. Orange dashed line shows rupture length if an 1812 rupture passed through FM. If 1812 terminated southeast of FM, the FM2 observation can be correlative with BFB as shown by green dashed line. PCT and FM7 are not correlated based on paleoenvironmental conditions at each site (see text for details). Only one earthquake, ca. 1550 A.D., can be connected through every site, and was as long as the 1857 rupture. B. Plot of lidar-derived cumulative displacements along the same stretch of the SSAF modified from Zielke et al. (2012). Vertical grey bars show 10-km bins of offset density with darker colors representing higher quality measurements. Black lines connect sections along strike in order to estimate offset distribution and length for successive earthquakes. We modified the plot by adding the color to the lines based on the sequence of ruptures from Figure 2A, to illustrate incompatibility between the two approaches; it is impossible to make the sequence of colors at each site match the sequence of colors predicted by the dating constraints (Figure 2A). Dashed circles highlight these locations. For example, if PC experienced 1857, 1812, and 1550 (red, orange, blue) and WW experienced 1857, 1812, and an earthquake around 1700 (red, orange, yellow), then the sequence of ruptures based on displacements incorrectly places the 1700 earthquake (yellow) earlier than the 1550 earthquake (blue). Similarly, as drawn, the penultimate event at BF (green) extends along the entire section of the fault and would incorrectly require this ca. 1750 earthquake to occur before older earthquakes at PC (1550, blue) and WW (1700, yellow). Zielke et al. (2015) proposed that the incompatibility results from rupture barriers that produce lower offsets not preserved in the geomorphology.



If rupture barriers play a role in the earthquake patterns on the SSAF, the rupture history determined from the paleoearthquake data (Figure 2A) might illuminate a barrier between the Frazier Mountain and Elizabeth Lake paleoseismic sites, just southeast of the Big Bend. Duan and Oglesby (2005) examined multicycle dynamic rupture models on a strike slip fault with this geometry, and find that earthquakes are preferentially generated on the fault section that is more parallel to plate motion (i.e. the Carrizo) and that resultant slip often continues just past the bend. These results produce a rupture pattern similar to that determined from paleoseismic studies (Figure 2A) and could be used to infer patterns in rupture directivity and epicenter location. However, other features of the fault may be at play and should be considered. For example, Fuis et al. (2012) show that between Frazier Mountain and Elizabeth Lake, the dip of the SSAF fault changes from moderately southwest to vertical.

### CONCLUSION

Using paleoearthquake ages on the SSAF, we show that a model designed to test for the longest possible ruptures can produce only one other 1857-length rupture in the last 700 years, ca. 1550 A.D. Given the model constraints, ruptures that are half the length of the 1857 earthquake (about ~160 km) are most common, translating to an Mw of 7.5. We further show that for the SSAF, the geomorphic record does not appear to resolve each individual rupture, indicating gully-forming storms occur on > 100 year intervals. Further, this analysis indicates that average per-event displacements are < 5 m and are less regular than suggested by the landscape analysis. The most notable pattern in the paleoseismic rupture histories is the more frequent earthquakes on the Carrizo and Big Bend sections of the fault, raising the possibility of a rupture barrier at the northwest end of the Mojave section.

**Acknowledgments:** Thanks to Olaf Zielke and Ramon Arrowsmith for conversations on this issue, Steve DeLong and Scott Bennett for thoughtful reviews. Any use of trade, firm, or product names is for descriptive purposes only and does not imply endorsement by the U.S. Government.

### References

Biasi, G. P. (2013). Maximum likelihood recurrence intervals for California paleoseismic sites, *U.S.G.S Open-File Report 2013-1165, Uniform California Earthquake Rupture Forecast Version 3 (UCERF3) – The Time-Independent Model, Appendix H*, 25 pp.

Duan, B., and D. D. Oglesby (2005), Multicycle dynamics of nonplanar strike-slip faults, *Journal of Geophysical Research: Solid Earth*, 110(B3), n/a-n/a, doi:10.1029/2004JB003298.

Field, E. H., et al. (2014), Uniform California Earthquake Rupture Forecast, Version 3 (UCERF3)—The Time-Independent Model,

*Bulletin of the Seismological Society of America*, 104(3), 1122-1180, doi:10.1785/0120130164.

Fuis, G. S., D. S. Scheirer, V. E. Langenheim, and M. D. Kohler (2012), A New Perspective on the Geometry of the San Andreas Fault in Southern California and Its Relationship to Lithospheric Structure, *Bulletin of the Seismological Society of America*, 102(1), 236-251, doi:10.1785/0120110041.

Gold, P. O., M. E. Oskin, A. J. Elliott, A. Hinojosa-Corona, M. H. Taylor, O. Keylos, and E. Cowgill (2013), Coseismic slip variation assessed from terrestrial lidar scans of the El Mayor-Cucapah surface rupture, *Earth and Planetary Science Letters*, 366, 151-162, doi:<http://dx.doi.org/10.1016/j.epsl.2013.01.040>.

Klinger, Y., M. Etchebes, P. Tapponnier, and C. Narteau (2011), Characteristic slip for five great earthquakes along the Fuyun fault in China, *Nature Geosci*, 4(6), 389-392, doi:<http://www.nature.com/ngeo/journal/v4/n6/abs/ngeo1158.html#supplementary-information>.

Milliner, C. W. D., J. F. Dolan, J. Hollingsworth, S. Leprince, F. Ayoub, and C. G. Sammis (2015), Quantifying near-field and off-fault deformation patterns of the 1992 Mw 7.3 Landers earthquake, *Geochemistry, Geophysics, Geosystems*, 16(5), 1577-1598, doi:10.1002/2014GC005693.

Salisbury, J. B., D. E. Haddad, T. Rockwell, J. R. Arrowsmith, C. Madugo, O. Zielke, and K. Scharer (2015), Validation of meter-scale surface faulting offset measurements from high-resolution topographic data, *Geosphere*, 11(6), 1884-1901, doi:10.1130/ges01197.1.

Scharer, K., R. Weldon, A. Streig, and T. Fumal (2014), Paleoseismicity at Frazier Mountain, California delimit extent and frequency of past San Andreas Fault ruptures along 1857 trace, *Geophysical Research Letters*, 41(13), 4527-4534, doi:10.1002/2014GL060318.

Scharer, K. M., G. P. Biasi, and R. J. Weldon (2011), A reevaluation of the Pallett Creek earthquake chronology based on new AMS radiocarbon dates, San Andreas fault, California, *Journal of Geophysical Research: Solid Earth*, 116(B12), n/a-n/a, doi:10.1029/2010JB008099.

Sieh, K. E. (1978), Slip along the San Andreas fault associated with the great 1857 earthquake, *Bulletin of the Seismological Society of America*, 68(5), 1421-1434, IN1421, 1435-1448.

Wesnousky, S. G. (2008), Displacement and Geometrical Characteristics of Earthquake Surface Ruptures: Issues and Implications for Seismic-Hazard Analysis and the Process of Earthquake Rupture, *Bulletin of the Seismological Society of America*, 98(4), 1609-1632, doi:10.1785/0120070111.

Zielke, O., J. R. Arrowsmith, L. Grant Ludwig, and S. O. Akciz (2012), High-Resolution Topography-Derived Offsets along the 1857 Fort Tejon Earthquake Rupture Trace, San Andreas Fault, *Bulletin of the Seismological Society of America*, 102(3), 1135-1154, doi:10.1785/0120110230.

Zielke, O., J. R. Arrowsmith, L. G. Ludwig, and S. O. Akciz (2010), Slip in the 1857 and Earlier Large Earthquakes Along the Carrizo Plain, San Andreas Fault, *Science*, 327(5969), 1119-1122, doi:10.1126/science.1182781.

Zielke, O., Y. Klinger, and J. R. Arrowsmith (2015), Fault slip and earthquake recurrence along strike-slip faults — Contributions of high-resolution geomorphic data, *Tectonophysics*, 638, 43-62, doi:<http://dx.doi.org/10.1016/j.tecto.2014.11.004>.



## Numerical Modelling of Tidal Notch Sequences on Rocky Coasts

Schneiderwind, Sascha (1), Kázmér, Miklos (2), Boulton, Sarah (3), Papanikolaou, Ioannis (4), Stewart, Iain (3), Reicherter, Klaus (1)

- (1) Neotectonics & Natural Hazards, RWTH Aachen University, Lochnerstr. 4-20, 52056 Aachen, Germany. [s.schneiderwind@nug.rwth-aachen.de](mailto:s.schneiderwind@nug.rwth-aachen.de)
- (2) Department of Palaeontology, Eötvös University, H-1117 Budapest, Pázmány Péter sétány 1/c, Hungary.
- (3) School of Geography, Earth and Environmental Sciences, Plymouth University, Plymouth, Devon PL4 8AA, UK.
- (4) Laboratory Mineralogy – Geology, Agricultural University of Athens, Iera Odos 75, Athina 118 55, Greece.

**Abstract:** Tidal notches have had the potential to form at sea level from ~6,000 years BP in the Mediterranean basin and preserve a symmetrical shape comparable to a quadratic polynomial. Statically determined, the roots are defined by the tidal range. However, gradual variations of eustatic sea-level rise and coseismic uplift in tectonically active regions contribute to vertical shifts of the erosional base at coastlines. As a consequence, the cliff morphology gets modified through time resulting in widening, deepening and separation of notches and possible overprinting of older features. In order to investigate successive modifications of coastal cliff morphology we developed a numerical model that considers the erosion rate, the erosion zone relative to sea-level, the regional sea-level curve, and tectonic uplift rates. The results show, that the present-day notch sequence from top descending to sea-level is not inevitably of decreasing age. Furthermore, the initiation of notch formation is not necessarily linked to the date of a certain seismic event.

**Key words:** Tidal Notches, digital modelling, Sea-Level Curve, extensional tectonics, Holocene.

### Introduction

Tidal notches are widely used as a sea-level marker. Notches form due to the contributions of ongoing horizontal erosion by chemical, physical and biological agents, they develop obvious ecological and morphological topographies that range from a few centimetres up to several metres deep. When these features are raised or submerged from present-day sea-level, palaeo-historic tectonic activity can be inferred. However, it remains unclear as to what present morphologies can reveal regarding the palaeo-magnitude and coseismic uplift/subsidence of historic earthquakes.

Biological erosion dominates notch formation on limestone coasts (e.g. Evelpidou et al., 2012). Frequently submerged by periodic tides horizontal galleries of endolithic bivalves are most active in the midlittoral zone, which extends across the tidal range (Pirazzoli, 1986). Endolithic bivalves act as the primary notch-forming agent and their habitat is limited to the tidal zone so the duration of sustained relative sea-level controls how deep a notch indentation develops. However, eustasy, isostasy, and vertical tectonic movements exhibit considerable spatial and temporal variability throughout the Holocene (Lambeck et al., 2004).

Boulton and Stewart (2015) compared local sea-level curves with associated regional uplift estimates and concluded that the highest elevation tidal notch on uplifting coasts dates to ~6,000 years BP in the Mediterranean. At that time the rate of eustatic sea-level rise decreased to ~1 mm/yr and reached gravitational equilibrium with the continental lithosphere (Carminanti et al., 2003; Stocchi et al., 2005) (Fig. 1). Since the Mid-

Holocene slow relative sea-level changes caused gradual changes of the erosional base at emerging coastlines. However, in seismically active regions, such as the extending Gulf of Corinth (central Greece), rapid displacements occur due to coseismic uplift of the coastlines that may not have exceeded the tidal range. As a consequence of both slow (eustatic) and rapid (tectonic) variations in the position of the erosional base, notch shape modification occurs. To distinguish between notch widening and new notch development is challenging (Fig. 2). It has to be expected, that the time period for notch formation might be short and the resulting indentation is only of minor scale, and that massive overprinting and degradation of older features has occurred since 6,000 years BP.

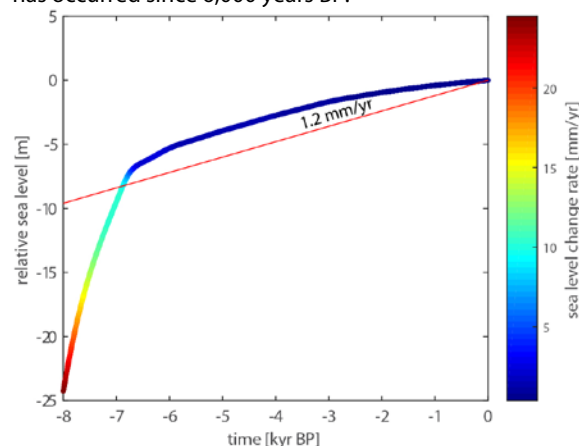


Fig. 1: Mid-Holocene sea-level curve for the Peloponnese, Greece (after Lambeck & Purcell, 2005). The gradient of sea-level rise and isostatic Holocene regional uplift (orange) are similar not until approximately 6,000 years BP.



In order to visualise the development of notch sequences incorporating eustatic and isostatic balances, erosion rates, coseismic uplift, and cliff steepness, we present a numerical model that simulates the migration of the erosional base through the Holocene. Well dated features can operate as inputs in order to verify the interpreted results or to indicate missed events due to notch degradation.

### Dynamic Notch formation

In the first instance, the gradient of relative sea-level change determines whether a tidal notch will develop or not.

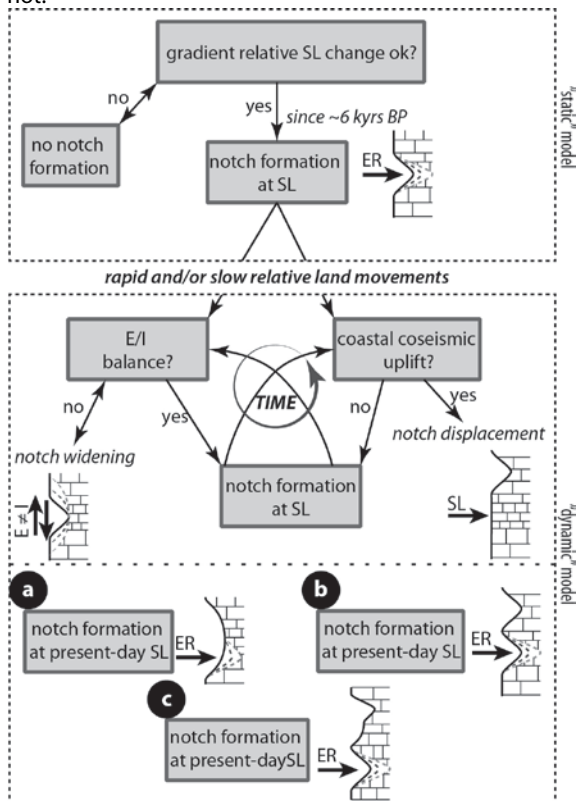


Fig. 2: Logic tree for tidal notch sequence evolution. The static notch formation model incorporates only the erosion rate (ER) to estimate the notch depth. The dynamic model considers gradual sea-level (SL) changes due to unbalanced eustasy (E) and isostasy (a), and coseismic land displacements. Resulting cliff shapes contain widened notches (1), emerged notches (b), or a combination of both (c).

For the Mediterranean, estimates of limestone erosion rates range from 0.2 - 1.0 mm/yr (Pirazzoli and Evelpidou, 2013). Thus, balanced conditions between eustasy and isostasy have to persist for at least 200 years to develop a significant 0.20 m deep notch. The notch height would approximately equal the tidal range for which estimates range from 0.3 - 0.4 m (Evelpidou et al., 2012). The coefficients of a quadratic polynomial can cover the requirements to describe such shapes (Fig. 3). Thus, in a static model notch depth is specified by erosion rate [mm/yr] x time [yr] of a constant erosional base. Minor

variations of sea-level change are not modelled here. The dynamic model calculates the parabolic erosion for every year considering both rapid and slow relative sea-level changes and computes the cumulative sum of erosional impacts. Using a local sea-level curve and information regarding ongoing isostatic and dated coseismic uplift events as inputs to control the migration of the erosional base enables the model to describe the vertical cliff morphology at a given moment.

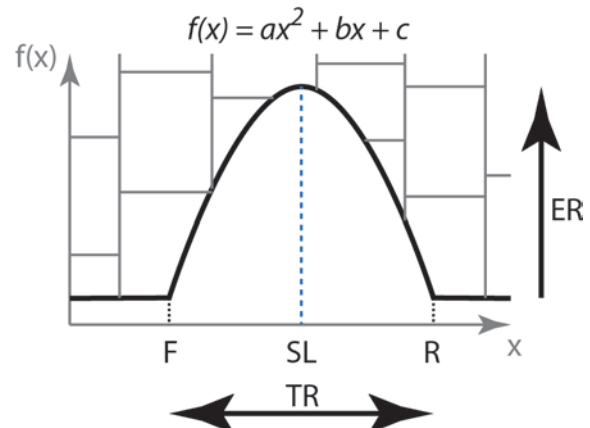


Fig. 3: A quadratic polynomial describes the depth ( $f(x)$ ) along a symmetrical notch profile. Floor (F) and roof (R) depict the roots separated by the tidal range (TR) along the x-axis. The erosion rate (ER) corresponds to  $c$  and determines the depth of the notch after one year. The coefficient  $b$  is null since the inflection point is at mean sea-level (SL). The coefficient  $a$  controls the gradient at  $f(0)$  and thus produces a curved or pointing shape.

The model assumptions are as follows:

- The erosion rate is consistent through time
- Erosion only effects the cliff within the tidal range with maximum impact at mean sea-level and gradual decrease towards the roof and floor (e.g., Antonioli et al., 2015)
- The affected lithology is homogeneous
- The initial cliff surface is smooth

### Results

The Mid-Holocene sea-level curve for Peloponnese (Greece) from Lambeck & Purcell (2005) shows a monotonically increasing shift (Fig. 1) and does not contain characteristics such as a mid-Holocene highstand (e.g. Kelletat, 2005) or punctuated variation (e.g. Goodman-Tchernov & Katz, 2015). When correcting this curve for the isostatic trend the resulting gradient indicates balanced conditions and suggests the period of notch formation was from ~6,500 years until today. In figure 4, a regional uplift rate of 1.2 mm/yr (Boulton & Stewart, 2015) is modelled. Using this uplift rate, relative sea-level change stagnated starting at ~6,000 years BP. However, today, a notch is present about 2 m above sea-level. However, slightly variable gradients within the past 3,000 years cause grazing towards the erosional zone and notch formation at the present-day sea-level. Vertical cliff sections above the present-day sea-level are



significantly different in shape than those predicted without coseismic uplift events.

Introducing coseismic uplift events creates a stepwise modification to the emerging coast function (Fig 5). Using the same regional uplift rate as before no submerged notches occur but vertical cliff sections above the present-day sea-level are significantly different in shape than predicted without coseismic uplift producing events. The most elevated notch is not as deep but significantly higher (at ~2.5 m) than the notch predicted in Figure 4. The uplift events lower the the erosional base. When sea-level is rising at ~1.2 mm/yr with a tidal range of 0.4 m, an uplift event of 0.22 m causes a prolongation of the erosive phase along a vertical section of sea cliff.

In the coseismic uplift model (Figure 5) initial notch formation begins prior to uplift event 2. Event 2 in figure 5 causes prolongation of the erosional phase of the initial notch. Contrarily, event 3 and 4 cause a lowering of the erosional base in a period of eustatic and isostatic balance (<6,000 BP). As a result, the erosional level significantly changes and results in the development of a new notch generation in response to each uplift event. In accordance to the applied sea-level curve no notch can be dated older than ~7,000 years BP.

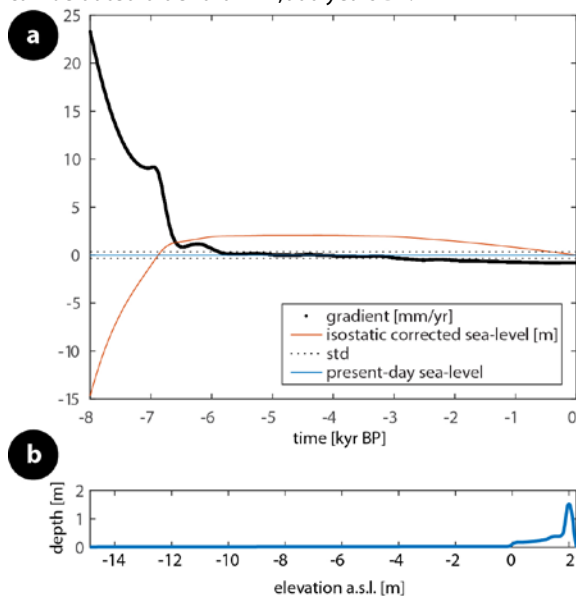


Fig. 4: Balancing eustatic and isostatic (1.2 mm/yr) agents (a) and the resulting notch profile (b) after 8 kyrs of a shifting erosional base in a tectonically stable setting. Cliff slope is 90°, Erosion rate is 0.5 mm/yr.

A more likely scenario is presented in figure 6. The cliff slope is not vertical and the seismic recurrence interval chosen is more suitable for the Peloponnese (Gaki-Papanastassiou et al., 2007). Furthermore, earthquake magnitudes are lowered to M6.5 producing only 0.11 m of coseismic uplift. The first notch develops at almost 6,500 years BP at an equivalent modern elevation of 2.2 m. Event 2 causes a quasi-relative-sea-level-stagnation since eustatic sea-level rise is slightly faster than the gravitational uplift at that time. At ~5,900 years BP the

roof of the initial notch gets significantly degraded and a younger generation notch forms at about 2.6 m (modern ASL). At 5,400 years BP, event 3 causes a lowering of the erosional base of 0.11 m and thus only widens the notch. Successive displacements of the erosional base are caused by events 4 and 5, at 4,500 and 3,600 years BP, respectively. Also, event 5 shifts the erosional base back to a level which occurred already 3,000 years ago. Subsequent coseismic events are accompanied by gradual relative sea-level variations. As a result, individual notches are widened and more separated than those that formed earlier.

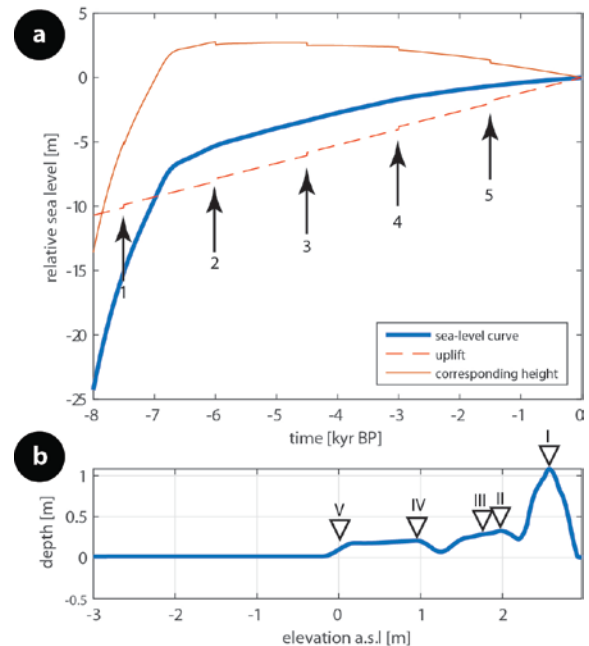


Fig. 5: a) Added five seismic events (arrows) of M7 of which each produced a coseismic uplift of 0.22 m. b) Resultant notch sequence. Triangles indicate individual notch generations: The oldest generation already began to develop prior to event 2 (I). (II) and (III) show generations formed due to coseismic uplift (Events 3 and 4). (IV) is the result from coseismic uplift and eustatic/isostatic disbalance. (V) depicts the present-day notch massively stretched due to ongoing disbalance.

## Discussion

Local sea-level curves can be highly dynamic, c. 8,000 years BP the rise in relative sea-level was considerable at 12-20 mm/yr (see Fig. 1); yet, Lambeck et al. (2014) highlights that 75% of mid-Holocene sea-level rise occurred from 6,700 to 4,200 years BP. In this stage, relative sea-level changed at 1.2 mm/yr and thus equals the herein modelled regional (gravitational) uplift rate. The shift of the erosional base appears to be mainly controlled by coseismic uplift during this period. Since 3,000 years BP, relative sea-level rise has been comparatively slow with rates < 1 mm/yr. As a result, the modelled notch sequence demonstrates how difficult it is to identify the specific timing of when notch formation began (see also Goodmen-Tchernov & Kratz, 2015).



Modern cliff morphology contains indentations, nips, and deepened sections that are not true notches. This geomorphology is a product of continuous notch formation, repeated overprinting, bedrock heterogeneity, storm surge elevations. Gradual sea-level change in combination with tectonic activity shifts the erosional base along the vertical axis. Therefore, it does not necessarily follow that drawdown results in a chronological sequence from old to young (see Fig. 6).

tidal notch sequences and thus contributes to palaeoseismological research.

**Acknowledgements:** T. M. Fernández-Steeger (RWTH Aachen University) is acknowledged for financial support and fruitful discussions. We thank Beau Whitney for his throughout review.

### References

- Antonioli, F., Lo Presti, V., Rovere, A., Ferranti, L., Anzidei, M., Furlani, S., Mastronuzzi, G., Orru, P.E., Scicchitano, G., Sannino, G., Spampinato, C.R., Paglirulo, R., Deiana, G., de Sabata, E., Sansò, P., Vacchi, M., and Vecchio, A., 2015. Tidal notches in Mediterranean Sea: a comprehensive analysis. *Quaternary Science Reviews* 119, pp. 66–84.
- Boulton, S. J.; Stewart, I. S. (2015): Holocene coastal notches in the Mediterranean region: Indicators of palaeoseismic clustering? In *Geomorphology* 237, pp. 29–37.
- Carminati, Eugenio; Doglioni, C.; Scrocca, D. (2003): Apennines subduction-related subsidence of Venice (Italy). In *Geophys. Res. Lett.* 30 (13).
- Evelpidou, N.; Kampolis, I.; Pirazzoli, P. A.; Vassilopoulos, A. (2012): Global sea-level rise and the disappearance of tidal notches. In *Global and Planetary Change* 92–93, pp. 248–256.
- Gaki-Papanastassiou, K., Papanastassiou, D., Maroukian, H.: Recent uplift rates at perachora Peninsula, east Gulf of Corinth, based on geomorphological-archaeological evidence and radiocarbon dates. *Hell. J. Geosc.* 42, pp. 45–56.
- Goodman-Tchernov, Beverly; Katz, Oded (2015): Holocene-era submerged notches along the southern Levantine coastline: Punctuated sea level rise? In *Quaternary International*.
- Kelletat, D. (2005): A Holocene Sea Level Curve for the Eastern Mediterranean from Multiple Indicators. *Z. Geomorph. N.F.* 137, pp. 1–9.
- Lambeck, Kurt; Antonioli, Fabrizio; Purcell, Anthony; Silenzi, Sergio (2004): Sea-level change along the Italian coast for the past 10,000yr. *Quat. Sc. Rev.* 23 (14–15), pp. 1567–1598.
- Lambeck, Kurt; Purcell, Anthony (2005): Sea-level change in the Mediterranean Sea since the LGM: model predictions for tectonically stable areas. In *Quaternary Science Reviews* 24 (18–19), pp. 1969–1988.
- Lambeck, Kurt; Rouby, Hélène; Purcell, Anthony; Sun, Yiyang; Sambridge, Malcolm (2014): Sea level and global ice volumes from the Last Glacial Maximum to the Holocene. In *Proceedings of the National Academy of Sciences of the United States of America* 111 (43), pp. 15296–15303.
- Pirazzoli, P. A. (1986): Marine notches. O. v. d. Plassche (Ed.): *Sea-Level Research*. Dordrecht: Springer Netherlands, pp. 361–400.
- Pirazzoli, Paolo A.; Evelpidou, Niki (2013): Tidal notches: A sea-level indicator of uncertain archival trustworthiness. *Palaeogeogr., Palaeoclim., Palaeoeco.* 369, pp. 377–384.
- Stocchi, P.; Spada, G.; Cianetti, S. (2005): Isostatic rebound following the Alpine deglaciation: impact on the sea level variations and vertical movements in the Mediterranean region. In *Geophys. J. Int.* 162 (1), pp. 137–147.
- Trenhaile, Alan S. (2014): Modelling tidal notch formation by wetting and drying and salt weathering. In *Geomorphology* 224, pp. 139–151.

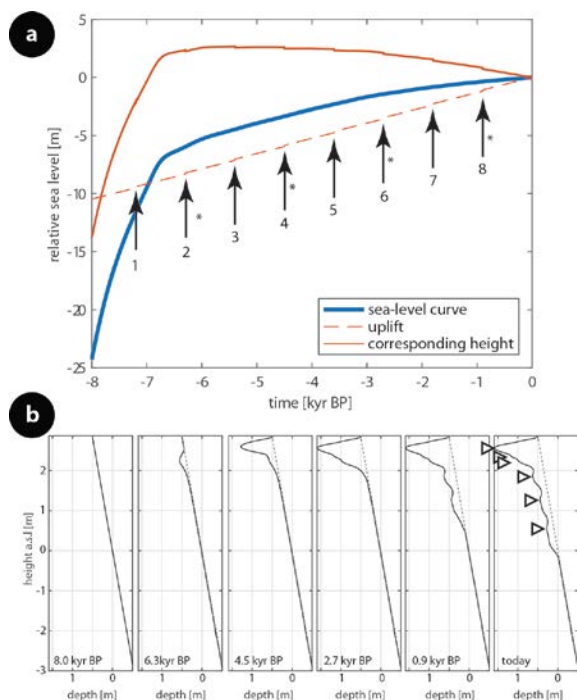


**Fig. 6:** a) 10 regularly separated M6.5 EQ with 0.11 m coseismic uplift (arrows). b) Notch profiles at a certain time during evolution of present day shape. Asterisk points on shown corresponding profile. Triangles indicate individual notch generations. Model input: Cliff slope is 80°, erosion rate is 0.5 mm/yr, and isostatic uplift is 1.2 mm/yr.

### Conclusion

Dependent on the region and associated local sea-level history, Holocene tidal notches can form beginning about 6,000–6,500 years BP in the Mediterranean Basin. Thereby, the very early stages of counterbalanced conditions might not result in the most elevated sea-level marker at present-day. As a consequence, a notch sequence from sea-level upwards does not necessarily adhere rigidly to a young to old chronology. Stages of almost-stagnation between regional sea-level rise and regional uplift (since approximately 4,000 years) tend to produce more space between individual notch generations. However, resulting notch shapes appear widened in comparison to older features formed 6,000–4000 years BP.

The model presented makes clear how slow an rapid processes bias each other and enables researchers to have an enhanced understanding of the evolution of



## The geometry of tidal notches – What do they reveal about coastal tectonics?

Schneiderwind, Sascha (1), Kázmér, Miklos (2), Boulton, Sarah (3), Papanikolaou, Ioannis (4), Stewart, Iain (3), Reicherter, Klaus (1)

- (1) Neotectonics & Natural Hazards, RWTH Aachen University, Lochnerstr. 4-20, 52056 Aachen, Germany. [s.schneiderwind@nug.rwth-aachen.de](mailto:s.schneiderwind@nug.rwth-aachen.de)
- (2) Department of Palaeontology, Eötvös University, H-1117 Budapest, Pázmány Péter sétány 1/c, Hungary.
- (3) School of Geography, Earth and Environmental Sciences, Plymouth University, Plymouth, Devon PL4 8AA, UK.
- (4) Laboratory Mineralogy – Geology, Agricultural University of Athens, Iera Odos 75, Athina 118 55, Greece.

**Abstract:** Tidal notches form at sea-level, predominantly on limestone coasts, during the Holocene. When present-day sea-level is different from distinct and stacked expressions coastal tectonic activities are inferred, in general. However, the relation between the offset of different notch generations and coseismic uplift produced from a single event remains a contentious issue. In order to review the evaluation of raised tidal notches in the frame of palaeoseismology, conceptual modelling of tidal notch sequence development provides new insights of morphological characteristics. High-resolution topographic data is able to provide the potential for the required accuracy to resolve those characteristics. The analysis of surface normal orientation and curvature enables the identification of tidal notches on steep cliffs and mapping of their spatial extent.

**Key words:** Tidal Notches, Holocene, Coastal Tectonics, t-LiDAR, Greece.

### Introduction

Tidal notches along steep rocky calcareous coastlines have been the subject of several studies in the past decades, mainly focussed on Holocene relative land movements sea-level variation and coastal tectonic processes. Resulting in obvious ecological and morphological topographies (Fig. 1) ranging from a few centimetres up to several metres deep, notches form at sea-level within the tidal range by continuous physical, chemical, and biological erosion (Pirazzoli, 1986). Assuming erosion rates between 0.2 – 1.0 mm/yr (Pirazzoli & Evelpidou, 2013), time periods of several decades to hundreds of years either in stable conditions or with balanced contributions of eustasy, isostasy and tectonics are required to form these distinct sea-level markers. Due to the rapidly rising post-LGM sea-level and slow crustal isostatic adjustments, such constant conditions were probably established not before 6 ka BP (Carminanti et al., 2003; Stocchi et al., 2005; Boulton & Stewart, 2015).

When the notches are found above or below the modern tidal range, coastal uplift or subsidence can be inferred, respectively. Warm, microtidal seas with active tectonics such as the Mediterranean provide beneficial conditions for studies that aim to unravel coastal tectonic activity (e.g. Pirazzoli et al., 1982, 1989, 1991; Rust & Kershaw, 2000; Stiros et al., 2000; Kershaw & Guo, 2001; Evelpidou et al., 2012a).

With a focus on Greek coastlines (Southwestern Crete and Eastern Gulf of Corinth), this paper aims to review existing knowledge about tidal notch formation, to provide new insights on reading exposures in terms of palaeoseismology, and to introduce a new methodology in order to extract evidence for coastal uplift in discrete events.

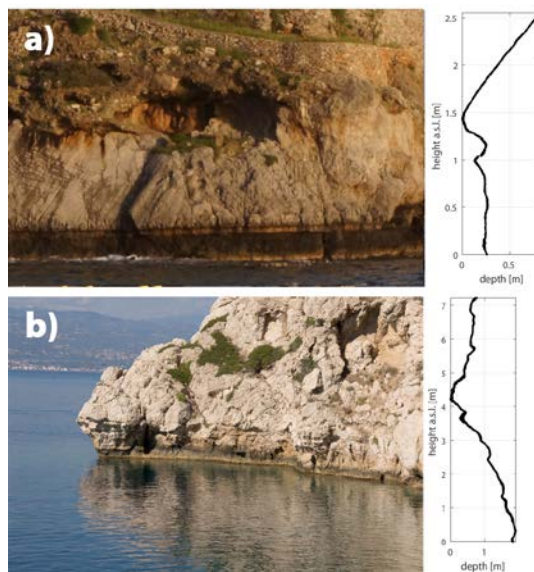


Fig. 1: Examples of palaeo sea-level markers and associated vertical profiles. a) Agio Pavlos (Southwestern Crete) raised by the 365 AD M8.5 earthquake. b) Heraion Lighthouse, Eastern Gulf of Corinth.

### Tidal notch formation

The term ‘tidal notch’ refers to a horizontal erosion feature at sea-level (Kelleter, 2005) due to the coeval action of chemical, physical, and biological impacts (Antonoli et al., 2015). Pirazzoli (1986) established a descriptive vertical classification based on objectively determinable characteristics. According to this study, tidal notches indicate the location of the midlittoral zone, which is vertically limited by the tidal range of approximately 0.4 m in the Mediterranean Sea (Evelpidou et al., 2012b) (Fig. 2).

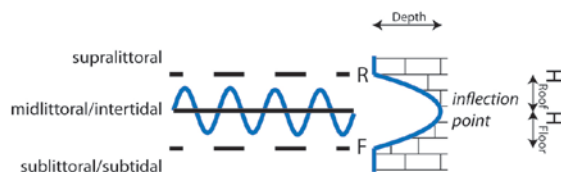


Fig. 2: Tidal notch formation at sea-level.

#### Chemical component

In the literature chemical erosion of calcareous cliffs is seen as a minor contributor only. Kelletat (2005) points out that dissolution of carbonates is not a common effect of seawater exposure, which is already saturated with  $\text{CaCO}_3$ . Only localised coastal sections might possess decreased saturation levels caused by submarine ground water discharge (Evelpidou et al., 2012b).

#### Physical component

Abrasion notches characterised by a well-rounded profile and a smooth surface are usually addressed separately. Their formation requires a nearby source of sand and pebbles that can be transported in suspension (Pirazzoli, 1986). Under such conditions the influence of biological erosion is likely decreased, if not completely extinguished since no organisms survive in these grinding environments (Kelletat, 2005).

A different type of physical erosion that occurs on limestone coasts is defined by the rock's resistance to wave action. Structural weaknesses such as cracks, fissures, joints, or faults can increase the potential of physical erosion. The rock is even more affected when turbulent water contains air that gets compressed when smashed against the rock and causes cavitation pitting (Antonioli et al., 2015).

#### Biological component

Biological erosion is commonly assumed to be the predominant agent in notch formation (Evelpidou et al., 2012b) and forms well-defined vegetational belts (Pirazzoli, 1986). The sublittoral zone of continuous immersion forms the habitat of grazing organisms like sea urchins that erode the underlying rock by abrading the surface with their hard teeth and radulas. Endolithic bivalves, such as the famous *Lithophaga lithophaga* as well as limpets and chitons live in galleries at mean sea level. The supralittoral zone is only affected at high tide. Here, bioerosion is mainly caused by epilithic algae and cyanobacteria.

#### The shape of tidal notches

The relative contribution of the aforementioned erosional mechanisms has not been quantified so far. Assuming a constant erosion rate along the tidal range and a periodical tide, the potential to graze a cliff within the tidal range is maximum at sea-level and decreases evenly towards zero at the upper and lower limit of tidal influence, respectively. One possible mathematical description for the decrease of effective erosion is a quadratic function with the tidal range and the

maximum erosion rate as inputs. Previous observations and sketches (e.g. Laborel et al., 1999; Cooper et al., 2007; Evelpidou et al., 2012a,b; Pirazzoli & Evelpidou, 2013; Taboroši and Kázmér, 2013; Trenhaile, 2015) support the hypothesis of a first order symmetrical V-/U-shaped notch (Pirazzoli, 1986) profile (Fig. 1a) with its retreat point (hereafter: inflection point) at mean sea level. The time controls the depth of a tidal notch if lithological, biological and climatic conditions are uniform. Deviations from symmetrical shapes occur when the cliff exposure is not sheltered to the open sea and when the cliff is not vertical. Furthermore, if the lithology is not homogeneous or intersected by structural weaknesses asymmetric shapes develop.

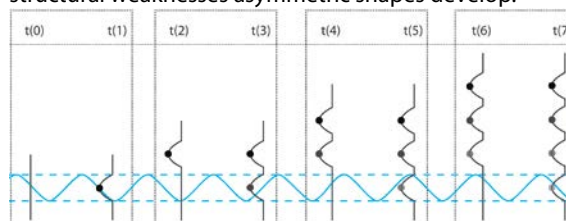


Fig. 3: General concept of raised notches. The initially straight cliff ( $t(0)$ ) suffers continuous erosion within the tidal range ( $t(1)$ ) with a maximum erosion rate at mean sea-level (dots). Rapid uplifting events (at  $t(2)$ ,  $t(4)$ , and  $t(6)$ ) raise the notches above the erosive zone.

#### Shape modification

In addition to exposure, and/or organic accretions (Pirazzoli, 1986), modification of the notches is also caused by processes that act differently in vertical and horizontal orientation. When sea-level rise and isostatic regional uplift occur at the same rate, a pseudo-stand still is produced and the erosional zone keeps its relative position along the cliff. Then the notch is only modified in its depth through time but keeps its height as long as the lithology is strong enough to support the weight of the overburden (Trenhaile, 2015). Vertical modification appears through slow and minor sea-level variations or due to rapid vertical land movements. Slow migration of the erosional zone only produces a widening of the existing notch while a rapid coast uplifting (or subsiding) event initiates the formation of a new notch (Fig. 3). When coastal uplift does not exceed the tidal range, the lower parts of the pre-existing notch will be overprinted. Furthermore, the amount of coseismic uplift in extensional tectonic settings ranges from  $\frac{1}{4}$  to  $\frac{1}{2}$  of the net slip per event (e.g. Papanikolaou et al., 2010). Thus, even moderate to strong events produce only a few decimetres of uplift which is not likely to exceed the entire tidal range.

#### Conceptual notch sequence model

The main assumptions for notch modelling are a normal curve distribution of erosion with its maximum at mean sea-level and its tips at low and high tide, respectively (Fig. 4).

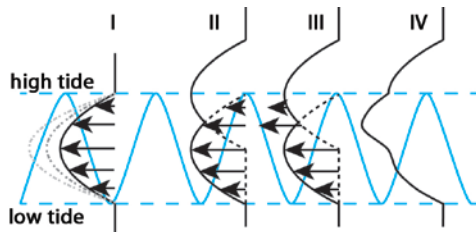


Fig. 4: Notch evolution incorporating a (I) normal distribution of erosion from low to high tide, and (II - IV) the effect of rapid land uplift which does not exceed the tidal range. (II) Raised older notch and theoretical erosion rate distribution. (III) Absolute erosion rates at the actual surface. (IV) Resulting cliff morphology exhibiting two notch generations.

Applying this model to the actual cliff's surface does not develop a classical ripple notch. Also, the resulting shape has its deepest indentation not at mean sea-level. The sum of afore and ongoing net erosion results in parts of the recent notch to be deeper than at mean sea-level. Furthermore, the resulting shape exhibits a significant potential for misinterpretation based on more than one uplifting events. Figure 5 shows the evolution of a notch sequence resulting from three earthquake events of the same magnitude and associated uplift each separated by the same time period.

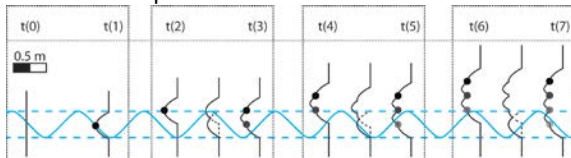


Fig. 5: Evolution of a notch sequence. M7 earthquakes at  $t(2)$ ,  $t(4)$ , and  $t(6)$  produce successive coastal uplifts of 0.22 m. Grey dots indicate former inflection points.

As a result, raised inflection points are not located at the deepest indentations of the sequence. Further, uplifts of more than half the tidal range do not produce a successive deepening of the cliff exposure. The inflection points only migrate vertically but are still existent on the exposed cliff. If the amount of uplift is less than half of the tidal range no remnants of pre-existing notches are preserved (Fig. 6).

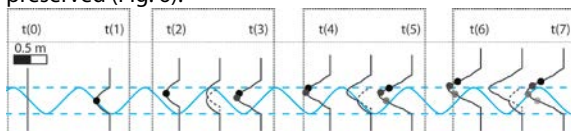


Fig. 6: Successive evolution of a notch sequence experiencing 3 earthquakes ( $t(2)$ ,  $t(4)$ , and  $t(6)$ ) of different magnitude (M6.5, M6.2, and M6.4) and uplift (0.11 m, 0.08 m, and 0.1 m). Grey dots indicate former inflection points

The usage of reasonable earthquakes and associated mean uplifts (in accordance with Wells & Coppersmith, 1994) produces a sequence with successive indentation into the cliff exposure, when still applying equal recurrence intervals. Furthermore, not only the lower parts of pre-existing notches but also their inflection points and even more towards the roof will degrade. As a result, the individual inflection points are only projections of previous relative mean sea-levels onto the

successively incised exposure and do not show any distinct geometrical evidence for their existence. In sheltered conditions the roof may be preserved and allow reconstructing the palaeoseismic history.

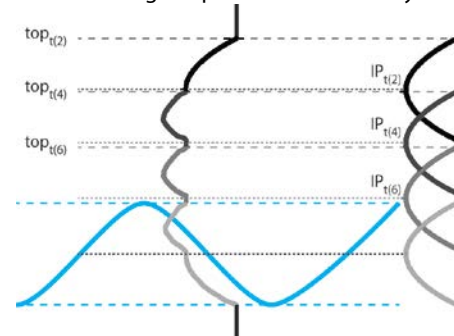


Fig. 7: Reading the sequence. The preserved top of each notch generation allows reconstructing associated inflection points (IP). This figure refers to the notch sequence of Fig. 5.

When assuming that the tidal range did not change through time and thus the parabolic shape intersects the levels of low and high tide, respectively, historic sea-levels can be reconstructed (Fig. 7). However, recognising this potentially minor feature might turn out to be challenging.

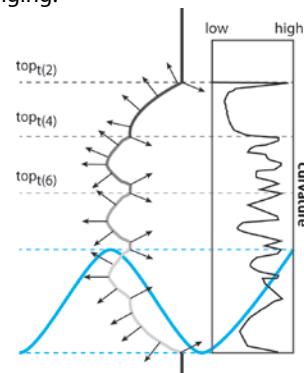
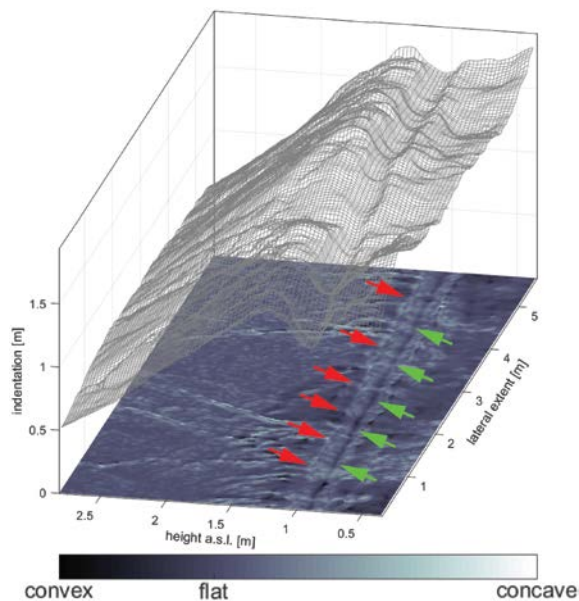


Fig. 8: Normal orientation and direction (arrows), and surface curvature along a vertical notch sequence.

### High-Resolution Laser Scanning

High resolution terrestrial laser scanning (TLS) offers the opportunity to evaluate an exposure not just by single vertical profiles (e.g. Kázmér & Taboróši, 2012) but in a full 3D-extent. The high accuracy and precision of the resulting point cloud data enables to detect minor changes in surface curvature and normal orientation (Fig. 8). The majority of surface normals of the concave cross-section of the notch is oriented towards the cliff (Fig. 8). Only a few knickpoints face towards the sea. However, when pointing downwards these normal vectors are located at the roof of a notch. Furthermore, the curvature represents the bend of a surface within a given radius. Thus, the combination of normal orientation and the amount of curvature points to remnants of older notch generations. The third dimension provided by TLS allows comparing the evolution of the curvature along the exposure and thus, verifying evidence for a raised tidal notch (Fig. 9).



convex flat concave  
Fig. 9: Laser scan from a distinct tidal notch at Agio Pavlos (Southwestern Crete). Concave (red) and convex (green) patterns represent the roof and the center of the notch, respectively.

## Conclusions

The symmetrical shape of tidal notches is the result of frequent immersion due to constant periodical tides. In sheltered conditions, a distinct notch floor and roof form at low and high tide, respectively. Ongoing erosion only affects the depth of a notch but not its height. Conceptual modelling showed that, following these assumptions, complex sequences of raised notches carry information on palaeo sea-levels. However, remnants of overprinted older features are difficult to recognise. High-resolution surface data, such as from TLS, can provide the required accuracy to analyse the orientation of normals and the curvature along an exposure.

**Acknowledgements:** The Hellenic Navy Hydrographic Service provided tidal range data from Posidonia. Thanks to C. Hilgers and his team (RWTH Aachen University) for the loan of the TLS System. T. M. Fernández-Steeger (RWTH Aachen University) is acknowledged for financial support.

## References

Antonoli, F., Lo Presti, V., Rovere, A., Ferranti, L., Anzidei, M., Furlani, S., Mastronuzzi, G., Orru, P.E., Scicchitano, G., Sannino, G., Spampinato, C.R., Paglirulo, R., Deiana, G., de Sabata, E., Sansò, P., Vacchi, M., and Vecchio, A., 2015. Tidal notches in Mediterranean Sea: a comprehensive analysis. *Quaternary Science Reviews* 119, pp. 66–84.

Boulton, S. J. and Stewart, I. S., 2015. Holocene coastal notches in the Mediterranean region: Indicators of palaeoseismic clustering? *Geomorphology* 237, pp. 29–37.

Carminati, E., Doglioni, C., Scrocca, D. (2003): Apennines subduction-related subsidence of Venice (Italy). *Geophys. Res. Lett.* 30 (13).

Cooper, F.J., Roberts, G.P., and Underwood, C.J., 2007. A comparison of 10<sup>3</sup>–10<sup>5</sup> year uplift rates on the South Alkyonides Fault, central Greece: Holocene climate stability

and the formation of coastal notches. *Geophys. Res. Lett.* 34 (14).

Evelpidou, N., Vassilopoulos, A., Pirazzoli, P. A. (2012a): Submerged notches on the coast of Skyros Island (Greece) as evidence for Holocene subsidence. *Geomorphology* 141–142, pp. 81–87.

Evelpidou, N., Kampolis, I., Pirazzoli, P. A., Vassilopoulos, A. (2012b): Global sea-level rise and the disappearance of tidal notches. *Global and Planetary Change* 92–93, pp. 248–256.

Kázmér, M. and Taboroši, D., 2012. Rapid Profiling of Marine Notches Using a Handheld Laser Distance Meter. *Journal of Coastal Research* 283, pp. 964–969.

Kelletat, D.H., 2005. Notches. *Encyclopedia of Coastal Science*. Edited by M. L. Schwartz. Springer, Dordrecht.

Kershaw, S. and Guo, L., 2001. Marine notches in coastal cliffs: indicators of relative sea-level change, Perachora Peninsula, central Greece. *Marine Geology* 179 (3–4), pp. 213–228.

Laborel, J., Morhange, C., Collina-Girard, J., and Laborel-Deguen, F., 1999. Littoral bioerosion, a tool for the study of sea level variations during the Holocene. *Bull. of the Geological Society of Denmark* 45, pp. 164–168.

Papanikolaou, I., Fomelis, M., Parcharidis, I., Lekkas, E.L., and Fountoulis, I.G (2010): Deformation pattern of the 6 and 7 April 2009, Mw=6.3 and Mw=5.6 earthquakes in L’Aquila (Central Italy) revealed by ground and space based observations. *Nat Hazards Earth Syst. Sci.*, 10, 73–87.

Pirazzoli, P. A. (1986): Marine notches. In Orson van de Plassche (Ed.): *Sea-Level Research*. Dordrecht: Springer Netherlands, pp. 361–400.

Pirazzoli, P. A., Laborel, J., Saliège, J. F., Erol, O., Kayan, I., Person, A. (1991): Holocene raised shorelines on the Hatay coasts (Turkey): Palaeoecological and tectonic implications. *Marine Geology* 96 (3–4), pp. 295–311.

Pirazzoli, P. A., Montaggioni, L. F., Saliège, J. F., Segonzac, G., Thommeret, Y., Vergnaud-Grazzini, C. (1989): Crustal block movements from Holocene shorelines: Rhodes Island (Greece). *Tectonophysics* 170 (1–2), pp. 89–114.

Pirazzoli, P. A., Thommeret, J., Thommeret, Y., Laborel, J., Montag-Gioni, L. F. (1982): Crustal block movements from holocene shorelines: Crete and antikythira (Greece). *Tectonophysics* 86 (1–3), pp. 27–43.

Pirazzoli, P. A. and Evelpidou, N. (2013): Tidal notches: A sea-level indicator of uncertain archival trustworthiness. *Palaeogeography, Palaeoclimatology, Palaeoecology* 369, pp. 377–384.

Rust, D. and Kershaw, S. (2000): Holocene tectonic uplift patterns in northeastern Sicily: evidence from marine notches in coastal outcrops. *Marine Geology* 167 (1–2), pp. 105–126.

Stiros, S.C., Laborel, J., Laborel-Deguen, F., Papageorgiou, S., Evin, J., and Pirazzoli, P.A., 2000. Seismic coastal uplift in a region of subsidence: Holocene raised shorelines of Samos Island, Aegean Sea, Greece. *Marine Geology* 170 (1–2), 41–58.

Stocchi, P., Spada, G., Cianetti, S. (2005): Isostatic rebound following the Alpine deglaciation: impact on the sea level variations and vertical movements in the Mediterranean region. *Geophys. J. Int.* 162 (1), pp. 137–147.

Taboroši, D. and Kázmér, M., 2013. Erosional and Depositional Textures and Structures in Coastal Karst Landscapes. Michael J. Lace, John E. Mylroie (Eds.): *Coastal Karst Land-forms*, vol. 5. Dordrecht: Springer Netherlands (Coastal Research Library), pp. 15–57.

Trenhaile, A.S., 2015. Coastal notches: Their morphology, formation, and function. *Earth-Sci Rev* 150, 285–304.

Wells, D. L. and Coppersmith, K. J. (1994): New empirical relationships among magnitude, rupture length, rupture width, rupture area, and surface displacement. *Bulletin of the Seismological Society of America* 84 (4), pp. 974–1002, A1–A4, B1–B11, C1–C49.



## Holocene paleo-seismicity of the Bollnäs fault , central Sweden

Colby A. Smith , Martin Sundh, Johan Nyberg, Björn Bergman, Henrik Mikko (1)

(1) Geological Survey of Sweden, Uppsala, Sweden

**Abstract:** Despite the intraplate setting, Fennoscandia experienced high-magnitude seismicity during the Holocene. Following deglaciation, preexisting bedrock faults were reactivated by a combination of tectonic and isostatic stresses. These so called post-glacial faults are well-documented in the north, but recent high-resolution digital elevation data show linear escarpments that appear to cut across glacial sediments in central Sweden, some 400 km south of previously mapped structures. One such feature lies just west of the town of Bollnäs and has undergone investigations to determine its origin.

**Key words:** Bollnäs, post-glacial, scarp, Sweden, Fennoscandia

### INTRODUCTION

The presence of post-glacial faults in Sweden has been known for decades (Lundqvist and Lagerbäck, 1976), but the recent availability of a high-resolution digital elevation model (DEM) (Lantmäteriet, 2015) has revealed new information about the location and complexity of post-glacial fault scarps (Mikko et al., 2015) .

Examination of the new DEM revealed a linear escarpment apparently cutting across glacial sediments and landforms near the town of Bollnäs (Fig. 1). In order to determine if this feature is a result of post-glacial fault rupture, investigations have been conducted

### DISCUSSION

Three lines of evidence support the interpretation that the escarpment results from post-glacial faulting. A) Trenches excavated across the scarp reveal faulted glacial sediments and landslides down the scarp overlain by undisturbed flat lying sediments (Fig. 2). B) Trenches atop an esker reveal water escape structures, interpreted to be seismites (Fig. 3). C) Numerous paleo-landslides exist in non-susceptible deposits on low-angle slopes (Fig. 4). The rupture dimensions suggest a paleo-seismic event of magnitude ~6.2 (Smith et al., 2014) according to the relationships reported by Wells and Coppersmith (1994). The stratigraphy of the trench indicates that faulting occurred shortly after deglaciation and is consistent with bog bottom dates from landslide scars that indicate sliding occurred prior to 10,200 calendar years before the present (Smith et al., 2014). These results are consistent with modeling results of fault instability following deglaciation (Wu, 1998).

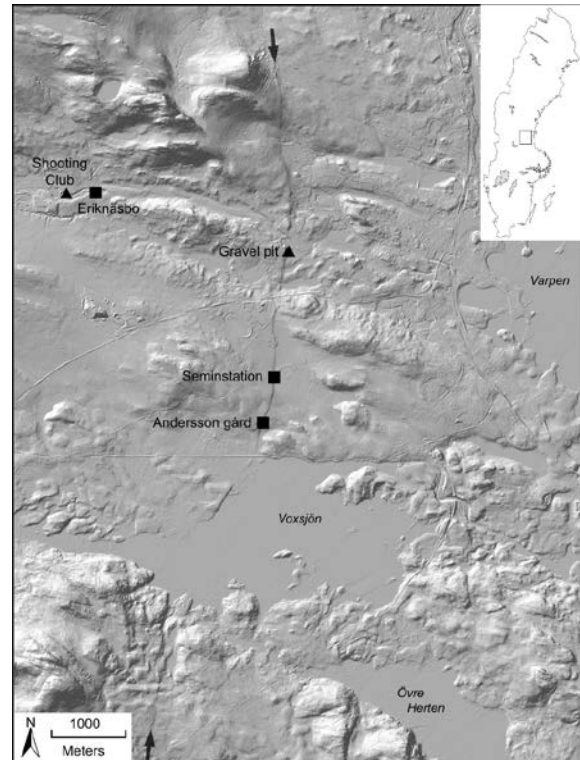


Fig. 1: Shaded relief DEM showing the east-facing Bollnäs scarp marked with arrows. The location within Sweden appears in the upper right corner. Trenches have been excavated at the black squares. Figure adapted from Smith et al. (2014).



Fig. 2: On the eastern side of the photo, varved glaciolacustrine clay conformably overlies till. The clay is truncated by till and the varves have been dragged into a nearly vertical orientation along the till clast. Figure adapted from Smith et al. (2014).



Fig. 3: Water-escape structures located in a flat upland environment about 2.5 km from the scarp. No evidence of rapid sedimentation by landsliding was found, and the water-escape structures are interpreted to result from liquefaction of sand during a paleoseismic event. Figure adapted from Smith et al. (2014).

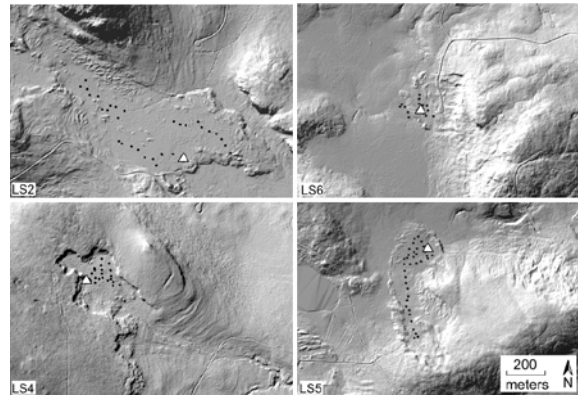


Fig. 4: Shaded relief DEM of landslides in till interpreted to be triggered by paleoseismicity. Radiocarbon dates of organic material overlying the landslides date to shortly after local deglaciation. Figure adapted from Smith et al. (2014).

**Acknowledgements:** Funding for this project was provided by the Swedish Nuclear Fuel and Waste Management Co (Svensk Kärnbränslehantering AB).

#### References

- Lantmäteriet, (2015). Gsd-Höjddata, Grid 2+.
- Lundqvist, J., Lagerbäck, R., (1976). The Pärve Fault: A late-glacial fault in the Precambrian of Swedish Lapland. *GFF* 98, 45–51.
- Mikko, H., Smith, C.A., Lund, B., Ask, M.V.S., Munier, R., (2015). LiDAR-derived inventory of post-glacial fault scarps in Sweden. Article LiDAR-derived inventory of post-glacial fault scarps in Sweden. *GFF* 137, 334–338.
- Smith, C.A., Sundh, M., Mikko, H., (2014). Surficial geology indicates early Holocene faulting and seismicity, central Sweden. *International Journal of Earth Sciences* 103, 1711–1724.
- Wells, D.L., Coppersmith, K.J., (1994). New Empirical Relationships among Magnitude, Rupture Length, Rupture Width, Rupture Area, and Surface Displacement. *Bulletin of the Seismological Society of America* 84, 974–1002.
- Wu, P., (1998). Intraplate earthquakes and Postglacial Rebound in Eastern Canada and Northern Europe. *Dynamics of the Ice Age Earth: A Modern Perspective* 603–628.



## Establishment of a comprehensive data base for seismic hazard assessment in Germany and Central Europe using historical, paleoseismic and neotectonic evidence

Thomas Spies (1), Diethelm Kaiser (1), Jörg Schlittenhardt (1), Klaus Reicherter (2), Jochen Hürtgen (2)

(2) BGR, Unit 'Seismic Hazard Assessment', Stilleweg 2, 30655 Hannover, Germany. Email: Thomas.Spies@bgr.de  
(1) Neotectonics and Natural Hazards Group, RWTH Aachen, Lochnerstr. 4-20, 52056 Aachen, Germany.

**Abstract:** Reliable seismic hazard assessment needs a data base comprising as much as possible complete historical and paleoseismic evidence and all available information on locations and properties of seismic sources, e.g. active faults and - supplementary in areas of moderate seismicity - also models of seismotectonic zones. The present project deals with these issues for Germany and Central Europe. Historical seismicity is being reviewed and a data base of existing paleoseismic evidence in Central Europe has been established recently. The German catalogue of historical seismicity of BGR covers 1200 years. Present work focuses on the re-evaluation of events by modern standards of historical research and seismological evaluation. Up to now the paleoseismic database does not cover all areas of significant seismicity in Central Europe so paleoseismic investigations are carried out in these areas. A data base of active faults and seismogenic structures will be compiled. Furthermore a comprehensive concept for the derivation of seismotectonic zoning will be developed.

**Key words:** Seismic hazard assessment, historical seismicity, paleoseismic evidence, active faults, Central Europe.

### INTRODUCTION

As recurrence intervals of the larger earthquakes in intraplate settings like Central Europe are in the order of many thousands of years, historical seismicity, paleoseismic and neotectonic evidence have to be taken into account to obtain reliable seismic hazard assessment, e.g., Vanneste et al. (2013) and Grützner et al. (2016). This includes the locations and properties of the seismic sources, e.g. active faults and models of the seismotectonic zones. The paper summarizes the compilation of the data for Germany and Central Europe. Historical seismicity is being reviewed on a regular basis (Leydecker, 1986 and 2011; Kaiser et al., 2014). A data base of existing paleoseismic evidence in Central Europe has been established recently and is being extended ("PalSeisDB", see Hürtgen et al., 2015). A data base of active faults and seismogenic structures will be compiled. Furthermore a comprehensive concept for the derivation of seismotectonic zoning will be developed.

### PROJECT CONTEXT

In 2011 a revised version of the German Nuclear Safety Standard, called KTA 2201.1 (Design of Nuclear Power Plants against Seismic Events) was published (KTA, 2011). It explicitly demands the use of paleoseismic studies which results have to be considered in the estimation of seismic hazard at the sites of the nuclear power plants. As a consequence the paleoseismic data base "PalSeisDB" was established as up to then no compilation of paleoseismic evidence existed.

The elaboration of the data base for seismic hazard assessment in Central Europe can be attributed to several

international activities. One is the SHARE project in which a harmonized seismic hazard model for whole Europe was established by several groups of leading experts in earthquake geology, seismology and seismic hazard assessment (Giardini et al., 2013). The results of the SHARE project which include catalogues of seismicity and a compilation of active faults in Europe have to be refined and supplemented at the regional and local scale.

Other international projects aiming at the improvement of the data base are the PEGASOS project in Switzerland (Probabilistic Seismic Hazard Analysis for Swiss Nuclear Power Plant Sites, Renault, 2014) and the CEUS project in the USA. In PEGASOS around 200 historical earthquakes with epicentral intensities larger than VI were re-evaluated by a team of historians and seismologists. Many events had to be rejected as fakes and the source parameters of most events were adjusted by a significant amount compared to previous estimations. A prominent example for the use of paleoseismic evidence is the CEUS project (Central and Eastern United States Seismic Source Characterization for Nuclear Facilities, CEUS-SSC, 2012) in which course the knowledge on seismicity and locations of seismic sources in this part of the United States could be greatly enhanced and incorporated into the seismic hazard assessment. The Central and Eastern United States show moderate seismicity like Central Europe which is considered here.

### HISTORICAL SEISMICITY

The historical seismicity of Germany and adjacent areas was compiled and published by Leydecker (1986) and updated by Leydecker (2011). It covers the time period of 800 AD up to present. Figure 1 displays the distribution of



events with epicentral intensities larger than VI which roughly is the lower bound for the damage of buildings. Beyond the German borders only events with epicentral intensities larger than VIII and up to 200 km distance are included completely in this catalogue.

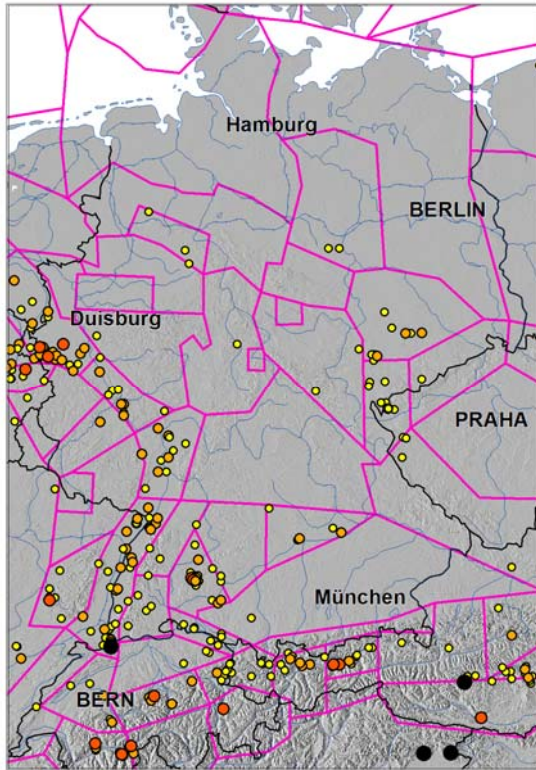


Fig. 1: Damaging earthquakes in the German Earthquake Catalogue: smallest size (yellow) indicates epicentral intensity range from VI-VII, followed by next larger size (orange) from VII-VIII, VIII-IX (red) and largest symbols indicating larger than IX in black (Leydecker, 2011). 391 events, time interval 800 AD up to present. Polygons mark the seismotectonic zones given by Leydecker & Aichele (1998).

The seismotectonic zone model of Leydecker & Aichele (1998) is displayed in Figure 1 as well. Moderate but significant seismicity is found in the Alpine Mountains in the South, in the Upper and Lower Rhine Graben in the West which are part of the European Rift system and the Swabian Jura related to the Upper Rhine Graben. A short review of the geological framework is given in Hürtgen et al. (2015).

Presently the German Earthquake Catalogue is being updated and extended in several ways. First the historical events and the instrumentally recorded events were combined in one common catalogue data base. It had to be extended to meet the different requirements in the documentation of instrumentally recorded seismicity on

one side and seismicity inferred from historical sources on the other side, see Kaiser et al. (2014).

A pilot study was performed to test the reliability of source parameters of the historical events which in most cases were not inferred from primary sources like newspaper articles and entries in chronicles but from compilations in secondary literature. In the 8 investigated cases the results of the study of the primary sources are not consistent with the source parameters in the catalogue (Hammerl, 2015). Thus in the future the study of primary sources by historians will be enhanced. This might also result in the identification of fakes meaning that the reported events in the historical sources cannot be attributed to an earthquake.

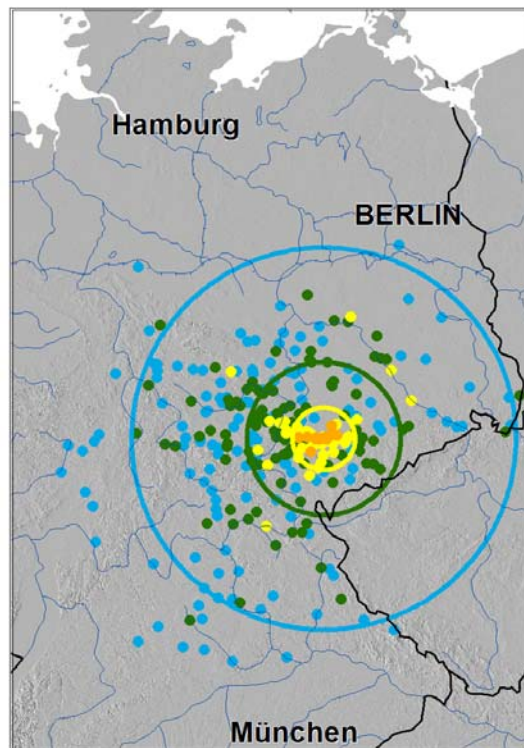


Fig. 2: Individual intensity data points for the event near the village of Posterstein in 1872. Blue points denote intensity IV, green points intensity V, yellow points intensity VI and orange points intensity VII. The displayed circles around the epicenter have the same areas as the isoseismal areas for IV to VI given in literature (Grünthal & Schwarz, 2001), VII not shown.

Furthermore the magnitudes of historical events will be determined in a systematic manner as up to now the catalogue only contains epicentral intensities for most historical earthquakes. Several strategies exist to succeed. One method was suggested by Johnston (1996) who inferred empirical relations of moment magnitude and the area of single isoseismals. An example is given in



Figure 2. It is the event near Posterstein in the Eastern part of Germany in 1872. Individual intensity data points are displayed and circles representing the areas of the obtained isoseismals by Grünthal & Schwarz (2001). A large scatter of the intensity data has to be stated and the method can deliver only imprecise values of  $M_w$ . Evaluation of the isoseismals IV to VII are in the range of 4.9 to 5.8 and  $M_w = 5.2$  is the average value. More reliable estimates of  $M_w$  can be obtained using well distributed intensity data points as input (Gomez-Capera et al., 2015). Therefore a comprehensive macroseismic catalogue will be compiled. The environmental seismic intensity scale will be applied when applicable (ESI 2007, see Michetti et al., 2007).

To increase the data base of historical events beyond the German borders the historical seismic catalogues of the neighboring countries are added successively, e.g., BRGM (2014) and Fäh et al. (2011).

#### PALEOSEISMIC EVIDENCE

Figure 3 shows a summary of the content of the paleoseismic data base "PalSeisDB" in relation to the seismotectonic zones (Hürtgen et al., 2015).

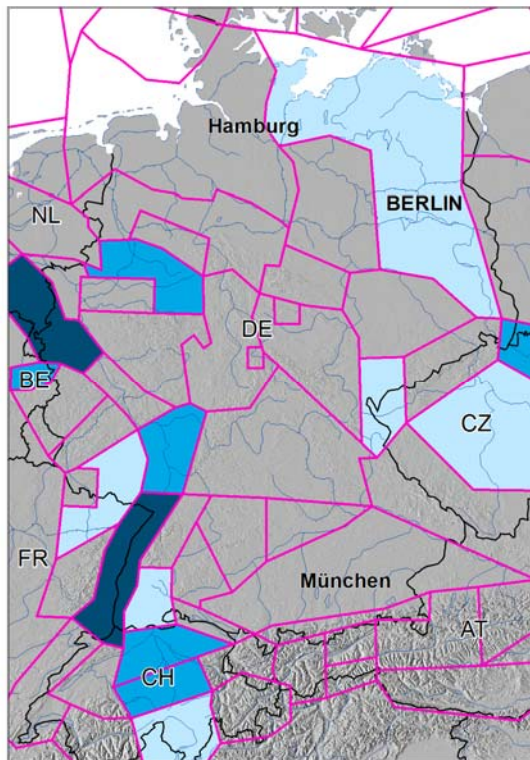


Fig.3: Dark areas denote a range of 4 to 17 entries in the paleoseismic data base, middle dark areas 2 – 4 entries, light areas one entry. Most of the zones do not contain any evidence, presumably for lack of investigation.

Although a lot of paleoseismic work has been performed in the last decades, paleoseismic evidence is sparse in Central Europe, both in terms of temporal and spatial distribution. The grey areas in Figure 3, where paleoseismic evidence is missing, should not be taken as a proof of absence of active tectonics, merely as sign of the lack of field investigations. Therefore, these areas have a potential as sites for future paleoseismic studies. Especially the Lower and Upper Rhine Graben are areas of great interest. Findings of seismically induced soft-sediment deformation features in the North German Basin also indicate a potential. Areas in southern Germany, the Swabian and Franconian Alb including the Franconian Lineament, are characterised by moderate seismic activity in historical and instrumental catalogues but the expected paleoseismic evidence has not been documented there, so far.

In the course of the current work field investigations in Northern Germany will be carried out first. Paleoseismic evidence has been found in exemplary cases (Brandes & Winsemann, 2013) but a systematic search has to be conducted. The focus will be on the identification of soft sediment deformation by seismic motion in the thick Quaternary sediments of the North German Basin.

#### DATA BASE OF ACTIVE FAULTS AND SEISMO-TECTONIC ZONE MODEL BASED ON NEOTECTONIC EVIDENCE

A comprehensive compilation of active faults in Central Europe is still missing, see Reicherter et al. (2008). In the SHARE catalogue of active faults in Europe mentioned above only few active faults of Central Europe are included (Giardini et al., 2013). Obviously all current neotectonic evidence has to be compiled on the basis of geological, active seismic, seismological, geomorphological and remote sensing studies to achieve such a data base. This work is currently prepared. The "Active Fault Map of Central Europe" and the database will be published in full detail and maintained in the future.

In regions of low and moderate seismicity it is usually not possible to attribute earthquake sources to fault structures. This is because the hypocenters are located in the crust, in Central Europe mostly well below 5 km depth, and it is not obvious how faults at the surface extend into the crust and because active faults are often buried beneath thick layers of weak sediments and/or faults might not be known. In seismic hazard assessment the spatial representation of the seismic sources in such regions is achieved by defining seismotectonic zones as areas or volumes of spatially homogeneous distribution of seismicity in terms of the frequency of events as a function of magnitude. Sometimes these zones are also used to consider seismic background activity of smaller magnitude events when faults can be directly represented in the assessment using their locations and their slip rates.



## INQUA Focus Group on Paleoseismology and Active Tectonics



paleoseismicity.org

The derivation of the seismotectonic zones was often based on the geographical distribution of seismicity (e.g. Leydecker & Aichele, 1998), as well as additionally using the fault patterns at the surface determined by remote sensing analysis (Burckhard & Grünthal, 2009). Currently a new approach is developed also taking into account the deep crustal structures determined by active seismic measurements and the geological and tectonic development of the crust in the past, e.g., see Malz et al. (2014) and Malz et al. (2015).

### DISCUSSION AND OUTLOOK

The current work comprises the compilation of historical seismicity, paleoseismic and neotectonic evidence to characterize the temporal and spatial distribution of seismicity in Central Europe which then can be used for reliable seismic hazard assessment. The comprehensive data base consists of the German Earthquake Catalogue including historical and instrumentally recorded seismicity, the paleoseismic database "PalSeisDB", the "Active Fault Map of Central Europe" and a new model of seismotectonic zones. Missing information is identified as well as the necessity of re-evaluation of data or sources. The acquisition of missing data, especially paleoseismic investigations, was started but obviously will need a lot of effort. The first new paleoseismic investigations are performed in the North German Basin. Also the evaluation of the primary historical sources which leads to reliable source parameters of historical seismicity needs a lot of effort from historians and seismologists.

### References

- Brandes, C., Winsemann, J. (2013). Soft-sediment deformation structures in NW Germany caused by Late Pleistocene seismicity. *International Journal of Earth Sciences*, 102, 2255-2274. doi:10.1007/s00531-013-0914-4.
- BRGM (2014). SISFRANCE Sismicité de la France Métropole. Bureau de Recherches Géologiques et Minières (BRGM), Electricité de France (EDF), Institut de Radioprotection et de Sûreté Nucléaire (IRSN). <http://www.sisfrance.net>, Date de dernière mise à jour: 01/01/2014.
- Burckhard, M., Grünthal, G. (2009). Seismic source zone characterization for the seismic hazard assessment project PEGASOS by the Expert Group 2 (EG1b). *Swiss Journal of Geosciences*, 102, 149-188. doi:10.1007/s00015-009-1307-3.
- CEUS-SSC (2012). Central and Eastern United States Seismic Source Characterization for Nuclear Facilities <http://www.ceus-ssc.com/>.
- Fäh, D. et al. (2011). ECOS-09 Earthquake Catalogue of Switzerland Release 2011 Report and Database. Public catalogue, 17. 4. 2011. Swiss Seismological Service ETH Zurich, Report SED/RISK/R/001/20110417.
- Giardini, D. et al. (2013). Seismic Hazard Harmonization in Europe (SHARE): Online Data Resource, doi: 10.12686/SED-00000001-SHARE.
- Gomez-Capera, A. A., Rovida, A., Gasperini, P., Stucchi, M., Viganò, D. (2015). The determination of earthquake location and magnitude from macroseismic data in Europe, *Bull Earthquake Eng* (2015) 13:1249–1280, DOI 10.1007/s10518-014-9672-3.
- Grünthal, G., Schwarz, J. (2001). Reinterpretation der Parameter des Mitteldeutschen Bebens von 1872 und Ableitung von Erdbebenzenarien für die Region Ostthüringen. - Thesis, *Wissenschaftliche Zeitschrift der Bauhaus-Universität Weimar*, 47, 1/2, 32-48.
- Grützner, C., Fischer, P., Reicherter, K. (2016). Holocene surface ruptures of the Rurrand Fault, Germany—insights from palaeoseismology, remote sensing and shallow geophysics. *Geophysical Journal International*, 204, 1662-1677. doi:10.1093/gji/ggv558.
- Hammerl, C. (2015). Vorstudie zur Neubewertung wichtiger historischer Erdbeben in Deutschland - Endbericht. In commission of the Federal Institute for Geosciences and Natural Resources (BGR), No. 212-4500093585, Vienna.
- Hürtgen, J., Spies, T., Schlittenhardt, J & Reicherter, K. (2015). PalSeisDB v1.0 - Paleoseismic Database of Germany and Adjacent Regions. In: Blumetti, A.M. et al. (eds), *Proceedings 6th International INQUA Meeting on Paleoseismology, Active Tectonics and Archeoseismology*. 19-24 April 2015, Pescina, Fucino Basin, Italy.
- Johnston, A. C. (1996). Seismic moment assessment of earthquakes in stable continental regions, *Geophys. J. Int.*, 125, 639-678.
- Kaiser, D., Bürk, D., Hartmann, G., Stelling, U. & Schlote, H. (2014). Integration of catalogues of historical and instrumentally recorded earthquakes in Germany in a common database – Concepts, uses, and products. Second European Conference on Earthquake Engineering and Seismology (2ECEES), Istanbul, [http://www.eaee.org/Media/Default/2ECEES/2ecces\\_esc/3202.pdf](http://www.eaee.org/Media/Default/2ECEES/2ecces_esc/3202.pdf).
- KTA (2011). Kerntechnischer Ausschuss 2201.1. Auslegung von Kernkraftwerken gegen seismische Einwirkungen Teil 1: Grundsätze. Fassung 2011-11.
- Leydecker, G. (1986). Erdbebenkatalog für die Bundesrepublik Deutschland mit Randgebieten für die Jahre 1000 - 1981. *Geologisches Jahrbuch*, E 36, 3-38.
- Leydecker, G. (2011). Erdbebenkatalog für Deutschland mit Randgebieten für die Jahre 800 bis 2008. *Geologisches Jahrbuch*. Reihe E, Heft 59, Hannover.
- Leydecker, G., Aichele, H. (1998). The seismogeographical regionalisation for Germany: the prime example of third-level regionalisation. *Geol. Jahrbuch*, E 55, 85-98.
- Malz, A., Kley, J., Jähne-Klingberg, F. (2014). Is past deformation of continental interiors a key to understanding modern intraplate seismicity? Poster T13B-4648, AGU Fall Meeting 2014, San Francisco.
- Malz, A., Madritsch, H., Kley, J. (2015). Improving 2D-seismic interpretation in challenging settings by integration of restoration techniques: a case study from the Jura fold-and-thrust belt (Switzerland). *Interpretation* 3(4), SAA37-SAA58. doi: 10.1190/INT-2015-0012.1.
- Michetti et al. (2007). Intensity Scale ESI 2007, in Mem. Descr. Carta Geologica d'Italia L. Guerrieri and E. Vittori (Editors), Servizio Geologico d'Italia, Rome, Italy, 74.
- Reicherter, K., Froitzheim, N., Jarosiński, M., Badura, J., Franzke, H.J., Hansen, M., Hübscher, C., Müller, R., Poprowa, P., Reinecker, J., Stackebrandt, W., Voigt, T., Eynatten, von, H., Zuchiewicz, W. (2008). Alpine tectonics II - Central Europe north of the Alps, in: *Geology of Central Europe* (McCann, T, ed.). Geological Society of London.
- Renault, P. (2014). Approach and challenges for the seismic hazard assessment of nuclear power plants: the Swiss experience. *Bollettino di Geofisica Teorica ed Applicata*, 55, 149-164. doi:10.4430/bgta0089.
- Vanneste, K., Camelbeeck, T., Verbeeck, K. (2013). A Model of Composite Seismic Sources for the Lower Rhine Graben, Northwest Europe. *Bulletin of the Seismological Society of America*. 103, 984–1007.



## Valley evolution of the Biala Łądecka drainage network during late Cenozoic, Lower Silesia, Poland

Stemberk, Jakub (1,2), Štěpančíková, Petra (2), Tábořík, Petr (1,2)

- (1) Department of Physical Geography and Geoecology, Charles University in Prague, Albertov 6, Prague 2, 128 43, Czech republic. Email: kuba.stemberk@gmail.com
- (2) Institute of Rock Structure and Mechanics, Academy of Sciences of the Czech Republic, Dpt. Engineering Geology, V Holešovičkách 41, Prague 8, 182 09, Czech Republic.
- (3) Institute of Hydrogeology, Engineering Geology and Applied Geophysics, Charles University in Prague, Albertov 6, Prague 2, 128 43, Czech republic.

**Abstract:** Biala Łądecka (Biala Kłodzka) river is located in Lower Silesia (Poland) and its valley separates Góry Złote Mts. (Rychlebské hory Mts.) on the northeast from Góry Bialskie Mts. on the southwest. We investigated geomorphology research of the Biala Łądecka river basin, in order to determine if Quaternary tectonic activity at the Sudetic Marginal Fault is contributing to the river's asymmetry. Previous research provided in adjacent area by L. Finckh and G. Göttinger (1931), W. Walczak (1954) and A. Ivan (1966), Biala Łądecka river used to flow across the Góry Złote Mts. directly to Oderská nížina Lowland during Pliocene; currently it flows to Nysa Kłodzka Basin. Our research was focused on analysis of all available cartographic materials (geological and topographic maps), available literature and own detail geomorphological mapping of selected landforms. Spatial distribution of these landforms such as gullies, erosion trenches, dellens, alluvial plains, alluvial fans, springs, swamps, river terraces, could potentially indicate recent tectonic activity in the studied area. Moreover, stream network parameters (measured using DEM data) such as changes in erosion intensity indicated in longitudinal and cross-section profiles, slope gradient and morphometric indexes, e.g. Stream Length (SL) index (Hack 1973), for Biala Łądecka river basin were analyzed. In selected places geophysical measures were used was also performed to discover locations of sediments of the Biala Łądecka paleoriver.

**Key words:** Biala Łądecka river, active tectonics, Góry Złote Mts. / Rychlebské hory Mts., Bělský fault, morphometric indexes, DEM analysis.

### Introduction:

The upper part of Biala Łądecka drainage and adjacent study area is located partly in Czech Republic, mainly in Poland (Fig. 1) and belongs to Bohemian Massif as a part of Epihercynian platform. It belongs to eastern part of the Sudety mountain system, specifically Rychlebské hory Mts. on the Czech side, Góry Złote and Góry Bialskie on the Polish side. It is represented by tectonically uplifted blocks with well-preserved NNE-SSW trending Variscan structure (the Staré Město unit and Śnieżnik unit) built almost exclusively of Precambrian metamorphic rocks and later granitoids (Kasza 1964, Don 2003). During the Pliocene and Pleistocene faults striking NW-SE to NNW-SSE were reactivated (Grygar and Jelínek, 2003) and movements on these



Fig. 2: Topographic map of the Rychlebské hory Mts. (Góry Złote Mts.) with marking the Bělský fault zone and the Sudetic Marginal Fault. BLV – Biala Łądecka valley, red line delineate the study area.

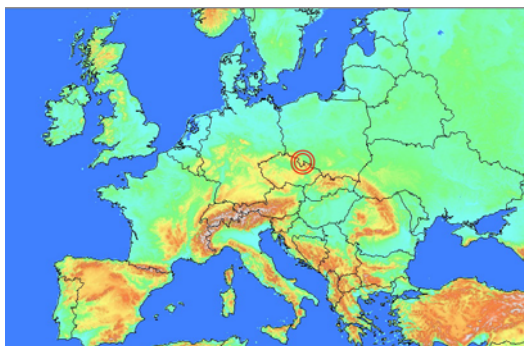


Fig. 1: Location.

faults influenced today's morphology of mountains. However the Bohemian Massif is considered as a tectonically inactive area, monitoring of micro-displacements directly on fault planes (eg. gauge TM-71 in Na Pomezí cave (Stemberk and Štěpančíková 2003) or GPS measurements have discovered recent tectonic activity in this part of the Bohemian Massif, (see eg. Cacoń and Dyjor, 1995, Schenk et al. 2003; Kontny 2004, Cacoń et al. 2005).



The main structure in study area is the 100km long Bělský fault (BF), in Poland called Bielawka fault or Trzebieszowice-Biala fault. It belongs to Elbe Fault System which is the zone of predominantly parallel NW-SE striking faults (eg. Sudetic Marginal Fault, Klepáčovský fault) traceable from the SE North Sea to the front of the Carpathian outer flysh nappes (Schenk et al. 2002). The zone has been active at least since Late Cretaceous time and underwent various types of movements during its evolution (Danišík et al. 2012). BF continues to SE through in Hrubý Jeseník Mts. and Nízký Jeseník Highland as a step-over fault of the Sudetic Marginal Fault and forms a 8 km wide fault zone with CO<sub>2</sub> mineral springs (eg. in Karlova Studánka, Dolní Moravice, etc.) (Hynie 1963). To the SE also Neogene and Quaternary volcanics (eg. Uhlířský vrch hill, Venušina sopka volcano) are placed in the zone (Buday et al., 1995). Historical (Guterch and Lewandowska-Marciniak 2002) and present seismicity has been documented in this area (eg. Špaček et al. 2006, Zedník et al. 2001). To the NW from the study area the BF location is uncertain, near Łądek Zdroj 3.83 – 5.46 Ma old volcano and 2 lava flows (Birkemajer 2002) may relate to the presence of the faults belong to BF zone.

The aim of this contribution is to show the likely possible young reconfiguration of upper part of Biala Łądecka drainage network caused by BF during the Cenozoic based on geomorphological evidences. Drainage network parameters may contain useful information about present and past tectonic movements (see eg. Burbank and Anderson 2001, Keller and Pinter 2002, etc.). The spatial distribution of selected landforms (eg. gullies, springs, swamps, linear shapes of relief, youngest erosion in drainage, etc.) based on detail geomorphological mapping was analyzed (see Fig. 3) and geophysical research was performed (see Fig. 4).

### Analysis and Discussion:

The analysis of drainage network of upper part of Biala Łądecka river basin discovered extreme asymmetry of the basin (asymmetry factor  $A_F = 31.5\%$ ) as visible on Fig. 3. It indicates the influence of tectonic movements on faults in this area during Cenozoic. Recent works about the Sudetic Marginal Fault, Rychlebské hory Mts. (Góry Złote Mts.) describe that the region have undergone 4-5 stages of uplift since Miocene (Badura et al. 2007), and also horizontal movements are determined on Sudetic Marginal Fault (Štěpančíková 2010, 2016, in prepare). In the BF zone sinistral sense of movement on main faults was suggested (same as on the Sudetic Marginal Fault) base on the valley offset of the Biala Łądecka river and Stříbrný potok brook. (see Fig. 3) Nowadays displacement of the Biala Łądecka river valley is nearly 2km since upper Pliocene when the valleys have started to downcutting (Ivan 1966). The offset of valley of the Stříbrný potok brook in BF zone is nearly 1.2 km. The rectangular bands in valley

direction occur mainly due to presence of lithostratigraphic boundaries and also due to probably horizontal tectonic movements.

Unfortunately nowadays valleys are free of any sediment suitable to date, even in many cases streams are flowing directly on bedrock. Holocene and Saal 1 river terraces of Biala Łądecka river are preserved in lower part of the valley.

Longitudinal profiles and SL indexes (Hack 1973) were constructed and calculated for all streams longer than 1 km based on 1m - LIDAR data (see Fig. 5 and Fig. 6). The SL indexes (Hack, 1973) were calculated for 100m long segments each 50 m of the stream following the formula  $SL = (\Delta H / \Delta L) L$ , where  $\Delta H / \Delta L$  is gradient of 100m long segment and L is the distance of midpoint from the stream beginning. The advantage of the SL index is to compare changes in channel slope of streams in different order. Afterwards it is possible to evaluate the relationships among tectonic activity, rock resistance and topography (Keller and Pinter 2002). Longitudinal profiles of streams are highly unbalanced due to presence of lithostratigraphic boundaries and also presence and movements of verified or suggested faults. Moreover these faults were based on SL indexes marked as active. The example of longitudinal profile of Bielawka river and its tributaries in combination with SL index position show plots on Fig. 5 and Fig. 6.

Morpholineaments represent the linear elements of the relief, such as linear sections of valleys, linear spatial distribution of selected landforms or linear structures directly visible from DEM. They can be associated with tectonic dislocations or lithostratigraphic boundaries (see eg. Badura et al. 2003, Štěpančíková 2005). Based on analyse of morpholineaments and linear arrangement of selected geomorphological landforms new traces of suggested faults were delineated, some of them were based on SL indexes marked as active (see Fig. 3).

ERT transect on the saddle between Biala Łądecka river basin and Stříbrný p. brook was surveyed to determine presence or absence of old river sediment. We did 5 ERT profiles with different electrode spacing (1m – 5m) and 3 DEMP profiles. No sediment presence was observed on this saddle indicating no river piracy between these rivers. Other ERT profile was surveyed to indicate the presence of the BF in this area. It appears as a 100m width zone dipping 60° to SSW, covered by a 2-5m thick weathered slope sediments. (see Fig. 4).

### Conclusion:

Despite the lack of datable or comparable sediments in valleys, no paleoseismic trenching and apparent low slip rates shows that combination of detailed geomorphological mapping, geophysical research and different kinds of DEM analyses are useful to determine valley evolution. These preliminary investigative techniques suggest the Bělský fault may have been active in the Quaternary. Additional research will build off of this work.



Fig. 3: A geomorphological map.

**Future work:**

The large alluvial fan is placed near Złoty Stok in mountain front (eg. Walczak 1954). Its evolution may relate with movements on the Sudetic Marginal Fault. We plan geophysical study in this area to discover stratigraphic position of this alluvial fan and also its spatial extent.

**Acknowledgements:**

This work was supported by the Grant Agency of Charles University in Prague (GAUK862213 - Multidisciplinary geophysical survey in investigation of landforms) and by Grant of Ministry of Education, Youth and Sports of the Czech Republic (LH12078 - Assessment of Tectonic Movements on Active Faults, Program KONTAKT II.).

**References:**

Badura, J., Zuchiewicz, W., Górecki, A., Sroka, W., Przybylski, B., Żyszkowska, M. (2003): Morphotectonic properties of the Sudetic Marginal Fault, SW Poland. *Acta Montana, Serie A* 24 (131), p21–49.

Badura, J., Zuchiewicz, W., Štěpančíková, P., Przybylski, B., Kontny, B., Cacoň, S. (2007): The Sudetic Marginal Fault: A Young Morphotectonic Feature at the NE Margin of the Bohemian Massif, Central Europe. *Acta Geodyn. Geomater.*, 4, p. 1-23.

Birkenmajer, K., Pécskay, Z., Grabowski, J., Lorenc, M.W., Zagożdżon, P.P. (2002): Radiometric dating of the Tertiary volcanics in Lower Silesia, Poland. II. K–Ar and palaeomagnetic data from Neogene basanites near Łądek Zdrój, Sudetes Mts. *Annales Societatis Geologorum Poloniae* 72, p119–129.

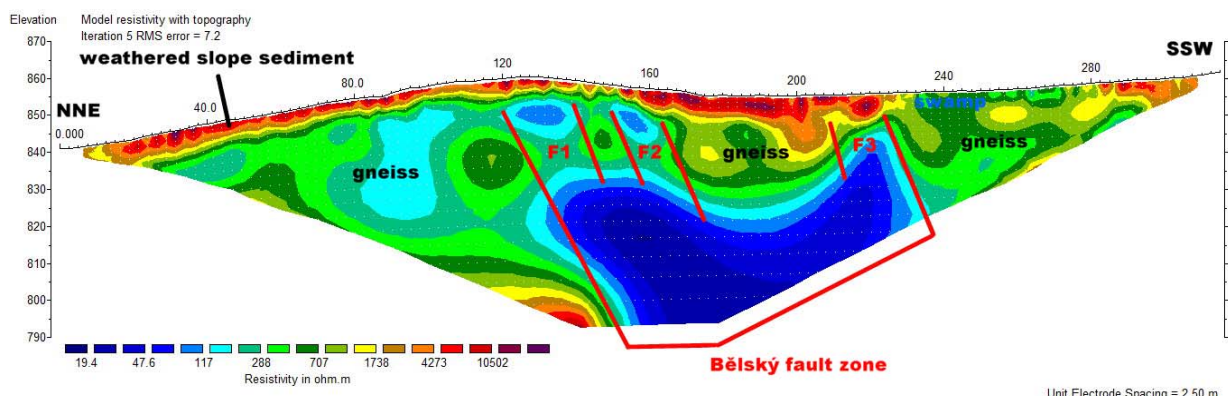


Fig. 4: Electrical Resistivity tomography (ERT) profile across the Bělský fault zone near nameless peak 928m.

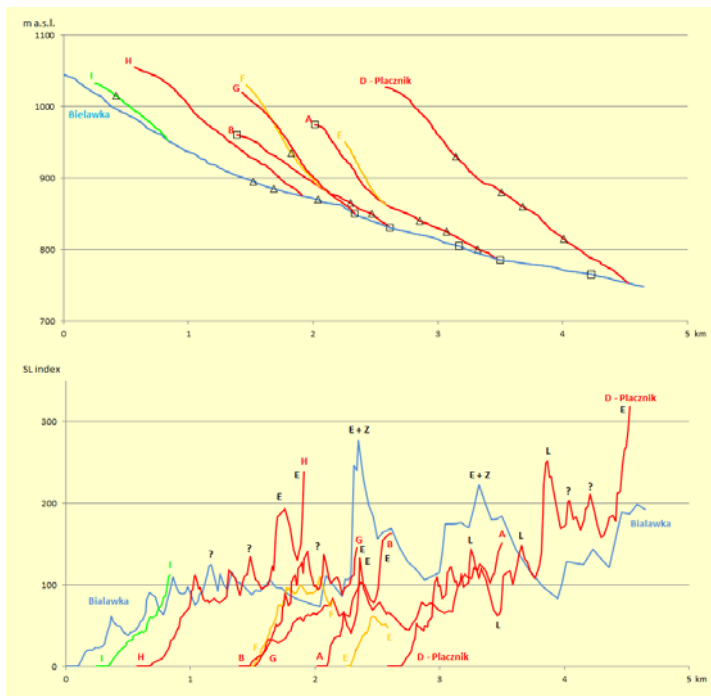


Fig. 5 Upper plot: Longitudinal profile of Bielawka brook with all tributaries, triangles identify places where brooks cross the faults; boxes identify places where brooks are following fault.

Fig. 6 Lower plot: SL index, reason of peaks: E – erosion, Z – fault, L – lithostratigraphic boundaries; ? – unknown reason.

Grygar R. and Jelínek J. (2003): The Upper Morava and Nysa pull apart grabens the evidence of neotectonic dextral transtension on the Sudetic Fault System. Acta Montana IRSM AS CR, ser. A, 24, p51 - 59.

Guterch B. and Lewandowska-Marciniak H. (2002): Seismicity and seismic hazard in Poland. Folia Quat., 73, p85-99.

Hack, J.T., 1973. Stream-profile analysis and stream-gradient index. Journal of Research of the U.S. Geological Survey, 1 (4), p421-429.

Hynie O. (1963): Hydrogeologie ČSSR II, Minerální vody. — Nakladatelství Československé akademie věd. Praha.

Ivan, A. (1966): Geomorfologické poměry severozápadní části Rychlebských hor. Theses, GÚ ČSAV, Brno, 120 p.

Kasza, L., (1964): Budowa geologiczna górnego dorzecza Białej Łądeckiej. Geologia Sudetica, Vol. 1, Krakow.

Keller, E.A., Pinter, N., (2002): Active tectonics—Earthquakes, Uplift and Landscape. Prentice Hall, New Jersey.

Kontny, B., 2004. Is the Sudetic Marginal Fault still active? Results of the GPS monitoring 1996–2002. Acta Geodynamica et Geomaterialia 1, 3 (135), p35-39.

Schenk, V., Schenková, Z., Cacoň, S., Kontny, B., Bosy, J., Kottnauer, P. (2003): To geodynamic interpretations of

Buday, T., Ďurica, D., Opletal, M., Šebesta, J. (1995): Význam bělského a klepáčovského zlomového systému a jeho pokračování do Karpat. Uhlí, rudy, geologický průzkum 2 (9), 275–282.

Burbank, D.W., Anderson, R.S., 2001. Tectonic Geomorphology. Blackwell Science, Oxford.

Cacoň, S., Dyjor, S., 1995. Neotectonic and recent crustal movements as potential hazard to water dams in Lower Silesia, SW Poland. Folia Quaternaria 66, p59–72.

Cacoň, S., Vyskočil, P., Talich, M., Kontny, B., Bosy, J., 2005. Deformation analysis of the

Polish Sudetes and Fore-Sudetic block. Reports on Geodesy 2 (73), p211–219.

Danišík, M., Štěpančíková P. and Evans N. (2012): Constraining long-term denudation and faulting history in intraplate regions by multi-system thermochronology - an example of the Sudetic Marginal Fault (Bohemian Massif, Central Europe), Tectonics 31, Tc2003, 19pp.

Don, J., Skácel, J., Gotowala, R. (2003): The boundary zone of the East and West Sudetes on the 1:50 000 scale geological map of the Velké Vrbno, Staré Místo and Šnieżnik Metamorphic Units. Geologia Sudetica, 2003, 35, p25–59.

Finckh, L. and Göttinger, G. (1931): Erläuterung zur geologischen Karten des Richenstein Gebirges, des Nesselkoppenkammes und des Neisse-Vorlandes, Wien, 108p.

GPS data monitored on the EAST SUDETEN network. Acta Montana, Serie A, No.24 (131), p87–97.

Stemberk J., Štěpančíková P. (2003): Tectonic setting and newly organised monitoring of recent deformation in the Rychlebské Hory Mts. Acta Montana, 24 (131), p153 – 161.

Špaček, P., Sýkorová, Z., Pazdírková, J., Švancara, J., Havíř, J. (2006): Present-day seismicity of the south-eastern Elbe Fault system (NE Bohemian Massif). Studia Geophysica Et Geodaetica 50, p233–258.

Štěpančíková, P. (2005): Selected analysis of the morphostructure of the NE part of the Rychlebské hory Mts. (Czech republic). Acta Geodyn. Geomater., 2, p59-67.

Štěpančíková, P., Hók, J., Nývlt, D., Dohnal, J., Sýkorová, I., Stemberk, J. (2010): Active tectonics research using trenching technique on the south-eastern section of the Sudetic Marginal Fault (NE Bohemian Massif, central, Europe). Tectonophysics, 485, p269–282.

Walczak, W. (1954): Pradolina Nysy i plejstocénski zmiany hydrograficzne na przedpolu Sudetów wschodnich. Polska Akademia Nauk, Instytut geografii, Warszawa.

Zedník, J., Pospíšil, J., Růžek, B., Horálek, J., Boušková, A., Jedlička, P. (2001): Earthquakes in the Czech Republic and surrounding regions in 1995-1999. Stud. Geophys. et Geod., 45, p267-282.



## Applicability of complex geophysical surveying in paleoseismic studies: three case studies from the Bohemian Massif

Štěpančíková Petra (1), Petr Tábořík (1, 2), Filip Hartvich (1), Jakub Stemberk (1, 2), Tomáš Fischer (2), Magda Karousová (2), Jan Vilhelm (2), Jakub Šíroky (2), Petr Špaček (3), Vratislav Blecha (2), Josef Pek (4), Thomas Rockwell (5), Michal Havaš (6)

(1) Institute of Rock Structure and Mechanics, Czech Academy of Sciences, V Holešovičkách 41, 18209, Prague 8, Czech Republic, Email:

[stepancikova@irmsm.cas.cz](mailto:stepancikova@irmsm.cas.cz)

(2) Faculty of Science, Charles University, in Prague, Albertov 6, Prague 2, 12843, Czech Republic

(3) Institute of Physics of the Earth, Faculty of Science, Masaryk University Brno, Tvrděho 12, 602 00 Brno, Czech Republic

(4) Geophysical Institute, Czech Academy of Sciences, Boční II/1401, 141 31 Prague 4, Czech Republic

(5) Dpt. of Geological Sciences, San Diego State University, 5500 Campanile Drive, San Diego, CA 92182-1020, California

(6) Faculty of Science, University of Ostrava, Chittussiho 10, 710 00 Slezská Ostrava, Czech Republic

**Abstract:** We present three case studies of paleoseismic surveys in the Bohemian Massif (Czech Republic) which were carried out in various geological environments. An extensive 2-D and 3-D geophysical survey preceded and accompanied the trenching. The trenching sites are situated on the faults reactivated in the Quaternary; in north-eastern Bohemian Massif on the Sudetic Marginal fault, at the contact of Bohemian Massif and the Carpathian Foredeep in the east (Holešov fault), and in the western Bohemian Massif on the Mariánské-Lázně fault in the Cheb basin. Combining paleoseismic trenching with geophysical surveys enabled verification and correlation of the results of geophysics with the lithology exposed in the trenches. The methods included geoelectrical surveying, electromagnetic surveying, shallow seismics and gravimetry. They enabled to trace the faults laterally and to the depth, to map the sediments offset by the faults. The studies from various geological environments show that the applicability of a specific geophysical method varies depending on the site conditions.

**Key words:** geophysical survey, paleoseismology, Sudetic Marginal Fault, Upper Morava basin, Mariánské-Lázně Fault, Bohemian Massif

During the last decade, several faults in the Bohemian Massif that were re-activated during Quaternary have been studied. We present three case studies from various geological environments where extensive 2-D and 3-D geophysical surveys preceded and accompanied paleoseismic trenching in order to trace the fault with no surface geological expression, to study the subsurface expression of the fault and extrapolate the geological information from trenches to the depth and laterally, to limit studied sedimentary bodies offset by the faults, etc.

The geophysical methods included (i) direct current (DC) geoelectrical surveying, i.e. electric resistivity tomography (ERT) and micro-scale resistivity profiling (mRP); (ii) electromagnetic (EM) surveying, i.e. ground penetrating radar (GPR) and dipole electromagnetic profiling (DEMP), and magnetotellurics (AMT); (iii) shallow seismic refraction (SSR) and seismic tomography (ST); and (iv) gravimetric survey (GS). Due to the trenching surveys that were conducted at the same sites, the results of geophysical measurements could be correlated with the lithology exposed in the trenches and the methods could be calibrated.

The first trenching site is **Bílá Voda**, situated in the north-eastern part of the Bohemian Massif where the

morphologically pronounced NW-trending Sudetic Marginal fault (SMF) controls the mountain front of the Sudeten mountains for ~140 km (Fig. 1).

The trenches exposed Paleozoic schist juxtaposed against Quaternary alluvium overlying the Miocene clayey sands, with the alluvium folded down into the fault zone. Classic features indicative of significant motion included rotation of clasts into the fault and the complete mismatch of units across the fault (Štěpančíková et al. 2011, 2013). Extensive trenching survey (18 trenches) enabled to identify beheaded alluvial fan, which is left-laterally offset from its supposed source valley at the best estimate of about  $37 \pm 8$  m.

A complex geophysical survey at Bílá Voda site was performed as follows: (i) pre-trenching geophysical searching for the exact fault location; (ii) detailed geophysical investigation alongside the trenching phase (to trace particular structures in the trenches vicinity), and (iii) extensive 3-D surveying of the wider area in order to distinguish high-conductive Miocene clayey sediments and the offset alluvial fan with low electrical conductivity. We used the following geophysical techniques: electrical resistivity tomography (ERT), audio-frequency magnetotellurics (AMT), shallow



seismic refraction/seismic tomography (SSR/SST), and ground penetrating radar (GPR). SSR and AMT methods were used to identify the SMF location at the field. For the exact position and course of the fault, detailed ERT measurements were employed.

north-western segment, and the allochthonous flysch of the Outer Western Carpathians and the underlying Karpatian sediments (Lower Miocene) of the Carpathian Foredeep in the south-eastern segment, by a minimum of 700- to 800-m vertical slip (Špaček et al. 2015).



Fig. 1. Location of the studied sites on digital elevation model (SRTM) of the Czech Republic. Red line – fault; SMF – Sudetic Marginal fault; HF – Holešov fault; MLF – Mariánské-Lázně fault; black rectangle – studied sites 1 – Bílá Voda, 2 – Brodek, 3 – Kopanina

Due to distinct lithologies and related different physical rock properties on the both sides of the fault, a strong horizontal gradient in electric resistivity clearly showed the fault position and allowed us to identify more resistive crystalline bedrock juxtaposed against conductive Miocene clayey sands covered by a veneer of the alluvial fan deposits. Also shallow seismics with the geophone interval 1 m showed the fault position however rather in the higher depth (8 m) due to similar velocities in the superficial part of the geological profile in the Quaternary sediments on the hanging wall and in the weathered bedrock in the footwall. ERT also revealed the limit of the alluvial fan deposits and their thickness, which helped in the interpretation of paleoseismic survey such as sense of the movements. The results of the GPR measurements were only poorly interpretable, namely due to strong signal attenuation in the fine-grain sediments. Nevertheless, they partly confirmed the extent of the alluvial fan sediments.

The second site **Brodek** is situated in the Upper Morava basin, a Late Cenozoic tectonically active region located at the contact of Bohemian Massif and the Western Carpathians' orogenic front in central Europe (Fig. 1). The site lies on the NW-trending Holešov fault, which controls the south-eastern basin margin. It offsets the Lower Badenian marine sediments (Middle Miocene) and the Plio-Quaternary fluviolacustrine sediments at its

Two trenches at the site Brodek exposed Badenian sandy clays juxtaposed against Quaternary fluvial sediments of probably Late Elsterian (400–460 ka) 'Brodek terrace' cut by the fault. 2-D and 3-D geophysical measurements applied at the site (ERT, DEMP, GPR) clearly distinguished between two different sedimentary units and, thus, indicated the position of the studied fault. The GPR images allowed to distinguish the main lithological limits, although the high clay content made the interpretation rather difficult. That is why the distinction of the thin inclined strata was enabled only due to availability of the trench log. The integrated interpretation with ERT data allowed cross-correlation and identification of some half-pronounced surfaces, although quasi-homogeneous blocks of high resistivity do not correlate with high reflectivity areas, which is uncommon (Fig. 2). Moreover, it enabled the elimination of incorrect interpretation of GPR images.

The third site, **Kopanina**, is situated in the western Bohemian Massif, in the Cenozoic Cheb basin, which is controlled by the NW-trending Mariánské Lázně fault in the NE and which is a part of Cheb-Domažlice graben on its intersection with NE-trending Eger rift. The area represents one of the seismically most active zones in central Europe, the Nový Kostel zone famous for the earthquake swarms and CO<sub>2</sub> emanation. Our trenching survey exposed the limit of the Oligocene to Holocene basin infill and revealed repeated movements within the



Mariánské-Lázně fault zone which tend to be successively younger from the basin margin towards the basin. The youngest documented faulting offsets the

main zones: (i) fine-grain sediments of the Vildstein formation of the Cheb basin (lower resistivity values, low intensity reflections), (ii) a coarse heterogeneous

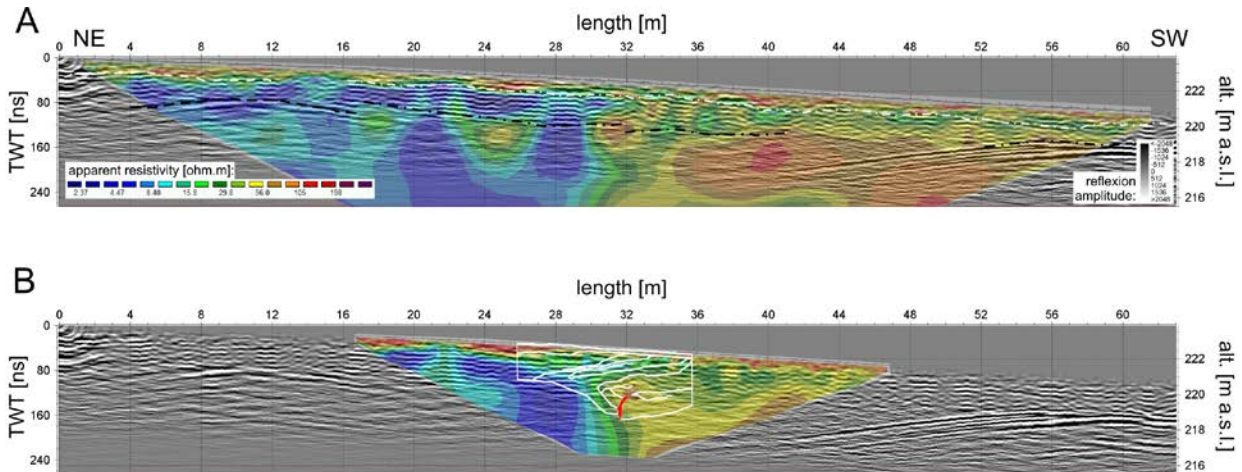


Fig. 2. Integrated interpretation of 100 MHz GPR (black-white scale) and ERT (color scale) sections and trench log (white full lines; red line – the fault). White and black dash-dot line - georadar interfaces. A – the ERT is with 1 m electrode spacing; B – the ERT is with 0.5 m electrode spacing)

radiometrically well dated Holocene colluvium (Fischer et al. 2012, Štěpančíková et al. 2015).

The paleoseismic trenching was combined with 2-D and 3-D geophysical surveys, which were performed at two different scales: (A) Shallow scale up to several tens of meters – the detailed survey was realised in order (i) to locate exact position of the MLF for trenching, as well as (ii) to extend information on fault properties (gained directly from the trench walls) laterally and to the depth, and (iii) to trace the faults as well as displaced sedimentary bodies. (B) The deep survey was focused on the subsurface manifestation of the MLF fault zone to the depth, naturally with smaller resolution.

Within the detailed survey, a combined geoelectrical survey was used. Electrical resistivity tomography (ERT), a direct current (DC) geoelectrical method, was used to depict 2-D vertical resistivity sections along the trench. Main geological structures as well as tectonic lines were identified in both trench walls and parallel ERT sections. A spatial distribution of the well-pronounced sedimentary body, cut (sheared) by fault, was determined on the basis of the 3-D electromagnetic (EM) survey employing two different EM methods: (i) high-frequency ground penetrating radar (GPR) with a shielded 250 MHz antenna, and (ii) dipole electromagnetic profiling (DEMP) measuring conductivity of the subsurface (conductometry). GPR measurements were performed in the dense grid of parallel profiles, finally interpreted as 3-D time (depth) slices. Similarly, the induction measurements of subsurface conductivity by means of DEMP were transferred to resistivity values and interpreted as depth resistivity slices. A combination and consequent integrated interpretations of the geoelectrical data sets allowed us to create a 3-D geoelectrical model with several zones of different resistivity values and different reflectivity of the EM signal. Our results confirmed three

sedimentary body with scattered concretions (higher resistivity values), and (iii) intensively argillaceous weathered crystalline rocks (mica-schists) (very low resistivity values, practically no reflections due to strong signal dispersion) (Fig. 3). Moreover, the spatial

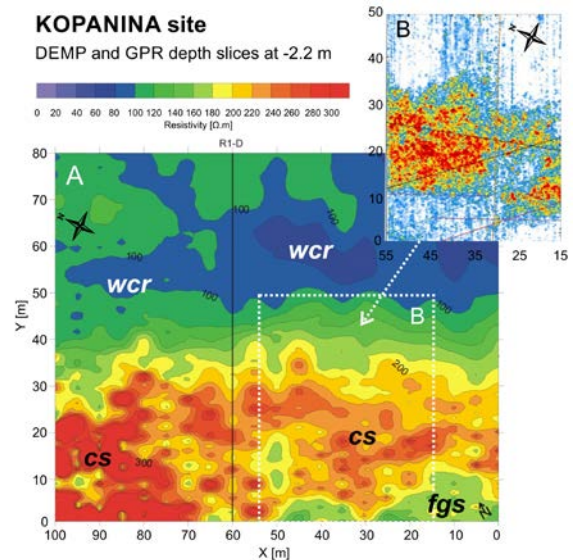


Fig. 3: 3-D geophysical survey at the Kopanina site – depth slices at ca. -2.2 m: (A) DEMP – areal apparent conductivity of the bedrock transferred to the apparent resistivity values; (B) inset of 3-D GPR depth slice. High reflectivity domains in radargram are corresponding to the high resistivity zones in DEMP pseudosection (depth slice). Lines in the GPR-slice indicating main fault structures were confirmed by trenching. Geological interpretation: **fgs** – fine-grained sediments of the Vildstein formation, **csb** – coarse heterogeneous sedimentary body with scattered concretions, **wcr** – intensively argillaceous weathered crystalline rocks.



## INQUA Focus Group on Paleoseismology and Active Tectonics



paleoseismicity.org

distribution of the coarse sedimentary body suggested right-lateral displacement along the fault line known from the trench most probably due to disruption of the sedimentary body by active faulting.

Deep geophysical surveying was performed to depict the MLF zone evidence to the depth. The geophysical complex consisted of the deep-range ERT sounding, seismic tomography and gravimetric survey. In contrast to detailed ERT measurements with high resolution using 1m electrode spacing, two very long profiles with length of 1 km and with 10 m electrode distance were measured in order to gain maximum possible depth of penetration. The deep ERT survey confirmed a steeply inclined low resistivity fault zone. The 2.5-dimensional modelling of microgravity data shows a steeply dipping density contrast between the basin infill and crystalline, which are separated by a wedge-like body with medium density. This agrees with a steep course of a rather wide fault zone indicated by low resistivity values and drop in velocity of seismic waves. This can be interpreted by deep and intensive disruption/weathering of the crystalline rocks along the fault.

The presented case studies showed the usefulness and applicability of an individual geophysical method depending on different geological conditions. Simultaneously, it showed how important is an integrated interpretation of different geophysical data sets, namely in terms of (i) cross-validation of the results of various geophysical techniques (even we often cannot compare methods directly due to its different physical parameters and/or measurement principles), (ii) reinterpretation and processing optimisation of the original geophysical models based on integrated interpretations, and finally (iii) improvement of final geological models.

Despite the certain difficulties, namely within data processing, which needs to be resolved, we would definitely recommend to use combined geophysical survey, especially an integrated interpretation of geophysical data sets, moreover together with trenching results.

**Acknowledgements:** The research was supported by Grant Agency of Czech Academy of Sciences, project No. IAA300120905 and Czech Science Foundation No.P210/12/0573, and No.16-10116J.

### References

- Fischer T., Štěpančíková P., Karousová M., Tábořík P., Flechsig C., Gaballah M. (2012). Imaging the Mariánské Lázně Fault (Czech Republic) by 3-D ground-penetrating radar and electric resistivity tomography. *Stud. Geophys. Geod.* 56: 1019-1036.
- Špaček P., Bábek O., Štěpančíková P., Švancara J., Pazdírková J., Sedláček J. (2015): The Nysa-Morava Zone: an active tectonic domain with Late Cenozoic sedimentary grabens in the

Western Carpathians' foreland (NE Bohemian Massif). *International Journal of Earth Sciences*: Volume 104, Issue 4 (2015), Page 963-990.

Štěpančíková P., Nývlt D., Hók J., Dohnal J. (2011): Paleoseismic study of the Sudetic Marginal Fault at the locality Bílá Voda (Bohemian Massif). In: *Earthquake geology and geoarchaeology: Science, Society and Critical facilities* (Grützner C., Pérez-López R., Fernández-Steege T., Papanikolaou I., Reicherter K., Silva P.G. and Vött A. eds). 2nd INQUA-IGCP-567 International Workshop, Corinth, (Greece). 239-242.

Štěpančíková P., Rockwell T., Hartvich F., Tábořík P., Stemberk J., Ortuño M., Wechsler N. (2013): Late Quaternary Activity of the Sudetic Marginal Fault in the Czech Republic: A signal of Ice Loading? In: *Seismic Hazard, Critical Facilities and Slow Active Faults* (C. Grutzner, A. Rudersdorf, R. Pérez-López, K. Reicherter, eds.) 4th International INQUA Meeting on Paleoseismology, Active tectonics and Archeoseismology, Aachen, Germany, 259-262.

Štěpančíková P., Tábořík P., Fischer, T., Hartvich, F., Karousová, M., Stemberk, J., Nováková, L. (2015): Holocene activity of the Mariánské Lázně Fault (Cheb basin, Bohemian Massif): youngest proved surface faulting in central Europe? In: Blumetti AM et al. (eds): Abstracts Volume 6th International INQUA Meeting on Paleoseismology, Active Tectonics and Archaeoseismology 19-24 April 2015, Pescina, Fucino Basin, Italy. *Miscellanea INGV*, n. 27, 478-480.



## Postglacial faults and paleolandslides in western Finnish Lapland

Sutinen, R.(1), Hyvönen, E.(1), Ruskeenieni, T. (2) and Middleton, M.(1)

- (1) Geological Survey of Finland, P.O. Box 77, 96101, Rovaniemi, FINLAND
- (2) Geological Survey of Finland, P.O. Box 96, 02151, Espoo, FINLAND

Northern Fennoscandia has experienced high-magnitude ( $M_w \approx 7-8.2$ ) late- or postglacial fault (PGF) activity attributable to lithospheric plate stresses and

glacio-isostatic rebound (Arvidsson, 1996, Olesen et al., 2004). The occurrence of PGFs includes bending of the crust that causes stress at the edge of the receding ice

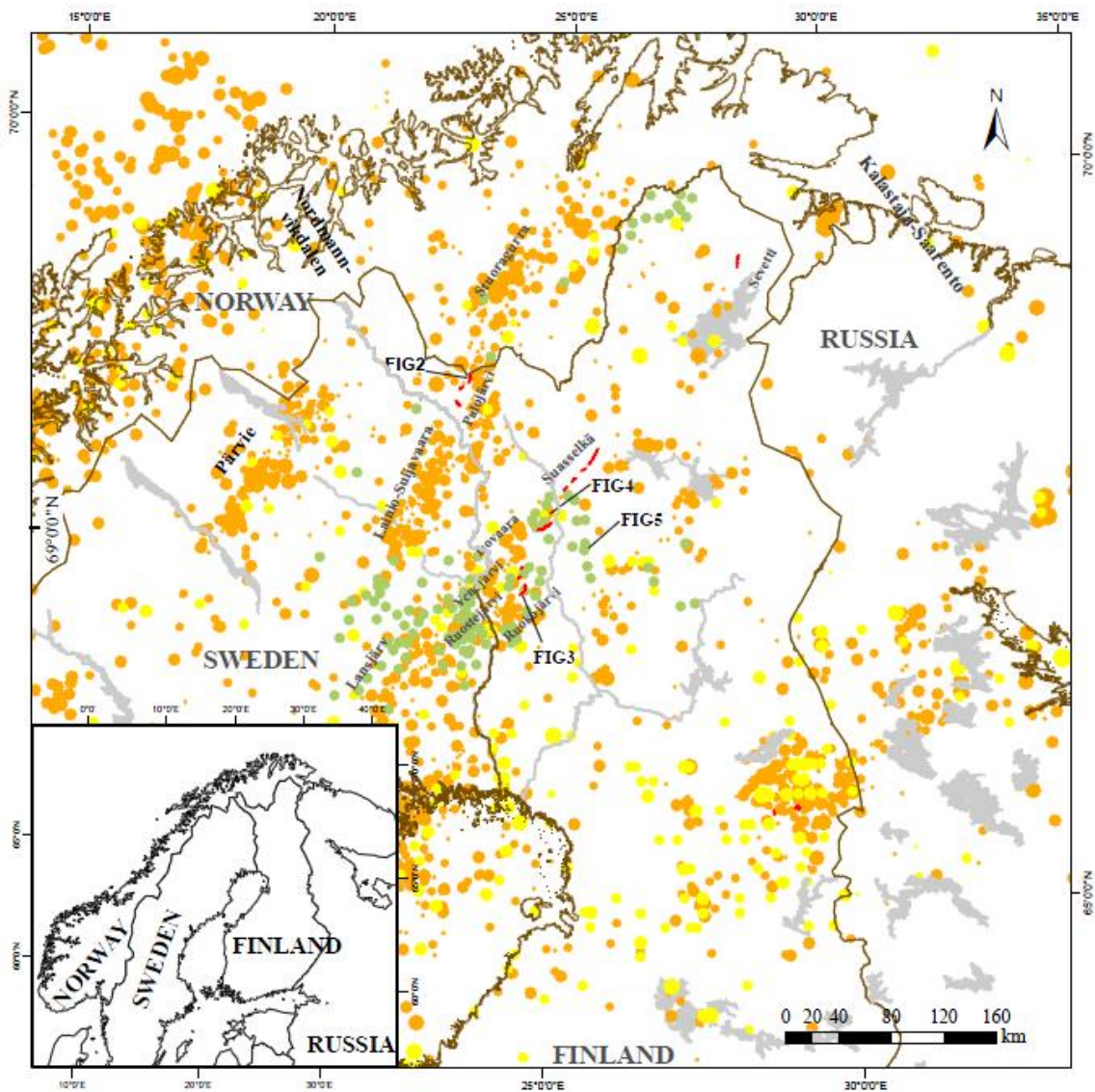


Fig. 1. Postglacial faults (red lines), paleolandslides (green dots) and recent seismic events (orange/yellow dots: [http://www.seismo.helsinki.fi/english/bulletins/catalog\\_northeurope.html](http://www.seismo.helsinki.fi/english/bulletins/catalog_northeurope.html)) in northern Fennoscandia (modified after Lagerbäck and Sundh, 2008; Kukkonen et al., 2010; Sutinen et al., 2014a; 2014b; Palmu et al., 2015).



sheets, hence the ice-marginal terrains were subjected to earthquakes (Stewart et al. 2000). The SW-NE trending geometry of the fault lines (Kuivamäki et al., 1998; Olesen et al., 2004; Lagerbäck and Sundh, 2008; Sutinen et al. 2014a; Fig. 1) suggests that primary forces would have been the lithospheric plate stresses, yet glacio-isostatic adjustment seems to have triggered/reactivated the old ruptures. In addition, instrumental data have indicated that a significant part of recent seismic activity spatially coincides with the old PGF lines in the Fennoscandian plate (Kukkonen et al., 2010; Fig. 1). The end-glacial or postglacial earthquakes have contributed to subaerial co-seismic deformations, such as landslides (Lagerbäck and Sundh, 2008; Sutinen et al., 2014b).

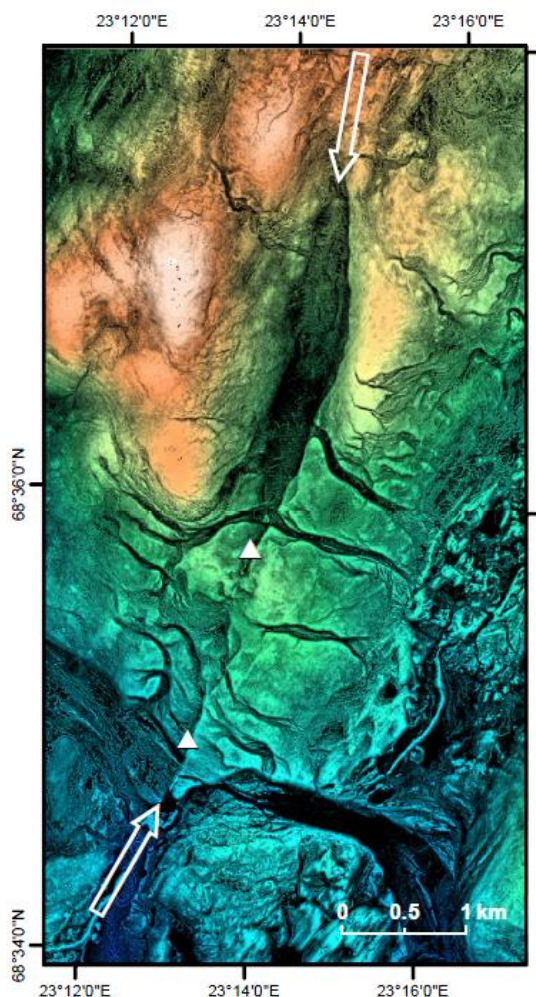


Fig. 2 (left). TDR (tilt derivative) enhanced LiDAR image of Palojärvi postglacial fault western Finnish Lapland (see location in Fig. 1). The vertical displacement is 4.3-6.8 m. The postglacial fault was verified by diamond drillings, the drilling sites are shown by triangles. Adopted from Sutinen et al. (2014a).

High-resolution LiDAR-based digital elevation models provide an efficient tool to detect PGF scarps and paleolandslides beneath forest canopies (Sutinen, et al., 2014a; 2014b; Palmu et al., 2015). The spatial distribution of these features tend to be coincidental hence suggesting that dating of landslide-buried organic materials will provide evidence on the frequency of the past earthquakes. To enhance faults and paleolandslides on the DEM we applied the tilt derivative (TDR) that is the arctangent of the ratio of a vertical to a combined horizontal derivative (see Sutinen et al., 2014 a). A TDR equalizes the amplitude of anomalies and thus emphasizes the structural/morphological features. All amplitudes are restricted to values between  $-90^\circ$  and  $90^\circ$  and the zero contours are located close to the source contact.

We percussion drilled through the paleolandslide accumulations to find buried organic materials and were able to reveal several samples for the C14 datings. In Kittilä, the buried organic sediments yielded 5050 yrs calBP (Fig 4). Other datings of the landslide buried sediments in western Finnish Lapland have yielded following ages: 1275, 1585, 5860, 10185 yrs calBP. In addition, basal peat samples yielded 9480 and 9510 yrs calBP from peat bogs developed on the foot wall of the Ruokojärvi postglacial fault, just next to the fault scarp in Kolari (Fig. 3). A good example of the young events is Tilkku paleoslide in Kittilä (Fig. 5; see location in Fig. 1), where the continuous borehole sample revealed gyttja beneath 2 m of landslide debris and yielded 1774 yr BP.

Our previous finding of landslide-buried woody remnants of birch yielded 9730 yrs calBP in Kittilä (Sutinen 2005). We therefore propose that earthquakes around 9500-10200 yrs calBP, 5000-5900 and 1200-1600 yrs calBP occurred in western Finnish Lapland. Historical earthquakes ( $M < 4$ ) are spatially coincidental with PGFs (Fig. 1), yet our results suggest that the recurrency interval of major earthquakes may be of the order of 4000 years within the Fennoscandian plate.

**Acknowledgements:** We appreciate field expertise by Ilkka Aro and Jukka Takalo as well as editorial help by Päivi Heikkilä at the Geological Survey of Finland, Rovaniemi.

## References

- Arvidsson, R. 1996. Fennoscandian earthquakes: whole crustal rupturing related to postglacial rebound. *Science* 274, 744-746.
- Kuivamäki, A., Vuorela, P., Paananen, M. 1998. Indications of postglacial and recent bedrock movements in Finland and Russian Karelia. Report YST-99, 92 p.
- Kukkonen, I., Olesen, O., Ask, M.V.S., PFDP Working Group. 2010. Postglacial faults in Fennoscandia: Targets for scientific drilling. *GFF* 132, 71-81.
- Lagerbäck, R., Sundh, M. 2008. Early Holocene faulting and paleoseismicity in northern Sweden. *Sveriges Geologiska Undersökning C836*, 80 pp.



- Olesen, O. Blikra, L.H. Braathen, A. Dehls, J.F. Olsen, L. Rise, L. Roberts, D. Riis, F. Faleide, J.I. Anda, E. 2004. Neotectonic deformation in Norway and its implications: a review. *Norwegian Journal of Geology* 84, 3-34.
- Palmu, J-P., Ojala, A.E.K., Ruskeeniemi, T., Sutinen, R., Mattila, J. 2015. LiDAR DEM detection of postglacial faults and earthquake induced landforms in Finland: a paleoseismic database. *GFF* 134:4, 344-352.
- Stewart, I.S. Sauber, J. and Rose, J. 2000: Glacio-seismotectonics: ice sheets, crustal deformation and seismicity. *Quaternary Science Reviews* 19, 1367-1389.
- Sutinen, R. 2005. Timing of early Holocene landslides in Kittilä, Finnish Lapland. *Geological Survey of Finland, Special Paper* 40, 53-58.
- Sutinen, R., Hyvönen, E., Middleton, M. and Ruskeeniemi, T. 2014a. Airborne LiDAR detection of postglacial

- faults and Pulju moraine in Palojärvi, Finnish Lapland. *Global and Planetary Change* 115, 24-32.
- Sutinen, R., Hyvönen, E. and Kukkonen, I. 2014b. LiDAR detection of paleolandslides in the vicinity of the Suasselkä postglacial fault, Finnish Lapland. *International Journal of Applied Earth Observation and Geoinformation* 27, 91-99.

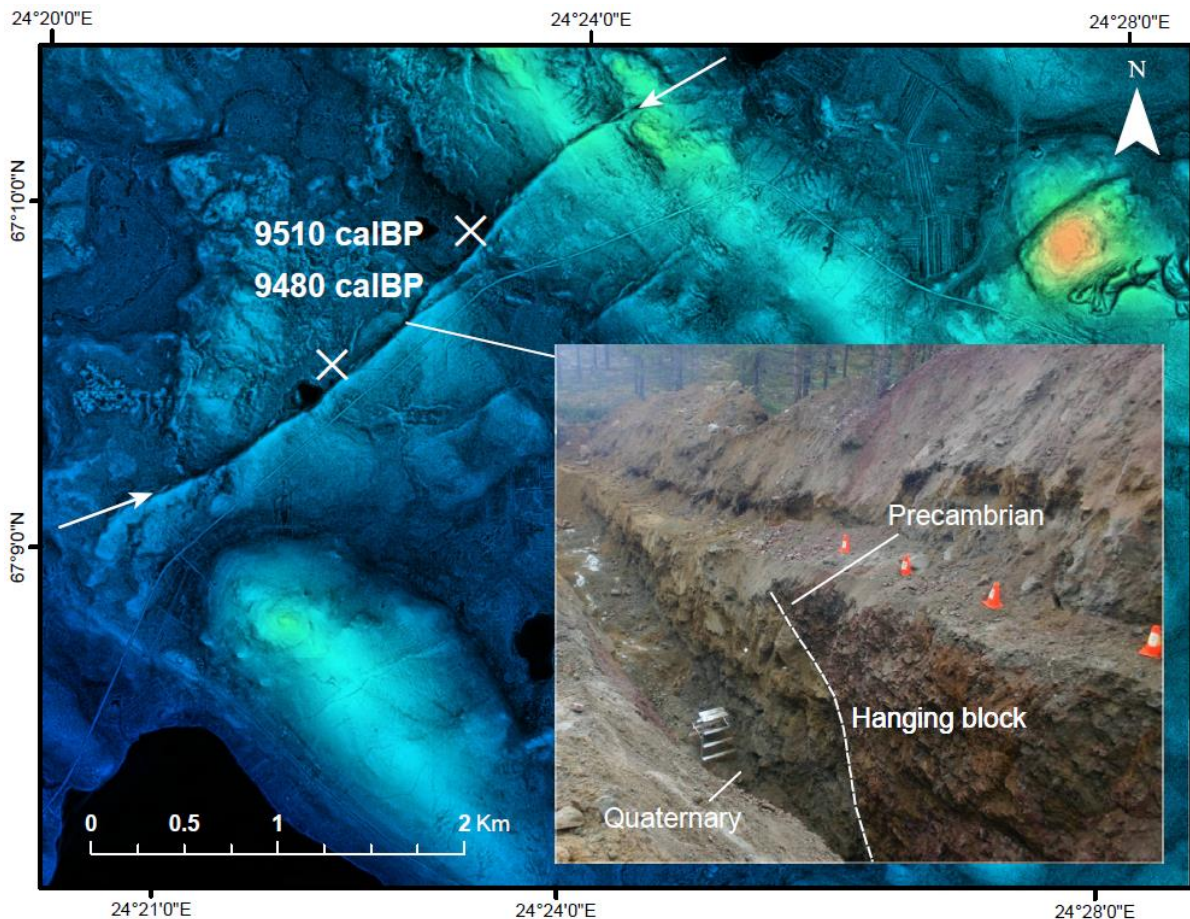


Fig. 3. TDR (tilt derivative) enhanced LiDAR image of Ruokojärvi postglacial fault in Kolari (shown by arrows; see Kuivamäki et al., 1998; Palmu et al., 2015), western Finnish Lapland (location in Fig. 1). The 6-m-high ramp opened in September 2012. The ages (crosses) are given for the basal peat samples next to the fault scarp.

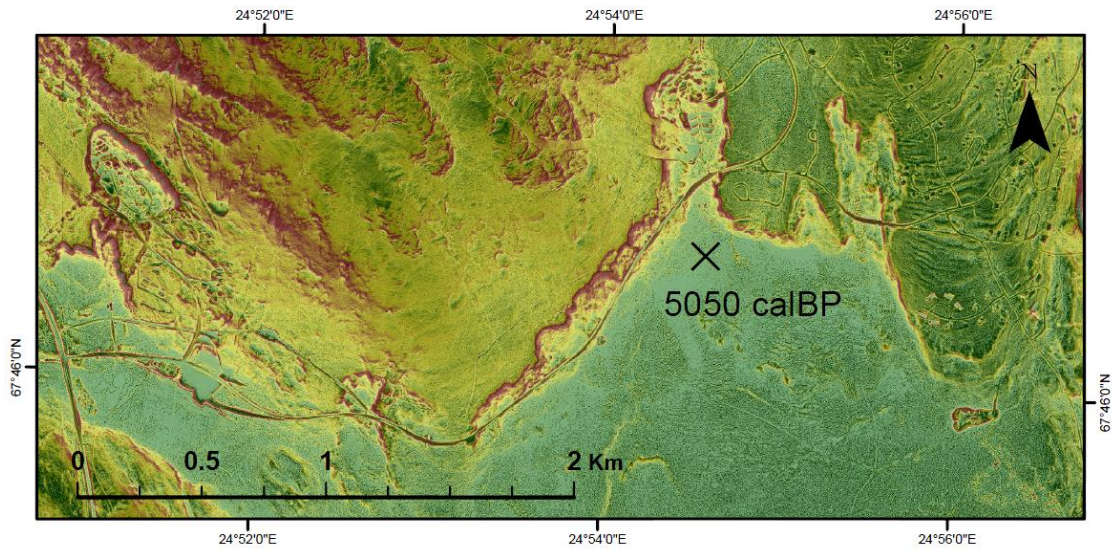


Fig.4. TDR (tilt derivative) enhanced LiDAR image showing rotational paleolandslides in Levi, Kittilä (location in Fig. 1). A cross indicates a percussion drill hole exhibiting peat/gyttja beneath six meters of slide debris (from north) yielding an age of 5055 cal yr BP. Adopted from Sutinen et al. (2014b).

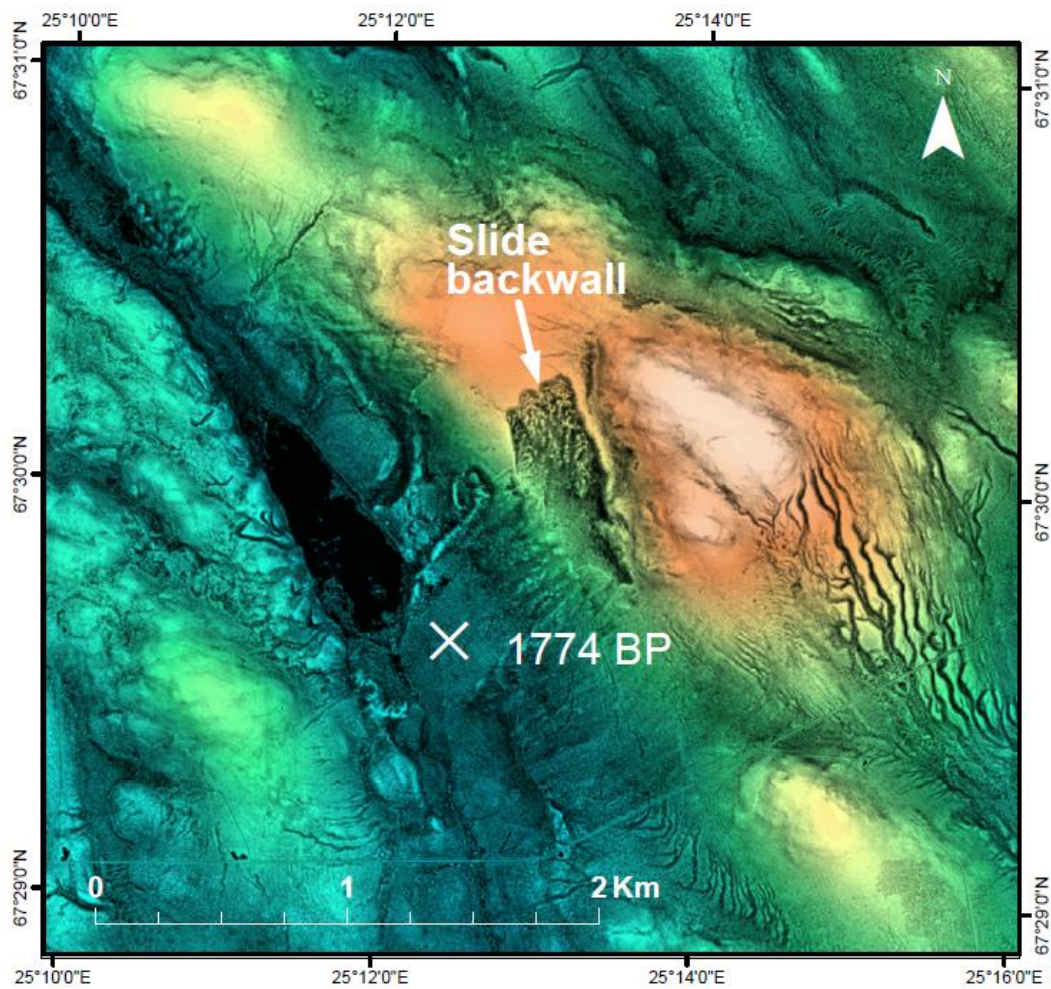


Fig.5. TDR (tilt derivative) enhanced LiDAR image showing rotational paleolandslide in Tilkua site, Kittilä (location in Fig. 1). A cross indicates a borehole site exhibiting gyttja beneath two meters of slide debris yielding an age of 1774 yr BP.



## Scarps associated with non-tectonic activity

Tatevossian, Ruben (1), Evgeniy Rogozhin (1)

(1) Institute of Physics of the Earth, RAS, 10 B. Gruzinskaya, Moscow, Russia. Email: ruben@ifz.ru

**Abstract:** The Ganges–Brahmaputra Delta (GBD), the world's largest delta, has been built from sediments eroded from the Himalayan collision. These sediments have prograded the continental margin of the Indian subcontinent by ca. 400 km, forming a huge sediment pile that is entering the Burma Arc subduction zone. The Rooppur NPP site is located in the central part of the GBD. Although the site is more than 300 km away from Indo–Burma subduction zone to the east and from Himalayan collision zone to the north, these global-scale structures govern to a great extent the seismicity and seismic hazard in the site vicinity. Scarps within the site were studied in three trenches. Inclined layers of the trench walls are interpreted as an evidence of erosion effect (not tectonic) caused by fluctuations of Ganges River flow-course.

**Key words:** Ganges–Brahmaputra Delta, scarp, trenching, liquefaction

### INTRODUCTION

The Ganges–Brahmaputra Delta (GBD) is located in a very complex region, where almost all known types of geodynamic regimes interact: continental collision, spreading, and subduction (Fig. 1).

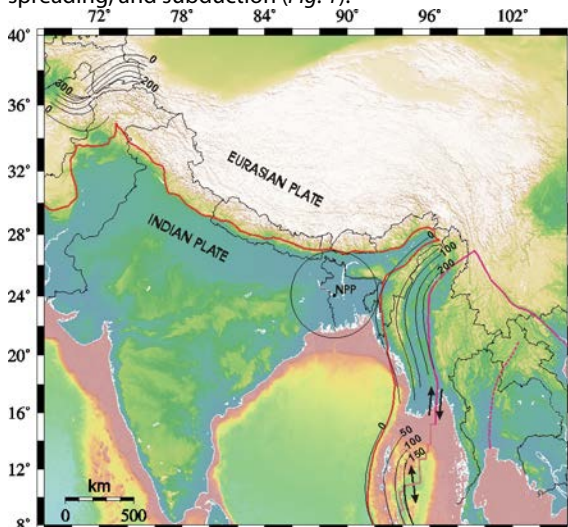


Fig. 1: General tectonic framework. Radius of circle around the Rooppur NPP site is 320 km. Red line shows Indian plate boundary. Black lines are depth isolines of downgoing slab; numbers are in km. Arrows show zone of spreading in the ocean and strike-slip fault limiting Burmese platelet. Tectonic scheme is taken from (DeMets et al., 1990)

Though the region is intensively studied at least since 1960s, details of its evolution, tectonic structure, and geodynamics are still debated. It is generally accepted that the GBD, the world's largest delta, has been built from sediments eroded from the Himalayan collision. These sediments have prograded the continental margin of the Indian subcontinent by ca. 400 km, forming a huge sediment pile that is entering the Burma Arc subduction zone. But where exactly starts the collision is not clear. More generally, whether there is tectonic activity within the GBD or it is a passive margin of Indian

subcontinent? The question is not only of academic interest, but a crucial issue with respect to the seismic hazard evaluation of the Rooppur Nuclear Power Plant (NPP) site, Bangladesh. For assessing the seismotectonic activity at near-region scale, two circumstances have to be kept in mind: a) knowledge on earthquake history is very poor (Martin & Szeliga 2010; Szeliga et al. 2010) and b) flat topography makes Digital Elevation Models (DEM) practically useless in the analysis to identify active tectonic structures. In such conditions, paleoseismological studies are most promising (The Contribution..., 2015).

### SEISMOTECTONIC BACKGROUND

Active faults and lineaments within 320 km of the site are plotted in Fig. 2 (Seismotectonic..., 2001). There are no active faults within 150 km from the site, but two lineaments are about ca. 30 km from the site.

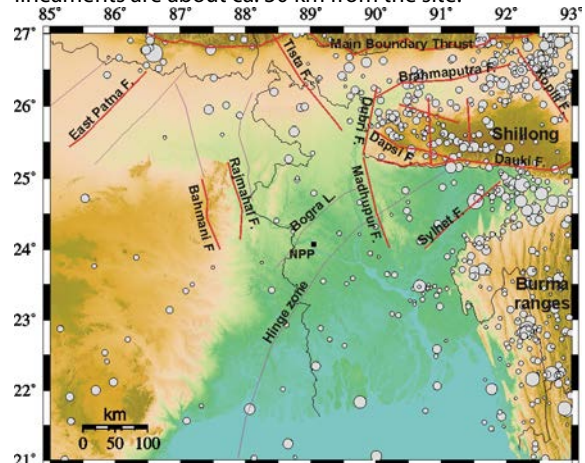


Fig. 2: Map of active faults and lineaments from to Seismotectonic Map of India (GSI, 2001). Earthquake epicenters are from to the ISC (International..., 2010). Solid red lines are faults; thin violet lines are lineaments

The Hinge zone is considered as the most important structural element close to NPP site: it is expressed in



gravity field and is interpreted to be a step in the basement at 15–20 km. There is no evidence of geological or earthquake activity associated with this zone. Shillong Plateau and Burma Ranges are the main seismically active zones. Bangladesh is characterized by diffuse seismicity; there are no earthquakes within 40 km radius around the site (according to instrumental data since 1964).

In this area of flat topography, Madhupur Fault bordering Madhupur Hills (only 28 m asl) from the West, is clearly expressed in the relief, which contrasts with the surrounding plain at 10 m asl. Therefore, elevation changes of less than 20 m are readable in the available DEM (with selected colour palette, intensity and angle of illumination).

Conclusion: there are no mapped active faults or earthquakes within the 40 km around the NPP site; there are no topographic elements of the DEM, close to the site, which can be interpreted as expressions of active faults. However, the region is located within complex geodynamic setting which requires more close and careful studies *in situ*.

#### SCARPS AND TRENCHING DATA

Linear features near the site were evaluated as candidates for potentially active tectonic zones (Fig. 3).

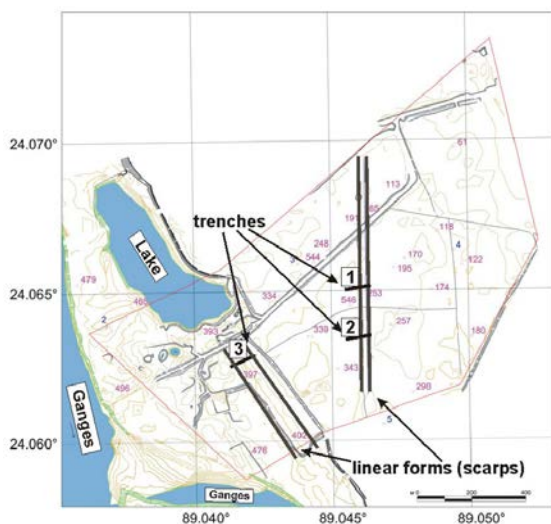


Fig. 3: Linear forms near the site and trenches (1 - 3). Numbers in violet are pits and holes dug to verify evidence of possible liquefaction

Photos show the expression of the linear features at surface (Figs. 4 & 5). We excavated three trenches that were 1.7 – 3.0 m deep, ca. 100 m long five holes up to 1.5 – 2 m deep and 26 pits as much as 4 m deep. The latter are located more or less homogeneously all over the site (Fig. 3). These excavations made it possible to obtain general view of structure and composition of the near-surface deposits.

To meet the extended abstract length, we do not provide a detailed description of the trench walls.



Fig. 4: The scarp near the pathway in eastern part of the NPP site. Total length of the scarp is more than 1 km



Fig. 5: Lower part of the slope slightly flooded to the east from the scarp

The trench #1 striking ENE crosses the scarp (Figs 6 & 7).



Fig. 6: Exposure in the central and eastern parts of trench #1 (NNW wall). Brown sandy and clayey loams are the dominant deposits

Photos and sketches give some understanding (Figs. 6 to 8) of the deposits. In general, three sections can be recognized in the NNW wall of the trench #1. In the eastern section of the trench near the lowered block on the surface up to 30 m flat-lying grayish-brown sandy loams with thin interlayers of grey quartz sands and grey-brownish clayey loams are present. In the upper



part of the cross-section under weak modern soil, there is a layer of yellow-grayish sands overlain by grayish-yellow sandy loams. In general the trench wall is dark brownish.

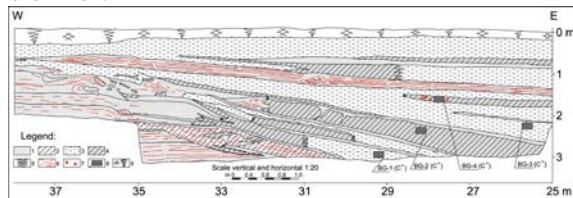


Fig. 7: Log of the trench # 1 NNW wall (central segment). The zone of structural inconformity between eastern and western segments is visible. Legend: 1 – sand fine; 2 – stratified sand; 3 – sandy loam; 4 – loamy sand 5 – the conventional boundaries of facies transition; 6 – textural features are represented in terms of layers; 7 – the individual shells of gastropods; 8 – areas sampling for age Dating ( $^{14}\text{C}$ ) (BG-1 is the number of samples); 9 – sod-soil horizon (together with the subsurface layer of sandy loam).

The second section of about 15 m coincides with gradient zone of the scarp. Here the trench was 3 m deep and exposed the following (from top to bottom): 1. Modern soil, grey, poor, podzolic – 10–20 cm; 2. Light-grey sandy loam, thick, dense – 70 cm; 3. Fine-grained light-grey quartz sand – 10–15 cm; 4. Stratified grey-brownish sandy loams – 50–70 cm (thickness increases eastward). Upper layers are horizontal. Only the base of layer 4 dips eastward at 2–5°. Deposits below include the following layers:

5. Yellowish-brown, fine-grained thin sand with small disharmonic folds (vertical or eastward inclined) – 20 cm; 6. Brownish clayey loams containing gastropod shells; the thickness increases eastward from 20 to 120 cm (4 samples for  $^{14}\text{C}$  are collected from different horizons); 7. Light-grey fine-grained sand – 10 cm; 8. Brownish clayey loams with sand interlayer – 90 cm; these clayey loams thinned westward to 40 – 50 cm and are replaced by poorly sorted quartz sand containing fractures filled with fine-grained sand, inclusions of clayey loams and humus fragments (“colluvial wedge” type). Inclination of these layers increases from 5 – 8° eastward from top to 10 to 15° at the base. The trench exposes an unconformable contact of the eastward inclined layers and horizontal layers of stratified micaceous fine-grained sand with visible thickness 80 cm.

The 50-m-long, western section of the trench is associated with uplifted block.



Fig. 8: The zone of interbedding in the trench # 1. Samples for  $^{14}\text{C}$  dating are shown by grey rectangles. Numbers are the sample numbers

It is characterized by horizontal thick layers of light yellow and grey-yellow micaceous sand with thin interlayers of light sandy loams and quartz sands. In the

intersection of the central and western parts of the trench, up to the top horizons, there is erosional contact of inclined layers characteristic of the first segment with the horizontal layers of older layers of the second section (Fig. 6).

We found similar features in trench #2, which is parallel to trench #1 and located about 200 m to the south (Fig. 9). The bedding in layers in the WSW segment of the trench #2 is almost horizontal. The general color is light-grey.

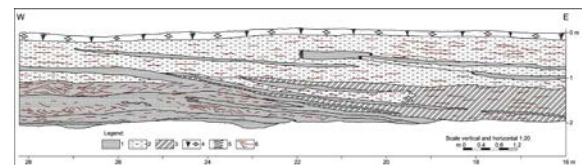


Fig. 9: Log of the trench # 2 NNW wall (central segment). Legend: 1 – sand; 2 – sand oblique; 3 – loam; 4 – sod-soil horizon (subsoil with thin clay sand); 5 – facies transitions between sediment section; 6 – textural features of the layers of the cut

In general, the trenches reveal the subsurface structure and stratigraphy of the Quaternary deposits beneath the topographic scarp in the central part of the Rooppur NPP site and lead to the following conclusion. The scarp is of erosion/deposition nature, not a tectonic, one because eastward inclined layers in the central part of both trenches uncomfortably overlay horizontal layers to the west from scarp, cutting them, and pinching out against them under different angles. Eastward from the scarp inclined younger layers of the transition zone (central segment of both trenches) become sub-horizontal at eastern segments.



Fig. 10: General view of the linear lowered element in the relief on the western part of the NPP site. The photo views toward the south



Fig. 11: General view of the linear feature in the western part of the NPP site. View of the photo is toward the south

The uplifted western side is characterized by light-grey and grey-brown clayey loams and the central part is



## INQUA Focus Group on Paleoseismology and Active Tectonics



paleoseismicity.org

characterized by dark brown clayey loams. The 115-m-long trench #3 was excavated in the western part of the site across a NNW-oriented linear feature (Fig. 10). The feature is 1 km long and is bounded by a 30-m-wide depression, which is lowered by 3-4 m. The trench #3 (Fig. 11) exposed the near-surface deposits beneath the scarp.

The cross-section of the NNW wall of the trench can be subdivided on three sections. The 60-m-long ENE segment contains dense, thick, light-grey and yellowish-grey, sandy loams interlayered with thin quartz, sometimes stratified sands. The layers are sub-horizontal in general, but in the western direction they dip gentle (1-3°). In the 40-m-long central part, below the modern soil and a layer of yellowish obliquely stratified quartz sand is a layer of dark-brown clayey loam (Fig. 11). The cross-section is erosional; it is conditioned by the ancient streamlet of Ganges passing here.

In addition to studies of Quaternary sediments in trenches, we studied the exposures in pit that were up to 4 m deep; the pits were more or less regularly distributed over the whole NPP site area. The main goal is to verify possible occurrences of seismites (liquefaction-induced structures). We omit description of pits but include several photos clearly showing absence of any trace of liquefaction (Fig. 12).



Fig. 12: Photographs of pit walls

We did not find either primary or secondary (liquefaction) evidence of paleo-events based on the absence of liquefaction features. The scarps are of erosion/deposition origin associated with paleo-channels of the nearby Ganges River.

### DISCUSSION

1. We stress that the absence of primary evidence of paleo surface dislocation in trenches is not enough to conclude that no paleoearthquakes have caused strong shaking at the site. The Kopili Fault (Fig. 2) has been mapped in the area, but Kumar et al. (2016) did not find direct evidence of ancient surface faulting. However they did report evidence of a paleoearthquake based on the wide-spread liquefaction phenomena in the fault zone. Their conclusion is supported by modern earthquake

activity associated with the Kopili Fault (Kayal et al., 2010). Comprehensive analysis of both primary and secondary effects can only be the basis for a sound conclusion on absence of paleoearthquake when "suspicious" topographic elements have been fully analyzed.

2. The fact that scarps can be generated due to phenomena other than earthquakes is an important conclusion. Few such cases are known. McCalpin (1992) reported on the scarp was a shoreline of Pleistocene Lake (Utah), and not a range-front fault scarp. Another example is when the scarps actually were fluvial terrace risers (Chile) (McCalpin, 2013).

3. Based on our results one can assume the GBD (at least its central part) is a passive margin of Indian subcontinent.

**Acknowledgements:** The study was partly supported by the Russian Foundation for Basic Research, project no. 14-05-00258. Authors are grateful to Jim McCalpin for the support. Comments of unknown reviewer improved greatly the paper.

### References

- DeMets, C., Gordan, R.G., Argus, D.F. and Stein, S. (1990). Current plate motions. *Geophys. J. Int.*, 101, 425-478.
- International Seismological Centre, *On-line Bulletin*, <http://www.isc.ac.uk>, Internat. Seis. Cent., Thatcham, United Kingdom, 2012.
- Kayal, J.R., S.S. Arefiev, S. Baruah, R. Tatevossian, N. Gogoi, M. Sanoujam, J.L. Gautam, D. Hazarika and D. Borah (2010). The 2009 Bhutan and Assam felt earthquakes (Mw 6.3 and 5.1) at the Kopili fault in the northeast Himalaya region. // *Geomatics, Natural Hazards and Risk* Vol. 1, No. 3, 273-281.
- Kumar, D., D.V. Reddy, Anand K. Pandey (2016). Paleoseismic investigations in the Kopili Fault Zone of North East India: Evidence from liquefaction chronology. // *Tectonophysics*, 674, 65-75.
- McCalpin, James, Robison, R.M., and Garr, J.D., 1992, Neotectonics of the Hansel Valley-Pocatello Valley corridor, northern Utah and southern Idaho in Hays, W.W. and Gori, P. (eds.), *Assessment of Regional Earthquake Hazards and Risk Along the Wasatch Front, Utah*, U.S. Geological Survey Professional Paper 1500-G, p. G1-G18.
- McCalpin, J.P., 2013, Survey for active faulting in the vicinity of the Siete Lagos damsite, Los Rios District, Chile, Final Report: unpublished report submitted to Aurum Consultores, Santiago, Chile by GEO-HAZ Consulting, Crestone, CO, Job. No. 2142, 88 p
- Martin S. & W. Szeliga (2010). A Catalog of Felt Intensity Data for 570 Earthquakes in India from 1636 to 2009. *Bulletin of the Seismological Society of America*, v. 100, No. 2, p. 562-569, doi: 10.1785/0120080328.
- Szeliga W., Hough S., Martin S., and Bilham R. (2010) Intensity, Magnitude, Location, and Attenuation in India for Felt Earthquakes since 1762. *Bulletin of the Seismological Society of America*, v. 100, No. 2, p. 570-584, doi: 10.1785/0120080329.
- Seismotectonic map of India and its environs. GSI, 2001.
- The Contribution of Palaeoseismology to Seismic Hazard Assessment in Site Evaluation for Nuclear Installations. IAEA-TECDOC-1767. VIENNA, 2015.



## Towards an Active Fault Assessment in the Southern Upper Rhine Graben

Thomas, Jessica (1), Stéphane Baize (2), Jochen Hürtgen (1), Klaus Reicherter (1), Edward Marc Cushing (2), Hervé Jomard (2)

(1) Neotectonics & Natural Hazards, RWTH Aachen University, Lochnerstr. 4-20, 52056 Aachen, Germany. Email: J.Thomas@nug.rwth-aachen.de

(2) Institut de Radioprotection et de Sûreté Nucléaire, BP 6, 92262 Fontenay-aux-Roses, France. Email: Stephane.baize@irsn.fr

**Abstract:** The Upper Rhine Graben (URG) is the central part of the Central European Cenozoic Rift System (ECRIS). The URG is limited by the Rhenish Massif in the North and the Jura thrust and fold belt in the South and is delimited by faults, which are supposed to be active especially at the eastern border of the URG. Most of the input data for fault-based SHA (seismic hazard assessment) models are highly uncertain to date, based upon sparse or hypothetical data. Especially missing are paleoseismic studies in the Freiburg area on the eastern border. To fill this gap, we did geophysical measurements in that area, including both shallow ground penetrating radar (GPR) profiles and electrical resistivity tomography (ERT) which show promising results indicating that one of the eastern boundary faults could be active relatively recently, setting the stage for a future trenching study.

**Key words:** Upper Rhine Graben, active faults, paleoseismology, pre-trench survey, geophysics

### INTRODUCTION

The Upper Rhine Graben belongs to the Central European Cenozoic Rift System (ECRIS) which extends over a length of 1100 km from the North Sea to the Mediterranean Sea and is one of the most tectonically active regions in

Central Europe. The ECRIS consists of several graben systems, amongst others, the Lower Rhine Graben (LRG), the Upper Rhine Graben (URG), the Bresse-Saône-Graben (BG) and the Limagne Graben (LG) (Fig. 1 A). The Upper Rhine Graben forms the central part of the ECRIS, bounded by the Jura fold and thrust belt to the South and

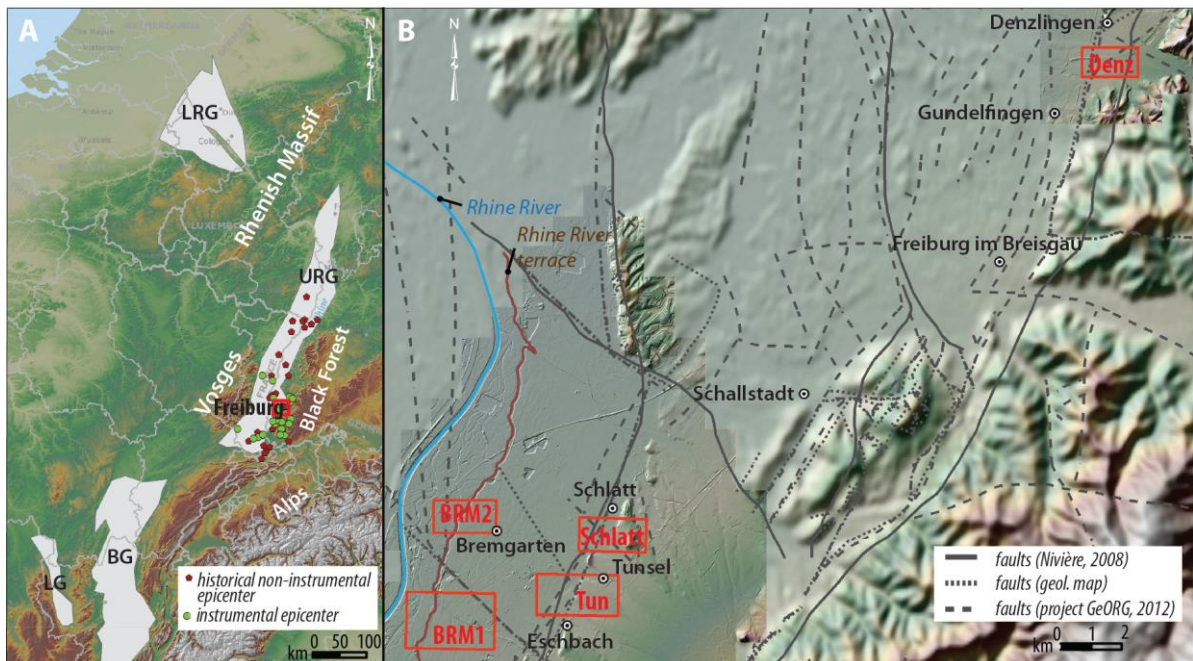


Fig. 1: A: Overview of the Central European Cenozoic Rift System (ECRIS) consisting of several graben systems, amongst others, the Lower Rhine Graben (LRG), the Upper Rhine Graben (URG), the Bresse-Saône-Graben (BG) and the Limagne Graben (LG). The URG is delimited by the Vosges and the Black Forest, two uplifted plateaus, to the west and east respectively and by the Rhenish Massif and the Alps to the north and south. The investigation area, presented in B, is marked as a red square near the city of Freiburg; In addition, the historical as well as instrumental epicenters in the URG are shown in in map A. DEM from SRTM data (green/red) and basemap from ESRI in the background. B: Extent of the five investigation areas, four in the south-west and one in the north-east of Freiburg im Breisgau (marked by red squares). In this publication only the first results of the investigation area at Denzlingen (Denz, north-east of Freiburg im Breisgau) are presented. DEM from LiDAR data (green/red) and SRTM data (green/red) in the background.



the Rhenish Massif to the North. The URG is 300 km long and up to 40 km wide and bordered on both sides by SSW-NNE striking Tertiary-age normal faults.

A brief overview at a seismicity map of the Upper Rhine Graben area reveals that the region is seismically active (cf. Fig. 1 A). The area has been hit recently by shallow and moderate earthquakes with intermediate intensities of VI-VII (1523, 1823, 1899, 1926; Fracassi et al., 2005; Nivière et al., 2008), but, historically, strong earthquakes damaged and devastated populated zones. The most damaging earthquake with an intensity of IX (SisFrance database, Fäh et al., 2009) occurred close to the Eastern Border Fault of the URG where it meets the front of the folded Jura of the Alps and significantly damaged the city of Basel in 1356 (Meghraoui et al., 2001; Ferry et al., 2005; Peters et al., 2005). Instrumental seismicity suggests that most of the URG is currently deforming under a transtensive (final parts) to transpressive (central segment) tectonic regime, caused by the crooked course of the rift valley (e.g. Illies & Greiner, 1979; Edel et al., 2006).

The southern URG (SURG) includes a series of critical facilities, including the French nuclear power plant of Fessenheim located close to faults, the activity of which has been suggested through preliminary geomorphological and geophysical studies, (e.g. Meghraoui et al., 2001; Nivière et al., 2008). Thus, fault-based SHA (seismic hazard assessment) studies should be developed, which could include a deterministic (scenario-based) approach (DSHA) and/or a probabilistic approach (PSHA). Whatever the approach, most of the input data in fault-based models are highly uncertain to date. They are mainly based upon sparse or hypothetical data. Especially the Freiburg area, located at the URG eastern border, is missing in paleoseismic studies and their crucial outcomes.

For a comprehensive hazard assessment of the location, detailed investigations of the faults are required. We plan to find an appropriate trenching site to add paleoseismological data because this approach has been proven to be worthwhile in the Rhine Graben, both to the North (Worms and Strasbourg) and to the South (Basel).

This would be done in order to definitely prove whether the faults ruptured the ground surface during the Quaternary, and to determine key fault parameters such as magnitude, age of large events, slip rates and/or return periods.

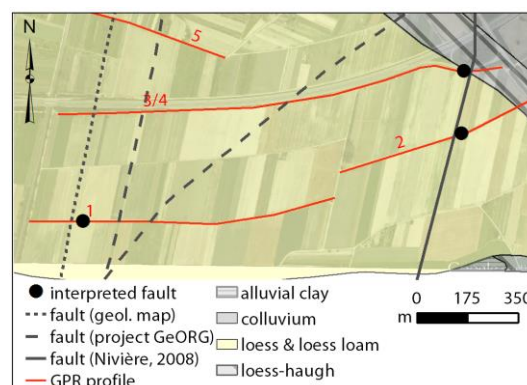


Fig. 2: Overview of the Denzlingen investigation site showing the location of faults provided by the geological map, the project GeORG (LGRB, 2012) and Nivière et al. (2008). The red lines show the location of the obtained GPR profiles shown in Fig. 3 and Fig. 4 A & B. The black circles mark the locations of the structures in the profiles interpreted as fault related.

In the URG a total of 14 trench studies have been already completed (e.g. Lemeille et al., 1999; Meghraoui et al., 2001; Peters et al., 2005) especially at the Western Border Fault. In the northern part, Pleistocene to Holocene slip along the Western Border normal fault has been proven by these trenches, in combination with geomorphological studies (Cushing et al., 2000; Peters et al., 2005).

This paper presents the first results of a pre-trenching geophysical survey carried out in the Freiburg area near the Eastern Border Fault in the URG in addition to the work of Hürtgen et al. (2015). The sites of investigation (Bremgarten, 1 & 2, Tunsel, Schlatt and Denzlingen; cf. Fig. 1 B) have been selected on the basis of the work of Lämmermann-Barthel et al. (2009), Nivière et al. (2008)

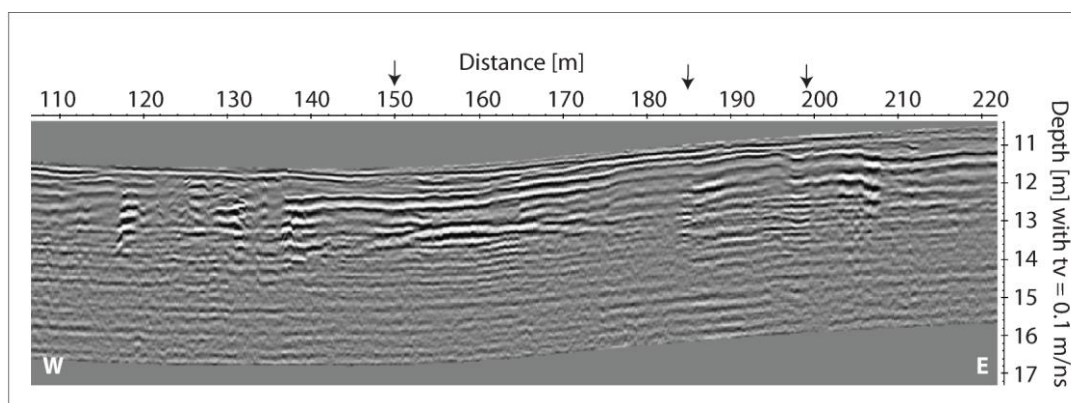


Fig. 3: Section of GPR profile 1 between 107 m and 222 m measured with the 270 MHz-antenna at the investigation site Denzlingen. The total length of the profile is 1075 m. The location is shown in Fig. 2. Arrows indicate some relevant features.



and the project GeORG (LGRB, 2012) and followed by a visual inspection in the field.

## METHODS

The investigations were conducted using ground penetrating radar (GPR), electrical resistivity tomography (ERT) and capacitive geoelectrics using the OhmMapper (OM) system consisting of a transmitter electronics and batteries along with two transmitting dipole cables. GPR and OM were used in order to provide information over relatively large areas with as much detail as possible. At selected places, additional measurements were made using DC-geoelectrics, because this method proved very useful for the verification of structures identified by GPR. The results were also compared to faults mapped in other projects such as the project GeORG (LGRB, 2012), the work of Nivière et al. (2008) and the faults visible in the geological maps to get a preferably high level of information for the validation of the results. Finally, the results of the geophysical measurements have been verified using high-resolution remote sensing data (5 m LiDAR data) and analysing the imprints in the morphology (e.g., erosional vs. morphotectonic features).

## RESULTS

The results presented here are only examples at the investigation area of Denzlingen located only a few kilometres north-east of Freiburg im Breisgau directly at the Eastern Main Border Fault in the SURG. Altogether a

total of several kilometres of GPR, ERT and OM surveys have been obtained in five different investigation areas around Freiburg in the SURG (cf. Fig. 1 B). The Freiburg area is agricultural with vineyards on the heights. The investigation site of Denzlingen is located within the graben above Quaternary sediments like sand, gravel or loess. Beside the Eastern Main Border Fault (Nivière et al., 2008), two fault traces of the geological map and one provided by the project GeORG (LGRB, 2012) are crossing this area (cf. Fig. 2). The surveys (GPR and OM) have been achieved across these fault traces and a scarplet striking SWW-NEE visible in the LiDAR data.

The most striking features, probably of tectonic origin and promising for further paleoseismological investigations, are visible in the Denzlingen profile 1 located in the south-west between 150 m and 200 m (cf. Fig. 3) and in the both profiles 2 and 3/4 located at the north-east at 444 m (cf. Fig. 4 A) and 1420 m (cf. Fig. 4 B) respectively. An overview of the location of these features is given in Fig. 2.

The GPR-Profile 1 is located directly across the faults shown on the geological map as well as the project GeORG (LGRB, 2012) (cf. Fig. 2). The first interesting feature is an unconformity of the reflectors at 2 m depth at 150 m along the profile (first black arrow in Fig. 3). The reflectors beneath this feature are dipping slightly to the west. Farther eastward at 185 m, the profile shows a sharp contrast at a depth of 1 to 3 m with a change of the reflection patterns (second black arrow in Fig. 3). The group of reflectors coming from the east are ending

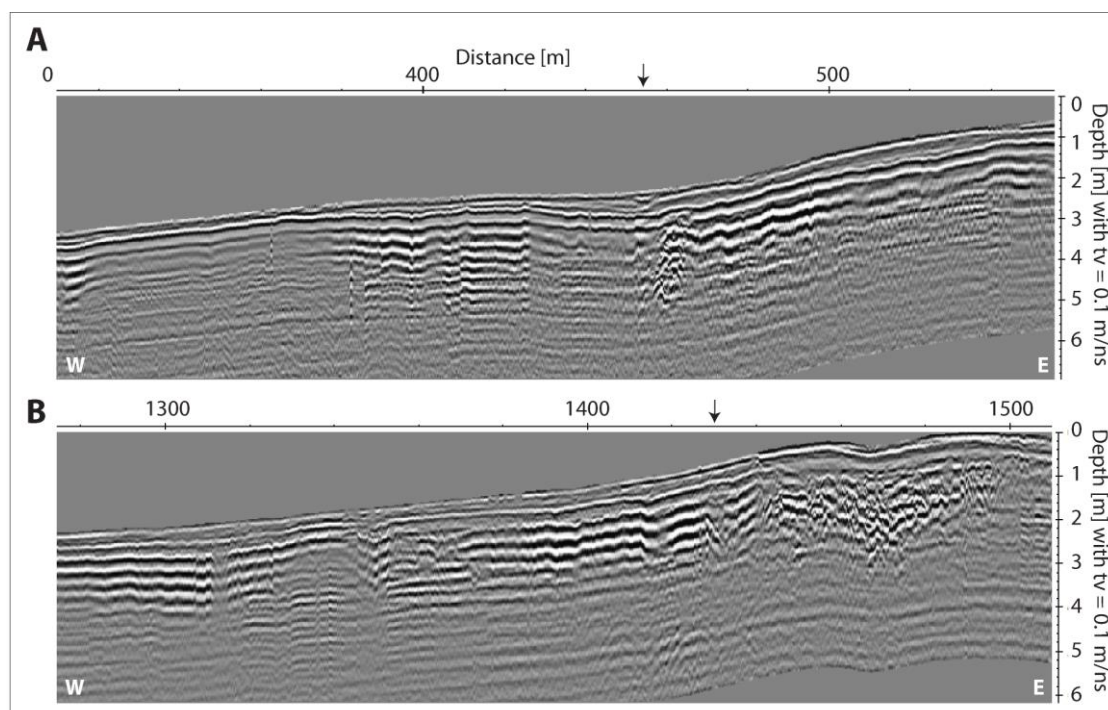


Fig. 4: A: section of GPR profile 2 between 0 m and 560 m measured with 270 MHz-antenna at the investigation site Denzlingen. The total length of the profile is 710 m. B: section of the combined GPR profile ¾ between 1280 m and 1510 m (end of line), measured with the 270 MHz-antenna at the investigation site Denzlingen. The location of both profiles is shown in Fig. 2. Arrows indicate some relevant features.



abruptly here. The reflectors above are dipping to the east at a high angle between 196 m and 200 m along the profile (third black arrow in *Fig. 3*). All of these structures are preliminarily interpreted as due to fault displacement and thus a tectonic origin.

The two GPR profiles 2 and 3/4 shown in *Fig. 4 A* and *Fig. 4 B* are located directly across the Main Border Fault in the west of profile 1 (cf. *Fig. 2*). Both profiles show an abrupt ending of continuous major reflectors coming from the east (marked by black arrows in *Fig. 4 A* and *Fig. 4 B*), the reflectors beneath 1 m depth abruptly bend down with a sharp contrast to the reflectors in the west. Moreover, there is a change of the dip angle to the west of some major continuous reflectors coming from the west and thus building a wedge-like feature. Similar features can be found in profile 3/4 at 1420 m and can be interpreted as originating from tectonic activity.

The locations of these structures found in profile 2 and 3/4 were in perfect accordance with a fault, which had been postulated by Nivière et al. (2008). In addition, a fault denoted in the geological map was confirmed in the profile 1 at the investigation area in Denzlingen.

## DISCUSSION & OUTLOOK

Presented here are only a few profiles with promising structures indicating a tectonic origin, but similar features were found in the GPR and ERT profiles obtained at the other four investigation areas shown in *Fig. 1 B*. All areas are cultivated areas and the shallow subsurface is modified due to agricultural use. Thus, an interpretation of the high-resolution shallow GPR-profiles is often difficult and ambiguous. For a detailed analysis of promising structures found with GPR further detailed investigations with ERT profiling or percussion drilling are necessary to compare and validate whether the features have a tectonic or erosional origin. For a comprehensive hazard assessment, detailed investigations of the interpreted faults are now required. We plan to perform all these preliminary investigations during the next year(s), starting with finding appropriate trenching sites from which to obtain relevant paleoseismological data, and determine key fault parameters, such as magnitude and age of large events.

**Acknowledgements:** Thanks to C. Clauser and his team of the institute of applied geophysics and geothermal energy (E.ON Energy Research Center, RWTH Aachen) for the loan of the ERT and OhmMapper.

## References

- Cushing, M., Lemeille, F., Cotton, F., Grellet, B., Audru, J.-C., Renardy, F., (2000). Paleo-earthquakes investigations in the Upper Rhine Graben (URG) in the framework of the PALEOSIS project. *Paleosis project* (ENV4-CT97-0578 EC Environment and Climate Research Programme), 1–9.
- Edel, J.B., Whitechurch, H., Diraison M., (2006). Seismicity wedge beneath the Upper Rhine Graben due to backwards Alpine push? *Tectonophysics* 428, 49–64.
- Fäh, D., Gisler, M., Jaggi, B., Kästli, P., Lutz, T., Masciadri, V., Matt, C., Mayer-Rosa, D., Rippmann, D., Schwarz-Zanetti, G., Tauber, J., Wenk, T. (2009). The 1356 Basel earthquake: An interdisciplinary revision. *Geophysical Journal International* 178, 351–374.
- Ferry, M., Meghraoui, M., Delouis, B., Giardini, D., (2005). Evidence for Holocene palaeoseismicity along the Basel-Reinach active normal fault (Switzerland): a seismic source for the 1356 earthquake in the Upper Rhine Graben. *Geophysical Journal International* 160, 554–572.
- Fracassi, U., Nivière, B., Winter, T., (2005). First appraisal to define prospective seismogenic sources from historical earthquake damages in southern Upper Rhine Graben. *Quaternary Science Review* 389, 1–33.
- Hürtgen, J., Jomard, H., Thomas, J., Reicherter, K., Baize, S., Röth, J., Cushing, M., Cinti, F.R., (2015). The Southern Upper Rhine Graben - A paleoseismological pre-site survey in the Freiburg area. In: *27 Abstracts Volume 6th International INQUA Meeting on Paleoseismology, Active Tectonics and Archeoseismology* (Blumetti, A.M., Cinti, F.R., De Martini, P.M., Galadini, F., Guerrieri, L., Michetti, A.M., Pantosti, D. & Vitorri, E. eds). 19–24 April 2015, Pescina, Fucino Basin, Italy, 220–223.
- Illies, J.H., Greiner, G., (1979). Holocene movement and state stress in the Rhine Graben rift system. *Tectonophysics* 52, 349–359.
- Lämmerrmann-Barthel, J., Neeb, I., Hinderer, M., Frechen, M., (2009). Last Glacial to Holocene fluvial aggradation and incision in the southern Upper Rhine Graben: Climatic and Neotectonic controls. *Quaternaire* 20, 1, 25–34.
- Lemeille F., Cushing M., Cotton F., Grellet B., Ménillet F., Audru J.-C., Renardy F., Fléhoc Ch., (1999). Evidences for Middle to Late Pleistocene faulting within the Northern Upper Rhine Graben (Alsace Plain, France). Traces d'activité pléistocène de failles dans le nord du Fossé du Rhin supérieur (Plaine d'Alsace, France). *Comptes Rendus de l'Académie des Sciences* 328, série II, n°12, 839–846.
- LGRB (Landesamt für Geologie, Rohstoffe und Bergbau), Regierungspräsidium Freiburg, (2012). Interreg IV Oberrhein, Projekt GeORG. Last checked: 13th January 2014 <http://geo.geopotenziale.eu/geonetwork/srv/de/main.home>
- Meghraoui, M., Delouis, B., Ferry, M., Giardini, D., Huggenberger, P., Spottke, I., Granet, M., (2001). Active normal faulting in the upper Rhine Graben and Paleoseismic Identification of the 1356 Basel earthquake. *Science* 293, 2070–2073.
- Nivière, B., Bruestle, A., Bertrand, G., Carretier, S., Behrmann, J., & Gourry, J.-C., (2008). Active tectonics of the southeastern Upper Rhine Graben, Freiburg area (Germany). *Quaternary Science Reviews* 27, 541–555.
- Peters, G., Buchmann, T., Connolly, P., van Balen, R., Wenzel, F., Cloetingh, S., (2005). Interplay between tectonic, fluvial and erosional processes along the Western Border Fault of the northern Upper Rhine Graben, Germany. *Tectonophysics* 406, 1–2, 39–66.



## The San Ramon Fault at the eastern border of Santiago city, Chile: paleoseismological implications from the linkage between piedmont units and fluvial terraces

Gabriel Vargas Easton (1), Rodrigo Rauld (1), Steven L. Forman (2), Tomás Iglesias (1), Yann Klinger (3), Sofía Rebolledo (1), Thomas K. Rockwell (4), José Luis Antinao (5), John Gosse (5), Stéphane Baize (6), Robin Lacassin (3), Rolando Armijo (3)

- (1) Departamento de Geología, CEGA, Universidad de Chile, Plaza Ercilla 803, Santiago. gvargas@ing.uchile.cl
- (2) Department of Geology, Baylor University, One Bear Place #97354, Waco, Texas 76798-7354, USA
- (3) Institut de Physique du Globe de Paris, Université Paris Diderot, UMR 7154 CNRS, 1 rue Jussieu, F-75005 Paris, France
- (4) Department of Geological Sciences, MC 1020, San Diego State University, San Diego, California 92182, USA
- (5) Earth Sciences Department, Dalhousie University, Halifax, Canada B3H 4J1
- (6) Institut de Radioprotection et de Sûreté Nucléaire, BP 17, 92262 Fontenay-aux-Roses, France

**Abstract:** The west-vergent San Ramón thrust fault is located along the eastern border of Santiago city, Chile, at the foot of the western slope of the main Andes Cordillera. Recent observations from a paleoseismological trench excavated across a 4-5 m height escarpment revealed two large ruptures of estimated magnitude Mw7.2-7.5 in the past 17,000-19,000 years; the last occurred nearly 8,000 years ago. New observations from additional trench support the idea of two major events in the last 17 ka. The geomorphology of deformed and tilted fluvial terraces that crosses the fault system indicates increasing incision rates toward the structural front, with 0.4 mm/year of tectonic vertical slip in the last ca. 86 ka. The consistency of Quaternary tectonic markers along the entire fault system supports its potential for generating strong earthquakes with superficial rupture; we estimate a probability of ca. 3% in the next hundred years for such an event.

**Key words:** Paleoseismology, San Ramón Fault, Santiago, Fluvial terraces, Seismic Hazard.

### INTRODUCTION

The San Ramón fault is an active west-vergent thrust fault system located along the eastern border of Santiago, capital city of Chile, at the foot of the western slope of the main Andes Cordillera (Armijo et al., 2010; Fig. 1). The structural system is constituted by segments in the order of 10-15 km length, evidenced by conspicuous 4 m to >100 m height scarps systematically located along the fault trace that affect Quaternary piedmont units, suggesting slip rate in the order of ~0.4-0.5 mm/year (Armijo et al., 2010; Rauld, 2011). Recent observations from a paleoseismological trench excavated across a prominent 4-5 m height escarpment revealed two last large episodes with superficial rupture, with the latest occurred nearly 8,000 years ago (Vargas et al., 2014; Fig. 2).

New geomorphological observations from additional trench, fault scarps and deformed fluvial terraces support the consistency of tectonic markers, as well as the capability of this fault to produce large earthquakes with superficial rupture, including the occurrence of two major events in the last 17 ka.

### PIEDMONT UNITS-DEVELOPMENT

Piedmont sediments affected by fault scarps along the eastern border of Santiago valley were previously grouped in three units assigned to the Early-Middle Pleistocene (older unit), Late Pleistocene (middle unit) and Late Pleistocene-Holocene (younger unit), respectively (Armijo et al., 2010; Rauld, 2011; Fig. 3). New geochronological results from radiocarbon and Optically

Stimulated Luminescence (OSL) analyses from sediments of the younger unit yielded ages ranging from 45-38 ka up to 1 ka. The older age is similar to the ages obtained from chlorine cosmogenic isotope analyses performed on block-rocks disposed on an alluvial surface of this last unit, which is affected by a prominent young fault scarp where two paleoseismological trenches were excavated (Vargas et al., 2014). In addition, this age is similar to those obtained from OSL analyses on outwash sediments located at 1300 m a.s.l., upstream along the Maipo river valley (Ormeño, 2007), interpreted as the result of the maximum advancement of glaciers during the Late Pleistocene at this latitude of the Andes of Central Chile. Thus, the available geochronological results suggest that the beginning of the deposition of the younger unit since the Late Pleistocene was driven by regional climate conditions characterized by higher precipitation rates that induced both alluviation along the piedmont of Santiago valley and glacier advancement in the adjacent Andes Cordillera.

The analysis of a paleoseismological trench dug across a young fault scarp affecting the younger unit revealed two last large earthquakes with superficial rupture in the last 17-19 ka (Vargas et al., 2014). Similar age around 16-17 ka have been found from OSL analyses in alluvial sediments taken in an adjacent trench in the same area, which confirm the previous chronostratigraphic interpretation. According Vargas et al. (2014), some alluviation occurred in this area after a penultimate large earthquake at ca. 17 ka, but it was less important after the last large earthquake at ca. 8 ka; arid climate conditions during the Early to Mid Holocene most probably contributed to the preservation of the fault



## INQUA Focus Group on Paleoseismology and Active Tectonics



paleoseismicity.org

scarp. The previous evidences suggest that active alluviation associated with the occurrence of torrential rainfalls prevailed during the latest Pleistocene in the region, but such torrents were rare, almost null, during the Early to Mid Holocene. Such a climate evolution agrees with previous regional paleoclimatic inferences from sites located to the south of this area that suggest colder climate and much higher precipitation during the Late Pleistocene until 21 ka, increasing aridity and then extreme dry conditions during the Early to Mid Holocene (Valero-Garcés et al., 2005; Jenny et al., 2002). The deposition of a modern alluvial unit began during the Late Holocene as suggested by the development of youngest alluvial fans that prograded within the Late Pleistocene-Holocene Unit (see Fig. 3, for example near the trenches location), crossing and concealing the fault scarps in some areas (Fig. 3). This is in agreement with higher lake levels -with respect to the Early Holocene- in the region since 5700 yr BP and especially after 3200 yr BP (Jenny et al., 2002), due to the onset of the influence of the modern El Niño episodes -warm phases of ENSO- that generally produces torrential rainfall episodes inducing alluviation along the subtropical western slope of South America (Jenny et al., 2002; Vargas et al., 2006).

### GEOMORPHOLOGY OF FLUVIAL TERRACES

Fluvial terraces located along the Mapocho and Maipo River valleys exhibit greater development once approaching the tectonic front associated to the San Ramón Fault (Fig. 3). In the Maipo River valley these terraces are particularly well exposed and have been grouped in 4 units, named T1 (the youngest), T2, T3 and T4 (the oldest). These terraces are characterized by fluvial and alluvial deposits with interbedded volcanic layers over erosional surfaces on rock substratum. The maximal ages obtained from ongoing OSL analyses from T1, T2 and T3 are 3-1 ka, 22-17 ka, and 86 ka, respectively; for T4 we suspect a Middle Pleistocene age based on extrapolation of incision rates estimated from the previous (Fig. 3). Together with the geomorphology of these terraces the geochronological data suggest increasing incision rates from upstream toward the tectonic front associated to the Quaternary activity of the fault, especially in the case of T2 and T3 which are well exposed and dated in this area (Fig. 3). T3 is, in particular, affected by a fault scarp and suggests a tectonic vertical offset in the order of 0.4 m/ka in the last ca. 86,000 years. The ages of T2 and T1 closely matches those found from piedmont units, suggesting also a climate control on their origin, similarly to the previous discussion. T1 is particularly well exposed upstream but exhibits scarce outcrops evidencing intense erosional processes in the area of the tectonic front.

### IMPLICATIONS FOR THE CHILEAN SEISMIC CODE AND URBAN DEVELOPMENT-NORMATIVE

Together with the previous observations (Armijo et al., 2010; Vargas et al., 2014), the new available data support the consistency of the geomorphologic tectonic markers

associated to the Late Quaternary activity of the San Ramón Fault along the entire piedmont of Santiago valley between the Mapocho and Maipo rivers. In addition to that, it's necessary to consider recent geophysical and seismological observations that revealed the structure at subsurface (Díaz et al., 2014), and the seismically active character of this fault system (Pérez et al., 2014), respectively. Thus, the available observations evidence the urgency to include changes in the Chilean Seismic Code (NCh433), as well as in urban development policies, particularly in the *Plan Regulador Metropolitano de Santiago*, to consider the possibility for crustal earthquakes and superficial rupture along active structures such as this fault, as already suggested in previous report (Seremi Minvu, 2012). One example of the relevancy of this matter is the seismic swarm occurred in 2007 along the intra-arc transpressional Liquiñe-Ofqui Fault System in the Patagonian Andes of Southern Chile, which included a  $M_w$ 6.2 earthquake that induced landslides, local tsunami waves and submarine superficial rupture causing destruction and fatalities in the Aysén Fjord, close to the city of Puerto Aysén (Legrand et al., 2011; Vargas et al., 2013).

From the available geochronological results, and taking the geomorphological and chronostratigraphic coherency of tectonic markers, it is possible to estimate a time-dependent earthquake probability of ca. 3% for the occurrence of a -characteristic- large earthquake with superficial rupture, similar to what we observed in the paleoseismological trenches, in the next hundred years.

**Acknowledgements:** Author thank project "Estudio de riesgo y modificación PRMS Falla San Ramón" (Seremi Minvu, 2012, Chilean Government). Additional funds from Centro de Excelencia de Geotermia de Los Andes (CEGA; Fondap project 15090013) are also acknowledged.

### References

- Armijo, R., R. Rauld, R. Thiele, G. Vargas, J. Campos, R. Lacassin & E. Kausel (2010). The West Andean Thrust, the San Ramón Fault, and the seismic hazard for Santiago, Chile. *Tectonics* 29, TC2007, doi:10.1029/2008TC002427.
- Díaz, D., A. Maksymowicz, G. Vargas, E. Vera, E. Contreras-Reyes & S. Rebolledo (2014). Exploring the shallow structure of the San Ramón thrust fault in Santiago, Chile (~33.5°S), using active seismic and electric methods. *Solid Earth* 5, 837-849, doi:10.5194/se-5-837-2014.
- Jenny, B., B.L. Valero-Garcés, R. Villa-Martínez, R. Urrutia, M.A. Geyh & H. Veit (2002). Early to mid-Holocene Aridity in Central Chile and the Southern Westerlies: The Laguna Aculco Record (34°S). *Quaternary Research* 58, 160-170, doi: 110.1006/qres.2002.2370.
- Legrand, D., Barrientos, S., Bataille, K., Cembrano, J. & A. Pavez (2011). The fluid-driven tectonic swarm of Aysén Fjord, Chile (2007) associated with two earthquakes ( $M_w$ 6.1 and  $M_w$ 6.2) within the Liquiñe-Ofqui Fault Zone. *Continental Shelf Research* 31, 154-161.
- Ormeño, A. (2007). Geomorfología dinámica del río Maipo en la zona cordillerana de Chile central e implicancias neotectónicas. Ms.Sc. Thesis, Universidad de Chile, 147 p.



Pérez A., J.A. Ruiz, G. Vargas, R. Rauld, S. Rebolledo & J. Campos (2014). Improving seismotectonics and seismic hazard assessment along the San Ramón Fault at the eastern border of Santiago city, Chile. *Natural Hazards* 71, 243-274, doi: 10.1007/s11069-013-0908-3.

Rauld, R.A. (2011). Deformación Cortical y Peligro Sísmico Asociado a la Falla San Ramón en el Frente Cordillerano de Santiago, Chile Central (33° S). PhD Thesis, Universidad de Chile, 311 p.

Seremi Minvu (2012). Estudio riesgo y modificación PRMS Falla San Ramón, IDN°640-27-LP10, Resumen Ejecutivo, 38 p.

Valero-Garcés, B.L., B. Jenny, M. Rondanelli, A. Delgado-Huertas, S.J. Burns, H. Veit & A. Moreno (2005). Palaeohydrology of Laguna de Tagua Tagua (34°30pS) and moisture fluctuations in Central Chile for the last 46 000 yr. *Journal of Quaternary Science* 20(7-8), 625-641, doi:10.1002/jqs.1988.

Vargas, G., Rutllant, J. & L. Ortlieb (2006). ENSO tropical-extratropical climate teleconnections and mechanisms for Holocene debris flows along the hyperarid coast of western South America (17-24°S). *Earth and Planetary Science Letters* 249(3-4), 467-483.

Vargas, G., Rebolledo S., Sepúlveda S., Lahsen, A., Thiele R., Townley B., Padilla C., Rauld R., Herrera M. & M. Lara (2013). Submarine earthquake rupture, active faulting and volcanism along the major Liquiñe-Ofqui Fault Zone and implications for seismic hazard assessment in the Patagonian Andes. *Andean Geology* 40(1), 141 -171.

Vargas G., Y. Klinger, T. Rockwell, S.L. Forman, S. Rebolledo, S. Baize, R. Lacassin, R. Armijo (2014). Probing large intra-plate earthquakes at the west flank of the Andes. *Geology*, doi:10.1130/G35741.1.

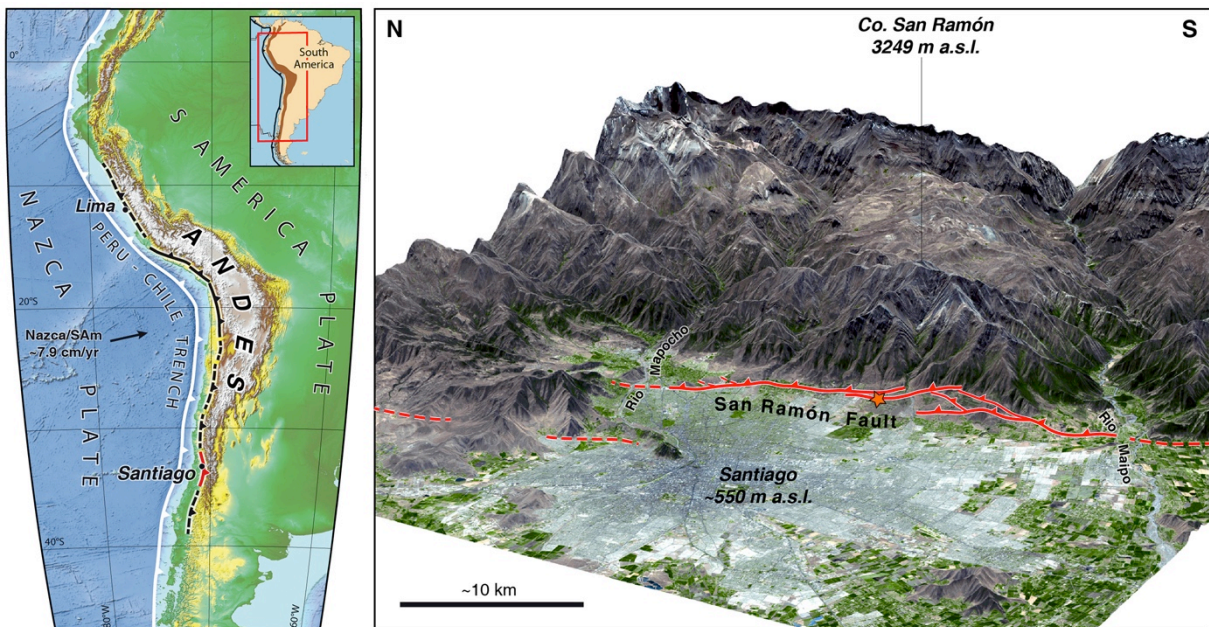


Fig. 1: Tectonic and geomorphologic context of the San Ramón Fault at the eastern border of Santiago, capital city of Chile. San Ramón Fault is a part of a major tectonic system, the West Andean Thrust, located at the western border of the main Andes Cordillera (Armijo et al., 2010). Star shows the location of paleoseismological trenches dug across a prominent young fault scarp (Vargas et al. 2014).

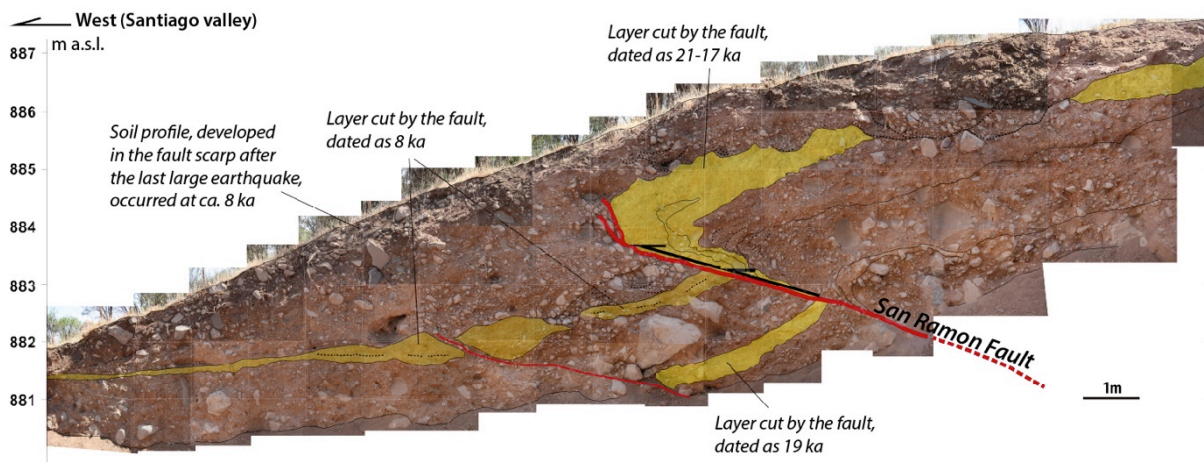


Fig. 2: Simplified version of a paleoseismological trench dug across a young fault scarp in the San Ramón Fault (Vargas et al., 2014).

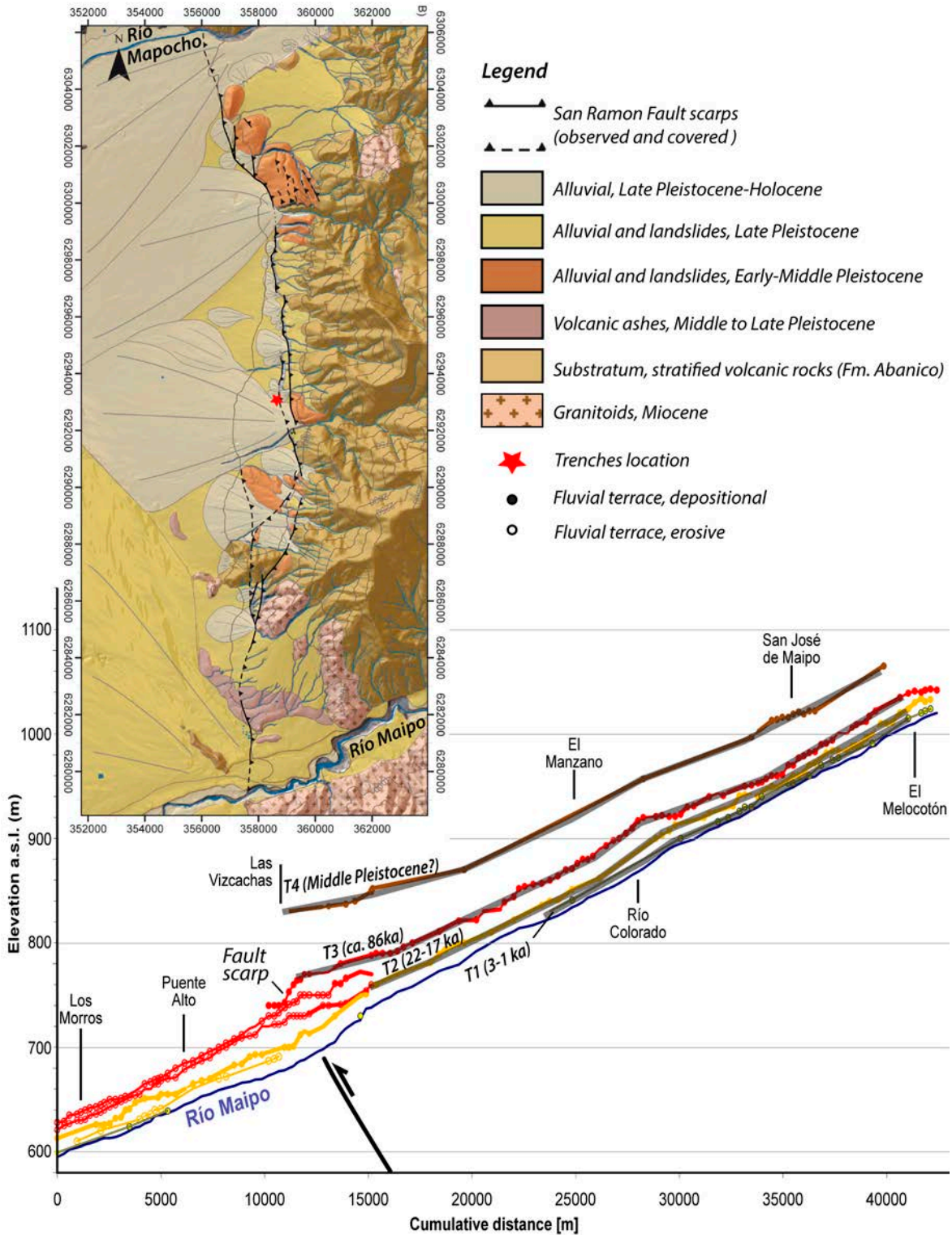


Fig. 3: Geomorphological chart of the piedmont at the eastern border of Santiago valley between the Mapocho and Maipo rivers, showing the three main alluvial units cut by the fault and the location of the paleoseismological trenches. The longitudinal profile shows the main fluvial terraces of the Maipo river (Ormeño, 2007; Rauld, 2011; this work).



## New evidences of the crustal origin of the seismic crisis of 2007 in the Aysén Region, Southern Chile

Angelo Villalobos-Claramunt (1), Gabriel Vargas (1), Andrei Maksymowicz (2), Galderic Lastras (3)

(1) Departamento de Geología, Facultad de Ciencias Físicas y Matemáticas, Universidad de Chile, Plaza Ercilla 803, Santiago, Chile. Email: angelovillalobos42@ug.uchile.cl

(2) Departamento de Geofísica, Facultad de Ciencias Físicas y Matemáticas, Universidad de Chile, Av. Blanco Encalada 2002, Santiago, Chile.

(3) Geociències Marines, Universitat de Barcelona, Barcelona E-08028, España.

**Abstract.** On April 21, 2007, a 6.2 Mw earthquake hit the Aysén Region, Southern Chile. This event corresponds to the largest earthquake in a sequence that started to be perceived on January 10, 2007, with a  $M_L < 3$  tremor and continued until February 2008. The affected area is characterized by the presence of the Liquiñe-Ofqui Fault Zone (LOFZ), corresponding to the main neotectonic and seismotectonic feature of Southern Chile. Here, we present new evidences obtained using reflection seismic profiles and high-resolution bathymetry that let us to constrain the seismic source to a crustal origin. It is established that the Punta Cola Fault (PCF), a branch of the LOFS, was responsible for the mainshock and generated surface rupture with fault scarps on the seafloor. Finally, identifying paleo-mass removals, we propose that at least three similar events have occurred in the area since the retreat of the glacier ice cap 12 ky ago.

**Keywords:** Aysén Earthquake, Liquiñe-Ofqui Fault Zone, Punta Cola Fault, surface rupture, seismic reflection method.

### INTRODUCTION

The Liquiñe-Ofqui Fault Zone (LOFZ) is a major transpressive fault system associated to Quaternary volcanoes along more than 1,000 km in the Patagonian Andes (Cembrano and Lara, 2009; Cembrano et al., 2002). This is a dextral structure sub-parallel to the Perú-Chile Trench which absorbs part of the oblique convergence between the Nazca and South America plates, additionally controlling the distribution of the Quaternary volcanic centres (Cembrano and Lara, 2009; Cembrano et al., 2002). The Aysén Fjord is a classical U-shaped submerged glacial valley oriented E-W to NW-SE characterized by steep slopes (Oppikofer et al., 2012) developed on granitoids of Cenozoic age and crossed by the LOFZ. In this area, the LOFZ is expressed like a duplex that includes the Punta Cola (PCF), Río Cuervo (RCF) and Quitralco (QF) faults, with both subaerial and subaqueous geomorphic Quaternary units as well as stratovolcanoes and monogenetic volcanic cones aligned or affected by the fault (Vargas et al., 2013). One of these volcanic features corresponds to the Cuervo Ridge located on the western boundary of the inner fjord, striking NE-SW (Figures 1, 2 and 3). Within this ridge has been inferred the presence of a submarine basaltic monogenetic cone (Lara, 2008), also elongated NE-SW, whose presence can be explained by local extension along a secondary fault (Vargas et al. 2013).

During 2007, a seismic crisis spans several months and included a major crustal Mw 6.2 earthquake which induced large landslides that generated local tsunami waves up to 10-40 m height (Van Daele et al., 2013). From geomorphic, structural and subaqueous observations, Vargas et al. (2013)

proposed that this last seismic crisis occurred along the LOFZ and that the major earthquake rupture, which reached the surface at the sea bottom, was produced along the N-S Punta Cola Fault, causing the largest landslides and subsequent tsunami waves. Van Daele et al. (2013) characterized the deformation and subaqueous features observed in the sea bottom as associated mostly to the penetration of the landslides into the fjord.

Here, from the analysis of seismic profiles and high resolution bathymetry data (Lastras et al., 2013), we focus on the last and previous superficial ruptures in the Aysén Fjord as well as on the implications of this findings for seismic hazard assessment in the Aysén region

### EVIDENCE OF SURFACE RUPTURE

A high resolution bathymetry (Figure 1) was used to identify the presence of topographical discontinuities in the seafloor, which have a generally rectilinear geometry with some slightly curved sections. These features have a similar orientation and in some cases are aligned with the structures mapped by Vargas et al. (2013). High density of escarpments can be observed on the northern flank of the fjord, 3.6 km NW from the Mentirosa Island, where the largest landslide was deposited (Oppikofer et al., 2012; Van Daele et al., 2013). These are characterized by two types of geometry, a set of sharp curved escarpments 370-750 m length that limit and enter into the landslide previously mapped (Van Daele et al., 2013; Lastras et al., 2013), and longitudinal sharp escarpments oriented NNE. It is proposed that the first group of scarps are related to the deposition of the landslide due to internal thrusting of the material,



while the second group resulted from the superficial

rupture associated to the mainshock.

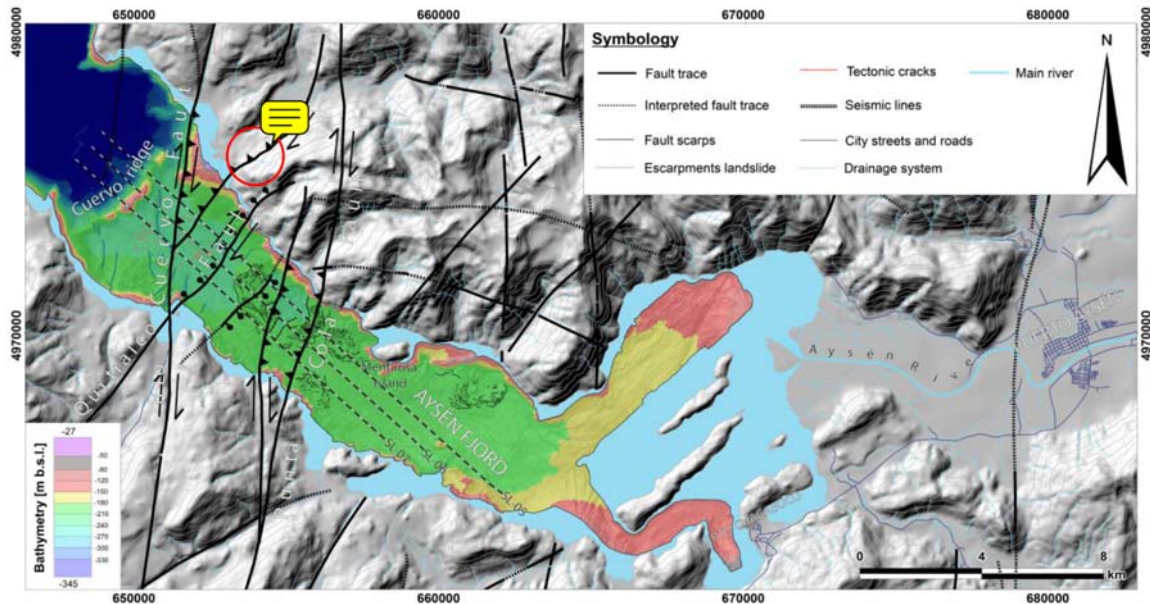


Fig. 1: Location of the sub-bottom seismic profiles obtained from the Aysén Fjord in the area of the 2007 seismic swarm and subaerial and submarine reliefs shown by the means of a Digital Elevation Model, based on 1:50,000 topographic sheets from the Chilean Army Geographic Institute (IGM) and bathymetric surface from DEFUTSA campaign. SLn: Seismic Line n.

The observation of seismic profiles revealed the main active structures that cut the sedimentary Late Pleistocene-Holocene infill of the fjord (Vargas et al., 2013). In the area where the dextral reverse ~ 20 km length Punta Cola Fault (PCF; Vargas et al., 2013) is projected into the fjord, we found a positive cross flower geometry affecting sediments (Figures 2 and 3), which narrows from north to south and presents an abrupt decrease in associated escarpments in the vicinity to the southern flank of the fjord. This is the most important structure studied in this work, characterized by complex deformation in sediments and with the largest volumetric strain. The vertical separation of the reflectors affected by the fault vary between ~ 2.1 and ~ 5.8 m. Reflectors are affected in deep and we observed also two more configurations with chaotic seismic facies similar to what resulted during the last seismic crisis at surface.

Approximately 2.5 km to the NW of the PCF we found the QF, one of the main branches of LOFZ characterized by a NE-SW orientation and dextral-normal kinematics (Cembrano et al., 2002, Thompson, 2002). Subsurface deformation in seismic profiles is characterized by a single vertical fault trace (Figures 2 and 3) with reflectors affected by the fault and separated between ~ 4 and ~ 4.8 m, showing maximum vertical offsets in deep and decreasing once approaching to the tip at surface.

The RCF, which is a dextral-reverse fault with NS orientation and ~ 40 km length (Vargas et al., 2013),

corresponds to the structure located in the vicinity of the Cuervo Ridge and is associated to several seismic sources with magnitudes  $M_w \leq 3.0$ . At subsurface it is expressed as two branches which generate a small pop-up (Figure 4) with vertical separations of reflectors ranging from ~ 1.4 to ~ 4.8 m. Similarly to the previous structure, it exhibits vertical displacements of the reflectors decreasing towards the tip of the rupture at surface.

## DISCUSSION

### ORIGIN OF THE SCARPS

The consistency between the observations from bathymetry and from seismic profiles points to a distinct origin for curved and rectilinear escarpments. The first are related to the quasi-instantaneous deposition of large submarine landslides, particularly associated to the large rockslide generated near Punta Cola (Oppikofer et al., 2012; Van Daele et al., 2013), producing fold-and-thrust structures and associated detachment located at 0.35-0.38 s (Figures 2 and 3). The second group, mostly rectilinear escarpments with higher vertical offsets, can be associated to a tectonic origin resulted from the expression at surface of the PCF's branches, evidencing also an after slip component in the strain, associated to the mainshock. The discrimination of these two types of submarine escarpments improves previous sedimentological (Van Daele et al., 2013) and tectonic (Vargas et al., 2013) interpretations.

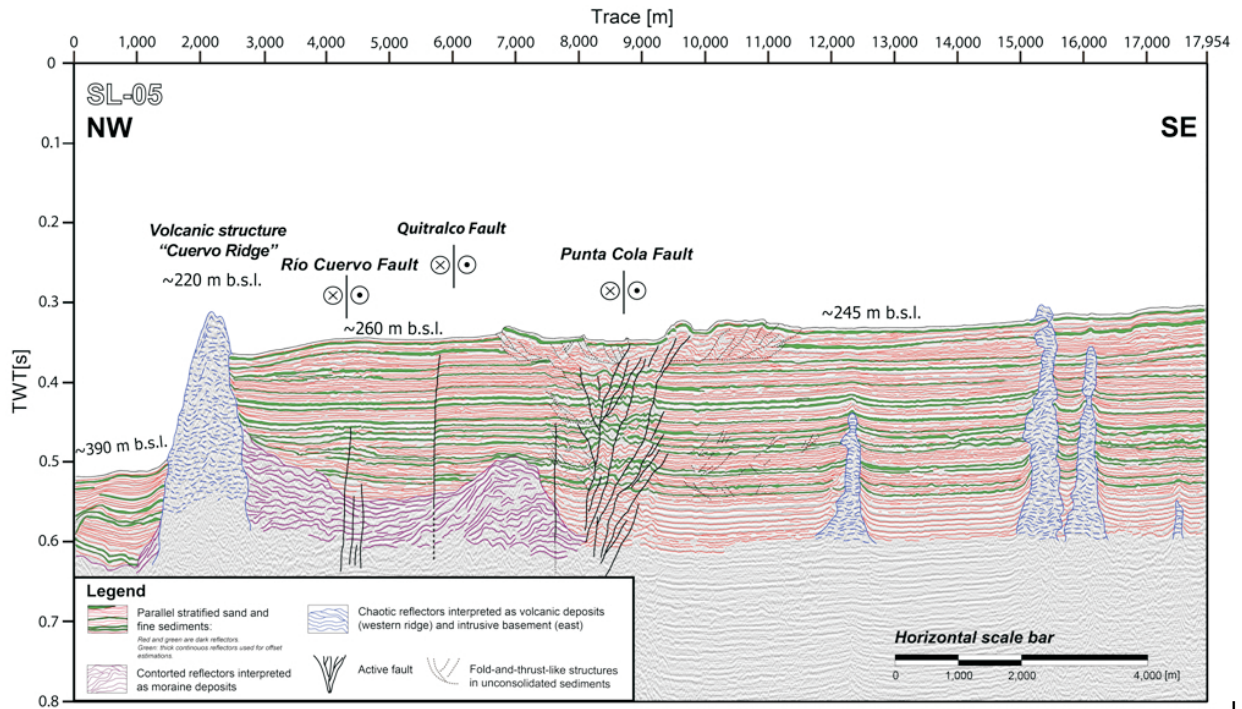


Fig. 2: Sub-bottom profile 5 (SL-05, Fig. 1). Interpretation realized on a sub-bottom profile. Vertical axis is in TWT (s). Green reflectors were used to calculate vertical offsets.

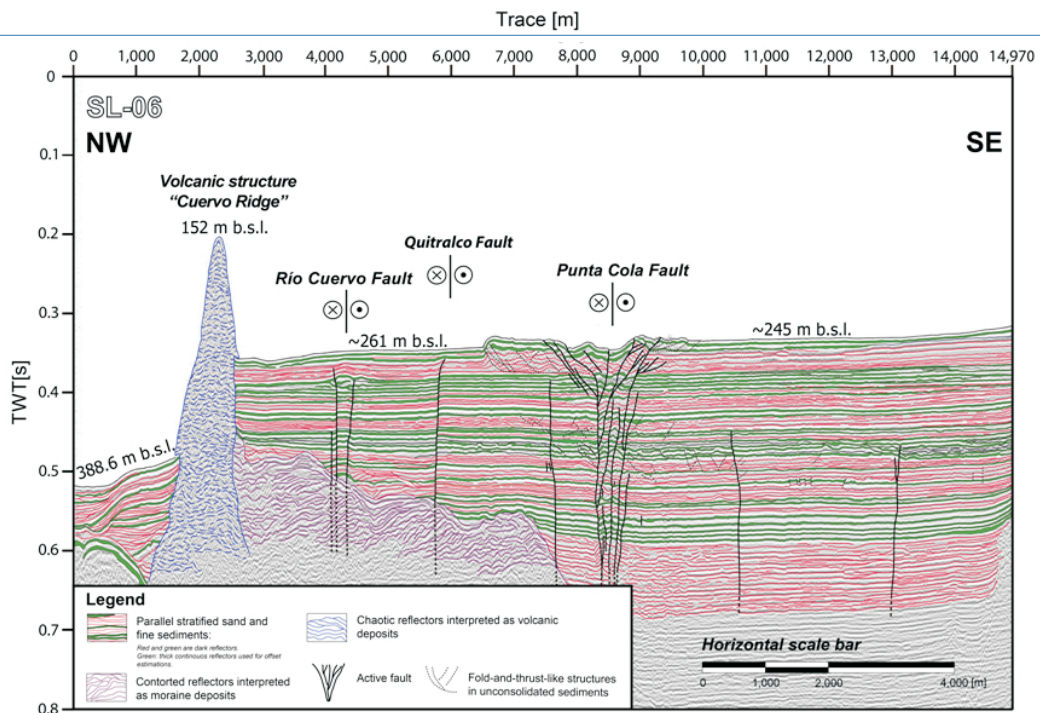


Fig. 3: Sub-bottom profile 6 (SL-06, Fig. 1). Interpretation realized on a sub-bottom profile. Vertical axis is in TWT (s). Green reflectors were used to calculate vertical offsets.

### EVIDENCES OF PALEO-EARTHQUAKES

The net displacement for the PCF as well as the two branches associated to the RCF were calculated/estimated using its vertical displacements

and rakes in nearby fault outcrops previously reported in the study area (Vargas et al., 2013). QF was not evaluated because we do not have any rake data. In the case of the PCF we only considered vertical displacements at its external branches,



because these structures define the boundary between the blocks that have been displaced by the fault zone, also we have selected with extreme caution the values on the top of the deformed reflectors to avoid the possible influence of fold-and-thrust-like structures in the estimations. These values of these estimates varies between  $\sim 2.1(9,01E-04)$  s and  $\sim 8.71$  m ( $6,45E-03$  s) with  $n = 23$ , in the case of the PCF. For RCF the average results for each vertical displacement at the fault trace (with  $n = 13$ ) correspond to  $\sim 5.24$  ( $3,94E-03$  s) and  $\sim 1.02$  m ( $6,12E-04$  s).

We used the Wells and Coppersmith (1994) empirical equations that link the displacement of a strike-slip fault with the moment magnitude of the earthquakes that it can generate, to assess the seismic potential of the faults. The results obtained are in apparent discrepancy with the magnitudes of the seismic events recorded during the seismic crisis (Agurto et al., 2013). This results from the fact that the vertical offsets recorded in the seismic profiles most likely correspond to an accumulation of multiple paleo-earthquakes and not only to the last event in 2007. As an example, evaluating the displacement that could be associated to the mainshock by using the same equations of Wells and Coppersmith (1994), we obtained 0.79, 0.49 and 0.59 m for reverse, strike-slip, and all kind of faults, respectively. Then, for the accumulated displacement observed today a considerable amount of paleo-earthquakes of the same magnitude or, alternatively, larger earthquakes are needed.

## CONCLUSION

We conclude that the 2007 seismic crisis in Aysén Fjord resulted from crustal deformation associated to active faulting along the main branches of the LOFZ, and that the Mw 6.2 earthquake was nucleated along the PCF causing surface rupture. Deformation of sediments in the Aysén Fjord, either directly affected by fault or associated to former submarine landslides deposits, evidence previous seismic surface ruptures particularly along the PCF, QF and RCF in the last 12,000 years, at least following the last ice sheet retreat, according radiocarbon results from volcanic ash layers overlaying glacial sediments in the area (Vargas et al., 2013).

**Acknowledgements:** We thank the research team and the crew of the DEFUTSA campaign to acquire and provide seismic and bathymetric data that made this work possible. Also we thank the support and reiterative help of the CEGA program. Finally, we appreciate the financial support of CONICYT, through its national scholarship PhD program.

## References

Agurto, H., Rietbrock, A., Barrientos, S., Bataille, K., Legrand, D. 2013. Seismo-tectonic structure of the Aysén Region, Southern Chile, inferred from the 2007 Mw = 6.2 Aysén earthquake sequence. *Geophysical Journal International*: 1-15.

- Cembrano, J., Lara, L. 2009. The link between volcanism and tectonics in the southern volcanic zone of the Chilean Andes: A review. *Tectonophysics* 471: 96-113.
- Cembrano, J., Lavenue, A., Reynolds, P., Arancibia, G., Lopez, G., Sanhueza, A. 2002. Late Cenozoic transpressional ductile deformation north of the Nazca-South America - Antarctica triple junction. *Tectonophysics* 354: 289-314.
- Lara, L. 2008. Holocene submarine volcanoes in the Aysén fjord, Patagonian Andes (44°S): Relations with the Liquiñe-Ofqui Fault Zone. *In* International Symposium on Andean Geodynamics (ISAG), No. 7, Abstracts Volume: 285-288. Nice.
- Lastras, G., et al. 2013. Landslides Cause Tsunami Waves: Insights From Aysén Fjord, Chile. *Eos Trans. AGU*, 94(34), 297
- Oppikofer, T., Hermanns, R.L., Redfield, T.L., Sepúlveda, S.A., Duhart, P., Bascañán, I. 2012. Morphologic description of the Punta Cola rock avalanche and associated minor rockslides caused by the 21 April 2007 Aysén earthquake (Patagonia, southern Chile). *Revista de la Asociación Geológica Argentina* 69 (3): 339 – 353.
- Thomson, S. 2002. Late Cenozoic geomorphic and tectonic evolution of the Patagonian Andes between latitudes 42°S and 46°S: An appraisal based on fission-track results from the transpressional intra-arc Liquiñe-Ofqui fault zone. *Geological Society of America Bulletin* 114 (9): 1159-1173.
- Vargas, G., Rebolledo, S., Sepúlveda, S.A., Lahsen, A., Thiele, R., Townley, B., Padilla, C., Rauld, R. Herrera, M.J., Lara, M. 2013. Submarine earthquake rupture, active faulting and volcanism along the major Liquiñe-Ofqui Fault Zone and implications for seismic hazard assessment in the Patagonian Andes. *Andean Geology* 40 (1): 141-171.
- Van Daele, M., Versteeg, W., Pino, M., Urrutia, R. De Batist, M. 2013 Widespread deformation of basin-plain sediments in Aysén fjord (Chile) due to impact by earthquake-triggered, onshore-generated mass movements. *Marine Geology* 337: 67–79.
- Wells, D.L., Coppersmith, K.J. 1994. New empirical relationships among Magnitude, Rupture Length, Rupture Width, Rupture Area, and Surface Displacement. *Bulletin of the Seismological Society of America* 84 (4): 974-1002.



## On the accuracy of topographic models derived from UAV photography

Neta Wechsler (1), Oded Katz (2), Amit Mushkin (2)

- (1) Department of Geosciences, Tel-Aviv University, Israel. netawe@post.tau.ac.il  
(2) Geological Survey of Israel, Jerusalem, Israel

**Abstract:** We use the new structure from motion approach in conjunction with UAV mapping in 2 sites, a devegetated valley and a collapsing coastal cliff. We show that in unconventional settings, UAV can perform with adequate accuracy and has the advantage of being low-cost, rapid and easy to utilize. Some sources of error are demonstrated and discussed.

**Key words:** Structure-from-Motion mapping, Coastal retreat, DEM, point clouds.

### INTRODUCTION

The use of automated photogrammetric methods to generate topographic models have become ubiquitous in recent years (Bemis et al. 2014, James & Robson, 2012; Westoby et al., 2012), a result of increasing availability of UAVs (unmanned aerial vehicles) equipped with high resolution digital cameras, of commercial and open-source processing software and of rising computing power. The cost of conducting a Structure-from-Motion (SfM) DEM model is now a small fraction of the cost of Airborne Lidar (ALSM) and takes considerably less time than using ground based Lidar (TLS) (Castillo et al. 2012). This allows for rapid-response mapping of geomorphic features, such as surface ruptures, extreme deposition /erosion events, etc. The accuracy of SfM mapping depends on many variables such as ground control, quality and number of images, shot angles and the site's dimensions (James & Robson, 2014, Johnson et al. 2014, Reitman et al. 2015). Due to the relative rapidity of acquisition and low costs, one of the emerging applications for SfM mapping is monitoring relatively short-term geomorphic changes by comparing time series. The results of such comparisons are highly dependent on the accuracy of SfM maps, and systematic model errors can induce further errors in the estimate of the changes. Here we compare topographic models acquired over various terrains using active (ALSM/TLS) and passive (SfM) mapping methods and discuss the merit of UAV-based models in different environments. Our goal is to establish the accuracy of UAV based SfM terrain modeling for repeat surveys, where the focus is capturing geomorphic changes over time.

#### Study areas

**Beteiha valley:** The first case study is located at the northern shores of the Sea of Galilee, Israel (Fig. 1a), where the Jordan River flows into the lake. An area of ~1 km<sup>2</sup> was recently devegetated by the Israel Park Service, offering a unique opportunity to map a part of the Dead Sea fault which crosses the valley (Wechsler et al. 2014) and was obscured by vegetation beforehand. A UAV

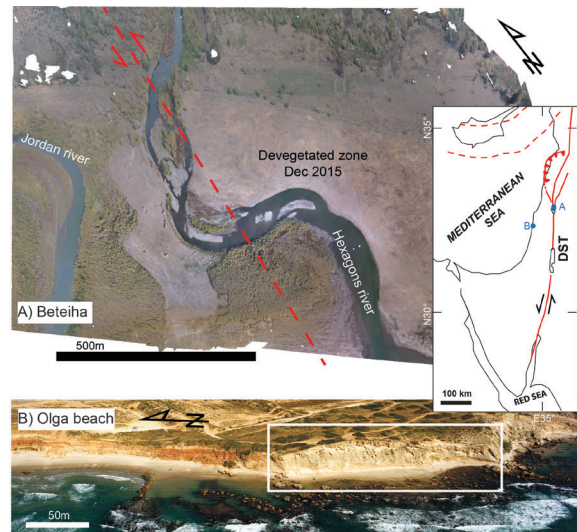


Fig. 1: Study areas. A) High resolution orthophoto generated from UAV photography above the Beteiha valley. The Dead-Sea fault is marked by dashed red line. B) The coastal cliffs at Olga beach. The white rectangle marks the study area, one of the sites where the cliff is being monitored along the Israel coast. Notice the narrow sand strip along the coast and the fallen boulders in the water. SfM mapping methods cannot map water surface due to changing light conditions. General location map on the right.

survey was conducted in the fall, before winter growth, in order to map the geomorphic signature of the fault. The mapped area was ~0.8 km<sup>2</sup>. A total of 380 photos were taken during 2 consecutive flights, covering the region of denudation.

**Coastal cliffs at Olga beach:** The second site is along the coastal cliffs of Israel (Fig. 1b). Here, the cliff is ~150m long and up to 20m high, and is composed of late-Pleistocene to Holocene age carbonate-cemented eolianites and paleosol layers (Yaalon, 1967). The cliff have been monitored for rate of retreat over several years using TLS surveys (Katz & Mushkin, 2013), ALSM being less useful for vertical cliff faces. A UAV mapping campaign was conducted along part of the cliff by the Geological Survey of Israel (GSI) as part of a multi-year



project for monitoring retreat rates along the coastal cliffs of Israel.

#### Data acquisition and processing workflow

We used a DJI Phantom-2-Vision 4-rotor drone with built-in 14 Megapixel camera for capturing over 350 photos during two flights at the Beteiha site, and the services of a commercial company (Terrascan labs) at the cliffs of Olga (herein termed Olga site), where they flew a UAV in January 2016. The DJI drone photos were processed according to the workflow outlined by Johnson et al. (2014), using Agisoft photoscan® to construct the point clouds from the photos and GEONpoints2grid utility to create high resolution DEMs. The commercial product included a filtered LAS point cloud and 4cm DEM raster which we had to register to the other datasets. We used Matlab® codes for cloud comparisons and ArcGIS Desktop for DEM comparisons. The ALSM DEM was acquired by the Geological Survey of Israel (GSI) and the TLS cloud was measured using Leica ScanStation2 at the beginning of 2015. Several ground control points were measured using RTK GPS at the Beteiha site. All UAV-generated clouds had very large point density – more than  $10^5$  points per  $m^2$ . This enabled us to create 5-10 cm per pixel DEM models almost without holes.

#### Direct cloud comparisons

At the **Beteiha** site we compare two consecutive flights processed separately, in order to examine the repeatability of the UAV mapping campaign. The two flights covered slightly different tracts and so we only compare the overlapping region, which included the degreaved region and the control points. We chose a

reference cloud and for each point computed the distance to its nearest neighbor in the other cloud (Fig 2.). This produces an unsigned distance value for each point in the reference cloud. As seen in Fig 2B, 95% of the distance values are smaller than 1.5m. Outliers include trees and area edges where clouds do not overlap, where larger differences can be seen. One significant error is an artifact in the middle of the model (Fig. 3), which might be the result of unfavorable shot angles which created some distortion (a hump) in one of the clouds (see James and Robson 2014). We therefore use the cloud without the hump as the data source for the DEM. The average error was 0.52m for direct cloud to cloud comparison, which is compatible with previously measured errors for areas on the order of 1  $km^2$  (James & Robson 2012, Johnson, 2014).

At the **Olga** site we compare the UAV to the TLS cloud (Fig. 3). We use the TLS as the reference cloud because it covered less of the cliff than the UAV. Due to the 18 month difference in acquisition, the later dataset (UAV) captured a large material slump that occurred between acquisitions. Here, 95% of the points were less than 1.2m away from each other, which is high given the scale of the cliff, but the average error is 0.33m, comparable to the results of James and Robson (2012). Sources of error include the slump, boulders moved by the sea, and registration errors (both clouds were not registered and had to be tied manually). Katz & Mushkin (2013) estimate the error between consecutive TLS scans to be less than 0.1m, making the UAV accuracy smaller than the TLS. However, the TLS suffers from line-of-sight obscuring and is more cumbersome and time consuming to operate. Additionally, some of the differences between the clouds can be improved upon by careful registration to a permanent reference frame.

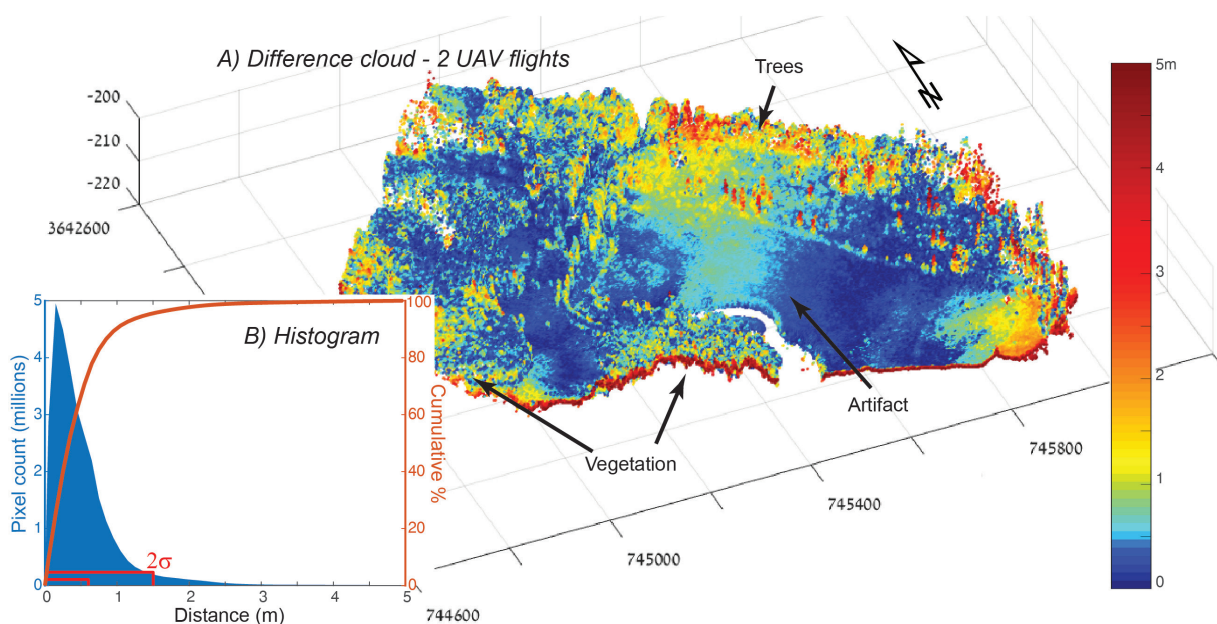


Fig. 2: Point clouds comparison for the Beteiha site. A) The points of a reference cloud, coloured by distance to nearest neighbouring point in the other cloud, plotted in 3D with x10 vertical exaggeration. B) A histogram of the distance distribution and cumulative percentage,  $1\sigma$  and  $2\sigma$  are marked in red.



*Topographic model (DEM) comparisons*

At the **Beteiha** site we use a 0.5m per pixel ALSM DEM product that was cleaned of vegetation returns during processing to compare with a 0.1m per pixel DEM model derived from the UAV cloud without the distortion artifact in the central area (Fig. 4), limited to a region where the point-count per pixel was larger than 3. There is a systematic error where the UAV model heights are higher than the ALSM model heights (dark red areas) in an area that was not devegetated, representing growth during the period between acquisitions. Focusing solely on the bare earth areas, the height difference is small, less than  $\pm 0.5m$ , showing very good agreement between the UAV and the ALSM models. Comparing the UAV model with an ALSM model without vegetation cleaning shows clearly the area where vegetation was removed, and we can actually estimate the amount of bio-matter removed. The SfM method cannot penetrate through foliage, as opposed to LiDAR measurements, which is one of its drawbacks, but its rapid deployment enabled capturing a model of the denudated earth.

At the **Olga** site we compare a 0.5m per pixel ALSM DEM with a 0.04m per pixel cloud derived product (Fig. 5). Due to the structure and topography of the coastal cliff, the DEM does not adequately represent the complexity of the cliff face, as it cannot model overhangs. Nevertheless, a comparison was made in order to examine the quality of the UAV DEM. One source of error was the UAV model lack of registration, and although we manually registered it to the ALSM DEM, there were mismatches in the vicinity of the cliff face and the boulders below it, as seen by the apparent movement of the boulders on the upper left part of Fig. 5. Additionally, here is an apparent removal of material at the center of the cliff, where a slump would have added material

rather than removed it. This error in cliff morphology is attributed to the limited ability of ALSM to model steep terrain (Johnson et al., 2014). All in all, the models are very similar with 95% of the points falling within 1m of each other and an average error of 0.31m per pixel, smaller than the spatial resolution of the ALSM. Here the UAV mapping method outperforms the ALSM in terms of modeling the cliff face and is better suited for monitoring coastal cliff retreat rates.

*Summary*

UAV mapping was used in two different environments and its absolute and relative accuracy was examined. We find in order to ensure best results, it is crucial to register the product using an adequate number of control points (Reitman et al. 2015). The level of accuracy depends on the scale of the mapped area and on the shot angles of the camera, among other things. The importance of shot-angles is demonstrated, by showing that even if the same camera is used over the same terrain at the same day and the clouds are registered with the same control points, the resulting models can be different. If an SfM mapping campaign is planned for long term change measurements, and it is not possible to use fixed markers for different scans, then it is advisable to register each model by accurately measuring control points and using the same frame of reference (i.e. total station, differential GPS, etc.) for the duration of the campaign. UAV mapping is becoming more accessible and prevalent in earth science research, so by acquainting ourselves with its capabilities and limits we can utilize this amazing tool better.

**Acknowledgements:** This project was partially supported by a GSI grant to O. Katz and A. Mushkin. The drone was generously loaned by the Dept. of Archaeology, Tel-Aviv University.

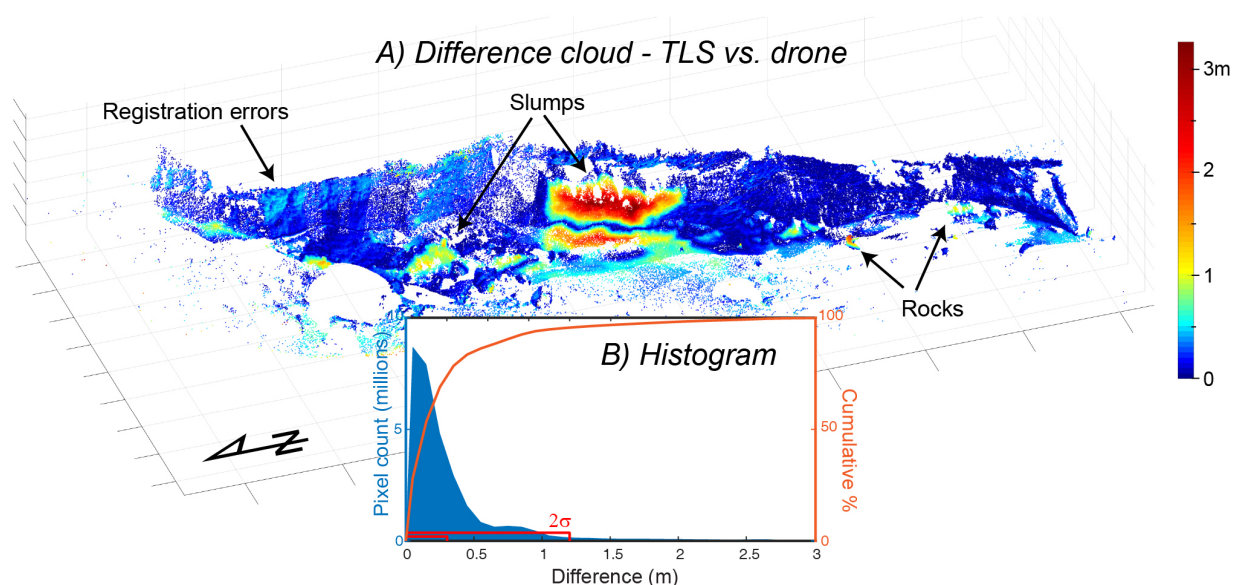


Fig. 3: Point cloud comparisons for the Olga site. A) & B) are the same as in Fig. 2. The TLS cloud did not cover the upper edge of the cliff and there are holes in the data due to line-of-site obscuring. The November 2015 slump is clearly seen, as well as smaller slumps. The narrowness of the beach limits the distance from which a TLS station can be operated but does not limit the UAV.



**References**

Bemis, S., S. Micklethwaite, D. Turner, M.R. James, S. Akciz, S. Thiele, and H.A. Bangash (2014). Ground-based and UAV-based photogrammetry: A multi-scale, high resolution mapping tool for structural geology and paleoseismology, *J. Struct. Geol.* 69, 163–178.

Castillo, C., R. Pérez, M.R. James, N.J. Quinton, E.V. Taguas, and J.A. Gómez (2012). Comparing the accuracy of several field methods for measuring gully erosion. *Soil Science Society of America Journal* 76, 1319–1332.

James, M.R., and S. Robson (2012). Straightforward reconstruction of 3D surfaces and topography with a camera: accuracy and geoscience application. *J. Geophys. Res.* 117, F03017.

James, M.R., and S. Robson (2014). Mitigating systematic error in topographic models derived from UAV and ground-based image networks. *Earth Surf. Process. Landf.* 39, 1413-1420.

Johnson, K., E. Nissen, S. Saripalli, J.R. Arrowsmith, P. McGarey, K. Scharer, P. Williams, and K. Blisniuk (2014). Rapid mapping of ultrafine fault zone topography with structure from motion. *Geosphere* 10(5), 969-986.

Katz, O., & A. Mushkin (2013). Characteristics of sea-cliff erosion induced by a strong winter storm in the eastern Mediterranean. *Quaternary Research*, 80(1), 20-32.

Reitman, N. G., S. E. Bennett, R. D. Gold, R. W. Briggs, & C. B. DuRoss (2015). High-Resolution Trench Photomosaics from Image-Based Modeling: Workflow and Error Analysis. *Bulletin of the Seismological Society of America*, 105, 2354-2366.

Wechsler, N., T. K. Rockwell, Y. Klinger, P. Štěpančíková, M. Kanari, S. Marco, & A. Agnon (2014). A paleoseismic record of earthquakes for the Dead Sea transform fault between the first and seventh centuries CE: nonperiodic behavior of a plate boundary fault. *Bulletin of the Seismological Society of America*, 104(3), 1329-1347.

Westoby, M.J., J. Brasington, N.F. Glasser, M.J. Hambrey, & J.M. Reynolds (2012). "Structure-from-Motion" photogrammetry: a low-cost, effective tool for geoscience applications. *Geomorphology* 179, 300-314.

Yaalon, D.H. (1967). Factors affecting the lithification of eolianite and interpretation of its environmental significance in the coastal plain of Israel. *J. Sed. Petrology* 37, 1189–1199.

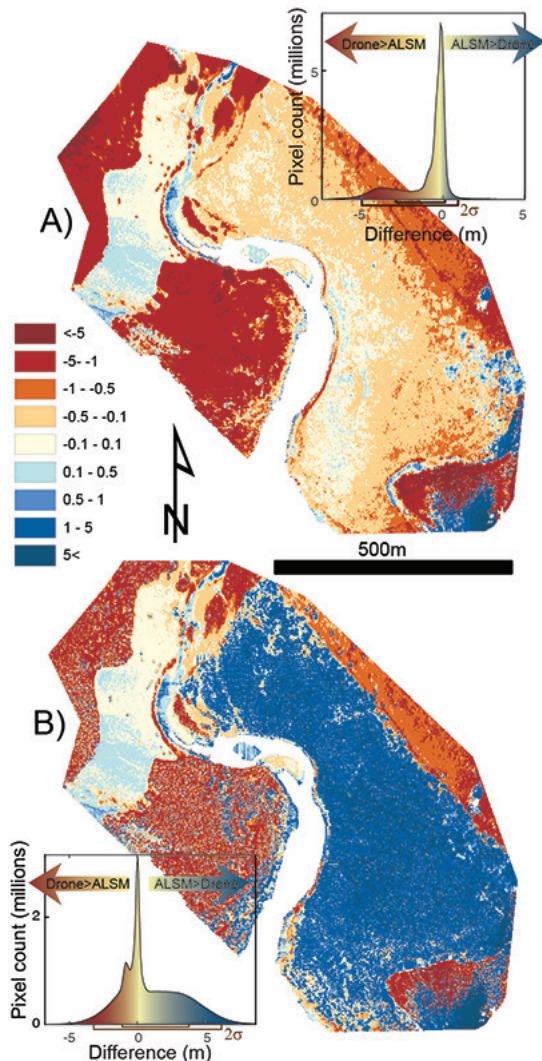


Fig. 4: Beteiha site ALSM-UAV differences, A) between cleaned ALSM and UAV DEMs. In the exposed zone the differences are smaller than 0.5m. B) Height difference between non-cleaned ALSM and UAV DEMs. Histograms represent the distance distribution, same as fig. 2.

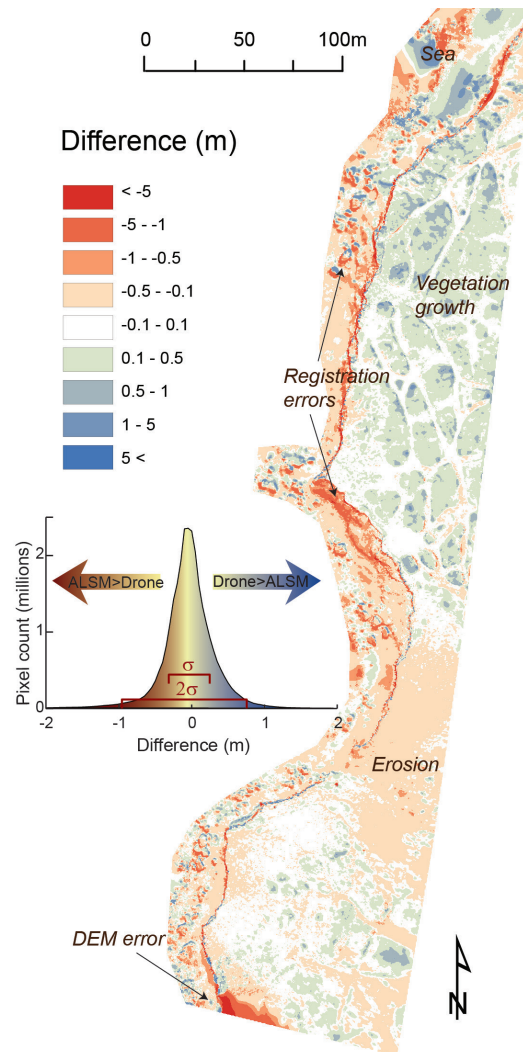


Fig. 5: Olga site ALSM-UAV height differences between DEMs. Histogram represents the distance distribution, same as fig. 2.



## Seismic source characterization in the Western Australia Shear Zone using 2D seismic data: an example from the Dampier fault zone

Whitney, Beau (1), Hengesh, James (2), Bergkamp, Bryan (3)

- 1) Centre for Energy Geoscience, The University of Western Australia, 35 Stirling Highway, Crawley, WA 6009, Australia; Beau.whitney@uwa.edu.au
- 2) Interface Geohazard Consulting, 20 Plumeria Pl., Lahaina, HI, 96761, USA; hengesh@gmail.com
- 3) Fugro Marine GeoConsulting, Inc., 6100 Hillcroft Ave., Houston, Texas, 77081, USA; bbergkamp@fugro.com

**Abstract:** The Western Australia Shear Zone (WASZ) is a system of active faults and folds along the reactivated passive margin of western Australia. The 180 km long Dampier fault zone, in the northern Carnarvon Basin, forms an 11 km wide fault zone across a reactivated Mesozoic graben. The northern fault section cross-cuts Quaternary age sediments producing a net down-to-the-north sense of displacement observed on 2D seismic transects. The east-west trending fault section is oblique to the dominantly northeast trending Mesozoic structural fabric of the Carnarvon basin, but sub-parallel to the structural trend of the offshore Canning basin. Fault offsets are estimated using displacements of several seismic horizons that extend across the area. The estimated slip rates for the Dampier fault range from 0.02 to 1.54 mm/yr, maximum earthquake magnitude estimates are on the order of  $M_w$  6.8 to 7.4, and recurrence intervals range between 1,000 and 183,000 years. The estimated slip rates are low, yet significant with respect to an intraplate tectonic setting. Rates within the WASZ are consistently higher than within adjacent non-extended cratonic terranes.

**Key words:** fault characterization, 2D seismic, intraplate seismic hazard

### INTRODUCTION

The Western Australia Shear Zone (WASZ) is a system of active faults and folds that extend along the reactivated passive margin of Australia through the Browse, Roebuck, and Carnarvon Basins (Fig. 1) (Whitney and Hengesh, 2013). The WASZ reoccupies older rift related structures that initially formed during periods of continental-scale fragmentation in the Paleozoic and Mesozoic Eras. Faults and folds within the WASZ have caused local inversion of older rift-era faults, in places have offset or folded the seafloor, folded late Pleistocene marine terraces, folded and faulted late Pleistocene alluvial deposits, and accommodated large historical earthquakes (Whitney, 2015).

The WASZ contains structures that share a consistent set of characteristics within a zone of concentrated historical seismicity. Reactivated faults and folds are within the formerly extended continental margin compared to adjacent cratonic domains. Seismicity and geomorphological indicators suggest a regional dextral-oblique sense of motion. Near surface fault expression is suggestive of a recent onset of reactivation. Seismicity and geologically derived strain indicators indicate rates of deformation vary systematically within the system decreasing from north to south. Earthquake recurrence within the WASZ is intermediate to plate boundary settings and Stable Continental Regions. Collectively, the WASZ extends 1,400 km along the North West Shelf from the plate boundary to the Cape Range. It then extends another 600 km through a system of faults and folds onshore within the southern Carnarvon Basin and

western edge of the Yilgarn craton (Whitney and Hengesh, 2015a, b; Hengesh and Whitney, 2015; Whitney et al., 2015a; Hengesh and Whitney, 2016).

The WASZ contains a number of seismic sources capable of generating earthquakes on the order of  $\sim M_w$  7.0-8.0 with recurrence on the order of  $10^3$ - $10^4$  years (Whitney and Hengesh, 2015; Hengesh and Whitney, 2015). In a broad sense, the shear zone accommodates differential motion between the subduction and collision zones that comprise the Indo-Australian northern plate boundary (Hengesh and Whitney, 2016). The transition from subduction to collision coincides with passive margin structures that are favorably aligned to be reactivated as dextral-transcurrent structures.

The WASZ consists of two subparallel fault zones in the Browse and Roebuck Basins referred to as the Inner (eastern) and Outer (western) Shelf fault zones (Hengesh and Whitney, 2015). These zones follow the basin margins and locally are associated with older basin bounding structures (Hengesh and Whitney, 2016). In the Carnarvon Basin, deformation in the WASZ is concentrated along the crustal transition between the inner (eastern) basin margin and older Archean crystalline rocks.

In this paper we present seismic source characteristics for the Dampier fault within the WASZ. The Dampier fault lies within the southern Inner Shelf fault zone in the Carnarvon Basin where the deformation transitions from two subparallel fault zones in the north to a single fault zone in the vicinity of Barrow Island (Hengesh and



Whitney, 2016; Whitney et al., *in revision*). A large restraining bend occurs inboard of Barrow Island where multiple fault segments from the southern Carnarvon Basin coalesce. The structural trend changes from northerly to northeasterly north of the restraining bend.

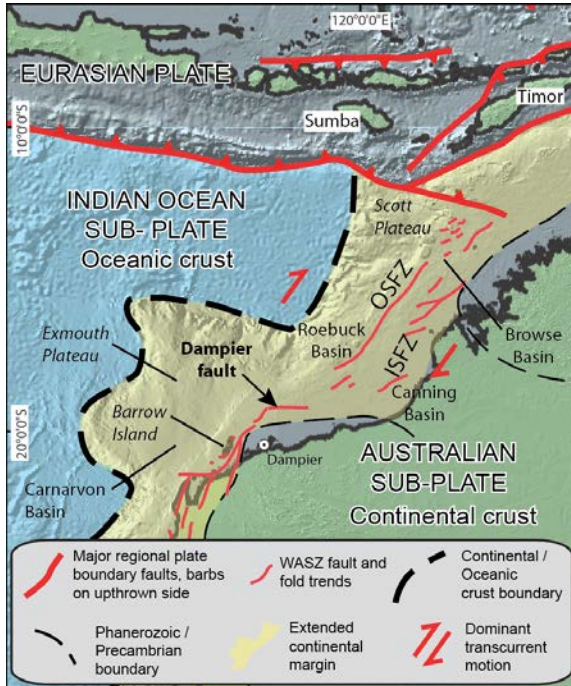


Fig. 1: Regional tectonic elements. OSFZ and ISFZ are Outer and Inner Shelf fault zones, respectively

## METHODS

We analyzed open-file 2D exploration data from Geoscience Australia data release (Cortese et al., 2014) using the seismic interpretation software package IHS Kingdom. We focus on the Quaternary period, which coincides with the timing of the most recent pulse of reactivation (Hengesh and Whitney, 2016). In the Carnarvon and Roebuck basins, 0.5 and 1.0 Ma reflectors have been identified in the shallow section (Gallagher et al., 2014). We constrain fault displacements, deformation style, fault extent, and compute slip rates based on the age and vertical offset of these seismic horizons. We convert two-way-travel time (TWT) to depth in the shallow section assuming a p-wave velocity of 1600 m/s.

We estimate maximum earthquake magnitude ( $M_{max}$ ) distributions for the Dampier fault using five different empirical relationships between fault length and magnitude, and rupture area and magnitude (Wells and Coppersmith, 1994; Hanks and Bakun, 2002; 2008; Ellsworth, 2003; Wesnousky, 2008). The minimum, average, and maximum magnitude values are derived from the range of lengths and areas used and the range of results derived from the five different equations. This approach captures the epistemic uncertainty in the fault

rupture characteristics and published empirical regressions (Table 1).

## RESULTS AND DISCUSSION

The Dampier fault zone is a 180 km long northeast trending structure that includes a southern transensional segment, a central transpressional segment, and a northern (east-west trending) transensional segment (Fig. 2). The east-west trending northern segment of the Dampier fault is ~60 to 91-km. The end of the fault roughly aligns with the projected trends of the Inner and Outer Shelf fault zones to the north, respectively (Fig. 1). The northern segment of the Dampier fault is traceable across multiple 2D lines (Fig. 2). Each segment maintains a similar expression along strike.

The western end of the northern segment of the Dampier fault forms an 11-km wide graben with a normal component of motion that displaces the Late Miocene horizon, and the overlying Quaternary section (Fig. 3). This fault (observed on line s136\_136\_24) has produced 0.15 to 0.18 second TWT (120 to 144 m) of down-to-the-north displacement of the Late Miocene horizon, 0.015 to 0.018 second TWT (11.8 to 14.3 m) of down-to-the-north displacement of a ~500 Ka Quaternary horizon (Gallagher et al., 2014), and 0.039 to 0.041 second TWT (30.8 to 32.5 m) of down-to-the-north displacement of a ~1.0 Ma Quaternary horizon (Table 2). The seabed is not deformed in this location, but the water depth here is only ~96 m and so this part of the continental shelf would have been abraded through current and wave action during multiple Pleistocene sea level lowstands.

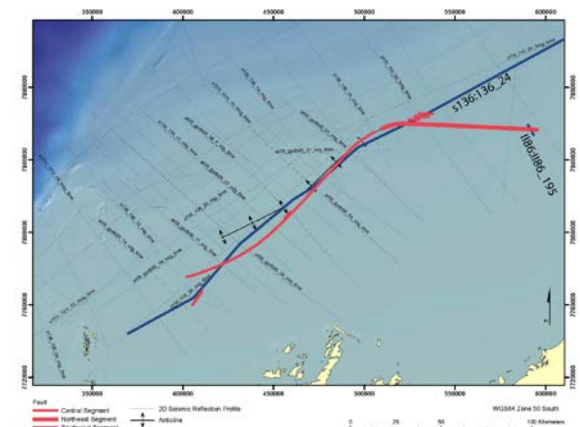


Fig. 2: 2D lines used to interpret and measure displacement on the Dampier fault. Blue lines are discussed in text.

The southern graben bounding fault dips 61° to the north and has similar form along strike. Its northern, south dipping counterpart is not consistently traceable. This may be due to poorer data coverage, or along strike changes in fault expression. The eastern end of the fault appears to deform the seabed reflector (Fig. 4). The data in this location are sparse and on this particular 2D line



(I186:I186-195) the data are truncated within the fault zone.

Faults within the WASZ broadly exhibit dominantly transcurrent motion and trend north-northeasterly (Hengesh and Whitney, 2016). The north segment of the Dampier fault appears to be located on a releasing bend north of the restraining Barrow Bend (Fig 1). To the north of the Dampier fault, dextral transcurrent motion is partitioned between two main fault zones (Inner and Outer Shelf). To the south, strain is concentrated on the Inner Shelf fault zone, which hugs the basin margin. The available 2D data allow measurements of vertical offsets, but do not allow us to assess horizontal slip rates across the fault. Due to the uncertainty and limitations of 2D data interpretation, we present a range of horizontal slip rate estimates by assuming a range of vertical to horizontal slip ratios. The dominant horizontal to

vertical slip ratios for strike slip faults commonly range from 1:1 to 10:1 [Wells and Coppersmith, 1994; K. Coppersmith pers. comm., 2015]. We apply these ratios to the minimum, average, and maximum slip rate values for the Dampier fault (Table 3).

Displacement values are the average of the mean maximum displacement values computed from surface rupture length and moment magnitude using the Wells and Coppersmith (1994) and the moment magnitude regressions from (Hanks and Bakun, 2002; 2008; Ellsworth, 2003; Wesnousky, 2008). Slip rates were computed from geological displacements described in the previous text. The recurrence distribution is calculated by dividing the maximum displacement by minimum slip rate, middle displacement by middle slip rate, and minimum displacement by maximum slip rate (Table 4).

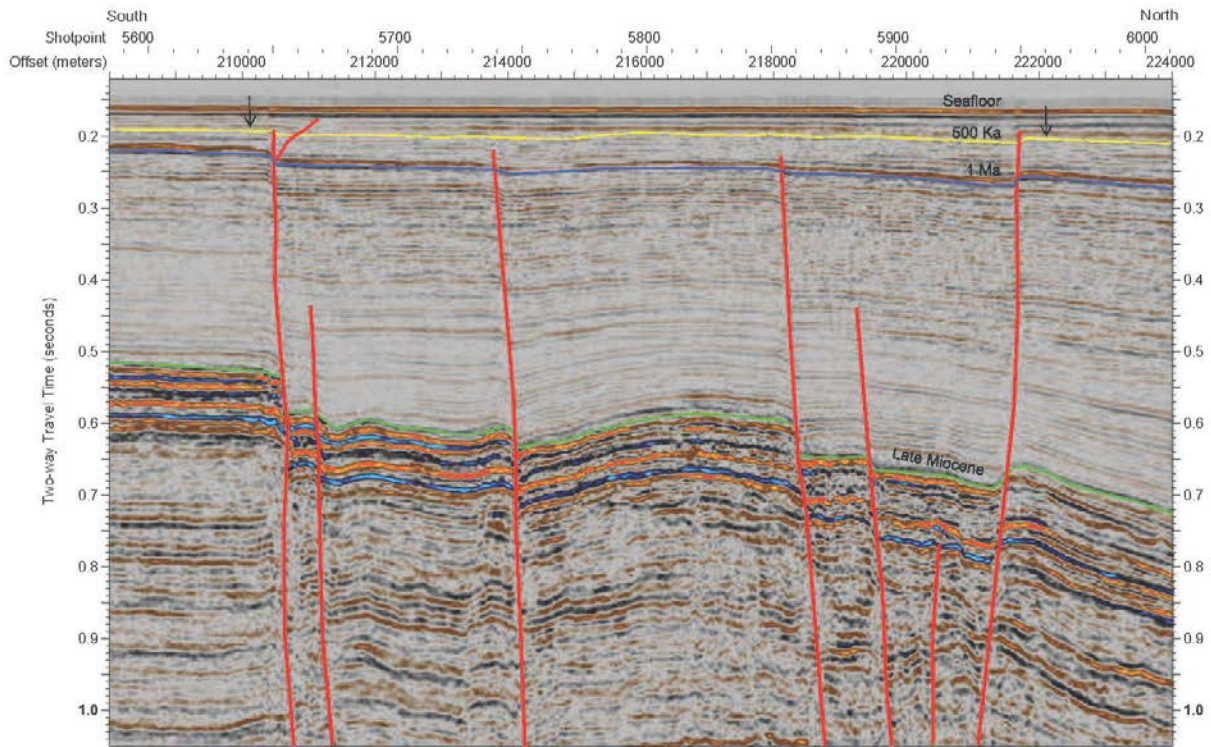


Fig. 3: Portion of seismic line s136:136\_24 showing faulting of the Late Miocene unconformity and Quaternary deposits (Gallagher et al., 2014) along the Dampier fault. Vertical scale in Two Way Time (seconds). Location shown on Figure 2.

Table 1. Mmax estimates for the northern segment (NS) of the Dampier fault. Magnitude values calculated using the Wells and Coppersmith (1994), Hanks and Bakun (2002; 2008), Ellsworth (2003), and Wesnousky (2008) relationships. Displacement values are the average of the mean maximum displacement values computed from surface rupture length and moment magnitude using the Wells and Coppersmith (1994) and the moment magnitude regressions listed above. Slip rates computed from geological displacements described in the text.

Sense of Slip	Estimated Rupture Length (km)		Min Rupture Width (km)		Max Rupture Width (km)		Estimated Rupture Area (km <sup>2</sup> )		Magnitude Distribution (Mw)		
	Min	Max	Min	Max	Min	Max	Min	Max	Min	Ave	Max
RL-SS	60	91	10	15	600	1365	6.8	7.1	7.4		



Table 2. Summary of displacement measurements across seismic line s136\_136\_24\_mig\_time on the Dampier fault (NS).

Shot Point Range	Horizon	Throw (sec TWT)		Displacement (m)		Period of Activity (Ma)		Estimated Fault Slip Rate (mm/yr)	
		Min	Max	Min	Max	Min	Max	Min	Max
5640-5950	500 ka	0.015	0.018	12	14	0.50	0.50	0.02	0.03
5650-5950	1.0 Ma	0.039	0.041	31	32	1.00	1.00	0.03	0.03
5600-5975	Late Miocene	0.150	0.180	120	144	1.00	3.00	0.04	0.14

Table 3. Summary of estimated vertical and horizontal slip rate values for the Dampier fault (NS).

Vertical Slip Rate (mm/yr)			Horizontal Slip Rate (mm/yr)		
Min	Ave.	Max	Min (1:1 H/V)	Mid (5:1 H/V)	Max (10:1 H/V)
0.02	0.08	0.14	0.02	0.40	1.40

Table 4. Recurrence estimates.

Ave of Mean MD for SRL&MW (m)			Slip Rate Models (mm/yr)			Recurrence (MD fx Mw)/slip rate		
Min	Mid	Max	Min	Mid	Max	Min	Mid	Max
1.61	2.54	3.66	0.020	0.400	1.540	1047	6356	183231

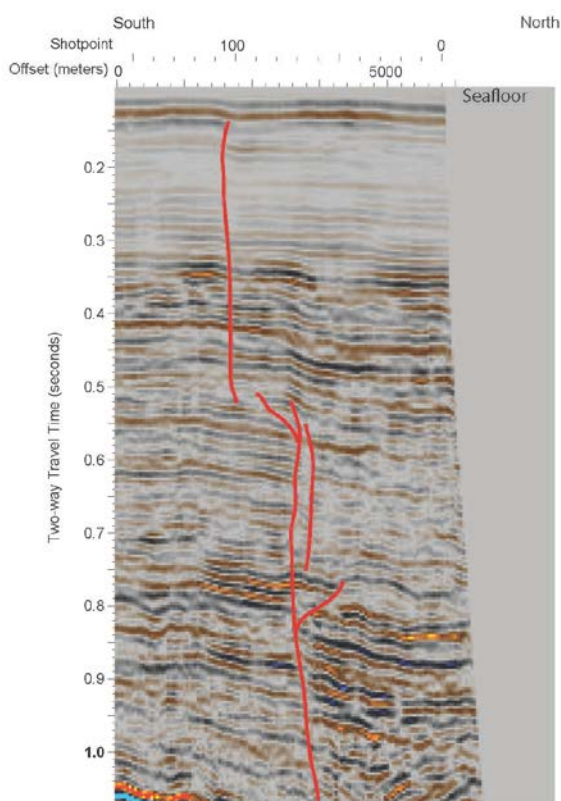


Fig. 4: Portion of seismic line II86:II86-195 showing deformation of the seabed. Location shown on figure 2.

## CONCLUSIONS

The Dampier fault zone consists of 180 km long northeast trending structures that includes a releasing and restraining bend. The Dampier fault zone displaces near seabed seismic horizons and locally deforms the seabed. The estimated slip rates for the Dampier fault

ranges from 0.02 to 1.54 mm yr<sup>-1</sup>. The Mmax distribution ranges from Mw 6.8 to 7.4, and the minimum, average and maximum recurrence intervals are 1,000, 6400, 183,000 years.

Mmax and recurrence estimates yield values which are consistent with other active faults in the WASZ (Whitney et al., 2015; Hengesh and Whitney, 2016). These values (10<sup>3</sup>-10<sup>4</sup> years) are intermediate to Stable Continental Regions (>10<sup>4</sup> years) and plate boundary (10<sup>2</sup>-10<sup>3</sup> years) settings. Rates within the WASZ are consistently higher and Mmax values are larger than adjacent non-extended cratonic terranes (Clark et al., 2012). The reactivated western margin of Australia should no longer be considered a Stable Continental Region.

**Acknowledgements:** We gratefully acknowledge the financial support provided by the Chevron Australia Business Unit (Project PDEP AES 12-P1ABU-82). This work forms part of the activities of the Centre for Energy Geoscience (CEG) and the Centre for Offshore Foundation Systems (COFS).

## References

- Clark, D., McPherson, A., and Van Dissen, R. 2012. Long-term behaviour of Australian stable continental region (SCR) faults. *Tectonophysics*. DOI: <http://dx.doi.org/10.1016/j.tecto.2012.07.004>
- Cortese, A., M. Tully, and A. Fleming (2014), 2014 Acreage Release Data Package. Geoscience Australia, Canberra.
- Ellsworth, W., 2003, Equations 4.5 and 4.5a in Working Group on California Earthquake Probabilities, 2003, Earthquake Probabilities in the San Francisco Bay Region: 2002–2031, USGS Open-File Report 2003-214.
- Gallagher, S. J., M. W. Wallace, P. W. Hoiles and J. M. Southwood (2014), Seismic and stratigraphic evidence for reef expansion and onset of aridity on the Northwest Shelf of Australia during the Pleistocene. *Marine and Petroleum Geology*, 57, 470-481.
- Hanks, T.C., and W.H. Bakun, 2002, A bilinear source-scaling model for M-log A observations of continental



## INQUA Focus Group on Paleoseismology and Active Tectonics



paleoseismicity.org

- earthquakes, *Bulletin of the Seismological Society of America*, v. 92, p. 1841-1846.
- Hanks, T.C., and W.H. Bakun, 2008, M-log A observations for recent large earthquakes, *Bulletin of the Seismological Society of America*, Vol. 98, No. 1, pp. 490-494, doi: 10.1785/0120070174.
- Hengesh, J.V., Whitney, B.B. 2015. Characterization of seismic sources within western Australia's newly reactivated transform margin. Australian earthquake engineering society and the New Zealand society for earthquake engineering, Tenth Pacific Conference on earthquake engineering, Sydney. No. 83, 8 pp.
- Hengesh, J.V., Whitney, B.B. 2016 (*accepted*). Transcurrent Reactivation of Australia's Western Passive Margin: a mechanism for Fragmentation of the Indo-Australian Plate. *Tectonics*.
- Wells, D. L., and K.L. Coppersmith (1994), New empirical relationships among magnitude, rupture length, rupture width, rupture area, and surface displacement. *Bulletin of the Seismological Society of America*, 84(4), 974-1002.
- Wesnousky, S., 2008, Displacement and geometrical characteristics of earthquake surface ruptures: Issues and implications for seismic-hazard analysis and the process of earthquake rupture, *Bulletin of the Seismological Society of America*, Vol. 98, No. 4, pp. 1609-1632, doi: 10.1785/0120070111.
- Whitney, B.B., Hengesh, J.V. 2013. Geological constraints on Mmax values from Western Australia: Implications for seismic hazard assessments. *Australian Geomechanics Society Journal. Western Australian Geotechnics*. Vol. 48, no 2. p. 15-26.
- Whitney, B.B., J.V. Hengesh, and D. Clark, 2014, The Western Australia shear zone, in *International Union for Quaternary Research (INQUA) Focus Group on Paleoseismology and Active Tectonics, 5th International INQUA Meeting on Paleoseismology, Active Tectonics and Archeoseismology (PATA)*, 21-27 September 2014, Busan, Korea, edited by Grutzner, C., J-H. Choi, P. Edwards, and Y-S. Kim, pp. 162-165, International Union for Quaternary Research.
- Whitney, B.B., 2015, Neotectonic deformation in the Western Australia Shear Zone, PhD Dissertation, The University of Western Australia.
- Whitney, B.B., and J.V. Hengesh, 2015a, Geomorphological evidence of neotectonic deformation in the Carnarvon Basin, Western Australia. *Geomorphology* 228, 579-596.
- Whitney, B.B., and J.V. Hengesh, 2015b, Geomorphological evidence for late Quaternary tectonic deformation of the Cape Region, coastal west central Australia. *Geomorphology*, 241, 160-174.
- Whitney, B. B., D. Clark, J.V. Hengesh, and P. Bierman, 2015a, Paleoseismology of the Mount Narryer fault zone, Western Australia: A multistrand intraplate fault system. *Geological Society of America Bulletin*, B31313-1.
- Whitney, B.B., J.V. Hengesh, and D. Gillam (*in revision*), Styles of fault reactivation within a formerly extended continental margin, North West Shelf, Australia, *Tectonophysics*.



### Shorter and variable recurrence intervals along the Cholame segment of the San Andreas Fault

Alana Williams, J Ramon Arrowsmith,

**Abstract:** Paleoseismicity data from the Cholame segment of the San Andreas fault (SAF) are important for testing earthquake recurrence models along the central SAF. Slip per event or few event information coupled with tightly constrained event age control is needed to build a catalog of paleoseismicity between the Parkfield and Carrizo sections of the SAF. We excavated five exploratory fault perpendicular trenches within an abandoned gypsum mine (35.253478, -119.585675) in the southeastern portion of the Cholame segment. The trenches did not reveal adequate preservation of rupture evidence to provide estimates for recurrence interval. In summer 2016, we will expand our earthquake geology research to promising new sites in the northern central portion of the Cholame segment.

**Key Words:** paleoseismology, active tectonics, San Andreas, Cholame, earthquake recurrence

#### Introduction

The Cholame segment of the southern San Andreas fault (SAF) is significant because it records the interaction between the creeping Parkfield segment to the northwest and the locked Carrizo segment to the southeast. Offset distributions have been reconstructed along this ~75 km long fault reach, but a more complete understanding of past ruptures for the Cholame section has not been forthcoming. Given its central position along the SAF, this lack of information places significant limitations on evaluating seismic hazard. New paleoseismic data on earthquake recurrence will lead to a better understanding of past rupture behavior and earthquake hazard analysis.

Large gaps in the paleoseismicity record and various interpretations of past earthquake offset pose challenges to modeling past fault behavior along the Cholame segment of the SAF. Sieh's extensive measurements (1978a) of geomorphic offsets along the Cholame segment of the SAF implied a characteristic slip of 3-4 m during the 1857 rupture and prior events (Figure 1). Re-investigation of surface offsets revised the estimates of 1857 offset along Cholame upward to 4-6 m (Lienkaemper, 2001; Zielke 2010, 2012). Three dimensional reconstruction of an offset gravel sheet at LY4 along the Cholame segment showed 3 m offset in 1857 across a few meter aperture (Young, et al., 2002). Current rupture models for the Cholame segment are constrained locally only by this limited offset information, the regional millennial scale SAF slip rate, and the behavior of the adjacent sections (Parkfield and Carrizo; Field, et al., 2013). Note for example that the paleoseismicity record along the Cholame section was insufficient for any maximum likelihood recurrence interval estimation by Biasi for the UCERF3 exercise (Biasi, 2013; UCERF3 Appendix H).

Assuming Cholame should slip at the SAF long term slip rate (~33mm/yr), and the 1857 rupture produced uniform slip of at least 3 m (Sieh, 1978a; Sieh and Jahns, 1984; Young, et al., 2002; Lienkaemper, 2001; Zielke, et al., 2010; 2012), there is a large slip deficit of that could accommodate a M7 rupture along the full length of the segment (Toke & Arrowsmith 2006) (Figure 1). More

importantly, this ~5 m deficit is too large to be released by creep alone (Lienkaemper, 2001). This prompted the investigation of the LY4 paleoseismic site by Stone et al. 2002, and Young et al. 2002. While no significant surface slip has been reported along the Cholame section since 1857, subsequent Parkfield events and creep have terminated around Highway 46 (northwest end of Cholame segment), and Young et al., 2002 report possible surface cracking at LY4 (35 km southeast of Highway 46).

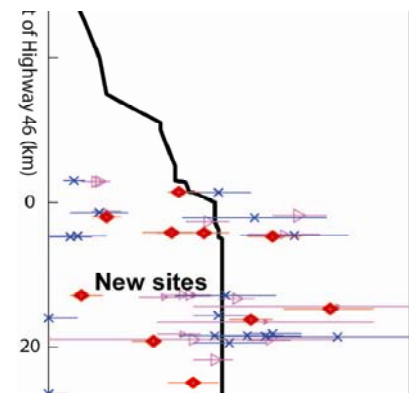


Figure 1 Slip deficit since 1857 accumulating at 3.3 cm/yr (black line) from Toke and Arrowsmith, 2006 accounting for post-1857 creep and Parkfield slip in the northwest. Symbols for offsets are scaled by reported quality. New sites are halfway between LY4 and Highway 46—southern Parkfield segment.

Young et al.'s measurement of  $3.0 \pm 0.7$  m slip on the 1857 earthquake is much smaller than the offsets measured on the neighboring Carrizo segment, and much larger than the Parkfield segment to the northwest, which suggests differences in fault properties (Sieh, 1978a; Hilley, et al., 2001). Young et al., 2002 interpreted 3 ground rupturing events, one of which was the 1857 event, followed by possible surface cracking. This corresponds with Stone et al.'s (2002) interpretation of 2-4 ground rupturing events, and provides a recurrence interval of 290-410 years. This longer recurrence rate differs from the hypothesis of more rapid Cholame recurrence intervals



(Sieh and Jahns, 1984; Young et al. 2002) derived from assumed lower slip/event in Cholame than Carrizo and uniform long term slip rate along strike. The poorly constrained geochronology at the previous Cholame excavations spurred the 2015 excavations detailed later in this report.

Slip/event is more variable than previously thought along the south central SAF (Akciz, et al., 2010 and Zielke, et al., 2010). Paleoseismic studies just southeast of the Carrizo segment at Frasier Mountain present evidence for 6 or 7 earthquakes (Figure 2) within the last 650 years, indicating a 90-110 year recurrence interval (Scharer et al., 2014). This is consistent with the Bidart record from Carrizo which implying surface rupture recurrence of  $88 \pm 41$  years (Akciz et al., 2010). Therefore, revisiting the poor geochronology and possible incomplete record at Cholame becomes more urgent.

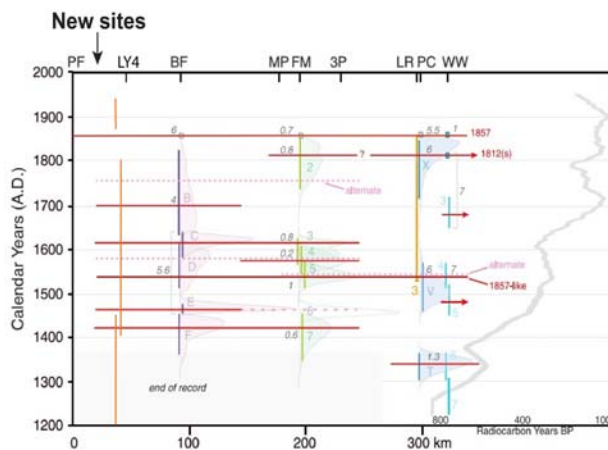


Figure 2 Correlation diagram for SSAF paleoearthquakes from Parkfield to Wrightwood showing location of new sites we propose to develop. The orange lines represent the 3 poorly dated events at LY4. The rest of the figure is adapted from Scharer et al. 2015. Shaded curves are earthquake age probability distributions; vertical bars show 95% confidence range for each earthquake. Paleoearthquakes are labeled by the letter or number used in the original reference (e.g., the five prehistoric earthquakes at Bidart Fan are identified as B, C, D, E, and F) [Weldon et al., 2004; Pruitt et al., 2009; Akciz et al., 2010; Scharer et al., 2011]. Grey numbers indicate horizontal displacement in meters (and vertical lowering for FM); bracket is used to signify when measurement is the cumulative total over several earthquakes. Solid red lines show possible ruptures based on Scharer's correlation of paleoearthquake ages among sites; lines arbitrarily end midway when no temporally correlative earthquake exists at the neighboring site.

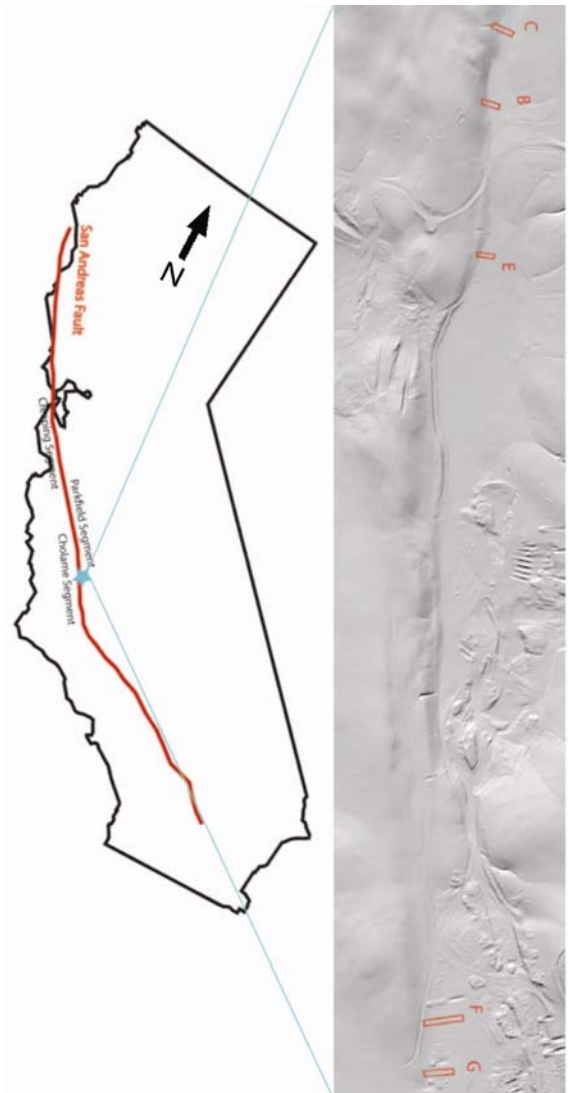


Figure 3 Map overview of California with a simplified SAF trace in red, and Gyp Mine site indicated by a blue star. The Creeping, Parkfield, and Cholame segments are labeled along the trace. Trench locations overlain on B4 high resolution topographic data.

### 2015 excavations

The Gypsum Mine location (Figure 3) is characterized by compelling tectonic landforms - steep, northeast-facing scarps and several sag ponds. In August 2015 we excavated five fault-perpendicular trenches focused on small alluvial fans deposited across the well-defined fault trace. Each trench was cleaned and photographed post excavation, and orthophotos were generated using Agisoft Photoscan. Logging was completed on the Agisoft models and charcoal samples were collected for radiocarbon analysis.

Trenches B and C exposed diamictons containing massive sandy silt and clay, poorly sorted pebble clasts, and gypsum



root casts. Trenches F and G (Figure 4) contain massive, tan, sandy silt soil with a gradual transition to silty clay bedrock, and moderately developed prismatic peds. The historic soil horizon displays horizontal partings. The soil becomes more indurated with depth. Bedrock is a dark brown to gray fractured mudstone, with poorly sorted blocky orange and white clasts. Trench G is slightly more bioturbated than Trench F and displays small vesicular fractures which may indicate fissure fill.

Trench E (Figure 5) is composed of fine clays interbedded with laminated sands and poorly sorted gravels that show deformation and liquefaction features similar to those seen in a south Carrizo sag trench (S. Akciz, UCLA). Three charcoal samples were collected from these beds, E1, E2, and E3, and we will compare their ages to the liquefaction features found in the south Carrizo trench.

Overall, the trenches excavated in this locality displayed a no discernable unit boundaries, variable sedimentation, and weak fault evidence. The sub-surface data is indicative of hundreds to thousands of years of surface stability, precluding the ability to preserve fine-scale evidence for recent events. The age control we will obtain from the dating of collected charcoal samples, coupled with the data we have collected, will be used to better interpret the geomorphological evolution of discontinuous sag settings along the Cholame segment of the SAF and help us improve the identification of prospective exploration sites along it.



Figure 5 Trench E panel of the southeast facing wall displaying liquefaction features. Interbedded fine sand and clay are outlined in yellow, poorly sorted gravels are outlined in orange.

#### 2016 earthquake geology efforts

In 2016, we plan to excavate across the SAF at new promising sites about 10 km northwest of the LY4 and about 23 km northwest of the Gypsum mine sites (Figure 4). Several of Sieh, Lienkaemper, and Zielke's offset measurements are located nearby the potential sites, in particular, the three favored for excavation. Sites 2, 4, and 5 (Figure 6) were chosen based on the compelling geomorphology. They are located along a steep scarp with a small shutter ridge, several drainages and well-located fault trace. The catchments and alluvial fans are reasonably sized indicating a strong likelihood of charcoal samples and an adequate sediment source which would minimize bioturbation and preserve datable bedded material. The local geology from which the site deposits are derived consists of reworked fine silt and sand, indicating these sites will likely be viable candidates for OSL dating methods.

#### Conclusion

The timing of rupture events along the Cholame segment remains poorly constrained, leaving the details of how the slip deficit is released unresolved and how ruptures occur along this important transitional segment of the southern SAF uncertain. The large distance spanning the Cholame segment and bounding sites (~75 km) provides adequate space for an M6-7 rupture to go unrecorded, indicating a gap in data for current hazard assessment. The current data suggest several rupture possibilities: (1) independent M6-7 rupture of the separate segments (Parkfield, Cholame, & Carrizo), (2) the reactivation of the 1857 reach (M7.8; possibly involving, triggered by or anticipated by Parkfield M6 events; Sieh, 1978a,b; Toke and Arrowsmith, 2006), (3) the occurrence of moderate ruptures in Cholame with minor continuation into the Carrizo segment, and/or (4) aseismic creep (Young et al., 2002).

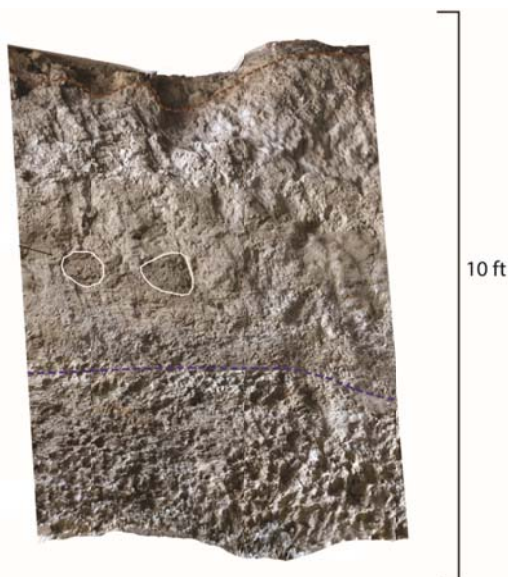


Figure 4 Trench G panel of the southeast facing wall. Zones of bioturbation are outlined in white. Bedrock transition is shown by the blue dashed line. The historic soil horizon is outlined by the brown dashed line.

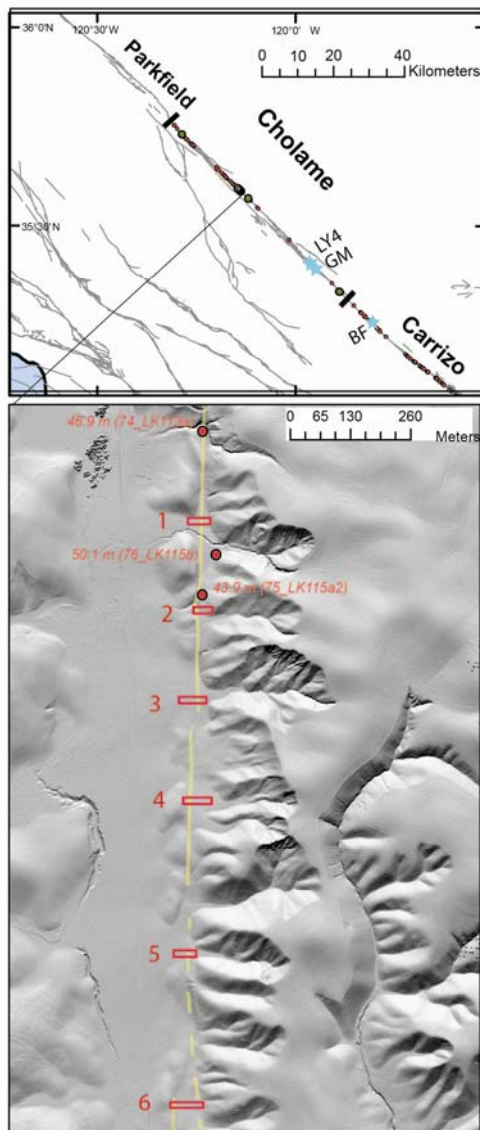


Figure 6 Map overview of the south central SAF with candidate sites indicated and details of the high quality geomorphology indicated with the sites overlain on B4 high resolution topographic data. Lidar shows regional active faults and offset measurement locations from Sieh, 1978a; Lienkaemper, 2001; and Zielke, 2012. B and C also include nearby offsets as tabulated by Zielke et al., 2012.

**Acknowledgements:** We gratefully acknowledge the financial support of the Southern California Earthquake Center, as well as the contributions of J. Barrett Salisbury, Sinan Akciz, and Tom Rockwell.

#### REFERENCES

Akciz, S. O., Grant Ludwig, L., Arrowsmith, J R., Zielke, O., Century-long average time intervals between earthquake ruptures of the San Andreas fault in the Carrizo Plain, California, *Geology*, 38, 9, p. 787-790, 2010.

Bemis, S., Micklethwaite, S., Turner, D., James, M., Akciz, S., Thiele, S., & Bangash, H. (n.d.). Ground-based and UAV-Based photogrammetry: A multi-scale, high-resolution mapping tool for structural geology and paleoseismology. *Journal of Structural Geology*, 163-178.

Field, E. H., Arrowsmith, J R., Biasi, G. P., Bird, P., Dawson, T. E., Felzer, K. R., Jackson, D. D., Johnson, K. M., Jordan, T. H., Madden, C., Michael, A. J., Milner, K. R., Page, M. T., Uniform California Earthquake Rupture Forecast, Version 3 (UCERF3)--The Time-Independent Model, *Bulletin of the Seismological Society of America*, Vol. 104, No. 3, pp. 1122-1180, doi: 10.1785/0120130164, 2014.

Hilley, G. E., Arrowsmith, J R., and Stone, E. M., Using microseismicity and surface offset data to define fault segment boundaries along low friction faults, with an example from the Cholame-Carrizo segment boundary along the San Andreas Fault, Southern California, *Bulletin of the Seismological Society of America*, 91, 427-440, 2001.

Lienkaemper, J. (2001). 1857 Slip on the San Andreas Fault Southeast of Cholame, California. *Bulletin of the Seismological Society of America*, 1659-1672.

Reitman, N., Bennett, S., Gold, R., Briggs, R., & Duross, C. (2015). High-Resolution Trench Photomosaics from Image-Based Modeling: Workflow and Error Analysis. *Bulletin of the Seismological Society of America*, 2354-2366.

Scharer, K., Weldon, R., Streig, A., & Fumal, T. (2014). Paleoearthquakes at Frazier Mountain, California delimit extent and frequency of past San Andreas Fault ruptures along 1857 trace. *Geophys. Res. Lett. Geophysical Research Letters*.

Sieh, K. E. (1978a). Slip along the San Andreas fault associated with the great 1857 earthquake, *Bulletin of the Seismological Society of America*, 68, 1421-1448.

Sieh, K. E. (1978b). Central California foreshocks of the great 1857 earthquake. *Bulletin of the Seismological Society of America*, 68(6), 1731-1749.

Sieh, K., & Jahns, R. (1984). Holocene activity of the San Andreas fault at Wallace Creek, California. *Geol Soc America Bull Geological Society of America Bulletin*, 883-883.

Stone, E.M., Grant, L., and Arrowsmith, J R., Recent rupture history of the San Andreas Fault southeast of Cholame in the northern Carrizo Plain, California, *Bulletin of the Seismological Society of America*, 92, 983-997, 2002.

Toke, N., & Arrowsmith, J. (2006). Reassessment of a Slip Budget along the Parkfield Segment of the San Andreas Fault. *Bulletin of the Seismological Society of America*, S339-S348.

Williams, A., (2015). Exploration of a new paleoseismic site in the Cholame section of the San Andreas fault, CA. Poster presented at the Annual Southern California Earthquake Center Conference, Palm Springs, CA.

Young, J., Arrowsmith, J., Collini, L., Grant, L., & Gootee, B. (2002). Three-Dimensional Excavation and Recent Rupture History along the Cholame Segment of the San Andreas Fault. *Bulletin of the Seismological Society of America*, 2670-2688.

Zielke, O., Arrowsmith, J., Ludwig, L., & Akciz, S. (2010). Slip in the 1857 and Earlier Large Earthquakes Along the Carrizo Plain, San Andreas Fault. *Science*, 1119-1122.

Zielke, O., Arrowsmith, J., Ludwig, L., & Akciz, S. (2012). High-Resolution Topography-Derived Offsets along the 1857 Fort Tejon Earthquake Rupture Trace, San Andreas Fault. *Bulletin of the Seismological Society of America*, 1135-1154.



## Fault slip behaviour of North Danghe Nanshan Thrust (NDNT) from high resolution topography data and paleoearthquakes

Shao Yanxiu (1,2), Wang Pengtao (1), Yuan Daoyang (1), Liu-Zeng Jing (2), Wu Zhao (1)

(1) Lanzhou Institute of Seismology, China Earthquake Administration, Lanzhou, 730000, China

(2) State Key Laboratory of Earthquake Dynamics, Institute of Geology, China Earthquake Administration, Beijing, 100029, China

Email: [shaoyx@geoidea.org](mailto:shaoyx@geoidea.org)

**Abstract:** New surveying and mapping technology, which can acquire high resolution topography quickly, is being used to study active tectonics in recent years. The results were great for earthquake reoccurrence model of large strike slip faults. Similar studies, however, were not carried out on active thrusts. We are studying earthquake reoccurrence model of North Danghe Nanshan thrust, which has different degree scarps, under because of thrusts' destruction. Our study is based on not only high resolution topography but also paleoearthquakes. Firstly, we used small Unmanned Aerial Vehicle (sUAV) and terrestrial LiDAR to construct high resolution Digital Elevation Model (DEM), and based on which to measure scarps along fault. We employed statistical methods such as probability density function to get accumulated slip distribution along fault and peak slip values. The number of earthquakes on different degree scarps were analysed according to slip distribution and peaks. Meanwhile, we also excavated trenches across different degree scarps to attain paleoearthquakes from successive depositional walls directly. The paleoearthquakes were compared with the result inferred from slip at last. Our primary result shows that it is valid to study active fault rupture mechanics from slip distribution, and slip behaviour of this thrust coincide with characteristic earthquake mode.

**Key words:** North Danghe Nanshan thrust, High resolution topography, Accumulated slip, Paleoearthquake

### Motivation

How earthquakes rupture and propagate are important topic to understand earthquake mechanics. Many recent studies on slip pattern of active faults using high resolution topography acquired by LiDAR (Hudnut et al., 2002; Oskin et al., 2007; Chen et al., 2015; Salisbury et al., 2015). Another low price photogrammetry method of sUAV is prevailing on mapping active tectonics (Bemis et al., 2014). Reliable cumulative slip distributions were characterised along large strike slip faults (Grant-Ludwig et al., 2010; Klinger et al., 2011; Ren et al., 2015; Haddon et al., 2016), and rupture modes of them were also proposed. However, these studies lacked support from paleoseismology, which is direct evidence for rupture modes.

Another issue is that few such studies using the new survey methods were carried out on reverse faults.

That may be because reverse fault systems have much more complex deformation structures and a relative lack of classic study sites. Because many destructive earthquakes were generated by reverse faults in history, it is very important to figure out active characteristic in dangerous compressional tectonic zone.

This study selects an ideal reverse type fault, North Danghe Nanshan Thrust (NDNT), which faulted alluvial terraces and preserves continuous multiple-event fault scarps including latest rupture high < 1m. These scarps offer opportunity to distinguish accumulated slip offset of older events.

### Geological Background

The NDNT is located west of the Qilian mountains, and adjacent to the eastern end of the South Altyn Tagh Fault. It plays a vital role in strain transfer from the Tibetan plateau to its eastern boundary (Mayer et al., 1998; Van der Woerd et al., 2001). The NDNT contains three segments from Subei in west to Yanchiwan in east, and is ~120 km long. Van der Woerd et al. (2001) mapped the west section in detail and estimated the vertical slip rate at ~5 mm/yr. Shao et al. (2011) investigated the middle and east segments, and found that thrust scarps had offset the latest alluvial fan surfaces by 0.5-1m and multiple similar high scarps were formed on older terraces; the latest rupture zone is ~40 km long. These deformation features indicate that the NDNT has ruptured many times during last few thousand years.

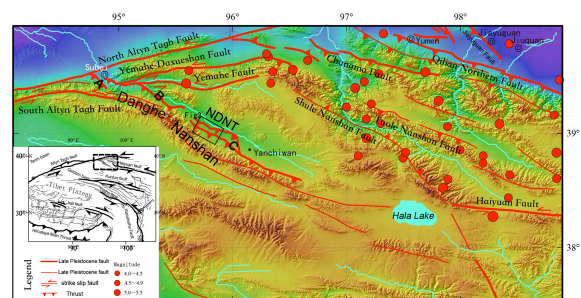


Fig.1. Active tectonic map of north Tibet Plateau  
Black box is study area  
A, B, C present three segments of NDNT



## Methods

We used terrestrial LiDAR and sUAV to scan east section of the NDNT, and resolution digital elevation model (DEM) was gotten after data processing. Scarp vertical throw along the fault was extracted from DEM. We also dug trenches across different high scarps to illustrate the number of events and its relation with scarps height.

## Primary results

The DEM data was calculated from ~5000 aerial photos covering ~ 3 km<sup>2</sup> area and point cloud of ~ 0.5 km<sup>2</sup> area, its resolutions about ~0.2 m and ~ 0.1 m respectively. We measured a few scarps primarily from the DEM data with GIS tools. Accumulated vertical slip was grouped into different value, and intervals between adjacent groups seems to be similar and likely same as minimal vertical offset ~ 0.7m (see Fig. 2).

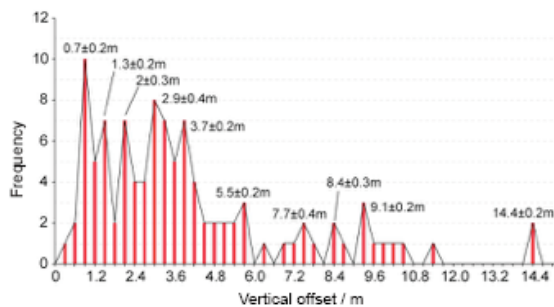


Fig. 2. Statistic result of scarp measurement

A paleoseismic trench across  $0.6 \pm 0.2$  m scarp show one earthquake ruptured around 700 B.P. with event indicator of paleosol and charcoal sample(see Fig. 3). We interpreted 4 events from another trench cutting ~ $2.6 \pm 0.3$  m high scarp based on indicators of colluvial deposit and paleosol.

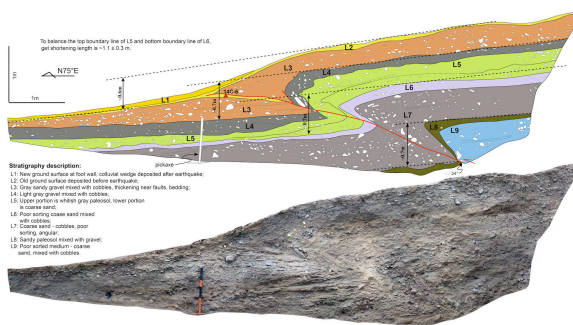


Fig. 3. Trench wall log

The primary results from accumulated slip distribution and paleoseismology show that NDNT has feature of characteristic earthquake reoccurrence mode, repetition

at same segment with similar earthquake magnitude > 7. Future work will focus on age determination of paleoearthquakes to get the interval age of reoccurrence and improve the slip mode.

**Acknowledgements:** This study was supported jointly by the Fundamental Research Funds of Lanzhou Institute of Seismology, China Earthquake Administration (grant 2012IESLZ08) and China National Special Fund for Earthquake Scientific Research in Public Interest (grant 201308012).

## References

- Bemis, Sean P., S. P., Micklethwaite, S., Turner D. et al. 2014. Ground-based and UAV-based photogrammetry: A multi-scale, high-resolution mapping tool for structural geology and paleoseismology. *Journal of Structural Geology*, 69: 163-178.
- Chen, T., Akciz, S. O., Hudnut, K. W. et al. 2015. Fault-Slip Distribution of the 1999 Mw 7.1 Hector Mine Earthquake, California, Estimated from Postearthquake Airborne LiDAR Data. *Bulletin of the Seismological Society of America*, 105(2A): 776-790.
- Grant-Ludwig, L. B., S. O. Akciz, G. R. Noriega et al. 2010. Variable slip on the San Andreas Fault in the Carrizo Plain, California, *Science* 327, 1117-1119, doi:10.1126/science.1182837.
- Haddon, E.K., Amos, C.B., Zielke, O., et al. 2016. Surface Slip during Large Owens Valley Earthquakes. *Geochem. Geophys. Geosyst.* doi:10.1002/2015GC006033.
- Hudnut, K. W., Borsa, A., Glennie, C., et al. 2002. High-resolution topography along surface rupture of the 16 October 1999 Hector Mine, California, earthquake (Mw 7.1) from airborne laser swath mapping. *Bulletin of the Seismological Society of America*, 92(4): 1570-1576.
- Klinger, Y., M. Etchebes, P. Tapponnier, et al. 2011. Characteristic slip for five great earthquakes along the Fuyun fault in China. *Nature Geoscience*, 4(6): 389-392.
- Meyer B., Tapponnier P., Bourjot L. et al., 1998. Crustal thickening in Gansu-Qinghai, lithospheric mantle subduction, and oblique, strike-slip controlled growth of the Tibet Plateau. *Geophys J. Int.*, 135: 1—47.
- Oskin, Michael E., Kimberly Le, and Michael D. Strane. 2007. Quantifying fault-zone activity in arid environments with high-resolution topography. *Geophysical Research Letters*, 34(23), DOI: 10.1029/2007GL031295.
- Ren Z., Zhang Z. Q., Chen T., et al. 2015. Clustering of offsets on the Haiyuan fault and their relationship to paleoearthquakes. *Geological Society of America Bulletin*, 128(1-2), 3-18.
- Salisbury, J. B., Haddad, D. E., Rockwell, T., et al., 2015. Validation of meter-scale surface faulting offset measurements from high-resolution topographic data. *Geosphere*, 11(6): 1-18, doi:10.1130/GES01197.1.
- Shao Yanxiu, Yuan Daoyang, Lei Zhongsheng et al. 2011. The features of earthquake surface rupture zone on Northern Margin Fault of Danghe Nanshan. *Technology of Earthquake Disaster Prevention*, 6(4):427-435.
- Van der Woerd J., Xiwei X., Haibing Let al., 2001. Rapid active thrusting along the north- western range front of the Tanghe Nan Shan (western Gansu, China). *J. Geophys. Res.*, 106: 30, 475-30, 504.